



HAL
open science

Temporal evolution of Amazonian laterites reconstructed from mineralogy, geochemistry and geochronology

Beatrix Heller

► **To cite this version:**

Beatrix Heller. Temporal evolution of Amazonian laterites reconstructed from mineralogy, geochemistry and geochronology. Geochemistry. Université Paris-Saclay, 2022. English. NNT : 2022UP-ASJ014 . tel-03917534

HAL Id: tel-03917534

<https://theses.hal.science/tel-03917534>

Submitted on 2 Jan 2023

HAL is a multi-disciplinary open access archive for the deposit and dissemination of scientific research documents, whether they are published or not. The documents may come from teaching and research institutions in France or abroad, or from public or private research centers.

L'archive ouverte pluridisciplinaire **HAL**, est destinée au dépôt et à la diffusion de documents scientifiques de niveau recherche, publiés ou non, émanant des établissements d'enseignement et de recherche français ou étrangers, des laboratoires publics ou privés.

Temporal evolution of Amazonian laterites reconstructed from mineralogy, geochemistry and geochronology

*Évolution temporelle des latérites d'Amazonie reconstituée par
minéralogie, géochimie et géochronologie*

Thèse de doctorat de l'université Paris-Saclay

École doctorale n° 579, Sciences mécaniques et énergétiques, matériaux et
géosciences (SMEMAG)

Spécialité de doctorat : Terre solide : géodynamique des enveloppes supérieures,
paléobiosphère

Graduate School : Géosciences, climat, environnement et planètes

Référent : Faculté des sciences d'Orsay

Thèse préparée dans les unités de recherche **GEOPS** (Université Paris Saclay, CNRS) et
IMPMC (Sorbonne Université, CNRS, IRD, MNHN), sous la direction de
Cécile GAUTHERON, Professeure, et la co-direction de
Thierry ALLARD, Directeur de Recherche

Thèse soutenue à Paris-Saclay, le 28 juin 2022, par

Beatrix HELLER

Composition du Jury

Cécile QUANTIN Professeure, Université Paris-Saclay	Présidente
Anicet BEAUVAIS Directeur de recherche, IRD	Rapporteur & Examineur
David SHUSTER Professeur, University of California	Rapporteur & Examineur
Jérôme GAILLARDET Professeur, Université de Paris	Examineur
Georgina KING Professeure assistante, Université de Lausanne	Examinatrice
Cécile GAUTHERON Professeure, Université Paris-Saclay	Directrice de thèse

Title : Temporal evolution of Amazonian laterites reconstructed from mineralogy, geochemistry and geochronology

Keywords : Geochronology, Laterite, Weathering, Iron Oxide, Kaolinite

Abstract : Laterites are deep stratified weathering profiles which form under tropical and subtropical climatic conditions commonly found at the Earth's continental surface. Although they are very widespread in (sub)tropical areas, many aspects of their genesis and evolution are still not well constrained. Previous studies have shown that they can be very old (Millions of years) and are therefore records of past climate, but little is known about their temporal evolution, notably in relation with climatic and geodynamic changes, due to the small quantity of age data and the difficulty to date this material.

The Guiana shield is of particular interest to study laterites as this area remained tectonically stable and in tropical latitudes since the Cretaceous, favoring the formation of very deep lateritic profiles. In this work, two areas were studied: the northeastern rim of the Guiana shield in French Guiana and the eastern rim of the shield in the Brazilian state of Amapá. In both areas, deep (>70 m) lateritic profiles developed on top of Paleoproterozoic basement rocks. The lateritic profiles were studied using mineralogical, geochemical and geochronological tools, notably (U-Th)/He dating and micro X-ray diffraction of supergene hematite and goethite and electron paramagnetic resonance spectroscopy (EPR) of kaolinite. In order to better understand the signification of hematite and goethite (U-Th)/He ages, a theoretical study on the He retention in these supergene minerals has been performed. The results allow to propose correction factors for the (U-Th)/He ages and to better apprehend the signification of these ages.

Results from the lateritic-bauxitic duricrust of Kaw mountain in French Guiana indicate that weathering started at least during the Oligocene and was favored during several episodes in the Middle Miocene and the Late Neogene. Coupling of geochronological, geochemical and mineralogical data allows to

distinguish between a period of ferruginous lateritic conditions and another one with bauxitic conditions indicating an important change in the weathering conditions. Comparison with other lateritic covers in northeastern French Guiana reveals that these periods also effected other sites in the area and that climate was the main driving force for the Late Neogene bauxitization.

In contrast, results from northern Brazil record weathering since the Late Cretaceous and indicate very discrete intervals of weathering at ca. 30 and 12 Ma. The Late Neogene bauxitization event recorded in French Guiana is absent in the studied samples and the therefore very well constrained (U-Th)/He ages, coupled to high resolution micro-XRD analyses, allow to establish a detailed precipitation chronology of the supergene iron (oxyhydr)oxide phases.

The results of the EPR analyses of purified kaolinites from two studied profiles indicate that kaolinite in the saprolites of the profiles formed probably several Myr to tens of Myrs ago. At Kaw, in French Guiana, EPR analyses of structural Fe impurities reveal that the kaolinites of the saprolite formed under near identical conditions over 70 m depth. In Amapá, the presence of rather young kaolinite at the top of the studied profile indicates relatively recent rejuvenation of kaolinite at the top but older kaolinite was preserved inside the duricrust as well as in the lower, saprolitic, part of the profile.

Finally, this thesis shows that a detailed combination of geochronological results coupled to mineralogical and geochemical analyses improves our understanding of tropical weathering processes and laterite formation by placing mineralogical and geochemical processes into a temporal framework.

Titre : Évolution temporelle des latérites d'Amazonie reconstituée par minéralogie, géochimie et géochronologie

Mots clés : Géochronologie, Latérites, Altération, Oxyde de Fer, Kaolinite

Résumé : Les latérites sont d'épais profils d'altération supergène se formant dans des conditions climatiques tropicales et subtropicales communément rencontrées à la surface de la Terre. Bien que très répandues dans les zones (sub)tropicales, beaucoup d'aspects de leur genèse et évolution ne sont pas bien contraints. Des études précédentes ont montré que les latérites peuvent être très anciennes, à l'échelle des millions d'années, et qu'elles constituent donc des archives des climats passés. Néanmoins, la dynamique de l'altération au cours du temps, associée aux forçages climatiques et géodynamiques est encore une question peu explorée, compte-tenu de la difficulté à dater les latérites et les processus de latéritisation.

Le bouclier guyanais présente un intérêt particulier pour étudier les latérites car cette région a été tectoniquement stable et à des latitudes tropicales depuis le Crétacé. Des profils latéritiques profonds (>70 m) du bord nord-est (Guyane Française) et est (état brésilien de l'Amapá) du bouclier guyanais ont été étudiés en combinant des approches minéralogiques, géochimiques et géochronologiques, incluant notamment la datation (U-Th)/He sur hématite et goéthite, et la spectroscopie de résonance paramagnétique électronique (RPE) sur kaolinite. Afin de mieux comprendre la signification des âges (U-Th)/He sur goéthite et hématite, un travail théorique sur la rétention de l'He dans ces minéraux supergènes a été effectué. Les résultats permettent ainsi de proposer des facteurs de corrections des âges (U-Th)/He.

En ce qui concerne les oxydes et hydroxydes de fer, les analyses de la cuirasse ferrugineuse-bauxitique de la montagne de Kaw en Guyane Française indiquent que l'altération a débuté au moins à l'Oligocène et qu'elle a été intense au cours de plusieurs épisodes du Miocène moyen et du Néogène supérieur. Le couplage des données géochronologiques, géochimiques et minéralogiques permet de distinguer des périodes de latéritisation ferrugineuse

et de latéritisation bauxitique, impliquant un changement important des conditions d'altération. La comparaison avec d'autres couvertures latéritiques du nord-est du bouclier guyanais montre que ces périodes ont aussi affecté d'autres sites dans la région et que le climat était le facteur le plus important pour la bauxitisation du Néogène tardif. Par contre, les cuirasses ferrugineuses latéritiques du nord du Brésil enregistrent une altération tropicale depuis la fin du Crétacé et indiquent deux épisodes discrets à environ 30 et 12 Ma. L'évènement de bauxitisation du Néogène tardif détecté en Guyane Française est absent dans ces échantillons et les âges (U-Th)/He, qui sont très reproductibles, permettent d'établir une chronologie de précipitation des phases d'oxydes et d'oxyhydroxydes de fer supergènes et de discuter de la durée des processus d'altération.

Les analyses par RPE ont été effectuées sur les kaolinites purifiées des deux profils étudiés. Une datation préliminaire suggère que les kaolinites des saprolites se sont formées il y a plusieurs millions ou dizaines de millions d'années. À Kaw, l'analyse par RPE du fer en impureté montre que les kaolinites de la saprolite se sont formées dans des conditions identiques sur presque 70 mètres de profondeur. En Amapá, on observe un rajeunissement relativement récent des kaolinites au sommet du profil, tandis que des kaolinites plus vieilles ont été préservées dans la cuirasse et dans la partie plus basse, saprolitique, du profil. L'analyse du fer structural montre des conditions de formation de kaolinite contrastées dans ce profil.

Ainsi, cette thèse montre qu'une approche géochronologique couplée aux analyses minéralogiques et géochimiques améliorent notre compréhension des processus d'altération tropicale, de formation et d'évolution des latérites, en les caractérisant et en les plaçant dans un cadre temporel.

Acknowledgements

This work would not have been possible without the support of several people who receive my special thanks. First of all I would like to thank my supervisors Cécile Gautheron and Thierry Allard. Thank you very much for having trusted in me and for having given me the opportunity to do this thesis. The last (nearly) four years were a great experience in many ways for me and you contributed considerably to that. Thank you for always being available for discussions, questions and support during experiments. Apart from teaching me a lot about science you clearly contributed to my French skills by explaining me everything with a lot of patience. Working with the two of you was a great experience and I hope that we will continue to do so in the future.

At this point I would also like to thank the French National Research Agency (ANR, RECA project) as well as the Source to Sink project (TOTAL-BRGM) for financing this beautiful project. I wish to thank Jean-Yves Roig and Renaud Couëffé from the BRGM without whom this project could not have been conducted as it was. Thank you for all the investment in the field work and also for the nice time spent together in the field. Equally, I would like to thank Guilherme Taitson Bueno, Raphael Themístocles Gomes Sobrinho, Caroline Sanchez, Gaël Monvoisin and Claire Ansart for the support in the field and the good conversations. Arnaud Heuret is thanked for sampling the duricrust samples from Connétable Island.

Anicet Beauvais and David Shuster are cordially thanked for their examiners' reports and constructive comments which helped to improve this manuscript and that will be very useful for the upcoming articles. Thank you also for the interesting discussion the day of the PhD defense. Furthermore I would like to thank Jérôme Gaillardet, Georgina King and Cécile Quantin for having participated to the jury and for the lively discussion which followed the presentation.

I am very grateful to Rosella Pinna-Jamme for her great analytical support. Discussing with you always made my days a little bit brighter. Guillaume Morin is cordially thanked for the private lessons on Rietveld refinement and for making the EPR-fitting possible. I appreciate the support of Benoît Baptiste, Ludovic Delbes and Imène Esteve for (micro-)XRD and SEM analyses. Frédéric Haurine and Pierre Burckel are thanked for the ICP-MS analyses and Christophe Falguères is thanked for the Gamma spectra. The team of the ARAMIS linear accelerator is

warmly thanked for the He⁺ irradiations. I am grateful to Silvana Bressan Riffel for her contribution to the sample preparation and analyses.

In the framework of the RECA project I had the opportunity to meet many interesting people. Thank you for the good discussion on laterites! Equally I would like to thank all my colleagues from GEOPS and the MINENV group at IMPMC who made me feel at home here in France! Special thanks are hereby given to Claire Ansart, Caroline Sanchez and Maximilien Mathian for the good company, the discussions on iron oxides, kaolinites, weathering in general and all the other topics on which we could exchange. Warmly thanked are also my PhD colleagues at Jussieu, Camille Baya, Pierre Lefevre, Quentin Boellert, Öykü Ataytür, Maëva Philippe and Karina Marques, for making the lunch breaks much funnier. I also would like to thank Silvia Niccolai for her mentoring support and the nice discussions while walking through Montrouge.

I would probably not be at the end of a thesis in geosciences without several people I had the possibility to cross. I am very grateful to István Dunkl who initiated me to (U-Th)/He dating and who still supports my work with some analyses here and there. I would like to thank Solveig Pospiech for always sharing her passion on geosciences with me. Thank you furthermore for being my long-term support regarding R and statistics. Mathias Hueck is thanked for the fruitful collaborations and his good friendship.

I would like to thank my friends in Paris who made me feel at ease in this country. A special thank goes to my flatmates and Thomas who supported me a lot, especially during these last weeks of writing.

In the end I would like to thank my family for always having supported my choices and reaching out for me for me wherever I am.

Content

ACKNOWLEDGEMENTS	4
CONTENT	6
I INTRODUCTION	9
REFERENCES	13
II METHODS	20
II.1 SAMPLING	20
II.2 OVERVIEW ON THE METHODS USED IN THIS THESIS	20
II.3 ANALYSES ON BULK SAMPLES	21
II.4 ANALYSES ON SEPARATED SUBSAMPLES.....	22
II.5 PRINCIPLE OF ELECTRON PARAMAGNETIC RESONANCE SPECTROSCOPY	31
II.6 CLAY MINERAL SEPARATION	35
REFERENCES	36
III REVEALING THE RADIATION DAMAGE AND AL-CONTENT IMPACTS ON HE DIFFUSION IN GOETHITE	41
ABSTRACT	41
III.1 INTRODUCTION	42
III.2 REVIEW OF ACTIVATION ENERGY EXPERIMENTAL LITERATURE DATA	44
III.3 COMPUTATIONAL DETAILS.....	47
III.4 RESULTS	52
III.5 DISCUSSION	59
III.6 CONCLUSION	68
ACKNOWLEDGMENTS	69
REFERENCES	69
IV READING THE CLIMATE SIGNALS HIDDEN IN BAUXITE	75
ABSTRACT	75
IV.1 INTRODUCTION	76
IV.2 GEOLOGICAL, GEOMORPHOLOGICAL AND CLIMATIC CONTEXT	78
IV.3 KAW MOUNTAIN GEOLOGY AND SAMPLING.....	82
IV.4 METHODS.....	86
IV.5 RESULTS	91
IV.6 DISCUSSION	107
IV.7 CONCLUSIONS	123
ACKNOWLEDGEMENTS.....	124
REFERENCES	124

V	PRECIPITATION CHRONOLOGY OF HEMATITE AND GOETHITE IN LATERITIC DURICRUSTS FROM EQUATORIAL BRAZIL.....	135
	ABSTRACT	135
	V.1 INTRODUCTION	136
	V.2 GEOLOGICAL, GEOMORPHOLOGICAL AND CLIMATIC CONTEXT	137
	V.3 TUCANO MINE GEOLOGY AND SAMPLING	144
	V.4 METHODS.....	146
	V.5 RESULTS	148
	V.6 DISCUSSION	160
	V.7 CONCLUSIONS	179
	ACKNOWLEDGEMENTS.....	180
	REFERENCES	180
VI	FRENCH GUIANA LATERITE AND BAUXITE EVOLUTION THROUGH TIME AND SPACE	189
	ABSTRACT	189
	VI.1 INTRODUCTION	189
	VI.2 GEOLOGY, GEOMORPHOLOGY AND CLIMATE OF THE CAYENNE AREA	192
	VI.3 SAMPLES	194
	VI.4 METHODS.....	200
	VI.5 RESULTS	201
	VI.6 DISCUSSION	215
	VI.7 CONCLUSIONS	235
	REFERENCES	235
VII	EPR SPECTROSCOPIC STUDY OF KAOLINITES FROM TWO LATERITIC PROFILES OF THE NORTHEASTERN AND EASTERN GUIANA SHIELD (KAW MOUNTAIN, FRENCH GUIANA AND TUCANO MINE AMAPÁ, BRAZIL).....	242
	ABSTRACT	242
	VII.1 INTRODUCTION	243
	VII.2 BACKGROUND	245
	VII.3 SAMPLES	249
	VII.4 METHODS.....	255
	VII.5 RESULTS AND DISCUSSION.....	260
	VII.6 CONCLUSIONS	303
	REFERENCES	304
VIII	CONCLUSIONS AND PERSPECTIVES	309
	VIII.1 CONCLUSIONS	309
	VIII.2 PERSPECTIVES.....	312
	REFERENCES	315

A. SUPPLEMENTARY MATERIAL FOR CHAPTER III	317
B. SUPPLEMENTARY MATERIAL FOR CHAPTER IV.....	322
FIGURES	322
TABLES	345
C. SUPPLEMENTARY MATERIAL FOR CHAPTER V.....	350
SUPPLEMENTARY OBSERVATIONS	354
D. SUPPLEMENTARY MATERIAL FOR CHAPTER VI.....	356
E. SUPPLEMENTARY MATERIAL FOR CHAPTER VII.....	358
RÉSUMÉ ÉTENDU EN LANGUE FRANÇAISE.....	371
INTRODUCTION	371
RESUME DU CHAPITRE III : REVELATION DE L'IMPACT DES DOMMAGES RADIOGENIQUES ET DE LA TENEUR EN AL SUR LA DIFFUSION DE L' ¹ He DANS LA GOETHITE	375
RESUME DU CHAPITRE IV : LIRE LES SIGNAUX CLIMATIQUES CACHES DANS LA BAUXITE	376
RESUME DU CHAPITRE V : CHRONOLOGIE DE LA PRECIPITATION DE L'HEMATITE ET DE LA GOETHITE DANS DES CUIRASSES LATERITIQUES DU BRESIL EQUATORIAL.....	378
RESUME DU CHAPITRE VI : ÉVOLUTION DES LATERITES ET BAUXITES DE GUYANE FRANÇAISE A TRAVERS LE TEMPS ET L'ESPACE	379
RESUME DU CHAPITRE VII : ÉTUDE SPECTROSCOPIQUE RPE DES KAOLINITES DE DEUX PROFILS LATERITIQUES DU BOUCLIER NORD-EST ET EST GUYANAIS (MONTAGNE DE KAW, GUYANE FRANÇAISE ET MINE DE TUCANO, AMAPA, BRESIL)	380
CONCLUSIONS.....	382
RÉFÉRENCES	383
CURRICULUM VITAE	390

I Introduction

Laterites are deep weathering profiles which develop under tropical and subtropical climatic conditions commonly found at the Earth's continental surface. They form at the interface of the geosphere, the hydrosphere, the biosphere and the atmosphere and their characteristics depend on the properties of these four spheres and a fifth, which is time. Laterites (here referred to as the entire weathering profile, including saprolite, ferruginous duricrust, and soil) represent the alteration of a rock to (sub)tropical Earth surface conditions and are predominantly composed of secondary minerals, named supergene minerals, that are formed during the weathering, such as clay minerals, iron (oxyhydr)oxides and aluminum (oxy)hydroxides, which are very stable in such climatic context (Tardy, 1997). Transformation of primary silicate minerals into secondary minerals includes liberation and leaching of alkali and earth alkali elements (Na, K, Ca, Mg) and transformation of CO₂ into dissolved carbon acid which is why the weathering process is an important agent in the global geochemical and atmospheric budget (Berner et al., 1983; Nahon, 1991; Lasaga et al., 1994). Intense tropical weathering leads to the residual accumulation of immobile elements such as Fe and Al but also trace elements like Ni, Au, Nb, Sc or Rare Earth Elements (REE) for which laterites are economically important resources (Patterson et al., 1994; Butt and Cluzel, 2013; Butt, 2016; Giovannini et al., 2017; Chassé et al., 2019). The geochemical and mineralogical composition of a laterite is strongly influenced by the climatic condition under which it forms, whereas the composition of the parental material plays a subordinate role (Bardossy and Aleva, 1990; Schellmann, 1994; Tardy, 1997). Seasonally contrasted tropical monsoonal climate favors the formation of ferruginous, "classical", laterites dominated by kaolinite, hematite, goethite (and quartz, depending on the protolith) (Tardy and Roquin, 1998). Very humid tropical climate linked to very well-drained conditions can lead to the development of lateritic bauxites, Al-enriched laterites in which kaolinite is no more stable and that are characterized by desilication and Al accumulation in form of Al (oxy)hydroxides (Valeton, 1972; Bardossy and Aleva, 1990; Carvalho et al., 1997; Valeton, 1999). Due to their long-term stability throughout the intertropical zone, which covers about 44% of the Earth's continental surface, laterites are archives of past climates (Tardy and Roquin, 1998). It has been proposed that laterites formed episodically throughout the Earth's history in periods with very favorable climate, but little is known about the duration, frequency and spatial extent of such weathering events (Prasad, 1983; Vasconcelos et al., 1994; Tardy and Roquin, 1998; Retallack, 2010; Vasconcelos et al.,

2015). Several studies have shown that laterites can be very old, especially in areas of tectonic quiescence, but there is still little information regarding their temporal evolution and their response to climatic and geodynamic changes (Vasconcelos et al., 1994; Beauvais et al., 2008; Monteiro et al., 2014; Allard et al., 2018; Mathian et al., 2019). As different climatic signals are potentially superposed in old and constantly exposed laterites, disentangling of the paleoclimatic information preserved in these archives is a complex task (Beauvais, 1999; Vasconcelos, 1999; Girard et al., 2000; Balan et al., 2005; Monteiro et al., 2014; Mathian et al., 2019).

While the processes controlling the geochemistry of major elements are known (see e.g., the weathering of primary silicates; Nahon, 1991), one major challenge in the study of laterites is to solve the lack of time constraints. It is already known that several generations of a same secondary mineral can coexist in a profile, but since they are mainly composed of clay minerals, iron (oxyhydr)oxides and aluminum (oxy)hydroxides, most conventional geochronological methods cannot be applied to laterites. K/Ar and $^{39}\text{Ar}/^{40}\text{Ar}$ dating has been applied with success to supergene Mn oxides from lateritic duricrusts (Vasconcelos et al., 1994; Ruffet et al., 1996; Beauvais et al., 2008; Beauvais and Chardon, 2013; Beauvais et al., 2016; Bonnet et al., 2016; Vasconcelos and Carmo, 2018) and provided a first temporal frame for discrete weathering periods in Brazil, Africa and India. However, K/Ar and $^{39}\text{Ar}/^{40}\text{Ar}$ dating requires the presence of K-bearing phases such as Mn oxides which are relatively scarce in laterites compared to iron oxides *sensu lato*, aluminum (oxy)hydroxides and kaolinite. Targeting the principal components of the laterite yields the potential to get a more complete and deepened understanding of their formation and evolution. Paleomagnetism has been successfully applied to the ferruginous parts of some lateritic profiles on different continents but this method becomes very imprecise if the latitudinal shift was small in the time interval of interest, as, e.g., for the Amazon craton during the Cenozoic period (Schmidt and Embleton, 1976; Schmidt et al., 1983; Kumar, 1986; Théveniaut and Freyssinet, 1999; Théveniaut and Freyssinet, 2002).

Hematite and goethite are the main constituents of the iron duricrust present in most lateritic profiles (Bardossy and Aleva, 1990; Tardy, 1997). These minerals can be dated by the (U-Th)/He method as they quantitatively retain He in their crystal structures (Lippolt et al., 1993; Shuster et al., 2005; Heim et al., 2006; Vasconcelos et al., 2013; Reiners et al., 2014; Balout et al., 2017; Deng et al., 2017; Hofmann et al., 2017; Farley, 2018). This approach has

been used successfully by a growing number of studies over the past three decades to constrain the ages of supergene iron (oxyhydr)oxides, but some essential aspects of the method, such as the diffusion parameters of He in goethite, remain poorly understood (Lippolt et al., 1998; Pidgeon et al., 2004; Monteiro et al., 2014; Riffel et al., 2016; Allard et al., 2018; Monteiro et al., 2018; Wells et al., 2019; dos Santos Albuquerque et al., 2020).

Kaolinite is present throughout the (near) totality of most lateritic profiles, including duricrusts in some cases, and is the major constituent of the saprolite which generally composes the thickest part of the lateritic profile. Natural kaolinites contain point defects created by ambient radiation which are stable over geological timescales and can be detected using electron paramagnetic resonance spectroscopy (EPR) (Clozel et al., 1994; Allard et al., 2012). Balan et al. (2005) were the first to use these defects in order to date kaolinite formation with a complete methodology, and since then this approach has been applied several of times to date kaolinites from laterites and lateritic soils (Allard et al., 2018; Mathian et al., 2019; Allard et al., 2020; Mathian et al., 2020). In the Amazon Basin lowlands, the EPR dating exercise revealed kaolinites of mid-Miocene to Quaternary ages that in several cases resulted from rejuvenation of previous, i.e. saprolitic, kaolinites. Therefore, in addition to crystal chemistry and Si isotopic results (see e.g. Balan et al., 2007; Guinoiseau et al., 2021), this confirmed the multiphase nature of weathering profiles. In such a context, one aim is to determine the record remaining in the profiles through the secondary minerals and not to determine necessarily when weathering processes began.

The Guiana shield, i.e. the northern part of the Amazon craton, is of particular interest to study laterites and bauxites as it has been tectonically stable and in tropical latitudes since the Cretaceous, favoring the development of deep lateritic profiles. Geomorphological models propose that its surface was shaped by a series of peneplanation events which alternated with phases dominated by weathering, leading to a staircase landscape (Choubert, 1957; King, 1962; McConnell, 1968; Blancaneaux, 1981; Aleva, 1984). Geochronological data from supergene Mn and Fe oxides from the Brazilian shield, the southern part of the Amazon shield, indicate episodic weathering throughout the Cenozoic (Vasconcelos et al., 1994; Ruffet et al., 1996; Monteiro et al., 2018). For the Guiana shield only few and very imprecise weathering age constraints exist, indicating a record of weathering since the Early to Mid-Cenozoic (Hammen and Wymstra, 1964; Wymstra, 1971; Théveniaut and Freyssinet, 1999; Théveniaut and Freyssinet, 2002). Owing to the scarcity of carbonates and lake sediments, there is a general

scarcity of paleoclimatic constraints for Amazonia, complicating the understanding of the evolution of this region which hosts the largest biodiversity of the world (e.g. Hoorn et al., 2010). Studying the laterites and bauxites of the Guiana shield yields thus the potential to deliver important information on the geological and paleoclimatic history of this region and to learn more about the formation and evolution of old lateritic and bauxitic profiles.

The main objectives of this thesis are

- i) to improve the understanding of laterite formation and evolution by placing mineralogical and geochemical processes into a temporal framework,
- ii) to find a method to disentangle the climatic signals hidden in laterites and lateritic duricrusts and
- iii) to allow new insights into the climatic and geomorphologic evolution of the Guiana shield.

In order to contribute to these objectives, two study areas were selected: a) the northeastern rim of the Guiana shield in French Guiana where several lateritic-bauxitic profiles developed supposedly since the Eocene and Miocene (Choubert, 1957; Théveniaut and Freyssinet, 2002) and where the current climate is extremely humid with more than 4000 mm precipitation / year (Groussin, 2001) and b) the eastern rim of the Guiana shield in the Brazilian state of Amapá, where ferruginous lateritic profiles developed possibly since the Late Cretaceous (Bardossy and Aleva, 1990) and where the current climate is more seasonally contrasted with approximately 2300 mm precipitation / year. The two profiles studied in more detail, Kaw mountain in French Guiana and the Tucano mine in Brazil, share important similarities such as their parental rocks (Paleoproterozoic schists), their elevation (ca. 300 m a.s.l.) and the depth of their profiles (>70 m), but differ in terms of their geomorphological setting, their proximity to the sea and the current amount of precipitation.

This thesis contains five major chapters (III-VII) and three smaller ones (I, II and VIII). Chapter II resumes the analytical mineralogical, geochemical and geochronological ((U-Th)/He and EPR dating) approaches used in this study and explains some subtleties in the context of this work. Chapter III presents an interdisciplinary theoretical study which investigates the controls of He diffusion in goethite by comparing published and re-evaluated experimental ³He and ⁴He diffusion data with theoretical ab-initio calculations. The results of this study allow us to define the controlling parameters of He diffusion in goethite and to propose adapted correction factors for goethite (U-Th)/He ages. Chapter IV is a detailed study of the lateritic-

bauxitic duricrust of Kaw mountain in French Guiana. I show how weathering conditions and climatic signals can be extracted from a large and complex dataset by coupling geochronological, mineralogical and geochemical data.

In Chapter V this approach is applied to ferruginous duricrusts from the second target area which is the Tucano mine in Amapá, Brazil. The results show very contrasting features when compared to those from Kaw mountain in French Guiana and permit a deepened understanding of small-scale processes happening during discrete weathering events.

In Chapter VI I present a study of lateritic duricrusts of three other sites in northeastern French Guiana giving insight into the evolution of these sites and allowing important conclusions on the regional climatic and geomorphologic evolution.

Two deep (> 70m) lateritic profiles from Kaw mountain and the Tucano mine are explored in Chapter VII. I examine EPR of purified kaolinites from different levels of these profiles together with bulk geochemistry. The results yield information on the formation conditions of kaolinite in these profiles and reveal that kaolinites precipitated under near identical conditions over >70m at Kaw but formed under more variable conditions in the Tucano mine. Preliminary kaolinite ages give constraints on the vertical age distributions in the profiles and show how some profile portions were affected by recent rejuvenation whereas others remained intact.

Chapter VIII resumes the final outcomes of this thesis and presents perspectives for future studies.

References

- Aleva G. J. J. (1984) Lateritization, bauxitization and cyclic landscape development in the Guiana Shield. In *Bauxite* (ed. L. Jacob Jr). A.I.M.E, New York, USA. pp. 297–318.
- Allard T., Balan E., Calas G., Fourdrin C., Morichon E. and Sorieul S. (2012) Radiation-induced defects in clay minerals: A review. *Nucl. Instruments Methods Phys. Res. Sect. B Beam Interact. with Mater. Atoms* **277**, 112–120.
- Allard T., Gautheron C., Bressan Riffel S., Balan E., Soares B. F., Pinna-Jamme R., Derycke A., Morin G., Bueno G. T. and do Nascimento N. (2018) Combined dating of goethites and kaolinites from ferruginous duricrusts. Deciphering the Late Neogene erosion history of Central Amazonia. *Chem. Geol.* **479**, 136–150.

- Allard T., Pereira L., Mathian M., Balan E., Taitson Bueno G., Falguères C. and do Nascimento N. R. (2020) Dating kaolinite from the Neogene Içá Formation and overlying laterites, central Amazonia, Brazil: Constraints for a stratigraphic correlation. *Palaeogeogr. Palaeoclimatol. Palaeoecol.* **554**.
- Balan E., Allard T., Fritsch E., Sélo M., Falguères C., Chabaux F., Pierret M. C. and Calas G. (2005) Formation and evolution of lateritic profiles in the middle Amazon basin: Insights from radiation-induced defects in kaolinite. *Geochim. Cosmochim. Acta* **69**, 2193–2204.
- Balan E., Fritsch E., Allard T. and Calas G. (2007) Inheritance vs. neoformation of kaolinite during lateritic soil formation: A case study in the Middle Amazon basin. *Clays Clay Miner.* **55**, 253–259.
- Balout H., Roques J., Gautheron C., Tassan-Got L. and Mbongo-Djimbi D. (2017) Helium diffusion in pure hematite ($\alpha\text{-Fe}_2\text{O}_3$) for thermochronometric applications: A theoretical multi-scale study. *Comput. Theor. Chem.* **1099**, 21–28.
- Bardossy G. and Aleva G. J. J. (1990) *Lateritic Bauxites*. Developmen., Elsevier Science, Amsterdam, The Netherlands.
- Beauvais A. (1999) Geochemical balance of lateritization processes and climatic signatures in weathering profiles overlain by ferricretes in Central Africa. *Geochim. Cosmochim. Acta* **63**, 3939–3957.
- Beauvais A., Bonnet N. J., Chardon D., Arnaud N. and Jayananda M. (2016) Very long-term stability of passive margin escarpment constrained by $^{40}\text{Ar}/^{39}\text{Ar}$ dating of K-Mn oxides. *Geology* **44**, 299–302.
- Beauvais A. and Chardon D. (2013) Modes, tempo, and spatial variability of Cenozoic cratonic denudation: The West African example. *Geochemistry, Geophys. Geosystems* **14**, 1590–1608.
- Beauvais A., Ruffet G., Hénocque O. and Colin F. (2008) Chemical and physical erosion rhythms of the West African Cenozoic morphogenesis: The ^{39}Ar - ^{40}Ar dating of supergene K-Mn oxides. *J. Geophys. Res. Earth Surf.* **113**, 1–15.
- Berner R. A., Lasaga A. C. and Garrels R. M. (1983) Carbonate-silicate geochemical cycle and its effect on atmospheric carbon dioxide over the past 100 million years. *Am. J. Sci.* **283**, 641–683.
- Blancaneaux P. (1981) *Essai sur le milieu naturel de la Guyane Française.*, Paris.

- Bonnet N. J., Beauvais A., Arnaud N., Chardon D. and Jayananda M. (2016) Cenozoic lateritic weathering and erosion history of Peninsular India from $^{40}\text{Ar}/^{39}\text{Ar}$ dating of supergene K–Mn oxides. *Chem. Geol.* **446**, 33–53.
- Butt C. R. M. (2016) The development of regolith exploration geochemistry in the tropics and sub-tropics. *Ore Geol. Rev.* **73**, 380–393.
- Butt C. R. M. and Cluzel D. (2013) Nickel laterite ore deposits: Weathered serpentinites. *Elements* **9**, 123–128.
- Carvalho A., Boulangé B., Melfi A. J. and Lucas Y. (1997) *Brazilian Bauxites*. eds. A. Carvalho, B. Boulangé, A. J. Melfi, and Y. Lucas, USP, FAPESP, ORSTOM, São Paulo, Paris.
- Chassé M., Griffin W. L., O'Reilly S. Y. and Calas G. (2019) Australian laterites reveal mechanisms governing scandium dynamics in the critical zone. *Geochim. Cosmochim. Acta* **260**, 292–310.
- Choubert B. (1957) *Essai sur la morphologie de la Guyane.*, Paris.
- Clozel B., Allard T. and Muller J. P. (1994) Nature and stability of radiation-induced defects in natural kaolinities: New results and a reappraisal of published works. *Clays Clay Miner.* **42**, 657–666.
- Deng X. D., Li J. W. and Shuster D. L. (2017) Late Mio-Pliocene chemical weathering of the Yulong porphyry Cu deposit in the eastern Tibetan Plateau constrained by goethite (U–Th)/He dating: Implication for Asian summer monsoon. *Earth Planet. Sci. Lett.* **472**, 289–298.
- Farley K. A. (2018) Helium diffusion parameters of hematite from a single-diffusion-domain crystal. *Geochim. Cosmochim. Acta* **231**, 117–129.
- Giovannini A. L., Bastos Neto A. C., Porto C. G., Pereira V. P., Takehara L., Barbanson L. and Bastos P. H. S. (2017) Mineralogy and geochemistry of laterites from the Morro dos Seis Lagos Nb (Ti, REE) deposit (Amazonas, Brazil). *Ore Geol. Rev.* **88**, 461–480.
- Girard J. P., Freyssinet P. and Chazot G. (2000) Unraveling climatic changes from intraprofile variation in oxygen and hydrogen isotopic composition of goethite and kaolinite in laterites: An integrated study from Yaou, French Guiana. *Geochim. Cosmochim. Acta* **64**, 409–426.
- Groussin J. (2001) Le Climat Guyanais. In *Atlas illustré de la Guyane* (ed. J. Barret). Laboratoire de Cartographie de la Guyane; Institut d'Enseignement Supérieur de Guyane. pp. 46–49.

- Guinoiseau D., Fekiacova Z., Allard T., Druhan J. L., Balan E. and Bouchez J. (2021) Tropical Weathering History Recorded in the Silicon Isotopes of Lateritic Weathering Profiles. *Geophys. Res. Lett.* **48**.
- Hammen van der T. and Wymstra T. A. (1964) A Palynological study on the Tertiary and Upper Cretaceous of British Guiana. *Leidse Geol. Meded.* **30**, 183–241.
- Heim J. A., Vasconcelos P. M., Shuster D. L., Farley K. A. and Broadbent G. (2006) Dating paleochannel iron ore by (U-Th)/He analysis of supergene goethite, Hamersley province, Australia. *Geology* **34**, 173–176.
- Hofmann F., Reichenbacher B. and Farley K. A. (2017) Evidence for >5 Ma paleo-exposure of an Eocene–Miocene paleosol of the Bohnerz Formation, Switzerland. *Earth Planet. Sci. Lett.* **465**, 168–175.
- Hoorn C., Wesselingh F. P., ter Steege H., Bermudez M. A., Mora A., Sevink J., Sanmartín I., Sanchez-Meseguer A., Anderson C. L., Figueiredo J. P., Jaramillo C., Riff D., Negri F. R., Hooghiemstra H., Lundberg J., Stadler T., Särkinen T. and Antonelli A. (2010) Amazonia Through Time : Andean Uplift, Climate Change, Landscape Evolution and Biodiversity. *Science (80-.)*. **330**, 927–931.
- King L. C. (1962) *Morphology of the Earth.*, Oliver and Boyd Publ. House, London.
- Kumar A. (1986) Palaeolatitudes and the age of Indian laterites. *Palaeogeogr. Palaeoclimatol. Palaeoecol.* **53**, 231–237.
- Lasaga A. C., Soler J. M., Ganor J., Burch T. E. and Nagy K. L. (1994) Chemical weathering rate laws and global geochemical cycles. *Geochim. Cosmochim. Acta* **58**, 2361–2386.
- Lippolt H. J., Brander T. and Mankopf N. R. (1998) An attempt to determine formation ages of goethites and limonites by (U+Th)-⁴He dating. *Neues Jahrb. Mineral. Monatshefte*, 505–528.
- Lippolt H. J., Wernicke R. S. and Boschmann W. (1993) ⁴He diffusion in specular hematite. *Phys. Chem. Miner.* **20**, 415–418.
- Mathian M., Aufort J., Braun J. J., Riotte J., Selo M., Balan E., Fritsch E., Bhattacharya S. and Allard T. (2019) Unraveling weathering episodes in Tertiary regoliths by kaolinite dating (Western Ghats, India). *Gondwana Res.* **69**, 89–105.
- Mathian M., Bueno G. T., Balan E., Fritsch E., Do Nascimento N. R., Selo M. and Allard T. (2020) Kaolinite dating from Acrisol and Ferralsol: A new key to understanding the landscape evolution in NW Amazonia (Brazil). *Geoderma* **370**.

- McConnell R. B. (1968) Planation Surfaces in Guyana. *Geogr. J.* **134**, 506–520.
- Monteiro H. S., Vasconcelos P. M., Farley K. A., Spier C. A. and Mello C. L. (2014) (U-Th)/He geochronology of goethite and the origin and evolution of cangas. *Geochim. Cosmochim. Acta* **131**, 267–289.
- Monteiro H. S., Vasconcelos P. M. P., Farley K. A. and Lopes C. A. M. (2018) Age and evolution of diachronous erosion surfaces in the Amazon: Combining (U-Th)/He and cosmogenic ^3He records. *Geochim. Cosmochim. Acta* **229**, 162–183.
- Nahon D. (1991) *Introduction to the petrology of soils and chemical weathering.*, Wiley, New York, USA.
- Patterson S. H., Kurtz H. F., Olson J. C. and Neeley C. L. (1994) *World Bauxite Resources - Geology and Resources of Aluminum.* U.S. Geolo., U.S. Geological Survey, Washington.
- Pidgeon R. T., Brander T. and Lippolt H. J. (2004) Late Miocene (U+Th)-4He ages of ferruginous nodules from lateritic duricrust, Darling Range, Western Australia. *Aust. J. Earth Sci.* **51**, 901–909.
- Prasad G. (1983) A review of the early Tertiary bauxite event in South America, Africa and India. *J. African Earth Sci.* **1**, 305–313.
- Reiners P. W., Chan M. A. and Evenson N. S. (2014) (U-Th)/He geochronology and chemical compositions of diagenetic cement, concretions, and fracture-filling oxide minerals in mesozoic sandstones of the Colorado Plateau. *Bull. Geol. Soc. Am.* **126**, 1363–1383.
- Retallack G. J. (2010) Lateritization and bauxitization events. *Econ. Geol.* **105**, 655–667.
- Riffel S. B., Vasconcelos P. M., Carmo I. O. and Farley K. A. (2016) Goethite (U-Th)/He geochronology and precipitation mechanisms during weathering of basalts. *Chem. Geol.* **446**, 18–32.
- Ruffet G., Innocent C., Michard A., Féraud G., Beauvais A., Nahon D. and Hamelin B. (1996) A geochronological $^{40}\text{Ar}/^{39}\text{Ar}$ and $^{87}\text{Rb}/^{87}\text{Sr}$ study of K-Mn oxides from the weathering sequence of Azul, Brazil. *Geochim. Cosmochim. Acta* **60**, 2219–2232.
- dos Santos Albuquerque M. F., Horbe A. M. C. and Danišík M. (2020) Episodic weathering in Southwestern Amazonia based on (U-Th)/He dating of Fe and Mn lateritic duricrust. *Chem. Geol.* **553**, 119792.
- Schellmann W. (1994) Geochemical differentiation in laterite and bauxite formation. *Catena* **21**, 131–143.

- Schmidt P. W. and Embleton B. J. J. (1976) Palaeomagnetic Results From Sediments of the Perth Basin, Western Australia, and their bearing on the timing of regional lateritization. *Palaeogeogr. Palaeoclimatol. Palaeoecol.* **19**, 257–273.
- Schmidt P. W., Prasad V. and Ramam P. K. (1983) Magnetic ages of some Indian laterites. *Palaeogeogr. Palaeoclimatol. Palaeoecol.* **44**, 185–202.
- Shuster D. L., Vasconcelos P. M., Heim J. A. and Farley K. A. (2005) Weathering geochronology by (U-Th)/He dating of goethite. *Geochim. Cosmochim. Acta* **69**, 659–673.
- Tardy Y. (1997) *Petrology of Laterites and Tropical Soils.*, Balkema, Rotterdam, The Netherlands.
- Tardy Y. and Roquin C. (1998) *Dérive des continents paléoclimats et altérations tropicales.*, BRGM, Orléans, France.
- Théveniaut H. and Freyssinet P. (1999) Paleomagnetism applied to lateritic profiles to assess saprolite and duricrust formation processes: The example of Mont Baduel profile (French Guiana). *Palaeogeogr. Palaeoclimatol. Palaeoecol.* **148**, 209–231.
- Théveniaut H. and Freyssinet P. (2002) Timing of lateritization on the Guiana Shield synthesis of paleomagnetic results. *Palaeogeogr. Palaeoclimatol. Palaeoecol.* **178**, 91–117.
- Valeton I. (1972) *Bauxites. Developmen.*, Elsevier, Amsterdam, The Netherlands.
- Valeton I. (1999) Saprolite-bauxite facies of ferralitic duricrust on paleosurfaces of former Pangaea. In *Palaeoweathering, Palaeosurfaces and Related Continental Deposits* (eds. M. Thiry and R. Simon-Coignon). Blackwell Science Ltd. pp. 153–188.
- Vasconcelos P. M. (1999) K-Ar and $^{40}\text{Ar} / ^{39}\text{Ar}$ Geochronology of weathering processes. *Annu. Rev. Earth Planet. Sci.* **27**, 183–229.
- Vasconcelos P. M. and Carmo I. de O. (2018) Calibrating denudation chronology through $^{40}\text{Ar}/^{39}\text{Ar}$ weathering geochronology. *Earth-Science Rev.* **179**, 411–435.
- Vasconcelos P. M., Heim J. A., Farley K. A., Monteiro H. and Waltenberg K. (2013) $^{40}\text{Ar}/^{39}\text{Ar}$ and (U-Th)/He $^{-4}\text{He}/^3\text{He}$ geochronology of landscape evolution and channel iron deposit genesis at Lynn Peak, Western Australia. *Geochim. Cosmochim. Acta* **117**, 283–312.
- Vasconcelos P. M., Reich M. and Shuster D. L. (2015) The paleoclimatic signatures of supergene metal deposits. *Elements* **11**, 317–322.

Vasconcelos P. M., Renne P. R., Brimhall G. H. and Becker T. A. (1994) Direct dating of weathering phenomena by $^{40}\text{Ar}/^{39}\text{Ar}$ and K-Ar analysis of supergene K-Mn oxides. *Geochim. Cosmochim. Acta* **58**, 1635–1665.

Wells M. A., Danišík M., McInnes B. I. A. and Morris P. A. (2019) (U-Th)/He-dating of ferruginous duricrust: Insight into laterite formation at Boddington, WA. *Chem. Geol.* **522**, 148–161.

Wymstra T. A. (1971) The palynology of the Guiana coastal basin. University of Amsterdam.

II Methods

II.1 Sampling

The samples analyzed in this thesis were collected during four field campaigns which took place in 2017, 2018, 2019, and 2021. In a first field trip in 2017 to French Guiana, prior to this thesis, the CDR duricrust samples were collected by a team of the French Geological Survey (BRGM, Jean-Yves Roig, Renaud Couëffé, Geoffrey Aertgeerts) and Paris Saclay University (Cécile Gautheron). A second field to French Guiana and Suriname took place in autumn 2018 with participants of the French Geological Survey (Jean-Yves Roig), Paris Saclay University (Gaël Monvoisin, Claire Ansart, Beatrix Heller) and Sorbonne University (Thierry Allard). During this field trip the duricrust samples KAWF, BAD and VID were sampled in French Guiana. Additionally a 75 m drill core (KAW18 samples) was drilled on Kaw mountain. Other samples (thesis of Claire Ansart) were sampled in Suriname. In 2019 a field trip was undertaken to northern Brazil with participants of the BRGM (Jean-Yves Roig), Paris Saclay University (Caroline Sanchez, Beatrix Heller), the Federal University of Goiás (Guilherme Taitson Bueno), and the Federal Institute of Amapá (Themístocles Raphael Gomes Sobrinho). During this field trip the TUC samples were taken in the Tucano Mine in the Brazilian state of Amapá. In 2021, the last samples analyzed for this thesis were taken by Arnauld Heuret (Cayenne University) on the island “Petit Connetable” in French Guiana (GC21 samples). All samples are described in detail in the corresponding chapters.

II.2 Overview on the methods used in this thesis

The following sections aim to give a short overview on the methods used in this thesis and some subtleties in the context of this work. They focus mainly on the methods used in the “(U-Th)/He chapters” III-VI as the “EPR-chapter” VII has a very specific and complex methodology which is presented in further detail in Chapter VII. Figure II-1 summarizes the methods used in Chapters IV-VI for lateritic duricrust samples. Ferruginous duricrust bulk samples were sawed into 1-2 cm thick slices. One slice per samples was crushed, finely ground and used for bulk XRD and geochemical analyses. For saprolite samples (Chapter VII) ca. 30g of sample material were finely ground and used for bulk XRD, geochemical analyses, and clay mineral purification.

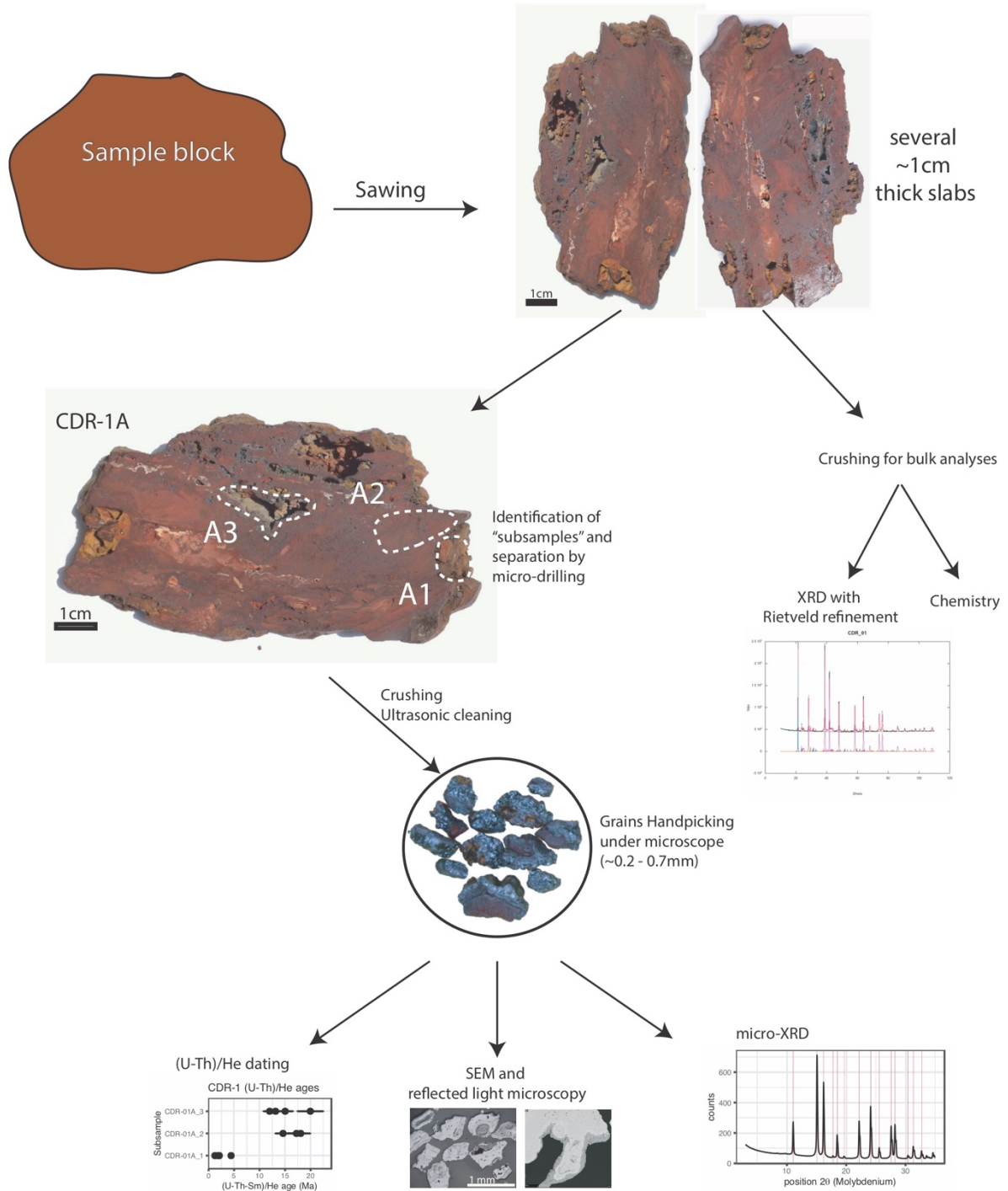


Figure II-1: Sample processing procedure followed in Chapters IV-VI. Duricrust blocks were sawed into slices, on piece was crushed and finely ground for mineralogical and geochemical analyses. Subsamples were separated by micro-drilling from the slices, crushed

II.3 Analyses on bulk samples

Powder XRD patterns were obtained for all bulk samples using identical measurement conditions which are described in detail in Chapter IV. In order to quantify the mineral phases

and to extract mineralogical information on the phases all duricrust bulk XRD pattern of Chapters IV-VI were refined with the Rietveld method (Rietveld, 1969) using the XND code (Berar and Baldinozzi, 1998). Table II-1 summarizes the refined minerals, the used crystallographic starting parameters and the extracted values. For further details and explanations see Chapter IV. Fe-Al substitutions of goethite and hematite were calculated after Schulze (1984) and Stanjek and Schwertmann (1992), respectively, and the hematite goethite ratio was calculated $RHG = \text{Hematite} / (\text{Hematite} + \text{Goethite})$. The samples for the EPR study (Chapter VII) were not refined.

Major and trace elements including rare earth element content were obtained on bulk samples on the same material as used for the XRD analyses. The analyses were performed on 1–2 g of material ground to < 100 µm at the Service d'Analyse des Roches et des Mineraux (SARM), Vandoeuvre-Les-Nancy, France. Analytical details and uncertainties are briefly described in Chapter IV and can be found at www.sarm.cnrs.fr.

Table II-1: Summary of the Rietveld refinement parameters.

Mineral	starting crystal parameters	refined parameters	calculated from the refinement parameters
Goethite	Forsyth et al. (1968)	scale-factor, unit cell parameters (a, b, c), line-width, anisotropic line-width*, Fe-site occupancy factor*	weight-fraction, Fe-Al substitution, Mean Coherent Domain (MCD) sizes
Hematite	Blake et al. (1966)	scale-factor, unit cell parameters (a = b, c), line-width, anisotropic line-width*, Fe-site occupancy factor*	weight-fraction, Fe-Al substitution, Mean Coherent Domain (MCD) sizes
Gibbsite	Saalfeld and Wedde (1974)	scale-factor, line-width*, orientation*2	weight-fraction
Kaolinite	Bish and Von Dreele (1989)	scale-factor, orientation*2, line-width*	weight-fraction
Anatase	Horn et al. (1972)	scale-factor, line-width*, unit cell*	weight-fraction
Rutile	Shintani et al. (1975)	scale-factor, line-width*, unit cell*	weight-fraction
Quartz	Antao et al. (2008)	scale-factor, line-width*, unit cell*	weight-fraction
Boehmite	Corbató et al. (1985)	scale-factor3	weight-fraction

*refined but not used for further investigation

¹: only refined when important amounts in sample

²: only refined when important amounts in sample and necessary

³: only refined for a limited number of samples

II.4 Analyses on separated subsamples

As indicated in Figure II-1, in each ferruginous duricrust bulk sample several distinct facies (here referred to as subsamples), showing macroscopically homogeneous texture, color, hardness and porosity were selected and separated by micro-drilling. Apparently

homogeneous, uniform and similar fragments were selected by handpicking under a binocular microscope. This procedure necessarily induces a bias. As the bulk samples are often very heterogeneous and complex, this relatively subjective subsampling procedure leads possibly to a certain lack of representation of the samples. This was enhanced by the fact that it was considered, that only very pure iron (oxyhydr)oxide phases, i.e. free of unretentive phases such as kaolinite, gibbsite or quartz, were prone for (U-Th)/He dating. It was furthermore assumed that only very dense and hard material would retain He in its structure.

Due to the microcrystalline and opaque character of the material handpicking was guided by looking at the colors, lusters and textures and it was tried to select grains which resembled each other as much as possible. To ensure the homogeneity of the subsamples it was attempted to increase the number of analyzed aliquots when possible.

II.4.1 Scanning electron microscopy and reflected light microscopy

Scanning electron microscopy (SEM) was primarily used to obtain images of the opaque Fe (oxyhydr)oxide grains. Handpicked grains of 0.2-2 mm size of the subsamples were mounted in epoxy resin discs and polished. This was done systematically for all subsamples of Chapters IV and V, but could only be done for some of the subsamples of Chapter VI due to a lack of time. Most mounted subsamples (53 out of 87) were investigated by SEM using a Zeiss ULTRA55 microscope coupled to an EDS (Bruker QUANTAX) at the IMPMC, Paris. All other mounted subsamples were studied using reflected light microscopy. High resolution secondary electron and backscattered electron mappings (pixel size = 120 or 150 nm) were obtained from 53 subsamples using the software ATLAS (Zeiss). Figure II-2 shows an example of these mappings which made it possible to study a large number of grains in great detail. This approach allowed to identify the homogeneity of the subsamples and to compare the selected grains at a very small scale. It showed that the handpicking procedure allowed selection of overall relatively similar grains. The mappings were used to identify the paragenesis, subsample texture and homogeneity of the Fe phases and to check systematically for mineral inclusions such as zircon or rutile. In selected areas major elements were quantified and element distribution maps were obtained using the EDS system.

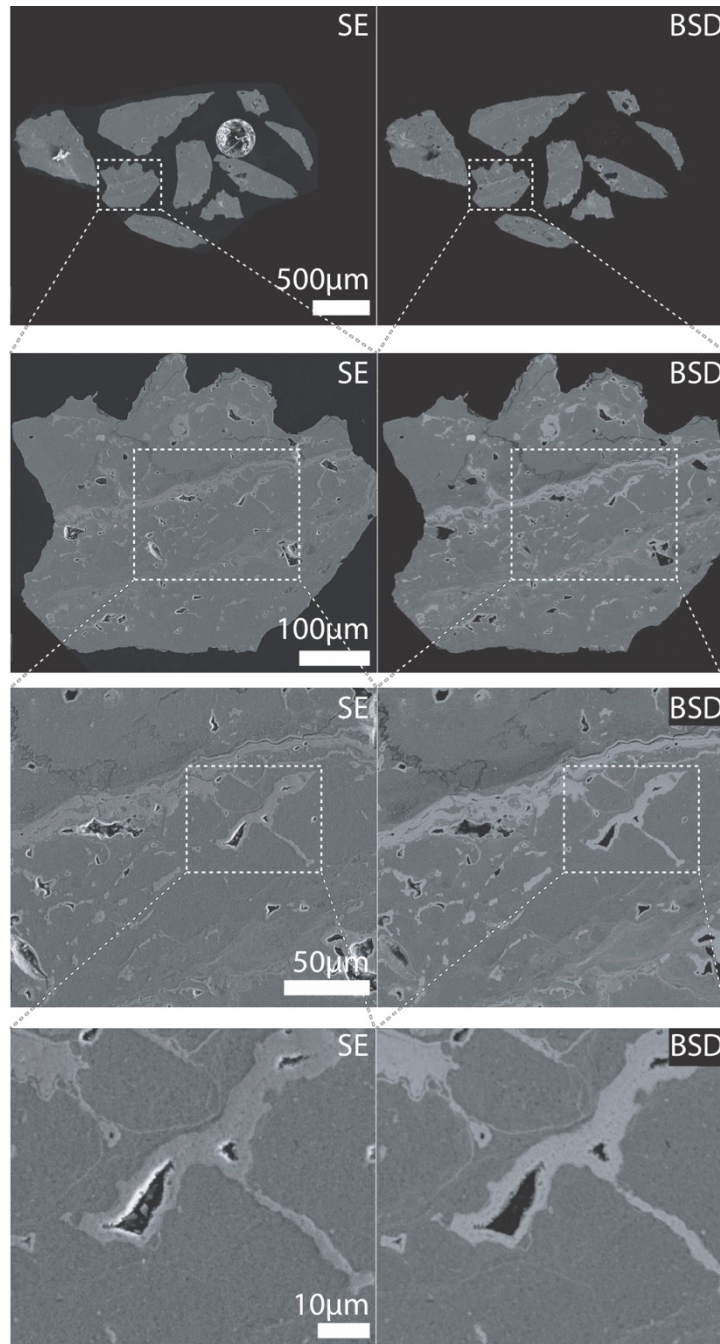


Figure II-2: Example of the secondary electron (SE) and back-scattered electron (BSD) mappings obtained by scanning electron microscopy. The pictures show the same area with different degrees of zooming. Note that the entire region shown at the top (several grains of one subsample) can be zoomed to the resolution of the picture at the bottom.

II.4.2 Micro X-ray diffraction

Given to the difficulty to characterize the mineralogical composition of the subsamples by optical methods and the often low amount of subsample material, in this thesis I applied a quantitative micro X-ray approach. Therefore individual subsamples grains of 250–700 μm size (ca. 20 - 100 μg , same size as for (U-Th)/He dating) were inserted into a boron silicate glass capillary (0.3 - 0.5 mm diameter) and analyzed at IMPMC laboratory, Paris, using a MM007HF

RIGAKU rotating Mo anode (1.2 kV) delivering a 100 μm -width micro beam. Figure II-3 shows the experimental setting which is described in detail in Marques et al. (in review). Two-dimensional XRD patterns were collected for 45–60 minutes in Debye-Scherrer geometry using a R-axis IV++ imaging double plate detector (300 \times 300 mm), the distance between the sample and the detector plate was 200 mm (Fig. II-3). Angle calibration and image integration to convert the 2D- into a 1D pattern were done using the FIT2D software (Hammersley, 2016). 1 to 5 grains were analyzed per subsample and for at least one grain per subsample the diffractogram was refined by the Rietveld method. Refinement was done as for the bulk samples (see above and Chapter IV) and important parameters are summarized in Table II-1.

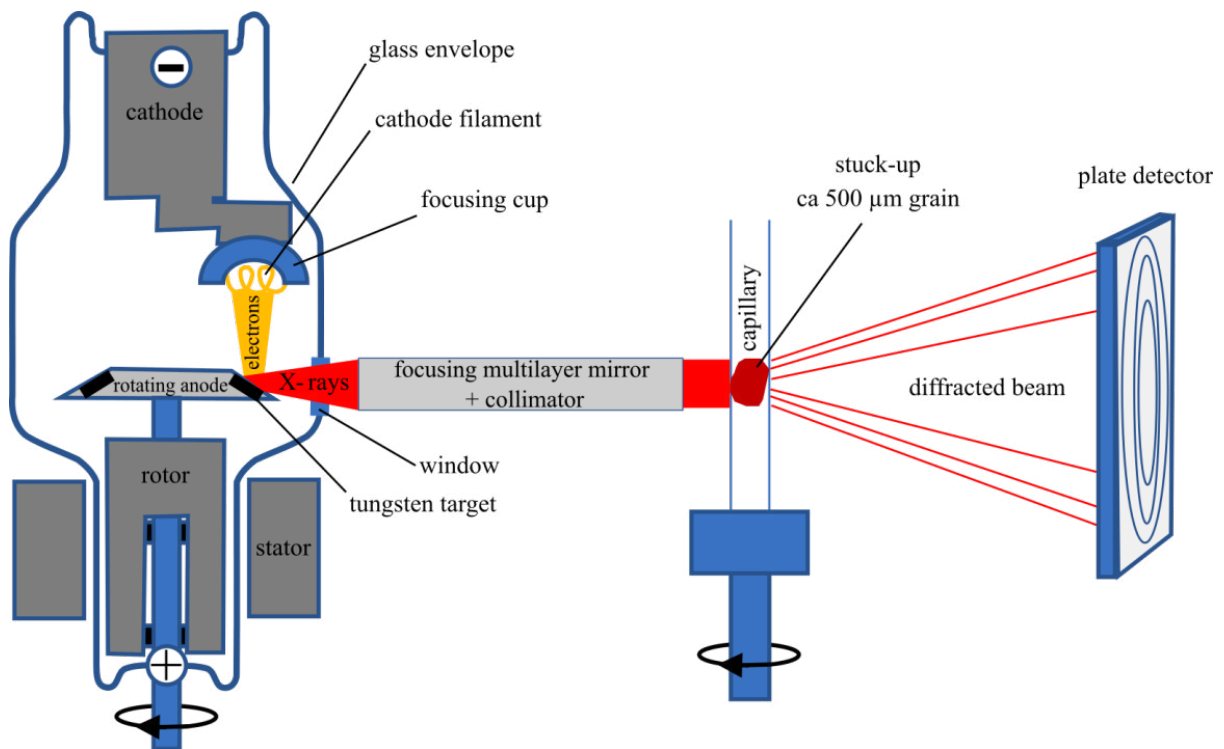


Figure II-3: Schema of the turning anode used for micro-XRD analyses of the Fe (oxyhydr)oxide grains (Figure by Marques et al., in review).

Figure II-4 shows examples of 4 different grains of the same subsample analyzed by micro-XRD. The X-ray diffraction pattern yield very similar results which was confirmed by Rietveld refinement of two of the grains (“XRD4” and “XRD4”) yielding very similar results (within error undistinguishable weight fractions of hematite, goethite and anatase and undistinguishable Gt-Al contents). Note that hematite-goethite ratio might be slightly different in the two other grains (“XRD2” and “XRD1”, Fig. II-4). For those subsamples where Rietveld refinement was done for more than one grain the results were generally very similar and concerned mainly the proportions of the mineral phases rather than the unit cell dimensions, coherent domain sizes or Fe-site occupations.

For several subsamples only one grain could be analyzed by micro-XRD. This is certainly not ideal but we consider that for the applied purpose (mainly identification of the phase and Al-content in the case of goethite and, to a lesser degree, mean coherent domain sizes) the analysis of one grain already yields the needed information.

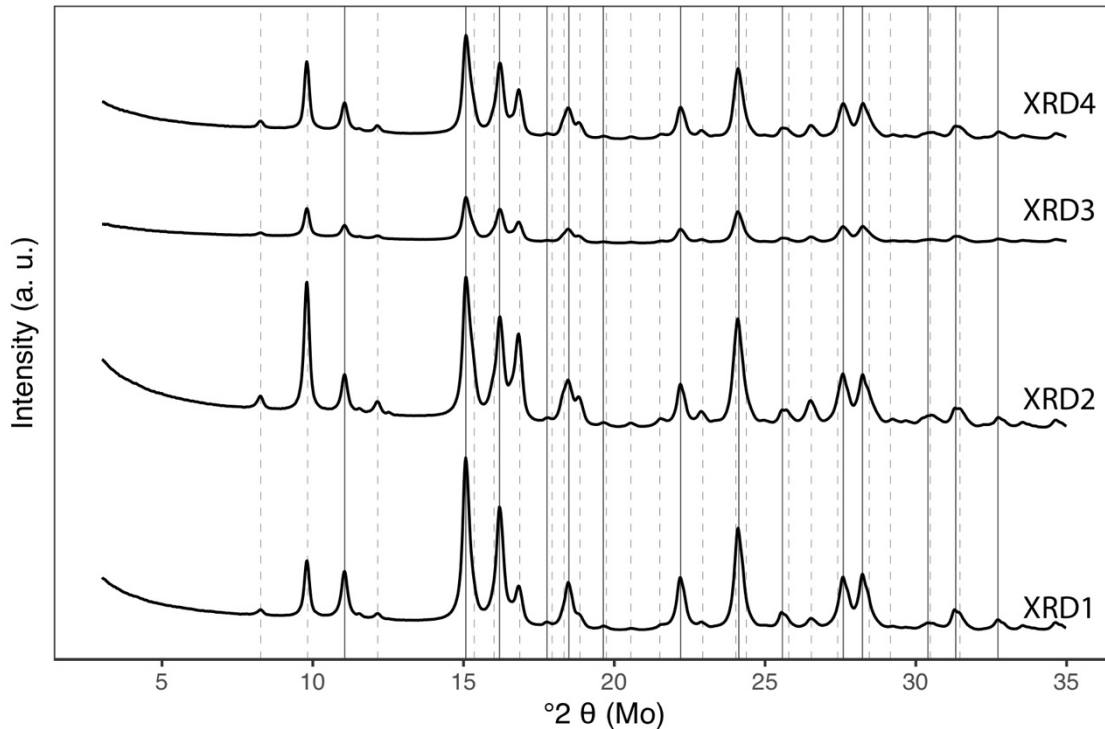


Figure II-4: XRD-pattern obtained through micro-XRD of 4 grains of subsample KAWF-4B_1G (Chapter KAWHE). Solid gray vertical lines indicate the positions of hematite peaks, dashed gray lines the position of goethite peaks. XRD3 and XRD4 were refined by the Rietveld method yielding very similar results (within error undistinguishable) with an 50:50 mixture of hematite and goethite. Note that the goethite proportion might be slightly greater in XRD2 and slightly smaller in XRD1.

The error of the Rietveld refinement is generally very small, especially regarding weight fractions and the fitted parameters of the predominant phases (>20%). The main error source of the micro-XRD results is the representativity of the grain and, in the case of large grains (e.g. 700 μm) the representativity of the selected spot ($\sim 100 \mu\text{m}$ size). However, comparison with the SEM images allows to have an overview about on the homogeneity of the subsample and to estimate the representativity of the micro-XRD results.

The goethite Fe-Al substitution was calculated from the c -parameter after Schulze, (1984). The error of the Al-substitution is generally calculated from the refinement error of the c -parameter plus the absolute error of the calibration, given by Schulze (1984) as $\pm 2.6 \text{ mol}\%$. This leads to relatively large error for our data. Note however, that the error of the relative differences between the Al-contents of the samples are better described by the error of the

Rietveld refinement and are overestimated when the calibration error of ± 2.6 mol% is included. For this reason, in some rare (indicated) cases only the refinement errors are given.

It shall be mentioned at this point that different conventions for the goethite classification exist. In Chapters IV-VI goethite is regarded as member of the *Pbnm* spacegroup with ($a = 4.598$ Å, $b = 9.951$ Å and $c = 3.018$ Å) and preferential crystal growth along the *c*-axis (e.g. Forsyth et al., 1968; Yang et al., 2014). In contrast, in Chapter II goethite is considered a member of the *Pnma* spacegroup : $a = 9.951$ Å, $b = 3.018$ Å and $c = 4.598$ Å with preferential crystal growth along the *b*-axis (Cornell and Schwertmann, 2003).

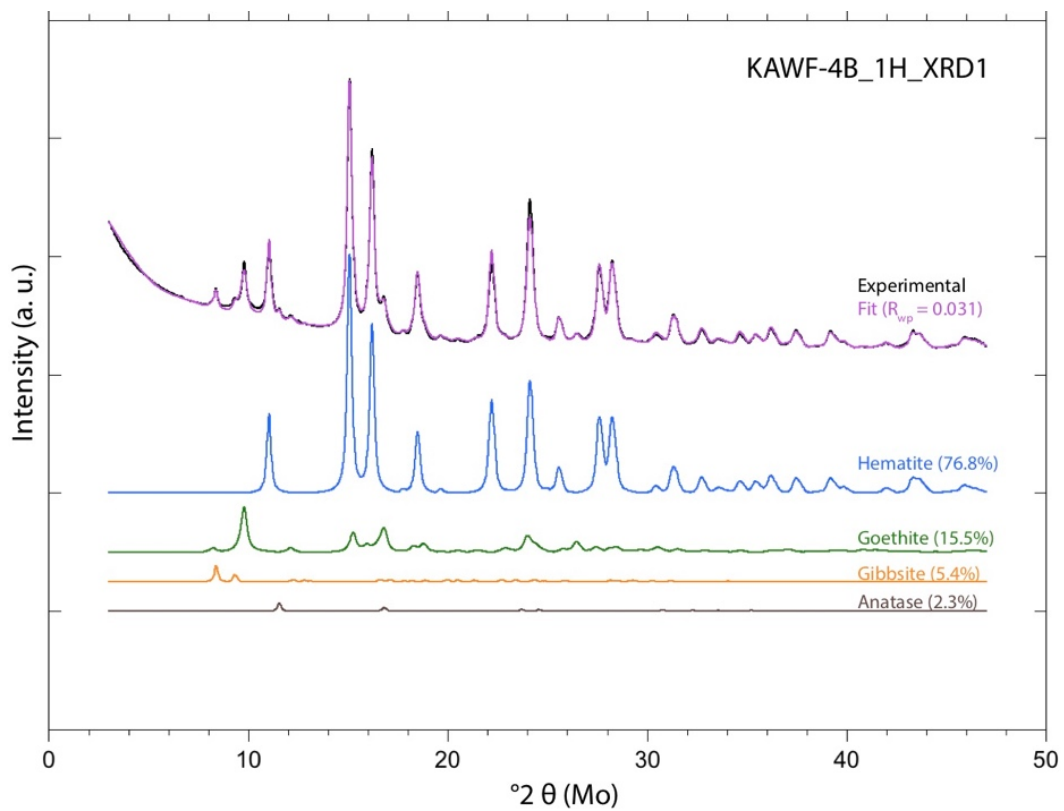


Figure II-5: Results of the Rietveld refinement of a grain of subsample KAWF-4B_1H analyzed by micro-XRD. The experimental diffractogram is shown in black, the obtained fit is overlain in violet. The R_{wp} -value indicates the quality of the fit (Toby, 2006). The resulting contributions of hematite (blue), goethite (green), gibbsite (yellow) and anatase (brown) are shown individually and the weight fraction is indicated in wt%.

II.4.3 (U-Th)/He geochronology

II.4.3.1 Concept

The radioactive decay of ^{238}U , ^{235}U , ^{232}Th and ^{147}Sm produces, apart from the final daughter isotopes ^{206}Pb , ^{207}Pb , ^{208}Pb and ^{143}Nd , α -particles (^4He nuclei, here always referred to as “He”). Each decay chain produces a different number of α -particles which can be expressed by the formula:

$$\begin{aligned} {}^4\text{He}_{all} = & 8 \times {}^{238}\text{U} \times (e^{\lambda_{238}t} - 1) \\ & + 7 \times {}^{235}\text{U} \times (e^{\lambda_{235}t} - 1) \\ & + 6 \times {}^{232}\text{Th} \times (e^{\lambda_{232}t} - 1) \\ & + 1 \times {}^{147}\text{Sm} \times (e^{\lambda_{147}t} - 1) \end{aligned} \quad (\text{II-1})$$

with decay constants $\lambda_{238} = 1.55125 \times 10^{-10}$, $\lambda_{235} = 9.8485 \times 10^{-10}$, $\lambda_{232} = 4.9475 \times 10^{-11}$, and $\lambda_{147} = 6.539 \times 10^{-12}$, where t is the elapsed time since “closure” of the system and ^{238}U , ^{235}U , ^{232}Th and ^{147}Sm are the amounts in moles (Zeitler, 2014). As the decay of ^{147}Sm produces only one ^4He having a half life time of 106 Ga while the decay of U and Th with half-life times of <4.47 Ga produces 21 ^4He , the latter are usually more important for the total ^4He production. Measuring both the amount of ^4He and of the parent isotopes makes it possible to calculate of duration of He accumulation (Farley, 2002; Zeitler, 2014). This procedure is actually the first isotope geochronological method used by Rutherford (1906) and Strutt (1905; 1908). The α -particles of the decay series are emitted with high kinetic energy and usually require tens of microns to come to rest in solid matter. In most minerals used for (U-Th)/He dating, the mean stopping distance is ~15-20 μm (Ketcham et al., 2011). Along its ejection path, the ^4He nucleus interacts with the crystal structure and captures two electrons to become a ^4He atom.

He, which is a noble gas, has a high diffusivity in solid phases. Thus the preserved amount of He in a crystal depends on the trapping potential of the mineral and diffusion that took place in the life of the dated phase. He diffusion kinetics in crystals is intensely studied and is controlled in first order by temperature and mineral type (Wolf et al. 1996; Zeitler et al. 1987) and, in the second order by grain size, thermal history, radiation damage and crystal chemistry (Shuster et al., 2006; Flowers, 2009; Gautheron et al., 2013; Guenther et al., 2013; Johnson et al., 2017). Depending on these parameters a mineral will retain (nearly) all, some, or none of the He produced. The closure temperature T_c is an empirical value introduced by Dodson (1973) that describes the retentivity of a mineral. T_c characterizes the temperature at

which, for a monotonic cooling, 50% of the produced He atoms are retained in the crystal. However it should be mentioned that due to the multiple factors which influence the He retention, crystals of the same mineral having experienced the same thermal history can have different T_c values.

11.4.3.2 Classical use of the (U-Th)/He method

The (U-Th)/He method is mainly used for applications in thermochronology (e.g. Farley, 2002; Gautheron and Zeitler, 2020). Generally minerals with a crystallization temperature lying considerably above their He closure temperature are used. The most commonly used minerals are zircon, titanite and apatite which have closure temperatures in the range of ca. 220 to <100°C for zircon and titanite and 110-50°C for apatite (e.g. Reiners et al., 1999; Farley, 2000; Stockli and Farley, 2004; Reiners, 2005). As these are temperatures commonly found in the Earth's shallow to mid-deep crust, the (U-Th)/He ages are generally related to the thermal history of the minerals rather than to their crystallization. For apatite and zircon He accumulation algorithms which include the effects of radiation damage on the retentivity exist and allow to reconstruct the cooling (and eventually reheating) history of the regarded minerals from their (U-Th)/He ages (Flowers et al., 2009; Guenther et al., 2013). Typical thermochronological applications are the exhumation of orogens or the subsidence history of sedimentary basins, but new developments enlarge constantly the field of applications (Ehlers and Farley, 2003; Reiners et al., 2005; Reiners and Brandon, 2006; Ault et al., 2019). However, with the increase of knowledge on He retention in minerals and active scientific community, the (U-Th)/He method has been used to other application including the geochronological one.

11.4.3.3 (U-Th)/He dating of supergene hematite and goethite

Several studies have shown that hematite and goethite can quantitatively retain He over geological timescales (Lippolt et al., 1993; Bahr et al., 1994; Lippolt et al., 1998; Shuster et al., 2005; Heim et al., 2006; Farley and Flowers, 2012; Vasconcelos et al., 2013; Reiners et al., 2014; Balout et al., 2017; Deng et al., 2017; Hofmann et al., 2017; Farley, 2018). The two minerals can thus be analyzed by the (U-Th)/He method. The supergene hematite and goethite minerals investigated in this thesis form at low temperature (ca. 20-35°C), significantly below their closure temperatures which are in the range of ca. 70-250 °C for hematite (as a function of the grain size and cooling rate, Farley, 2018) and not yet defined for goethite (see Chapter III for

details), but it has been shown that goethite partially retains He at ambient temperature of geological timescales (Shuster et al., 2005; Heim et al., 2006; Vasconcelos et al., 2013; Deng et al., 2017; Hofmann et al., 2017). As the samples did not suffer any significant reheating through geological processes (e.g. burial or metamorphism), He basically started to accumulate since the mineral precipitation and was not significantly lost due to major reheating (although some He is probably always lost). The (U-Th)/He ages are thus precipitation ages and do not contain a thermochronological information *sensu strictu*.

Several studies (Lippolt et al., 1993; Bahr et al., 1994; Farley and Flowers, 2012; Balout et al., 2017; Farley, 2018) focused on the He diffusion behavior in hematite and allowed determination of the diffusion kinetics of He in this minerals. Supergene hematite is composed of very small crystallites of 10s to 1000s of nm size. Due to this very small grain size, some of the produced He is lost by diffusion, even at surface temperature. According to the aforementioned studies we estimated a 5% He loss for hematite in this study.

He diffusion studies on goethite revealed rather variable values for diffusive loss in goethite, ranging from 2 to 20% (Shuster et al., 2005; Heim et al., 2006; Vasconcelos et al., 2013; Deng et al., 2017; Hofmann et al., 2017). These studies did not allow to determine which parameters controlled He diffusion in goethite. In order to better understand the He diffusion behavior in goethite a theoretical study has been conducted. This study is presented in Chapter III and proposes the following correction factors for goethite (U-Th)/He ages: for Al-poor goethite (<10 mol% Fe-Al substitution) 15 ± 10 % diffusive loss correction for samples with radiation damage densities $< 1\times 10^{15}$ α/g , 10 ± 7 % diffusive loss correction for radiation damage densities from 1×10^{15} to 1×10^{16} α/g , and 5 ± 5 % diffusive loss correction for radiation damage densities $> 1\times 10^{16}$ α/g and for Al-rich goethite (>10 mol% Fe-Al substitution) $5\pm 5\%$ diffusive loss correction independent of the radiation damage. These correction factors were applied for the goethite (U-Th)/He ages of Chapters V and VI.

II.4.3.4 Ultrasound test

The possible effect of He loss through ultrasonic cleaning was tested by comparing material of the same subsample cleaned for a long time (ca. 30 minutes or more and showing rounding) with material cleaned for a short time (2-5 minutes). The data is presented in Figure II-6. Generally, there was no systematic difference in the obtained ages. Only one subsample very rich in large kaolinite booklets showed signs of He-loss (not presented as the data was

excluded). Note that long ultrasonic cleaning was only used in at the beginning of the thesis for the sample preparation of some of the samples of Chapter IV. For the samples of Chapters V and VI ultrasound times were kept as short as possibly.

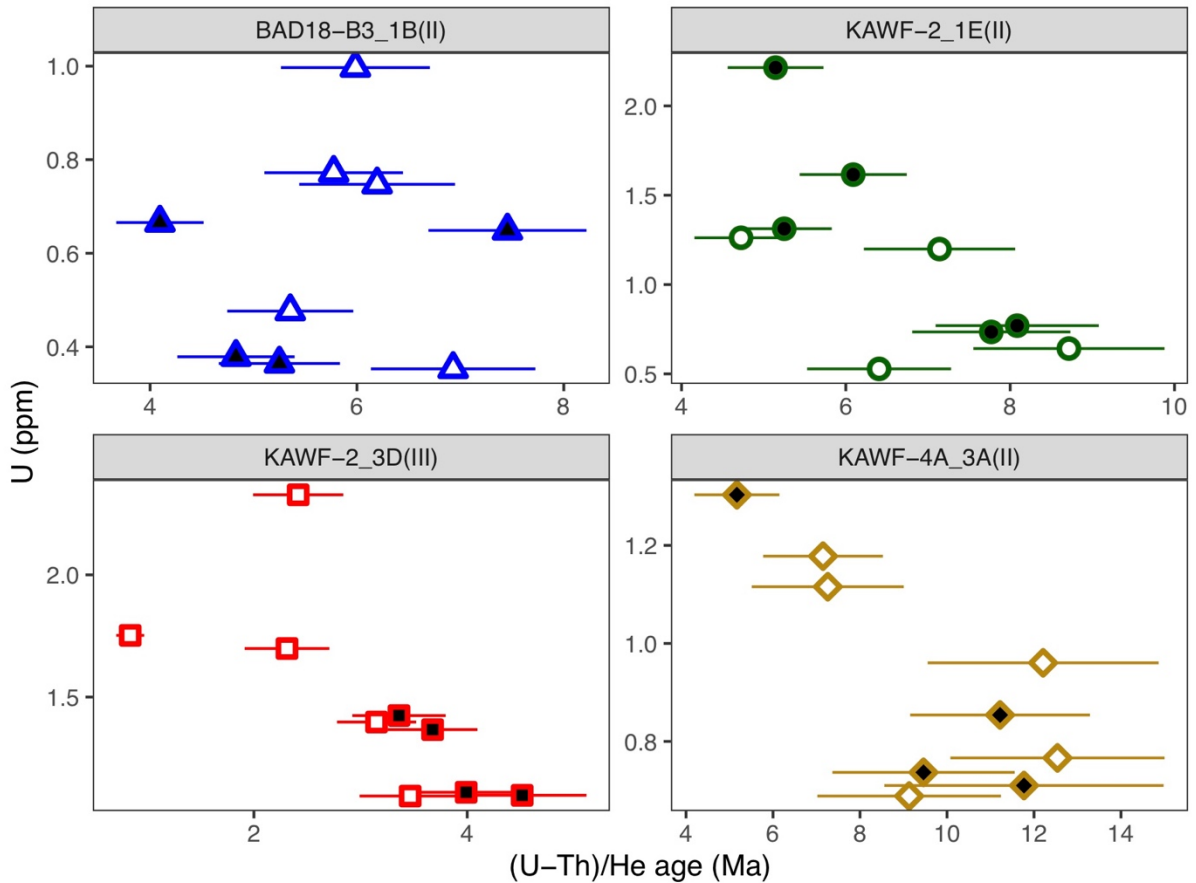


Figure II-6: (U-Th)/He ages versus U concentrations for four subsamples with some material cleaned for a long time (30 minutes or more, filled symbols) in an ultrasonic bath and some material cleaned for a short time (2-5 minutes, empty symbols) in ultrasonic bath. The data does not indicate any systematic He loss through long ultrasonic cleaning.

II.5 Principle of electron paramagnetic resonance spectroscopy

Since electron paramagnetic resonance spectroscopy (EPR) is not so commonly used in geosciences, the principle of this method is briefly described in the following section. The electron paramagnetic resonance spectroscopy concerns the chemical species with unpaired electrons, the so-called paramagnetic centers, such as free radicals, some ions of transition elements, electron defects. It is a very sensitive technique that can detect concentrations as low as atomic ppb and is non destructive.

The electrons of the material get discrete levels of energy of spins when submitted to a magnetic field (Zeeman effect). An electromagnetic wave in the microwave range (typically

several GHz) produces transitions between these levels of energy (Fig. II-7). The absorption of the microwave energy quantum concerns only transitions of unpaired electrons. For technical reasons the resulting spectrum is recorded at a fixed microwave frequency as a function of the magnetic field that ranges within some thousands gauss in standard setting such as the X-band (circa 9.4 GHz).

The resonance condition necessary to produce a signal is:

$$h\nu = g\beta H \quad (\text{II-2})$$

where h is the Planck constant, ν is the hyperfrequency (GHz), β the Bohr Magneton and H the magnetic field.

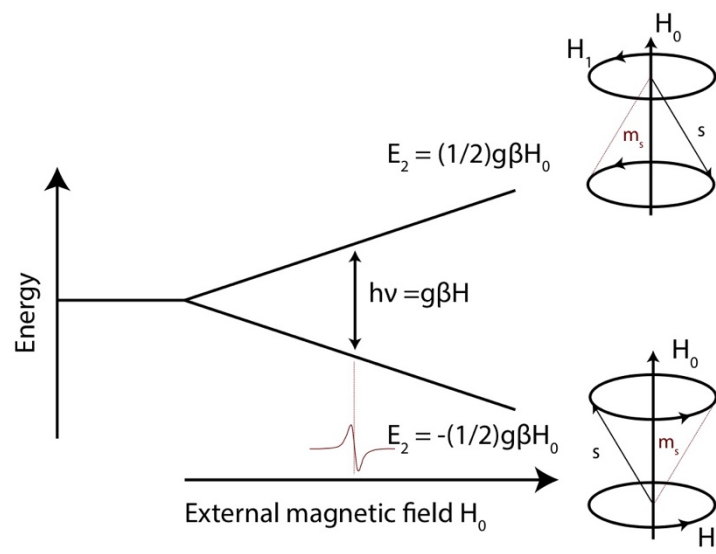


Figure II-7: The Zeeman effect for $S = \frac{1}{2}$. The magnetic field produces a precession of the magnetic moment of the electron around its axis, and induces $2S+1$ energy levels. The spin S flips when going from one energy level to the other, when the resonance condition is fulfilled. Figure modified from Allard (1994)

The parameter g is a tensor relating the hyperfrequency to the magnetic field and the principal values of which are characteristic of the paramagnetic species. An example of species with $S=1/2$ is the radiation-induced defect O^- encountered in kaolinite, as its electronic structure is $1s^2 2s^2 2p^5$.

For species with several unpaired electrons, the total spin is ≥ 1 and the resulting interaction is the fine structure, due to the magnetic interaction of other electrons (spin-orbit coupling) and the electric interaction of the crystal field. A good example concerning kaolinite is the structural Fe^{3+} ($3d^5$) with 5 unpaired electrons and total spin of $5/2$. In configuration of low symmetry (not cubic) the symmetry of the crystal field is important and induces a splitting

of the fundamental level at zero magnetic field (Fig. II-8). Consequently, the Zeeman sub-levels are no more equally spaced.

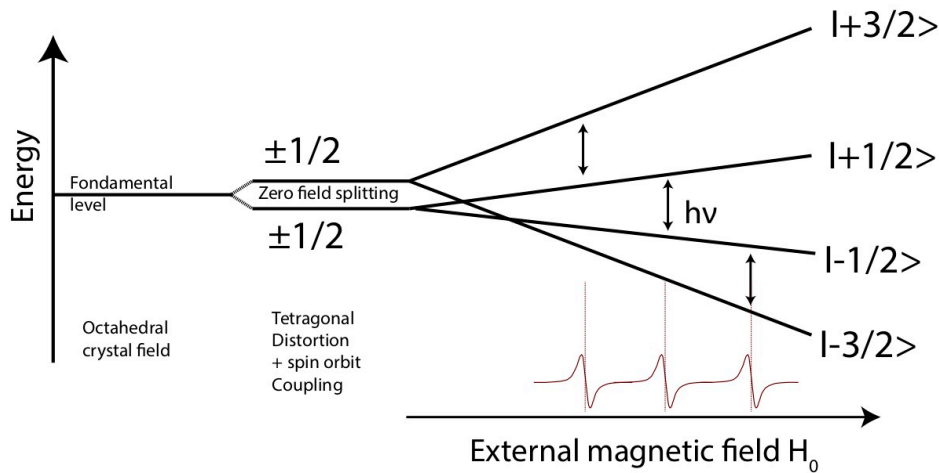


Figure II-8: Fine structure for a $S=3/2$ total spin. In low symmetry crystal fields, a zero field splitting is observed. Figure modified from Allard (1994)

The coupling between the electronic spin and the nuclear spin is the hyperfine structure. The nucleus with non-zero nuclear spin creates locally a magnetic field which decomposes the Zeeman sub-level in $2I+1$ resonances that are, in a first approximation, equally spaced (Fig. II-9). The hyperfine structure is characterized by the hyperfine constant A (magnetic field separation between hyperfine peaks). Examples of isotopes with non-zero nuclear spins that are always or often present in kaolinites are ^{27}Al ($I=5/2$) and ^{51}V ($I=7/2$). The resulting interaction of these nuclei with the $S=1/2$ are complex spectra.

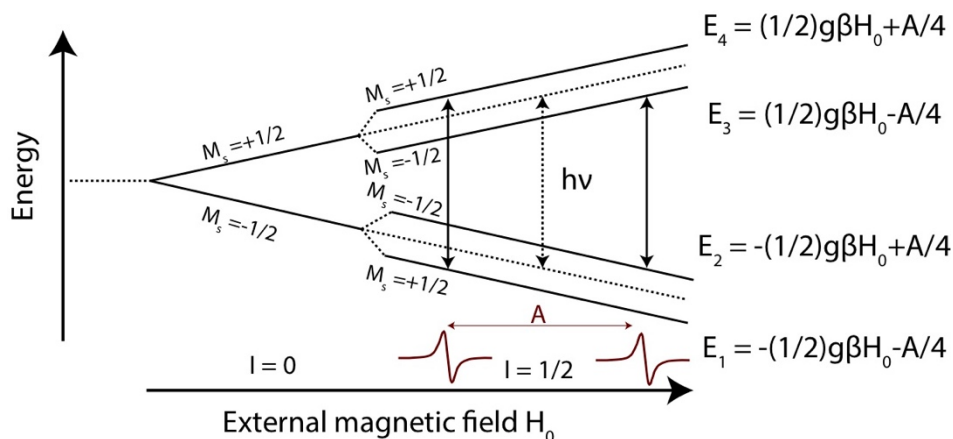


Figure II-9: Hyperfine structure for $S=1/2$, and nuclear spin $I=1/2$ that induces a constant splitting of the energy levels. The resulting spectrum shows $2I+1$ transitions. Figure modified from Allard (1994)

In a mineral submitted to an external magnetic field, the unpaired electron experiences various interactions that define the possible energy levels of the system. The Hamiltonian energy operator \mathcal{H} expresses these interactions and allows one to calculate the energies of the

electronic levels as a function of H (Calas, 1988). Considering the main interactions concerned in EPR, it can be written:

$$\begin{aligned} \mathcal{H} &= \mathcal{H}_{SS} + \mathcal{H}_Z + \mathcal{H}_{IS} \\ &= S.\mathbf{D}.S + \beta S.\mathbf{g}.H + S.\mathbf{A}.I \end{aligned} \quad (\text{II-3})$$

where \mathbf{D} , \mathbf{g} , \mathbf{A} are the tensors related to the fine structure, Zeeman interaction and hyperfine coupling, respectively, and S is the total electronic spin, I the nuclear spin. The code ZFSfit (Morin and Bonnin, 1999) used in our study (see Chapter VII) calculates this full Hamiltonian and allows one to fit the EPR signals encountered in kaolinite (see also Balan et al., 1999) but this operation is complex when several signals are superimposed in the same region.

The EPR analysis was performed on powders in our study, meaning that all orientations of crystallites are present in the magnetic field. This is responsible for spectra that display an anisotropy of the g tensor, which can be assimilated to an ellipsoid with g_x , g_y , g_z principal values (Fig. II-10). An example of axial spectrum with $g_{//}$ (g_z) and g_{\perp} ($g_y=g_x$) defining a revolution ellipsoid is given for the radiation-induced defect in kaolinite named A-center (see Chapter VII).

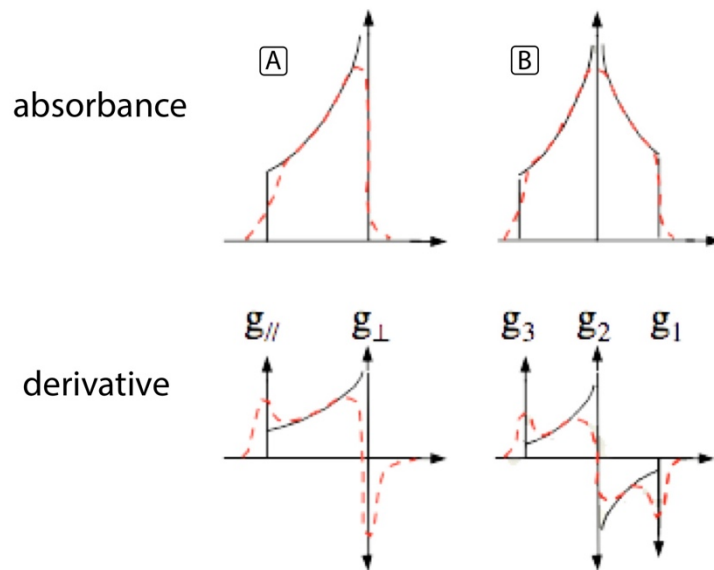


Figure II-10: EPR of powder : spectra of absorbance and first derivative in axial (A) and orthorhombic (B) symmetry of the g tensor. Specific points of the spectra allow one to determine the principal values of g. Figure modified from Allard (1994)

II.6 Clay mineral separation

II.6.1 Procedure

For kaolinite purification 8g of ground sample material (<200 μm) were filled into a 250ml Teflon centrifugation tube. Deferration was performed following the citrate-bicarbonate- dithionite (CBD) procedure of Mehra and Jackson (1960), which dissolves all Fe^{3+} oxides in the broad sense, irrespective of their nature or crystallinity. To do so, a citrate-bicarbonate solution was prepared with 78.42 g sodium citrate, 9.34 g bicarbonate and 1 L of MilliQ water. 200 ml of this solution were added to the sample and then 4.0 g of dithionite were added. The mixture was well mixed and heated during 1h to 1:15 h (depending on the incident temperature) in a Bain Marie at 80-95°C, agitating regularly. Afterwards the mixture was centrifugated during 10 minutes at 5000 turns per minute (tpm) and the supernatant, containing the dissolved and then complexed Fe was discarded. The CBD procedure was repeated until the liquid was completely transparent and colorless, and the remaining solid sample did not contain visible traces of Fe minerals anymore. For most saprolite samples 4-6 CBD cycles were necessary whereas for duricrust samples up to 13 cycles were done in order to dissolve most of the Fe.

Afterwards, the solid wet samples were washed 3-4 times with MilliQ water by agitating the suspension during 15-30 minutes for every washing cycle. Every time, the water was separated by centrifugating the samples 10-20 minutes with 10,000 tpm and pouring away the liquid. For clay separation the samples were brought into suspension and this suspension was centrifugated during 17 minutes at 500 tpm to recover < 2 μm fraction in the supernatant. The latter was filled into 1L beakers and kept aside. The last two steps were repeated 4-5 times in order to extract the maximum of the clay fraction. When necessary, the suspension was agitated in a ultrasonic bath prior to centrifugation. The separated liquid containing the clay fraction <2 μm was subsequently centrifugated 15 minutes at 10 000 tpm in order to recover the solid clay fraction. If necessary, organic material contained in the clay fractions was dissolved using hot H_2O_2 (done for 2 samples). The purified clay fractions were then filled into small Teflon recipients and dried at ca. 50°C in a stove. Once dried, the material was gently crushed in an agate mortar in order to disaggregate and disorientate the clay minerals.

II.6.2 Analyses on purified kaolinites

The purified kaolinites were then studied by powder XRD and electron paramagnetic resonance (EPR) spectroscopy. The Gaité index, indicative of structural ordering in kaolinite, and the amount of structural Fe³⁺ substituting Al³⁺ in the kaolinite structure were calculated from the EPR spectra (Gaité et al., 1997; Balan et al., 2000). For samples selected for EPR dating (Balan et al., 2005), dosimetry curves were obtained after artificial irradiation of the kaolinite with He⁺ ions at the ARAMIS linear accelerator (Orsay, France). Preliminary ages (without usual corrections) were calculated from the paleodoses obtained through the dosimetry curves and dose-rates calculated from the bulk concentration of radioelements. All steps of the relatively complex kaolinite dating procedure are explained in Chapter VII.

References

- Allard T. (1994) La Kaolinite: un dosimètre des rayonnements naturels. Application au traçage de migrations anciennes de radioéléments dans la géosphère. Université Paris VII.
- Antao S. M., Hassan I., Wang J., Lee P. L. and Toby B. H. (2008) State-of-the-art high-resolution powder X-ray diffraction (HRPXRD) illustrated with rietveld structure refinement of quartz, sodalite, tremolite, and meionite. *Can. Mineral.* **46**, 1501–1509.
- Ault A. K., Gautheron C. and King G. E. (2019) Innovations in (U–Th)/He, Fission Track, and Trapped Charge Thermochronometry with Applications to Earthquakes, Weathering, Surface-Mantle Connections, and the Growth and Decay of Mountains. *Tectonics* **38**, 3705–3739.
- Bahr R., Lippolt H. J. and Wernicke R. S. (1994) Temperature-induced ⁴He degassing of specularite and botryoidal hematite: a ⁴He retentivity study. *J. Geophys. Res.* **99**.
- Balan E., Allard T., Boizot B., Morin G. and Muller J. P. (2000) Quantitative measurement of paramagnetic Fe³⁺ in kaolinite. *Clays Clay Miner.* **48**, 439–445.
- Balan E., Allard T., Boizot B., Morin G. and Muller J. P. (1999) Structural Fe³⁺ in natural kaolinites: New insights from electron paramagnetic resonance spectra fitting at X and Q-band frequencies. *Clays Clay Miner.* **47**, 605–616.
- Balan E., Allard T., Fritsch E., Sélo M., Falguères C., Chabaux F., Pierret M. C. and Calas G. (2005) Formation and evolution of lateritic profiles in the middle Amazon basin: Insights from radiation-induced defects in kaolinite. *Geochim. Cosmochim. Acta* **69**, 2193–2204.

- Balout H., Roques J., Gautheron C., Tassan-Got L. and Mbongo-Djimbi D. (2017) Helium diffusion in pure hematite ($\alpha\text{-Fe}_2\text{O}_3$) for thermochronometric applications: A theoretical multi-scale study. *Comput. Theor. Chem.* **1099**, 21–28.
- Berar J. F. and Baldinozzi G. (1998) XND code: From X-ray laboratory data to incommensurately modulated phases. *Rietveld Model. complex Mater. CPD Newsl.* **20**, 3–5.
- Bish D. L. and Von Dreele R. B. (1989) Rietveld refinement of non-hydrogen atomic positions in kaolinite. *Clays Clay Miner.* **37**, 289–296.
- Blake R. L., Hessevick R. E., Zoltai T. and Finger L. W. (1966) Refinement of the hematite structure. *Am. Mineral. J. Earth Planet. Mater.* **51**, 123–129.
- Calas G. (1988) Electron paramagnetic resonance. *Rev. Mineral. Geochemistry* **18**, 513–571.
- Corbató C. E., Tettenhorst R. T. and Christoph G. G. (1985) Structure refinement of deuterated boehmite. *Clays Clay Miner.* **33**, 71–75.
- Cornell R. M. and Schwertmann U. (2003) *The Iron Oxides. Structure, Properties, Occurrences and Uses.*, Wiley-VCH, Weinheim, Germany.
- Deng X. D., Li J. W. and Shuster D. L. (2017) Late Mio-Pliocene chemical weathering of the Yulong porphyry Cu deposit in the eastern Tibetan Plateau constrained by goethite (U–Th)/He dating: Implication for Asian summer monsoon. *Earth Planet. Sci. Lett.* **472**, 289–298.
- Dodson M. H. (1973) Closure temperature in cooling geochronological and petrological systems. *Contrib. to Mineral. Petrol.* **40**, 259–274.
- Ehlers T. A. and Farley K. A. (2003) Apatite (U–Th)/He thermochronometry: Methods and applications to problems in tectonic and surface processes. *Earth Planet. Sci. Lett.* **206**, 1–14.
- Farley K. A. (2002) (U–Th) / He Dating: Techniques, Calibrations, and Applications. *Rev. Mineral. Geochemistry* **47**, 819–844.
- Farley K. A. (2000) Helium diffusion from apatite: General behavior as illustrated by Durango fluorapatite. *J. Geophys. Res.* **105**, 2903–2914.
- Farley K. A. (2018) Helium diffusion parameters of hematite from a single-diffusion-domain crystal. *Geochim. Cosmochim. Acta* **231**, 117–129.

- Farley K. A. and Flowers R. M. (2012) (U-Th)/Ne and multidomain (U-Th)/He systematics of a hydrothermal hematite from eastern Grand Canyon. *Earth Planet. Sci. Lett.* **359–360**, 131–140.
- Flowers R. M. (2009) Exploiting radiation damage control on apatite (U-Th)/He dates in cratonic regions. *Earth Planet. Sci. Lett.* **277**, 148–155.
- Flowers R. M., Ketcham R. A., Shuster D. L. and Farley K. A. (2009) Apatite (U-Th)/He thermochronometry using a radiation damage accumulation and annealing model. *Geochim. Cosmochim. Acta* **73**, 2347–2365.
- Forsyth J. B., Hedley I. G. and Johnson C. E. (1968) The magnetic structure and hyperfine field of goethite (α -FeOOH). *J. Phys. C Solid State Phys.* **1**, 179.
- Gaite J.-M., Ermakoff P., Allard T. and Muller J.-P. (1997) Paramagnetic Fe³⁺: a Sensitive Probe for Disorder in Kaolinite Origins of Line Broadening. *Clays Clay Miner.* **45**, 496–505.
- Gautheron C., Barbarand J., Ketcham R. A., Tassan-Got L., van der Beek P., Pagel M., Pinna-Jamme R., Couffignal F. and Fialin M. (2013) Chemical influence on α -recoil damage annealing in apatite: Implications for (U-Th)/He dating. *Chem. Geol.* **351**, 257–267.
- Gautheron C. and Zeitler P. K. (2020) Noble Gases Deliver Cool Dates from Hot Rocks. *Elements* **16**, 303–309.
- Guenther W. R., Reiners P. W., Ketcham R. A., Nasdala L. and Giester G. (2013) Helium diffusion in natural zircon: radiation damage, anisotropy, and the interpretation of zircon (U-Th)/He thermochronology. *Am. J. Sci.* **313**, 145–198.
- Hammersley A. P. (2016) FIT2D: a multi-purpose data reduction, analysis and visualization program. *J. Appl. Crystallogr.* **49**, 646–652.
- Heim J. A., Vasconcelos P. M., Shuster D. L., Farley K. A. and Broadbent G. (2006) Dating paleochannel iron ore by (U-Th)/He analysis of supergene goethite, Hamersley province, Australia. *Geology* **34**, 173–176.
- Hofmann F., Reichenbacher B. and Farley K. A. (2017) Evidence for >5 Ma paleo-exposure of an Eocene–Miocene paleosol of the Bohnerz Formation, Switzerland. *Earth Planet. Sci. Lett.* **465**, 168–175.
- Horn M. S. C. F., Schwebdtfeger C. F. and Meagher E. P. (1972) Refinement of the structure of anatase at several temperatures. *Zeitschrift für Krist. Mater.* **136**, 273–281.

- Johnson J. E., Flowers R. M., Baird G. B. and Mahan K. H. (2017) "Inverted" zircon and apatite (U–Th)/He dates from the Front Range, Colorado: High-damage zircon as a low-temperature (<50 °C) thermochronometer. *Earth Planet. Sci. Lett.* **466**, 80–90.
- Ketcham R. A., Gautheron C. and Tassan-Got L. (2011) Accounting for long alpha-particle stopping distances in (U–Th–Sm)/He geochronology: Refinement of the baseline case. *Geochim. Cosmochim. Acta* **75**, 7779–7791.
- Lippolt H. J., Brander T. and Mankopf N. R. (1998) An attempt to determine formation ages of goethites and limonites by (U+Th)-⁴He dating. *Neues Jahrb. Mineral. Monatshefte* **11**.
- Lippolt H. J., Wernicke R. S. and Boschmann W. (1993) ⁴He diffusion in specular hematite. *Phys. Chem. Miner.* **20**, 415–418.
- Mehra O. P. and Jackson M. L. (1960) Iron oxide removal from soils and clays by a dithionite-citrate system buffered with sodium bicarbonate. *Clays Clay Miner.* **7**, 317–327.
- Morin G. and Bonnin D. (1999) Modeling EPR Powder Spectra Using Numerical Diagonalization of the Spin Hamiltonian. *J. Magn. Reson.* **136**, 176–199.
- Reiners P. W. (2005) Zircon (U–Th)/He Thermochronometry. *Rev. Mineral. Geochemistry* **58**, 151–179.
- Reiners P. W. and Brandon M. T. (2006) Using thermochronology to understand orogenic erosion. *Annu. Rev. Earth Planet. Sci.* **34**, 419–466.
- Reiners P. W., Chan M. A. and Evenson N. S. (2014) (U–Th)/He geochronology and chemical compositions of diagenetic cement, concretions, and fracture-filling oxide minerals in mesozoic sandstones of the Colorado Plateau. *Bull. Geol. Soc. Am.* **126**, 1363–1383.
- Reiners P. W., Ehlers T. A. and Zeitler P. K. (2005) Past, present, and future of thermochronology. *Rev. Mineral. Geochemistry* **58**, 1–18.
- Reiners P. W., Farley K. A. and Sciences P. (1999) Helium diffusion and (U–Th)/He thermochronometry of titanite. *Geochim. Cosmochim. Acta* **63**, 3845–3859.
- Rietveld H. M. (1969) A profile refinement method for nuclear and magnetic structures. *J. Appl. Crystallogr.* **2**, 65–71.
- Rutherford E. (1906) *Radioactive Transformations.*, Charles Scribner's Sons, New York, USA.
- Saalfeld H. and Wedde M. (1974) Refinement of the crystal structure of gibbsite, Al(OH)₃. *Zeitschrift für Krist. Mater.* **139**, 129–135.
- Schulze D. G. (1984) The influence of aluminium on iron oxides. VIII. Unit-cell dimensions of Al-substituted goethites and estimation of Al from them. *Clays Clay Miner.* **32**, 36–44.

- Shintani H., Sato S. and Saito Y. (1975) Electron-density distribution in rutile crystals. *Acta Crystallogr. Sect. B Struct. Crystallogr. Cryst. Chem.* **31**, 1981–1982.
- Shuster D. L., Flowers R. M. and Farley K. A. (2006) The influence of natural radiation damage on helium diffusion kinetics in apatite. *Earth Planet. Sci. Lett.* **249**, 148–161.
- Shuster D. L., Vasconcelos P. M., Heim J. A. and Farley K. A. (2005) Weathering geochronology by (U-Th)/He dating of goethite. *Geochim. Cosmochim. Acta* **69**, 659–673.
- Stanjek H. and Schwertmann U. (1992) The influence of aluminum on iron oxides. Part XVI: Hydroxyl and aluminum substitution in synthetic hematites. *Clays Clay Miner.* **40**, 347–354.
- Stockli D. F. and Farley K. A. (2004) Empirical constraints on the titanite (U–Th)/ He partial retention zone from the KTB drill hole. *Chem. Geol.* **207**, 223–236.
- Strutt R. J. (1908) On the accumulation of helium in geological time. *Proc. R. Soc. London* **81A**, 272–277.
- Strutt R. J. (1905) On the radio-active minerals. *Proc. R. Soc. London* **76A**, 88–101.
- Toby B. H. (2006) R factors in Rietveld analysis: How good is good enough? . *Powder Diffraction* **21**, 67–70.
- Vasconcelos P. M., Heim J. A., Farley K. A., Monteiro H. and Waltenberg K. (2013) $^{40}\text{Ar}/^{39}\text{Ar}$ and (U-Th)/He $^{-4}\text{He}/^3\text{He}$ geochronology of landscape evolution and channel iron deposit genesis at Lynn Peak, Western Australia. *Geochim. Cosmochim. Acta* **117**, 283–312.
- Yang H., Lu R., Downs R. T. and Costin G. (2014) Goethite, α -FeO(OH), from single-crystal data.
- Zeitler P. K. (2014) U-Th / He Dating. In *Encyclopedia of Scientific Dating Methods* (eds. J. W. Rink and J. Thompson). Springer, Dordrecht. pp. 1–14.

III Revealing the radiation damage and Al-content impacts on He diffusion in goethite

Fadel Bassal¹, Beatrix Heller^{2,3}, Jérôme Roques¹, Hilal Balout¹, Laurent Tassan-Got¹, Thierry Allard³, Cécile Gautheron^{2*}

¹ Université Paris-Saclay, CNRS/IN2P3, IJCLab, 91405 Orsay, France

² Université Paris-Saclay, CNRS, GEOPS, 91405, Orsay, France

³ IMPMC, UMR 7590, CNRS, Sorbonne Université, MNHN, IRD, 4 place Jussieu, F-75252 Paris cedex 05, France

(Manuscript in review at Chemical Geology)

Abstract

Since several dozens of years, the (U-Th)/He chronological method on goethite has been more and more applied to date laterite formation and evolution or ore-deposit formation. However, questions remain on possible He loss by diffusion due to the polycrystalline structure of goethite and associated underestimation of the (U-Th)/He age. Helium loss was estimated to range from 2 to 30%, but no relation or models have been produced to explain such values. To clarify the situation, we firstly performed a complete review of experimental He diffusion data in natural goethite, that reveals the link between activation energy and He loss with the damage dose. To understand He diffusion behavior in goethite and model the He loss, natural defect and alpha damage as well as the chemical composition and growth structure effect on He diffusion have been investigated thanks to a multi-scale study. We used numerical simulations combining the Density Functional Theory at the atomic scale and Kinetic Monte Carlo simulations at the macroscopic scale. We found that He diffusion is purely anisotropic along the preferential elongated axis (i.e. *b*-axis) and He leaks out easily in defect-free goethite and Al-goethite. The consequence of this anisotropy is that crystallographic defects and alpha damage strongly lower the He diffusivity in goethite and Al-goethite by obstructing the diffusion channel or trapping He along the *b*-axis. Defect and damage impact on He diffusion is even larger for Al-goethite. The obtained He diffusion parameters for goethite containing defect and damage are similar to the activation energy and He diffusional loss obtained in natural goethite from the literature. This allows one to demonstrate the systematic

dependence of the diffusion coefficient with damage dose and the impact of Al on He retention. He atoms are retained only at the favor of obstructions blocking the diffusion and vacancies trapping them in the goethite structure. The consequence of the diffusive behavior is that a part of He diffuses out of the crystal until sufficient damage accumulated along the *b*-axis. The diffusion domain size is the channel length along the *b*-axis rather than the whole crystallite size. To correct the He loss this study proposes estimation of the He retention and needed corrections for different types of goethite.

III.1 Introduction

The Earth's continental surface undergoes erosion and weathering processes that affect its morphology. During hydrolyzation of the rocks at the surface, chemical elements are transferred between the different compartments of the critical zone during weathering (Brantley and Lebedeva, 2011). The release of most soluble chemical elements from the parent rock will also lead to the precipitation of secondary phases such as clays and oxides (e.g., iron oxides and oxyhydroxides; Nahon, 2003; Nahon and Tardy, 1992), which retain the less soluble elements such as Al, Fe, or Ti. Goethite, $\alpha\text{-FeO(OH)}$, is one of the most common iron oxyhydroxides developed in those environments and the most abundant phase of iron(III) at the Earth's surface (Cornell and Schwertmann, 2004). Goethite can contain up to 33% of Al substitution and some dozen to hundreds of ppm of trace and rare earth elements, including U, Th and Sm (Ault et al., 2019; Shuster et al., 2005). Principally goethite is found in soils (e.g. laterites), sediments, and ore deposits and it is the main constituent of limonite (yellow-red ochres) (Dutrizac and Soriano, 2018). In addition to hematite ($\alpha\text{-Fe}_2\text{O}_3$), this ferric iron oxyhydroxide is one of the most thermodynamically stable forms of iron oxides at ambient conditions in the presence of water.

Goethite and hematite crystallization are key markers of the Earth's surface evolution and are related to weathering products that are linked to climatic and geodynamical changes (Vasconcelos et al., 2015). Accessing the timing of hematite and goethite precipitation provides important constraint on the evolution of weathering covers and reconstruction of continental surfaces. One important tool for dating hematite and goethite is the (U–Th)/He chronometry. This methodology is based on the radioactive alpha decay of U, Th and Sm that produces He nuclei (alpha particle) which are (partially) retained in the crystal structure (see review of Ault et al., 2019). The (U–Th)/He age interpretation depends therefore on our knowledge of the He

loss by diffusion in the target mineral. Helium is a noble gas that is thermally activated and diffuses from neighboring insertion sites following the Arrhenius law (Farley, 2000). The diffusion rate depends on the energy barrier between sites and the probability of jumping to one of the neighboring insertion sites. He atoms always vibrate due to temperature, even at surface temperature, and have a probability to jump to the next neighboring insertion sites. Even for He retentive minerals such as apatite and zircon for example (Farley, 2000; Reiners, 2005), He atoms diffuse at surface temperature, but thanks to the large size of the crystal compared to the diffusional size (dozens to hundreds of angstroms compared to hundreds of micrometers), He is significantly retained. However, for polycrystalline samples composed of dozens of nano- to micrometer sized crystallites, like it is the case for hematite and goethite, radiogenic He can diffuse out of the crystallites (e.g. Farley, 2018; Shuster et al., 2005; Gautheron and Zeitler, 2020). For hematite, a significant amount of diffusion experiments and calculation have been performed leading to similar values of few percent of He diffusion loss (e.g., Balout et al., 2017b; Evenson et al., 2014; Farley, 2018; Farley and Flowers, 2012; Lippolt et al., 1993). However, goethite (U-Th)/He (GHe) ages, on the contrary to hematite, seem to necessitate larger He diffusion correction. $^4\text{He}/^3\text{He}$ studies indicate diffusive He loss ranging from some percent (Hofmann et al., 2017) to 10-30 percent (Deng et al., 2017; Heim et al., 2006; Shuster et al., 2005). The distribution of crystallite sizes of those samples was not detailed in the latter contributions leading to unknown information about the diffusion domain size. In addition, the different parameters that might modify He diffusion in goethite such as chemical substitution, defect or radiation damage have never been investigated.

To bring additional information on the He retention process and the impact of iron-aluminum substitution, crystallographic defects and radiation damage on He diffusivity in goethite, we conducted a multi-scale theoretical study. We aim to develop an atomic-level understanding of the He-diffusion mechanism in goethite using a computational chemistry approach. Finally, the impacts of iron-aluminum substitution and crystallographic defects on the He diffusivity in goethite were investigated and resulting obstruction and trapping impact of defect and damage were modeled. All those data were compared to existing He diffusion literature data (Deng et al., 2017; Heim et al., 2006; Hofmann et al., 2017; Shuster et al., 2005; Vasconcelos et al., 2013) and used to predict the He diffusion behavior in goethite crystal for the purpose of goethite (U-Th)/He geological dating.

III.2 Review of activation energy experimental literature data

To our knowledge, six studies (Deng et al., 2017; Heim et al., 2006; Hofmann et al., 2017; Reiners et al., 2014; Shuster et al., 2005; Vasconcelos et al., 2013) have been conducted under-vacuum step heating diffusion experiments on polycrystalline goethite samples. All of these studies, except the one from Reiners et al. (2014) measured both natural ^4He as well as ^3He produced by proton bombardment in order to define the percentage of He lost by diffusion (Shuster and Farley, 2005). While five studies define the fraction of ^4He lost by diffusion using $^4\text{He}/^3\text{He}$ data, only two studies (Reiners et al., 2014; Shuster et al., 2005) report diffusion coefficients for He diffusivity in goethite. As the diffusion domains (i.e. crystallite size) of those samples are not known, extraction of diffusion data from those data should be taken with caution as demonstrated by Farley (2018). For this reason, to compare all available data with our theoretical results, we extracted only the diffusion parameter activation energy (E_a) from the diffusion experiments in the afore mentioned studies that provide $^4\text{He}/^3\text{He}$ diffusion data. Some experiments had to be rejected as their heating schedules were not suited for the calculation of the diffusion parameters. The linear parts of the diffusion experiments were fitted by least square regression. Only heating steps with temperatures $<250^\circ\text{C}$ were taken into consideration as above this temperature goethite transforms into hematite at ambient pressure. Furthermore, the activation energy (E_a) was generally retrieved from low ^3He and ^4He release fractions ($<10\%$ of the total gas for 92% of the used data), leading to its reliable estimation. Some experiments contained isothermal steps which had to be omitted for regression as they lead to an offset in Arrhenius plots. In this case several linear regressions (one for each linear portion) were calculated, and a mean was obtained from the different regressions. Arrhenius diagrams of all used diffusion experiments indicating the steps selected for regression can be found in the supplementary material (Appendix A). Errors on the E_a parameter correspond to the uncertainties of the linear regressions. The purpose of this work is to qualitatively compare the whole dataset highlighting the large differences and not to extract precise E_a value. The obtained activation energy values range from 1.21 ± 0.7 to 2.00 ± 0.17 eV (or 117 ± 17 to 193 ± 17 kJ/mol) (Table III-1).

In addition, the radiation damage densities (α -doses) of the literature samples were calculated, using the U and Th concentrations and the damage accumulation duration, which in our case is the (U-Th)/He age of the samples. We assumed that the crystallization age of the goethite is equivalent to the diffusive loss corrected (U-Th)/He ages. Unfortunately, for the data

by Heim et al. (2006) no U and Th contents were available, as the weight of the dated aliquots was not determined for this study. Then we estimated the U and Th contents using a U content of 25 ± 24 ppm, which is a typical value for supergene goethite, and the reported Th/U ratio.

Figure III-1 presents the compilation of the obtained activation energy E_a (in eV per particle) versus the diffusive loss fraction obtained from $^4\text{He}/^3\text{He}$ data (Fig. III-1A) and the damage density of the goethite (Fig. III-1B). The investigation of the activation energy retrieved from the literature data demonstrates that He diffusion is complex in goethite, with an almost unretentive He diffusion behavior at surface temperature for some goethites to more retentive ones. In addition, it highlights the role of radiation damage which seems to modify the He activation energy. A summary of the evaluated diffusion experiments and the obtained activation energy can be found in Table III-1.

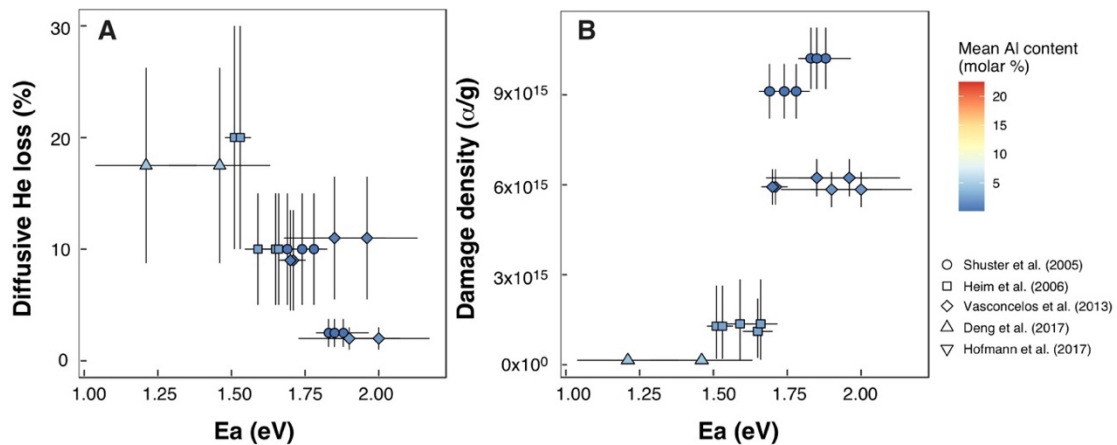


Figure III-1: Diffusive He loss fractions and activation energy (E_a) extracted from literature data of Deng et al. (2017); Heim et al. (2006); Hofmann et al. (2017); Shuster et al. (2005); Vasconcelos et al. (2013): (A) He diffusive loss extracted from $^4\text{He}/^3\text{He}$ data as a function of the activation energy E_a (in eV/particle). (B) Estimated damage density versus the activation energy E_a (in eV/particle). Shapes indicate the references, color the mean Al content of the samples. Note that the activation energy is given in eV unit to be coherent with the value of the theoretical study from this contribution, but conversion to kJ/mol is easily obtained as $1 \text{ eV} = 96,485 \text{ kJ/mol}$.

Revealing the radiation damage and Al-content impacts on He diffusion in goethite

Table III-1: Overview of published diffusion experiments by Deng et al. (2017), Heim et al. (2006), Hofmann et al. (2017), Shuster et al. (2005) and Vasconcelos et al. (2013) and extraction of the activation energy (E_a) from these experiments.

Reference	sample	Isotope	^4He	s	U	Th	(U-Th)/He	σ	Al	σ	Damage	Damage	Damage	E_a	$\pm\sigma$	E_a	$\pm\sigma$
			loss				age				dose	dose min	dose max				
			(%)	(ppm)			(Ma)	(molar%)			(a/g)			(kJ/mol)	(eV)		
Shuster et al. (2005)	BAH-F124-111.2	4	2.5	1.3	65.9	0.2	47.5	4.9	0.1		1.0×10^{16}	9.2×10^{15}	1.1×10^{16}	182	8	1.9	0.1
	BAH-F124-111.2	3	2.5	1.3	65.9	0.2	47.5	4.9	0.1		1.0×10^{16}	9.2×10^{15}	1.1×10^{16}	176	4	1.8	0
	BAH-F124-111.2	3 (given value)	2.5	1.3	65.9	0.2	47.5	4.9	0.1		1.0×10^{16}	9.2×10^{15}	1.1×10^{16}	178	3	1.9	0
	BAH-F124-114	4	10	5	228.1	0	12.3	1.6	0.2		9.1×10^{15}	8.2×10^{15}	1.0×10^{16}	168	8	1.7	0.1
	BAH-F124-114	3	10	5	228.1	0	12.3	1.6	0.2		9.1×10^{15}	8.2×10^{15}	1.0×10^{16}	171	3	1.8	0
	BAH-F124-114	3 (given value)	10	5	228.1	0	12.3	1.6	0.2		9.1×10^{15}	8.2×10^{15}	1.0×10^{16}	163	2	1.7	0
Heim et al. (2006)	YAN-02-01-A	3	10	5	ca. 25±24*	Th/U=0.9	11.4	1.4	2.5	1.7	1.1×10^{15}	2.3×10^{14}	2.2×10^{15}	159	5	1.7	0.1
	YAN-02-01-A	4	10	5	ca. 25±24*	Th/U=0.9	11.4	1.4	2.5	1.7	1.1×10^{15}	2.4×10^{14}	2.2×10^{15}	160	5	1.7	0.1
	YAN-02-01-D1	3	10	5	ca. 25±24*	Th/U=0.3	15.7	2.3	2.5	1.7	1.4×10^{15}	1.7×10^{14}	2.9×10^{15}	154	4	1.6	0.1
	YAN-02-01-D1	4	10	5	ca. 25±24*	Th/U=0.3	15.7	2.3	2.5	1.7	1.4×10^{15}	1.7×10^{14}	2.9×10^{15}	161	6	1.7	0.1
	YAN-02-01-D2	3	20	10	ca. 25±24*	Th/U=0.5	14.2	3.5	2.5	1.7	1.3×10^{15}	2.0×10^{14}	2.6×10^{15}	145	3	1.5	0
	YAN-02-01-D2	4	20	10	ca. 25±24*	Th/U=0.5	14.2	3.5	2.5	1.7	1.3×10^{15}	2.0×10^{14}	2.6×10^{15}	148	4	1.5	0
Vasconcelos et al. (2013)	LybP02-09-A1	4	9	4.5	38.3	88.7	30.7	3.1	0.5		5.9×10^{15}	5.3×10^{15}	6.5×10^{15}	166	4	1.7	0
	LybP02-09-A1	3	9	4.5	38.3	88.7	30.7	3.1	0.5		5.9×10^{15}	5.3×10^{15}	6.5×10^{15}	164	4	1.7	0
	LynP02-09-A2	4	2	1	36.8	91.4	30.7	3.1	1.9		5.8×10^{15}	5.3×10^{15}	6.4×10^{15}	183	17	1.9	0.2
	LynP02-09-A2	3	2	1	36.8	91.4	30.7	3.1	1.9		5.8×10^{15}	5.3×10^{15}	6.4×10^{15}	193	17	2	0.2
	LynP02-09-A3	4	11	5.5	39.6	96.1	30.7	3.1	0.9		6.2×10^{15}	5.6×10^{15}	6.9×10^{15}	190	17	2	0.2
	LynP02-09-A3	3	11	5.5	39.6	96.1	30.7	3.1	0.9		6.2×10^{15}	5.6×10^{15}	6.9×10^{15}	179	17	1.9	0.2
Deng et al. (2017)	ZK1217-91	3	17.5	8.8	19.1	0.3	2.4	0.2	4.3	4.2	1.5×10^{14}	1.4×10^{14}	1.7×10^{14}	117	17	1.2	0.2
	ZK1217-91	4	17.5	8.8	19.1	0.3	2.4	0.2	4.3	4.2	1.5×10^{14}	1.4×10^{14}	1.7×10^{14}	141	17	1.5	0.2
Deng et al. (2017)	4673	3	10.3	5.2	0.8	0.5	0.41	0	4.35	4.2	1.2×10^{12}	1.1×10^{12}	1.3×10^{12}				
	4673	4	10.3	5.2	0.8	0.5	0.41	0	4.35	4.2	1.2×10^{12}	1.1×10^{12}	1.3×10^{12}				
	ZK1217-20	3	14.3	7.2	40.5	0.4	4.42	0.1	4.35	4.2	5.8×10^{14}	5.2×10^{14}	6.4×10^{14}				
	ZK1217-20	4	14.3	7.2	40.5	0.4	4.42	0.1	4.35	4.2	5.8×10^{14}	5.2×10^{14}	6.4×10^{14}				
Hofmann et al. (2017)	FH-F1-BR01-irr	3	6.2	3.1	4.2	85.5	22.7**	9.2	22.5	13	1.8×10^{15}	1.6×10^{15}	2.0×10^{15}				
	FH-F1-BR01-irr	4	6.2	3.1	4.2	85.5	22.7**	9.2	22.5	13	1.8×10^{15}	1.6×10^{15}	2.0×10^{15}				
	FH-F2-BR04-irr	3	4.1	2.1	5.8	94	18.9**	0.7	22.5	13	1.7×10^{15}	1.6×10^{15}	1.9×10^{15}				
	FH-F2-BR04-irr	4	4.1	2.1	5.8	94	18.9**	0.7	22.5	13	1.7×10^{15}	1.6×10^{15}	1.9×10^{15}				
	FH-F3-BR03-3rdlayer-irr3	3	2.5	1.3	NA	NA	NA	NA	22.5	13	NA	NA	NA				
	FH-F3-BR03-3rdlayer-irr3	4	2.5	1.3	NA	NA	NA	NA	22.5	13	NA	NA	NA				
	FH-F4-BR05-4thlayer-irr4	3	1.9	1.0	8.1	65.4	18.9**	0.9	22.5	13	1.5×10^{15}	1.3×10^{15}	1.6×10^{15}				
	FH-F4-BR05-4thlayer-irr4	4	1.9	1.0	8.1	65.4	18.9**	0.9	22.5	13	1.5×10^{15}	1.3×10^{15}	1.6×10^{15}				
	FH-F5-BR05-core-irr3	3	6.4	3.2	8.1	65.4	18.9**	0.9	22.5	13	1.5×10^{15}	1.3×10^{15}	1.6×10^{15}				
	FH-F5-BR05-core-irr3	4	6.4	3.2	8.1	65.4	18.9**	0.9	22.5	13	1.5×10^{15}	1.3×10^{15}	1.6×10^{15}				

III.3 Computational details

We optimized an orthorhombic crystal structure model (Fig. III-2A) with the *Pnma* space group according to the international tables of crystallography (Hahn, 1996). The crystal lattice is composed of a unit cell containing 4 FeO(OH) groups (Fig. III-2A) and characterized by the following parameters: $a = 9.951 \text{ \AA}$, $b = 3.018 \text{ \AA}$ and $c = 4.598 \text{ \AA}$, with crystal growing preferentially along the *b*-axis (Cornell and Schwertmann, 2004). Note that different conventions for naming the axes exist so that $a = 4.598 \text{ \AA}$, $b = 9.951 \text{ \AA}$ and $c = 3.018 \text{ \AA}$ can be found commonly in the literature (e.g., Yang et al., 2006).

Firstly, the periodic-DFT computational approach (Hohenberg and Kohn, 1964; Kohn and Sham, 1965), has been used to study the He-diffusion in a goethite crystal, an approach that has successfully been used to study the He and Ne diffusion in hematite (Balout et al., 2017a; Balout et al., 2017b) and zircon (Gautheron et al., 2020), and He diffusion in apatite (Djimbi et al., 2015; Gerin et al., 2017). The details about the DFT calculations can be found in previous works (Bassal et al., 2020). After a first stage of computational simulations to adjust calculation parameters, interstitial sites were investigated for He insertion into the crystal model. Later, the Minimum-Energy Pathway (MEP) of the He diffusion process between two interstitial stable sites has been characterized using the Nudged-Elastic Band (NEB) method (Jónsson et al., 1998). In this respect, the migration energy (E_{mig}) between interstitial sites has been calculated.

In summary, the DFT calculation allows one to determine the insertion sites and the He insertion energies. The migration energy between the insertion sites is obtained using MEP calculation between insertion sites. The migration energy can be converted into activation energy for isotropic diffusion (Balout et al., 2017a). In case of the presence of trapping defects, an effective activation energy can be calculated by adding to the migration energy the difference between the insertion energies (Gautheron et al., 2020). Finally, in case of anisotropic diffusion, the KMC calculation allows one to calculate the effective activation energy along each axis, that incorporates the different insertion sites, migration and effective activation energies (Djimbi et al., 2005).

III.3.1 Lattice construction

First, a supercell characterized by $(\vec{v}_1 \times 3\vec{v}_2 \times 2\vec{v}_3)$ was defined in such a way that this supercell is large enough to avoid the volume relaxation after adding one He atom into the

crystal structure. The supercell was computed by duplicating the goethite unit cell in the three dimensions of space, one time according to the a -axis, three times according to the b -axis and two times according to the c -axis. This supercell was considered to investigate the He insertion in defect-free pure goethite (Fig. III-2A). Then, the impact of Fe-Al substitution on the He diffusivity in goethite was examined. The substitution of Fe by Al atoms leads to the replacement of the typical Fe–O bonds by new shorter Al–O bonds, due to the difference of Van der Waals radius of the Al atom compared to the Fe atom (Fig. III-2B). Consequently, Fe-Al substitution induces a global contraction of the overall size of the goethite crystal depending on the substitution percentage. Moreover, the Fe-Al substitution modifies the magnetic properties and the Néel temperature of goethite (Fleisch et al., 1980). For the purpose of this study, we studied the influence of Fe-Al substitution by replacing one pair of Fe atoms by one pair of Al atoms (substitution fraction = 8.33%), two pairs of Fe atoms by two pairs of Al atoms (substitution fraction = 16.66%) and three pairs of Fe atoms by three pairs of Al atoms (substitution fraction = 25%). As the Al^{3+} is a diamagnetic cation and thus substituting paramagnetic Fe^{3+} by diamagnetic Al^{3+} perturbs the spin neutrality of our system, we choose to substitute Fe with Al atoms in such a way that each pair of Al atoms substitutes one pair of opposite-spin Fe atoms. This computational strategy was chosen according to DFT studies in the literature. It is worth noting that the Fe-Al substitutions were, intentionally, localized around the chosen sites in the crystal lattice, in order to make visible the Fe-Al substitution effect on the He diffusion, until the extreme situation. To develop a rational understanding of the impact of the Fe-Al substitution on He diffusion we increase systematically the local Fe-Al substitution, and thus increase the local Fe-Al constraint on the insertion site until the point that adding supplement Al atoms does not significantly impact the crystal structure. In this case constraints reach the maximum level (the highest local constraints).

Finally, crystallographic intrinsic defects and irradiation damage were investigated (see Bassal et al. (2020) for additional and complete details). Defect such as Schottky defect was performed by the elimination of a complete group of $\text{FeO}(\text{OH})$ from the goethite supercell ($\vec{v}_1 \times 3\vec{v}_2 \times 2\vec{v}_3$) inducing the formation of a crystal vacancy, which is considerably large and reduces significantly the constraints once a He atom occupies the free space generated by the crystal defect. A second type of defect was created based on the work of Blanchard et al. (2010) for hematite, by considering the elimination of one Fe atom from the octahedral unit of the crystal system. In this case, 3 H atoms were added in such a way that each H atom ensures a

new covalent bond with each O atom to replace the 3 removed Fe–O bonds. In the following, this type of defect will be named as hydrated defect. Different positions of H atoms have been examined to find the most stable structure. A third case of damage caused by radioactive alpha recoil decay was investigated theoretically as large damage of several dozens of nanometers in size. Although this type of damage cannot be computed directly by DFT due to the limited supercell size, its impact on the He diffusion in goethite can be simulated and computed considering an insertion site with an insertion energy of zero eV. In other words, the cavity (amorphized area), generated by the recoil damage, is large enough to minimize the constraints on the new insertion site created inside the cavity.

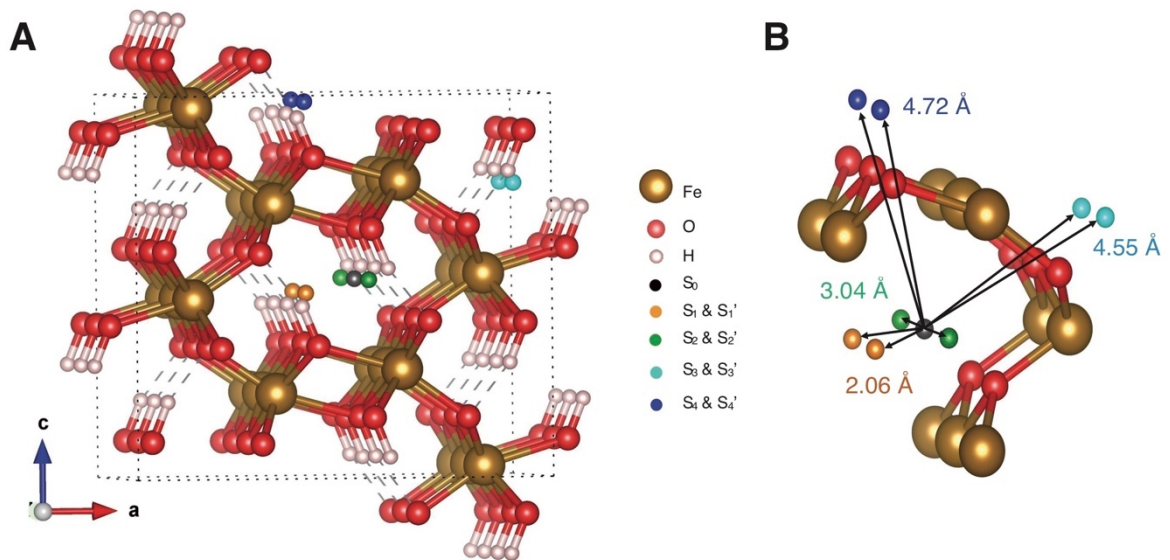


Figure III-2: (A) The $(\vec{v}_1 \times 3\vec{v}_2 \times 2\vec{v}_3)$ super-cell used to investigate the He insertion into goethite (Fe in brown, O in red, H in white). Point in black correspond to the interstitial site position S_0 . Points in orange, green, cyan and bleu corresponds to the neighbor interstitial sites to S_0 . (B) Different insertion sites (S_1 , S_2 , S_3 , S_4) in the vicinity of S_0 site, with the associated distance, where the OH are not reported.

III.3.2 Atomic scale

Periodic DFT (Hohenberg and Kohn, 1964; Kohn and Sham, 1965) calculations were investigated for energy minimizations of goethite crystal structures (unit cell, supercell, and supercell with one He atom) and thus to determine the different He insertions sites. The supercell was selected as having a low volume expansion (+1.86%) and characterized by $a = 9.997 \text{ \AA}$, $b = 9.124 \text{ \AA}$ and $c = 9.178 \text{ \AA}$. All calculations were spin-polarized, considering the magnetic properties of goethite, due to the presence of iron atoms. Simulations were carried out with the Vienna Ab initio Simulation Package (VASP) (Kresse and Furthmüller, 1996; Kresse

and Hafner, 1993) using the generalized gradient approximation (GGA), in particular, the PBE (Perdew et al., 1996) functional exchange correlation potential.

After the optimization of the supercell, all insertion sites (interstitial and vacancy sites) were identified and investigated in the whole crystal structure. The insertion energy is the energy difference between the complex system (super-cell + He atom) and the separated systems (super-cell without He atom) – equation (III-1):

$$E_{insertion} = E_{system} - (E_{goethite} + E_{He}) \quad (III-1)$$

To describe the He jumps between two neighboring interstitial sites (between one interstitial site and its neighboring vacancy site), inside the crystal goethite structure, we used the NEB method (Jónsson et al., 1998), which is a method to simulate the minimum energy pathway (MEP) of He migration and to provide the energy barrier between two given initial and final states of a transition process. The NEB method is a chain-of-states method (Elber and Karplus, 1987; Pratt, 1986) in which a chain (string) of images (He atoms at differences positions) is used to describe the minimum energy pathway (MEP). The saddle point of the obtained optimized MEP corresponds to the transition state (TS) of the migration process. The Climbing Image NEB (CI-NEB) method (Henkelman et al., 2000) was used for more accuracy on the transition state: After a regular NEB calculation, a more rigorous convergence is carried out in the saddle point. Then, the exact migration barrier can be calculated, and the jump probability can be determined using the vibration frequencies. Vibrational Frequencies, NEB and CI-NEB calculations have been performed using the VASP TST Tools (source, codes, scripts) of the University of Texas in Austin (<https://theory.cm.utexas.edu/vtsttools/>).

For any possible jump between sites the NEB method computes the energy barrier between the initial and final states. It corresponds to the so-called migration energy E_{mig} , defined by the equation (III-2):

$$E_{mig} = E - E^{init} \quad (III-2)$$

where E^{init} and E are, respectively, the initial and transition states energies.

According to the Transition State Theory (TST) (Vineyard, 1957; Voter, 1986) the jump rate of the He atom Γ can be expressed as:

$$\Gamma = \nu_0 e^{\frac{-E_{mig}}{k_B T}} \quad (III-3)$$

The attempt frequency, ν_0 , can be defined using the Vineyard approximation (Vineyard, 1957), based on the frequencies of the He atom, derived from the harmonic approximation of

the energy landscape, at the ground and transition states (see Bassal et al., 2020 for more details).

Afterward, the jump probabilities for all possible transitions $S_0 \rightarrow S_{1,2,3\dots n}$ between an initial site S_0 and all the neighboring ones $S_{1,2,3\dots n}$ can be calculated. For each initial site, S_0 , the total probability of jump, Γ^{Tot} , can be obtained as the sum of the probabilities of jump from this site S_0 to all its neighbors. The residence time is calculated as the inverse of the total jump probability corresponding to the time required for passing from the initial site to the neighboring ones.

III.3.3 Macroscopic scale

When the crystal is homogeneous, like a perfect periodic lattice, it is possible to derive analytically the diffusion coefficient from the above-defined jump rates. On the contrary if accidents, like obstructions or trapping sites, are spread randomly the periodicity is broken and the favored tool giving the diffusion coefficient is a Monte Carlo simulation of the random walk between the sites. This simulation is named Kinetic Monte Carlo (KMC) (Bortz et al., 1975; Gillespie, 1976) and it follows the time-dependent trajectories of the He atom motion using the transition rates determined from the atomic scale described above.

The simulation is run at a given temperature T and the diffusion coefficient is derived from the spread of the displacement of the He atom for an ensemble of trajectories. For example if the variance of the displacement along x is noted v_x , the diffusion coefficient, D_x , at temperature T is based on the Einstein (1905) equation (III-4).

$$D_x = \frac{v_x}{2t} \quad \text{(III-4)}$$

where t is the mean time to run the trajectory. The same relation applies for the coordinates y and z . In the goethite and zircon cases the diffusion coefficient along the three directions are very different, revealing the highly anisotropic nature of the diffusion and justifying the explicit calculation of values along the coordinates.

He diffusion is a thermally activated process and can be described by the Arrhenius law (Arrhenius, 1889; Laidler, 1996) and equation (III-5):

$$D = D_0 \times e^{\frac{-E_a}{k_B \times T}} \quad \text{(III-5)}$$

where D_0 is a temperature-independent factor, k_B is the Boltzmann constant and T is temperature in kelvin. The activation energy (E_a) corresponds to the energy that one atom

needs to jump from one free site to a free neighbor one. The same simulation is repeated for different temperatures and the coefficient D is calculated for each simulation. Using the Arrhenius law, in particular its logarithmic form, the activation energy E_a and the pre-exponential factor D_0 can be extracted using equation (III-6):

$$\ln(D) = -E_a \left(\frac{1}{k_B \times T} \right) + \ln(D_0) \quad (\text{III-6})$$

In this case, E_a and D_0 correspond respectively to the slope and the intercept of the obtained curve in a plot of $\ln(D)$ vs. $\frac{1}{T}$.

III.4 Results

III.4.1 Theoretical goethite FeO(OH) structure

In the case of defect-free FeO(OH) goethite, four types of interstitial insertion sites are identified and they are located inside the free spaces in the open channels between the octahedral units (Fig. III-2A). Two symmetric stable interstitial sites S_0 and S_1 are identified inside the channel, in such a way that each site occupies a middle position from its two adjacent hydrogen atoms. These two symmetric sites repeat periodically along the main axis of each channel following a zig-zag pathway. From this point of view, each interstitial site S_0 is surrounded by 4 equivalent neighbors: 2 neighboring sites (S_2 and S_2') on the same hydrogen line along the main axis of the open channel (the b -axis) and 2 equivalent neighboring sites (S_1 and S_1') localized beside on the second line of hydrogen atoms. Figure III-2B presents the different symmetric insertion sites and the distances between each pair of sites. Longitudinally, a distance of 3.04 Å between two successive sites is found, whereas a diagonal distance of 2.06 Å between two successive sites is obtained. All insertion sites are characterized by an insertion energy of 1.38 eV (Table III-2). In this case we can define two types of He jump inside the same channel: the diagonally jump characterized by a distance of 2.06 Å, and the longitudinally one characterized by a distance of 3.04 Å (Fig. III-2B). Furthermore, two additional types of transition can be defined considering the periodicity of the interstitial sites in the adjacent and parallel channels. For each interstitial site S_0 , we can identify a first pair of neighbor sites, S_3 and S_3' , which is located in the first adjacent channel and located diagonally from the initial site S_0 (Fig. III-2B). These sites are characterized by a distance of 4.55 Å from S_0 . Moreover, we can identify a second pair of neighbor sites, S_4 and S_4' , which is located in the second adjacent channel, and located vertically from S_0 . These sites are characterized by a distance of 4.72 Å from S_0 (Fig. III-2B).

Four pairs of atomic jumps between the initial site S_0 and its four pairs of neighbor sites are defined as illustrated on Figure III-2B: $S_0 \rightarrow S_1$ & $S_0 \rightarrow S_1'$, $S_0 \rightarrow S_2$ & $S_0 \rightarrow S_2'$ (inside-channel jumps) and $S_0 \rightarrow S_3$ & $S_0 \rightarrow S_3'$, $S_0 \rightarrow S_4$ & $S_0 \rightarrow S_4'$ (between-channels jumps). Thus, four types of migration pathways could be identified and are characterized by their migration energies $E_{mig(S_0 \rightarrow S_1)}$, $E_{mig(S_0 \rightarrow S_2)}$, $E_{mig(S_0 \rightarrow S_3)}$, $E_{mig(S_0 \rightarrow S_4)}$.

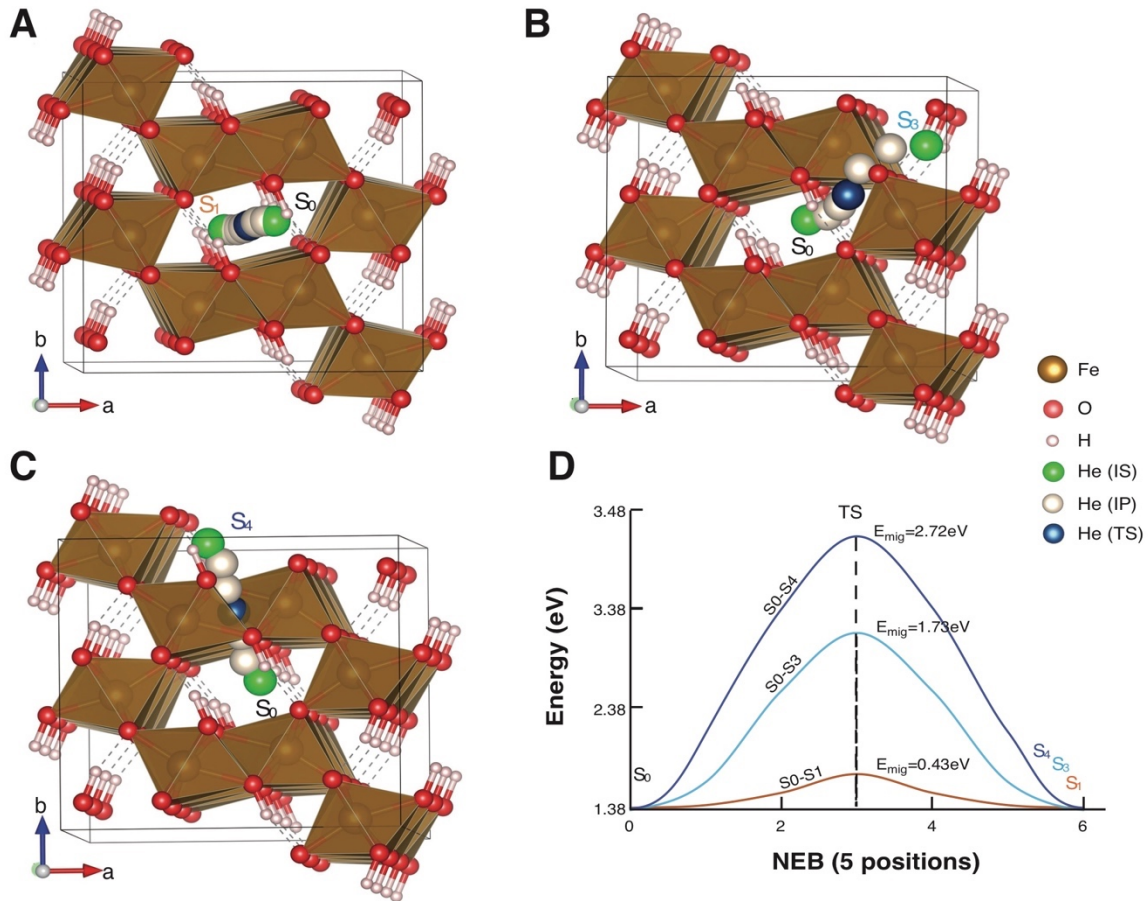


Figure III-3: Migration pathways of $S_0 \rightarrow S_1$ inside-channel atomic jump (A) and $S_0 \rightarrow S_3$ and $S_0 \rightarrow S_4$ between-channel atomic jumps (B and C) of He atom in defect-free pure goethite and their corresponding MEPS plot diagram (D). The pathways consist of 5 system positions. He atoms at the initial and final equilibrium states are represented by green spheres. He atom at the transition states is represented by dark blue spheres. IS, IP and TS refer to Insertion Site, Intermediate Position and the Transition State.

Figure III-3 presents the results for each migration energy calculated between the insertion sites. For the $S_0 \rightarrow S_1$ diagonal jump, the migration pathway is characterized by a migration energy of 0.43 eV (Table III-2, Figs. III-3A and D), whereas the migration energy for the $S_0 \rightarrow S_2$ longitudinal jump (inside-channel) along the b -axis between 2 successive sites S_0 and S_2 , is higher with a value of 10 eV (Table III-2; not presented in Fig. III-3). Finally, migration energy to the neighboring sites S_3 and S_4 , yield value of $S_0 \rightarrow S_3$ of 1.73 eV and $S_0 \rightarrow S_4$ of 2.72 eV (Table III-2, Figs. 3B, C and D). The $S_0 \rightarrow S_2$, $S_0 \rightarrow S_3$ and $S_0 \rightarrow S_4$ migration energies are high and

disable those jumps. This shows that the diffusion in goethite is possible only along $S_0 \rightarrow S_1$ (y direction, b -axis). The pre-exponential factor D_{0y} can be deduced from the normal frequencies at the site and the transition point, it is equal to $13.6 \times 10^{-4} \text{ cm}^2 \cdot \text{s}^{-1}$.

III.4.2 Theoretical Fe-Al goethite structure

The defect-free substituted Fe-Al goethite structure is subject to a global volume contraction of several percent in the case of substitution by one, two and three Fe-Al pairs, respectively (Table III-2). This contraction is localized mainly around the two interstitial sites S_0 and S_1 . Depending on the positions of the Fe-Al substitutions along the channel, interstitial sites do not have the same constraints and the same insertion energy. The latter in this case depends on the Fe-Al substitutions steric constraints on the interstitial site (distances of the site from Al atoms). Figure III-4 sketches the effect of the Al along the pathway when 1, 2 and 3-Al pairs are substituted. In the case of a 1 pair, close to the Al atoms the sites are named S_0' and S_1' and their insertion energy amounts to 1.53 eV (Table III-2), slightly higher than for S_0 and S_1 due to the local shrinking of the channel. In the case of substitution by two Fe-Al pairs, the He insertion energy rises up to 1.63 eV for S_0' and 1.76 eV for S_1'' (Table III-2), whereas in the case of three Fe-Al pairs, the He insertion energy is 1.63 eV for S_0' and S_1' , and 1.73 eV for S_0'' and S_1'' (Table III-2).

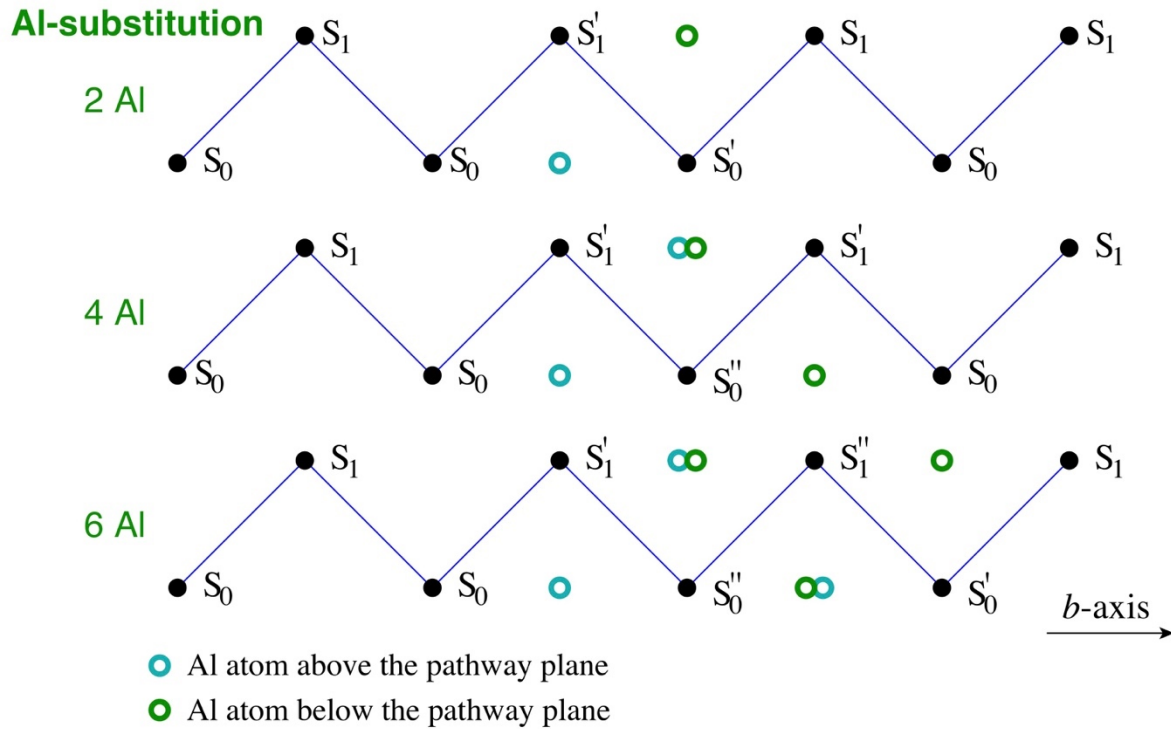


Figure III-4: Schematic representation of the pathway along the b -channel when 1, 2 or 3 pairs of Fe atoms are substituted by Al atoms. The open circles mark the approximate position of Al, cyan when they are above the pathway plane, green when they are below. Close to the Al atoms the sites S_0 and S_1 go up in energy and they are labelled with ' and '' according to the impact of the level of shrinking of the channel.

The migration energy was only computed for the inside-channel diagonal jump. In the case of one pair of Al the migration energy E_{mig} , for the $S_0' \rightarrow S_1'$ jump is about 0.42 eV (Fig. III-5). By symmetry for the reverse direction $S_1' \rightarrow S_0'$ the migration energy is the same. This barrier is almost the same as in the non-substituted case, however the effective activation energy is higher because the diffusing atom has first to climb up to S_0' (or S_1') before crossing this barrier. Indeed, it can be demonstrated, and confirmed by the KMC simulation, that the effective barrier is the sum of 0.42 eV and the energy difference $S_1' - S_0 = 0.15$ eV. In the case of two pairs of Al, the migration energies for the jumps $S_1'' \rightarrow S_0'$ and $S_0' \rightarrow S_1''$ are respectively 0.42 eV and 0.55 eV, but again the effective activation energy is higher as the energy difference $S_1'' - S_0 = 0.38$ eV has to be added to 0.42 eV. In the case of three pairs of Al, E_{mig} between S'' sites remains constant at 0.42 eV and the effective activation energy is $0.42 + 0.35 = 0.77$ eV. It is clear that, with two pairs of Al centered around the insertion site we reach the maximum level of Fe-Al substitution contribution on the He diffusion. Adding other Al atoms (for example three pairs of Al or more) will not change the insertion energy (max ~ 1.76 eV), even the migration energy (max ~ 0.42 eV) (Table III-2, Fig. III-5). We did not compute the migration energies for the jumps

to S_2 , S_3 and S_4 (trans-channel jumps), because considering the high energy barriers (i.e. migration energy) calculated for this type of atomic jump in the case of the pure goethite, the energy barriers of these transitions will be higher given the additional constraint of the Fe-Al substitution. However, the diffusion behavior between pure goethite and Fe-Al substituted goethite slightly diverge. The constraints due to the Fe-Al substitutions lead to increase the insertion energy of He atom by 10 – 28 % compared to FeO(OH) goethite. The migration energies are similar compared to that found in the case of pure goethite lattice and range from 0.42 to 0.55 eV (Table III-2, Figs. III-3 and III-5). Effective activation energies are, in these cases, between 0.57 to 0.93 eV depending on the Fe-Al substitution constraints contribution. The corresponding pre-exponential factor D_{0y} is $127 \times 10^{-4} \text{ cm}^2 \cdot \text{s}^{-1}$ and can increase up to $846 \times 10^{-4} \text{ cm}^2 \cdot \text{s}^{-1}$. The effective migration energy is slightly different from the migration energy (Table III-2).

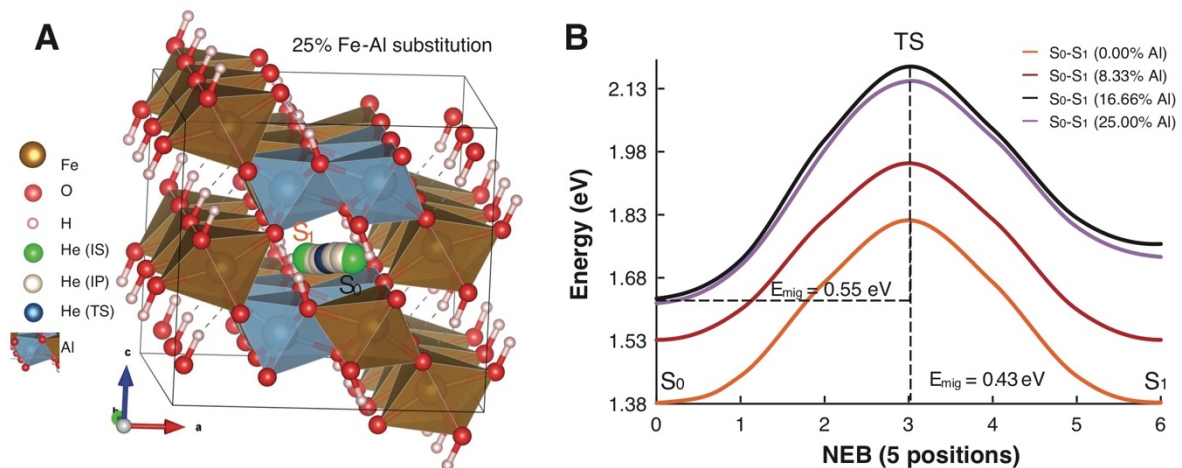


Figure III-5: Migration pathway of $S_0 \rightarrow S_1$ atomic jump of He atom in the case of 25% Fe-Al substituted defect-free goethite (A) and the MEPs comparative plot diagram depending of Fe-Al substitution portion for 8.3%, 16.6% and 25.0% Fe-Al substitution percentages (B). The pathways consist of 5 linked system positions. He atoms at the initial and final equilibrium states are represented by green spheres. He atom at the transition state is represented by dark blue sphere. IS, IP and TS refer to Insertion Site, Intermediate Position and the Transition State.

III.4.3 Goethite containing defects

The three types of defects (hydrated defect, Schottky defect and radiation damage) modeled in this study present different migration energy (i.e., energy barriers), depending on the defect size. For all cases and similarly to the Fe-Al substituted goethite, the migration energies for the between-channel atomic jumps ($S_0 \rightarrow S_2$, $S_0 \rightarrow S_3$ and $S_0 \rightarrow S_4$) have not been

computed, because of the high energy barriers expected for these types of atomic jumps (see Section III.4.2).

In case of small defect such as crystallographic hydrated defect, the formation of a new stable insertion site S_{vacancy} (S_4), inside the small vacancy, is generated by the elimination of the Fe atom and the addition of 3 H atoms. In this case, the insertion energy of a He atom inside the generated free spaces is about 1.40 eV (Table III-2, Fig. III-6A). Intermediate site TS_H which is more stable compared to TS^*_H allows the migration to the site $S_{1'}$ characterized by a lower insertion energy of 1.23 eV (Fig. III-6A). The migration energy and effective activation energy between the vacancy to the crystal lattice are similar and of 0.60 eV (Table III-2).

In the case of the creation of a larger defect such as the FeO(OH) Schottky defect where one complete group of FeO(OH) is eliminated of the goethite structure, a new insertion site S_{vacancy} (called in this case S_{00}) is formed (Fig. III-6B). This new site is localized inside the generated free space of the crystallographic vacancy and characterized by an insertion energy of 0.52 eV (Table III-2). The He migration between the crystallographic vacancy (site S_{00}) and the adjacent unoccupied channel (site S_1) is characterized by an energy barrier (E_{mig}) of 1.08 eV (Table III-2, Fig. III-6B) which corresponds to the migration energy difference between the new interstitial site S_{00} and the transition state $TS^!$. Again, the effective activation energy is higher as He has to reach TS. The calculation of the effective activation energy, has also been obtained by using KMC calculation for FeO(OH) goethite and goethite containing one and two pairs of Al substitution and E_a values are of 1.29, 1.43 and 1.79 eV respectively (Table III-2).

Revealing the radiation damage and Al-content impacts on He diffusion in goethite

Table III-2: Structural properties of goethite ($\vec{v}_1 \times 3\vec{v}_2 \times 2\vec{v}_3$) super-cell and He insertion energies for interstitial sites (S_0 and S_1) and vacancy sites (S_{00} and S_H), from PBE+U Density Functional Theory simulations. Migration energy of He in goethite depending on the Fe-Al substitution portion and the crystal defect type (vacancy size), and volume contraction of the crystal model depending on the Fe-Al substitution portion, in goethite. KMC calculation results for the D_0 and effective activation energy for the different case.

Supercell	$(\vec{v}_1 \times 3\vec{v}_2 \times 2\vec{v}_3)$			%V	$E_{insertion}$ (eV)			E_{mig} (eV)				D_0	Effective
	a (Å)	b (Å)	c (Å)	contraction	S_0	S_1	($S_{vacancy}$)	$S_0 \rightarrow S_1$	$S_0 \rightarrow S_2$	$S_0 \rightarrow S_3$	$S_0 \rightarrow S_4$	($\text{cm}^2 \cdot \text{s}^{-1}$)	(eV)
Defect-free crystal													
Pure goethite	9.997	9.124	9.178	0	1.38	1.38	-	0.43	10	1.73	2.72	13.6×10^{-4}	0.43
1 pair Fe-Al 8%	9.956	9.079	9.149	1.2	1.53	1.53	-	0.42	-	-	-	127×10^{-4}	0.57
2 pairs Fe-Al 16%	9.906	9.044	9.122	2.37	1.76	1.63	-	0.55	-	-	-	846×10^{-4}	0.93
3 pairs Fe-Al 25%	9.864	9.001	9.096	3.51	1.73	1.63	-	0.53	-	-	-	-	-
								$S_{vacancy} \rightarrow S_1$					
Defect crystal													
Hydrated defect FeO(OH)	9.967	9.155	9.244	-	1.28	1.23	1.4	-	-	-	-	-	0.6
Schottky defect													
FeO(OH)	9.951	9.197	9.229	-	1.3	1.24	0.52	-	-	-	-	-	1.29
1 pair Fe-Al substitution	-	-	-					-	-	-	-	-	1.43
2 pairs and more Fe-Al substitution	-	-	-					-	-	-	-	-	1.79
Recoil damage													
FeO(OH)	-	-	-		-	-	-	-	-	-	-	-	1.81
1 pair Fe-Al substitution	-	-	-		-	-	-	-	-	-	-	-	1.95
2 pairs and more Fe-Al substitution	-	-	-		-	-	-	-	-	-	-	-	2.31

Finally, we associated a recoil damage as a large free space which is large enough to minimize the constraints and cancel the interaction to neighbors on the new generated site $S_{vacancy}$ inside this free space. In another word, compared to the Schottky defect vacancy, the free space is much larger in such a way that the constraints on the $S_{vacancy}$ be negligible. The He jump trajectory between the new generated vacancy site and its neighboring interstitial site (S_1 inside the channel) is similar to that obtained in the case of FeO(OH) Schottky defect, but the energy barrier is higher. As the constraints on the He atom inside the vacancy is considerably minimized (insertion energy ~ 0 eV, Table III-2), the maximum energy barrier to ensure the He jump outside the vacancy increase from 1.81 to 2.31 eV for the different goethite compositions (Table III-2).

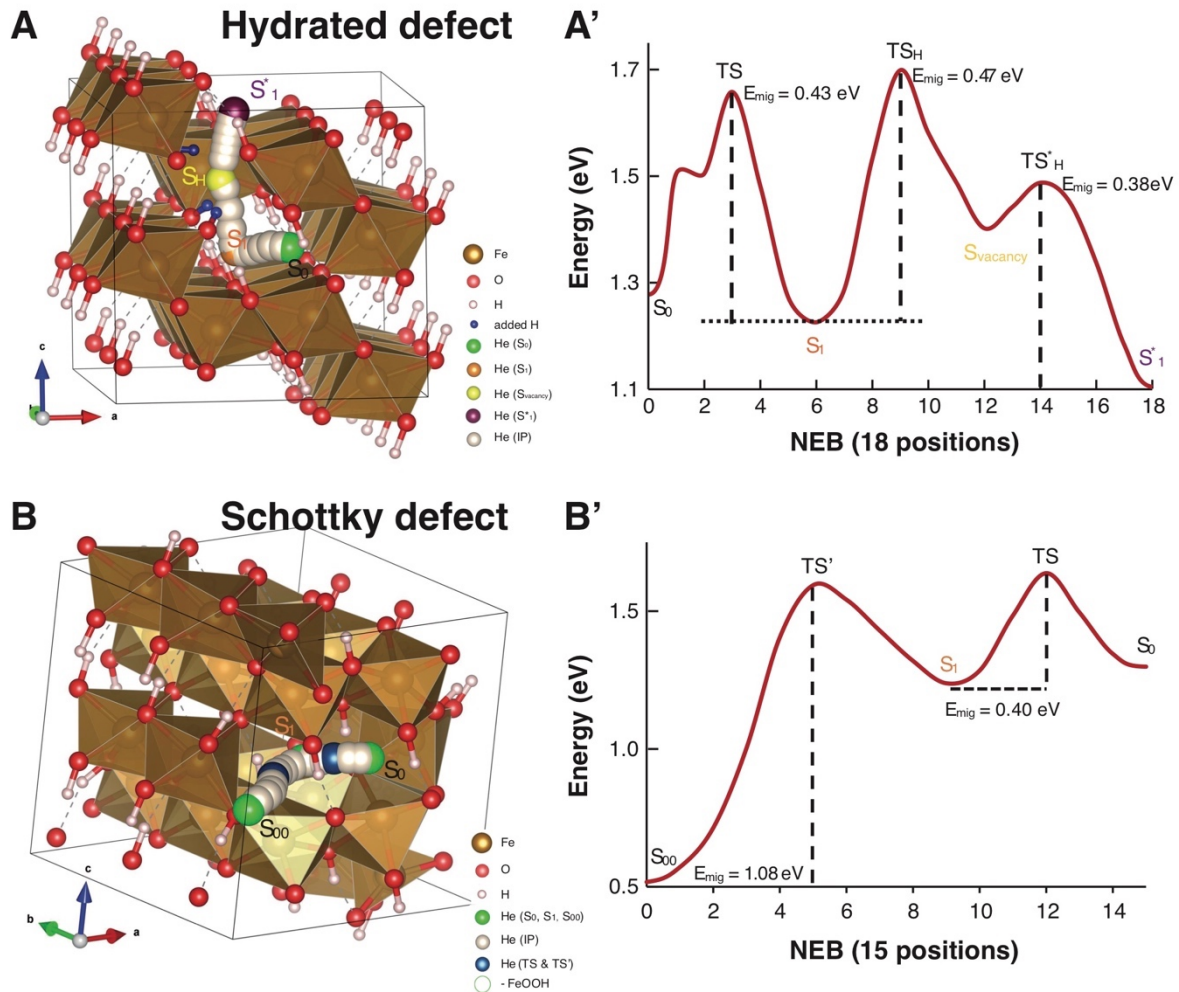


Figure III-6: (A) Migration pathway of $S_0 \rightarrow S_1 \rightarrow S_{vacancy} \rightarrow S^*_{1}$ atomic jumps and their MEPs plot diagram in the case of hydrated Fe vacancy. (A') He atoms at the equilibrium states are represented by green, orange, yellow, and plum spheres. The $S_{vacancy}$ (S_4) corresponds to the position of He atom inside the hydrated Fe vacancy site. TS_H and TS^*_H correspond to the transition states for the He jumps outside the hydrated Fe vacancy (to the 2 neighbor unoccupied channels). (B) Migration pathway of $S_{00} \rightarrow S_1 \rightarrow S_0$ atomic jumps of He atom and their corresponding MEPs plot diagram in the case of FeO(OH) Schottky defect. (B') The pathway consists of 14 linked system positions. He atoms at equilibrium states are represented by green spheres. He atoms at the transition states (TS & TS') are represented by dark blue spheres. IS , IP and TS refer to Insertion Site, Intermediate Position and the Transition State.

III.5 Discussion

III.5.1 He diffusion in defect-free FeO(OH) and AlFeO(OH) goethite

He diffusion computation results for the FeO(OH) goethite and Al-substituted goethite $Al_xFe_{1-x}O(OH)$ indicate that He diffuses mainly along the main axis of the unoccupied channel ($S_0 \rightarrow S_1$) along the b -axis, to form a global zig-zag pathway of He jumps characterizing an anisotropic migration pathway. The diffusion will spread only along the b -channel, because the migration energy to jump from S_0 to S_2 or S_3 or S_4 is very high and no diffusion will be possible at low temperature (Table III-2). The direct jump $S_0 \rightarrow S_2$ is energetically unfavorable, due to its

high migration energy of 10 eV. In this respect, to jump from S_0 to S_2 He atom needs to jump twice, $S_0 \rightarrow S_1$ and then $S_1 \rightarrow S_2$, with an energetic effort of 0.43 eV for each step to arrive to the final site S_2 , instead of overcoming the high energy barrier of the direct longitudinal jump (10 eV, Table III-2). In addition, the high energy barriers along $S_0 \rightarrow S_3$ and $S_0 \rightarrow S_4$ sites are also very high compared to the energy barrier along $S_0 \rightarrow S_1$ (1.73 and 2.72 eV, Table III-2) and the atomic jumps between channels require high temperature. KMC simulations performed in this study gives an effective activation energy of 0.43 eV that is identical to the migration energy along $S_0 \rightarrow S_1$. This confirms that no He atoms can migrate along the other directions. Consequently, migrations between-channels could not be expected at lower temperature value such as Earth surface temperature (i.e., 10-40°C). He diffusion in goethite is then purely anisotropic and can only develop along the b -axis. This is a specific case, although anisotropic diffusion is common to several minerals, as zircon (Gautheron et al., 2020) for example, goethite is the extreme case where only a 1D diffusion is possible.

From the theoretical calculations obtained for pure goethite and Al-goethite we can conclude that He is not retained in the goethite structure even at surface temperature, as using those activation energy and frequency factor values, an (U-Th)/He age of 0 will be obtained for any kind of thermal history. Al substitutions increase He retention but not sufficiently to retain He at surface temperature. These results reveal that the Fe-Al substitution has minor impact on the He diffusivity, as even with the maximum constraints of Fe-Al substitution, the activation energy (0.93 eV) remains insufficient to retain the He atom at low temperature. For both pure goethite and Fe-Al substituted goethite, diffusion is strongly anisotropic and is characterized by relatively low activation energy.

These results are in contradiction with the He-retention revealed experimentally in natural goethite (Deng et al., 2017; Heim et al., 2006; Hofmann et al., 2017; Shuster et al., 2005; Vasconcelos et al., 2013) (Fig. III-1). However, this is expected as the natural He diffusion data exhibit a complex behavior (Fig. III-1), where differences in He retention (obtained from the $^4\text{He}/^3\text{He}$ data) related to alpha dose are observed. In addition, strong discrepancy between results obtained using theoretical and experimental approaches has already been reported for zircon (Gautheron et al., 2020; Reich et al., 2007; Saadoune et al., 2009).

III.5.2 He diffusion in goethite containing defect or radiation damage

He diffusion data from natural goethite suggests that radiation damage strongly impacts He retention, and the theoretical approach brings a detailed insight about the phenomena. As

already discussed, diffusion along the other directions ($S_0 \rightarrow S_2$, $S_0 \rightarrow S_3$ and $S_0 \rightarrow S_4$) is energetically hindered by the high barrier and cannot occur at low temperature, implying that the strong He retentivity should be associated with the blocking of the He diffusion in goethite along the b -channel axis (y -axis). All different kinds of defects or pathways obstruction associated with alpha damage can affect He diffusion. Vacancies slow down diffusion by trapping He whereas pathway obstruction along the b -axis will also affect diffusion by hindering the He to reach the open end of the channel. In the peculiar case of 1D diffusion the obstruction is very efficient because it cannot be bypassed.

Different types of defects such as hydrated defect, Schottky defect and recoil damage on He diffusion have been investigated in goethite and Al-goethite structures. Hydrated defect cannot be a valid defect candidate for trapping He as this defect only slightly modifies the insertion energy compared to defect-free pure goethite (1.23 eV compared to 1.38 eV respectively, Table III-2). The 3 added hydrogen atoms reduce the vacancy size and then increase the steric constraints on the He atom once it is inserted inside the hydrated Fe vacancy (Fig. III-6A). Consequently, this damage type will not trap He, as the energy barriers are too low and no He will be retained leading to an (U-Th)/He age of 0 for any kind of thermal history (Table III-2).

On the other hand a Schottky defect impacts the He retention because the insertion energy strongly drops down to 0.52 eV, implying that the vacancy is lower than normal diffusion sites by 0.86 eV, and it has an efficient trapping effect, especially at low temperature because the effective activation energy is 1.28 eV. The presence of Schottky defect in Fe-Al substituted goethite modifies even more the He diffusivity due to the contribution of the Fe-Al substitution constraints. The effective activation energy increases to 1.43 eV and even to 1.79 eV depending on the Fe-Al substitution constraints contribution. Even if the Schottky defect is a valid candidate to trap He and slow down diffusion, because the computed E_a values are in the range of the ones estimated for natural goethite, the trapping energy of this defect cannot explain the higher E_a value of ~ 2 eV in natural goethite (Fig. III-1A). To compare more quantitatively the diffusion results, we computed the closure temperature (Dodson, 1973) using a cooling rate of $10^\circ\text{C}/\text{Myr}$ and a diffusion domain of $0.1 \mu\text{m}$. This yields interesting results as the value increases with the Al content, from 21°C for a pure goethite to 52°C for one Al pair substitution to 132°C for two Al pair substitution. Similar behavior can be obtained when looking at the He retention factor (t'/t) using an arbitrary isothermal holding time of $t=100$ Myr with a temperature of 25°C .

The simulated (U-Th)/He age (t') for this holding time is modeled using HeFTy software (Ketcham, 2005), and the He retention factor (t'/t) will increase from 0 up to 1. Those values are also in the low range of the ones obtained for natural goethite (Fig. III-1), showing that this type of defect is a valid candidate to trap He in the goethite structure.

Finally, recoil damage produced during alpha decay of U and Th in natural goethite is the most accountable defect to explain He retention as the effective computed maximum activation energies range between 1.81, 1.95 and 2.31 eV depending on Fe-Al substitution constraints (Table III-2). Those values are in complete agreement with the highest E_a values obtained on natural goethite (Fig. III-1 and Table III-1). In addition, the obtained closure temperatures present highly retentive values, with T_c of 137°C for a pure goethite, 168°C for one pair Al substitution and 148°C for two pairs Al substitution, and for each case the consequence is that the He retention factor (t'/t) is equal to 1. This shows that radiation damage seems to be the main parameter governing He diffusion, as already suggested, and modeled for apatite and zircon crystal, showing the importance of damage modifying He behavior in minerals (i.e., Farley, 2000; Reiners, 2005; Shuster et al., 2006). The experimental and theoretical results show in addition that the Al-content in goethite has an impact on the He diffusion in goethite containing damage.

III.5.3 Modelling He diffusion in macroscopic natural goethite samples

The main results of the theoretical study, supported by the available data, can be summarized as follows:

- 1) He diffusion occurs only along the b -axis, it is a pure 1D diffusion along the b -channels. In a defect-free crystal the diffusion is very fast, and the He is immediately released.
- 2) As a consequence of the 1D diffusion, any obstructing atom in the b -channel blocks the diffusion because the energy barrier to jump in a parallel channel is too high.
- 3) Any vacancy can trap the He which will stay there at surface temperature.

This picture is comparable to diffusion in zircon, but goethite is an extreme case owing to the high barrier to jump into a parallel channel which makes the diffusion purely 1D. According to 1) any open pristine channel releases the He it receives from the α decays. This has to be modified by the fact that α -decays produce obstruction-vacancy pairs which bring some retention by the mechanisms 2) and 3). The scope of the model is to quantify this retention effect. The mineral crystallites are generally small of the order of $\sim 0.1 \mu\text{m}$, and

contain a limited number of diffusion sites, but they are lumped in a compact configuration which can close the diffusion channels for the internal ones. For those channels the retention is complete even if they are not damaged because He cannot escape at the end of the channels. The other crystallites may have channels opened on one side and closed on the other side if they have grown up from a heap of other crystallites, and they may be opened on both sides if they are free. We focus now on those fully or half-opened channels.

Right after the goethite crystallization, the channel is almost devoid of obstructions and traps, so that He diffuses quickly, reaches the open end and is released. The irradiation displaces crystal atoms thereby producing obstructions. The deposition of one obstruction in the channel already has a retention effect in case of closure at one end: only He which is deposited in the open segment escapes, the rest been kept inside. In this picture the probability to escape is the ratio of the length of that segment to the total length of the channel. The density of obstructions increases linearly in time, so that the open segment decreases and the escape probability drops. Trapping vacancies are created as well in the channel. Obviously, He deposited between traps or between traps and obstructions have no chance to get out of the channel. However, the traps behave in a different way than obstructions. To illustrate the phenomenon let us consider a damage in the vicinity of the open end of the channel. Would it be an obstruction, a He located between it and the aperture would escape surely. For a trap it is not always the case because along its diffusion path the He atom may still fall into the trap, so that the trap has a distant action. It can be proved from a theoretical study of the random walk that the probability to escape is proportional to the distance to the trap of the initial location of the He. When the He location neighbors the vacancy the probability is 0, whereas when it is close to the channel aperture, it is 1. As a consequence, in average, He atoms located in the terminal open segment have the probability $\frac{1}{2}$ to escape (it was 1 for an obstruction).

The above considerations lead to a modelling of the impact of obstructions and traps. We consider a segment of length of the crystallite L (L is arbitrary), representative of the b -channel. Obstructions are placed randomly on the segments, so that their average inter-distance be $\langle d \rangle$. The same is done for traps. If no trap/obstruction is present in the segment, the He release fraction is 1. If the end defect (the closest to the aperture) is an obstruction at distance l from the open side, the contribution to the release fraction is l/L . If it is a vacancy the contribution is $l/(2L)$. The result depends obviously on the locations of obstructions and traps, so we consider many configurations, about 10^6 , having the same $\langle d \rangle$ and we average the

release fraction over all configurations. As the result depends only on the ratio $\langle d \rangle / L$, we plot the release fraction versus this quantity in Figure III-7A. The continuous curve corresponds to a channel open at both sides, whereas the dashed one is for a channel closed on one side, giving a lower release as expected. For a large $\langle d \rangle$ the concentration of obstructions and vacancies is low, and often the channels does not even contain any defect, it leads to a total release (fraction equal to 1). When $\langle d \rangle$ is small the open segments at each side shorten and the release fraction drops in proportion to $\langle d \rangle$.

So far, we only considered a given $\langle d \rangle$, or equivalently a given concentration of defects. This concentration builds up linearly in time and one has to integrate the released fraction over time. Due to the above-mentioned linearity the integration depends only on the final concentration of defects. If we denote $x = \langle d \rangle / L$, and $X = \langle d_f \rangle / L$, where $\langle d_f \rangle$ is the final mean distance, the final release fraction of the channel is given in eq. (III-7):

$$F = \frac{1}{T} \int_0^T f(\langle d \rangle / L) dt = X \int_X^\infty \frac{f(x)}{x^2} dx \quad (\text{III-7})$$

where $f(x)$ is the suited function plotted in Figure III-7A. The right-hand form of the above equation results from the $1/t$ dependence of $\langle d \rangle$. The integrated release fraction depends only on the ratio of the final mean distance $\langle d_f \rangle$ to the channel length L . Those quantities can be related to more physical ones.

The formula of the elementary mesh of the crystal is $\text{Fe}_4\text{O}_4(\text{OH})_4$ and it contains 2 sites distant by 1.5 Å along the b-channel. Therefore, in 1g of crystal the total number of sites is 3.4×10^{21} . This crystal is subject to α emissions. According to the simulation package SRIM (Ziegler, 2008) an α decay displaces on average 1700 atoms, creating as many vacancies and obstructions. Let us denote D the α dose in 10^{15} α/g , the number of obstructions or vacancies in 1 g is $1.7 \times 10^{18} \times D$. The average distance between obstructions/vacancies, expressed in number of sites, is $3.4 \times 10^{21} / (1.7 \times 10^{18} \times D) = 2000/D$. Taking into account the inter-site distance the mean distance $\langle d \rangle$ between obstructions/vacancies, expressed in μm is $\langle d_{\mu\text{m}} \rangle = 0.3/D$, and finally $X = 0.3 / (L_{\mu\text{m}} D)$, which is used to calculate the integrated release fraction F .

Figure III-7B presents the dependence of the release fraction with the dose D for different channel lengths. The continuous curves are for channels open on both sides, the dashed ones are for channels open on one side only, the other side being closed by the contact with another crystallite. The longer the channel length, the lower the release fraction. At short times this fraction is always equal to 1 because without damage the diffusion is fast and free in the channel. It should be stressed that the release does not depend on dimensions other than

the channel length. This is a consequence of the 1D diffusion and the high energy barrier to jump to a neighboring channel.

Considering the complexity of the structure of crystallites, the simulations were done one step further, at least in a statistical way. As already mentioned, some crystallites may have their *b*-channels closed at both sides due to the tight contact with other crystallites which grew up from the former. For those closed crystallites the release fraction is always 0, whatever their length. The other crystallites, fully open or half open along the elongated *b*-axis direction, have a distribution of lengths. As there is no available information about the statistical distribution of lengths, we just consider a few test cases to illustrate the behavior. We assume that 60% in volume of the channels are closed on both sides and that 40% are open on one side only. This is representative of an internal block of closed crystallites from which half open crystallites grew up. We considered two possible crystallite lengths: 0.1 μm and 0.5 μm and a mixture of the two lengths with the same probability. The results are plotted in Figure III-7C. The low dose release dropped down to 0.4 due to the absence of contribution from the 60% closed channels, and the population of mixed lengths shows up as intermediate between its end members. The comparison of experimental results from natural goethite samples, quantum calculation and modeling demonstrate that He diffusion in goethite is governed by the influence of hydrated, Schottky defects and/or recoil damage. The defects/damage will create pathway obstructions and traps and modify strongly the He diffusion. In addition, we demonstrate theoretically that goethite with Al will be more retentive compared to a pure goethite crystal. Finally, we also show that even if the crystallite size plays a role, as soon as crystallites are intergrowing and damage dose accumulates, He is strongly retained in goethite. The main outcome in this picture is that the He loss is not governed by an activation energy. It is completely determined by the geometrical assembly of the crystallites where the important size is the length of the elongated *b*-axis and by the density of obstructions and vacancies, which can be accounted also in a geometrical way.

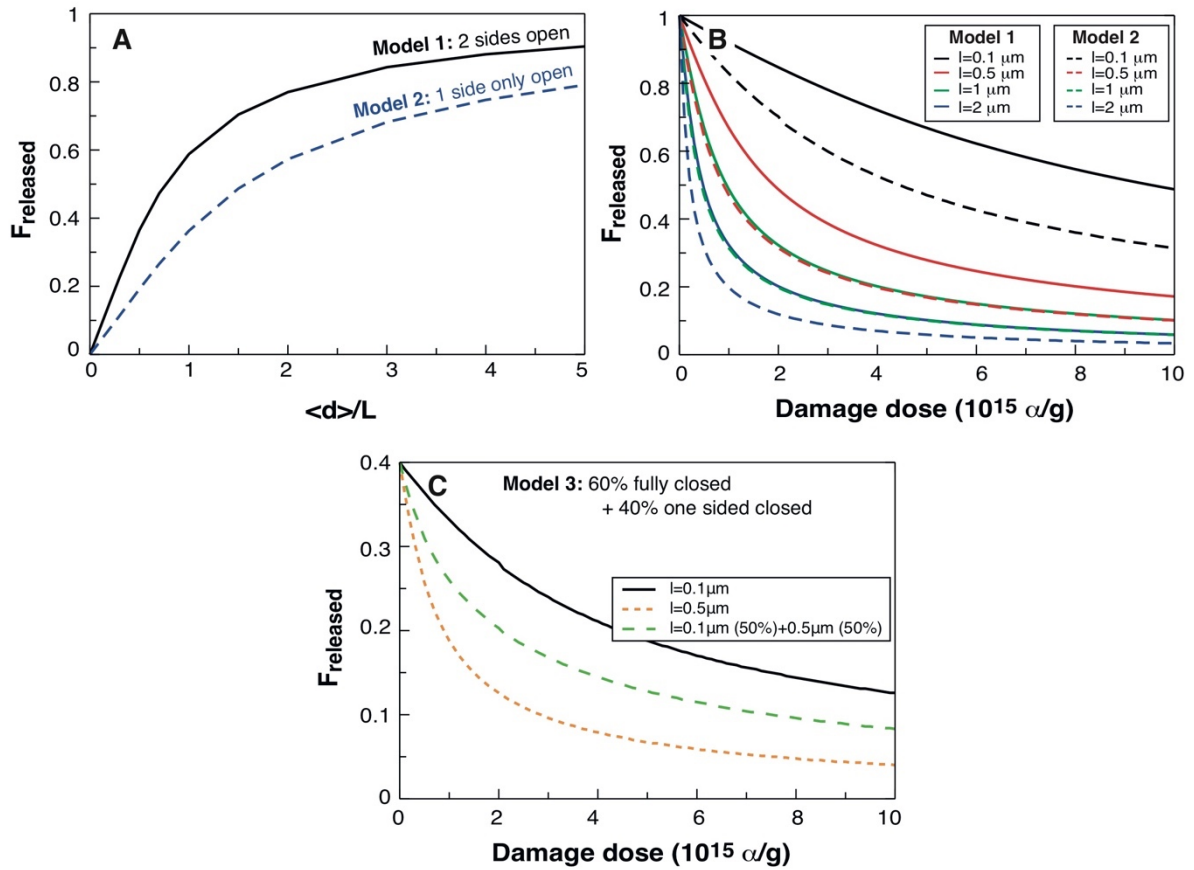


Figure III-7: Modeled released He fraction as a function of the irradiation dose. (A) Steady release fraction for fully open channels (continuous) and half-open channels (dashed). (B) Integration of the functions displayed in (A) over the time accounting for the variation of defect concentration for fully open channels (continuous) and half-open ones (dash). (C) Release fraction for a population of crystallites made of 60% closed channels and 40% half-open having two possible lengths (0.1 and 0.5 μm) and of mixture of them.

III.5.4 Discussion on He retention data based on the model

Experimental data as reported in Figures III-1 and III-8 illustrate that the activation energy and He loss fraction correlate with the radiation damage density of natural samples. The samples with higher damage density loosed less He. This is perfectly in line with the theoretical results which predict that radiation damage lowers the He diffusivity by pathway obstruction and creation of traps, and that those mechanisms are particularly efficient in the case of pure 1D diffusion. The correlation of the two values indicates that they are closely related as expected. In detail, diffusive He loss is anti-correlated with the damage dose (Fig. III-8), indicating that He retention seems to be linked to the radiation damage that reduces diffusion along the b-axis. In addition, Figure III-8 illustrates that the samples by Hofmann et al. (2017) have a different behavior than the other samples. Although the samples of Hofmann et al. (2017) have comparably low damage densities, they are very retentive and loosed less He

than expected. The high Al contents of these samples (10-35%) could be a reason for the increased retentivity as our calculations show that Al substitution leads to an increase of the activation energy.

One main result of the DFT calculation, and the modelling based on its result, is that He diffusion in goethite is purely anisotropic and fast along the *b*-axis, implying that He is retained only at the favor of obstructions blocking the diffusion and vacancies trapping the atoms in the goethite structure. The computed activation energy for radiation damaged goethite along the *b*-axis is in the range of the value obtained along the other *a*-*c* plan ($S_0 \rightarrow S_3$ $E_a=1.73$ eV; Table III-2). In case of highly damaged goethite, diffusion along the *b*-axis will be similar to diffusion along the *a*-*c*-plan leading to a more isotropic diffusion. As a consequence, the GHe system has potential to be used as a thermochronometer in case of buried goethite. However, the thermal history could be only obtained with the determination of the diffusion domain size.

Our results imply that the crystallite size will play a role for low damaged goethite and will then progressively become a secondary parameter. In addition, the blocking by closed ends of the channels either due to the compact packing will in addition reduces He loss by diffusion. Due to the one-dimensional diffusion behavior the only relevant dimension is the channel length. Figure III-7C shows a dependence with this crystallite length, but it is entangled with other quantities like the fraction of fully closed channels. In fact, all experimental He diffusion data have been obtained on goethite with different crystallite sizes (~ 200 nm to μm in size), even if the information is mainly missing in some studies (Deng et al., 2017; Heim et al., 2006; Hofmann et al., 2017; Reiners et al., 2014; Shuster et al., 2005; Vasconcelos et al., 2013). One can also observe on Figure III-8A that He is significantly blocked in goethite for different crystallite sizes, and for a dose higher than $\sim 6 \times 10^{15}$ α/g , He diffusive loss is around 10% or lower. It is important to note that He diffusive loss obtained on natural samples is also similar for the same damage dose and overlap to each other. However, for natural goethite, the other end of crystallite prism is probably also blocked due to natural defects and intergrowths. The crystallization habit (botryoidal, mixed crystallites) should be an important feature that will help He retention by blocking crystallite prism ends. In addition, in the future, the determination of the He diffusion behavior for highly damaged goethite (i.e., very rich U-Th and old goethite samples) would be important to estimate the possible interconnection of damage leading to a change in He retention, as observed in zircon (Ketcham et al., 2013).

Based on this study we can develop a good understanding of the He diffusion in goethite and define the key factors like crystal defects, obstructions, and Fe-Al substitution on the He retention. As He is almost completely lost from the crystal before sufficient damage is accumulated, (U-Th)/He ages in goethite are underestimated. We propose to apply adapted diffusion correction factors for (U-Th)/He dating depending on the radiation damage density and the Al content of the samples. For samples with little Al, we propose the following correction factors depending on the radiation damage density, following the results of the published $^4\text{He}/^3\text{He}$ diffusive loss data presented in Figure III-8B and 8C: $15\pm 10\%$ diffusive loss correction for samples with radiation damage densities $< 1\times 10^{15}$ α/g , $10\pm 7\%$ diffusive loss correction for radiation damage densities from 1×10^{15} to 1×10^{16} α/g , and $5\pm 5\%$ diffusive loss correction for radiation damage densities $> 1\times 10^{16}$ α/g (Fig. III-8B). For samples containing a significant amount of Al no major correction is needed and we propose to apply a $5\pm 5\%$ diffusive loss correction (Fig. III-8C).

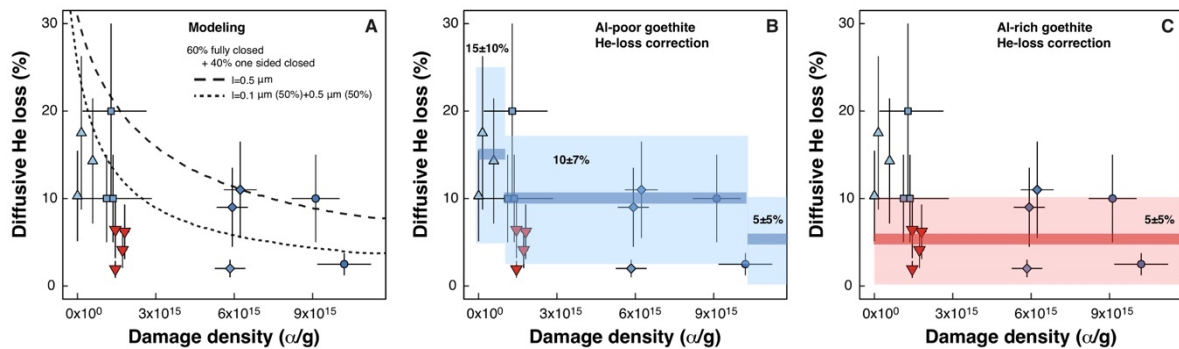


Figure III-8: Diffusion He loss values evolution as a function of the damage density. (A) comparison with simulation results shown on Fig. III-7C for a $0.5 \mu\text{m}$ and a mixing between crystallite of 0.5 and $0.1 \mu\text{m}$ are additionally reported. (B) and (C) proposed He loss correction for Al-poor goethite and Al-rich goethite respectively. Filled blue filled symbols goethite with low Al content (< 5 wt%) and filled red symbols represent samples with high Al content of the samples (> 20 wt%). Circles: Shuster et al. (2005); squares: Heim et al. (2005); diamonds: Vasconcelos et al. (2013); triangles: Deng et al. (2017) and inverted triangles: Hofmann et al. (2017).

III.6 Conclusion

He diffusion in goethite has been investigated for the purpose of the understanding of the (U-Th)/He chronometer, as He can be lost by diffusion due to the finely divided and polycrystalline structure of goethite. A complete review of experimental He diffusion data in natural goethite has been performed allowing us to qualitatively evaluate the He activation energy for all data and reveal the strong link of the activation energy and He diffusion loss with the damage dose. The investigation of He diffusion in goethite was performed thanks to a multi-

scale study, where we modeled the possible role of Al chemical substitution, defects produced during crystal growth together with alpha damage on He diffusion. The calculation shows that He diffuses easily in defect-free and Al-Fe goethite only along the *b*-axis that is the elongated axis of goethite, as the energy needed to migrate along the *a* and *c*-axis is unfavorable, leading to a pure anisotropy. By trapping He atoms, crystallographic defects and alpha-recoil damage lower the He diffusivity in goethite, by creating pathway obstructions and traps, a process that is even larger for Al-goethite. The obtained He diffusion parameters for defect goethite are similar to He diffusion data obtained in natural goethite from the literature, allowing us to demonstrate the systematic evolution of the diffusion coefficients with damage dose and the impact of Al on He retention. Finally, the He retention in goethite is also governed by the crystallite size that is the channel length along the *b*-axis and damage density, the latter becoming the most important parameter when damage accumulates. The only possible diffusion direction, along the *b*-channels, makes the release highly dependent on the way the crystallites are clustered because the channels can be closed by tight contact, thereby stopping any diffusion. We finally propose a He loss correction ranging from 15±10 % to 5±5 % for goethite containing little Al substitution depending on the damage dose, and 5±5 % for goethite containing a large amount of Al.

Acknowledgments

This study and F. Bassal and B. Heller salaries have been funded by the Agence National de la Recherche – grant no. ANR-17-CE01-0012 – RECA: Reconstructing the climate impact on laterite formation. All calculations were performed on the HPC cluster of the radiochemistry team at the “Institut de Physique Nucléaire d’Orsay” (Orsay, France). We would like to thank Christophe Diarra for his precious help in managing the IPNO cluster (GRIF) and Guillaume Morin for the meaningful discussions during the writing. Ken Farley is thanked for the exchange about Heim et al. (2006) contribution. Associated editor C. France-Lanord and the two anonymous reviewers are thanked for their help in improving the manuscript.

References

Arrhenius, S. (1889) Über die Dissociationswärme und den Einfluss der Temperatur auf den Dissociationsgrad der Elektrolyte. Für Phys. Chem. 4U, 96.

- Ault, A.K., Gautheron, C. and King, G.E. (2019) Innovations in (U-Th)/He, fission-track, and trapped-charge thermochronometry with applications to earthquakes, weathering, surface-mantle connections, and the growth and decay of mountains. *Tectonics* 38, 3705-3739.
- Balout, H., Roques, J., Gautheron, C. and Tassan-Got, L. (2017a) Computational investigation of the interstitial neon diffusion in pure hematite, α -Fe₂O₃. *Computational Materials Science* 128, 67-74.
- Balout, H., Roques, J., Gautheron, C., Tassan-Got, L. and Mbongo-Djimbi, D. (2017b) Helium diffusion in pure hematite (α -Fe₂O₃) for thermochronometric applications: a theoretical multi-scale study. *Computational and Theoretical Chemistry* 1099, 21-28.
- Bassal, F., Roques, J. and Gautheron, C. (2020) Neon diffusion in goethite, α -FeO(OH): A theoretical multi-scale study. *Physics and Chemistry of Minerals* 47, 14.
- Blanchard, M., Morin, G., Lazzeri, M. and Balan, E. (2010) First-principles study of the structural and isotopic properties of Al- and OH-bearing hematite. *Geochim. Cosmochim. Acta.* 74, 3948–3962.
- Bortz, A.B., Kalos, M.H. and Lebowitz, J.L. (1975) A new algorithm for Monte Carlo simulation of Ising spin systems. *J. Comput. Phys.* 17, 10-18.
- Brantley, S.L. and Lebedeva, M. (2011) Learning to read the chemistry of regolith to understand the Critical Zone. *Annu. Rev. Earth Planet. Sci.* 39, 387-416.
- Cornell, R.M. and Schwertmann, U. (2004) *The Iron Oxides: Structure, Properties, Reactions, Occurrences and Uses.*
- Deng, X.D., Li, J.-W. and Shuster, D. (2017) Late Mio-Pliocene chemical weathering of the Yulong porphyry Cu deposit in the eastern Tibetan Plateau constrained by goethite (U-Th)/He dating: Implication for Asian summer monsoon. *Earth Planet. Sci. Lett.* 472, 289-298.
- Djimbi, D.M., Gautheron, C., Roques, J., Tassan-Got, L., Gerin, C. and Simoni, E. (2015) Impact of apatite chemical composition on (U-Th)/He thermochronometry: an atomistic point of view. *Geochim. Cosmochim. Acta.* 167, 162-176.
- Dodson, M.H. (1973) Closure temperature in cooling geochronological and petrological systems. *Contributions to Mineralogy and Petrology* 40, 259-274.
- Dutrizac, J.E. and Soriano, C. (2018) Behaviour of the rare earths during goethite (α -FeOOH) precipitation from sulphate-based solutions. *Hydrometallurgy* 176, 87-96.

- Einstein, A. (1905) Über die von der molekularkinetischen Theorie der Wärme geforderte Bewegung von in ruhenden Flüssigkeiten suspendierten Teilchen. *Ann. Phys.* 322, 549–560.
- Elber, R. and Karplus, M. (1987) A method for determining reaction paths in large molecules: Application to myoglobin. *Chem. Phys. Lett.* 139, 375-380.
- Evenson, N.S., Reiners, P.W., Spencer, J.E. and Shuster, D. (2014) Hematite and Mn oxide (U-Th)/He dates from the Buckskin-Rawhide detachment system, western Arizona: gaining insights into hematite (U-Th)/He systematics. *American Journal of Science* 314, 1373-1435.
- Farley, K.A. (2000) Helium diffusion from apatite: general behavior as illustrated by Durango fluorapatite. *Journal of Geophysical Research* 105, 2903-2914.
- Farley, K.A. (2018) Helium diffusion parameters of hematite from a single-diffusion-domain crystal. *Geochim. Cosmoch. Acta* 231, 117-129.
- Farley, K.A. and Flowers, R. (2012) (U-Th)/Ne and multidomain (U-Th)/He systematics of a hydrothermal hematite from Eastern Grand Canyon. *Earth Planet. Sci. Lett.* 359-360, 131-140.
- Fleisch, J., Grimm, R., Grübler, J. and Gütlich, P. (1980) Determination of the aluminum content of natural and synthetic aluminogoethites using Mössbauer spectroscopy. *J Phys.* 41, 169-170.
- Gautheron, C., Djimbi, D.M., Roques, J., Balout, H., Ketcham, R.A., Simoni, E., Pik, R., Seydoux-Guillaume, A.M. and Tassan-Got, L. (2020) A multi-method, multi-scale theoretical study of He and Ne diffusion in zircon. *Geochim. Cosmochim. Acta.* 268, 348-367.
- Gautheron, C. and Zeitler, P.K. (2020) Noble Gases Deliver Cool Dates from Hot Rocks. *Elements* 16, 303-309.
- Gerin, C., Gautheron, C., Oliviero, E., Bachelet, C., Djimbi, D.M., Seydoux-Guillaume, A.M., Tassan-Got, L., Sarda, P., Roques, J. and Garrido, F. (2017) Influence of vacancy damage on He diffusion in apatite investigated at atomic to mineralogical scales. *Geochim. Cosmochim. Acta.* 197, 87-103.
- Gillespie, D.T. (1976) A general method for numerically simulating the stochastic time evolution of coupled chemical reactions. *J. Comput. Phys.* 22, 403–434.
- Hahn, T. (1996) *International Tables of Crystallography*, International Union of Crystallography London

- Heim, J.A., Vasconcelos, P., Shuster, D., Farley, K.A. and Broadbent, G. (2006) Dating paleochannel iron ore by (U-Th)/He analysis of supergene goethite, Hamersley province, Australia. *Geology* 34, 173-176.
- Henkelman, G., Uberuaga, B.P. and Jónsson, H. (2000) A climbing image nudged elastic band method for finding saddle points and minimum energy paths. *The Journal of Chemical Physics* 113, 9901.
- Hofmann, F., Reichen, B. and Farley, K.A. (2017) Evidence for >5Ma paleo-exposure of an Eocene–Miocene paleosol of the Bohnerz Formation, Switzerland. *Earth Planet. Sci. Lett.* 465, 168-175.
- Hohenberg, P. and Kohn, W. (1964) Inhomogeneous Electron Gas. *Phys. Rev.* 136, B864–B871.
- Jónsson, H., Mills, G. and Jacobsen, K.W. (1998) Nudged Elastic Band Method for Finding Minimum Energy Paths of Transitions.
- Ketcham, R.A. (2005) Forward and inverse modelling of low-temperature thermochronology data, in: Reiners, P.W.a.E., T.A. (Ed.), *Low temperature thermochronology: techniques, interpretations and applications. Reviews in mineralogy and geochemistry*, pp. 275-314.
- Ketcham, R.A., Guenther, W.R. and Reiners, P.W. (2013) Geometric analysis of radiation damage connectivity in zircon, and its implications for helium diffusion. *American Mineralogist* 98, 350-360.
- Kohn, W. and Sham, L.J. (1965) Self-Consistent Equations Including Exchange and Correlation Effects. *Phys. Rev.* 140, A1133–A1138.
- Kresse, G. and Furthmüller, J. (1996) Efficiency of ab-initio total energy calculations for metals and semiconductors using a plane-wave basis set. *Computational Materials Science* 6, 15-50.
- Kresse, G. and Hafner, J. (1993) Ab initio molecular dynamics for liquid metals. *Phys. Rev. B.* 47, 558(R).
- Laidler, K.J. (1996) A glossary of terms used in chemical kinetics, including reaction dynamics (IUPAC Recommendations 1996). *Pure Appl. Chem.* 68, 149.
- Lippolt, H., Wernicke, R.S. and Boschmann, W. (1993) ⁴He Diffusion in Specular Hematite. *Phys. Chem. Minerals* 20, 415-418.
- Nahon, D. (2003) Weathering in tropical zone. Significance through ancient and still active mechanisms. *C. R. Geoscience* 335, 1109-1119.

- Nahon, D. and Tardy, Y. (1992) Chapter I.3 - The Ferruginous Laterites. Handbook of Exploration Geochemistry 4, 41-55.
- Perdew, J.P., Burke, K. and Ernzerhof, M. (1996) Generalized Gradient Approximation Made Simple. Phys. Rev. Lett. 77, 3865-3868.
- Pratt, L.R. (1986) A statistical method for identifying transition states in high dimensional problems. J. Chem. Phys. 85, 5045-5048.
- Reich, M., Ewing, R.C., Ehlers, T. and Becker, U. (2007) Low-temperature anisotropic diffusion of helium in zircon: Implications for zircon (U-Th)/He thermochronometry. Geochim. Cosmochim. Acta. 71, 3119-3130.
- Reiners, P.W. (2005) Zircon (U-Th)/He thermochronometry, in: Reiners, P.W., Ehlers, T.A. (Eds.), Thermochronology, Reviews in Mineralogy and Geochemistry, pp. 151-179.
- Reiners, P.W., Chan, M.A. and Evenson, N.S. (2014) (U-Th)/He geochronology and chemical compositions of diagenetic cement, concretions, and fracture-filling oxide minerals in Mesozoic sandstones of the Colorado Plateau GSA Bulletin 126, 1363-1383.
- Saadoune, I., Purton, J.A. and De Leeuw, N.H. (2009) He incorporation and diffusion pathways in pure and defective zircon $ZrSiO_4$: A density functional theory study. Chem. Geol. 258, 182-196.
- Shuster, D. and Farley, K.A. (2005) $^4He/^3He$ thermochronometry: theory, practice, and potential complications, in: Reiners, P.W. a.E., T.A. (Ed.), Low-temperature thermochronology: techniques, Interpretations, and Applications.
- Shuster, D., Flowers, R. and Farley, K.A. (2006) The influence of natural radiation damage on helium diffusion kinetics in apatite. Earth Planet. Sci. Lett. 249, 148-161.
- Shuster, D., Vasconcelos, P., Heim, J. and Farley, K.A. (2005) Weathering geochronology by (U-Th)/He dating of goethite. Geochim. Cosmochim. Acta 69, 659-673.
- Vasconcelos, P.M., Heim, J.A., Farley, K.A., Monteiro, H. and Waltenberg, K. (2013) $^{40}Ar/^{39}Ar$ and (U-Th)/He – $^4He/^3He$ geochronology of landscape evolution and channel iron deposit genesis at Lynn Peak, Western Australia. Geochim. Cosmochim. Acta. 117, 283-312.
- Vasconcelos, P.M., Reich, M. and Shuster, D. (2015) The paleoclimatic signatures of supergene metal deposits. Elements 11, 317-322.
- Vineyard, G.H. (1957) Frequency factors and isotope effects in solid state rate processes. Journal of Physics and Chemistry of Solids 3, 121-127.

- Voter, A.F. (1986) Classically exact overlayer dynamics: Diffusion of rhodium clusters on Rh(100). *Phys. Rev. B.* 35, 6819-6829.
- Yang, H., Lu, R., Downs, R.T. and Costin, G. (2006) Goethite, [alpha]-FeO(OH), from single-crystal data. *Acta Crystallogr. Sect. E.* 62, i250–i252.
- Ziegler, J.F. (2008) SRIM-2008 The stopping range of ions in matter. United States Naval Academy, Annapolis.

IV Reading the climate signals hidden in bauxite

Available online at www.sciencedirect.com**ScienceDirect***Geochimica et Cosmochimica Acta* 323 (2022) 40–73**Geochimica et
Cosmochimica
Acta**www.elsevier.com/locate/gca

Reading the climate signals hidden in bauxite

Beatrix M. Heller^{a,b,*}, Silvana Bressan Riffel^{a,c}, Thierry Allard^b,
Guillaume Morin^b, Jean-Yves Roig^d, Renaud Couëffé^d, Geoffrey Aertgeerts^e,
Alexis Derycke^a, Claire Ansart^a, Rosella Pinna-Jamme^a, Cécile Gautheron^a

^a *GEOPS, Université Paris Saclay, CNRS, Bat. 504, 91405 Orsay cedex, France*^b *IMPMC, UMR 7590, CNRS, Sorbonne Université, MNHN, IRD, 4 place Jussieu, 75252 Paris cedex 05, France*^c *UFRGS, Federal University of Rio Grande do Sul, Av. Bento Gonçalves, 9500, Institute of Geosciences, 91509-900 Porto Alegre, Brazil*^d *BRGM, 3 avenue Claude Guillemin, BP 6009, 45060 Orléans Cedex 2, France*^e *BRGM, Domaine de Suzini, BP 10552, 97333 Cayenne Cedex 2, France*

Received 21 October 2021; accepted in revised form 15 February 2022; Available online 22 February 2022

DOI: 10.1016/j.gca.2022.02.017

Abstract

The dynamics of tropical weathering through time with the formation and long-term evolution of laterite associated with climatic and geodynamic forcing is still a poorly explored issue. To better access this, we focused on lateritic-bauxitic duricrusts from the well-explored, 300 m high Kaw mountain in northeastern French Guiana. Macroscopically homogeneous Fe (oxyhydr)oxides-rich subsamples were separated from 10 bulk samples. Bulk- and subsamples were investigated by mineralogical and geochemical analyses and (U-Th)/He geochronology. The samples show a large heterogeneity on the macro- and microscopic scale reflecting different stages of duricrust formation and evolution through processes of dissolution and (re)precipitation of Fe (oxyhydr)oxides. The 284 (U-Th)/He ages obtained for goethite α -(Fe, Al)OOH and hematite α -Fe₂O₃ range from 30.5 ± 3.1 to <0.8 Ma and show large variability within a sample. The oldest hematite and Al-poor goethite subsamples precipitated since 30 Ma and formed while kaolinite was stable. Precipitation of Fe-minerals increased since ~14–12 Ma but still happened under ferruginous lateritic, non-bauxitic conditions. The dissolution and (re)precipitation of Fe minerals, Al-substitution in goethite, and the overall enrichment in Th, as well as gibbsite precipitation indicate an intensification of weathering and a shift towards bauxitic conditions since the end of the Miocene. The Th-, U-, and Al-rich Fe phases formed in this late episode of intense weathering partially replace the oldest, often Th- and U-poor phases

leading to a considerable age spread. We claim that this episode of intensified weathering, which had its peak at ca. 6-2 Ma, corresponds to the bauxitization of the lateritic cover of Kaw mountain.

Our proposed model of lateritization since at least 30 Ma and bauxitization since the late Miocene provides new constraints on the timescale and intensity of weathering at Kaw mountain. The onset of lateritization in French Guiana (Kaw region) is potentially older than ca. 30 Ma and was possibly synchronous with the development of bauxites in neighboring countries, and differences in the Paleogene weathering intensity might be due to different drainage capacities of the parental material. Late Neogene bauxitization suggests a regional increase in precipitations and drainage potentially linked to increased incision owing to local uplift.

Finally, we confirm that a detailed combination of geochronological results coupled to mineralogical and geochemical analyses improves our understanding of tropical weathering processes and duricrust formation by placing mineralogical and geochemical processes into a temporal framework.

IV.1 Introduction

Lateritic bauxites are weathering products in which Al and Fe accumulated, often forming economically important Al-deposits (Valeton, 1972; Bardossy and Aleva, 1990; Patterson et al., 1994; Carvalho et al., 1997). While classical laterites, deep stratified weathering profiles, often capped by a ferruginous duricrust but without important Al enrichment, form under tropical and subtropical climatic conditions commonly found at the Earth's continental surface, more specific conditions are required for bauxite formation (Prasad, 1983; Bardossy and Aleva, 1990; Schellmann, 1994; Tardy and Roquin, 1998; Valeton, 1999). Extensive studies linked to exploration activities and global comparison have shown that suitable climatic conditions with monsoonal seasonal variations and high precipitations are necessary (Bardossy and Aleva, 1990; Tardy, 1997; Tardy and Roquin, 1998). Thus, the potential process leading to bauxites is favored in equatorial regime but they can be found in broader intertropical latitude (Bardossy and Aleva, 1990). Iron-rich/ferruginous laterites form preferentially under more seasonally contrasted monsoonal (sub)tropical climate, whereas aluminum-rich/ bauxitic laterites (referred to as bauxites) require generally a more humid, less contrasted tropical climate (Tardy et al., 1991; Tardy, 1997; Tardy and Roquin, 1998). In

addition, specific drainage conditions with high permeability of the host rock and strong dissection of the surface are also essential for the formation of bauxites (Bardossy and Aleva, 1990). Ferruginous and bauxitic laterites are thus archives of past climate and landscape (Tardy and Roquin, 1998), containing information on the evolution of the continental surfaces, especially in areas of tectonic quiescence prone to weathering (e.g., Allard et al., 2018; Balan et al., 2005; Monteiro et al., 2014, 2018; Riffel et al., 2015; Vasconcelos et al., 2019, 1994).

However, several aspects of their genesis are not well understood and there is a lack of time constraints for their formation, evolution and relation with climatic change, mostly because absolute dating of bauxites remains a challenging task. Whenever ferruginous laterites and bauxites are covered by sediments, they can be dated indirectly by determining the age of the under- and overlying formations, whereas dating of uncovered weathering surfaces is more complicated.

The mineralogy of ferruginous laterites and bauxites is rather simple, consisting mainly of secondary minerals such as kaolinite, iron oxides and oxyhydroxides, and aluminum hydroxides. However, these minerals are not suitable for conventional geochronological methods. K-Ar and ^{40}Ar - ^{39}Ar dating of manganese oxides was used in numerous studies of lateritic duricrusts (see e.g. Beauvais et al., 2008; Vasconcelos et al., 1994, 2015; Ruffet et al., 1996; Vasconcelos, 1999; Vasconcelos and Carmo, 2018). This method requires K-bearing phases such as some Mn oxides, but such minerals are rare in laterites, in contrast to Fe oxides *sensu lato*, kaolinite, or gibbsite. Paleomagnetic dating of the ferruginous parts of the profiles is possible but becomes very imprecise when the latitudinal shift of the target area was insignificant during the time interval of interest. Goethite and hematite, the main constituents of the Fe duricrust (Tardy, 1997), which is equally present in most bauxites (Bardossy and Aleva, 1990), can be dated using the (U-Th)/He method as they quantitatively retain He at Earth surface conditions as shown by ^4He and $^4\text{He}/^3\text{He}$ diffusion experiments and *ab-initio* calculations (Shuster et al., 2005; Heim et al., 2006; Vasconcelos et al., 2013; Reiners et al., 2014; Balout et al., 2017; Deng et al., 2017; Hofmann et al., 2017; Farley, 2018). This approach has been used by a growing number of studies over the last three decades, but uncertainty remains on some essential aspects such as the diffusion parameters of He in goethite (Lippolt et al., 1998; Pidgeon, 2003; Pidgeon et al., 2004; Shuster et al., 2012; Danišik et al., 2013; Vasconcelos et al., 2013; Monteiro et al., 2014, 2018; Riffel et al., 2016; Hofmann et al., 2017; Allard et al., 2018; Wells et al., 2019). In pedogenic iron duricrusts, the petrological relationship

between the different phases is often very complex due to multiple cycles of dissolution of previously formed phases followed by reprecipitation (Nahon, 1991; Tardy, 1997). Geochronological analysis of this material thus requires an understanding of the relationships between the target phases (Monteiro et al., 2014).

The Kaw Mountain ridge in northeastern French Guiana is covered by a thick weathering profile first discovered in the 19th century (Leprieur, 1848). An extensive exploration campaign in the 1950s revealed the existence of a large, though uneconomic, bauxitic Al deposit with ca. 42 Mt of Al-ore with 42 wt% Al on average (Choubert, 1956). The area has been tectonically stable and in intertropical latitudes at least since the Cretaceous. Geomorphological studies estimate an Oligocene to Miocene age for this paleosurface (Choubert, 1957; Blancaneaux, 1981), and a paleomagnetic study indicates an Eocene age (Théveniaut and Freyssinet, 2002). Note however, that peneplanation, lateritization, and bauxitization might have happened over a long time interval (Bardossy and Aleva, 1990). In this context, the timing of the bauxitization of this surface remains unclear.

In this study we combine (U-Th)/He dating of iron (oxyhydr)oxides from the lateritic-bauxitic iron duricrust of Kaw mountain with detailed high resolution mineralogical and geochemical analyses. Our data reveal a complex story of precipitation, dissolution, transformation, and mixing processes in a very active weathering system. Despite some substantial age spreading which will be discussed in detail, the careful analysis of the dataset allows determination of periods with enhanced Fe mineral precipitation, enables insights into variations of the weathering intensity and thereby into the bauxitization process.

IV.2 Geological, geomorphological and climatic context

IV.2.1 Geological history of the Guiana shield

The Amazonian craton forms the core of the South American continent and is composed of two parts, a northern one called Guiana shield and a southern one, called Brazilian or Guaporé shield, that are divided by the Amazonas-Solimões Basin, which hosts the world's largest river, the Amazon (see Fig. IV-1A). Apart from minor Archean cores, most of the craton was formed during the Paleoproterozoic Trans-Amazonian orogeny (ca. 2.2-1.95 Ga) and later Paleo-, Meso-, and Neoproterozoic accretionary events on its southwestern border (Cordani and Teixeira, 2007). After the Panafrican/Brasiliano orogeny at the end of the Neoproterozoic,

the Amazonian Craton was located next to the West African craton, where it remained until the Mesozoic opening of the Atlantic. During the Paleozoic, marine and terrestrial sediments were deposited in a huge E-W intracontinental rift known as the Amazonas-Solimões Basin which was episodically filled later, during Cretaceous and Cenozoic times.

Low-temperature thermochronological data from the Northeastern part of the Guiana shield indicate that the basement rocks have been near the surface since ca. 90 Ma (Derycke et al., 2021). In the Guiana basin, the coastal sedimentary basin at the northeastern rim of the shield, sediments started to deposit in the Cretaceous on top of the Precambrian basement (Wong, 1994). In the onshore part of this basin (coastal plains of Guyana, Suriname and French Guiana), Paleocene to Early Eocene sediments were deeply weathered during the Late Eocene and Oligocene, leading to the formation of the coastal bauxites (Hammen and Wymstra, 1964; Wymstra, 1971; Bardossy and Aleva, 1990; Wong, 1994; Monsels and Van Bergen, 2019), and producing the “Bauxite Hiatus” in the sedimentary sequence of the Guiana basin, but afterwards sedimentation continued during the Cenozoic.

West of the Guiana shield uplift of the Andes started in the early Cenozoic but mountain building first peaked by the Late Oligocene to Early Miocene (~23 Ma) and was most intense during Middle to Late Miocene (~12 Ma) and Early Pliocene (~4.5 Ma) (Hoorn et al., 2010; Sundell et al., 2019). Closure of the Panama Isthmus occurred at ~3.5 to 2.7 Ma (Coates, 1992; Bartoli et al., 2005). A large foreland basin developed where sediments from the Andes started to accumulate. However, until the Late Miocene the drainage system was different from today's and the Acre and Solimões basins were drained towards the Northwest. Establishment of the drainage towards the east, a process called transcontinentalisation, occurred definitively around ca. 9-8 Ma, leading to the development of the Amazon Fan located in the North of the mouth of the Amazon (e.g. Figueiredo et al., 2009; Hoorn et al., 2017). Since then, more than 4000 m of sediments accumulated in the Amazon fan, more than the half of them during the last 2.4 Myr, loading an enormous weight on the plate (Figueiredo et al., 2009).

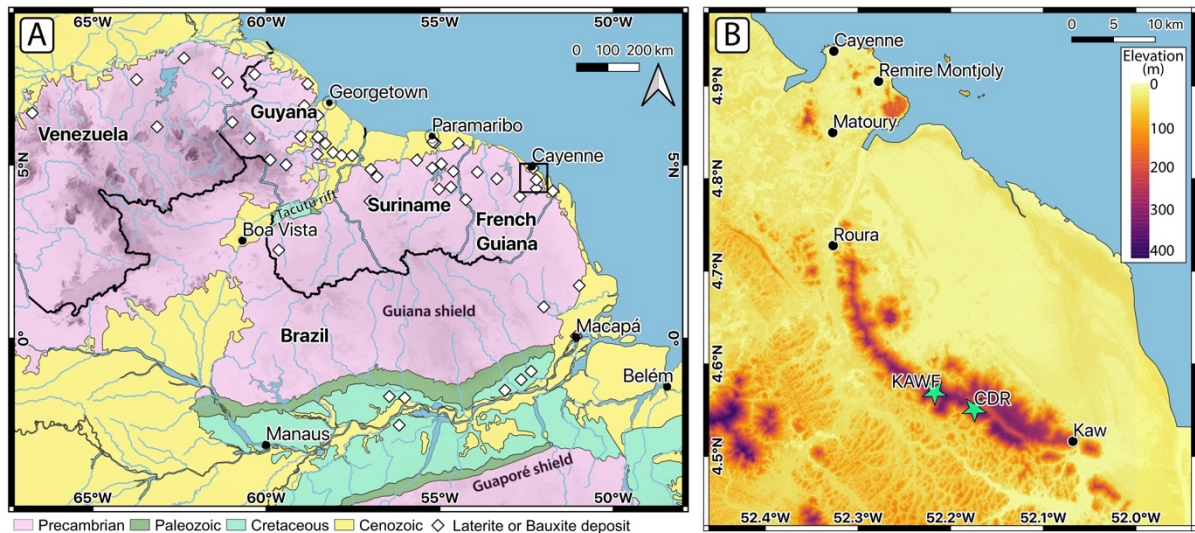


Figure IV-1: (A) Geological map of the Guyana Shield (after Gómez et al. (2019) modified according to Mendes et al. (2012) and Baker et al. (2015)) with documented laterite and bauxite deposits (white diamonds, after Bardossy and Aleva (1990)). The underlying Digital Elevation model indicates the relief (dark = high). (B) Digital Elevation model of northeastern French Guiana with Kaw mountain ridge (between Roura and Kaw) and sampling locations (stars).

IV.2.2 Geomorphology of the Guiana Shield

The Guiana Shield has a slightly domed structure intersected by the Tacutu rift that separates an eastern and a western domain (Fig. IV-1). One of the geomorphological characteristics of the Guiana Shield is the occurrence of several planation surfaces, the most remarkable of these surfaces are the so called “tepui” in Venezuela, flat table mountains with elevations of >2000 m (Briceño and Schubert, 1990). All high elevation surfaces >1000 m of the Guiana shield are only recognized west of the Tacutu rift. Geomorphological studies on the Guiana shield and the South American platform propose the existence of several surface planation levels with different ages of peneplanation from late Cretaceous to Quaternary (Choubert, 1957; King, 1962; McConnell, 1968; Blancaneaux, 1981; Aleva, 1984; Bardossy and Aleva, 1990). According to these models high elevation surfaces are supposed to be older than low elevation surfaces. A good summary of surfaces, elevations and assigned ages for the Guiana Shield can be found in Bardossy and Aleva (1990) and Théveniaut and Freyssinet (2002). Note that assignment of the ages and elevations of these surfaces appears to be sometimes inconsistent when comparing different authors (Choubert, 1957; King, 1962; McConnell, 1968; Blancaneaux, 1981; Aleva, 1984; Bardossy and Aleva, 1990).

IV.2.3 Weathering age constraints

Age constraints on paleosurfaces are mainly of relative nature. Stratigraphic relationships with sedimentary deposits are provided in Central Amazonia where most bauxites rest on (and so postdate) the Alter do Chão Formation considered to be late Cretaceous and early Cenozoic (Putzer, 1984; Hoorn et al., 2010). In Cenozoic coastal basins of Suriname and Guyana, bauxites developed on top of Paleocene to Early Eocene sediments are overlain by Oligocene to Miocene sediments (Hammen and Wymstra, 1964; Aleva, 1981; Bardossy and Aleva, 1990). Age dating by paleomagnetism indicates Eocene to recent ages for a number of lateritic covers in northern French Guiana (Théveniaut and Freyssinet, 1999; Théveniaut and Freyssinet, 2002). No other studies exist in French Guiana and all published geochronological literature is on the southern part of the Guiana shield and on the Guaporé shield. Allard et al. (2018) dated ferruginous duricrusts in western Amazonia developed on top of Precambrian intrusive rocks and Neogene sediments. Using (U-Th)/He geochronology of Fe oxides as well as electron paramagnetic resonance dating of kaolinites, they obtained Mid to Late Neogene ages. Mathian et al. (2020) obtained late Neogene and Quaternary ages on kaolinites from ferralsols and Acrisols from the same area whereas Balan et al. (2005), who studied weathering profiles north on Manaus, obtained Early Paleogene to late Neogene kaolinite ages in weathered Alter do Chão sediments and soils located north of Manaus.

Several studies on absolute age dating of supergene Fe and Mn minerals exist for the Guaporé Shield (Vasconcelos et al., 1994; Ruffet et al., 1996; Shuster et al., 2005; Shuster et al., 2012; Monteiro et al., 2018; dos Santos Albuquerque et al., 2020), most of them from the Carajás area. Results cover a wide range of ages, mainly from 80 Ma to recent and exhibit discrete periods of intense weathering: the most common data are indicative of the Eocene, Early Oligocene, Middle Miocene, Pliocene, and Pleistocene and some older ages in the case of dos Santos Albuquerque et al. (2020). A ^3He exposure age of 7 Ma for the Carajás plateau indicates very slow erosion rates for that area (Monteiro et al., 2018).

IV.2.4 French Guiana climatic condition

Nowadays, French Guiana is located in the tropics north of the equator and most of the country (including the study area) has a tropical rainforest climate ("Af") after the Köppen climate classification (Beck et al., 2018), defined by >60mm precipitation in the driest month. At sea level the mean annual temperature is equal to or above 25°C and the difference between

mean temperatures of the warmest and coolest months does not exceed 5°C. While temperatures are rather constant and similar over the Guianas, precipitation shows a large variability in this region (Bovolo et al., 2012). French Guiana has two rainy seasons, one from May to June/July and another one in December and January. The main dry season is from July to November; from February to April rain is reduced but French Guiana lacks a second dry period (Bovolo et al., 2012). The Northeast of French Guiana is the most humid area of the country with mean annual precipitations exceeding 3000 mm, locally, notably in the area of Kaw, exceeding 4000 mm (Groussin, 2001; Bovolo et al., 2012; Ringard et al., 2015).

IV.3 Kaw mountain geology and sampling

IV.3.1 Kaw mountain study area: geology, geomorphology and paleomagnetic data

The Roura-Fourgassié-Kaw mountain ridge (in the following referred to as Kaw mountain) is a ~40 km long, 200-320 m elevation convex-shaped ridge in northeastern French Guiana (Fig. IV-1B). It stretches SE-NW parallel to the coastline at ~20 km inland. Its basement is composed of acid to intermediate metavolcanites of the Paleoproterozoic Paramaca unit (2.14-2.16 Ga) (Delor et al., 2003), metamorphosed under greenschist metamorphic conditions and affected by subvertical banding. The top of the ridge is capped by a thick lateritic-bauxitic cover which is very heterogeneous with strong variations in thickness, color, texture and composition (Choubert, 1956). The mean composition is 42 wt% Al₂O₃, 30 wt% Fe₂O₃, 4 wt% TiO₂, 1.7 wt% SiO₂, 22 wt% H₂O for the 42 Mt bauxite reserve, but extreme values of the Al-Fe rich crust range from white bauxite with 64 wt% Al₂O₃ and 1.5 wt% Fe₂O₃ to Fe-laterite with 6 wt% Al₂O₃ and 60 wt% Fe₂O₃ (Choubert, 1956; Blancaneaux, 1981). Gibbsite is the main Al-mineral, whereas boehmite is rare. A drilling close to Camp Caiman revealed 20 m of bauxite overlying (at least) 50 m of clays and saprolite, and reached the altered rock at a depth of 70 m (bottom of the drilling). According to Choubert (1956), the mean thickness of the bauxitic crust is 5.5 m, but higher thicknesses up to 20 m were observed, especially close to the rim of the plateau, at cliffs, and at long angle slopes. Choubert (1956) observes a link between the schistosity and bauxite thickness, with thicker bauxitic crust perpendicular to the schistosity (i.e. steep schistosity). Flanks of the Kaw Mountain expose stair-like morphology with lateritic steps, cliffs, numerous rolled blocks and entire slid shields are described. Caves, generally situated below the duricrust, are common. In flat areas, bauxite often appears as floats sat on clays (Choubert, 1956).

Choubert (1957) and later Blancaneaux (1981) assign the flat surface of Kaw mountain to the “second peneplain” or “surface II” for which they consider – based on large-scale geomorphological models – an Oligocene to Lower Miocene age, equivalent to the Early Velhas level of King (1962) in northern Brazil. The first published attempt of dating of the lateritic surface has been undertaken by Théveniaut and Freyssinet (2002) who did paleomagnetic dating of the iron duricrust at the top of the ridge. The authors obtained an Eocene to Miocene age for the weathering surface. Their interpretation of the Eocene age and the Miocene age corresponds to the actual paleosurface and to strong uplift during the last 10 Ma, respectively.

IV.3.2 Bulk samples

Ten ferruginous duricrust samples from two transects were collected for the purpose of this study (Fig. IV-2). Sample locations and descriptions can be found in Table IV-1. The first transect descends the northern flank of the mountain ridge; four samples collected in situ at the surface (CDR-01-04) were sampled along a path called “Sentier d’observation des Coqs de roche” at elevations of 307-220 m. The second transect is west of the “CDR” transect and descends the southern flank of the ridge starting at “Camp Caiman” (Fig. IV-2). Six samples (KAWF-1 to KAWF-5 and KAW18-10B) were collected at elevations of 300-220 m. Two samples (KAWF-5 and KAW18-10B2) were taken at the top of the ridge, one sample (KAWF-4) was collected in the bed of a small creek which runs over a massive duricrust (Fig. IV-2). Descending the flank further down from the sampling point of KAWF-4, the small creek runs continuously over the duricrust (Fig. B-1A of the Electronic Supplement). Suddenly, at ca. 220 m elevation, the duricrust ends in a ca. 3.5 m high cliff producing a small waterfall with a pond at its base (Fig. B-1B of the Electronic Supplement). Two samples, KAWF-3 and KAWF-2, which represent different parts of the duricrust, were taken at this spot (Fig. IV-2 and Fig. B-1B). Another sample, KAWF-1, was sampled at the other side of the pond from a giant duricrust block of ca. 4m x 6m x 3m (Fig. IV-2). The sample was taken about 1m above the ground. Although this block is probably not in situ we assume that due to its immense size it has not been turned around or transported very far.

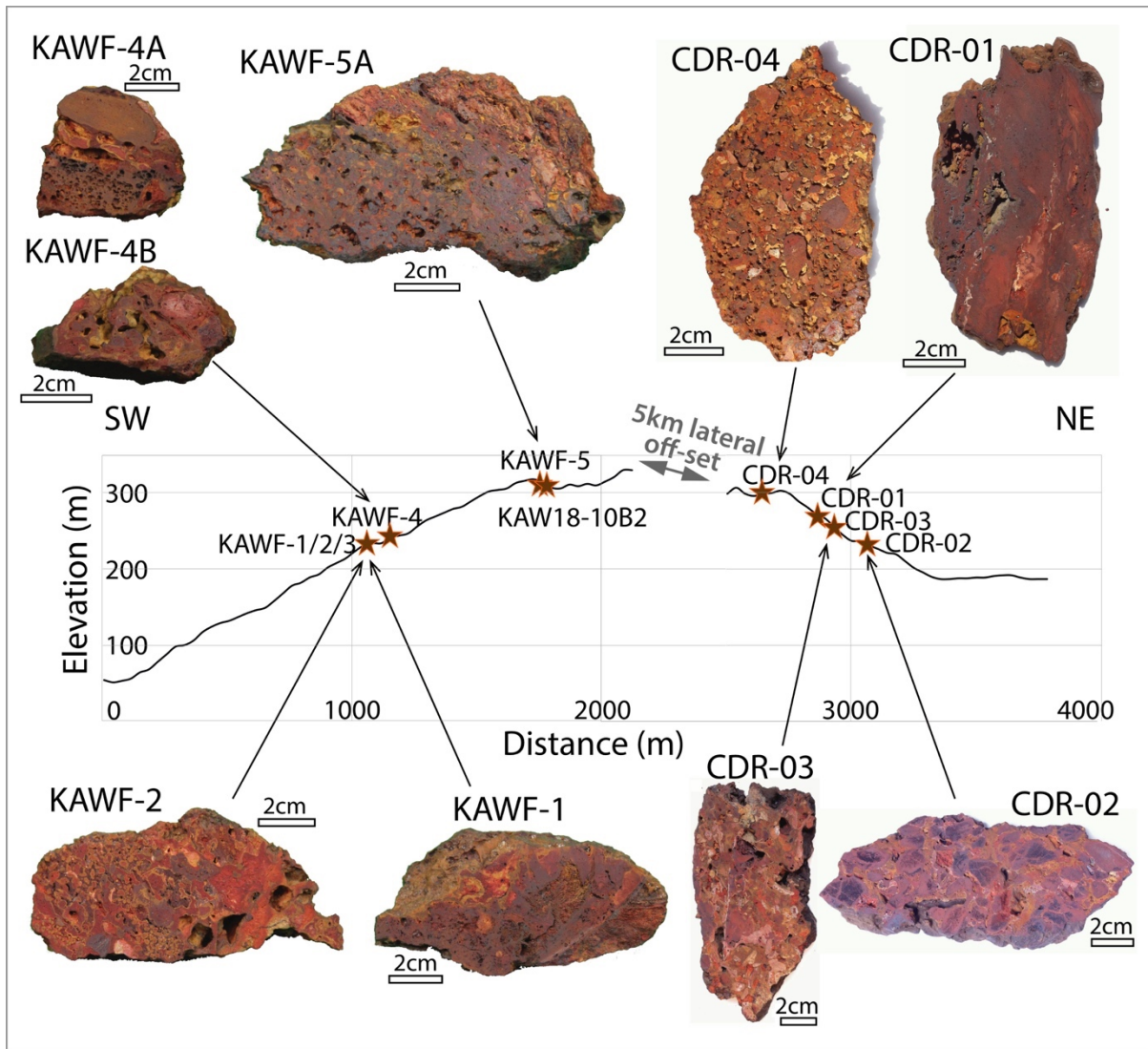


Figure IV-2: Elevation profile of the two sampled transects on the northern (CDR) and southern (KAWF) flanks of the ridge (for locations see Figure IV-1) with pictures of the analyzed samples.

Reading the climate signals hidden in bauxite

Table IV-1: Sample locations and sample description.

Flank (transect)	Sample	Latitude	Longitude	Elevation (m)	outcrop	analysed blocks	description	material used for bulk XRD and bulk chemistry
North (CDR)	CDR-01	4.55263	-52.17262	271	surface, in situ	CDR-01A CDR-01B	Massive, overall red sample. The matrix is fine grained, mainly dark red but locally beige-pink. Metallic, anthracite colored Fe minerals crystallized botryoidally in big voids. The outer surface of the sample is denser than the matrix and brownish black. The two blocks are very similar	slice of CDR-01A
North (CDR)	CDR-02	4.55482	-52.17158	222	surface, in situ	CDR-02	Composed of black cm-sized altered pisoliths cemented in a ochre-beige porous matrix. Towards their outer rim and along veins in their interior the pisoliths are often denser and more metallic. As for the other samples the outermost coating is denser and brown to black	slice of CDR-02
North (CDR)	CDR-03	4.55317	-52.1723	256	surface, in situ	CDR-03	Vermiform to massive, sometimes slightly pisolitic structure. The colors range from red-violet, to ochre, beige and greenish-beige. The beige parts of the matrix are often less consolidated than the rest of the sample. The densest parts of the sample are red-violet domains which are sometimes more blackish towards the rims and resemble similar ones observed in sample CDR-04C.	slice of CDR-03
North (CDR)	CDR-04	4.55095	-52.17452	307	surface, in situ	CDR-04A CDR-04C	Nodular/psolitic structure. Red to blackish and orange nodules and pisolites of varying size (0.1-2cm) are cemented in an extremely porous fine-grained matrix colored from beige to ochre and brown. Sometimes the nodules are coated and cemented by a black glassy layer More massive structure than CDR-04A, dominating color is red. Beige ochre fine grained domains coexist with red to red-violet finely porous matrix. Blackish denser veins and coatings crosscut the matrix and delimitate the different domains. Rarely reddish-black micropisolites / nodules exist.	slice of CDR-04A slice of CDR-04C
South (KAWF)	KAWF-1	4.56364	-52.2175	220	from side of giant bloc (ca. 4x6x3m) next to waterfall, ca. 1m above ground	KAWF-1	Massive structure dominated by a red matrix. Locally the matrix is yellow or dark brown, clear boundaries are often not visible. Inside a big cavity, glassy black, at the surface yellow orange, botryoidal minerals crystallized	pieces of slice of KAWF
South (KAWF)	KAWF-2	4.56364	-52.2175	220	at diff next to waterfall, ca. 2 m below surface, in situ	KAWF-2	Red-yellow sample with a rather nodular structure. mm-sized red dull nodules with a yellow rim are in a red to blackish red, sometimes red-whitish fine grained porous matrix. Locally red-blackish pisolites or nodules of different size and porosity occur in the matrix. Big voids are often covered by a brown glassy coating.	slice of KAWF-2
South (KAWF)	KAWF-3	4.56364	-52.2175	220	surface, in situ, at head of waterfall	KAWF-3	The outer surface of the sample is made up by a thick dense dark gray coating with metallic luster. Inside it has a massive structure with dull red and yellow domains which resemble the "taches" described by Tardy (1993) for the "horizon tacheté" (mottled zone)	several cm-sized pieces of KAWF-3
South (KAWF)	KAWF-4	4.56406	-52.21775	250	surface, in situ, from bed of a small creek which runs over massive duricrust (material broke into small pieces during sampling)	KAWF-4A KAWF-4B	Ochre-reddish and very porous sample containing pores of different sizes. Red bean shaped domains of different porosity and hardness, sometimes yellow at their rim alter with ochre brown domains of different forms. The latter are either more dense but not very hard or harder, very porous with many big pores (mm sized) and matrix-character. Some big voids are filled with white rather unconsolidated material. Massive to slightly pisolitic structure with big voids. Sample is dominated by a red matrix with yellow veins and coatings. Locally the matrix is red-whitish and less consolidated.	several cm-sized pieces of KAWF-4
South (KAWF)	KAWF-5	4.56875	-52.21766	300	face, in situ or big b	KAWF-5A KAWF-5B	Sample 5A has one pisolitic part where small micropisolites of ca. 0.1-0.3cm size are cemented in a orange-ochre fine grained matrix. Locally they are additionally cemented by a black dense glassy phase. The pisolitic part of the sample grades into a matrix dominated part where a poorly consolidated fine grained orange-red-yellow matrix is crosscut by black glassy to metallic veins. KAWF-5B is similar to the matrix dominated part of KAWF-5A. Towards the outer surface the material is black, massive hard and dense with some small pores and locally bright veins crosscutting.	slice of KAWF-5A slice of KAWF-5B
South (KAWF)	KAW18-10_B2	4.56897	-52.21697	300	10cm below surface	KAW18-10_B2	Composed of 0.5-1.5cm-sized black pisolites sampled at 10cm depth from a pisolite-soil mixture. Reddish more porous and edgy nodules were equally present in the same horizon but were not analyzed here. Two pisolites which are black and dense at the surface and red-violet to orange at the inside were used for geochronological analyses. Three other pisoliths with the same outer aspect were used of mineralogical and geochemical analysis.	several pisolites separated from matrix (not presented)

IV.4 Methods

IV.4.1 Bulk sample analyses

IV.4.1.1 Petrological observations

For petrological observations and subsequent analyses, bulk sample blocks (mainly dm-sized) were sawed into several 1-2 cm thick slices. For samples where more than one block was analyzed, notably those which broke into smaller pieces during sampling in the field, each block was given a specific name (letter after sample number, e.g. KAWF-5A). The slices were observed using a hand lens and a binocular microscope and different mineralogical phases and subsamples of Fe-minerals (in the following always referred to as subsamples) were identified and described. Generally, one slice (or several small pieces in the case of broken samples) was used for bulk analyses. A schema visualizing the preparation procedure can be found in Figure B-2 of the Electronic Supplement.

IV.4.1.2 X-Ray Diffraction

Sample slices/pieces were crushed in a steel and subsequently finely ground in an agate mortar. The material was loaded in hollowed inox sample holders (32 mm diameter and 3 mm depth) and the sample surface was leveled using a rough glass plate in order to limit preferential orientation. Powder X-ray diffraction (XRD) analyses were performed at the IMPMC laboratory, Paris, France, with a Panalytical™ XPert-Pro® Diffractometer equipped with an X'Celerator® detector. Powder data were collected in Bragg-Brentano geometry using Co-K α radiation counting in continuous mode over the 3-110° 2 θ range with an angular step of 0.01670° for 4 h. The powder XRD patterns were refined by the Rietveld method using the XND code including anisotropic pseudo-Voigt line-shape parameters (Berar and Baldinozzi, 1998). Crystal structures data reported by Forsyth et al. (1968), Blake et al. (1966), Saalfeld and Wedde (1974), Bish and Von Dreele (1989), Horn et al. (1972), Shintani et al. (1975), and Corbató et al. (1985) for goethite, hematite, gibbsite, kaolinite, anatase, rutile and boehmite respectively, were taken as starting parameters for the refinements. In the XND code, structure factors were corrected for anomalous scattering factors calculated from Cromer (1983). Scale factors and line-width parameters were refined for all phases, while unit-cell parameters were refined for goethite, hematite, anatase and rutile only. Although they were not further interpreted in the present study, anisotropic line-width parameters were freely refined for goethite and hematite

in order to take into account for anisotropy of the crystallite shapes (Fritsch et al., 2005; Dublet et al., 2015), which was required to correctly match observed line-shapes. Once a satisfying fit (with low weighted profile R-factor (R_{wp}), see Toby (2006)) was obtained, the weight-fraction $w(p)$ of each phase p was calculated from its refined scale factor using the classical formalism by Snyder and Bish (1989) and assuming $\sum w(p)=1$. The ratio of hematite to goethite (RHG) was calculated as $RHG = \text{hematite} / (\text{hematite} + \text{goethite})$. Al for Fe substitution rate in the goethite structure was calculated by applying the linear regression of Schulze (1984) to the Rietveld-refined value of the c unit-cell parameter ($Pbnm$ space group), the c dimension being the less sensitive to non-stoichiometry in goethite (Schulze, 1984; Wolska and Schwertmann, 1993). Al-substitution rates of hematites were too low in the samples studied to be accurately determined from the a unit-cell parameter, owing to the effect of non-stoichiometry on the hematite unit-cell dimensions (Stanjek and Schwertmann, 1992). Although this parameter value was not interpreted in the present study, the site occupancy factor of the Fe site was freely refined for goethite and hematite to account for both Al for Fe substitution and non-stoichiometry, which was necessary to correctly match observed intensities (Wolska and Schwertmann 1993; Stanjek and Schwertmann, 1992). Uncertainties on our reported Al mol% values in goethite includes the uncertainty on the refined c value plus the ± 2.6 mol% uncertainty reported by Schulze (1984) on the regression.

IV.4.1.3 Geochemical analyses

Major and trace elements including rare earth element content were obtained on bulk samples on the same material as used for the XRD analyses. The analyses were performed on 1-2 g of material ground to $<100 \mu\text{m}$ at the Service d'Analyse des Roches et des Mineraux (SARM), Vandoeuvre-Les-Nancy, France. Major elements (and Sc) were determined by ICP-OES iCap6500, trace elements by ICP-MS iCapQ after alkali fusion. Analytical uncertainties vary from $<2\%$ to 25% for major element concentration from $>10 \text{ wt}\%$ to $<0.05 \text{ wt}\%$ and from $<5\%$ to 20% for trace element concentrations between $100 \mu\text{g/g}$ and $0.1 \mu\text{g/g}$. Further analytical details can be found at www.sarm.cnrs.fr.

IV.4.2 Analyses on separated subsamples

In each bulk sample, several distinct facies, showing apparently homogeneous texture, color, hardness and porosity were identified. Those were separated by micro-drilling using a Dremel multi tool, gently crushed in a steel mortar in order to obtain 0.1-2 mm sized fragments and then cleaned in ultrasound with MilliQ water and Ethanol. Single grains were then selected and handpicked under a binocular microscope for mineralogical and geochronological analyses. Each of these individual subsamples was assigned a systematic name consisting of the bulk sample (profile+number), the block of sample (if more than one piece was sampled), the type of phase, ranging from the assumed oldest to the assumed youngest (number) and a letter for the specific subsample. Individual subsample fragments are here referred to as grains. A table containing the descriptions of all separated subsamples is reported in the Electronic Supplement (Table B-1).

IV.4.2.1 Scanning Electron microscopy analyses and reflected light microscopy

Representative hematite and goethite grains of all subsamples were mounted in epoxy resin discs, polished, and investigated using reflected light and Scanning Electron microscopes (SEM). All subsamples were observed under reflected light. SEM analyses were performed using a Zeiss ULTRA55 microscope coupled to an EDS (Bruker QUANTAX) at the IMPMC, Paris. High resolution secondary electron and backscattered electron mappings (pixel size = 120 nm) were obtained from 30 subsamples using the software ATLAS (Zeiss). These mappings were used to identify the paragenesis, subsample texture and homogeneity of the Fe phases and to check systematically for mineral inclusions such as zircon or rutile. In selected areas major elements were quantified and element distribution maps were obtained using the EDS system.

IV.4.2.2 Subsample XRD analysis

X-ray diffraction patterns of subsamples were obtained in two ways: i) by powder diffraction of finely crushed handpicked grains using the same measurement settings as described for the bulk samples (see above) but scanning over the 3-120° 2 θ -range and counting for 6 h (done for 4 subsamples) and ii) by analyzing individual handpicked grains (done for 67 grains from 30 different subsamples) in Debye-Sherrer geometry using Mo K α radiation. For this latter analysis, a single grain of 250-700 μm size (ca. 20–100 μg) from selected subsamples

was inserted into a boron silicate glass capillary (0.3-0.5 mm diameter) and analyzed at IMPMC laboratory, Paris, using a MM007HF RIGAKU rotating Mo anode (1.2 kV) delivering a 100 μm -width micro beam. For each subsample, 1 to 5 grains were analyzed. Two-dimensional XRD patterns were collected for 45-60 minutes in Debye-Scherrer geometry using a R-axis IV++ imaging double plate detector (300 x 300 mm), the distance between the sample and the detector plate was 200 mm. Angle calibration and image integration to convert the 2D- into a 1D pattern were done using the FIT2D software (Hammersley, 2016). For 32 of the individual grains (generally one per subsample) the diffractograms were refined by the Rietveld method using the same XND code and procedure as described for the bulk samples. RHG and Fe-Al substitution in goethite were calculated as for the bulk samples.

IV.4.2.3 (U-Th)/He geochronological analysis

Microscopically pure single grains of 250-700 μm size were handpicked under a binocular microscope and filled individually into 1x1 mm Nb capsules (purity 99.95%) for the (U-Th)/He analysis. 4 to 10 aliquots were analyzed per subsample. By weighing the empty and the filled Nb tubes the weight of the oxide grains was determined (10-250 μg , median = 63 μg). Degassing and analysis of the He content were conducted with two He extraction lines at GEOPS laboratory Orsay, France, coupled to (i) a Quadrupole mass spectrometer (QuadStar Pfeiffer, used for 237 of 284 analyses) and (ii) a VG5400 magnetic sector mass spectrometer, (used for 47 of 284 analyses). Each capsule was filled into a copper (Quadrupole line) or inox (VG line) planchet containing 49 positions (Gautheron et al., 2021). 8 capsules with fragments of the Durango apatite age standard and 3 capsules of a goethite internal standard, which serves as U and age standard, were measured with the oxides in each planchet, 1 Durango every 7 samples. Each capsule was heated during 30 minutes at a temperature <1000 °C (up to a barely visible light glow of the capsule) using an IR diode laser. The temperature was regularly checked in order to avoid U volatilization as this has been described by Hofmann et al. (2020) and Vasconcelos et al. (2013). Examples indicating that no significant U loss seems to have affected our samples can be found in Figure B-3 of the Electronic Supplement. For details on the degassing protocol see Gautheron et al. (2021).

For U and Th analyses the iron oxyhydroxide grains (including the Nb capsules) were filled into Teflon vials and digested during 24 h on a 100°C hot plate using an acid mixture of 50 μl of HNO_3 5N, 50 μL of a ^{235}U , ^{230}Th and ^{149}Sm spike in HNO_3 5N, 400 μL 48% HCl ultra-pure

and 100 μL 30% HF ultra-pure. Afterwards the solutions were evaporated to dryness (3 h at 100°C) and redissolved in 1.9 mL HNO_3 1N (1h at 100°C). 1.5 mL of solution were taken and transferred to polypropylene vials where they were re-diluted with 500 μL HNO_3 1N. Durango fragments degassed with the Fe oxides were dissolved according to the protocol described by Gautheron et al. (2021).

U, Th and Sm analyses were performed on a ThermoFisher Element XR HR-ICPMS at GEOPS, Orsay, France or an Agilent ICP-QMS 7900 at IPGP, Paris, France and quantification was done by isotope dilution method. The analytical error for U, Th and He is 5 % at 1 σ . For ages younger than ~ 0.8 Ma, the age determination is less accurate associated with the U-Th series disequilibrium that changes the He production rate (Farley, 2002). Because we used a ^{235}U and ^{230}Th spike adapted for the determination of age older than 0.8 Ma, no precise age can be calculated. We therefore only indicate that the ages are < 0.8 Ma (this concerns only 3 out of the 284 ages of our dataset).

As large fragments were used for (U-Th)/He dating, alpha ejection (loss of the alpha particles produced in the outer 15-25 μm of a crystal, for details see Farley et al., (1996)) is balanced by He implantation and no alpha ejection correction is necessary. The possible effect of He loss through ultrasonic cleaning was tested by comparing material of the same subsample cleaned for a long time (ca. 30 minutes or more) with material cleaned for a short time (2-5 minutes). There was no systematic difference in the obtained ages.

IV.4.2.4 He diffusion loss correction

Supergene hematite and goethite are generally composed of crystallites that have a very small size in the 10s to 100s nm scale (e.g., Vasconcelos et al., 2013). Although several studies have shown, that, even for those small crystallite sizes, hematite and goethite can quantitatively retain He over geologic timescales (Shuster et al., 2005; Heim et al., 2006; Vasconcelos et al., 2013; Balout et al., 2017; Deng et al., 2017; Hofmann et al., 2017; Farley, 2018), a certain proportion of the produced He is lost by diffusion. For microcrystalline hematite diffusive loss is expected to be ca. 2-5% (Balout et al., 2017; Farley, 2018), whereas microcrystalline goethite loses ca. 2-20% of its radiogenic He over short to moderate geological timescales (Shuster et al., 2005; Heim et al., 2006; Vasconcelos et al., 2013; Deng et al., 2017; Hofmann et al., 2017). As diffusion losses are different for hematite and goethite and not equally well characterized for the two minerals, we adapted the diffusion correction factor to

the mineralogy of the subsamples. For subsamples composed mainly of hematite (RHG > 0.5), we applied a diffusion correction of 5 % (i.e. adding 5 % to the raw age) and an error of 10 % (+analytical error if greater than this). For subsamples composed mainly of goethite (RHG < 0.5), we applied a diffusion correction of 10 % as proposed by Shuster et al., (2005). We decided to use 15 % error (+analytical error if greater than this) for goethite instead of 10 % error proposed by Shuster et al., (2005), as the studies by Deng et al., (2017) and Hofmann et al., (2017) have shown that He diffusivity in goethite might be more complex than formerly expected and He losses might differ significantly between different types of goethite. Note that the applied errors largely exceed the analytical error of the He, U, Th, and Sm measurements (generally ca. 2-5 %). Correction factors are given per aliquot in Table IV-3.

IV.5 Results

IV.5.1 Mineralogy and geochemistry of bulk samples

The mineralogy quantification obtained with the XRD diffractograms is presented in Table IV-2. Sample KAW18-10B2 is left out, as the analyzed nodules do not represent the bulk sample. All samples contain hematite, goethite, gibbsite, and anatase in detectable amounts, while kaolinite, boehmite and rutile exist only in some of the samples in detectable quantities. The hematite-goethite ratio (RHG) ranges from 0.92 to 0.06 (Table IV-2). Gibbsite contents range from 2.9 to 34.4 wt%, anatase contents from 0.9 to 2.7 wt%. The widespread presence of gibbsite coupled to the absence of kaolinite indicates the bauxitic character of the samples. Al-substitutions in goethite range from 5 to 25 mol% (Table IV-2). Note that these are mean values for each sample and higher and lower values might occur in different parts of the samples. The amounts of hematite and goethite for the bulk samples are presented on Figure IV-3A and highlight two distinct samples with extreme hematite or goethite amounts (CDR-01 and KAWF-5B, respectively).

The major element data of the analyzed samples are reported in Table IV-2. Fe_2O_3 and Al_2O_3 range from 55.1 to 81.2 wt% and 9.2 to 25.0 wt%, respectively, and are the major components. SiO_2 contents are very low, ranging from 0.3 to 4.4 wt%, similar to TiO_2 ranging from 0.9 to 3.1 wt%. P_2O_5 contents are up to 0.7 wt%, MnO contents up to 0.08 wt%. MgO, NaO and K_2O are generally below the limit of detection. The loss of ignition, mainly related to structural water of goethite, gibbsite and kaolinite ranges from 6.9 to 17.9 wt%. Figure IV-3B

shows the Fe_2O_3 and Al_2O_3 quantities of the analyzed samples, and a strong correlation between the Fe_2O_3 content and the Al_2O_3 content can be observed.

Analyses of U and Th can be found in Table IV-2, other trace elements and rare earth elements are reported in Table B-2 of the Electronic Supplement.

Table IV-2: Bulk composition of the analyzed duricrust samples

		CDR-01	CDR-02	CDR-03	CDR-04A	CDR-04C	KAWF-1	KAWF-2	KAWF-3	KAWF-4	KAWF-5A	KAWF-5B
Hematite	wt%	75.5	62.1	39.4	19.5	33.5	32.3	33.2	36.1	33.6	17.0	5.0
abs. error	wt%	0.5	0.5	0.9	0.8	1.2	1.2	1.6	1.2	1.3	1.7	0.3
Goethite	wt%	7.0	26.5	34.4	70.5	29.8	54.5	39.4	42.1	54.3	53.8	82.6
abs. error	wt%	0.8	1.5	1.5	0.4	2.0	1.1	1.6	1.3	1.3	1.4	0.1
Gibbsite	wt%	14.7	8.8	23.5	7.0	34.4	2.9	23.7	17.0	9.5	27.7	11.9
abs. error	wt%	0.7	0.4	0.5	0.3	0.6	0.5	0.8	0.4	0.6	0.7	0.6
Anatase	wt%	2.8	2.7	2.8	0.9	2.4	1.4	1.2	1.5	1.4	1.5	0.6
abs. error	wt%	0.6	0.3	0.3	0.2	0.5	0.3	0.3	0.3	0.3	0.4	0.2
Kaolinite	wt%	bld	bld	bld	1.7	bld	8.9	2.5	2.1	0.3	bld	bld
abs. error	wt%	bld	bld	bld	0.3	bld	0.7	0.9	0.4	0.6	bld	bld
Rutile	wt%	bld	bld	bld	0.4	bld	bld	bld	0.8	0.6	bld	bld
abs. error	wt%	bld	bld	bld	7.2	bld	bld	bld	0.4	0.2	bld	bld
Boehmite	wt%	bld	bld	bld	0.1	bld	bld	bld	0.4	0.2	bld	bld
abs. error	wt%	bld	bld	bld	0.1	bld	bld	bld	0.4	0.2	bld	bld
RHG ¹	Hm/(Hm+Gt)	0.92	0.70	0.53	0.22	0.53	0.37	0.46	0.46	0.38	0.24	0.06
Gt c ²	Å	3.0058	2.9906	2.9996	2.9920	3.0034	3.0048	2.9889	2.9813	2.9838	3.0150	3.0160
abs. error	Å	0.0179	0.0041	0.0042	0.0024	0.0053	0.0017	0.0038	0.0031	0.0029	0.0039	0.0024
Gt Al-substit	mol%	11	19	14	19	12	11	20	25	23	5	5
abs. error	mol%	12.8	5.0	5.0	4.0	5.6	3.6	4.8	4.4	4.3	4.8	4.0
R _{wp} ³		0.018	0.013	0.017	0.010	0.022	0.015	0.015	0.013	0.014	0.019	0.017
Fe ₂ O ₃	wt%	81.24	78.77	61.51	66.44	54.98	71.03	55.07	60.38	66.73	57.98	71.63
Al ₂ O ₃	wt%	9.15	10.19	20.23	14.09	24.98	11.46	23.37	20.56	16.01	20.56	10.65
SiO ₂	wt%	0.35	0.48	0.32	1.28	0.32	4.35	1.53	1.39	0.46	0.82	1.24
TiO ₂	wt%	2.45	1.24	1.84	1.26	1.49	0.90	1.70	1.73	2.18	3.12	1.97
P ₂ O ₅	wt%	0.10	0.15	0.15	0.23	0.15	0.73	0.14	0.17	0.17	0.22	0.38
MnO	wt%	0.02	bld	bld	0.07	bld	0.02	0.05	0.02	0.04	0.06	0.08
LOI ⁴	wt%	6.86	9.37	15.59	16.46	17.92	12.25	18.26	16.20	14.56	17.35	14.60
U	µg/g	0.43	0.85	0.77	1.24	0.70	1.13	1.94	1.55	1.70	1.69	2.61
Th	µg/g	3.30	8.54	4.43	8.75	4.08	4.87	12.80	11.80	11.60	3.80	2.06

RHG¹: ratio hematite goethite; Gt c²: goethite unit cell c-parameter; R_{wp}²: weighted profile R-factor (see Toby, 2006)

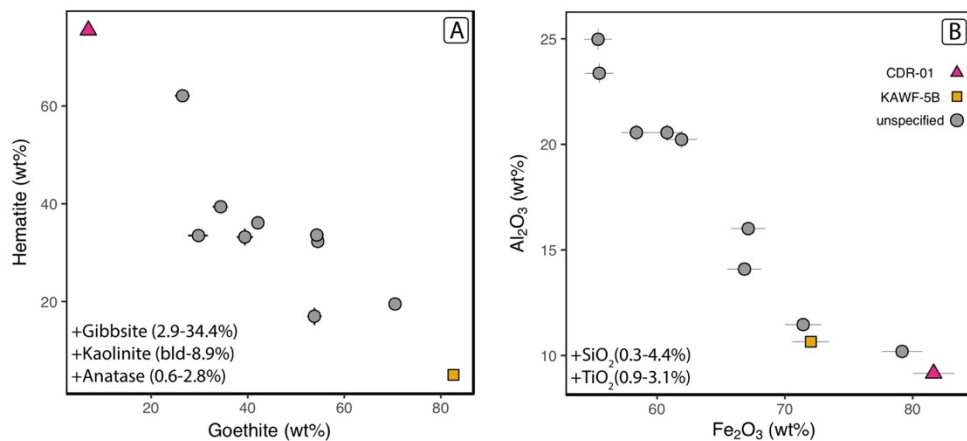


Figure IV-3: Bulk data of the dated duricrust samples. (A) shows the amounts of hematite and goethite obtained through Rietveld refinement of the bulk XRD data, (B) shows the Fe_2O_3 and Al_2O_3 content from the geochemical analyses. The pink triangles correspond to sample CDR-01, the yellow squares to sample KAWF-5B, the grey circles to all other samples. For data see Table IV-2.

IV.5.2 SEM analyses

The SEM analyses reveal that some subsamples are relatively uniform (Fig. IV-4A-B), while many show complex textures, intergrowths, structures of redissolution, or different phases of precipitation (Fig. IV-4C-L). Selected typical SEM images are presented in Figure IV-4 to illustrate the main petrological and mineralogical textures observed on the Kaw samples.

The SEM images show that in some subsamples all kaolinites have been dissolved and only phantoms of ancient kaolinites remain (Fig. IV-4D-E), while in other subsamples (especially those of KAWF-1) kaolinites of varying size are present and not dissolved (Fig. B-4 of the Electronic Supplement). Hematite and goethite occur either as two separated phases seeming to have crystallized one after another (Fig. IV-4G-I) or are intimately connected eventually indicating processes of phase transformation (Fig. IV-4J-L). Element mapping shows that Al contents can vary a lot inside individual grains, with examples that are available in Figure B-5 of the Electronic Supplement. Some subsamples show minor zircon or rutile inclusions, but these minerals are generally rare and very small (up to 5 μm , mostly $<2 \mu\text{m}$ on the long axis). The eventual significance of these inclusions on the (U-Th)/He ages will be discussed further below.

SEM images and analyses reveal the complexity of the samples; what seems one phase at macroscopic scale is often a mixture of at least two phases and even more at microscopic scale. Often hematite and goethite, sometimes also anatase, kaolinite, and gibbsite appear in the same grains. Separation of these different phases for (U-Th)/He chronology is often not possible due to the small scale of the intergrowths. In these cases, mixed ages are expected to be obtained.

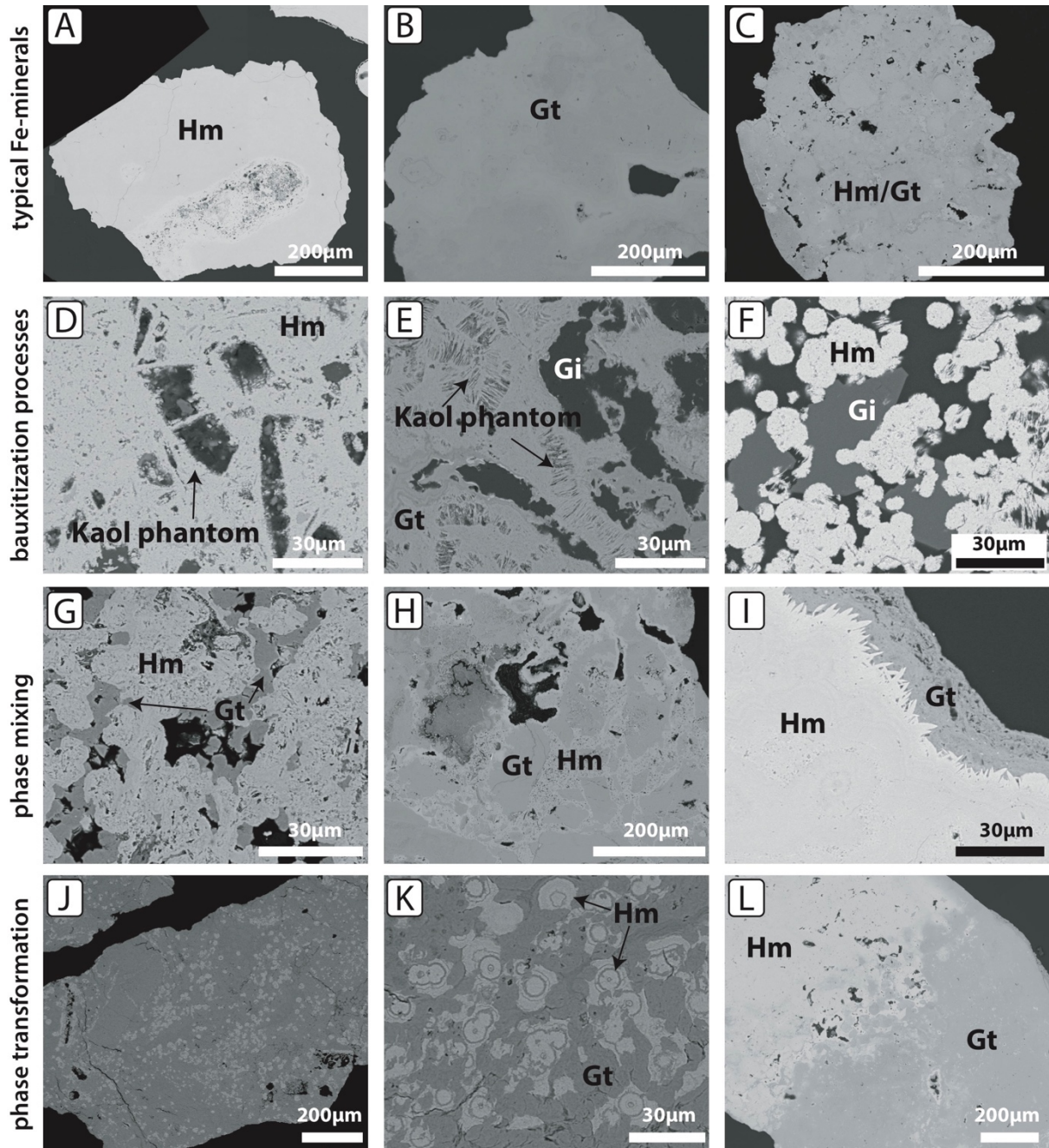


Figure IV-4: Scanning Electron microscopy images of representative grains of hematite and goethite. (A) Well-crystallized, botryoidal hematite coating less pure and porous matrix (CDR-01B_3). (B) Well-crystallized glassy black goethite (KAWF-1A_5CII). (C) Typical texture of a porous pisolith composed mainly of hematite (KAWF-5A_1A). (D) Internal hollows created by the dissolution of kaolinite (arrow) (CDR-01A_2). (E) Goethite grain with kaolinite dissolution features ("phantoms", black arrows) and late stage gibbsite (Gi) filling porosity (KAWF-4A_3A). (F) Micro-nodules of hematite with late stage μm -sized gibbsite (CDR-02_D2). (G-I) phase mixing of hematite (Hm) and goethite (Gt). (G) Goethite crystallized in voids cementing hematite aggregates (CDR-02_E2). (H) Goethite showing brecciated texture cemented by late-stage hematite (KAWF-5B_1B). (I) Pure and well-crystallized hematite coated by late-stage porous Al-rich goethite (CDR-01B_3). (J) Goethite (dark gray) grain with many small hematite spots (bright gray) (KAWF-5B_2AII). (K) Zoomed image of (J), showing concentric hematite pisoids in a goethite matrix partly overlapping the pisoids. We interpret these features as hydration features representing the transformation of hematite into goethite. (L) Grain composed of hematite and goethite from the outermost coating of sample CDR-01 showing the progressive hydration of the hematite (CDR-01A_1).

IV.5.3 XRD analyses of subsamples

Results of the single grain XRD Rietveld analyses (Tables B-3 and IV-3) show that the subsamples are in many cases composed of mixtures of hematite and goethite but pure phases also occur. Anatase is common in small amounts, whereas gibbsite, kaolinite, and rutile are rarely detectable in the selected subsamples. Al-substitutions in goethite range from 0 to 29 mol% and are similar to the values obtained for the bulk samples (Table IV-1).

IV.5.4 (U-Th)/He dating

A total of 284 Fe oxyhydroxide grains were successfully dated by (U-Th)/He dating, with generally at least 4-5 aliquots per subsample. Data are reported on Tables IV-3 and B-4 (Durango apatite data). In order to test the reproducibility of the results we dated up to 10 aliquots for some subsamples. Figure 5 shows graphs of all obtained age data. The He ages corrected for diffusive loss range from 30.5 ± 3.1 to < 0.8 Ma and cover basically the entire range in between with a main peak at ca. 2 Ma. The oldest ages are all found on the northern flank of the mountain ridge with the oldest ages being obtained at the lowest elevation in sample CDR-02. On the southern flank the age distribution is more homogeneous with similar maximum ages of 12-15 Ma at all elevations.

For most analyzed (bulk) samples and subsamples, inter- and intra-subsample age range exceeds analytical uncertainty, varying from some to many percent (see Fig. IV-5A). Age distributions are different in every sample. U, Th, and Sm concentrations are generally low in the samples ranging from 0.05 to 5.2 ppm for U (median=0.9 ppm), 0 to 33 ppm for Th (median=6 ppm), and 0 to 6 ppm for Sm (median = 1 ppm). Figures IV-5B and IV-5C present U and Th versus age graphs for the data set. A Th/U versus age graph for all samples as well as individual age vs U, Th and Th/U graphs for every sample can be found in Figures B-6A-D of the Electronic Supplement. Actinide concentration versus age trends differ in between the samples. While several samples (e.g., CDR-01, CDR-02, KAWF-4) show an enrichment in actinides towards younger ages this trend is inverted or more complex in other samples. Some subsamples show systematic variations of age with U or Th and selected examples will be presented in detail further down.

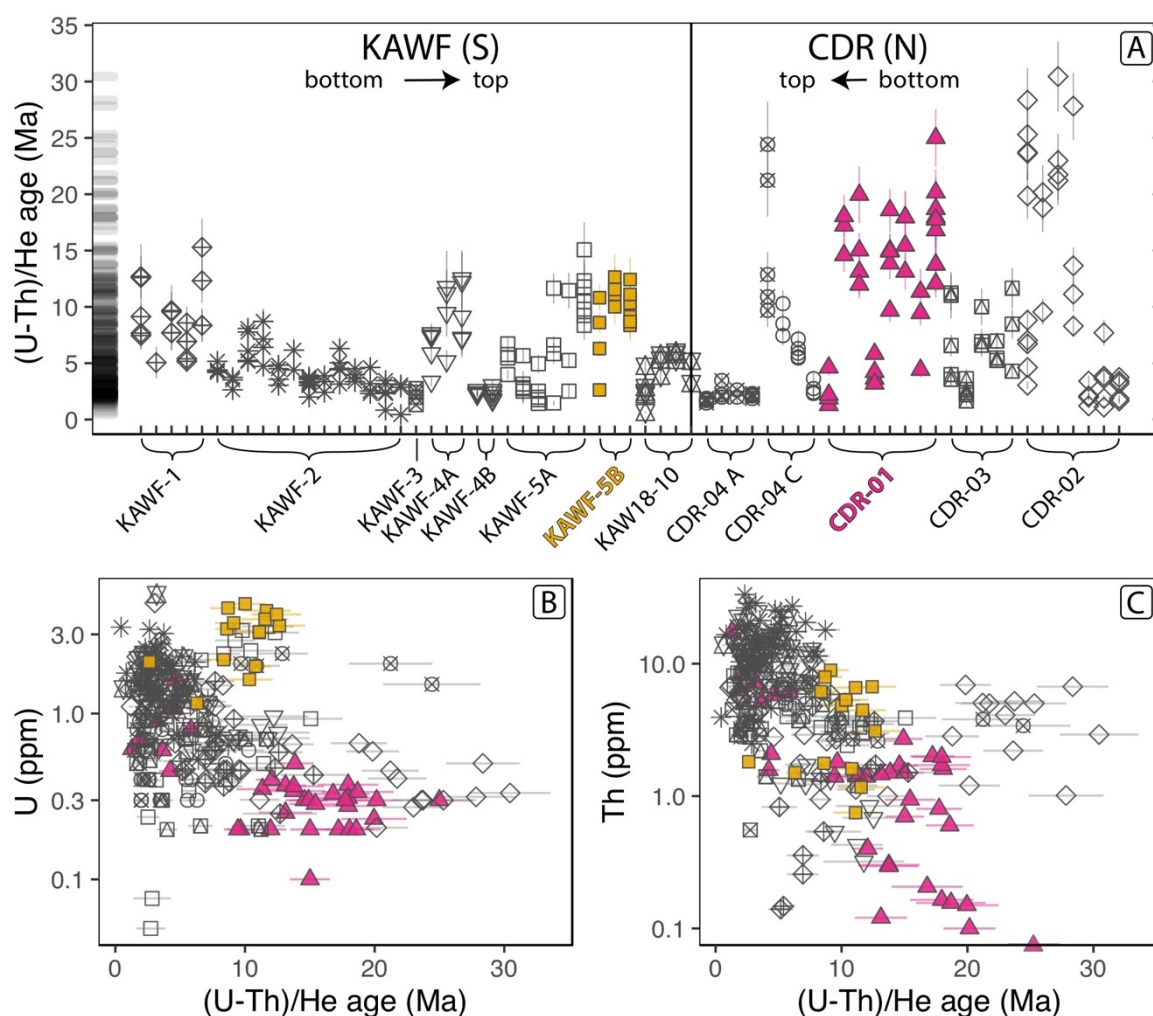


Figure IV-5: Representation of all obtained (U-Th)/He ages from the Kaw mountain ridge. (A) shows the ages for every individual subsample ($n=284$). Every vertical line is one subsample, color and shape represent the different bulk samples which are ordered from South to North. Grey bars at the left hand side indicate the overall data density. (B) and (C) show the ages for every sample relative to their U and Th concentrations (y-scales are logarithmic). Colors and shapes are as in A according to the samples. Several samples show correlations ages with U or Th concentrations but clear differences are visible between the different samples. For data see Table IV-3, individual plots for every sample can be found in Figure A6 of the Electronic Supplement.

IV.5.5 Detailed description of the (U-Th)/He, mineralogical and petrological results of two selected samples

The results of samples CDR-01 and KAWF-5 are presented in more detail, as those samples are characterized by extreme mineralogical, geochemical and geochronological features (Figs. IV-3 and IV-6). For all other samples, pictures of the samples indicating the dated subsamples and showing the obtained ages can be found in Figure B-7 of the Electronic Supplement.

IV.5.5.1 CDR-01

Figures IV-6A-D show a detailed portrait of sample CDR-01. Macroscopically this very hematitic (bulk analysis 75 wt% hematite, Table IV-2) sample is rather simple being composed

of a fine-grained hematite-gibbsite matrix (subsamples CDR-01A_2 and CDR-01B_2, ratio hematite - gibbsite varies as macroscopically visible in color variations), some small cavities where botryoidal hematite crystallized (subsamples CDR-01A_3 and CDR-01B_3) and an outer coating composed of goethite (subsamples CDR-01A_1 and CDR-01B_1). The results from the two macroscopically very similar blocks are very coherent in terms of mineralogy (SEM), Th and U concentrations and (U-Th)/He ages and are thus treated together. Figures IV-4A, -4D, -4I, and 4L show SEM images of the subsamples of sample CDR-01. The matrix is very fine-grained and rather homogeneous (Fig. IV-4D). Phantoms of kaolinite (i.e. holes with forms of kaolinite booklets indicating dissolved kaolinite) are visible suggesting that hematite formed while kaolinite was stable and possibly in equilibrium with kaolinite (Fig. IV-4D). In some voids large crystals of gibbsite crystallized seeming to post-date hematite crystallization. SEM images of the cavity fillings show that the botryoidal hematite that surrounds the matrix is very dense and pure (see Fig IV-4A and -4I), and EDS analyses indicate that this botryoidal hematite contains less aluminum than the matrix. Some of the mounted grains of subsample CDR-01B_3 show a thin layer of fine-grained goethite coating the botryoidal hematite (see Fig IV-4I).

Matrix and cavity filling (subsamples CDR-01A_2, CDR-01B_2, CDR-01A_3 and CDR-01B_3) yield similar, albeit rather spread, ages of mainly 25-10 Ma (Fig. IV-6A). Geochemically they differ, with the cavity fillings being poorer in Th than the matrix. Note that it was very difficult to select pure grains of the botryoidal filling and often a small fraction of matrix was attached in the analyzed aliquots. The outermost coating (subsamples CDR-01A_1 and CDR-01B_1) yields clearly younger ages of 5.8 to 1.3 Ma and shows an enrichment in Th and U compared to matrix and cavity with a Th/U ratio similar to the matrix though (Fig. IV-6B-C-D). One aliquot from the matrix yields an age of 4.4 ± 0.7 Ma and has an U content more similar to subsample 1 (coating). The aliquots of subsamples CDR-01A_3 and CDR-01B_3 show an increase in Th towards younger ages (Figs. 6C and A8D), indicating either continuous precipitation under changing conditions or mixture with a younger phase richer in Th. We remark that that inside subsample 1 (coating) there is a tendency towards higher Th contents with younger age. The sample shows an overall increase in Th and U concentration towards younger ages (Fig. IV-6C, calculated correlation coefficients are given in Figure B-8 of the Electronic Supplement).

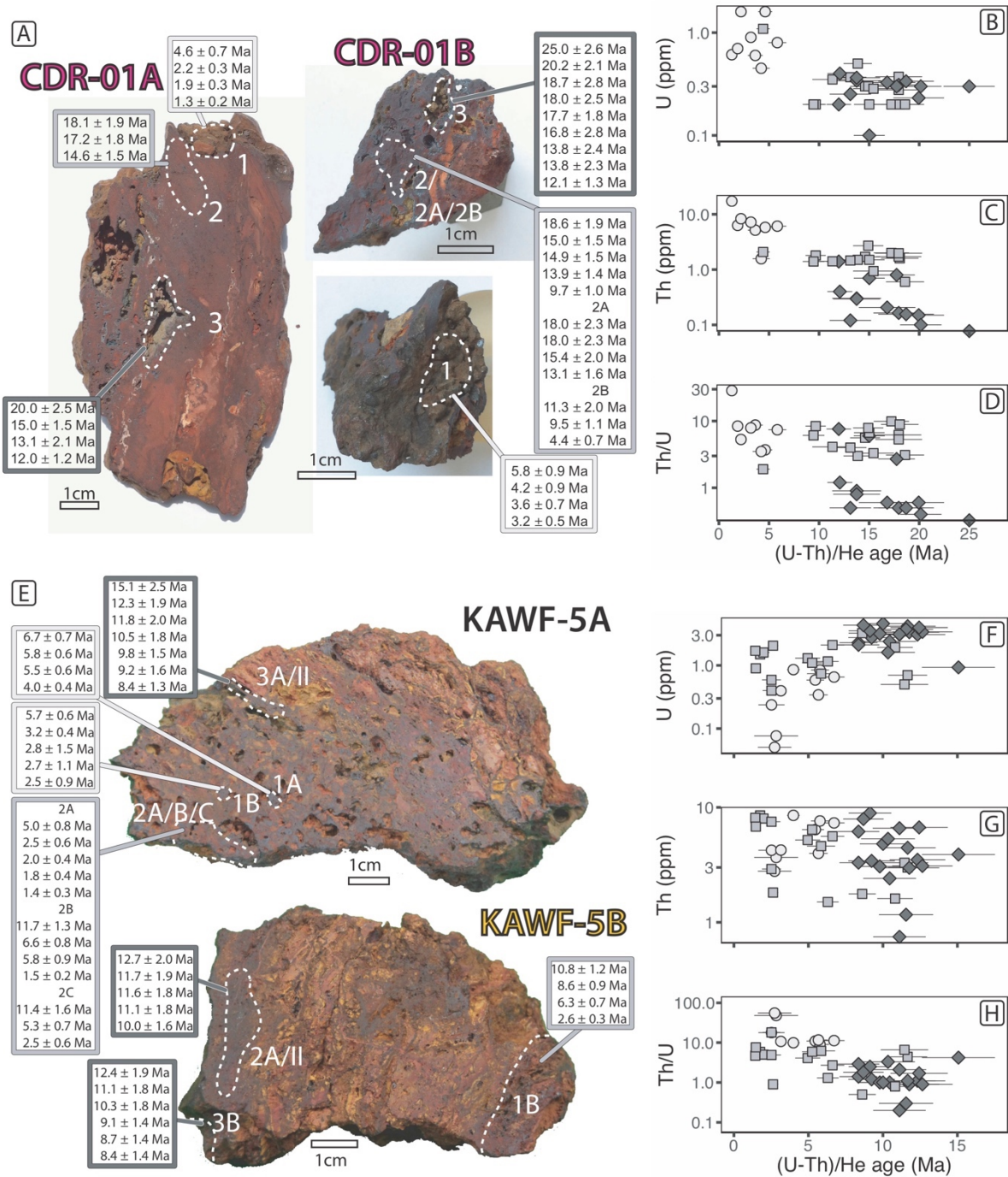


Figure IV-6: Samples CDR-01 (A-D) and KAWF-5 (D-H). (A) shows a picture of the two analyzed blocks of sample CDR-01 with the locations of the separated subsamples and the obtained (U-Th)/He ages. (B-D) show the ages relative to their corresponding U and Th concentrations and the Th/U ratios. Colors are as boxes in A, shapes refer to specific subsamples. The sample and some of the subsamples such as A3 and B3 show a clear increase in U and Th concentrations towards younger ages (y-scales are logarithmic). For calculated regressions see Fig. B-8 of the Electronic Supplement. (E) shows a picture of the two analyzed blocks of the sample KAWF-5 with the locations of the separated subsamples and the obtained (U-Th)/He ages. Subsamples 2A, B, C were sampled at the same locations but differ in terms of color and texture (2A: black glassy gt, 2B: brown reddish Gt/Gt-Hm mix, 2C: metallic porous fragments, similar to pisoliths). (F-H) show the ages relative to their corresponding U and Th concentrations and the Th/U ratios. Colors are as in E, subsamples were grouped into of Al-poor Gt (dark gray diamonds), pisoliths (bright gray circles) and rather mixed phases (medium gray squares). U concentrations (F) are higher in the older subsamples and decrease towards younger ages with a slight re-increase for the youngest ages (subsamples KAWF-5A_2A). Th concentrations (G) cover the same range for all ages but aliquots of the same subsample have often similar concentrations. Th/U ratios (H) increase towards younger ages mainly due to U decrease (see F) and vary by two orders of magnitude. The small hematite pisoliths (subsamples KAWF-5A_1A and 1B) have clearly higher Th/U ratios than the older goethite subsamples. For calculated regressions see Fig. B-9 of the Electronic Supplement.

IV.5.5.2 KAWF-5

Different from sample CDR-01, KAWF-5 contains very little hematite and is composed mainly of goethite and gibbsite (see Table IV-2 and Fig. IV-3A). Figure IV-6E presents the two analyzed blocks which differ slightly in texture and bulk composition (see Tables IV-1 and IV-2). Figures IV-4J and IV-4K show SEM images of subsample KAWF-5B_2AII. This subsample yields reproducible ages of 12.7 ± 2.0 to 10.0 ± 1.6 Ma. Interestingly the subsample is not very homogeneous on the microscopic scale. Anatase is common in this subsample (Table B-3) and many of the analyzed grains present small concentric hematite pisoids which occur inside dense goethite or along phase boundaries (Figs. IV-4J and -4K). On the polished surface they appear as small craters which could either indicate a volume loss compared to the goethite or a polishing effect. They probably result from hydration of hematite into goethite. Al substitution in these goethite subsamples is low with ca. 5 mol% Al but higher than in the small hematite pisoids according to EDS analyses (Fig. B-5B of the Electronic Supplement). Scarce kaolinite dissolution structures are visible in the goethite. The pisolith subsamples (KAWF-5A_1A and KAWF-5A_1B) are generally very fine-grained (Fig. IV-4C). They vary in porosity in between them but have rather homogeneous structures. Spherical textures are common and resemble those observed in other pisoliths of the other samples. Voids are filled with later hematite and goethite phases, and fragments containing parts of the pisolith cortex show transformation into goethite. Subsample KAWF-5B_1B shows very chaotic features. While some areas resemble those of the massive goethite grains, others have brecciated structures which are cemented by a fine-grained hematite matrix (Fig. IV-4H). Sporadically fine-grained porous hematite matrix is intergrown with fine grained gibbsite.

Figures IV-6E-H show details of the dated subsamples from the two blocks of this sample. The ages range from 15 to 1 Ma but show some systematic differences from sample CDR-01. The oldest ages (8-15 Ma) occur all in goethite from more or less massive veins or coatings (KAWF-5A_3AII, KAWF-5B_2AII and KAWF-5B_3B). Pisoliths composed of hematite or a hematite-goethite mix yield younger ages ranging from 6.7 ± 0.7 to 2.5 ± 0.9 Ma (KAWF-5A_1A and KAWF-5A_1B). The youngest occur in vitreous goethite which cements /coats the hematite pisoliths (KAWF-5A_2A). Note that this vitreous goethite has different U and Th content than the older goethite subsamples. Different from most other samples, U contents decrease from old to young whereas Th contents cover the same range for all ages but are rather constant for each subsample (except KAWF-5A_2) (Table IV-3). Subsamples KAWF-5A_2B (slightly more

brownish and less vitreous than KAWF-5A_2A) and KAWF-5A_2C (more metallic and porous, rather resembling pisolith material) were picked from the same separate as KAWF-5A_2A and might be mixtures between older massive veins, the pisoliths and the late vitreous goethite. The age versus U and age versus Th/U graphs (Figs. IV-6F and -6H and Fig. B-9 of the Electronic Supplement) support this assumption.

Examples of age vs U and Th correlations of other (sub)samples are presented in Figures B-10 and B-11 of the Electronic Supplement.

IV.5.6 Relation of micro-XRD with chemistry and (U-Th)/ages

The micro-XRD results obtained on individual grains are compared to the U, Th and age data (bulk and from (U-Th)/He data) and reported in Figure IV-7. The highest U contents occur in samples and subsamples with a RHG close to 0 (pure goethite), and subsamples with RHG close to 1 (pure hematite) have very low U contents (Fig. IV-7A, but note that there is also U-poor goethite). Th content correlates with Al-substitution in goethite with high Th concentrations occurring in Al-rich goethite (Figs. IV-7B and B-12). Bulk samples and subsamples/grains show the same trends for U versus RHG and Th versus goethite Al-substitution.

The oldest ages correspond to rather pure hematite (RHG = 1) and, to a minor degree, goethite (RHG = 0) subsamples, whereas mixed subsamples (RHG around 0.5) are generally young (Fig. IV-7C and Table IV-3). Age correlates with the Al-content of goethite; towards younger ages goethite gets increasingly richer in Al (Fig. IV-7D and Table IV-3, one clear exception is botryoidal goethite from subsample KAWF-5CII which has ages of 9-5 Ma and lacks any Al).

Note that geochronological and mineralogical data were not obtained on the same aliquots. The mineralogical characterization by Rietveld refinement used 1-2 grains per subsample whereas (U-Th)/He data correspond to several (3-10) aliquots of each subsample. Therefore, the micro-XRD data does not represent the same diversity as the (U-Th)/He data which leads to the sometimes poorer correlation of the subsample/grain data compared to the bulk analyses.

Reading the climate signals hidden in bauxite

Sample	generation	aliquot	weight µg	4He mol	4He mol/g	²³⁸ U ng	²³² Th ng	¹⁴⁷ Sm ng	²³⁸ U ppm	²³² Th ppm	¹⁴⁷ Sm ppm	²³² Th ppm	¹⁴⁷ Sm ppm	Sm (total) ppm	Th/U	raw age Ma	corrected age Ma	error corrected age %	diffusion correction factor	predominant mineral	RHG	Goethite Fe-Al- substitution
KAWF-5A	KAWF-5A_2A	K5A2A3	81	2.14E-15	2.64E-11	0.14	0.65	0.020	1.70	8.10	0.30	2.00	2.00	4.7	1.3	1.4	0.3	10	Gt			
KAWF-5A	KAWF-5A_2A	K5A2A4	63	3.84E-15	6.09E-11	0.08	0.33	0.020	1.30	5.20	0.30	2.00	2.00	4.1	4.5	5.0	0.8	10	Gt			
KAWF-5A	KAWF-5A_2A	K5A2A5	55	8.64E-16	1.57E-11	0.03	0.16	0.000	0.59	2.91	0.07	0.47	0.47	4.9	2.3	2.5	0.6	10	Gt			
KAWF-5A	KAWF-5A_2B	K5A2B1	74	6.25E-15	8.44E-11	0.05	0.22	0.000	0.70	3.00	0.00	0.00	0.00	4.4	11.1	11.7	1.3	5	Gt-Ht-mix			
KAWF-5A	KAWF-5A_2B	K5A2B2	90	1.70E-15	1.88E-11	0.08	0.62	0.030	0.90	6.80	0.40	2.67	2.67	7.6	1.4	1.5	0.2	5	Gt-Ht-mix			
KAWF-5A	KAWF-5A_2B	K5A2B3	32	3.66E-15	1.14E-10	0.07	0.18	0.010	2.10	5.60	0.50	3.33	3.33	2.7	6.3	6.6	0.8	5	Gt-Ht-mix			
KAWF-5A	KAWF-5A_2B	K5A2B4	26	1.43E-15	5.50E-11	0.02	0.12	0.010	0.74	4.60	0.23	1.53	1.53	6.2	5.6	5.8	0.9	5	Gt-Ht-mix			
KAWF-5A	KAWF-5A_2C	K5A2C1	36	2.50E-15	6.94E-11	0.04	0.23	0.020	1.10	6.40	0.60	4.00	4.00	5.9	5.0	5.3	0.7	5	Ht			
KAWF-5A	KAWF-5A_2C	K5A2C2	25	1.87E-15	7.50E-11	0.01	0.08	0.000	0.50	3.30	0.00	0.00	0.00	6.6	10.9	11.4	1.6	5	Ht			
KAWF-5A	KAWF-5A_2C	K5A2C3	20	5.35E-16	2.68E-11	0.01	0.15	0.000	0.40	7.50	0.20	1.33	1.33	18.0	2.4	2.5	0.6	5	Ht			
KAWF-5A	KAWF-5A_3AII	K5A3AII1	87	1.20E-14	1.38E-10	0.08	0.34	0.000	0.93	3.89	0.05	0.32	0.32	4.2	13.7	15.1	2.5	10	Gt		0.00	
KAWF-5A	KAWF-5A_3AII	K5A3AII2	49	8.03E-15	1.64E-10	0.13	0.17	0.010	2.75	3.42	0.14	0.93	0.93	1.2	8.4	9.2	1.6	10	Gt		0.00	
KAWF-5A	KAWF-5A_3AII	K5A3AII3	35	8.16E-15	2.33E-10	0.12	0.10	0.010	3.35	2.98	0.19	1.28	0.9	10.7	11.8	11.8	2.0	10	Gt		0.00	
KAWF-5A	KAWF-5A_3AII	K5A3AII4	58	8.92E-15	1.54E-10	0.14	0.14	0.010	2.39	2.41	0.12	0.79	1.0	9.5	10.5	10.5	1.8	10	Gt		0.00	
KAWF-5A	KAWF-5A_3AII	K5A3AII5	56	1.04E-14	1.86E-10	0.18	0.17	0.007	3.17	3.06	0.12	0.83	1.0	8.9	9.8	1.5	10	Gt		0.00		
KAWF-5A	KAWF-5A_3AII	K5A3AII6	40	9.46E-15	2.36E-10	0.12	0.14	0.006	3.07	3.50	0.14	0.92	1.1	11.2	12.3	1.9	10	Gt		0.00		
KAWF-5A	KAWF-5A_3AII	K5A3AII7	48	6.02E-15	1.25E-10	0.11	0.16	0.005	2.29	3.30	0.11	0.75	1.4	7.6	8.4	1.3	10	Gt		0.00		
KAWF-5B	KAWF-5B_1B	K5B1B1	63	8.05E-15	1.28E-10	0.12	0.10	0.006	1.93	1.61	0.10	0.64	0.8	10.3	10.8	1.2	5	Gt-Ht-mix		0.51		
KAWF-5B	KAWF-5B_1B	K5B1B2	86	1.39E-14	1.61E-10	0.28	0.15	0.006	3.23	1.77	0.07	0.45	0.5	8.2	8.6	8.6	0.9	5	Gt-Ht-mix		0.51	
KAWF-5B	KAWF-5B_1B	K5B1B3	78	2.63E-15	3.37E-11	0.16	0.14	0.006	2.05	1.82	0.08	0.51	0.9	2.5	2.6	0.3	5	Gt-Ht-mix		0.51		
KAWF-5B	KAWF-5B_1B	K5B1B5	111	5.40E-15	4.86E-11	0.13	0.17	0.010	1.15	1.50	0.09	0.60	1.3	6.0	6.3	6.3	0.7	5	Gt-Ht-mix		0.51	
KAWF-5B	KAWF-5B_2AII	K5B2AII1	110	1.96E-14	1.78E-10	0.34	0.08	0.010	3.08	0.75	0.12	0.81	0.2	10.1	11.1	11.1	1.8	10	Gt		0.13	
KAWF-5B	KAWF-5B_2AII	K5B2AII2	100	2.81E-14	2.81E-10	0.46	0.48	0.020	4.59	4.81	0.17	1.15	1.0	9.1	10.0	10.0	1.6	10	Gt		0.13	
KAWF-5B	KAWF-5B_2AII	K5B2AII4	50	1.47E-14	2.94E-10	0.21	0.22	0.010	4.17	4.45	0.23	1.51	1.1	10.6	11.7	1.9	10	Gt		0.13		
KAWF-5B	KAWF-5B_2AII	K5B2AII5	57	1.47E-14	2.58E-10	0.19	0.18	0.010	3.39	3.09	0.14	0.93	0.9	11.5	12.7	2.0	10	Gt		0.13		
KAWF-5B	KAWF-5B_2AII	K5B2AII6	87	1.96E-14	2.26E-10	0.32	0.10	0.010	3.71	1.17	0.09	0.62	0.3	10.5	11.6	11.6	1.8	10	Gt		0.13	
KAWF-5B	KAWF-5B_3B	K5B3B1	48	7.14E-15	1.49E-10	0.08	0.26	0.000	1.60	5.33	0.08	0.53	3.3	9.4	10.3	1.8	10	Gt		0.00		
KAWF-5B	KAWF-5B_3B	K5B3B2	57	1.47E-14	2.58E-10	0.18	0.38	0.010	3.10	6.59	0.11	0.75	2.1	10.1	11.1	1.8	10	Gt		0.00		
KAWF-5B	KAWF-5B_3B	K5B3B3	69	9.82E-15	1.42E-10	0.15	0.43	0.010	2.11	6.16	0.11	0.71	2.9	7.6	8.4	1.4	10	Gt		0.00		
KAWF-5B	KAWF-5B_3B	K5B3B4	85	2.14E-14	2.52E-10	0.30	0.76	0.010	3.52	8.92	0.11	0.73	2.5	8.3	9.1	1.4	10	Gt		0.00		
KAWF-5B	KAWF-5B_3B	K5B3B5	52	1.75E-14	3.37E-10	0.21	0.35	0.007	3.96	6.69	0.14	0.95	1.7	11.3	12.4	1.9	10	Gt		0.00		
KAWF-5B	KAWF-5B_3B	K5B3B6	52	1.37E-14	2.64E-10	0.22	0.41	0.006	4.33	7.92	0.11	0.74	1.8	7.9	8.7	1.4	10	Gt		0.00		

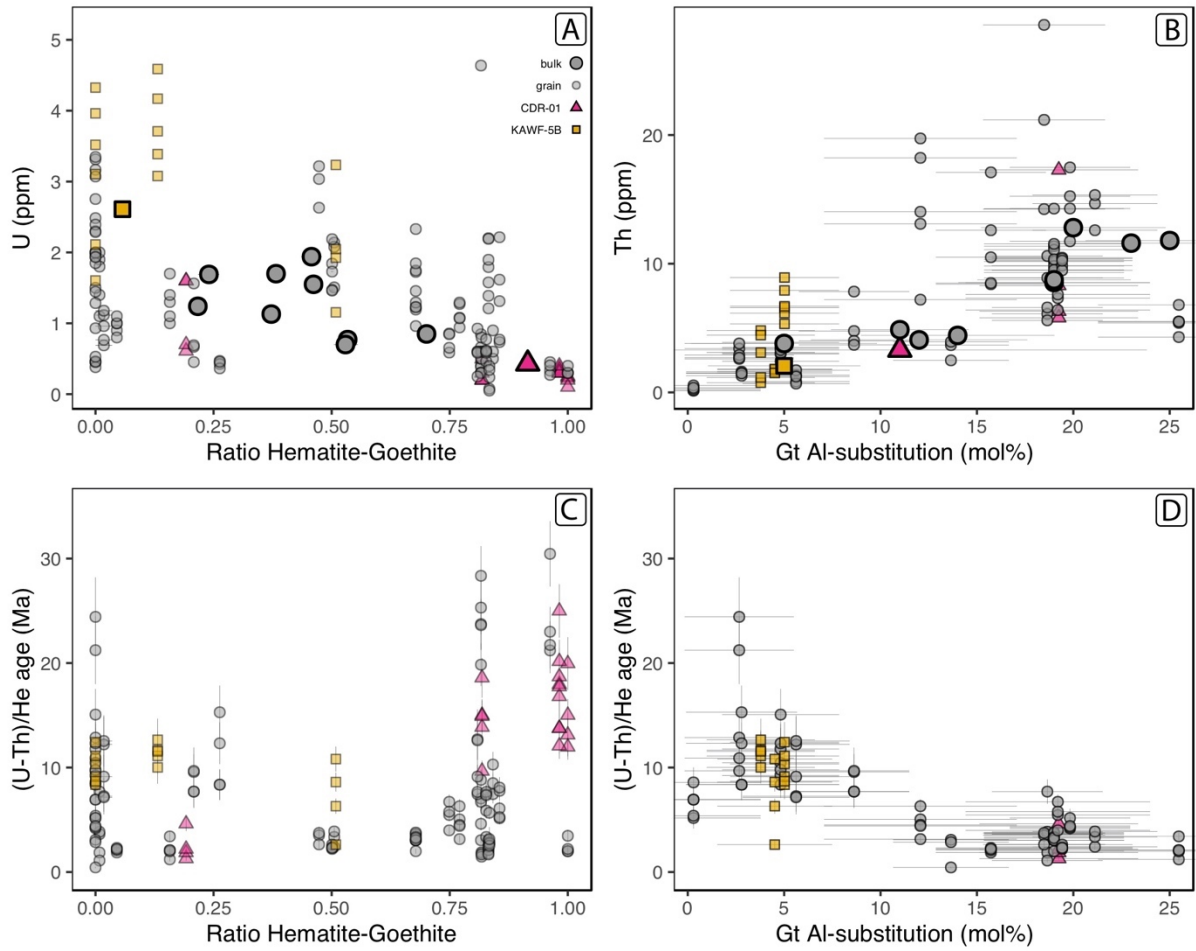


Figure IV-7: Relation of mineralogy and (U-Th)/He data for the analyzed samples and subsample. (A): Ratio hematite-goethite calculated as hematite (wt%)/(hematite(wt%) + goethite (wt%)) versus U concentration in bulk samples and dated grains. (B) shows the Th concentration of the bulk samples and dated grains versus the Al-substitution in goethite for samples and subsamples containing more than 20% goethite. (C) presents the obtained (U-Th)/He ages versus the ratio hematite-goethite, (D) shows (U-Th)/He ages versus Al-substitution in goethite for subsamples containing more than 20% goethite. Pink triangles correspond to sample CDR-01, yellow squares to sample KAWF-5B, grey circles to all other samples. Note that mineralogical data was only obtained for a subset of the dated subsamples.

IV.6 Discussion

IV.6.1 (U-Th)/He age distribution

The (U-Th)/He ages obtained on the lateritic duricrust samples show a very broad distribution entirely covering the range from the 30.5 ± 3.1 to < 0.8 Ma (Table IV-3), illustrating a long history of hematite and goethite precipitation. Interestingly, the ages often correlate with U and Th (Figs. IV-6, B-6, B-8-B-11), which show a considerable variation. This indicates on one hand the existence of different populations of hematite and goethite and, on the other hand, the eventual mixing of the latter. Our geochronological data set shows substantial intra- and inter-subsample age ranges which largely exceed analytical uncertainty (Figs. IV-5 and B-

6). In order to extract geological meaningful information from these data we will therefore discuss the possible reasons of this data distribution and their importance.

Loss or gain of either He or actinide elements can impact the (U-Th)/He ages and in the following different parameters, such as rich U-Th mineral inclusions, He loss due to diffusion, porosity, or wildfire, that can lead to uninterpretable ages, are discussed. Firstly, too old ages can result from neighboring or inclusion of actinide rich minerals such as zircon that will increase the He budget without impacting the U-Th contents (Vasconcelos et al., 2013; Monteiro et al., 2014) or through loss of U by volatilization during degassing as described by Vasconcelos et al. (2013) and Hofmann et al. (2020). We carefully checked many of the subsamples by SEM and only little very small (<5 μm often <2 μm) zircon and rutile inclusions were found. As rutile has generally low U and Th contents (Meinhold, 2010) similar to those observed in our subsamples, such small inclusions are not supposed to significantly increase the ages. Zircon inclusions could be problematic, but according to Vermeesch et al. (2007) and Gautheron et al. (2012) the error, which can result from inclusions of such small size (compared to the ca. 500 μm aliquots), is in the range of 0-20 % depending on the amount of zircon crystals and their U and Th content. Zr content in the bulk samples shows no enrichment (100-260 ppm) compared to the mean upper continental crust (193 ppm, Rudnick and Gao, 2013) indicating no major presence of zircon in our samples.

Secondly, the U content is consistent between the dated subsamples and the bulk samples (Fig. IV-7A) indicating no detectable loss of U during the degassing procedure. Figure B-3 of the Electronic Supplement shows examples of several subsamples with age-U relationships showing a positive or no correlation of (U-Th)/He ages and U, indicating that no major U loss leading to erroneously old ages affected the samples. Furthermore, the heating temperature during degassing was controlled and an internal goethite standard was systematically analyzed with the samples. It is therefore little probable that our data set contains erroneously old ages. Note at this point that the three oldest ages come from three different subsamples (CDR-02_2A, CDR-02_2D and CDR-02_2E) of the same bulk sample but overlap within error.

Thirdly, He loss can lead to erroneously young ages, associated with He lost (ca. 2-20 %) due to the polycrystalline nature of hematite and goethite (Shuster et al., 2005; Heim et al., 2006; Vasconcelos et al., 2013; Balout et al., 2017; Deng et al., 2017; Hofmann et al., 2017; Farley, 2018). However, our adapted He loss diffusion correction and the large error applied

allows one to correct for this issue, even if this correction does not include eventual He loss due to porosity or poor crystallinity. The Fe-minerals dated here are often porous (e. g. Fig. IV-4C, -4F, -4G). If pores are empty, alpha-particles are not stopped when going through them, ejection is thus not a problem. However, if the pores are filled with water, the alpha particles will be slowed down or stopped. The mean distance of alpha particles in water is $\sim 35 \mu\text{m}$ (Palmer and Akhavan-Rezayat, 1978) (versus $\sim 15 \mu\text{m}$ in hematite and goethite, Ketcham et al., (2011)). In water filled pores $> 35 \mu\text{m}$ all alpha particles will therefore be stopped, whereas only some alpha particles will be stopped in pores $< 35 \mu\text{m}$ (depending on their incident energy and the size of the pore). Porosity and intergrown unretentive phases have no impact on He diffusivity if the pores (or unretentive phases) are small and unconnected. However, interconnected porosity (or large unretentive phases) can accelerate diffusion as He might escape along these fast diffusion pathways and be lost.

The above analysis shows that there are only few factors that can lead to erroneously old ages (zircon inclusions and U evaporation) and we do not consider that they have had a major influence on our dataset. Even if uncontrolled He loss by diffusion through interconnected porosity and unretentive phases might also play a role, we believe that measured U, Th, Sm, and He content of this study are robust and that the (U-Th)/He ages are mainly related to weathering processes, i.e. iron oxyhydroxide precipitation, dissolution and reprecipitation. For discussion of the mechanisms of these processes in lateritic iron crusts see Monteiro et al., (2014). Thus, gain of U and Th can mainly occur by later addition of Th and U bearing phases. When addition happens significantly after initial precipitation this will lead to mixed ages between the initial and the later phase. The effect of this mixing upon the measured ages will depend on the endmember ages, respective concentrations of U and Th in the initial and the added phases and the proportions of the latter. As shown in Figure IV-4, the dated subsamples are often not homogeneous at microscopic scale and some of the dated aliquots represent a small-scale mixture of several phases of the same or different mineralogy. The commonly observed trends of age with U or Th support this assumption (Figs. IV-5 and IV-6). To test the mixing of minerals with different U-Th content and ages, a simple mixing model has been performed and results for different phase mixing scenarios of a 20 Ma old phase with a 2 Ma old phase with various actinide content are reported in Figure IV-8 as well as Figure B-13 and Table B-5 of the Electronic Supplement. Depending on the actinide concentrations in the two phases, the apparent mixed age, i.e. age that would be obtained from the measured

amount of He, U and Th, varies a lot. The order of magnitude of change will depend on the two endmembers age value. If the older phase has low actinide concentrations and the younger one high concentrations, the mixed age gets considerably younger even when containing small amounts of the younger phase. For example, in scenario 1 (phase 1 = 20 Ma, 0.3 ppm U, and 0.3 ppm Th and phase 2 = 2 Ma, 2 ppm U, and 10 ppm Th, pink squares in Fig. IV-8), a mixing of 90 % : 10 % leads to an extreme rejuvenation of the age (mixed age ca. 10 Ma). On the contrary, scenario 2 (phase 1 = 20 Ma, 2ppm U, and 10ppm Th and phase 2 = 2Ma, 0.3ppm U and 0.3 ppm Th, yellow circles in Fig. IV-8) with a 40 % : 60 % mixing produced an age at still 18 Ma. However, in the latter case small amounts of the old phase mixed in the young phase led to significantly older ages. For more extreme concentration differences, the age varies even more abruptly. For equal concentrations in both phases the age changes linearly with the proportion of the phases (grey triangles in Fig. IV-8).

The mixing examples show, how even small amounts of a second phase can significantly change the measured ages. If old phases are actinide-poor, as it is the case for most of our samples (Figs. IV-5B and -5C), small amounts of an actinide-rich younger phase can considerably lower and spread the ages. On the other hand, the mixing scenario 2 shows that an old phase which is actinide rich can incorporate large amounts of an actinide poor younger phase without this leading to a spread of the data. This could explain the rather homogeneous ages observed in the older subsamples of sample KAWF-5 (Fig. IV-6). In addition, the complex age versus U/Th relations observed in our dataset coupled to the SEM microscale petrological images indicate that in our samples and probably also in some of the individual subsamples, more than 2 phases are being mixed. The impact of the mixing onto the ages depends strongly on the actinide concentrations. The fact that in most samples the youngest subsamples are actinide rich might be one principal reason for the large age range observed in our dataset.

We assume that most age spreading inside individual subsamples is due to mixing of phases related to multiple redissolution/reprecipitation processes. Depending on the proportions of the mixed phases, maximum and minimum ages of each subsample might be of smaller or greater importance. For old subsamples, the oldest ages are endmembers with potential geological significance. In contrast, the younger ages of the same subsamples might probably be a product of phase mixing related to later overgrowths or posterior precipitation of material in voids. Overlapping maximum ages in similar subsamples – such as subsamples CDR-02_2A, CDR-02_2D and CDR-02_2E which yield the three oldest ages of our dataset (Fig.

IV-5 and Table IV-3) – indicate that these ages have probably a geologic significance (see also Monteiro et al., (2014)). For the youngest subsamples, the situation is slightly different as mixing of previously existing material with the new material might lead to older ages. This could probably be the case when a coating forms on top of an ancient matrix by hydration of the latter as for example in CDR-01A_1 (see also Fig. IV-4L). We should therefore regard both maximum and minimum ages of the dated subsamples in order to extract geologically significant information from the present data set (Fig. IV-9A-B). Maximum ages are more relevant in the older subsamples while minimum ages might give insight into the last event(s) that affected the samples.

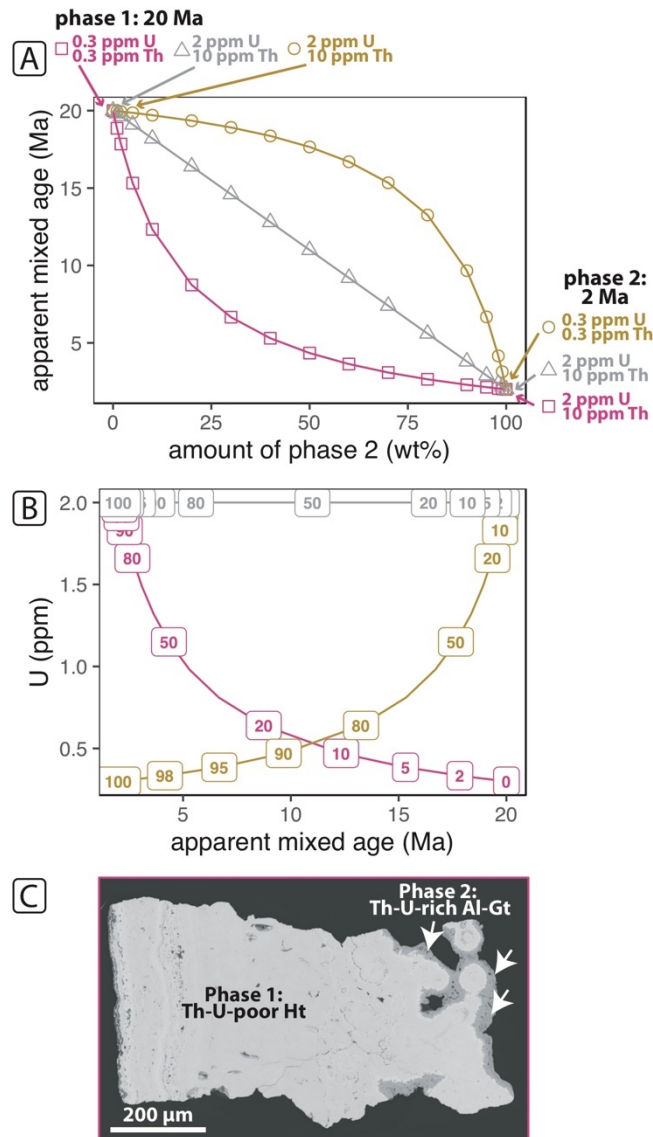


Figure IV-8: Theoretical phase mixing scenarios of two phases with different ages, 20 Ma and 2 Ma, and different actinide concentrations. (A) shows the mixed apparent ages which would be measured as a function of the percentage of phase 2. Actinide concentrations for all phases and scenarios are indicated in the corresponding colors. The evolution of the age varies strongly in between the different scenarios. When actinide concentrations are lower in phase 1 than in phase 2 (pink rectangles), the age drops quickly even with low amounts of phase 2. When phase 1 is richer in actinides than phase 2 (yellow circles), the age drops slowly in the beginning and very fast at the end. For equal concentrations in both phases (grey triangles), the relation between age and proportion of phase 2 is linear. B shows the apparent mixed ages relative to the total U concentrations, colors are as in A. The labels indicate the percentage of phase 2 in the mixing. For scenario 1 (pink rectangles) the addition of 10% of phase 2 leads to drop of age from 20 to 10 Ma whereas in scenario 2 (yellow circles) an amount of 60% of phase 2 lead only to a minor drop from 20Ma to 18 Ma. The graph for Th vs mixed age looks very similar and can be found together with the Th/U graph in Fig. B-13 of the Electronic Supplement. (C) shows an example of a grain composed mainly of Th and U poor Hematite but which shows a small Gt rim (see white arrows). We suppose that these rims observed in some of the grains of subsample CDR-01B_3 are composed of late stage U and Th rich Al Gt and lead to the dispersed ages of this subsample which correlate with U and Th. Assumed endmember ages and actinide concentrations resemble those of scenario 1.

IV.6.2 (U-Th)/He ages, mineralogy and chemistry variation: insight for dissolution and recrystallisation processes

The comparison of the mineralogy and mineral chemistry with the age data gives insight into the evolution of the duricrust system. The oldest ages (30-25 Ma), obtained on subsamples

from samples CDR-02 and CDR-01, are composed of hematite with none or very few goethite (see Table IV-3, Figs. IV-7 and IV-9B). These subsamples have (compared to the other subsamples) low U concentrations and very low to intermediate Th concentrations (see Figs. IV-5 and IV-9C). Goethite starts to precipitate since ca. 25-20 Ma (CDR-04A_3B) but is more common since ca. 14 to 13 Ma (KAWF-5 and KAWF-4, Fig. IV-9B). These early goethite subsamples are very Al poor (2-6 mol%) and contain only small amounts of hematite (Figs. IV-7 and IV-9D). Most of them have high U and low to intermediate Th concentrations (see yellow squares in Fig. IV-5, IV-6F and IV-6G). Since ca. 13-10 Ma, hematite and goethite are more intimately mixed (Fig. IV-7C) and goethite gets increasingly enriched in Al. The subsamples with ages <5 Ma are predominantly composed of goethite (Fig. IV-9B) and these young goethite subsamples contain the highest amounts of Al-substitution (Fig. IV-9D). From 10-8 Ma on, U and Th concentrations get more diverse and increase in some subsamples (Figs. IV-5B, -5C and -9C).

The observed temporal evolution of the Al-rich hematite and goethite minerals seems to highlight important insight into the weathering processes. The Al-content and stability of hematite and goethite are strongly linked to the activity of water, the elements (Si, Al, Fe) in solution, the minerals they are associated with (kaolinite, gibbsite, quartz), the temperature and the grain size as shown by Tardy and Nahon (1985); Trolard and Tardy (1987) and Tardy (1997) who studied in detail Al-goethite and Al-hematite in ferricretes (iron crusts) and bauxites. On the scale of a lateritic weathering profile, Al-substitutions in goethite and hematite increase from the bottom to the top (Fitzpatrick and Schwertmann, 1982; Fritsch et al., 2005). When percolating fluids are rich in silica, Al-substitution in hematite and goethite is low and kaolinite forms. Tardy and Nahon (1985) propose that primary hematite forms mainly in small pore spaces associated with kaolinite. When conditions get undersaturated and kaolinite gets unstable and is slowly replaced by hematite, the hematite gets richer in Al. Al-rich goethite forms in the first stages of the rehydration of Al-rich hematite, the highest Al-substitutions in goethite occur with the maximum dissolution of kaolinite. When percolating fluids are Si-poor and Al-rich, Al-goethite precipitates together with gibbsite. Tardy and Nahon (1985) report 2-20 mol% Al-substitution in goethite when the latter is associated with kaolinite in ferricretes and 18-27 mol% Al-substitution when it is associated with gibbsite in bauxites. For bauxites, Bardossy and Aleva (1990) describe high Al-substitution in primary goethite and hematite (i.e.

formed with gibbsite / boehmite) and low Al-substitution in secondary goethite and hematite such as fissure fillings or crusts.

This allows some important interpretations regarding the conditions of sample formation. The first hematite subsamples, which precipitated since 30 Ma, formed while kaolinite was stable, possibly even in equilibrium with the latter, in line with the mechanism proposed by Tardy and Nahon (1985). The kaolinite minerals were completely dissolved later and only their phantoms remain (Fig IV-4C and -4D). The oldest goethite subsamples are Al-poor with Al-substitutions <6 mol% (Fig. IV-9D), indicating stability with kaolinite and absence of gibbsite. Only since ca. 8 Ma Al-rich goethite precipitates, and the Al-contents in goethite increase towards younger ages (Fig. IV-9D). High Al-substitutions in goethite can be found in coatings of small pisoliths and the outermost coatings, i.e. where rehydration happens, as well as in the matrix where goethite is associated with gibbsite. The sample textures indicate many dissolution and reprecipitation cycles. This might also lead to a local enrichment of Al if the more mobile Fe is lixiviated and the less mobile Al reprecipitates at the same place. The amount of Fe in the solution can either be completely removed from the system or reprecipitate elsewhere in form of very pure, Al-poor goethite (for example KAWF-1A_5CII).

The Th and U concentrations of the dated grains give equally some information on the precipitation conditions of the Fe-minerals. Th is a very immobile element and, as can be seen in Figure IV-7B, shows a very similar behavior as Al. The first subsamples show rather low concentrations of Th <10 ppm (Fig. IV-5C and -9C, median Th concentration for grains >10 Ma = 1.7 ppm Th). Since 10 Ma, Th concentrations and also Th/U ratios start to increase (median Th concentration for grains <10 Ma = 7.3 ppm Th). The highest Th concentrations (10-33 ppm Th) can be found in small pisoliths which are in the process of rehydration and in the outermost rehydration coatings. The lowest Th concentrations (<0.5 ppm) can be found in the very pure, Al-poor botryoidal goethite and hematite of subsamples KAWF-1A_5CII and CDR-01_3 (Fig. IV-6C, Table IV-3). While Al can come either from the dissolution of kaolinite or dissolution/precipitation cycles of Fe minerals, the Th enrichment and the increase of the Th/U ratio we can observe since 10 Ma are probably due to dissolution/precipitation cycles of Fe minerals as kaolinite does not incorporate significant quantities of Th (Braun et al., 1993). The increase in Th (and Al) indicates therefore that there is an increase of dissolution/precipitation cycles of Fe minerals since 10 Ma (Fig. IV-9).

On the contrary, U shows a different behavior than Th. U concentrations are not linked to the Al-content of goethite but seem to be linked to the amount of goethite compared to hematite, indicating that U is mainly contained in goethite (Fig. IV-7A). Under oxidizing conditions U forms Uranyl, which is much more mobile than Th and is transported with the fluids. The strong affinity of U for iron oxides is well documented as well in adsorption as in coprecipitation contexts (Hsi and Langmuir, 1985; Manceau et al., 1992; Bruno et al., 1995). Thus, Fe minerals precipitated directly from the fluids with a high water activity might be more prone to be U-rich. This could explain why goethite is generally U richer and hematite, which forms with relatively low water activity, either in small pores or from dehydration of Gt, tends to be U poorer.

IV.6.3 Timing of lateritization and bauxitization and relation with local geomorphology

Low-temperature thermochronological studies from rocks from the basement of the Guiana Shield in north eastern French Guiana indicate that the rocks are exhumed close to the surface at ca. 90 Ma (Derycke et al., 2021). This age can be regarded as maximum age constraint for the onset of weathering processes. The (U-Th)/He ages obtained in our study show that surface weathering on Kaw mountain started at least at the beginning of the Oligocene (oldest ages found in our samples). However, these ages have to be considered as minimum age constraint for the onset of weathering. To form a lateritic profile with a duricrust and (more or less) well-crystallized hematite and goethite, it needs a favorable climate and time (Beauvais and Colin, 1993; Vasconcelos et al., 2015). The age of the oldest duricrusts will thus not correspond to the onset of weathering.

The (U-Th)/He results do not provide any information on what happened in between 90 and 30 Ma. It is possible that older Fe minerals exist in the duricrust of Kaw mountain but that we did not sample them. The different age distributions in our samples show how much the samples vary in terms of age and composition. Furthermore, it is very likely that older Fe minerals were not preserved as they got dissolved later on. Tardy (1997) explains that in an evolving duricrusted lateritic profile, the duricrust is formed lower, at the interface with the fluctuating water table, while it is degraded/dismantled higher in the profile at the interface with the soil cover. Owing to this degradation/dismantling process, Fe migrates downwards and the duricrust gets rejuvenated at its bottom (e.g. Beauvais (1999) and Beauvais (2009) who described this degradation process resulting in a secondary ferruginisation front migrating

downward in lateritic profiles in Central Africa). Therefore, lateritic duricrust gets younger at its bottom and older at its top. This constant rejuvenation of the duricrust is then one reason why old ages might not be preserved in an evolving duricrust system.

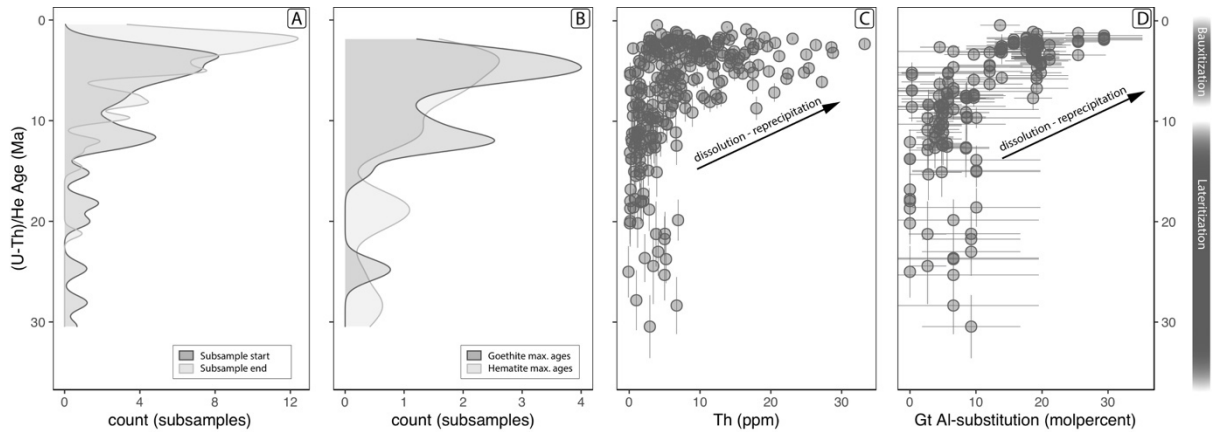


Figure IV-9: (A) shows Kernel density estimates of the maximum (dark gray) and minimum (bright gray) ages of our dated subsamples. (B) shows Kernel density estimates of the maximum ages of hematite (bright gray) and goethite (dark gray) subsamples. Very mixed subsamples (predominant mineral in Table IV-3 = hematite-goethite-mix) are not represented. (C) shows Th concentrations vs (U-Th)/He ages for all dated grains. (D) shows (U-Th)/He ages versus Al-substitution in goethite for subsamples analysed by micro-XRD with more than 20% goethite. Al-substitutions are mean values by subsample whereas all (U-Th)/He ages for these subsamples are plotted.

The overall age distribution (Fig. IV-10) of our results which shows a more or less exponential decrease towards older ages and resembles in its general shape those of other authors (Monteiro et al., 2014, 2018; dos Santos Albuquerque et al., 2020) could result from (more or less) continuous weathering with permanent dissolution and reprecipitation cycles under relatively constant conditions. However, our petrological, mineralogical and geochemical results allow a deeper insight and imply an important change in the weathering conditions. From our results, a lateritic system with precipitation of ferruginous duricrust has been set in place at the beginning of the Oligocene. Weathering probably continued during the Oligocene and Early Miocene but, from the few ages we obtain between 30 and 14 Ma (probably many of them being mixed ages), it is impossible to identify discrete events. Subsample onsets (i.e. maximum ages) are at 30-27 Ma (CDR-02), 25-24 Ma (CDR-01 and CDR-04C), 20-18 Ma, around 15 Ma and, more significantly, from ~14 to 13 Ma on (Fig. IV-9A). The maximum age peak at ~12 Ma, that postdates the Middle Miocene Climate Optimum (MMCO, 17-14.5 Ma (Flower, 1999; Herold et al., 2011)) by 2-3 Myr, could indicate very favorable weathering conditions (Fig. IV-9). As explained in Section IV.6.2, these old subsamples crystallized while kaolinite was stable without incorporating major amount of Al, indicating the presence of a “classical”/ ferruginous

lateritic system without formation of gibbsite and / or bauxite (Fig. IV-9). The distribution of hematite and goethite within this period of ferruginous lateritization, with a predominance of hematite from 30 to 14 Ma and Al-poor goethite appearing significantly only since ~14 Ma (Fig. IV-9B), indicates, that the climate might have developed from hotter and/or more arid seasonally contrasted monsoonal climate with preferential precipitation of hematite to more humid (and/or eventually cooler) seasonally contrasted monsoonal climate with preferential precipitation of goethite (Trolard and Tardy, 1987; Tardy and Roquin, 1998).

The 10-8 Ma period seems to record a change towards more intense weathering conditions which peak at 6-2 Ma. Under these intense weathering conditions kaolinite got unstable, Fe-mineral recycling became faster and the formerly ferruginous laterite was bauxitized. Whether weathering was continuous or characterized by discrete events during the last 10 Myr is not possible to say from our data. Both a continuous intensification of weathering since 10 Ma with a peak between 6 and 2 Ma as well as a short-lasting bauxitization event at ca. 3-2 Ma associated with strong mineral recycling could produce the observed results. The intense phase mixing makes a differentiation of the two processes impossible.

Ages > 15 Ma are obtained exclusively in samples collected on the northern flank of the mountain ridge (Fig. IV-5A). This flank is more exposed to the predominant wind directions and is closer to the sea, possibly leading to higher precipitations. Bardossy and Aleva (1990) observe at other bauxite sites more alteration on elevated luv-sides than on lee-sides. Spatial distribution of ages > 15 Ma only on NE flank could either be a sampling effect or indicate that conditions favorable for Fe-duricrust formation were set in place earlier on the NE flank than on the SW flank. With the available sampling material, this question cannot be answered.

There is no significant difference between the samples collected at the top and those coming from the flanks of the ridge. However, KAWF-1, which was sampled from a giant detached block, shows some different features compared to the other samples, notably the abundance of kaolinite, the scarcity of gibbsite and young ages <5 Ma. This could indicate a disconnection, i.e. break off, from the overall duricrust system at the beginning of the bauxitization phase through dissolution of an important amount of material just below the duricrust. The stair-like morphology observed on the flanks of Kaw mountain (Choubert, 1956), as well as the caves which exist below the duricrust at several places, might be related to the same phenomenon which could thus be synchronous to the bauxitization at the end of Neogene.

IV.6.4 Regional and climatic context of the lateritization and bauxitization of Kaw Mountain

IV.6.4.1 Comparison with available age data: highlighting the climate signals

Figure IV-10 compares the results obtained in this study with available geochronological data from Amazonia. While all existing (U-Th)/He data correspond to sites faraway (> 1000 km) from our study area, the paleomagnetism data of Théveniaut and Freyssinet (2002) were obtained on Kaw mountain and nearby duricrusts in French Guiana and Suriname. For Kaw, the authors obtain ages of ca. 50 ± 10 Ma, 13-10 Ma and very recent ages. A Mid to Late Miocene age obtained on a sample from lower elevations (220 m) of Kaw mountain is very similar to the age peak we observed in our dataset at ca. 14-12 Ma. Three other samples from Kaw of Théveniaut and Freyssinet (2002) yield magnetic poles which fall in between the 10 Ma paleopole and the recent magnetic pole (Fig. IV-10). While the authors assign these results to recent reworking on top of the duricrust, it is possible that this signal is related to the intense weathering phase we observe in our samples in the late Neogene. Their results for the low elevation units in the Cayenne area (Cayenne Units 2 and 3, Fig. IV-10) and from the Surinamese Moengo deposit with values of ca. 10-8 Ma show an overlap with our data. Due to the large uncertainty of paleomagnetism ages however, a more detailed comparison is not possible.

The available (U-Th)/He and ^{40}Ar - ^{39}Ar data from supergene Fe and Mn oxides from Amazonia (Vasconcelos et al., 1994; Ruffet et al., 1996; Shuster et al., 2005, 2012; Allard et al., 2018; Monteiro et al., 2018; dos Santos Albuquerque et al., 2020) presented in Figure IV-10 derive from areas more than 1000 km away from Kaw mountain and located mainly South of the Amazon River. Different from our data, most of the aforementioned studies comprise much older ages spanning over large parts of the Cenozoic up to the Paleozoic (dos Santos Albuquerque et al., 2020). Although the compilation of all (U-Th)/He data (Fig. IV-10) shows an increase in age density since the Pliocene, this feature is much less pronounced in the literature data when compared to our dataset. Age density curves are obviously biased by the number of aliquots dated per subsample and the chosen subsamples and should therefore not be overinterpreted. Nevertheless, the comparison shows the importance of the Late Neogene bauxitization event for our samples. In any case, the comparably older ages obtained from the high elevation samples (ca. 700m) from the Carajás area (Vasconcelos et al., 1994; Ruffet et al., 1996; Shuster et al., 2005, 2012; Monteiro et al., 2018) are consistent with the geomorphological models, which sustain the idea of older surface ages on high elevation

surfaces and younger ages in low elevation surfaces (Choubert, 1957; King, 1962; McConnell, 1968; Blancaneaux, 1981; Bardossy and Aleva, 1990; Briceño and Schubert, 1990).

The ^{40}Ar - ^{39}Ar data by Vasconcelos et al. (1994) and Ruffet et al. (1996) show a peak at 15-10 Ma, similar to the peak we observe in our data at 14-12 Ma. Note that this peak is just shortly after the MMCO (17-14.5 Ma). The $\delta^{18}\text{O}$ isotope curve (Zachos et al., 2008) in Figure IV-10 indicates a general temperature decrease since the MMCO. This is compatible with or observed hematite-goethite distribution (Fig. IV-9B) which could result either from a shift from more arid (ca. 30 to 14 Ma) to more humid climate (since ~14 Ma) or from a decrease in temperature with higher temperatures from 30 to 14 Ma and lower temperatures since ~14 Ma (Trolard and Tardy, 1987; Tardy and Roquin, 1998).

Despite of the general temperature decrease since the MMCO, periods of warm climate (with global mean temperatures 2 – 4°C higher than those of preindustrial climate) existed during the Pliocene, notably during the Pliocene Climatic Optimum (ca. 4.4 – 4.0 Ma, Fedorov et al., 2013) and the mid-Pliocene Warm Period (mPWP, 3.3 – 3.0 Ma, (Haywood et al., 2013). During the mPWP the intertropical convergence zone was shifted northwards leading to a dryer South American Summer Monsoon over intertropical South America (Pontes et al., 2020) but eventually increasing precipitations north of the equator and accelerating weathering in the Guianas. Our proposed bauxitization could thus be linked to increased precipitation during the mPWP.

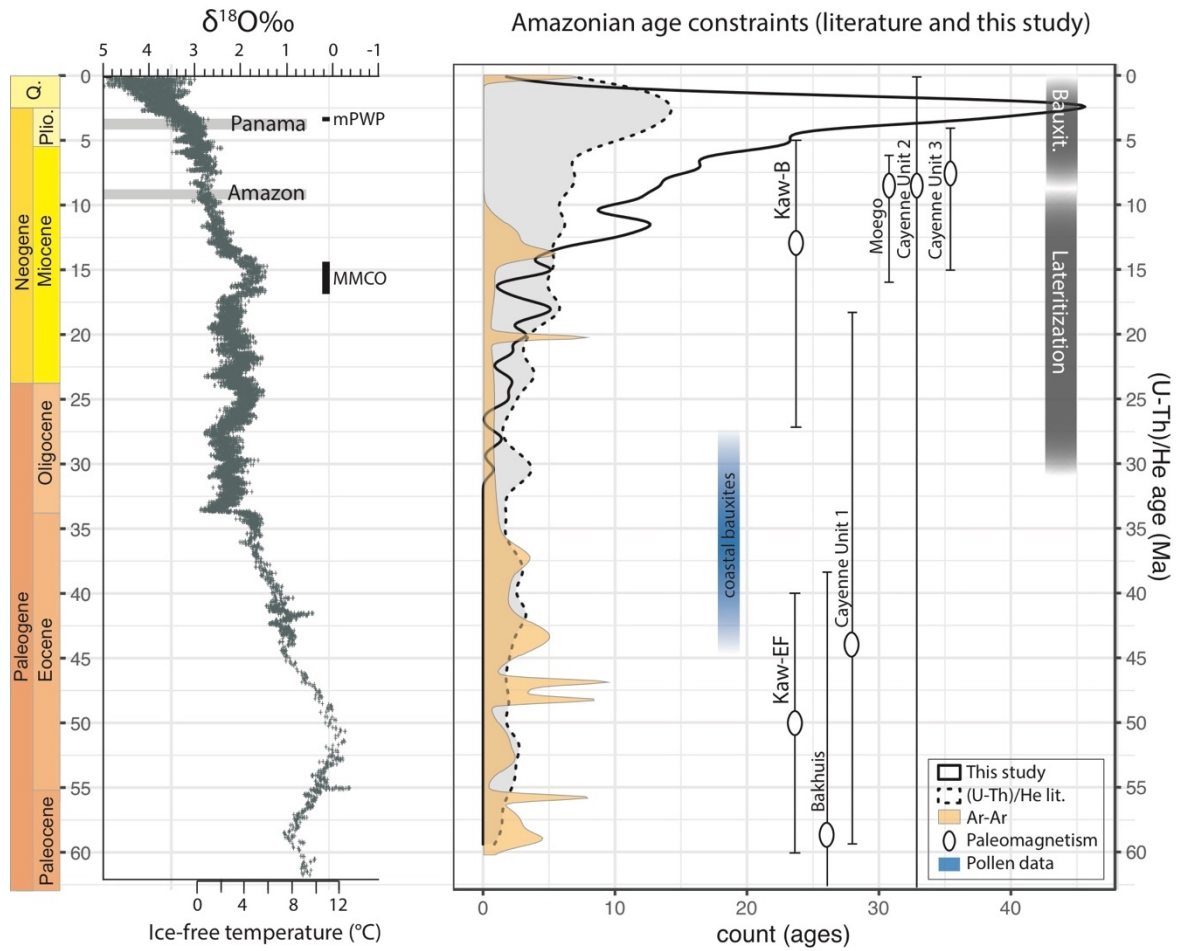


Figure IV-10: Compilation of available climate data, main geologic events in Amazonia, published geochronological data and our new data for the last 60 Myr. $\delta^{18}\text{O}$ data from Zachos et al. (2008) is a proxy for the global temperature, MMCO= Middle Miocene Climate Optimum, mPWP = mid-Pliocene Warm Period. Age constraints for laterites and bauxites in Amazonia: Black solid line: Kernel density distribution of our age data. Literature data: the grey Kernel density curves shows the available (U-Th)/He ages of supergene Fe- and Mn minerals from the Amazon craton from (Shuster et al., 2012; Allard et al., 2018; Monteiro et al., 2018; dos Santos Albuquerque et al., 2020). Note that only ages <60 Ma are shown. Data from Shuster et al. (2005) is not plotted as their samples are included in the dataset of Monteiro et al. (2018). Orange density curve: probability density plot of the ^{39}Ar - ^{40}Ar data of Vasconcelos et al. (1994) and Ruffet et al. (1996) on the Southern part of the Amazon craton. Where available, plateau ages were used, otherwise isochron ages. Ellipses with vertical error bars: paleomagnetism ages of Théveniaut and Freyssinet (2002) for different sites in French Guiana (including Kaw) and Suriname. Note that the location of “KAW-EF” is at ca. 300m elevation and location of “KAW-B” at ca. 220m. The blue bar shows the supposed age of the coastal bauxites in Suriname and Guyana (Hammen and Wymstra, 1964; Bardossy and Aleva, 1990).

IV.6.4.2 Comparison with other bauxites of the Amazonian craton

Most of the bauxites of the coastal plain in Guyana and Suriname are underlain and capped by sediments. Detailed sedimentological palynological studies of the under- and overlaying sediments (Hammen and Wymstra, 1964; Wymstra, 1971) allow the determination of a Late Eocene to Oligocene age of the bauxitization event. In the sediments of the coastal plain this phase is recognized as the so called “Bauxite Hiatus” (Wong, 1994). Other important hiatuses occur at the Cretaceous-Tertiary boundary and near the base of the Miocene (Wong,

1986; Wong, 1994), and palynological results indicate that large parts of the Miocene are missing in the sedimentary record (Wymstra, 1971; Wong, 1986), supporting the existence of several weathering episodes during the Cenozoic.

In contrast, no reliable age data exists for the generally uncovered bauxites formed on top of the basement rocks of the Guiana shield and on top of the Cretaceous-Paleogene sediments of the Amazonas basin. Bardossy and Aleva (1990) propose a Late Cretaceous or Early Tertiary origin for several of them, but also mention, that they often seem to have a polyphase origin and that bauxitization might largely postdate lateritization and continue today.

The Late Eocene to Oligocene age of the coastal bauxites in Suriname and Guyana overlaps with our oldest ages and underlines the geological significance of the latter. However, this raises the question why in the coastal belt bauxites are produced whereas at Kaw ferruginous laterites are developed. While unequal precipitation could be one reason, differences in the drainage capacities due to the different parental material could also be responsible for this different evolution, as Bardossy and Aleva, (1990) have shown that drainage is one of the key parameters controlling bauxite formation, whereas parental rock composition plays a subordinate role (Schellmann, 1994). The bauxites of the coastal belt are generally on top of highly permeable arkosic sandstones which are possibly better drained than the schists of the Paramaca formation at Kaw. As explained in Section 6.3, the (U-Th)/He ages of the Fe oxyhydroxides are minimum estimates for the onset of alteration. It is thus possible that lateritic (but not bauxitic) cover of Kaw mountain developed isochronal to the coastal bauxites in the neighboring country.

IV.6.5 Implications for the regional climate and geology

Our results show that tropical climate, allowing the formation of laterite, exists at Kaw since at least 30 Ma. As the late Neogene bauxitization event had a strong impact on the preexisting Fe-duricrust, we cannot say if these conditions have lasted continuously since then or not. The peak of maximum subsample ages at 12-14 Ma suggests that favorable conditions existed during the Middle Miocene. From 30 to 12 Ma the climate might have been more seasonally contrasted tropical climate, as lateritic duricrust, but not bauxitic duricrust was formed. The distribution of hematite and goethite suggests that there might have been a

transition from hotter and dryer to more humid and/or eventually cooler seasonally contrasted tropical climate during this period.

Bardossy and Aleva (1990) have shown that the formation of lateritic bauxites requires some specific conditions when compared to ferruginous laterites. These are notably a humid tropical monsoonal climate and very good drainage conditions. The shift to increasing bauxitic conditions observed in our samples potentially indicates change in local climate including better drainage conditions in the Late Neogene.

Due to the lack of lake sediments or carbonates little is known about the climatic variations in Amazonia throughout the last Myr. However, the major geological changes which affected the area throughout the Cenozoic, notably several uplift episodes of the Andes (Rodríguez Tribaldos et al., 2017) and the closure of the Panama isthmus (Coates, 1992; Bartoli et al., 2005), have potentially influenced the regional climate. While temperatures might have been more or less stable due to the position in tropical latitudes with variations mainly connected to global temperature variations, precipitation patterns might have changed more significantly. Studies of the current climate of the Guianas show that the area is subject to a rather complex precipitation pattern with considerable small-scale variation whereas temperatures show less variation (Bovolo et al., 2012; Ringard et al., 2015). The intensity increase of weathering processes observed in our dataset since the end of the Neogene indicates probably an increase in precipitation. On the one hand, enhanced precipitation could be a local feature. Nowadays the area of Kaw mountain is the area with the highest precipitations in French Guiana. This pattern might have been set in place at the end of the Neogene. On the other hand, there could have been a more regional change in precipitation patterns in Amazonia possibly related to the closure of the Panama Isthmus at ca. 3.5-2.7 Ma (Coates, 1992; Bartoli et al., 2005) with influence on oceanic currents and wind pattern in the area or to the mid-Pliocene Warm Period. The results from Western Amazonia (Allard et al., 2018; Mathian et al., 2020) yielding similar weathering ages support this possibility.

Improvement of the drainage conditions (Bardossy and Aleva, 1990) could additionally have intensified the weathering processes at Kaw in the late Neogene. Due to the already developed weathering mantle, the permeability of the parental material was likely increased. Bardossy and Aleva, (1990) describe that bauxites occur mainly on highly dissected plateaus, but the temporal relationship of incision and bauxitization is not totally clear. Augmented incision inducing better drainage could have been triggered by relative movements of the

continent (uplift) or the sea level (drop). With the Miocene transcontinentalization of the Amazon river, sediments from the Andes started to deposit in the Amazon fan from around 11 Ma (Figueiredo et al., 2009; Hoorn et al., 2017). In a short period of time, mainly since 6.8 Ma and even more since 2.4 Ma, huge masses of sediments have been deposited in the fan (> 4000 m), leading to an enormous weight pushing down the plate (Figueiredo et al., 2009). Flexural uplift owing to this sediment loading on the margin was suggested by Figueiredo et al., (2009) and Sapin et al., (2016). The bauxitization event, which could have lasted several Myr or less, could therefore be linked to increased uplift of the Guyana shield. A coupled process with uplift leading to locally increased precipitation due to change of the relief could also have possibly triggered the bauxitization process. Comparative studies at other sites would be needed in order to find an answer to this question.

IV.7 Conclusions

Our new data shed light onto an area so far only poorly constrained by weathering geochronology. The lateritic bauxitic cover of Kaw Mountain (French Guiana) records weathering since at least the Oligocene. The oldest Fe minerals dated in this study formed during or after kaolinite formation under ferruginous lateritic (not aluminous lateritic) conditions ca. 30 Ma ago. Ferruginous lateritic conditions with precipitation of hematite and Al-poor goethite and stability of kaolinite prevailed during the Early and Middle Miocene. Precipitation of Fe-minerals became more common at 14-10 Ma. Increase in phase mixing, Fe-Al-substitution in goethite, Th concentration and Th/U ratio as well as gibbsite precipitation imply an intensification of the weathering conditions during the Late Miocene, the Pliocene and Early Pleistocene, starting at ca. 10 Ma with a peak at 6-2 Ma. We assume that this intensification of weathering is responsible for the bauxitization of the weathering surface of Kaw mountain. The Th and U rich Fe minerals formed during this late stage of intense weathering got mixed with the preexisting Fe minerals leading to a strong spreading of the bulk (U-Th)/He ages.

Comparison with nearby bauxites indicates that the onset of weathering at Kaw could have been synchronous to the formation of the coastal bauxites in Suriname and Guyana. The different intensity of the Paleogene weathering which produced bauxites on top of the sedimentary rocks in Suriname and Guyana and ferruginous lateritic cover on top of the

basement rocks at Kaw might be due to the different drainage capacities of the parental material.

The Late Neogene bauxitization event that we observe in our data has not yet been described in the area. Bauxitization at Kaw could have been caused either by a regional or global change in precipitation, possibly by flexural uplift owing to sedimentary loading in the Amazon fan leading to increased incision and thus increased drainage, or a combination of these processes with uplift leading to changes in the local precipitation pattern. Finally, this study reveals that climatic signal hidden in ferruginous laterite and bauxite could be revealed by combining geochronological results with mineralogical and geochemical analyses.

Acknowledgements

This work is funded and carried out in the framework of the BRGM-TOTAL project Source-to-Sink and the French funding Agency ANR RECA-ANR-17-CE01-0012-01 project. Frédéric Haurine and Pierre Burckel are warmly thanked for the ICP-MS analysis, Ludovic Delbes and Benoît Baptiste for support with XRD analyses and Imène Esteve for help with SEM analyses. The editor Jeffrey Catalano, Florian Hofmann and two anonymous reviewers helped to improve this manuscript with their constructive comments.

References

- Aleva G. J. J. (1981) Essential differences between the Bauxite Deposits along the Southern and Northern Edges of the Guiana Shield, South America. *Econ. Geol.* **76**, 1142–1152.
- Aleva G. J. J. (1984) Lateritization, bauxitization and cyclic landscape development in the Guiana Shield. In *Bauxite* (ed. L. Jacob Jr). A.I.M.E, New York, USA. pp. 297–318.
- Allard T., Gautheron C., Bressan Riffel S., Balan E., Soares B. F., Pinna-Jamme R., Derycke A., Morin G., Bueno G. T. and do Nascimento N. (2018) Combined dating of goethites and kaolinites from ferruginous duricrusts. Deciphering the Late Neogene erosion history of Central Amazonia. *Chem. Geol.* **479**, 136–150.
- Baker P. A., Fritz S. C., Silva C. G., Rigsby C. A., Absy M. L., Almeida R. P., Caputo M., Chiessi C. M., Cruz F. W., Dick C. W., Feakins S. J., Figueiredo J., Freeman K. H., Hoorn C., Jaramillo C., Kern A. K., Latrubesse E. M., Ledru M. P., Marzoli A., Myrbo A., Noren A., Piller W. E., Ramos M. I. F., Ribas C. C., Trnadade R., West A. J., Wahnfried I. and

- Willard D. A. (2015) Trans-Amazon Drilling Project (TADP): Origins and evolution of the forests, climate, and hydrology of the South American tropics. *Sci. Drill.* **20**, 41–49.
- Balan E., Allard T., Fritsch E., Sélo M., Falguères C., Chabaux F., Pierret M. C. and Calas G. (2005) Formation and evolution of lateritic profiles in the middle Amazon basin: Insights from radiation-induced defects in kaolinite. *Geochim. Cosmochim. Acta* **69**, 2193–2204.
- Balout H., Roques J., Gautheron C., Tassan-Got L. and Mbongo-Djimbi D. (2017) Helium diffusion in pure hematite ($\alpha\text{-Fe}_2\text{O}_3$) for thermochronometric applications: A theoretical multi-scale study. *Comput. Theor. Chem.* **1099**, 21–28.
- Bardossy G. and Aleva G. J. J. (1990) *Lateritic Bauxites*. Developmen., Elsevier Science, Amsterdam, The Netherlands.
- Bartoli G., Sarnthein M., Weinelt M., Erlenkeuser H., Garbe-Schönberg D. and Lea D. W. (2005) Final closure of Panama and the onset of northern hemisphere glaciation. *Earth Planet. Sci. Lett.* **237**, 33–44.
- Beauvais A. (2009) Ferricrete biochemical degradation on the rainforest-savannas boundary of Central African Republic. *Geoderma* **150**, 379–388.
- Beauvais A. (1999) Geochemical balance of lateritization processes and climatic signatures in weathering profiles overlain by ferricretes in Central Africa. *Geochim. Cosmochim. Acta* **63**, 3939–3957.
- Beauvais A. and Colin F. (1993) Formation and transformation processes of iron duricrust systems in tropical humid environment. *Chem. Geol.* **106**, 77–101.
- Beauvais A., Ruffet G., Hénocque O. and Colin F. (2008) Chemical and physical erosion rhythms of the West African Cenozoic morphogenesis: The $^{39}\text{Ar}\text{-}^{40}\text{Ar}$ dating of supergene K-Mn oxides. *J. Geophys. Res. Earth Surf.* **113**, 1–15.
- Beck H. E., Zimmermann N. E., McVicar T. R., Vergopolan N., Berg A. and Wood E. F. (2018) Present and future köppen-geiger climate classification maps at 1-km resolution. *Sci. Data* **5**, 1–12.
- Berar J. F. and Baldinozzi G. (1998) XND code: From X-ray laboratory data to incommensurately modulated phases. *Rietveld Model. complex Mater. CPD Newsl.* **20**, 3–5.
- Bish D. L. and Von Dreele R. B. (1989) Rietveld refinement of non-hydrogen atomic positions in kaolinite. *Clays Clay Miner.* **37**, 289–296.

- Blake R. L., Hessevick R. E., Zoltai T. and Finger L. W. (1966) Refinement of the hematite structure. *Am. Mineral. J. Earth Planet. Mater.* **51**, 123–129.
- Blancaneaux P. (1981) *Essai sur le milieu naturel de la Guyane Française.*, Paris.
- Bovolo C. I., Pereira R., Parkin G., Kilsby C. and Wagner T. (2012) Fine-scale regional climate patterns in the Guianas, tropical South America, based on observations and reanalysis data. *Int. J. Climatol.* **32**, 1665–1689.
- Braun J. J., Pagel M., Herbilln A. and Rosin C. (1993) Mobilization and redistribution of REEs and thorium in a syenitic lateritic profile: A mass balance study. *Geochim. Cosmochim. Acta* **57**, 4419–4434.
- Briceño H. O. and Schubert C. (1990) Geomorphology of the Gran Sabana, Guayana Shield, southeastern Venezuela. *Geomorphology* **3**, 125–141.
- Bruno J., De Pablo J., Duro L. and Figuerola E. (1995) Experimental study and modeling of the U(VI)-Fe(OH)₃ surface precipitation/coprecipitation equilibria. *Geochim. Cosmochim. Acta* **59**, 4113–4123.
- Carvalho A., Boulangé B., Melfi A. J. and Lucas Y. (1997) *Brazilian Bauxites*. eds. A. Carvalho, B. Boulangé, A. J. Melfi, and Y. Lucas, USP, FAPESP, ORSTOM, São Paulo, Paris.
- Choubert B. (1957) *Essai sur la morphologie de la Guyane.*, Imprimerie Nationale, Paris.
- Choubert B. (1956) *Les Gisements de bauxite de la Guyane Française*. ORSTOM, Paris, 15 p.
- Coates A. G. (1992) Closure of the Isthmus of Panama: the near-shore marine record of Costa Rica and western Panama. *Geol. Soc. Am. Bull.* **104**, 814–828.
- Corbató C. E., Tettenhorst R. T. and Christoph G. G. (1985) Structure refinement of deuterated boehmite. *Clays Clay Miner.* **33**, 71–75.
- Cordani U. G. and Teixeira W. (2007) Proterozoic accretionary belts in the Amazonian Craton. In *4-D Framework of Continental Crust: Geological Society of America Memoir 200* (eds. R. D. J. Hatcher, M. P. Carlson, J. H. McBride, and J. . Martínez-Catalán). Geological Society of America, Boulder, CO. pp. 297–320.
- Cromer D. T. (1983) Calculation of anomalous scattering factors at arbitrary wavelengths. *J. Appl. Crystallogr.* **16**, 437–437.
- Danišík M., Evans N. J., Ramanaidou E. R., McDonald B. J., Mayers C. and McInnes B. I. A. (2013) (U-Th)/He chronology of the Robe River channel iron deposits, Hamersley Province, Western Australia. *Chem. Geol.* **354**, 150–162.

- Delor C., Lahondère D., Egal E., Lafon J. M., Cocherie A., Guerrot C., Rossi P., Truffert C., Théveniaut H., Phillips D. and Avelar V. G. de (2003) Transamazonian crustal growth and reworking as revealed by the 1:500,000-scale geological map of French Guiana (2nd edition). *Geol. la Fr.* **2-3-4**, 5–57.
- Deng X. D., Li J. W. and Shuster D. L. (2017) Late Mio-Pliocene chemical weathering of the Yulong porphyry Cu deposit in the eastern Tibetan Plateau constrained by goethite (U–Th)/He dating: Implication for Asian summer monsoon. *Earth Planet. Sci. Lett.* **472**, 289–298.
- Derycke A., Gautheron C., Barbarand J., Bourbon P., Aertgeerts G., Simon-Labric T., Sarda P., Pinna-Jamme R., Boukari C. and Haurine F. (2021) French Guiana margin evolution: From Gondwana break-up to Atlantic opening. *Terra Nov.*, 1–8.
- Dublet G., Juillot F., Morin G., Fritsch E., Fandeur D. and Brown G. E. (2015) Goethite aging explains Ni depletion in upper units of ultramafic lateritic ores from New Caledonia. *Geochim. Cosmochim. Acta* **160**, 1–15.
- Farley K. A. (2002) (U–Th) / He Dating: Techniques, Calibrations, and Applications. *Rev. Mineral. Geochemistry* **47**, 819–844.
- Farley K. A. (2018) Helium diffusion parameters of hematite from a single-diffusion-domain crystal. *Geochim. Cosmochim. Acta* **231**, 117–129.
- Farley K. A., Wolf R. A. and Silver L. T. (1996) The effects of long alpha-stopping distances on (U–Th)/He ages. *Geochim. Cosmochim. Acta* **60**, 4223–4229.
- Fedorov A. V., Brierley C. M., Lawrence K. T., Liu Z., Dekens P. S. and Ravelo A. C. (2013) Patterns and mechanisms of early Pliocene warmth. *Nature* **496**, 43–49.
- Figueiredo J., Hoorn C., van der Ven P. and Soares E. (2009) Late Miocene onset of the Amazon River and the Amazon deep-sea fan: Evidence from the Foz do Amazonas Basin. *Geology* **37**, 619–622.
- Fitzpatrick R. W. and Schwertmann U. (1982) Al-substituted goethite—An indicator of pedogenic and other weathering environments in South Africa. *Geoderma* **27**, 335–347.
- Flower B. P. (1999) Warming without high CO₂? *Nature* **399**, 313–314.
- Forsyth J. B., Hedley I. G. and Johnson C. E. (1968) The magnetic structure and hyperfine field of goethite (α -FeOOH). *J. Phys. C Solid State Phys.* **1**, 179.

- Fritsch E., Morin G., Bedidi A., Bonnin D., Balan E., Caquineau S. and Calas G. (2005) Transformation of haematite and Al-poor goethite to Al-rich goethite and associated yellowing in a ferralitic clay soil profile of the middle Amazon Basin (Manaus, Brazil). *Eur. J. Soil Sci.* **56**, 575–588.
- Gautheron C., Pinna Jamme R., Derycke, A. A., Hadi F., Sanchez C., Haurine F., Monvoisin G., Barbosa D., Delpech G., Maltese J., Sarda P. and Tassan-Got L. (2021) Analytical protocols and performance for apatite and zircon (U-Th)/He analysis on quadrupole and magnetic sector mass spectrometer systems between 2007 and 2020. *Geochronology*.
- Gautheron C., Tassan-Got L., Ketcham R. A. and Dobson K. J. (2012) Accounting for long alpha-particle stopping distances in (U-Th-Sm)/He geochronology: 3D modeling of diffusion, zoning, implantation, and abrasion. *Geochim. Cosmochim. Acta* **96**, 44–56.
- Gómez J., Schobbenhaus C., Montes N. E. and Compilers (2019) *Geological Map of South America 2019. Scale 1:5 000 000.*,
- Groussin J. (2001) Le Climat Guyanais. In *Atlas illustré de la Guyane* (ed. J. Barret). Laboratoire de Cartographie de la Guyane; Institut d'Enseignement Supérieur de Guyane. pp. 46–49.
- Hammen van der T. and Wymstra T. A. (1964) A Palynological study on the Tertiary and Upper Cretaceous of British Guiana. *Leidse Geol. Meded.* **30**, 183–241.
- Hammersley A. P. (2016) FIT2D: a multi-purpose data reduction, analysis and visualization program. *J. Appl. Crystallogr.* **49**, 646–652.
- Haywood A. M., Hill D. J., Dolan A. M., Otto-Bliesner B. L., Bragg F., Chan W. L., Chandler M. A., Contoux C., Dowsett H. J., Jost A., Kamae Y., Lohmann G., Lunt D. J., Abe-Ouchi A., Pickering S. J., Ramstein G., Rosenbloom N. A., Salzmann U., Sohl L., Stepanek C., Ueda H., Yan Q. and Zhang Z. (2013) Large-scale features of Pliocene climate: Results from the Pliocene Model Intercomparison Project. *Clim. Past* **9**, 191–209.
- Heim J. A., Vasconcelos P. M., Shuster D. L., Farley K. A. and Broadbent G. (2006) Dating paleochannel iron ore by (U-Th)/He analysis of supergene goethite, Hamersley province, Australia. *Geology* **34**, 173–176.
- Herold N., Huber M. and Müller R. D. (2011) Modeling the miocene climatic optimum. Part I: Land and atmosphere. *J. Clim.* **24**, 6353–6373.

- Hofmann F., Reichenbacher B. and Farley K. A. (2017) Evidence for >5 Ma paleo-exposure of an Eocene–Miocene paleosol of the Bohnerz Formation, Switzerland. *Earth Planet. Sci. Lett.* **465**, 168–175.
- Hofmann F., Treffkorn J. and Farley K. A. (2020) U-loss associated with laser-heating of hematite and goethite in vacuum during (U-Th)/He dating and prevention using high O₂ partial pressure. *Chem. Geol.* **532**.
- Hoorn C., Bogotá-A G. R., Romero-Baez M., Lammertsma E. I., Flantua S. G. A., Dantas E. L., Dino R., do Carmo D. A. and Chemale F. (2017) The Amazon at sea: Onset and stages of the Amazon River from a marine record, with special reference to Neogene plant turnover in the drainage basin. *Glob. Planet. Change* **153**, 51–65.
- Hoorn C., Roddaz M., Dino R., Soares E., Uba C., Ochoa-Lozano D., Mapes R. (2010) The Amazonian craton and its influence on past fluvial systems (Mesozoic-Cenozoic, Amazonia). In *Amazonia: landscape and species evolution. A look into the past*. Hoorn C. and Wesselingh F.P. (Eds). Wiley-Blackwell. 103-122
- Hoorn C., Wesselingh F. P., ter Steege H., Bermudez M. A., Mora A., Sevink J., Sanmartín I., Sanchez-Meseguer A., Anderson C. L., Figueiredo J. P., Jaramillo C., Riff D., Negri F. R., Hooghiemstra H., Lundberg J., Stadler T., Särkinen T. and Antonelli A. (2010) Amazonia Through Time : Andean Uplift, Climate Change, Landscape Evolution and Biodiversity. *Science*. **330**, 927–931.
- Horn M. S. C. F., Schwebdtfeger C. F. and Meagher E. P. (1972) Refinement of the structure of anatase at several temperatures. *Zeitschrift für Krist. Mater.* **136**, 273–281.
- Hsi C.-K. D. and Langmuir D. (1985) Adsorption of uranyl onto ferric oxyhydroxides: Application of the surface complexation site-binding model. *Geochim. Cosmochim. Acta* **49**, 1931–1941.
- Ketcham R. A., Gautheron C. and Tassan-Got L. (2011) Accounting for long alpha-particle stopping distances in (U-Th-Sm)/He geochronology: Refinement of the baseline case. *Geochim. Cosmochim. Acta* **75**, 7779–7791.
- King L. C. (1962) *Morphology of the Earth: A Study and Synthesis of World Scenery.*, Oliver and Boyd Publ. House, Edinburgh and London, 699 p.
- Leprieur (1848) Exploration géologique du bassin de la Comté (Guyane Française). *Bull. la Société Géologique la Fr.* **5**, 251–254.

- Lippolt H. J., Brander T. and Mankopf N. R. (1998) An attempt to determine formation ages of goethites and limonites by (U+Th)-⁴He dating. *Neues Jahrb. Mineral. Monatshefte* **11**.
- Manceau A., Charlet L., Boisset M. C., Didier B. and Spadini L. (1992) Sorption and speciation of heavy metals on hydrous Fe and Mn oxides. From microscopic to macroscopic. *Appl. Clay Sci.* **7**, 201–223.
- Mathian M., Bueno G. T., Balan E., Fritsch E., Do Nascimento N. R., Selo M. and Allard T. (2020) Kaolinite dating from Acrisol and Ferralsol: A new key to understanding the landscape evolution in NW Amazonia (Brazil). *Geoderma* **370**.
- McConnell R. B. (1968) Planation Surfaces in Guyana. *Geogr. J.* **134**, 506–520.
- Meinhold G. (2010) Rutile and its applications in earth sciences. *Earth-Science Rev.* **102**, 1–28.
- Mendes A. C., Truckenbrod W. and Nogueira A. C. R. (2012) Análise faciológica da formação Alter do Chão (Cretáceo, Bacia do Amazonas), próximo à cidade de Óbidos, Pará, Brasil. *Rev. Bras. Geociencias* **42**, 39–57.
- Monsels D. A. and Van Bergen M. J. (2019) Bauxite formation on Tertiary sediments in the coastal plain of Suriname. *J. South Am. Earth Sci.* **89**, 275–298.
- Monteiro H. S., Vasconcelos P. M., Farley K. A., Spier C. A. and Mello C. L. (2014) (U-Th)/He geochronology of goethite and the origin and evolution of cangas. *Geochim. Cosmochim. Acta* **131**, 267–289.
- Monteiro H. S., Vasconcelos P. M. P., Farley K. A. and Lopes C. A. M. (2018) Age and evolution of diachronous erosion surfaces in the Amazon: Combining (U-Th)/He and cosmogenic ³He records. *Geochim. Cosmochim. Acta* **229**, 162–183.
- Nahon D. (1991) *Introduction to the petrology of soils and chemical weathering.*, Wiley, New York, USA.
- Palmer R. B. J. and Akhavan-Rezayat A. (1978) The stopping power of water, water vapour and aqueous tissue equivalent solution for alpha particles over the energy range 0.5-8 MeV. *J. Phys. D. Appl. Phys.* **11**, 605–616.
- Patterson S. H., Kurtz H. F., Olson J. C. and Neeley C. L. (1994) *World Bauxite Resources - Geology and Resources of Aluminum*. U.S. Geolo., U.S. Geological Survey, Washington.
- Pidgeon R. T. (2003) Application of (U-Th)/ He Geochronology To Date Hematite and Other Iron Minerals Produced During Weathering. *Advances*, 321–323.

- Pidgeon R. T., Brander T. and Lippolt H. J. (2004) Late Miocene (U+Th)-⁴He ages of ferruginous nodules from lateritic duricrust, Darling Range, Western Australia. *Aust. J. Earth Sci.* **51**, 901–909.
- Pontes G. M., Wainer I., Taschetto A. S., Sen Gupta A., Abe-Ouchi A., Brady E. C., Chan W. Le, Chandan D., Contoux C., Feng R., Hunter S. J., Kame Y., Lohmann G., Otto-Bliesner B. L., Peltier W. R., Stepanek C., Tindall J., Tan N., Zhang Q. and Zhang Z. (2020) Drier tropical and subtropical Southern Hemisphere in the mid-Pliocene Warm Period. *Sci. Rep.* **10**, 1–11.
- Prasad G. (1983) A review of the early Tertiary bauxite event in South America, Africa and India. *J. African Earth Sci.* **1**, 305–313.
- Putzer, H. 1984. The geological evolution of the Amazon basin and its mineral resources. In: *The Amazon: Limnology and Landscape Ecology of a Mighty Tropical River and its Basin* (ed. H. Sioli). Dr W. Junk Publishers, Dordrecht, pp. 15–46.
- Reiners P. W., Chan M. A. and Evenson N. S. (2014) (U-Th)/He geochronology and chemical compositions of diagenetic cement, concretions, and fracture-filling oxide minerals in mesozoic sandstones of the Colorado Plateau. *Bull. Geol. Soc. Am.* **126**, 1363–1383.
- Riffel S. B., Vasconcelos P. M., Carmo I. O. and Farley K. A. (2015) Combined ⁴⁰Ar/³⁹Ar and (U-Th)/He geochronological constraints on long-term landscape evolution of the Second Paraná Plateau and its ruiniform surface features, Paraná, Brazil. *Geomorphology* **233**, 52–63.
- Riffel S. B., Vasconcelos P. M., Carmo I. O. and Farley K. A. (2016) Goethite (U–Th)/He geochronology and precipitation mechanisms during weathering of basalts. *Chem. Geol.* **446**, 18–32.
- Ringard J., Becker M., Seyler F. and Linguet L. (2015) Temporal and spatial assessment of four satellite rainfall estimates over French Guiana and north Brazil. *Remote Sens.* **7**, 16441–16459.
- Rodríguez Tribaldos V., White N. J., Roberts G. G. and Hoggard M. J. (2017) Spatial and temporal uplift history of South America from calibrated drainage analysis. *Geochemistry, Geophys. Geosystems* **18**, 2321–2153.
- Rudnick R. L. and Gao S. (2013) *Composition of the Continental Crust*. 2nd ed., Elsevier Ltd.

- Ruffet G., Innocent C., Michard A., Féraud G., Beauvais A., Nahon D. and Hamelin B. (1996) A geochronological $^{40}\text{Ar}/^{39}\text{Ar}$ and $^{87}\text{Rb}/^{87}\text{Sr}$ study of K-Mn oxides from the weathering sequence of Azul, Brazil. *Geochim. Cosmochim. Acta* **60**, 2219–2232.
- Saalfeld H. and Wedde M. (1974) Refinement of the crystal structure of gibbsite, $\text{Al}(\text{OH})_3$. *Zeitschrift für Krist. Mater.* **139**, 129–135.
- dos Santos Albuquerque M. F., Horbe A. M. C. and Danišík M. (2020) Episodic weathering in Southwestern Amazonia based on (U–Th)/He dating of Fe and Mn lateritic duricrust. *Chem. Geol.* **553**, 119792.
- Sapin F., Davaux M., Dall’asta M., Lahmi M., Baudot G. and Ringenbach J.-C. (2016) Post-rift subsidence of the French Guiana hyper-oblique margin: From rift-inherited subsidence to Amazon deposition effect. *Geol. Soc. Spec. Publ.* **431**, 125–144.
- Schellmann W. (1994) Geochemical differentiation in laterite and bauxite formation. *Catena* **21**, 131–143.
- Schulze D. G. (1984) The influence of aluminium on iron oxides. VIII. Unit-cell dimensions of Al-substituted goethites and estimation of Al from them. *Clays Clay Miner.* **32**, 36–44.
- Shintani H., Sato S. and Saito Y. (1975) Electron-density distribution in rutile crystals. *Acta Crystallogr. Sect. B Struct. Crystallogr. Cryst. Chem.* **31**, 1981–1982.
- Shuster D. L., Farley K. A., Vasconcelos P. M., Balco G., Monteiro H. S., Waltenberg K. and Stone J. O. (2012) Cosmogenic ^3He in hematite and goethite from Brazilian “canga” duricrust demonstrates the extreme stability of these surfaces. *Earth Planet. Sci. Lett.* **329–330**, 41–50.
- Shuster D. L., Vasconcelos P. M., Heim J. A. and Farley K. A. (2005) Weathering geochronology by (U–Th)/He dating of goethite. *Geochim. Cosmochim. Acta* **69**, 659–673.
- Snyder D. B. and Bish D. L. (1989) Quantitative analysis. *Mineral. Soc. Am. Rev. Mineral.* **20**, 101–144.
- Stanjek H. and Schwertmann U. (1992) The influence of aluminum on iron oxides. Part XVI: Hydroxyl and aluminum substitution in synthetic hematites. *Clays Clay Miner.* **40**, 347–354.
- Sundell K. E., Saylor J. E., Lapen T. J. and Horton B. K. (2019) Implications of variable late Cenozoic surface uplift across the Peruvian central Andes. *Sci. Rep.* **9**, 1–12.
- Tardy Y. (1997) *Petrology of Laterites and Tropical Soils.*, Balkema, Rotterdam, The Netherlands.

- Tardy Y., Kobilsek B. and Paquet H. (1991) Mineralogical composition and geographical distribution of African and Brazilian periatlantic laterites. The influence of continental drift and tropical paleoclimates during the past 150 million years and implications for India and Australia. *J. African Earth Sci.* **12**, 283–295.
- Tardy Y. and Nahon D. (1985) Geochemistry of laterites, stability of Al-goethite, Al-hematite, and Fe³⁺-Kaolinite in bauxites and ferricretes: an approach to the mechanism of concretion formation. *Am. J. Sci.* **285**, 865–903.
- Tardy Y. and Roquin C. (1998) *Dérive des continents paléoclimats et altérations tropicales.*, BRGM, Orléans, France.
- Théveniaut H. and Freyssinet P. (1999) Paleomagnetism applied to lateritic profiles to assess saprolite and duricrust formation processes: The example of Mont Baduel profile (French Guiana). *Palaeogeogr. Palaeoclimatol. Palaeoecol.* **148**, 209–231.
- Théveniaut H. and Freyssinet P. (2002) Timing of lateritization on the Guiana Shield synthesis of paleomagnetic results. *Palaeogeogr. Palaeoclimatol. Palaeoecol.* **178**, 91–117.
- Toby B. H. (2006) R factors in Rietveld analysis: How good is good enough? . *Powder Diffr.* **21**, 67–70.
- Trolard F. and Tardy Y. (1987) The stabilities of gibbsite, boehmite, aluminous goethites and aluminous hematites in bauxites, ferricretes and laterites as a function of water activity, temperature and particle size. *Geochim. Cosmochim. Acta* **51**, 945–957.
- Valeton I. (1972) *Bauxites*. Developmen., Elsevier, Amsterdam, The Netherlands.
- Valeton I. (1999) Saprolite-bauxite facies of ferralitic duricrust on paleosurfaces of former Pangaea. In *Palaeoweathering, Palaeosurfaces and Related Continental Deposits* (eds. M. Thiry and R. Simon-Coignon). Blackwell Science Ltd. pp. 153–188.
- Vasconcelos P. M. (1999) K-Ar and ⁴⁰Ar / ³⁹Ar Geochronology of weathering processes. *Annu. Rev. Earth Planet. Sci.* **27**, 183–229.
- Vasconcelos P. M. and Carmo I. de O. (2018) Calibrating denudation chronology through ⁴⁰Ar/³⁹Ar weathering geochronology. *Earth-Science Rev.* **179**, 411–435.
- Vasconcelos P. M., Farley K. A., Stone J., Piacentini T. and Fifield L. K. (2019) Stranded landscapes in the humid tropics: Earth's oldest land surfaces. *Earth Planet. Sci. Lett.* **519**, 152–164.
- Vasconcelos P. M., Heim J. A., Farley K. A., Monteiro H. and Waltenberg K. (2013) ⁴⁰Ar/³⁹Ar and (U-Th)/He -⁴He/³He geochronology of landscape evolution and channel iron

- deposit genesis at Lynn Peak, Western Australia. *Geochim. Cosmochim. Acta* **117**, 283–312.
- Vasconcelos P. M., Reich M. and Shuster D. L. (2015) The paleoclimatic signatures of supergene metal deposits. *Elements* **11**, 317–322.
- Vasconcelos P. M., Renne P. R., Brimhall G. H. and Becker T. A. (1994) Direct dating of weathering phenomena by $^{40}\text{Ar} / ^{39}\text{Ar}$ and K-Ar analysis of supergene K-Mn oxides. *Geochim. Cosmochim. Acta* **58**, 1635–1665.
- Vermeesch P., Seward D., Latkoczy C., Wipf M., Günther D. and Baur H. (2007) α -Emitting mineral inclusions in apatite, their effect on (U-Th)/He ages, and how to reduce it. *Geochim. Cosmochim. Acta* **71**, 1737–1746.
- Wells M. A., Danišík M., McInnes B. I. A. and Morris P. A. (2019) (U-Th)/He-dating of ferruginous duricrust: Insight into laterite formation at Boddington, WA. *Chem. Geol.* **522**, 148–161.
- Wolska E. and Schwertmann U. (1993) The mechanism of solid solution formation between goethite and diaspore. *Neues Jahrb. für Mineral. Monatshefte* **5**, 213–223.
- Wong T. (1994) The Paleocene-Eocene succession in the Guiana Basin. *Bull. la Société belge Géologie* **T.103**, 281–291.
- Wong T. E. (1986) Outline of the stratigraphy and the geological history of the Suriname coastal plain. *Geol. en Mijnb.* **65**, 223–241.
- Wymstra T. A. (1971) The palynology of the Guiana coastal basin. University of Amsterdam.
- Zachos J. C., Dickens G. R. and Zeebe R. E. (2008) An early Cenozoic perspective on greenhouse warming and carbon-cycle dynamics. *Nature* **451**, 279–283.

V Precipitation chronology of hematite and goethite in lateritic duricrusts from equatorial Brazil

Beatrix M. Heller^{1,2}, Cécile Gautheron¹, Caroline Sanchez¹, Guilherme Taitson Bueno³, Themístocles Raphael Gomes Sobrinho⁴, Jean-Yves Roig⁵, Rosella Pinna Jamme¹, Thierry Allard²

¹ : Université Paris-Saclay, CNRS, GEOPS, 91405, Orsay, France

² : IMPMC, UMR 7590, CNRS, Sorbonne Université, MNHN, IRD, 4 place Jussieu, 75252 Paris cedex 05, France

³ : Universidade Federal de Goiás, Instituto de Estudos Socioambientais, Av. Esperança, s/n - Samambaia, Goiânia - GO, 74001-970, Brazil.

⁴ : Instituto Federal do Amapá, Rodovia BR-210, Km 03, S/n - Brasil Novo, AP, 68909-398, Brazil

⁵ : BRGM, 3 avenue Claude Guillemin, BP 6009, 45060 Orléans Cedex 2, France

(Manuscript in preparation for submission to *Geochemistry, Geophysics, Geosystems*)

Abstract

We present a new coupled (U-Th)/He geochronological, mineralogical and geochemical data set of supergene hematite and goethite from a lateritic profile developed on top of Paleoproterozoic schists and BIFs in the area of Serra do Navio, Amapá, Brazil. The (U-Th)/He ages present mostly reproducible ages for each sub-samples, with hematite age ranging from 69.4 ± 3.5 to 16.0 ± 0.8 Ma and goethite from 40.2 ± 2.8 to 8.7 ± 0.9 Ma. Those results indicate that the studied area undergoes lateritic weathering since the Late Cretaceous / Early Paleogene as well as the presence of two discrete weathering events at ~ 30 and ~ 12 Ma with durations of ca. 6 Ma both. In situ mineralogical investigation of the dated subsamples show that these weathering events correspond to the predominant precipitation of hematite (30 Ma) and goethite (12 Ma) and allow insight into the mineralogical and geochemical evolution of the lateritic duricrust. While a canga layer formed on top of the BIFs is composed mainly of relatively coarse-grained hematite and goethite, the duricrusts formed on top of the schists are generally fine grained. During the two discrete weathering events, crystallite sizes tend to increase towards younger ages, goethite becomes richer in Al, U, Th and Sm and is increasingly mixed with kaolinite. The discrete weathering events recorded in this dataset correspond probably to periods with relatively hotter and / or dryer tropical monsoonal climate (~ 30 Ma) and more humid and/ or cooler tropical monsoonal climate (~ 12 Ma). In between these events

and since 8 Ma apparently no hematite and goethite precipitated, indicating that the climate was either unfavorable for keeping the duricrust system active, or the water table dropped significantly, due to uplift or sea level changes, leading to erosion rather than duricrust formation.

V.1 Introduction

Laterites are thick weathering profiles which form under (sub)tropical climatic conditions. Although they are very widespread in (sub)tropical area, many aspects of their genesis and evolution are still not well constrained. Previous studies have shown that they can be very old, especially in (sub)tropical areas of tectonic quiescence, but little is known about their temporal evolution, notably in relation with climatic and geodynamic changes, due to a lack of age data and the difficulty to date this material (e.g. Vasconcelos et al., 1994; Ruffet et al., 1996; Monteiro et al., 2014; Monteiro et al., 2018). The mineralogy of lateritic profiles is generally very simple as they consist mainly of secondary minerals such as kaolinite, Fe (oxyhydr-) oxides and aluminum hydroxides (Tardy, 1997). Whenever K-bearing phases such as supergene Mn oxides are present, weathering ages can be obtained through K-Ar and ^{40}Ar - ^{39}Ar dating. Unfortunately, many laterites lack these minerals.

However, hematite and goethite, which are the principal components of the lateritic iron duricrust generally present at the top of lateritic profiles can be dated by (U-Th)/He geochronology as they quantitatively retain He over moderate geological timescales (Lippolt et al., 1993; Shuster et al., 2005; Heim et al., 2006; Vasconcelos et al., 2013; Reiners et al., 2014; Balout et al., 2017; Deng et al., 2017; Hofmann et al., 2017; Farley, 2018). Several studies have used this methods recently in order to better constrain weathering events and processes (Lippolt et al., 1998; Pidgeon, 2003; Monteiro et al., 2014; Riffel et al., 2016; Allard et al., 2018; Monteiro et al., 2018; Wells et al., 2019; dos Santos Albuquerque et al., 2020). However, most published (U-Th)/He datasets of supergene hematite and goethite present very spread and often poorly reproducible ages (Lima, 2008; Monteiro et al., 2014; Hofmann et al., 2017; Monteiro et al., 2018; dos Santos Albuquerque et al., 2020; Gautheron et al., 2022; Heller et al., 2022). This is probably related to complex weathering histories and mixing of different phases and generations of iron minerals (Heller et al., 2022). Although the (U-Th)/He age distributions of the aforementioned studies often show some dominant age peaks which allow one to determine periods with increased weathering activity, discrete weathering events can

only be scarcely identified. Furthermore, strong mixing and very spread ages make it difficult to put different precipitation processes into a temporal framework and to determine the duration of the weathering events.

In order to overcome the problems related to intense phase mixing and to find out more about the characteristics and durations of weathering events, this study focuses on ferruginous lateritic duricrust samples with relatively simple textures (generally one type of hematite and 1-2 types of goethite with few macroscopic intergrowths) from an area with contrasted tropical monsoonal climate. From geochronology, geochemistry and fine mineralogy data, our aim is to reveal generations of iron (oxyhydr)oxides formed in contrasting conditions and question the record of discrete weathering episodes as highlighted in previous studies devoted to Amazonia. More specifically, we present a new (U-Th)/He dataset of supergene hematite and goethite from a lateritic weathering profile developed on top of Paleoproterozoic schists and banded iron formations of the eastern rim of the Guiana shield, an area where previous geomorphologic studies led to propose peneplanation and weathering periods since the Cretaceous (Choubert, 1957; King, 1962; McConnell, 1968; Blancaneaux, 1981; Aleva, 1984; Bardossy and Aleva, 1990). In our study, the dataset stands out for its rather exceptional reproducibility, which allows the discrimination of one poorly resolved weathering event starting in the Late Cretaceous/ Early Paleogene and two discrete weathering events during the Early Oligocene and Middle Miocene. Combination with high-resolution mineralogical and geochemical analyses allows one to establish a precipitation chronology and enables insights into the mineralogical and geochemical evolution of the duricrust system.

V.2 Geological, geomorphological and climatic context

V.2.1 Regional geology of Amapá state, Northern Brazil

The Amazon craton sets in the northern part of South America can be divided in a northern part called Guiana shield and a southern one called Brazilian or Guaporé shield (Fig. V-1A-B). They are separated by the Amazonas-Solimões basin which hosts the Amazon river. The Amazon craton comprises two Archean cores, the Itamaca block in Venezuela and the Amapá block in Northern Brazil, but was mainly formed during the Paleoproterozoic Trans-Amazonian orogeny (ca. 2.2-1.95 Ga) as well as later accretionary events which happened during the Paleo-, Meso- and Neoproterozoic at its southwestern border (Cordani and Teixeira, 2007). From the end of the Neoproterozoic until the Mesozoic opening of the Atlantic, the

Amazon craton was located next to the West African craton. During the Paleozoic, the Amazonas-Solimões basin was formed and filled with marine and terrestrial sediments. Basin filling continued episodically later during Cretaceous and Cenozoic times.

During the Mesozoic (at ca. 200 Ma) a large volume of magmatic rocks associated to the Central Atlantic Magmatic Province intruded the Amazon craton (Marzoli et al., 1999). Low-temperature thermochronological data from the Guiana shield in French Guiana suggest that its basement rocks have been close to the surface since ca. 90 Ma (Derycke et al., 2021).

The state of Amapá is located at the southeastern rim of the Guiana shield (Fig. V-1B). To the south the shield is covered by Paleozoic Sediments of the Amazonas basin which are overlain by the Cretaceous to Early Cenozoic Alter do Chão formation (Putzer, 1984; Hoorn et al., 2010) and younger, mainly Holocene sediments (Fig. V-1B). To the east the shield is capped by the sediments of the Amapá Coastal plain (ACP), which compose the onshore sediments of the Foz do Amazonas basin. While it was for a longtime thought that many of these sediments belonged to the Miocene Barreiras formation which crops out at many places of the northern and northeastern coast of Brazil, recent studies have shown that the oldest sediments in the ACP, which cover the deeply weathered basement, are actually Pleistocene in age (Bezerra et al., 2015). These Pleistocene sediments are often weathered themselves. Incision preceded deposition of the youngest, Holocene sediments, which are related to the ongoing sedimentation of the Amazon river.

The sediments of the equatorial Brazilian margin record a complex story of sea level changes and subsidence since the onset of rifting (ca. 140 Ma) and drifting (ca. 100 Ma). Note that shelf sedimentation was different north and east of the mouth of the Amazon river. The offshore part of the Foz do Amazonas basin (north of the mouth of the Amazon) mainly documents a marine filling since the Cretaceous with deposition of deep-water mudstones and siltstones which lasted until the Paleocene (Fig. V-1D) (Figueiredo et al., 2007). From the late Paleocene to the late Miocene (ca. 62– 8 Ma), the basin was dominated by mixed carbonate-siliciclastic shelf sediments (Figueiredo et al., 2007; Cruz et al., 2019) (Marajó and Amapá Formations). Deposition of the Amapá carbonates occurred during four major cycles (I: Paleocene to early Eocene, II: middle Eocene, III: late Eocene to late Oligocene, IV: Early to middle Miocene) interrupted by subaerial exposure (Carozzi, 1981; Wolff and Carozzi, 1984; Cruz et al., 2019). Note that deposition of the carbonates took place contemporaneously with siliciclastic sedimentation on the inner shelf, which explains the difference with the ages

indicated in Figure V-1D. Since the Late Miocene the carbonates were stepwise buried due to siliciclastic input; the youngest age of the carbonates has been repeatedly revised (Carozzi, 1981; Wolff and Carozzi, 1984; Figueiredo et al., 2009; Cruz et al., 2019). It has been a matter of debate whether the breakdown of the carbonate platform was linked to the transcontinentalization of the Amazon river, i.e. emplacement of its drainage to the east, which occurred finally during the late Miocene at 9.4 to 8.0 Ma (Figueiredo et al., 2007; Figueiredo et al., 2009; Hoorn et al., 2017; van Soelen et al., 2017; Cruz et al., 2019). A recent study shows that carbonate sedimentation continued at the northeastern shelf of Amapá until 3.7 Ma while it had already stopped further South (Cruz et al., 2019).

To the east of the mouth of the Amazon sedimentation was different, but equally strongly influenced by sea level changes (Rossetti, 2001; Rossetti et al., 2013; Nogueira et al., 2021). After the Cretaceous until the late Oligocene, there was a long period of non-deposition, sub aerial exposure with erosion and weathering, probably related to a drop in sea-level under tropical to subtropical conditions (Fig. V-1D, unconformities "S1+S2") (Rossetti, 2001; Rossetti, 2004; Rossetti et al., 2013). Two important transgressions, possibly related to eustatic sea-level highstands, occurred during the i) Late Oligocene – Early Miocene and ii) Early to Middle Miocene, leading to deposition of carbonates (Pirabas Formation) and siliciclastic sediments (Barreiras Formation) along the northern and northeastern Brazilian coast (Rossetti, 2001; Rossetti et al., 2013). The maximum flooding was during the Langhian (at ca. 15.2 Ma) and was followed by an important eustatic sea level fall, which started in the Late Langhian and had its climax during the Serravallian / Early Tortonian (~11.8-7.3 Ma) (Nogueira et al., 2021). The base of the Barreiras formation, which is either an erosional or a gradual contact, is estimated to be late Oligocene to Early or Middle Miocene in age (Fig. V-1D) (Rossetti et al., 2013; Nogueira et al., 2021). An unconformity with paleosol exists within in Barreiras Formation ("S3"). The top of the Barreiras sediments is strongly weathered and an early (Rossetti 2013) to middle (Nogueira 2021, Rossetti 2004) Miocene age has been proposed as the end of deposition. The Tortonian sea-level drop led to progressive progradation of the deposition and to aerial exposure of the Barreiras formation, resulting in a stop of deposition, erosion and lateritization of the Barreiras sediments (Nogueira 2021, Rossetti 2004). This unconformity ("S4") is overlain by the late Pleistocene Post-Barreiras sediments.

Precipitation chronology of hematite and goethite in lateritic duricrusts from equatorial Brazil

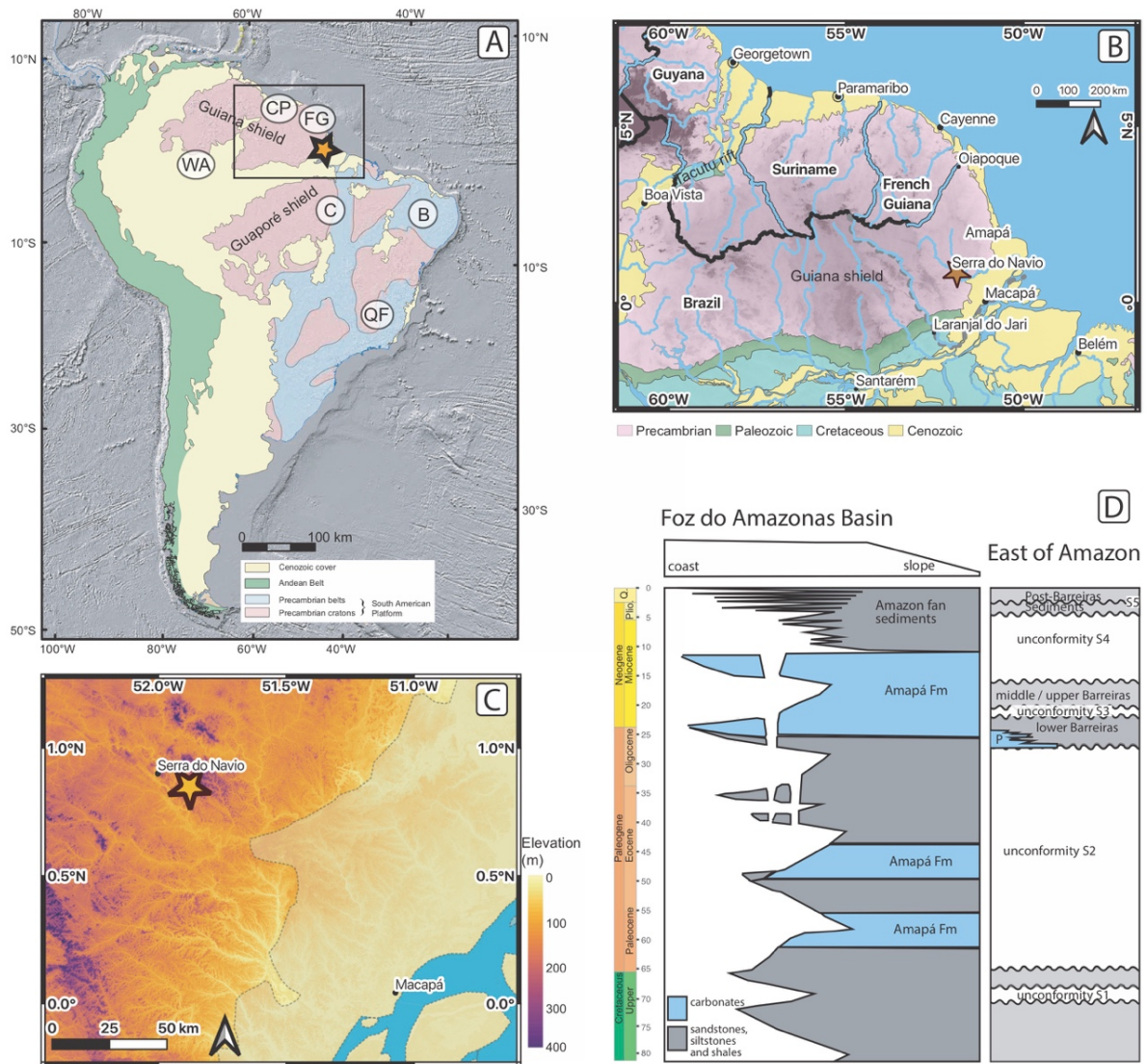


Figure V-1: Geological setting of the study site. (A) Overview map showing the main tectonic domains of South America, modified from Cordani et al. 2016. Paleozoic and Mesozoic covers of the South American Platform are not differentiated. Note that for reasons of simplicity the Cretaceous-Paleogene Alter do Chão Formation is included in the Cenozoic cover in (A). Letters indicate areas for which weathering age data exists: CP: Coastal Plain of Guyana and Suriname; FG: French Guiana; WA: Western Amazonia; C: Carajás; B: Borborema Province; QF: Quadrilátero Ferrífero. (B) Geological map of the working area, based on from Gómez et al. (2019), modified after Baker et al. (2015) and Mendes et al. (2012). Dashed line indicates the border of Amapá state (C) Digital Elevation model of the study area. Yellow-gray overlay indicates the area where Cenozoic sediments crop out. (D) Simplified sedimentary section of the Foz do Amazonas Basin (after (Figueiredo et al., 2007; Nogueira et al., 2021)) and of the sedimentary successions East of the mouth of the Amazon (after (Rossetti, 2004; Rossetti et al., 2013)).

Since the transcontinentalization of the Amazon, huge masses of sediments (>4000 m) coming from the Andes have been deposited in the Foz do Amazonas basin and since then developed the Amazon mega fan (Damuth and Flood, 1985). Sedimentation in the Amazon fan became more intense since 2.4 Ma (Figueiredo et al., 2009). An uplift of the forebulge related to the enormous weight of these sediments has been proposed in the literature (Driscoll and Karner, 1994; Rodger et al., 2006; Figueiredo et al., 2009; Watts et al., 2009). According to Watts et al. (2009) the sedimentary load and the related flexure created crustal stresses susceptible up to hundreds of kilometers away. However, structural analyses of Neogene and

Quaternary structures in the area of the mouth of the Amazon have shown that most Neogene structures are actually related to intraplate stress, reactivation of preexisting structures promoted by activity along oceanic fracture zones and transform faults of the Brazilian equatorial margin, as well as tectonism in the Andean region (Rossetti, 2014).

V.2.2 Geomorphology of the Guiana shield and its eastern rim

The Guiana shield has a generally domed structure and can be divided into an eastern and a western part, which are separated by the Tacutu rift (Fig. V-1B). It comprises planation surfaces of different elevations for which ages from the Cretaceous to recent have been suggested by several authors (Choubert, 1957; King, 1962; McConnell, 1968; Blancaneaux, 1981; Aleva, 1984; Bardossy and Aleva, 1990). These authors propose that the highest surfaces are the oldest and the lowest are the youngest ones. While elevation exceeds 2000 m in the western part, the eastern part has a generally flatter relief with mountains <1000 m. In Amapá the highest elevations can be found in its northwestern part at the border to French Guiana whereas towards the coast elevations become lower. In the cratonic area the landscape is generally formed by smooth hills with elevations of 200 to 800 m (Fig. V-1C). The coastal plains are flat with some isolated mountains (100 to 400 m) and a generally very low relief of 0 to 30m (Fig. V-1C). The different planation surfaces are suggested to follow the domed structure of the shield and thus to flatten towards the coast (Blancaneaux, 1981). Bardossy and Aleva (1990) propose a late Cretaceous age for elevations of 300 m in Eastern Amapá.

V.2.3 Weathering age frame

The geologic record of the Amazon craton and its onlapping sediments shows that several episodes of intense weathering affected the rocks in this area. While in the case of weathered sediments the age of weathering can be constrained (or at least bracketed) by the age of the under- and overlying sediments, absolute dating of weathering products is needed in order to shed light on the weathering history of uncapped sediments or basement rocks.

Some weathering age constraints exist for rocks of the Guiana shield and its onlapping sediments. The economically important bauxite deposits in the Coastal plain of the Guiana basin in Suriname and Guyana could be dated to be Late Eocene-Oligocene in age based on pollen analyses in the under- and overlying sediments (Hammen and Wymstra, 1964; Wymstra,

1971). Two recent studies of Heller et al. (2022) and Ansart (2022) on bauxitic-lateritic covers developed on top of Paleoproterozoic basement rocks in Northeastern French Guiana and Suriname, respectively, indicate long and complex weathering histories at least since the Oligocene. In French Guiana (U-Th)/He geochronological dating of supergene hematite and goethite coupled to mineralogical and geochemical analyses indicates ferruginous lateritic weathering since at least 30 Ma years, with an increase in goethite precipitation at 14-12 Ma and bauxitization during the Late Neogene (Heller et al., 2022). The dataset from Suriname (Ansart, 2022) implies the existence of a bauxitization phase before 14 Ma and supports intensification of weathering during the Late Neogene. A Paleomagnetic study from the same area suggests weathering possibly since the Eocene and during the Miocene but due to the small latitudinal shift of South America during the Cenozoic, these paleomagnetic ages are only poorly constrained (Théveniaut and Freyssinet, 2002).

(U-Th)/He ages from supergene hematite and goethite developed on top of Miocene sediments in the Western Amazon basin (Fig. V-1A) yield late Miocene to Pliocene ages (Allard et al., 2018). Kaolinite EPR ages from the same authors and by Mathian et al. (2020), who studied saprolites and soils developed in top of Precambrian granites, indicate Mid to Late Neogene ages. In contrast, the study of Guinoiseau et al. (2021) on silicon isotopes in EPR dated kaolinites from weathered Lower Cretaceous to Paleogene sediments of the Alter do Chão Formation close to Manaus (Balan et al., 2005) allow to distinguish two main weathering episodes around 35-20 Ma and 8-6 Ma. Similarly, Gautheron et al. (2022) who performed (U-Th)/He data in hematite and goethite from lateritic duricrust developed over Alter do Chão and Cenozoic sediments record also two main weathering phases from 42 to 18 Ma and 8 to 2 Ma.

Several studies comprising weathering age data exist for the Brazilian shield south of the Amazon. ^{40}Ar - ^{39}Ar data of supergene Mn oxides (Vasconcelos et al., 1994; Ruffet et al., 1996) and (U-Th)/He data from supergene goethite (Shuster et al., 2005; Monteiro et al., 2018), both from the Carajás area (Fig. V-1A), indicate the existence of several episodes of weathering since the Late Cretaceous in that area. Lateritic duricrust samples analyzed by dos Santos Albuquerque et al. (2020) record weathering going possibly back to the Paleocene.

Weathering age data (^{40}Ar - ^{39}Ar on Mn oxides and (U-Th)/He on hematite and goethite) exists also for the Borborema province (Fig. V-1A) and nearby outcrops of the Barreiras Formation located in northeastern Brazil (Lima, 2008). The ^{40}Ar - ^{39}Ar data from 31 to 0.8 Ma with major peaks at 28, 10, 5.5 and 1.5 Ma and a high data density between the Middle Miocene

and the Pliocene (Lima, 2008). (U-Th)/He age data span from the Middle Eocene to the Pleistocene with peaks at 17, 14-8 and 3 Ma (Lima, 2008).

The sedimentary record of eastern Amazonia, mainly south and southeast of the Amazon, contains a number of weathered paleosurfaces (Fig. V-1D) (Rossetti, 2004). The oldest of these surfaces, S1, often marked by a strong kaolinitization, occurs on top of Late Cretaceous deposits (Rossetti 2001, 2004, 2013). The next unconformity, S2, is on top of a weathered so called “semi-flint” with unknown age (Rossetti, 2004). When these two surfaces are amalgamated (i.e. the two unconformities correspond to the identical surface and no sediments are in between them), a thick lateritic paleosol with hexagonal branched concretions is present (Rossetti, 2004). The age of these two surfaces is only poorly constrained but must lie between the Cretaceous (underlying sediments) and the Late Oligocene or Early Miocene (overlying sediments). The two unconformities are overlain by the Late Oligocene to Early Miocene Pirabas and lower Barreiras formation, which are truncated by a third unconformity, S3, represented by a Paleosol but no lateritization (Fig. V-1D). However, according to Rossetti (2004), bauxites formed where the three paleosurfaces (S1+S2+S3) are amalgamated. The third unconformity is overlain by the Middle to Late Miocene sediments of the middle and upper Barreiras formation, which are covered by lateritic paleosol. While sedimentary analyses indicate an Serravallian or Tortonian onset of weathering (11-8 Ma) and relation with the Tortonian sea-level fall (Rossetti, 2004; Nogueira et al., 2021), goethite (U-Th)/He ages obtained on these laterites at two places in northern and northeastern Brazil (Lima, 2008; Rossetti et al., 2013) indicate a slightly older age of 17-16 Ma for the onset of weathering. A fifth and last unconformity is observed between the Plio-Pleistocene “Post-Barreiras 1” sediments and the Holocene “Post-Barreiras 2” sediments but shows no strong weathering (Rossetti, 2004).

Very recent weathering in eastern Amazonia is indicated by the fact that the Pliocene sediments of the ACP, slightly further north, are equally strongly weathered (Bezerra et al., 2015).

V.2.4 Climate of Amapá

According to Alvares et al. (2013) and Beck et al. (2018), the state of Amapá has tropical monsoon climate (Am) in the Köppen climate classifications with mean annual temperatures > 26°C, < 60 mm rainfall in the driest month and mean annual precipitations between 2300 and

>3000 mm. The main dry season is from July to November and precipitation are the highest between March and May. Mean annual precipitations vary in between different regions of Amapá (Gomes Sobrinho and Sotta, 2011), and for the area of Serra de Navio, values of 2300 mm and 2500 mm of mean annual precipitation have been reported (Forti et al., 2000; Gomes Sobrinho and Sotta, 2011).

V.3 Tucano mine geology and sampling

V.3.1 Tucano mine: location, geology, weathering mantle

The Tucano gold mine (Great Panther, Canada) is located in a hilly landscape close to the villages Pedra Branca do Amaparí and Serra do Navio in Amapá, northern Brazil (Fig. V-1B, lat = 0° 50,742' S, long = 51° 52,631' W). It belongs to the Paleoproterozoic NW-SE striking Vila Nova greenstone belt which is composed of metabasalts (Jornal Formation) and metasediments of clastic and chemical origin (Serra do Navio and Serra da Canga Formations) and hosts a number of important Mn, Au and Fe deposits, as well as some minor Cr, Sn and Ta deposits (Melo et al., 2003; Scarpelli and Horikava, 2017). According to Scarpelli and Horikava (2017) the Jornal formation corresponds to the Paramaca formation in French Guiana. The metasediments (clastic sediments, carbonates, cherts, iron oxides) of the Paleoproterozoic Serra da Canga and the Serra do Navio formations are metamorphosed under amphibolite facies conditions with local retrograde metamorphism into greenschist facies along fractures, faults and shear zones. In the open mining pit TAP AB1 (Fig. V-2A) vertically dipping banded iron formations (BIFs) and quartz-mica schists of the Serra da Canga formation crop out. They show a gradual transition (several m large) and are locally intruded by granitic sills and dykes (Fig. V-2). Scarpelli and Horikava (2017) describe that the layers of silicated and oxide banded iron formations contain silicates of iron, magnesium and calcium, often accompanied with carbonates. A N-S striking, hydrothermally altered, shear zone located at the contact between BIFs and schists crosses the mine and composes the main Au mineralization zone. In the mine, the rocks are deeply weathered, especially close to the hydrothermally altered mineralization zone (Scarpelli and Horikava, 2017), and saprock occurs down to at least 120m below the original landsurface (ca. 300-260m a.s.l.). This is in line with studies from the area which report supergene alteration reaching depths of 50-60 m and more than 100 m in more carbonatic zones (Scarpelli and Horikava, 2017; Scarpelli and Horikava, 2018).

Precipitation chronology of hematite and goethite in lateritic duricrusts from equatorial Brazil

On the top of the schist profile a ca. 1.5-2 m thick lateritic duricrust formed which is covered by a soil layer and underlain by a clay-rich layer. A mottled zone is absent and the clay layer turns directly into the vertically dipping thick saprolites.

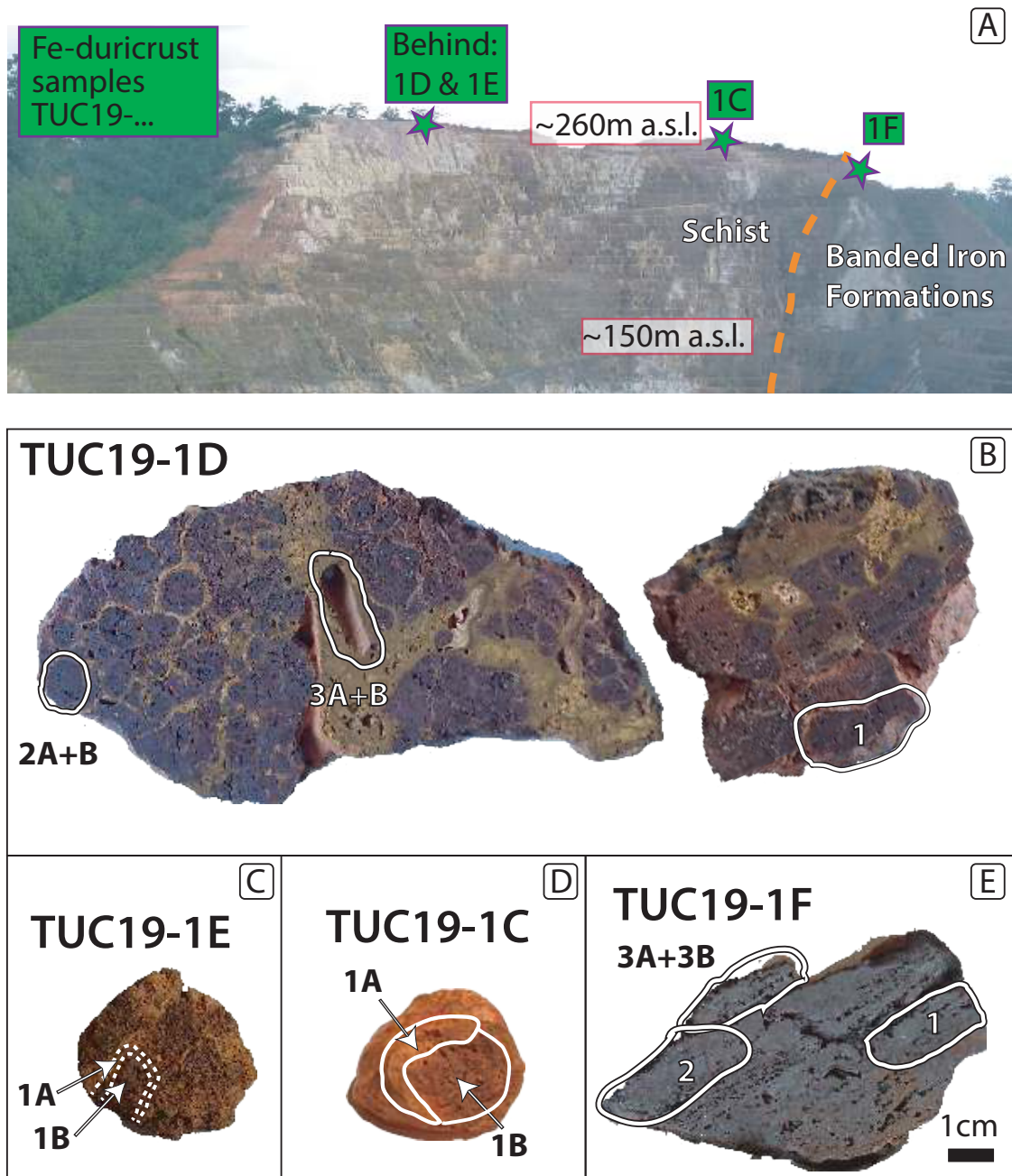


Figure V-2: Pictures of the Tucano mine (A) and the analyzed samples (B-E). (A) shows the upper part of the mining pit where the samples studied here were collected. Sampling sites are indicated by green stars. Outcrop pictures can be found in Figure A1 of the Electronic Supplement. (B) shows pictures of sample TUC19-1D indicating where the subsamples were separated. Subsample TUC19-1D_4 was separated from another slice, a picture can be found in Figure C-2 of the supplementary material. (C), (D), and (E) show sample images for samples TUC19-1E, -1C and -1F, respectively. For B-D see scale in F which corresponds to B-E. Note that for sample TUC19-1E the entire small sample block was crushed and subsample separation was conducted under the binocular microscope.

V.3.2 Samples

For this study, 4 samples of ferruginous lateritic duricrust were investigated (Fig. V-2). 3 samples were taken in the duricrust horizon developed above the schists (see Fig. C-1 of the supplementary material for outcrop pictures). Sample TUC19-1D (Fig. V-2B) was taken in the upper part of a massive duricrust and has a nodular to pisolitic texture with dark red nodules and pisoliths, often with a darker rim (but without multiple concentric layers) and set in a yellow-ochre matrix (Figs. V-2A and C-1A, C-2 of the supplementary material). Sample TUC19-1E (Figs. V-2C and C-1B of the supplementary material) was taken at the same spot as TUC19-1D but ca. 1.2 m below the latter. The samples resemble each other but TUC19-1E is more matrix-dominated with abundant fine-grained material and fewer pisoliths. Sample TUC19-1C (Fig. V-2D) was taken ca. 150 m further west. At that place, the duricrust is not massive but composed of separated pisoliths of ochre brown color (outside) which are surrounded by a fine grained ochre matrix (see Fig. C-1C of the Electronic Supplement).

Sample TUC19-1F corresponds to a several cm thick, supergene canga layer formed directly on top of rather intact BIFs about 80 m further west from the sampling site of TUC19-1C (see Fig V-2). TUC19-1F has a very massive structure, is dark gray to black and very hard.

V.4 Methods

V.4.1 Bulk analyses

The sample blocks were sawed into 1-2 cm thick slices and observed petrographically. One slice of each sample was crushed in steel mortar and finely ground in an agate mortar for mineralogical and geochemical analyses of the bulk samples. For sample TUC19-1C both 2-3 pisoliths and the matrix (sample "TUC19-1C (matrix)") were analyzed separately. Note that the fine fraction represents ca. 30 wt% of the bulk sample. For analytical procedures of the bulk samples see Heller et al. (2022).

V.4.2 Subsample analyses

Macroscopically homogeneous hematite and goethite subsamples were separated from the sample slices by micro-drilling using a Dremel multi tool. These separates were gently crushed in a steel mortar in order to obtain fragments of 0.1 to 2 mm size and named systematically according to the sample block, the separated region, and the subsample.

Descriptions of all subsamples can be found in Table C-1 of the supplementary material. For mineralogical and geochronological analyses, microscopically pure and homogeneous grains of 300-700 μm size were selected under a binocular microscope. Scanning electron microscopy, $\mu\text{-XRD}$ and (U-Th)/He analyses were performed as explained in Heller et al. (2022). Different from Heller et al. (2022) secondary electron and backscattered electron mappings were obtained for all subsamples with a pixel size of 150 nm. Micro-XRD analyses were performed for one grain per subsample, and (U-Th)/He ages were determined for 3-6 grains. Note that grains of subsample TUC19-1C_1B were not dated as this material was very soft and considered not to be datable. Rietveld refinement of micro-XRD patterns was performed using the same code (XND) and parameters used in Heller et al. (2022), but additionally quartz was refined using the crystal parameters of Antao et al. (2008) and the minimum crystallite sizes (i.e. mean coherent domains) of hematite and goethite were calculated from the obtained peak widths. In order to correct for instrumental peak width, Nacalf (XPertPro powder diffraction) and LaB6 (Mo rotating anode) standard materials were analyzed and refined. Different from the study by Heller et al. (2022), Al-substitutions in hematite were calculated from the a unit-cell parameter according to Stanjek and Schwertmann, (1992). The given error corresponds to the refinement error only. Note however that the obtained values are rather approximative because precipitation temperature and non-stoichiometry also influence the a unit-cell parameter (Stanjek and Schwertmann, 1992).

Hematite and goethite quantitatively retain He over geological timescales, but due to their generally microcrystalline structure, some part of the radiogenic He is lost by diffusion and a diffusive loss correction is thus required (Lippolt et al., 1993; Shuster et al., 2005; Heim et al., 2006; Vasconcelos et al., 2013; Reiners et al., 2014; Balout et al., 2017; Deng et al., 2017; Hofmann et al., 2017; Farley, 2018). According to the propositions of Chapter III and Heller et al. (2022), we used a $5 \pm 5\%$ correction for hematite (7 subsamples), $5 \pm 5\%$ for Al-rich goethite (> 10 mol% Al-Fe substitution, not present in this data set), $10 \pm 7\%$ for goethite with an alpha damage dose $> 1 \times 10^{15}$ (2 subsamples) and $15 \pm 10\%$ for goethite with a dose $< 1 \times 10^{15}$ (4 subsamples). If the analytical error was larger than the error of the diffusion correction, the total error was increased accordingly.

In order to avoid U volatilization, which can occur due to too strong heating during He degassing and which results in too old ages (Vasconcelos et al., 2013; Hofmann et al., 2020), the samples were degassed using the minimum laser intensity needed in order to visibly heat

the samples (dark orange glow, corresponding to temperatures $<980^{\circ}$, see Gautheron et al., 2021). For this temperature range, U volatilization is minor ($\leq 10\%$) or absent (Hofmann et al., 2020), indicating that the maximum error of this on our data is about 10%. Results presented in Heller et al. 2022, as well as the generally very reproducible results of this study, indicate that in the used degassing setting U-volatilization does not seem to be a major problem.

Some aliquots (notably hematite from sample TUC19-1F) showed a very retentive degassing behavior as indicated by the fact that 2-3 degassing cycles were needed in order to degas comparably small amounts of He. Assuming that an amount of gas similar to the amount extracted in the second (or third) extraction cycle remained in the grains, would increase the ages by approximately 10-20%.

V.5 Results

V.5.1 Bulk mineralogy and geochemistry

The results from mineralogical and geochemical bulk analyses are resumed in Table V-1 (mineralogy, major elements, U and Th), Table C-2 of the supplementary material (trace element including rare earth element concentrations) and Figure V-3. The following section describes the composition of the duricrust samples but does not consider the matrix material of sample TUC19-1C, which has a slightly different composition. All duricrust samples contain hematite (65.2-13.2 wt%), goethite (48.2-31.5 wt%) and kaolinite (25.5-2.1 wt%). Most of these samples contain also anatase (≤ 0.8 wt%), gibbsite (≤ 9.8 wt%), quartz (≤ 0.5 wt%) and rutile (≤ 0.4 wt%). Maghemite was detected in sample TUC19-1F but was not quantified. The hematite-goethite ratios, calculated as $RHG = \text{hematite} / (\text{hematite} + \text{goethite})$, range from 0.67 ± 0.02 to 0.20 ± 0.02 and Fe-Al substitution in goethite from 9.5 ± 3.3 to 2.9 ± 3.8 mol% (when including the calibration error of ± 2.6 mol%). Fe_2O_3 content ranges from 59.4 to 94.1 wt%, Al_2O_3 content from 12.2 to 0.5 wt%, SiO_2 content from 12.1 to 0.8%, TiO_2 content from 0.7 to 0.03 wt% and MnO content from 0.3 to 0.02 wt%. The loss of ignition ranges from 11.7 to 3.7 wt% and P_2O_5 , MgO, Na_2O and K_2O contents are either low (<0.22 wt%) or below the limit of detection (see Table V-1). U concentrations vary from 8.3 to 2.1 ppm, Th concentrations from 25.7 to 0.5 ppm and Sm concentrations from 1.2 to 0.5 ppm. For all other elements see Tables V-1 and C-1. Generally, samples TUC19-1C, -D and -E, which resemble also macroscopically have a rather similar geochemical and mineralogical signature whereas sample TUC19-1F shows a different pattern (Fig. V-3). This is reflected in the rare earth element (REE) pattern (Fig. V-3C). Note that

Precipitation chronology of hematite and goethite in lateritic duricrusts from equatorial Brazil

the fine grained matrix material of sample TUC19-1C (TUC19-1C (matrix)) is composed primarily of kaolinite (47.8 wt%), Al-rich goethite (38.7wt% with 28.3 mol% Al-substitution), quartz (7.1 wt%), and anatase (3.2 wt%) and has a different chemical composition (see Fig. V-3 and Tables V-1 and C-2). In addition, its REE pattern is very different when compared to the duricrust samples and to the Fe rich nodules.

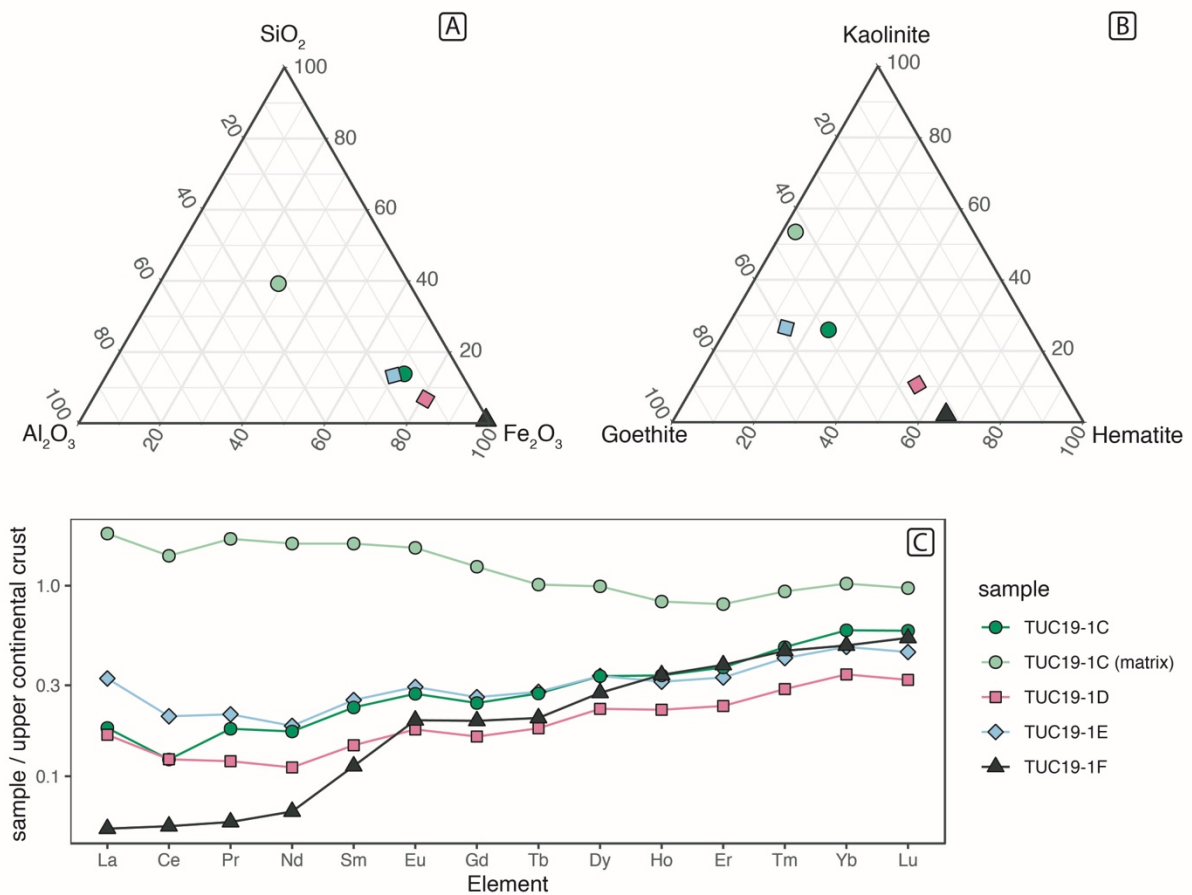


Figure V-3: Bulk sample mineralogy and geochemistry. (A) Ternary diagram of the main oxides for the analyzed bulk samples. (B) Ternary diagram for kaolinite, hematite and goethite, which are the main components of all studies samples (for data see Table V-1). (C) Rare earth element pattern for the analyzed bulk samples, normalized to upper continental crust according to Rudnick and Gao (2013).

Precipitation chronology of hematite and goethite in lateritic duricrusts from equatorial Brazil

Table V-1: Mineralogical and geochemical composition of the bulk samples. Mineral compositions and characteristics as Fe-Al substitution and mean coherent domain sizes (MCD) were obtained through Rietveld refinement.

		TUC19-1C	TUC19-1D	TUC19-1E	TUC19-1F	TUC19-1C(matrix)
Hematite	wt%	24.6	48.5	13.2	65.2	2.9
abs. error	wt%	1.7	1.4	1.8	1.1	0.8
Goethite	wt%	48.2	31.5	54.2	32.2	38.7
abs. error	wt%	1.1	1.7	1.2	1.8	3.5
Gibbsite	wt%	bld	9.8	7.7	0.4	bld
abs. error	wt%	bld	1.2	0.5	0.3	bld
Anatase	wt%	0.8	0.5	0.5	bld	3.2
abs. error	wt%	0.3	0.4	0.4	bld	0.7
Kaolinite	wt%	25.5	9.4	24.3	2.1	47.8
abs. error	wt%	0.8	0.9	0.5	0.9	1.3
Rutile	wt%	0.4	bld	0.1	bld	0.4
abs. error	wt%	0.3	bld	0.2	bld	0.4
Boehmite	wt%	bld	bld	bld	bld	bld
abs. error	wt%	bld	bld	bld	bld	bld
Quartz	wt%	0.5	0.3	bld	0.1	7.1
abs. error	wt%	0.2	0.2	bld	0.2	0.3
RHG¹		0.34	0.61	0.20	0.67	0.07
abs. error		0.02	0.02	0.02	0.02	0.02
Goethite Al-subst.	mol%	9.5	7.7	7.4	2.9	28.3
abs. error (total)	mol%	3.3	4.1	3.4	3.8	8.0
abs. error (refinement)	mol%	0.7	1.5	0.8	1.2	5.4
Hematite Al-subst.	mol%	6.3	4.1	4.4	2.7	bld
abs. error	mol%	2.1	1.0	2.7	1.5	bld
Hm MCD[110]	nm	20.9	22.8	23.7	77.7	bld
abs. error	nm	1.85	1.15	3.55	7.2	bld
Hm MCD[001]	nm	10.8	11.5	13	77.7	bld
abs. error	nm	1.2	0.7	2.55	7.2	bld
Gt MCD[100]	nm	33.8	18.3	22.5	40.4	19.8
abs. error	nm	3.3	3.4	2.45	8.5	6.1
Gt MCD[010]	nm	41.4	26.8	30.7	43.4	59.2
abs. error	nm	5.6	7.2	4.45	12.55	6
Gt MCD[001]	nm	328.6	31.8	36.4	295.9	59.2
abs. error	nm	78.95	4.85	2.9	147.2	2.9
Fe₂O₃	wt%	63.1	71.8	59.4	94.1	24.1
Al₂O₃	wt%	12.2	10.9	14.3	0.5	26.5
SiO₂	wt%	12.1	6.0	11.4	0.8	32.6
TiO₂	wt%	0.72	0.60	0.68	0.03	1.44
P₂O₅	wt%	bld	bld	0.10	0.16	0.13
MnO	wt%	0.02	0.05	0.03	0.29	0.07
MgO	wt%	bld	bld	0.03	0.23	0.06
CaO	wt%	bld	0.04	0.05	bld	bld
Na₂O	wt%	bld	bld	bld	bld	bld
K₂O	wt%	bld	bld	bld	bld	0.48
LOI²	wt%	11.5	10.1	13.0	3.7	14.7
U	ppm	8.0	5.3	8.3	2.1	5.4
Th	ppm	25.7	22.3	19.5	0.5	22.5

RHG¹: ratio hematite goethite; LOI²: loss of ignition

V.5.2 Subsample mineralogy

V.5.2.1 Samples TUC19-1C, TUC19-1D, TUC19-1E

The samples of the duricrust on top of the schists show very similar mineralogical characteristics and are therefore described together. The micro-XRD results which are resumed in Table V-2 and Figure V-4 show that the subsamples are generally composed of hematite, goethite and kaolinite. Small amounts of anatase and gibbsite were detected in some subsamples. All subsamples show a strong predominance of either hematite or goethite and calculated hematite goethite ratios (RHG) are very close to 1 or 0 for all subsamples. Several goethite subsamples (TUC19-1C_1A, TUC19-1D_3A, TUC19-1E_1A) contain important amounts of kaolinite (51- 9 wt%, Fig. V-4D).

The hematite subsamples, which resemble each other a lot, are generally very fine grained and have slightly anisotropic shapes with mean coherent domain sizes of 19 to 65 nm in [110] direction and 9-38 nm in [001] direction (Fig. V-4B). Fe-Al substitution extracted from the Rietveld refinement indicates relatively moderate Al-substitutions of 5-10 mol% (Fig. V-4A). Note that up to 16 mol% Al-substitution have been reported for hematite in contrast to a maximum value of 33 mol% Al-substitution in goethite (Cornell and Schwertmann, 2003). Typical SEM images are presented in Figure 5. Pores of variable sizes (>120 μm to < 3 μm) are very common and many of them, especially the bigger ones, have angular shapes (Fig. V-5A-5D). Sometimes, rounded minerals rests of undefined composition can be found inside these pores (Fig. V-5D and Figure C-3A of the supplementary material). Mineral inclusions of variable composition and size (quartz, Fe-oxides, zircon, anatase, gibbsite and an undefined Al-Si-Mg-Ca phase) were observed in the mounted hematite grains (Fig. 5C). Occasionally bigger pieces of dense hematite resembling the one of sample TUC19-1F occur as inclusions in the fine grained porous hematite (Fig. 5C). A partly dissolved zircon grain was found in one pore, possibly indicating a reduced stability of this mineral phase in our samples (Fig. 5D). Rarely bigger kaolinite booklets (up to 35 μm) were observed. Some grains (subsample T1D4) show fracture or porosity filling with relatively pure goethite (Fig. 5B).

The goethite subsamples are generally less porous and contain less inclusions than the hematite subsamples (Figs. V-5E-G). They differ in terms of purity and density (Figs. V-4C and V-4D); black, veinlike goethite (TUC19-1D_2B, TUC19-1D_3B, Fig. V-5E) was found to be the purest and densest. However, some grains of subsample TUC19-1D_3B have matrix-like material richer in kaolinite attached to them. More brownish and dull goethite (TUC19-1C_1A,

Precipitation chronology of hematite and goethite in lateritic duricrusts from equatorial Brazil

TUC19-1D_3A, TUC19-1E_1A, Figs. V-5F-5H) contains generally higher amounts of kaolinite (9-51 wt %, Fig. V-4D). Sometimes a layering (different shades of gray in BSE images, e.g. Figs. V-5F and V-5G), related either to variation of the kaolinite content or Al-substitution is visible. Rietveld refinement indicates rather isotropic crystallite shapes with mean coherent domain sizes of 10-35 nm (Fig. V-4E).

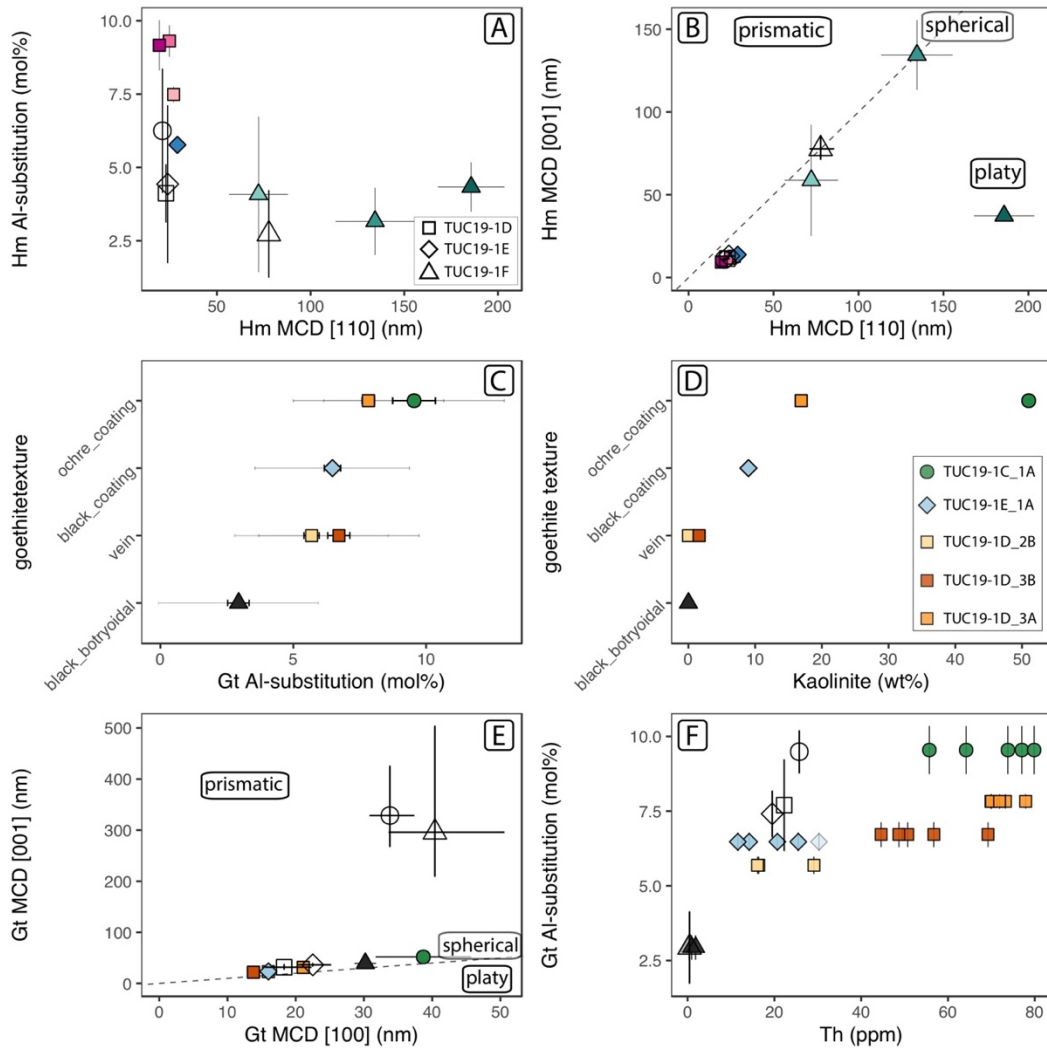


Figure V-4: Mineralogical characteristics of the analyzed goethite and hematite subsamples showing contrasting conditions of formation (A) Hematite (Hm) Fe-Al-substitution versus the size of the Mean Coherent Domains of the crystallites (direction [110]) obtained through Rietveld refinement. Filled symbols correspond to subsample analyses, empty symbols correspond to bulk samples. (B) Hematite minimum crystallite sizes (mean coherent domains) in [110] and [001] directions. Labels indicate the shapes of the crystallites according to the [110] vs [001] ratio. The dashed line indicates the 1-1 line which corresponds to approximately spherical or equant crystallites. (C) Goethite (Gt) textures versus the goethite Fe-Al-substitution. Thicker black error bars show the error of the Rietveld refinement whereas thin error bars show the error including the error of the calibration. Note that the Rietveld error is sufficient when only relative differences are regarded. (D) Goethite textures versus the amount of kaolinite mixed with goethite in the analyzed grains. (E) Goethite minimum crystallite sizes (mean coherent domains) in [100] and [001] directions. Labels indicate the shapes of the crystallites according to the [110] vs [001] ratio. The dashed line indicates the 1-1 line, which corresponds to approximately spherical or equant crystallites. A figure zooming on the subsample data can be found in Figure A6 of the supplementary material. (F) Goethite Fe-Al-substitution versus the Th concentration of the analyzed subsamples and bulk samples (bigger empty symbols). Only the refinement error if the Al-substitution is given.

Precipitation chronology of hematite and goethite in lateritic duricrusts from equatorial Brazil

Table V-2: Results of the Rietveld refinement of the subsample grains.

sample_XRD subsample	T1C1A_XRD1 TUC19-1C_1A	T1C1B_XRD1 TUC19-1C_1B	T1D1_XRD1 TUC19-1D_1	T1D2A_XRD1 TUC19-1D_2A	T1D2B_XRD1 TUC19-1D_2B	T1D3A_XRD1 TUC19-1D_3A	T1D3B_XRD1 TUC19-1D_3B	T1D4_XRD1 TUC19-1D_4	T1E1A_XRD1 TUC19-1E_1A	T1E1B_XRD1 TUC19-1E_1B	T1F1_XRD1 TUC19-1F_1	T1F2_XRD1 TUC19-1F_2	T1F3A_XRD1 TUC19-1F_3A	T1F3B_XRD1 TUC19-1F_3B	T1F1bohr_XRD1 TUC19-1Fbohr_1
Hematite	wt%	76.5	92.8	100.0	1.6	0.7	bid	96.8	bid	92.6	91.2	93.5	97.6	0.7	54.9
abs. error	wt%	0.2	0.1	bid	0.2	0.1	bid	0.1	bid	0.1	bid	0.1	0.1	0.4	0.3
Goethite	wt%	47.6	6.1	bid	98.3	82.4	98.3	1.1	90.1	7.0	6.6	6.5	2.4	99.3	45.0
abs. error	wt%	0.3	0.8	bid	0.0	0.2	0.0	0.3	0.6	0.2	0.7	1.0	2.3	0.0	0.5
Gibbsite	wt%	bid	bid	bid	0.1	bid	bid	0.5	bid	bid	bid	bid	bid	bid	bid
abs. error	wt%	bid	bid	bid	0.2	bid	bid	0.6	bid	bid	bid	bid	bid	bid	bid
Anatase	wt%	1.4	0.1	bid	bid	bid	bid	bid	0.1	bid	0.1	bid	bid	bid	bid
abs. error	wt%	0.5	0.1	bid	bid	bid	bid	bid	0.1	bid	0.1	bid	bid	bid	bid
Kaolinite	wt%	51.0	19.0	1.0	bid	16.9	1.6	1.6	9.0	0.4	1.9	bid	bid	bid	bid
abs. error	wt%	0.8	0.7	0.3	bid	0.5	0.5	0.7	0.7	0.3	1.1	bid	bid	bid	bid
Rutile	wt%	bid	bid	bid	bid	bid	bid	bid	bid	bid	bid	bid	bid	bid	bid
abs. error	wt%	bid	bid	bid	bid	bid	bid	bid	bid	bid	bid	bid	bid	bid	bid
Quartz	wt%	bid	bid	bid	bid	bid	bid	bid	bid	bid	0.2	bid	bid	bid	bid
abs. error	wt%	bid	bid	bid	bid	bid	bid	bid	bid	bid	0.3	bid	bid	bid	bid
RHG	wt%	0.95	0.94	1.00	0.02	0.01	bid	0.99	bid	0.93	0.93	0.94	0.98	0.01	0.55
abs. error	wt%	0.00	0.01	bid	0.00	0.00	bid	0.00	bid	0.00	bid	0.01	0.02	0.00	0.00
Goethite Al-subst.	mol%	9.5	13.7	bid	5.7	7.8	6.7	11.0	6.5	10.7	7.1	2.7	10.4	2.9	2.8
abs. error total	mol%	3.4	4.6	bid	2.9	2.8	3.0	15.8	2.9	4.3	9.4	8.0	24.1	3.0	3.2
abs. error refinement	mol%	0.8	4.4	2.0	0.3	0.2	0.4	13.2	0.3	1.7	6.8	5.4	21.5	0.4	0.6
Gt c-parameter	Å	3.0078	2.9962	3.0006	bid	3.0145	3.0127	3.0053	3.0132	3.0057	3.0121	3.0198	3.0063	3.0193	3.0196
Hematite Al-subst.	mol%	bid	7.5	9.3	bid	bid	bid	9.2	bid	5.8	4.3	3.2	4.1	2.7	2.5
abs. error (refinement)	mol%	bid	0.4	0.3	0.5	bid	bid	0.9	bid	0.2	0.8	1.1	2.7	bid	0.8
Ht a-parameter	Å	5.0313	5.0314	5.0292	bid	bid	bid	5.0294	bid	5.0335	5.0353	5.0367	5.0356	5.0373	5.0375
Ht MCD[110]	nm	64	27	25	25	25	bid	19	bid	29	186	134	72	bid	228
abs. error	nm	0	0	0	bid	bid	bid	0	bid	0	18	21	16	bid	35
Ht MCD[001]	nm	bid	13	12	12	12	bid	9	bid	14	37	134	59	bid	41
abs. error	nm	0	0	0	bid	bid	bid	0	bid	0	3	21	34	bid	5
Gt MCD[100]	nm	39	31	16	16	21	14	bid	16	21	28	38	36	30	37
abs. error	nm	7	9	0	0	1	0	bid	0	4	29	33	bid	2	7
Gt MCD[010]	nm	52	37	31	23	32	22	bid	24	32	30	39	48	39	68
abs. error	nm	5	0	3	0	0	1	bid	0	5	39	33	bid	1	11
Gt MCD[001]	nm	52	37	31	23	32	22	bid	24	32	30	39	48	39	68
abs. error	nm	5	0	3	0	0	1	bid	1	5	39	33	bid	1	11
R _{wp} -value		0.0587	0.0291	0.03	0.0424	0.0241	0.0306	0.0503	0.0309	0.0275	0.0468	0.0766	0.0931	0.039	0.031

V.5.2.2 *Sample TUC19-1F*

The TUC19-1F subsamples show very different textures and characteristics than other samples. Note that we use the word “texture” in the geological (not pedological) sense as smaller (cm and mm-sized) macroscopic and microscopic features including particle size, the geometric aspects of its constituent particles and crystals/crystallites and their mutual spatial relations. As in the bulk sample, maghemite was detected in several of the subsamples. Hematite is the dominant mineral of most subsamples but botryoidal goethite was observed in subsample TUC19-1F_1 and is the main component of subsample TUC19-1F_3B. The crystallites are much bigger than in the other samples and Rietveld refinement indicates crystallites with a predominantly anisotropic platy shape with mean coherent domain (MCD) sizes of 70-200 nm in [110] direction and 30-130 nm in [001] direction (Fig. 4B). Rietveld refinement indicates Fe-Al substitution of ca. 4 mol% for the hematite subsamples of TUC19-1F, but note that the errors calculated from the Rietveld refinement are very large. The hematite grains are generally very dense and hard (Fig. 5I). In more porous zones, preferential crystal growth orientations can be observed (Fig. 5J). Inclusions are very rare but occasionally small (< 10 μm) grains of quartz, a W-Ca phase, a Ca-P phase, and a Ca-Mg phase were observed by SEM-EDS. Angular pores reminding forms of ancient grains occur; sometimes they are filled with kaolinite (Fig. C-3B of the supplementary material). Some of the mounted hematite grains have small pieces of goethite attached to them.

The goethite of subsamples TUC19-1F_3B (dated and analyzed mineralogically) and TUC19-1F_1 (analyzed only mineralogically) is botryoidal, dense and very pure (i.e. without mineral inclusions or Al-substitution) (Fig. 5K). Nevertheless, the mounted grains show that goethite grew on top of the hematite and some grains contain both minerals (Fig. 5L). Prism lengths were estimated to ca. 40-60 μm under the binocular microscope; the SEM images indicate sublayers of ca. 3-20 μm width. Rietveld refinement indicates mean coherent domains with slightly prismatic shape and 30-60 nm size (Fig. V-4E and C-6 of the supplementary material). Fe-Al-substitution in the goethite is very low with ca. 3 mol% (Figs. V-4D and V-4F).

Precipitation chronology of hematite and goethite in lateritic duricrusts from equatorial Brazil

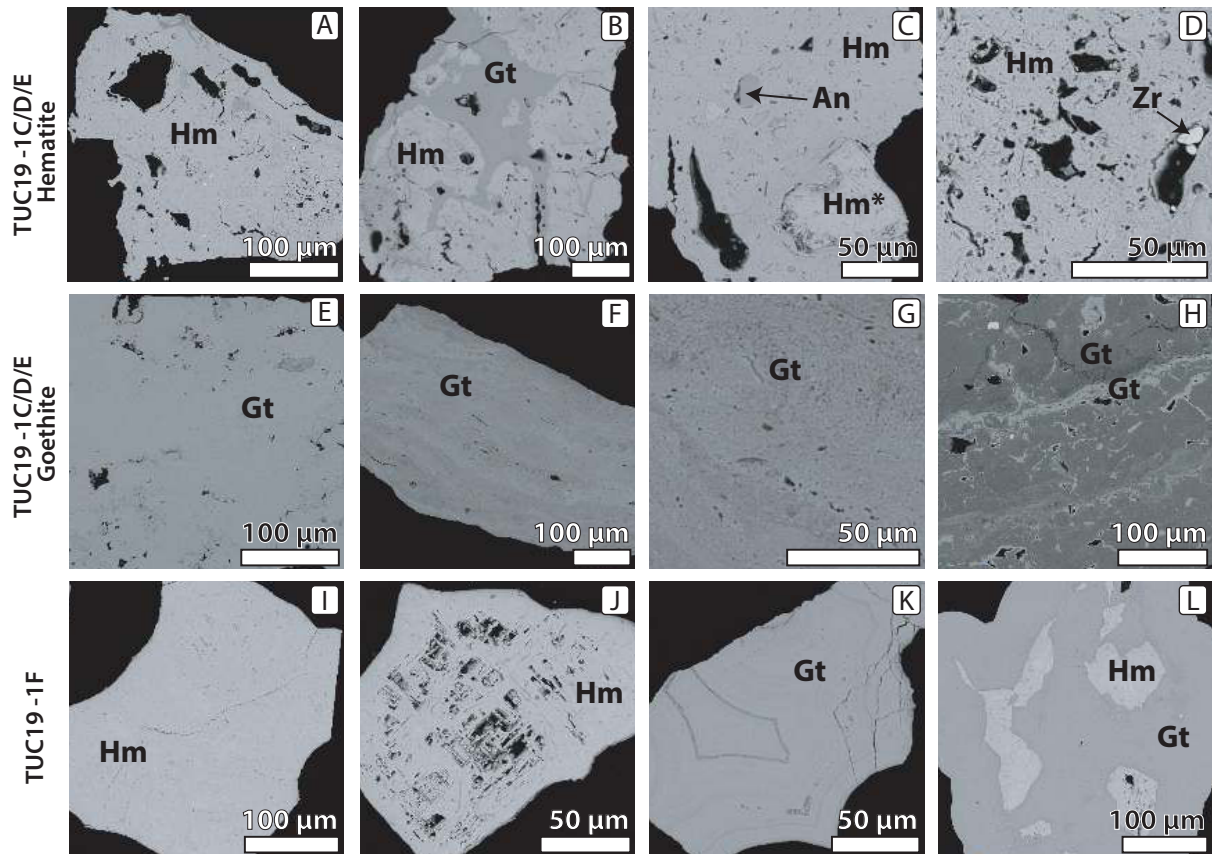


Figure V-5: Back-scattered electron images of aliquots of subsamples selected for dating. (A) Fine grained hematite grain with angular pores of different sizes, typical for the hematite subsamples from TUC19-1C/D/E (TUC19-1D_2A). (B) Hematite grain with dense fracture-filling goethite forming veins (TUC19-1D_4). (C) Hematite grain with a large inclusion of differently textured hematite (Hm*), an anatase inclusion (An) and (more or less) angular pores of different sizes (TUC19-1D_4). (D) Porous hematite showing a pore with a small, rounded, possibly already partly dissolved, zircon grain (TUC19-1D_2A). (E) Fine grained, rather dense and pure goethite (TUC19-1D_3B). (F) Fine grained goethite, probably mixed with very fine grained kaolinite, showing a slightly layered texture (TUC19-1D_3A). (G) Zoomed image of a goethite grain from the same subsample as (F), showing a fine grained texture with small pores (TUC19-1D_3A). (H) Goethite grain showing two types of goethite (darker gray = fine-grained goethite intergrown with kaolinite and brighter gray = purer and denser goethite coating pores and veins) (TUC19-1C_1A). (I) Dense homogeneous hematite grain typical for the hematite subsamples of sample TUC19-1F (TUC19-1F_3A). (J) More porous hematite grain of sample TUC19-1F showing platy crystallite growth (TUC19-1F_2). (K) Pure and dense botryoidal goethite grain representative for the goethite of sample TUC19-1F (TUC19-1F_3B). Botryoidal goethite grown on top of dense hematite (TUC19-1F_1).

V.5.3 (U-Th)/He Geochronology

67 (U-Th)/He geochronological ages were successfully obtained on 13 subsamples and cover a range from 69.4 ± 3.5 to 8.7 ± 0.9 Ma. Figure V-6 presents all ages, and data is reported in Table V-3. U concentrations in the aliquots range from 19 to 0.1 ppm, Th concentrations from 80 ppm to <bld and Sm concentrations from 20 ppm to <bld.

Precipitation chronology of hematite and goethite in lateritic duricrusts from equatorial Brazil

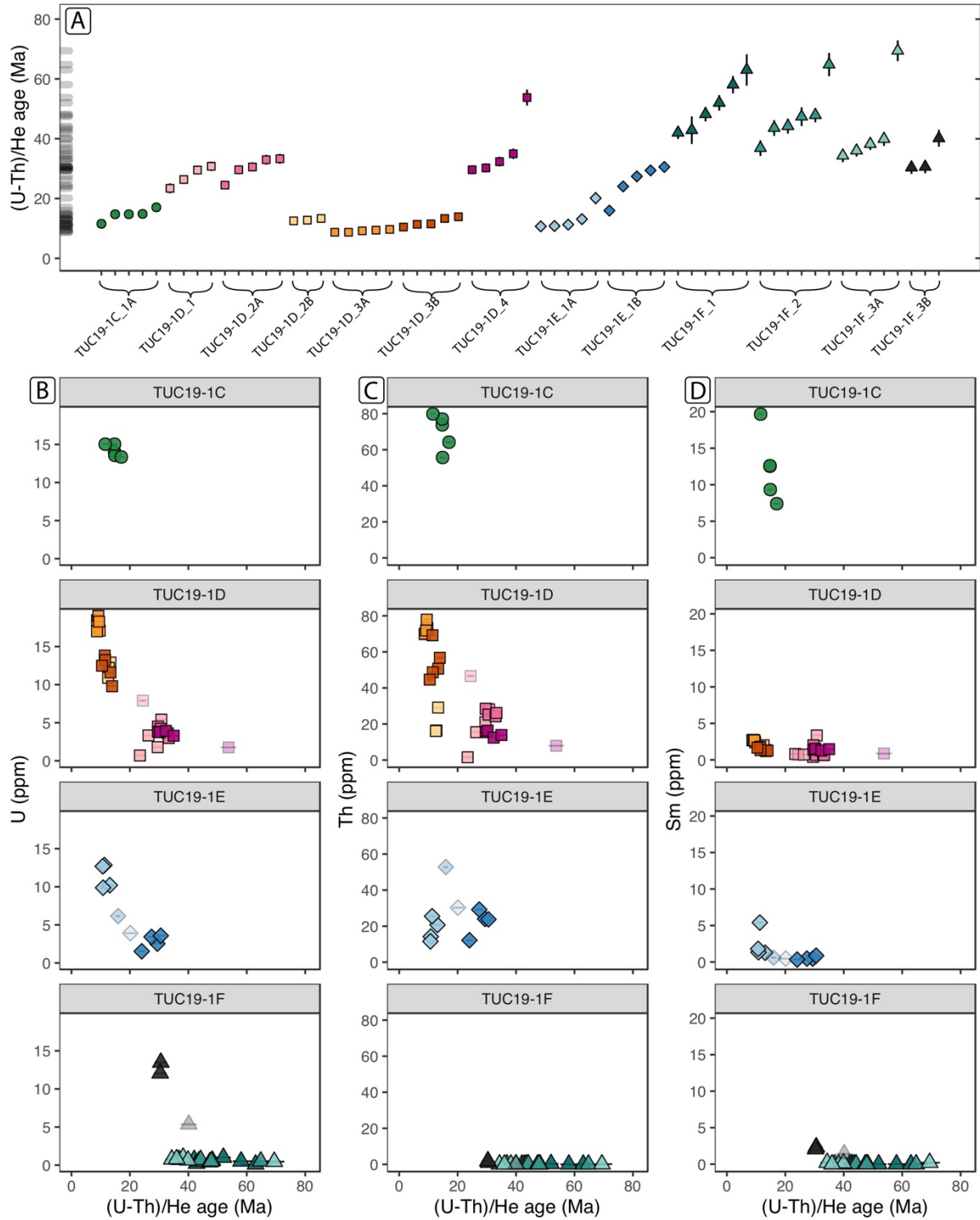


Figure V-6: (U-Th)/He ages obtained in this study. (A) Ranked order plot of all obtained ages. Shapes correspond to the bulk-samples, colors are specific for every subsample. (U-Th)/He ages versus U (B), Th (C), and Sm (D) concentrations for all dated aliquots. Shapes and colors are as in (A). Semi-transparent symbols correspond to ages considered as mixed ages and not used for interpretation. Additional Figures showing the (U-Th)/He age vs U and Sm concentration with adapted x- and y-scales can be found in Fig. C-4 of the supplementary material.

The aliquots with (U-Th)/He ages from 69 to 35 Ma, principally from sample TUC-1F, yield rather spread ages and showed a very retentive degassing behavior. Despite the rather

spread ages, a shift in median ages is visible between the three hematite subsamples TUC19-1F_1 (median = 50 Ma), TUC19-1F_2 (median = 46 Ma) and TUC19-1F_3A (median = 38 Ma). The goethite subsample TUC19-1F_3B shows a correlation of age with U (Fig. V-6B). Subsamples TUC-19-1F_1, -2 and 3A do not show significant correlations with U, but when regarded altogether, the ages correlate significantly with U ($R^2 = 0.24$, p-value = 0.0048, see Fig. C-5 of the electronic supplement for the fit and explanation of R^2 and p-value).

In contrast to the old subsamples, the younger subsamples show often very well defined ages and yield very reproducible geochronologic results. In several subsamples (e.g. TUC19-1D_2B, TUC19-1D_2C, TUC19-1D_2D) all obtained ages overlap within error. In other subsamples this is true for a part of the dated aliquots (e.g. in TUC19-1C_1A three aliquots yield an nearly identical result of 14.7 to 14.8 Ma). For the samples TUC19-1C, TUC19-1D, and TUC19-1E the ages concentrate around 30 and 12 Ma. U and Th concentrations are generally higher in the younger subsamples and lower in the older subsamples. Some samples and subsamples show correlation with U, Th or Sm, e. g. in TUC19-1D U with age ($R^2 = 0.77$, p-value = 2×10^{-9}) and Th with age ($R^2 = 0.53$, p-value = 1.7×10^{-5}) and U with age in TUC19-1E ($R^2 = 0.80$, p-value = 0.0005) (see Figs. V-6 and C-4). Some ages of the dataset can clearly be identified as a result of phase mixing (see Heller et al. 2022 for details on the result of phase mixing on (U-Th)/He ages). These mixed ages (semi-transparent symbols in Figs. V-6-8), which can generally be identified as their ages and U, Th or Sm concentrations fall onto a mixing line (or curve) in between two well defined age populations, are excluded from the discussion as they do not bear a geological meaning. Taking this into consideration, the results obtained in this study indicate discrete episodes of hematite and goethite precipitation at ca. 30 and 12 Ma.

There is a strong relation between the geochronological, geochemical and mineralogical results. Figure V-7 shows the concentrations of U, Th and Sm as a function of the RHG. U seems to be principally contained in goethite as aliquots from goethite subsamples have U concentrations >10 ppm, whereas aliquots from hematite subsamples have generally U contents < 6 ppm (Fig. V-7A). Th and Sm show similar trends with high concentration in goethite and low concentrations in hematite. However, the contrast weaker than for U as several goethite subsamples have low Th concentrations similar to the hematites (Figs. V-7B and V-7C).

The samples show a strong link between the obtained ages and the subsample mineralogy (Fig. V-7D). For samples TUC19-1C, -1D, and -1E, hematite and goethite correspond to the age populations at 30 and 12 Ma respectively. In sample TUC19-1F the oldest ages

Precipitation chronology of hematite and goethite in lateritic duricrusts from equatorial Brazil

correspond all to hematite subsamples and the only goethite subsample yields ages of ca. 30 Ma.

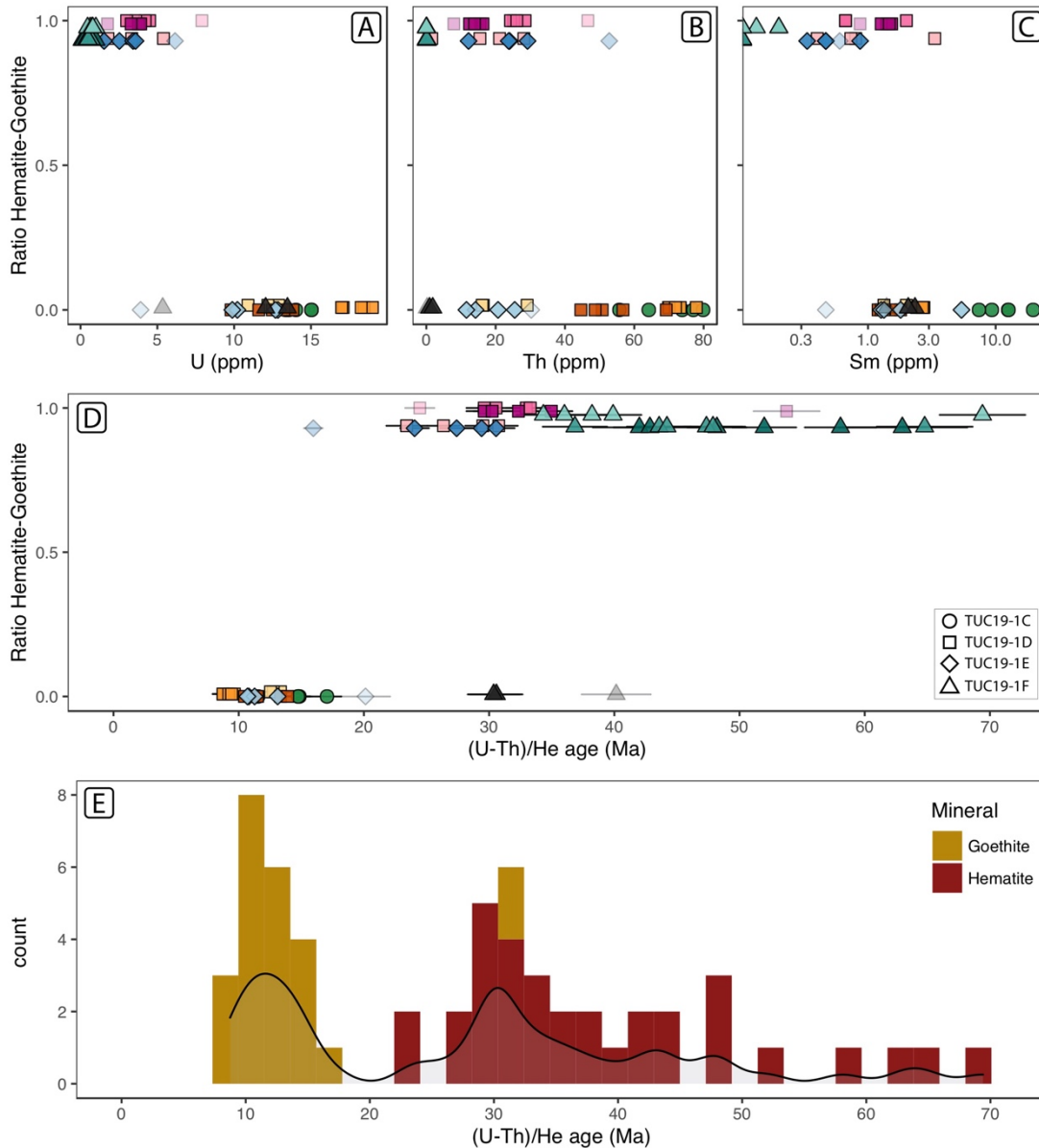


Figure V-7: Relation of the geochemical and geochronological data with the ratio hematite-goethite (RHG). (A) U vs RHG, (B) Th vs RHG and (C) Sm vs RHG. (D) shows the obtained (U-Th)/He ages as a function of the RHG. Shapes in (A-D) are according to the (bulk) sample (see legend in (D)), colors are according to the subsamples and as in Figures V-4 and V-6. Semi-transparent symbols are considered mixed ages and are not included in (E). (E) Histogram and Kernel density plot of the obtained (U-Th)/He ages (red = hematite, yellow = goethite).

The old hematite subsamples of TUC19-1F are composed of very large, sometimes platy crystallites and the hematite is poor in Al with ca. 4 mol% Al-substitution (Fig. V-4A and V-B). As crystallite size calculation by XRD is problematic for such large crystallites and the grains analyzed by micro-XRD might not be fully representative of the subsamples, we prefer not to

interpret the variation in crystallite size observed between the subsamples of sample TUC19-1F.

Figure V-8 shows the ages relative to the mineralogical parameters obtained through Rietveld refinement concerning all subsamples of the schist-duricrusts (i.e. all except TUC19-1F). The 4 hematite subsamples with ages around 30 Ma (TUC19-1D_1, TUC19-1D_2A, TUC19-1D_4, TUC19-1E_1B) show an increase in crystallite size towards younger ages (Fig. V-8A). This seems to be coupled to a decrease in Al-substitution, but note that the unit cell a -parameter of hematite, from which the Al-substitution is calculated, is influenced by non-stoichiometry, making this measure less robust (Fig. C-6C of the supplementary material).

The goethite subsamples show a correlation of Th with the Al-substitution in goethite (Fig. V-4F). The Th enrichment is stronger in the analyzed subsamples when compared to the bulk. This is probably a dilution effect as in the bulk samples goethite is mixed with hematite and kaolinite. The four goethite subsamples of samples TUC19-1D and TUC19-1E show an enrichment in Th towards younger ages (Fig. V-8C). Subsample TUC19-1CA lies off this trend with a considerably higher Al-substitution. Note that this subsample shows generally rather different mineralogical and geochemical characteristics when compared to the goethite subsamples from samples TUC19-1D and TUC19-1E (greater Mean Coherent Domain size and kaolinite content Fig. V-4). The goethite subsamples of TUC19-1D and TUC19-1E show, just as some of the hematite subsamples, an increase in crystallite sizes towards younger ages (Fig. V-8B). Some of the subsamples contain considerable amounts of kaolinite. Figure V-4D shows that this is the case especially for the yellow-ochre colored coatings. Note however, that the large amount of kaolinite obtained by micro-XRD in subsample TUC19-1C_1A (51 wt%) might not be fully representative as EDS analyses of mounted grains and bulk sample XRD (Table V-1) indicate lower values. Goethite subsamples rich in kaolinite have generally also higher Fe-Al substitutions (Fig. V-4C and V-4D). The amounts of kaolinite increase towards younger ages in the subsamples of samples TUC19-1D and TUC19-1E (Fig. V-8D).

Precipitation chronology of hematite and goethite in lateritic duricrusts from equatorial Brazil

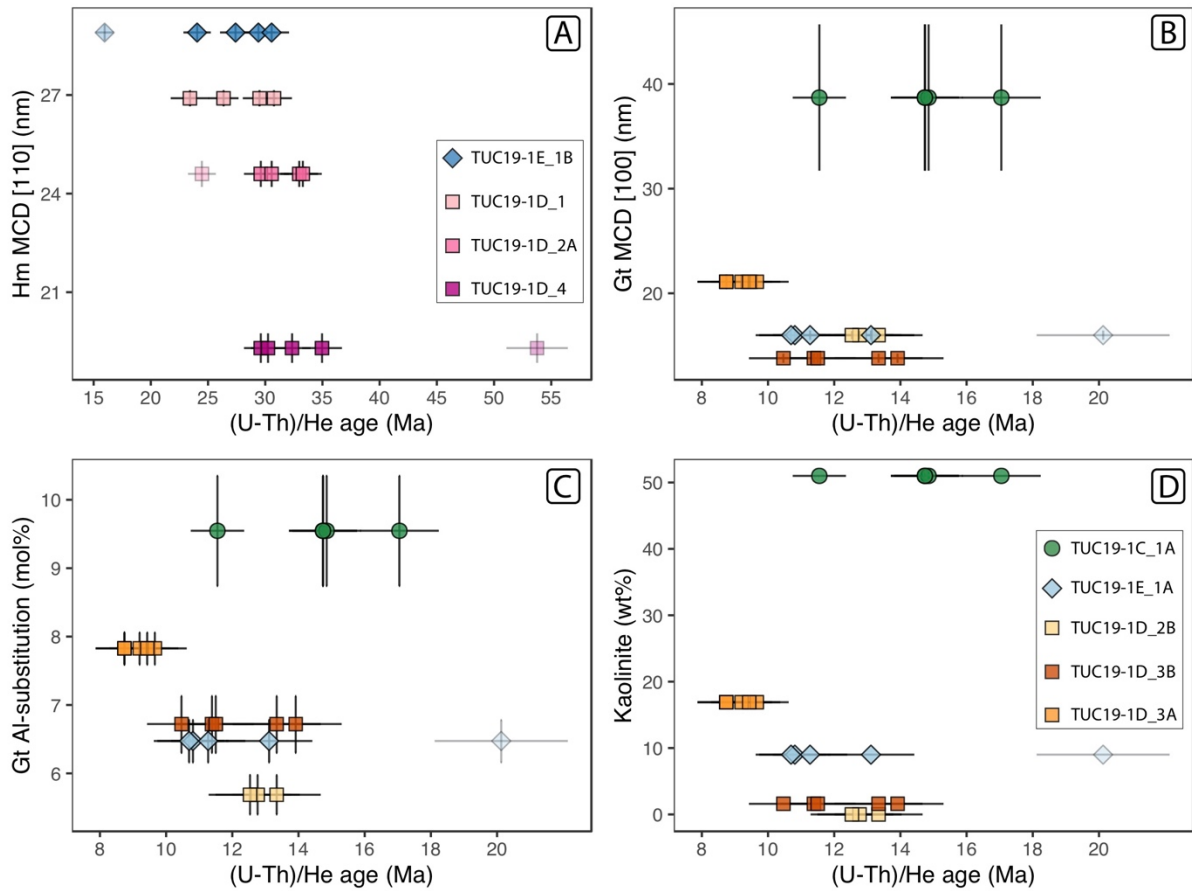


Figure V-8: Evolution of the determined (U-Th)/He ages with the mineralogical characteristics of the analyzed hematite (A) and goethite (B-D) subsamples. Only samples above the schist are presented. (A) (U-Th)/He ages versus approximated crystallite sizes ([110 direction], MCD = mean coherent domain) for the analyzed hematite subsamples. (B) (U-Th)/He ages versus approximated crystallite sizes ([100 direction]) for the analyzed goethite subsamples. (C) (U-Th)/He ages versus Fe-Al-substitution in goethite for the goethite subsamples. Note that in order to focus on the relative differences only the refinement error of the Al-substitution is shown and the error of the calibration (± 2.6 mol%) is not included. (D) (U-Th)/He ages versus the amount of kaolinite mixed with goethite in the goethite subsamples. Similar supplementary figures can be found in Fig. C-6 of the supplementary material.

V.6 Discussion

V.6.1 (U-Th)/He age distribution

V.6.1.1 Weathering onset and possible reason for the spread of the oldest ages

The onset of the weathering-record is not easy to define as the results of sample TUC19-1F yield rather spread ages between 70 and 40 Ma. Although the maximum ages of the three hematite subsamples of TUC19-1F overlap within error (Fig. V-6A), an age difference between the subsamples seems to be present comparing the median ages of these subsamples. Taking the three hematite subsamples of TUC19-1F together, the age data show a general correlation with the U concentration (Fig. C-5 of the Electronic Supplement). As the younger goethite generation of this subsample (TUC19-1F_3B) has considerably high U concentration (Fig. V-6B,

V-7D), a factor 10 to a factor 100 higher than the hematite, it is possible that a part of the age spread observed in this bulk sample is due to phase mixing. Presence of small pieces of goethite attached to some of the mounted hematite grains supports this assumption. Due to the extreme actinide concentration gradient between hematite and goethite, the samples are extremely sensitive to phase mixing and already very small amount of an U-rich phase can have a strong impact on the ages.

The hematite grains of TUC19-1F showed a very retentive degassing behavior but as explained in Section V.4 incomplete degassing related to the high retentivity can only account for ca. 20% age difference and can thus not explain the observed spread. Likely the high retentivity is linked to the rather large crystallite size of the TUC19-1F hematite but accumulated alpha damage related to the old age of the sample might also have enhanced the retentivity as this has been shown to be the case in magnetite and goethite (Chapter III and Bassal et al., 2022).

Zircon inclusions were only rarely observed in the subsamples of TUC19-1F and if they were present, they were very small (few μm). However, we cannot exclude that some He implantation from small zircons might have slightly impacted (i.e. increased) the ages. This might occur as with our analytical procedure He from zircon inclusions is included in the He budget but the corresponding actinide mother elements are likely not included in the measured actinide budget since zircon is not dissolved in the used acid mix. This can lead to “parentless” He and too old ages. Note however that the error produced by small (100 times smaller than host grain, i.e. $< 5\mu\text{m}$ here) and rare U- and Th-rich inclusions is $\leq 10\%$ in apatite (Vermeesch et al., 2007). In any case, the three oldest ages which yield results between 69 and 63 Ma belong to different subsamples and overlap within error. This supports a geological significance of these ages (Monteiro et al., 2014). Although, due to the aforementioned reasons, we cannot define the onset of weathering precisely, the data indicate a record of weathering since the late Cretaceous or Early Paleogene, which is an important result for the knowledge of the weathering record in the Amapá state.

V.6.1.2 Discrete weathering events

The subsamples of samples TUC19-1C, -1D and -1E yield results that are more reproducible than those of TUC19-1F (Fig. V-6A). This is even surprising as the samples are sometimes very porous, extremely fine grained, or rather soft and can contain, in the case of

some goethite subsamples, important amounts of kaolinite. All of these factors were previously rather considered to have a negative impact on the (U-Th)/He reproducibility but have not been investigated in this regard so far. The present study shows that these parameters might have no major impact on the (U-Th)/He age reproducibility. Hematite and goethite are generally not very mixed in our subsamples, as indicated by the μ XRD and SEM results. The age populations at ~30 and ~12 Ma can thus be clearly assigned to the precipitation of hematite and goethite, respectively (Fig. V-7D). The only exception is subsample TUC19-1F_3B. While this is the only goethite subsample with ages of ~30Ma, sample TUC19-1F still follows the same systematics as the other samples with all hematite subsamples being considerably older than the goethite subsamples.

The youngest ages of obtained in this study belong to subsample TUC19-1D3A and yield an age of 8 Ma (Fig. V-6A). This indicates that formation of the massive Fe duricrust was probably completed by then.

Precipitation chronology of hematite and goethite in lateritic duricrusts from equatorial Brazil

Table V-3: (U-Th)/He data of all obtained ages.

Bulk Sample	Subsample	Aliquot weight µg	⁴ He mol	⁴ He error mol	⁴ He mol/g	U ng	Th ng	¹⁴⁷ Sm ng	U ppm	Th ppm	Sm total ppm	Th _U ratio	raw age Ma	corrected age Ma	error corr. Ma	age Ma	correction factor %	predominant mineral	RHG	mixedage
TUC19-1C	TUC19-1C_1A	T1C1A5	62	1.47E-13	5.35E-16	8.64E-12	0.83	3.98	0.07	13.35	64.18	1.11	7.4	4.8	15.5	17.1	10	Gt	0.00	no
TUC19-1C	TUC19-1C_1A	T1C1A2	51	9.82E-14	4.19E-16	8.22E-12	0.69	2.84	0.07	13.56	55.70	1.40	9.3	4.1	13.5	14.9	10	Gt	0.00	no
TUC19-1C	TUC19-1C_1A	T1C1A1	105	2.36E-13	4.91E-16	4.67E-12	1.47	7.75	0.20	14.02	73.81	1.88	12.5	5.3	13.4	14.7	10	Gt	0.00	no
TUC19-1C	TUC19-1C_1A	T1C1A3	55	1.34E-13	5.80E-16	1.05E-11	0.83	4.24	0.10	15.03	77.03	1.89	12.6	5.1	13.4	14.7	10	Gt	0.00	no
TUC19-1C	TUC19-1C_1A	T1C1A4	30	5.80E-14	3.93E-16	1.31E-11	0.45	2.40	0.09	15.03	79.86	2.95	19.7	5.3	10.5	11.6	10	Gt	0.00	no
TUC19-1D	TUC19-1D_1	T1D11	124	2.36E-13	5.80E-16	4.68E-12	0.67	3.49	0.06	5.40	28.13	0.50	3.3	5.2	29.3	30.8	5	Ht	0.94	no
TUC19-1D	TUC19-1D_1	T1D13	76	7.58E-14	4.46E-16	5.87E-12	0.14	1.61	0.00	1.79	21.12	0.06	0.4	11.8	28.1	29.5	5	Ht	0.94	no
TUC19-1D	TUC19-1D_1	T1D16	82	7.58E-14	4.33E-16	5.28E-12	0.27	1.27	0.01	3.33	15.46	0.11	0.7	4.6	25.1	26.4	5	Ht	0.94	no
TUC19-1D	TUC19-1D_1	T1D14	69	8.92E-15	3.75E-16	5.43E-12	0.05	0.11	0.01	0.70	1.54	0.12	0.8	2.2	22.3	23.4	5	Ht	0.94	no
TUC19-1D	TUC19-1D_2A	T1D2B4	50	8.03E-14	4.15E-16	8.30E-12	0.15	1.30	0.00	3.00	26.10	0.10	0.7	8.7	31.7	33.3	5	Ht	1.00	no
TUC19-1D	TUC19-1D_2A	T1D2A3	76	1.20E-13	6.25E-16	8.22E-12	0.27	1.85	0.01	3.60	24.30	0.10	0.7	6.7	31.4	33.0	5	Ht	1.00	no
TUC19-1D	TUC19-1D_2A	T1D2A2	65	1.03E-13	6.25E-16	9.61E-12	0.27	1.64	0.01	4.20	25.20	0.10	0.7	6	29.1	30.6	5	Ht	1.00	no
TUC19-1D	TUC19-1D_2A	T1D2A1	65	1.12E-13	4.46E-16	6.86E-12	0.29	1.85	0.02	4.50	28.50	0.30	2.0	6.3	28.2	29.6	5	Ht	1.00	no
TUC19-1D	TUC19-1D_2A	T1D2A4	44	1.07E-13	4.91E-16	1.12E-11	0.35	2.05	0.01	7.90	46.60	0.10	0.7	5.9	23.3	24.5	5	Ht	1.00	yes
TUC19-1D	TUC19-1D_2B	T1D2B1	32	3.97E-14	3.93E-16	1.23E-11	0.41	0.93	0.01	12.90	29.10	0.20	1.3	2.3	11.6	13.3	15	Gt	0.02	no
TUC19-1D	TUC19-1D_2B	T1D2B2	66	6.25E-14	4.24E-16	6.42E-12	0.80	1.08	0.01	12.20	16.40	0.20	1.3	1.3	11.1	12.8	15	Gt	0.02	no
TUC19-1D	TUC19-1D_2B	T1D2B3	31	2.68E-14	3.84E-16	1.24E-11	0.34	0.50	0.01	10.90	16.10	0.30	2.0	1.5	10.9	12.5	15	Gt	0.02	no
TUC19-1D	TUC19-1D_3A	T1D3A1	39	6.25E-14	4.37E-16	1.12E-11	0.67	2.86	0.01	17.10	73.24	0.36	2.4	4.3	8.4	9.7	15	Gt	0.01	no
TUC19-1D	TUC19-1D_3A	T1D3A5	46	7.58E-14	4.02E-16	8.73E-12	0.84	3.58	0.02	18.27	77.90	0.40	2.7	4.3	8.2	9.4	15	Gt	0.01	no
TUC19-1D	TUC19-1D_3A	T1D3A4	45	7.14E-14	4.10E-16	9.12E-12	0.85	3.23	0.02	19.00	71.88	0.41	2.7	3.8	8	9.2	15	Gt	0.01	no
TUC19-1D	TUC19-1D_3A	T1D3A2	92	1.25E-13	4.91E-16	5.33E-12	1.56	6.43	0.04	17.00	69.90	0.40	2.7	4.1	7.6	8.7	15	Gt	0.01	no
TUC19-1D	TUC19-1D_3A	T1D3A3	36	5.35E-14	4.28E-16	1.19E-11	0.66	2.52	0.01	18.45	70.02	0.41	2.7	3.8	7.6	8.7	15	Gt	0.01	no
TUC19-1D	TUC19-1D_3B	T1D3B2	24	3.66E-14	3.61E-16	1.51E-11	0.24	1.36	0.00	9.80	56.74	0.19	1.3	5.8	12.1	13.9	15	Gt	0.00	no
TUC19-1D	TUC19-1D_3B	T1D3B1	38	5.80E-14	4.24E-16	1.12E-11	0.44	1.93	0.01	11.60	50.73	0.18	1.2	4.4	11.6	13.3	15	Gt	0.00	no
TUC19-1D	TUC19-1D_3B	T1D3B4	33	4.42E-14	2.23E-16	6.76E-12	0.44	1.61	0.01	13.23	48.69	0.20	1.3	3.7	10	11.5	15	Gt	0.00	no
TUC19-1D	TUC19-1D_3B	T1D3B3	24	3.88E-14	3.88E-16	1.62E-11	0.33	1.66	0.01	13.82	69.22	0.27	1.8	5	9.9	11.4	15	Gt	0.00	no
TUC19-1D	TUC19-1D_3B	T1D3B5	31	3.52E-14	3.84E-16	1.24E-11	0.39	1.38	0.01	12.49	44.60	0.25	1.7	3.6	9.1	10.5	15	Gt	0.00	no
TUC19-1D	TUC19-1D_4	T1D45	45	4.46E-14	3.97E-16	8.82E-12	0.08	0.36	0.01	1.76	7.93	0.13	0.9	4.5	51.2	53.8	5	Ht	0.99	yes
TUC19-1D	TUC19-1D_4	T1D44	95	1.12E-13	4.91E-16	5.17E-12	0.31	1.32	0.02	3.29	13.90	0.22	1.5	4.2	33.3	35.0	5	Ht	0.99	no
TUC19-1D	TUC19-1D_4	T1D43	102	1.16E-13	4.33E-16	4.24E-12	0.40	1.27	0.02	3.92	12.46	0.19	1.3	3.2	30.8	32.3	5	Ht	0.99	no
TUC19-1D	TUC19-1D_4	T1D42	95	1.12E-13	4.91E-16	5.17E-12	0.36	1.55	0.02	3.77	16.94	0.23	1.5	4.3	28.8	30.2	5	Ht	0.99	no
TUC19-1D	TUC19-1D_4	T1D41	111	1.25E-13	4.91E-16	4.42E-12	0.42	1.72	0.02	3.82	15.49	0.21	1.4	4.1	28.2	29.6	5	Ht	0.99	no

Precipitation chronology of hematite and goethite in lateritic duricrusts from equatorial Brazil

Table 3 (continued)

Bulk Sample	Subsample	Aliquot weight µg	⁴ He mol	⁴ He error mol	⁴ He mol/g	U ng	Th ng	¹⁴⁷ Sm ng	U ppm	Th ppm	¹⁴⁷ Sm ppm	Sm total ppm	Th_U_ratio	raw age Ma	corrected age Ma	error corr. age Ma	correction factor %	predominant mineral	RHG	mixedage
TUC19-1E	TUC19-1E_1A	T1E1A5	66	6.69E-14	4.37E-16	6.62E-12	0.26	2.00	0.00	3.91	30.27	0.07	0.5	17.5	20.1	2.0	15	Gt	0.00	yes
TUC19-1E	TUC19-1E_1A	T1E1A1	113	1.07E-13	4.91E-16	4.34E-12	1.15	2.34	0.02	10.21	20.69	0.19	1.3	11.4	13.1	1.3	15	Gt	0.00	no
TUC19-1E	TUC19-1E_1A	T1E1A3	27	2.68E-14	3.70E-16	1.37E-11	0.35	0.69	0.02	12.85	25.50	0.81	5.4	9.8	11.3	1.1	15	Gt	0.00	no
TUC19-1E	TUC19-1E_1A	T1E1A2	36	2.41E-14	3.93E-16	1.09E-11	0.36	0.51	0.01	9.88	14.19	0.20	1.3	9.4	10.8	1.1	15	Gt	0.00	no
TUC19-1E	TUC19-1E_1A	T1E1A4	26	2.01E-14	3.52E-16	1.36E-11	0.33	0.30	0.01	12.69	11.57	0.27	1.8	9.3	10.7	1.1	15	Gt	0.00	no
TUC19-1E	TUC19-1E_1B	T1E1B5	46	6.69E-14	4.46E-16	9.70E-12	0.16	1.09	0.01	3.58	23.77	0.13	0.9	29.1	30.6	1.5	5	Ht	0.93	no
TUC19-1E	TUC19-1E_1B	T1E1B1	87	1.07E-13	4.46E-16	5.13E-12	0.22	2.09	0.01	2.53	24.01	0.07	0.5	28	29.4	1.5	5	Ht	0.93	no
TUC19-1E	TUC19-1E_1B	T1E1B2	76	1.12E-13	4.91E-16	6.46E-12	0.26	2.22	0.01	3.42	29.20	0.07	0.5	26.1	27.4	1.4	5	Ht	0.93	no
TUC19-1E	TUC19-1E_1B	T1E1B3	64	3.48E-14	3.88E-16	6.06E-12	0.10	0.78	0.00	1.53	12.18	0.05	0.3	22.9	24.0	1.2	5	Ht	0.93	no
TUC19-1E	TUC19-1E_1B	T1E1B4	49	7.58E-14	4.28E-16	8.74E-12	0.30	2.59	0.00	6.15	52.77	0.09	0.6	15.2	16.0	0.8	5	Ht	0.93	yes
TUC19-1F	TUC19-1F_1	T1F14	145	7.14E-15	3.70E-16	2.55E-12	0.02	0.01	0.00	0.10	0.00	0.00	0.0	60	63.0	5.3	5	Ht	0.93	no
TUC19-1F	TUC19-1F_1	T1F13	164	2.45E-14	3.88E-16	2.37E-12	0.08	0.00	0.00	0.50	0.00	0.00	0.0	55.3	58.1	2.9	5	Ht	0.93	no
TUC19-1F	TUC19-1F_1	T1F19	129	3.75E-14	6.25E-16	4.84E-12	0.13	0.04	0.01	1.00	0.30	0.00	0.0	49.5	52.0	2.6	5	Ht	0.93	no
TUC19-1F	TUC19-1F_1	T1F18	137	2.14E-14	3.97E-16	2.90E-12	0.09	0.00	0.00	0.60	0.00	0.00	0.0	45.9	48.2	2.4	5	Ht	0.93	no
TUC19-1F	TUC19-1F_1	T1F17	85	4.91E-15	3.70E-16	4.36E-12	0.02	0.00	0.00	0.20	0.00	0.00	0.0	40.8	42.8	4.6	5	Ht	0.93	no
TUC19-1F	TUC19-1F_1	T1F12	203	3.03E-14	3.79E-16	1.87E-12	0.14	0.00	0.00	0.70	0.00	0.00	0.0	40	42.0	2.1	5	Ht	0.93	no
TUC19-1F	TUC19-1F_2	T1F25	76	1.29E-14	3.79E-16	4.99E-12	0.04	0.00	0.00	0.50	0.00	0.00	0.0	61.7	64.8	3.9	5	Ht	0.94	no
TUC19-1F	TUC19-1F_2	T1F26	187	2.28E-14	4.19E-16	2.24E-12	0.09	0.01	0.00	0.50	0.10	0.00	0.0	45.6	47.9	2.4	5	Ht	0.94	no
TUC19-1F	TUC19-1F_2	T1F23	94	9.82E-15	3.75E-16	3.99E-12	0.04	0.00	0.00	0.40	0.00	0.00	0.0	45.1	47.4	3.2	5	Ht	0.94	no
TUC19-1F	TUC19-1F_2	T1F22	85	1.47E-14	3.97E-16	4.67E-12	0.06	0.01	0.00	0.70	0.10	0.00	0.0	42.1	44.2	2.5	5	Ht	0.94	no
TUC19-1F	TUC19-1F_2	T1F21	117	1.25E-14	3.84E-16	3.28E-12	0.05	0.01	0.00	0.50	0.10	0.00	0.0	41.5	43.6	2.6	5	Ht	0.94	no
TUC19-1F	TUC19-1F_2	T1F24	68	8.92E-15	3.57E-16	5.25E-12	0.04	0.01	0.00	0.70	0.10	0.00	0.0	35.1	36.9	2.6	5	Ht	0.94	no
TUC19-1F	TUC19-1F_3A	T1F3A3	126	2.19E-14	3.66E-16	2.90E-12	0.06	0.01	0.00	0.46	0.11	0.03	0.2	66.1	69.4	3.5	5	Ht	0.98	no
TUC19-1F	TUC19-1F_3A	T1F3A2	94	1.25E-14	3.61E-16	3.84E-12	0.06	0.01	0.00	0.63	0.08	0.02	0.1	38	39.9	2.3	5	Ht	0.98	no
TUC19-1F	TUC19-1F_3A	T1F3A1	90	1.83E-14	3.84E-16	4.26E-12	0.09	0.00	0.00	1.00	0.00	0.00	0.0	36.4	38.2	2.0	5	Ht	0.98	no
TUC19-1F	TUC19-1F_3A	T1F3A5	102	1.52E-14	3.75E-16	3.67E-12	0.08	0.00	0.00	0.80	0.00	0.00	0.0	34.3	36.0	2.0	5	Ht	0.98	no
TUC19-1F	TUC19-1F_3A	T1F3A4	75	1.03E-14	3.52E-16	4.70E-12	0.06	0.00	0.00	0.75	0.05	0.03	0.2	32.7	34.3	2.2	5	Ht	0.98	no
TUC19-1F	TUC19-1F_3B	T1F3B1	87	9.37E-14	4.91E-16	5.64E-12	0.47	0.02	0.02	5.35	0.24	0.21	1.4	36.5	40.2	2.8	10	Gt	0.01	yes
TUC19-1F	TUC19-1F_3B	T1F3B2	71	1.47E-13	6.69E-16	9.43E-12	0.96	0.07	0.02	13.47	0.94	0.35	2.3	27.8	30.6	2.1	10	Gt	0.01	no
TUC19-1F	TUC19-1F_3B	T1F3B3	57	1.07E-13	4.24E-16	7.44E-12	0.69	0.11	0.02	12.05	1.85	0.31	2.1	27.6	30.4	2.1	10	Gt	0.01	no

V.6.2 Possible reasons for the observed age differences

Due to their high reproducibility the (U-Th)/He ages presented in this study allow new insight into the formation and evolution processes of lateritic duricrusts and the precipitation chronology of different phases of Fe (oxyhydr)oxides. The involved processes on small to outcrop scale will be discussed in the following.

V.6.2.1 Possible reasons for different ages on top of schists and BIFs

On the outcrop scale, the samples show a very clear feature: sample TUC19-1F, a canga layer formed on top of the BIFs, contains much older ages than duricrust samples formed on top of the schists (Figs. V-2 and V-9). Due to the small distance between the samples, this observation cannot be linked to climatic differences and must be related either to different durations of duricrust formation or to different preservation of the duricrusts. This could mean that while a canga layer on top of the extremely iron rich BIF (unweathered BIFs have typical Fe contents of 20-40 wt%, Klein, 2005) formed and well crystallized hematite precipitated, no duricrust formed on top of iron-poorer the schists (schist saprolite from the Tucano in 120m depth mine has an Fe₂O₃ content of 6 wt%, see Chapter VII, and the upper and middle continental crust have mean compositions of 5 and 6 wt% Fe₂O₃, respectively, Rudnick and Gao, 2013). The very different availability of Fe could be a reason for such different processes. This is supported by observations of Lascelles (2006) who report extremely rapid weathering of BIFs, especially when these are rich in ferrous carbonate and silicate (an exposed siderite drill core was completely oxidized within 3 yr), as it is partially the case in the Tucano BIFs (Scarpelli and Horikava, 2017). Alternatively this could mean that while the canga layer formed on top of the BIFs during the Early Paleogene, a ferruginous duricrust formed on top of the schists. In this case, this duricrust would have been recycled later on in a way that only the signal since ca. 30 Ma remained. As our samples shows very homogeneous ages of ~30 and ~12 Ma on top of the schists, contain no textures indicating multiple cycles of dissolution and reprecipitation, and only one considerably older age exists (T1D45, probably a grain containing a large canga inclusion as this has been observed by SEM and the U, Th, and Sm concentrations support this, as presented in Figs. V-5D and V-6B-D), this hypothesis seems not very probable. Otherwise an older duricrust on top of the schists could have been eroded as this material was likely less resistant to erosion compared to the canga on top of the BIFs. In the Tucano mine the BIFs and schist show a rather gradual and sedimentological transition but nevertheless, a shear zone passes in between them. No major post-Cretaceous reactivation of shear zones is documented

for the Guyana shield and the area is considered to have been stable since the Cretaceous. However, Cenozoic sediments in the area indicate Neogene reactivations (Rossetti, 2014) and it could be possible, that reactivation of the shear zone including a vertical movement of the schist block lead to uplift of the latter and preferential erosion of a formerly formed duricrust on top of the schists. Although no existing data directly supports this hypothesis, the general long life of shear zones with several cycles of reactivation has been documented (Holdsworth et al., 1997). Shear zone activity as a reason for different weathering ages on both side of the shear zone leading to unequal erosion can therefore be considered as a possible but little probable hypothesis. The explanation, that it is much easier and faster to create an indurated duricrust on top of very iron rich BIFs than on top of intermediate schists (Fe content likely 5 to 10 times smaller), seems simpler and more logical.

V.6.2.2 Age differences and similarities between duricrusts above the schist

Samples TUC19-1D and TUC19-1E, which were sampled at the same spot but at different depths (difference of ca. 1.2 m), yield indistinguishable results (Fig. V-6). The existing model of duricrust formation proposes that the duricrust is formed at its bottom, at the contact with the water table, and is dismantled at its top at the interface with the soil (Tardy, 1997). Iron is leached at the top and migrates to the bottom rejuvenating the soft nodular horizons to form a new duricrust, which is more goethitic than hematitic. (Beauvais, 2009). According to the proposed model we would expect younger ages in TUC19-1E, but in our samples, we cannot see any difference in age between samples TUC19-1D and 1E (Fig. V-6A). TUC19-1E contains more kaolinite than TUC19-1D (see Table V-1 and Figure V-3), a feature which was also visible in the field as TUC19-1E has a bigger proportion of matrix (see Fig. C-1 of the supplementary material). Unfortunately the bottom of the duricrust was not cropping out at the sampling point, but pisolitic duricrust some 10s of meters away has a thickness of approximately 2 m and likely the massive duricrust of samples TUC19-1D and -1E has a similar thickness. Nevertheless, the two samples might not be fully representative of upper and lower duricrust. The identical ages of TUC19-1D and -1E could indicate that on top of the schists in the Tucano mine duricrust formation happened in several well defined, rather short intervals and was not a long lasting process with slow downward formation of the duricrust horizon.

Interestingly, sample TUC19-1C_1A yields slightly older goethite ages (including three nearly identical results of 14.7 ± 1.0 to 14.9 ± 1.0 Ma) than samples TUC19-1D and -1E and the observed enrichment of Th and substituted Al, as well as the Sm concentration, lie off the

trends of the other two samples (Figs. V-6 and V-8). Although the results from TUC19-1C_1A partially overlap within error with the oldest goethite analyses of samples TUC19-1D (13.3 ± 1.3 Ma) and -1E (13.1 ± 1.3 Ma), this indicates slightly offset goethite precipitation. A possible reason could be the proximity of sample TUC19-1C with the BIFs where Fe might be more easily available. Alternatively, the age difference could be related to different precipitation mechanisms. This latter mechanisms will be rediscussed further down with the processes of hematite and goethite precipitation.

V.6.3 Paragenesis of the discrete weathering events

A very remarkable feature of the data set is the strong bimodal distribution of age and mineralogy (Figures V-7 and V-9). Figure V-9 summarizes the timing of the hematite and goethite precipitations. On top of the schists, the age population at ~ 30 Ma is uniquely composed of hematite whereas the age population at ~ 12 Ma is uniquely composed of goethite (Fig. V-9). Hematite generally constitutes pisolith interiors and sometimes massive features in TUC19-1D (Fig. V-2B) whereas goethite forms rims around the pisolith core and cavity coatings, some veins and is contained in the yellow clay-rich matrix (Figs. V-2, -9 and C-1 of the supplementary material).

V.6.3.1 *Predominance of hematite precipitation at ~ 30 Ma*

The clear bimodal distribution is somehow surprising as Tardy and Nahon (1985) and Tardy (1997) explain how hematite and goethite can form synchronously in different settings of the duricrust, as a function of the pore size and water activity. On the other hand, it has been shown that hematite and goethite form preferentially under different climatic conditions (Tardy and Roquin, 1998; Cornell and Schwertmann, 2003). Whereas hematite is favored under hotter and dryer conditions, goethite is favored under cooler and more humid conditions (Trolard and Tardy, 1987; Tardy and Roquin, 1998; Cornell and Schwertmann, 2003). In soils around the globe goethite occurs often without hematite (i.e. hematite/(hematite+goethite) ratio (RHG) = 0), especially at higher latitudes. However, the opposite is rarely the case and soils which contain supergene hematite (they occur at lower latitudes) have generally RHG values between 0 and 0.79 and hence contain some goethite (Cornell and Schwertmann, 2003).

The published (U-Th)/He datasets containing both supergene hematite and goethite (dos Santos Albuquerque et al., 2020; Gautheron et al., 2022; Heller et al., 2022) apparently do not show such a strong separation of hematite and goethite with time. Note that in several studies the mineralogy is not reported for each aliquot or only one mineral (mainly goethite) was analyzed (Monteiro et al., 2014; Riffel et al., 2016; Monteiro et al., 2018), making a direct comparison difficult. The goethite in sample TUC19-1F is synchronous with the hematite in samples TUC19-1D and -1E that can be explained by Fe remobilization in the already existing, predominantly hematitic duricrust TUC19-1F (Fig V-9). The weathering event which led to the precipitation of hematite above the schists allowed mobilization of Fe and precipitation of goethite in large cavities in the canga layer. Note that the goethite in TUC19-1F_3B is mineralogically very different from ~12 Ma old goethite in the other samples (Figs. V-4 and V-5). Due to the different parental materials (abundance of clays above of the schists versus canga layer poor in kaolinite on top of the BIFs) and therefore different types of porosity (many small pores above the schists and predominantly larger pores in the canga), differences in the water activity might have led to precipitation of botryoidal goethite in the canga and fine grained hematite on top of the schists. This is in line with the processes proposed by Tardy and Nahon (1985) and Tardy (1997).

However, the absence of 30 Ma goethite on top of the schists is surprising. On the one hand, exclusively hematite could have formed at 30 Ma on top of the schists, on the other hand goethite could have formed but was recycled or not preserved later on. Primary hematite in duricrusts is supposed to form in the small pore space associated with kaolinite (Tardy and Nahon, 1985; Tardy, 1997). While the kaolinite disappears, the hematite gets enriched in Al (Tardy, 1997). Although the 30 Ma hematite subsamples are generally poor in kaolinite (<2 wt%), their pisolithic structure (Fig. V-9), their small grain size (Fig V-4) and their moderate to elevated Al contents support the hypothesis that they formed in a classical duricrust setting associated with kaolinite. The often large pores present in the hematite (Fig. V-5A) indicate that other minerals were (still) stable while hematite precipitated. These minerals were apparently dissolved later. Rounded mineral remains observed in some pores (e.g Figs. V-5D and C-3A of the supplementary material) favor this interpretation. Surprisingly, different from what would be expected, the 30 Ma old hematite subsamples seem to show a slight decrease in Al-substitution towards younger ages (Fig. A6C of the supplementary material). Note however that the a-parameter of the hematite unit cell, from which the Al-substitution is calculated, is

also sensible to differences of the precipitation temperature and non-stoichiometry (Stanjek and Schwertmann, 1992; Cornell and Schwertmann, 2003), reducing the robustness of the calculated Al-substitution in hematite.

Nevertheless this evaluation does not resolve the question whether goethite coprecipitated with hematite or not. If no goethite coprecipitated, which seems possible as we do not find any goethite of that age, this would imply formation conditions favorable for the precipitation of hematite but not for the precipitation of goethite. The nature of these conditions will be discussed further down.

V.6.3.2 Formation conditions of the goethite subsamples

V.6.3.2.1 Goethite of sample TUC19-1C

The age population at ~12 Ma is composed uniquely of goethite. The mineralogical analyses show that these goethite subsamples, which precipitated in a rather short time interval from 15-9 Ma with a clear peak at 12 Ma (Fig. V-7B), show different mineralogical and geochemical characteristics. The oldest of these goethite subsamples is TUC19-1C_1A which corresponds to the coating of a rather large (ca. 4 cm) pisolith (Figs. V-2, V-9). Such pisolith coatings are often rich in Al and are considered to form from rehydration of the Al-rich hematite composing the core of the pisolith (Tardy, 1997). This is in line with our mineralogical data showing an Al-rich hematite core (Table V-2, subsample TUC19-1C_1B, Fe-Al substitution = 7.5 mol%, a medium value for hematite which can incorporate up to 16 mol% Al) and 9.5 mol% Fe-Al substitution in the goethite coating (a moderate value for goethite, which incorporates up to 33 mol% Al, but the highest observed in our dataset), similar to the results obtained for the bulk sample (Table V-1). A possible explanation of the slightly older ages of this subsamples compared to the other goethite subsamples could be, that it is faster to rehydrate hematite very locally into goethite than to dissolve some of the hematite, transport the Fe and reprecipitate goethite from the solution elsewhere.

V.6.3.2.2 Goethite of samples TUC19-1D and TUC19-1E

The goethite subsamples from the massive duricrust (TUC19-1D and TUC19-1E) yield ages between 13.9 ± 1.4 and 8.7 ± 0.9 Ma. These subsamples have different characteristics when compared to the pisolith coating of subsample TUC19-1C_1A, such as lower Al-

substitutions and smaller crystallite sizes (Fig. V-8). The excellent reproducibility of these ages (inside subsamples TUC19-1D_2B, -3A, and -3B (nearly) all obtained ages overlap within error) suggests that observed small age differences in between the subsamples are not due to He retentivity inaccurate correction but reflect the weathering process. Furthermore several parameters such as Al-substitution, grain size and kaolinite content seem to evolve with time when comparing the subsamples.

The veinlike subsamples (TCU19-1D_2B and TUC19-1D_3B), which are generally black, dense, and pure contain little or no kaolinite, are very fine grained and contain relatively low amounts of Al. These are the goethite subsamples which precipitated first, probably from the first remobilized Fe. The oldest ages ranging from 13.3 ± 1.3 to 12.5 ± 1.3 Ma can be found in the goethite veins close to the hematite (subsample TUC19-1D_2B) whereas the veins further away (TUC19-1D_3B) yield slightly younger ages of 13.9 ± 1.4 to 10.5 ± 1.0 Ma (Fig. V-9). Subsample TUC19-1E_1A, a black coating, yields ages similar to TUC19-1D_3B, yet less well defined ranging from 13.1 ± 1.3 to 10.7 ± 1.1 Ma. The rather low Th and Al contents of this subsample (TUC19-1E_1A) indicate that it resembles the veinlike goethite and does not represent a coating formed by direct hydration of hematite.

The yellow-ochre coating (TUC19-1D_3A) yields younger ages from 9.7 ± 1.0 to 8.7 ± 0.9 Ma, which show a partial overlap with those of subsamples TUC19-1D_3B and TUC19-1E_1A and no overlap with subsample TUC19-1D_2B. This observed age difference indicates that this ochre coating, rich in kaolinite, was the last goethite that precipitated (Fig. V-9).

Summing up the data suggests that in samples TUC19-1D and -1E, the characteristics of goethite evolved with time. As presented in Figure V-9, at first black goethite veins precipitated close to hematite (subsample TUC19-1D_2B), then black veins precipitated further away (TUC19-1D_3B and TUC19-1E_1A) and only afterwards the ochre coating, rich in kaolinite, precipitated. Thereby, the fluids from which the goethite precipitated, became progressively enriched in U, Th and Sm (see Fig. V-6 and C-4) and Al-substitution and grain size of the goethite increased.

Precipitation chronology of hematite and goethite in lateritic duricrusts from equatorial Brazil

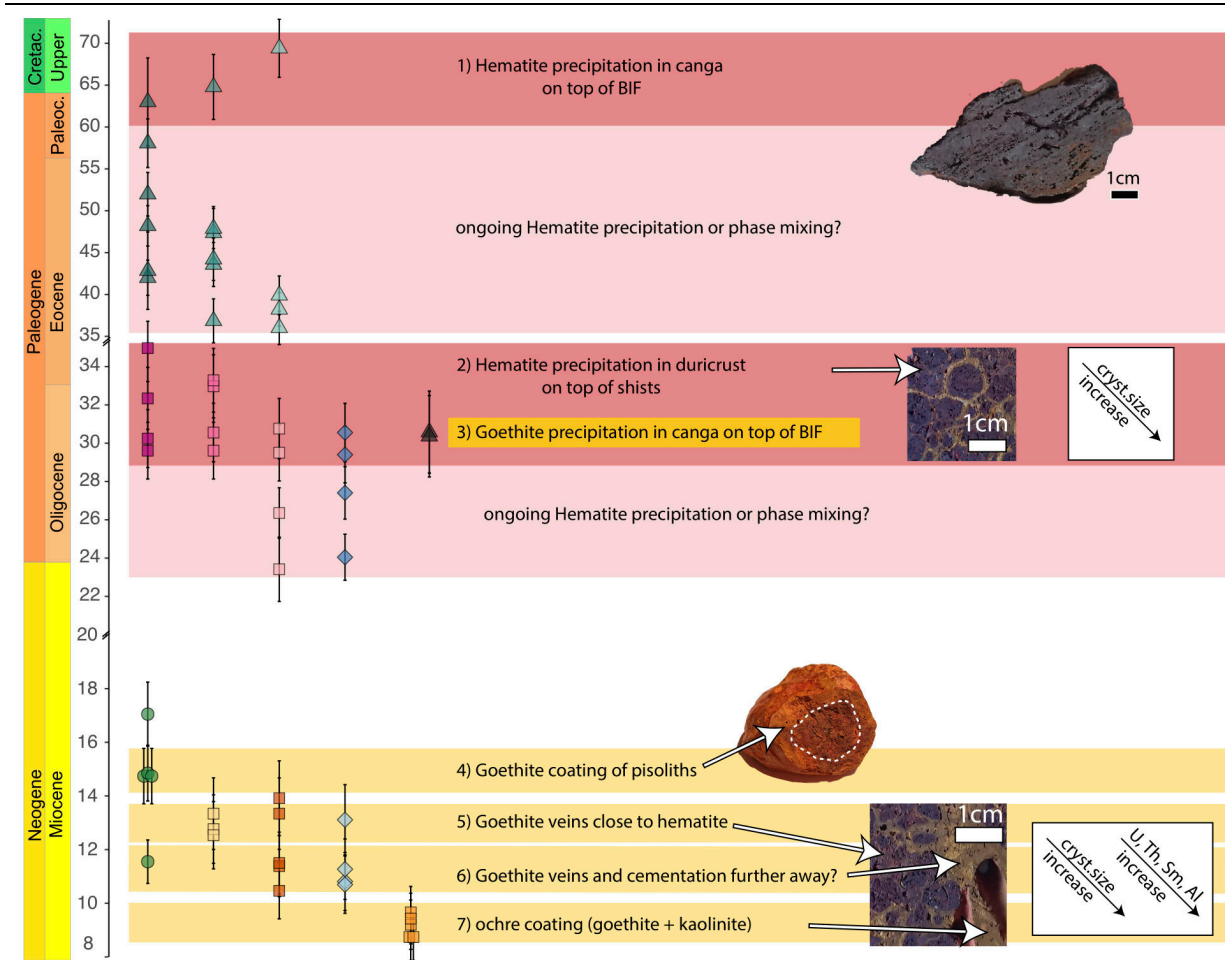


Figure V-9: Precipitation chronology of the studied duricrust samples with ages for all separated subsamples (left hand of the graph). Symbol shapes (triangles = TUC19-1F, squares = TUC19-1D, diamonds = TUC19-1E and circles = TUC19-1C) and colors of the ages are as in Figures V-4 to V-7. Red boxes indicate phases of Hematite precipitation, yellow boxes correspond to goethite precipitation. White boxes highlight mineralogical and geochemical trends for the corresponding time intervals.

V.6.3.2.3 Absence of inclusions

In contrast to the 30 Ma old hematite subsamples, the goethite subsamples contain little big pores and inclusions. On the one hand this can be linked to the fact that hematite and goethite form through different processes (veins are generally not very porous) and on the other hand maybe other minerals (e.g. quartz) had already been dissolved prior to the goethite precipitation event. Alternatively, dissolution of inclusions and precipitation of goethite might have happened in parallel. The fact that most dissolution pores are empty and not filled with goethite could support this hypothesis. As, at least above the schists, most former inclusions have been dissolved (or nearly dissolved, see Fig. C-3A of the supplementary material) we cannot say much about their composition neither about the fluid conditions needed in order to dissolve them. Probably they were composed of quartz grains and other more or less weathering-resistant minerals. The observation that even zircon grains are partially dissolved

(Fig. V-5D) is very interesting as this mineral is considered to be one of the most resistant ones. However, it has already been stated that zircon, especially when highly radiation damaged, i.e. metamict, was not stable under lateritic conditions (Carroll, 1953; Balan et al., 2001; Delattre et al., 2007). As the parental rocks of the schists are very old (Paleoproterozoic), the zircons are probably very metamict and therefore less resistant against weathering.

V.6.3.3 Implications for the weathering conditions and the precipitation mechanisms

As explained above at ~30 Ma only hematite is preserved above the schists whereas some goethite precipitates in the large pores in the canga above the BIFs. The strong predominance of hematite possibly indicates rather hot and / or dry seasonally contrasted tropical climate (Tardy and Roquin, 1998).

The important and rather massive precipitation of goethite at ~12 Ma implies the presence of another important weathering event. The characteristics of the goethite minerals, which are rather poor in Al (considering that goethite can contain up to 30 mol% Fe-Al substitution), rich in kaolinite and scarce of gibbsite, imply that this weathering event happened under ferruginous lateritic and non-bauxitic conditions. Strong precipitation could have led to an upward movement of the water table and thereby to hydration of the former base of the duricrust system. Like this, some hematite could have been transformed into goethite directly, e.g. in the coatings of pisoliths (such as subsample TUC19-1C_1A). However, precipitation of veinlike goethite cannot be explained by direct hydration, i.e. a local process, and indicates a certain mobility and transport of Fe. Tropical soils have often relative acid pH conditions (von Uexküll and Mutert, 1995), linked to the scarcity of alkaline elements and the humic acids produced by vegetation. This facilitates the dissolution of hematite and goethite. Like this, Fe could have been remobilized and veinlike goethite precipitated in cavities, voids and fractures. As discussed above, dissolution of mineral inclusions in hematite and goethite precipitation might have been isochronous. Parallel to the dissolution of mineral inclusions matrix minerals such as quartz might have been progressively dissolved and could have reinforced the relative Fe accumulation in the duricrust. Goethite precipitated in function of favorable climatic conditions. The fact that no hematite coprecipitated with goethite indicates that possibly the climate was too wet or cool for hematite precipitation and that water activity in larger size porosity was too high.

However, the change from hematite-dominated system at ~30 Ma to goethite-dominated system at ~12 Ma could also be a change in microclimate (i.e. humidity and temperature of the soil / upper regolith) only without a change in macroclimate (climate sensu strictu) (although some macroclimate change must have happened as there was a gap in Fe mineral precipitation). A possible change in soil microclimate could be related to local drainage conditions. While the soil was better drained it was generally dryer and hematite precipitation was possible. When the system was less drained, micro-conditions were wetter and goethite precipitated. Similar effects with preferential hematite and goethite precipitation have been observed in soils as a function of drainage and exposition (Cornell and Schwertmann, 2003 and references therein). A change in water table height could thus explain the shift from a hematite-dominated system to a goethite-dominated system.

V.6.4 Duration of the weathering events

The very good reproducibility of our data allows us to constrain the durations of the two discrete weathering events. For the weathering event at ca. 30 Ma the ages of the hematite above the schist and the goethite in the canga range from 35 to 23 Ma, but most ages (15 out of 20) are between 35 and 29 Ma with an age peak at 30 Ma (Figs. V-6 and V-9). Median ages of the subsamples range from 32.3 to 27.4 Ma. This indicates a duration of ca. 5-8 Ma for this weathering event.

For the event at ca. 12 Ma, the age data indicate that it lasted from ca. 15 Ma (3 identical ages TUC19-1C_1A) to 9 Ma (5 ages of subsample TUC19-1D_3A which overlap within error), i.e. ca. 6 Ma. The detailed analyses of our dataset shows how during this event different subsamples with different characteristics precipitate one after another, supporting the fact that the ages cover the duration of the weathering event (Fig. V-9).

V.6.5 Effect of the weathering history onto the age distribution

The presented dataset stands out for its remarkable reproducibility when compared to similar datasets (Monteiro et al., 2014; Allard et al., 2018; Monteiro et al., 2018; Wells et al., 2019; dos Santos Albuquerque et al., 2020; Heller et al., 2022). Heller et al (2022) have shown that phase mixing of different supergene Fe (oxyhydr)oxide phases with different ages and actinide compositions can lead to significant age spread in (U-Th)/He ages. In that study, a late

Neogene bauxitization event leading to numerous cycles of dissolution and reprecipitation is likely responsible for the strong age spread observed in their data. Although the dataset presented here contains some mixed ages, most subsamples yield highly reproducible (U-Th)/He results. The rather simple weathering history recorded in our dataset with two discrete weathering events and the absence of bauxitic conditions could be responsible for this data quality.

V.6.6 Regional comparison and climatic and geodynamic implications

V.6.6.1 *Pre-Oligocene/ Early Paleogene weathering*

Our data with maximum hematite ages between 69 and 63 Ma and numerous ages between 60 Ma and 30 Ma indicate that the basement rocks in Amapá are exposed to the surface since the late cretaceous or Early Paleogene. Several authors propose a Cretaceous peneplanation event for the Guiana shield (Choubert, 1957; McConnell, 1968; Bardossy and Aleva, 1990) and even for the entire cratonic basement of South America (King, 1962). Although this Cretaceous “Gondwana” surface is suggested to appear generally at higher elevations, several authors explain that the surfaces dip towards the coastline and Bardossy and Aleva, (1990) propose a Late Cretaceous age for the upper planation surface in the Serra do Navio area to which our sampling site belongs. Our data confirm that hypothesis and comprise the first late Cretaceous / Early Paleogene weathering data for the Guyana shield. Figure V-10 compares our results to existing weathering age data from the South American Platform. Results from Brazilian shield south of the Amazon yield similar results with ^{40}Ar - ^{39}Ar ages up to 70 Ma (Vasconcelos et al., 1994; Ruffet et al., 1996) and (U-Th)/He ages up to 80 Ma (Monteiro et al., 2018). These data derive from areas with considerably higher elevations (Carajás, ca. 700-800m), supporting the existence of a regional extent of a Late Cretaceous. Paleocene paleosurface which was (and is) sloped northward.

From our data, no discrete weathering events can be determined for this first episode of weathering which formed the canga layer on top of the BIFs. The preservation of only hematite but no goethite from that time interval could indicate a rather hot and dry climate for that period. During the Late Cretaceous / Early Paleogene global temperature were generally higher than today (Zachos et al., 2008; Westerhold et al., 2020) but had not yet reached their peak of the Early Eocene Climate Optimum (53-51 Ma, (Zachos et al., 2008)).

Precipitation chronology of hematite and goethite in lateritic duricrusts from equatorial Brazil

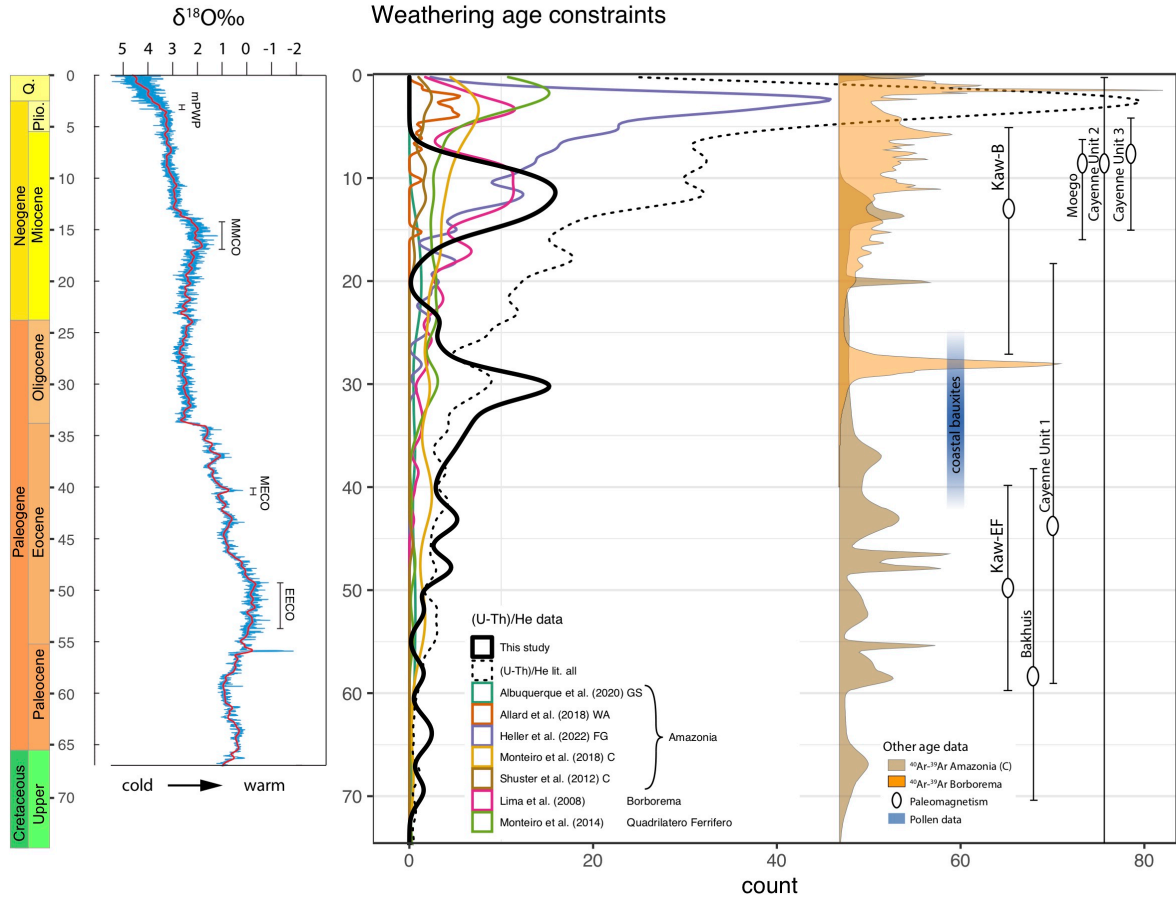


Figure V-10: Data of this study in the context of published weathering age data and global temperature variations in the Cenozoic. Left panel: blue and red curve show the Cenozoic global benthic $\delta^{18}\text{O}$ curve from (Westerhold et al., 2020) smoothed over 20 kyr (blue) and 1 Ma (red). The right panel shows published weathering age constraints for Amazonia and other cratonic areas of Brazil. Empty curves correspond to Kernel Density estimates of published (U-Th)/He data from Amazonia (GS = Guaporé Shield, WA = Western Guiana, FG = French Guiana, C = Carajás) and other areas in Brazil (Lima, 2008; Shuster et al., 2012; Monteiro et al., 2014; Allard et al., 2018; Monteiro et al., 2018; dos Santos Albuquerque et al., 2020; Heller et al., 2022). The black dashed curve summarizes the cited (U-Th)/He studies included, the black dense line represents this study. Note that for better visibility the density data of our study is multiplied by a factor of 4. The filled curves on the right hand side represent probability density plots of ^{39}Ar - ^{40}Ar data on supergene Mn oxides from the Carajás area in Amazonia (Vasconcelos et al., 1994; Ruffet et al., 1996) and the Borborema province in northeastern Brazil (Lima, 2008). Black ellipses show the Paleomagnetic ages by Théveniaut and Freyssinet (2002), the blue bar indicates the age of the coastal bauxites in Suriname and Guyana based on Pollen data by Hammen and Wymstra (1964).

V.6.6.2 Oligocene weathering

Our data indicates the presence of an important weathering event at ca. 30 Ma which led to the massive precipitation of hematite on top of the schists and to precipitation of goethite inside the canga sample on top of the BIFs. The age of 30 Ma appears in several weathering age data sets from Amazonia and South America. The oldest ages of Heller et al. 2022 are around 30 Ma, whereas the dataset of Monteiro et al. (2018) shows an important peak at 30 Ma and ^{40}Ar - ^{39}Ar ages with a peak at 28 Ma from the Borborema province (Lima 2008) record this age, too. The coastal bauxites in Suriname and Guyana are supposed to have

formed during the Late Eocene and Oligocene (Hammen and Wymstra, 1964; Wymstra, 1971). This lies slightly before our ages but note the pollen data do not allow a very precise dating of these bauxites. Sedimentary records from the Guiana basin indicate that weathering lasted during the entire Oligocene (Wong, 1986) which is very compatible with the weathering observed in our data. (U-Th)/He age by Monteiro et al. (2014) on cangas from Southeastern Brazil show an important age peak at ca. 30 Ma (Fig. V-10). A recent study of Shaw et al. (2021) also indicates weathering at ca. 30 Ma for one of their sampling sites which is nowadays located in the Chilean Andes. During the Oligocene global temperatures were higher than now but lower than during the Eocene (e.g. Westerhold et al., 2020; Zachos et al., 2008). The temperature curve of Westerhold et al. (2020) in Figure V-10 shows an excursion towards higher $\delta^{18}\text{O}$ values at ca. 30 Ma. Whether the weathering event recorded in our samples is related to this increase cannot be determined here. In any case, our data implies that at 30 Ma contrasted tropical monsoonal climate, allowing the formation of a lateritic duricrust prevailed on the eastern rim of the Guyana shield. The strong predominance of hematite precipitation in our samples for this time interval possibly indicates that the climate was rather hot and / or dry at that time. Heller et al. (2022) report similar results for the northeastern rim of the Guiana shield. The data from other sites do not allow a more precise characterization of the climate.

Although our data shows a very clear peak at 30 Ma, the weathering event likely lasted several Millions of years. The ages spread between 35 and 23 Ma but most data (15 of 20) lie between 35 and 29 Ma and half of the analyses yields ages between 31 and 29 Ma. This time period corresponds to an interval of non-deposition in the sedimentary succession East of the mouth of the Amazon (Rossetti, 2001; Rossetti, 2004; Rossetti et al., 2013) and carbonate deposition in the Foz do Amazonas basin (Carozzi, 1981; Wolff and Carozzi, 1984; Cruz et al., 2019) (Fig. V-1D). According to Haq et al. (1987) the global sea-level was low at that time. The laterites associated with the unconformities S1 and S2 documented by Rossetti (2004) could have formed during the same time interval as our samples but due to the lack of age data for the former, this can only be assumed.

V.6.6.3 What happened between the two weathering events?

The absence of data between 23 and 17 Ma indicates either that the climatic conditions did not allow the precipitation the Fe minerals, for example due to too dry or cool climate or that the water table dropped so low that the duricrust system stopped being active. Possible reasons for such a drop of the water table could be a dryer climate, uplift of the continent or

drop of the sea-level. The unconformity S3 found between the lower and middle Barreiras Formation, deposited during the Late Oligocene/Early Miocene and Middle-Late Miocene, respectively, probably formed during the Early / Middle Miocene (Fig. V-1D) (Rossetti, 2004). This unconformity, associated with a paleosol, indicates erosion but no major weathering. An Early to Middle Miocene erosion phase is compatible with our data and could account for a drop of the water table and associated stop of iron (oxyhydr)oxide precipitation in the duricrust.

V.6.6.4 Middle to Late Miocene weathering

The next discrete weathering event recorded in our dataset peaks at 12 Ma. Goethite ages range from 17 to 8 Ma but most ages (19 out of 23) lie between 15 and 9 Ma. At least on the scale of our dataset only goethite precipitated at that time. This possibly indicates a wetter and or / cooler monsoonal climate.

Weathering ages of 12 Ma are equally recorded in (U-Th)/He the data sets of Heller et al., (2022), Lima (2008), Shuster (2012). The data set of Monteiro et al (2018) comprises such ages but the data seems to be very continuous and possibly mixed and do not show a discrete weathering event at that time. ^{40}Ar - ^{39}Ar data from Vasconcelos et al., (1994) and Ruffet et al., (1996) show a peak at ca. 14 Ma which precedes the peak observed in our data. ^{40}Ar - ^{39}Ar ages obtained from the weathered top of the Barreiras formation range from 13-7 Ma (Lima, 2008) and are in line with the unconformity age proposed by Rossetti (2004) and Nogueira et al. (2021) but in contrast with the age proposed by Rossetti (2013). ^{40}Ar - ^{39}Ar data of 13-7 Ma by de Oliveira Carmo and Vasconcelos (2006) indicate surface weathering at that time in Southeastern Brazil.

Similar to the here presented data, the data of Heller et al. (2022) show the predominance of goethite relative to hematite from 14 Ma on. The authors interpret this as a shift towards a more humid or cooler climate. The global temperature curves of Zachos et al. (2008) and Westerhold et al. (2020) indicate a temperature decrease at that time which succeeds the MMCO (17-14.5 Ma). Whereas cooler temperatures are compatible with the favored precipitation of goethite relative to hematite (Trolard and Tardy, 1987; Tardy and Roquin, 1998), a simple temperature decrease cannot explain the extensive precipitation of goethite.

V.6.6.5 Possible causes for the Miocene weathering

Whether this iron (oxyhydr)oxide precipitation increase is related to an increase in precipitation or an upwards movement of the water table, leading to mobilization of Fe, cannot be resolved from our data. However, comparison with the global sea level curve (Haq et al., 1987) and sequence stratigraphic analyses of coastal and shelfal sediments of eastern Amazonia (Rossetti, 2001; Nogueira et al., 2021) indicate an important sea-level drop at that time. Theoretically, an important sea-level drop is expected to enhance erosion in the hinterland rather than induce an uplift of the water table and enhance weathering. It is therefore little probable, that a sea-level change induced this weathering and likely, that enhanced precipitation accounts for the abundant precipitation of goethite.

V.6.6.6 The absence of more recent weathering

The complete lack of ages <8 Ma indicates that something changed after this weathering event. This could have been a change in climate or a change of the water level, leading to a stop of the duricrust formation.

Many of the existing weathering age data sets comprise a many Late Neogene ages (Lima, 2008; Shuster et al., 2012; Allard et al., 2018; Monteiro et al., 2018; Heller et al., 2022). Heller et al. (2022) propose a late Neogene bauxitization event for their samples in NE French Guiana. The fact that the Pliocene sediments of the ACP are strongly weathered underline the presence of Late Neogene (or Holocene) weathering close to our study area. The complete absence of Late Neogene ages in our dataset is thus very surprising. Additionally the current climatic conditions should allow lateritization and precipitation of Fe minerals. The fact that we do not record any ages younger than 8 Ma could be related to the fact that the water table dropped significantly and the study area was target of erosion. The fact that in the eastern area of the Guiana shield many lateritic profiles show erosion at their top and set in rather dissected landscapes indicate the presence of at least one or several periods of erosion after formation of the laterites. The youngest ages of the weathering record are concomitant with the transcontinentalisation of the Amazon river, where large amount of sediment started to be deposit in the Foz do Amazonas basin. The change in the drainage system could have prevented younger weathering in the Amapá state. It is furthermore possible, and suggested by the current climate, that weathering still affected the study area but did not lead to the precipitation of well crystallized Fe minerals. The fine grained, clay-rich matrix could possibly

have formed since then and may contain diffuse, fine grained goethite formed during the last 8 Ma. It should also be kept in mind that the sampling is possibly not completely representative and younger phases of iron oxides precipitated elsewhere.

V.7 Conclusions

Our new mineralogical, geochemical and geochronological data show that weathering in the eastern area of the Guyana shield started probably during the Later Cretaceous or Early Paleogene indicating that this area possibly corresponds to the so called “Gondwana” surface proposed in the literature. Basically all old ages occur in a canga layer formed on top of BIFs whereas duricrust samples developed on top of schists record weathering only since the Late Paleogene. This could eventually indicate that producing a lateritic duricrust is facilitated and faster on top of iron rich BIFs than on top of intermediate schists. The dataset stands out due to its remarkable age reproducibility which allows the discrimination of two weathering events at 30 Ma and 12 Ma which probably lasted ca. 6 Ma both and correspond to the precipitation of large amounts of hematite at 30 Ma and goethite at 12 Ma. Rietveld analyses of the dated subsamples allow insight into the mineralogical evolution of the duricrust and show that during the two weathering events the crystallite sizes of hematite and goethite increase towards younger ages. Four well defined goethite subsamples show that over a short time interval goethite gets increasingly richer in Al, U, Th and Sm and gets increasingly mixed with kaolinite. The weathering events recorded here appear equally in other weathering age data sets of northern South America and probably represent phases of relatively hot and or dry contrasted tropical climate at 30 Ma and comparably cooler and / or more humid contrasted tropical climate at 12 Ma. In between these events and since 8 Ma, Fe mineral precipitation seems to have ceased. This could either be due to climatic changes towards climatic conditions less favorable for keeping the duricrust system active, or be related to a significant drop of the water table, linked to continental uplift or sea-level drop and evoking erosion instead of duricrust formation. Widespread weathering observed in the area during the Late Neogene or even later suggests that a drop of the water table is a more probable explanation.

Acknowledgements

The Great Panter company (Canada) is warmly thanked for access to the Tucano mine and Anderson Jastes is thanked for support during field work in the mine. Frédéric Haurine and Pierre Burckel are warmly thanked for the ICP-MS analysis, Ludovic Delbes and Benoît Baptiste for support with XRD analyses and Imène Esteve for help with SEM analyses. Guillaume Morin is thanked for discussion and help with the Rietveld refinement.

References

- Aleva G. J. J. (1984) Lateritization, bauxitization and cyclic landscape development in the Guiana Shield. In *Bauxite* (ed. L. Jacob Jr). A.I.M.E, New York, USA. pp. 297–318.
- Allard T., Gautheron C., Bressan Riffel S., Balan E., Soares B. F., Pinna-Jamme R., Derycke A., Morin G., Bueno G. T. and do Nascimento N. (2018) Combined dating of goethites and kaolinities from ferruginous duricrusts. Deciphering the Late Neogene erosion history of Central Amazonia. *Chem. Geol.* **479**, 136–150.
- Alvares C. A., Stape J. L., Sentelhas P. C., De Moraes Gonçalves J. L. and Sparovek G. (2013) Köppen's climate classification map for Brazil. *Meteorol. Zeitschrift* **22**, 711–728.
- Ansart C. (2022) Evolution des latérites du bouclier Amazonien, rapport de Mineralogie, géochronologie et géochimie. Université Paris Saclay, France.
- Antao S. M., Hassan I., Wang J., Lee P. L. and Toby B. H. (2008) State-of-the-art high-resolution powder X-ray diffraction (HRPXRD) illustrated with rietveld structure refinement of quartz, sodalite, tremolite, and meionite. *Can. Mineral.* **46**, 1501–1509.
- Baker P. A., Fritz S. C., Silva C. G., Rigsby C. A., Absy M. L., Almeida R. P., Caputo M., Chiessi C. M., Cruz F. W., Dick C. W., Feakins S. J., Figueiredo J., Freeman K. H., Hoorn C., Jaramillo C., Kern A. K., Latrubesse E. M., Ledru M. P., Marzoli A., Myrbo A., Noren A., Piller W. E., Ramos M. I. F., Ribas C. C., Trnadade R., West A. J., Wahnfried I. and Willard D. A. (2015) Trans-Amazon Drilling Project (TADP): Origins and evolution of the forests, climate, and hydrology of the South American tropics. *Sci. Drill.* **20**, 41–49.
- Balan E., Allard T., Fritsch E., Sélo M., Falguères C., Chabaux F., Pierret M. C. and Calas G. (2005) Formation and evolution of lateritic profiles in the middle Amazon basin: Insights from radiation-induced defects in kaolinite. *Geochim. Cosmochim. Acta* **69**, 2193–2204.

- Balan E., Neuville D. R., Trocellier P., Fritsch E., Muller J. P. and Calas G. (2001) Metamictization and chemical durability of detrital zircon. *Am. Mineral.* **86**, 1025–1033.
- Balout H., Roques J., Gautheron C., Tassan-Got L. and Mbongo-Djimbi D. (2017) Helium diffusion in pure hematite (α -Fe₂O₃) for thermochronometric applications: A theoretical multi-scale study. *Comput. Theor. Chem.* **1099**, 21–28.
- Bardossy G. and Aleva G. J. J. (1990) *Lateritic Bauxites*. Developmen., Elsevier Science, Amsterdam, The Netherlands.
- Bassal F., Roques R., Corre M., Brunet F., Ketcham R., Schwartz S., Tassan-Got L. and Gautheron C. (2022) Role of defects and radiation damage on He diffusion in magnetite: implication for (U-Th)/He thermochronolog. *Minerals in press*.
- Beauvais A. (2009) Ferricrete biochemical degradation on the rainforest-savannas boundary of Central African Republic. *Geoderma* **150**, 379–388.
- Beck H. E., Zimmermann N. E., McVicar T. R., Vergopolan N., Berg A. and Wood E. F. (2018) Present and future köppen-geiger climate classification maps at 1-km resolution. *Sci. Data* **5**, 1–12.
- Bezerra I. S. A. A., Nogueira A. C. R., Guimarães J. T. F. and Truckenbrodt W. (2015) Late pleistocene sea-level changes recorded in tidal and fluvial deposits from Itaubal Formation, onshore portion of the Foz do Amazonas Basin, Brazil. *Brazilian J. Geol.* **45**, 63–78.
- Blancaneaux P. (1981) *Essai sur le milieu naturel de la Guyane Française.*, Paris.
- Carozzi A. V (1981) Porosity models and oil exploration of Ampa carbonates, Paleogene, Foz do Amazonas Basin, offshore NW Brazil. *J. Pet. Geol.* **4**, 3–34.
- Carroll D. (1953) Weatherability of Zircon. *J. Sediment. Petrology* **23**, 106–116.
- Choubert B. (1957) *Essai sur la morphologie de la Guyane.*, Paris.
- Cordani U. G. and Teixeira W. (2007) Proterozoic accretionary belts in the Amazonian Craton. In *4-D Framework of Continental Crust: Geological Society of America Memoir 200* (eds. R. D. J. Hatcher, M. P. Carlson, J. H. McBride, and J. . Martínez-Catalán). Geological Society of America, Boulder, CO. pp. 297–320.
- Cornell R. M. and Schwertmann U. (2003) *The Iron Oxides. Structure, Properties, Occurences and Uses.*, Wiley-VCH, Weinheim, Germany.

- Cruz A. M., Reis A. T., Suc J. P., Silva C. G., Praeg D., Granjeon D., Rabineau M., Popescu S. M. and Gorini C. (2019) Neogene evolution and demise of the Amapá carbonate platform, Amazon continental margin, Brazil. *Mar. Pet. Geol.* **105**, 185–203.
- Damuth J. E. and Flood R. D. (1985) Amazon Fan, Atlantic Ocean. In *Submarine Fans and Related Turbidite Systems* (ed. A. H. Bouma). Springer, New York, USA.
- Delattre S., Utsunomiya S., Ewing R. C., Boeglin J. L., Braun J. J., Balan E. and Calas G. (2007) Dissolution of radiation-damaged zircon in lateritic soils. *Am. Mineral.* **92**, 1978–1989.
- Deng X. D., Li J. W. and Shuster D. L. (2017) Late Mio-Pliocene chemical weathering of the Yulong porphyry Cu deposit in the eastern Tibetan Plateau constrained by goethite (U–Th)/He dating: Implication for Asian summer monsoon. *Earth Planet. Sci. Lett.* **472**, 289–298.
- Derycke A., Gautheron C., Barbarand J., Bourbon P., Aertgeerts G., Simon-Labric T., Sarda P., Pinna-Jamme R., Boukari C. and Haurine F. (2021) French Guiana margin evolution: From Gondwana break-up to Atlantic opening. *Terra Nov.*, 1–8.
- Driscoll N. W. and Karner G. D. (1994) Flexural deformation due to Amazon Fan loading: A feedback mechanism affecting sediment delivery to margins. *Geology* **22**, 1015–1018.
- Farley K. A. (2018) Helium diffusion parameters of hematite from a single-diffusion-domain crystal. *Geochim. Cosmochim. Acta* **231**, 117–129.
- Figueiredo J., Hoorn C., van der Ven P. and Soares E. (2009) Late Miocene onset of the Amazon River and the Amazon deep-sea fan: Evidence from the Foz do Amazonas Basin. *Geology* **37**, 619–622.
- Figueiredo J. J. P., Zalán P. V. and Soares E. F. (2007) Bacia da foz do Amazonas. *Bol. Geociencias da Petrobras* **15**, 299–309.
- Forti M. C., Boulet R., Melfi A. J. and Neal C. (2000) Hydrogeochemistry of a small catchment in Northeastern Amazonia: A comparison between natural with deforested parts of the catchment (Serra do Navio, Amapa State, Brazil). *Water. Air. Soil Pollut.* **118**, 263–279.
- Gautheron C., Pinna Jamme R., Derycke, A. A., Hadi F., Sanchez C., Haurine F., Monvoisin G., Barbosa D., Delpech G., Maltese J., Sarda P. and Tassan-Got L. (2021) Analytical protocols and performance for apatite and zircon (U–Th)/He analysis on quadrupole and magnetic sector mass spectrometer systems between 2007 and 2020. *Geochronology*.

- Gautheron C., Sawakuchi A. O., dos Santos Albuquerque M. F., Cabriolu C., Parra M., Ribas C. C., Pupim F. N., Schwartz S., Kern A. K., Gómez S., de Almeida R. P., Horbe A. M. C., Haurine F., Miska S., Nouet J., Findling N., Riffel S. B. and Pinna-Jamme R. (2022) Cenozoic weathering of fluvial terraces and emergence of biogeographic boundaries in Central Amazonia. *Glob. Planet. Change* **212**, 103815.
- Gomes Sobrinho T. R. and Sotta E. D. (2011) Caracterização climatológica do módulo 4 da Floresta Estadual do Amapá-FLOTA/AP: dados preliminares. In *IV Simpósio Internacional de Climatologia* Sociedade Brasileira de Meteorologia, João Pessoa, Brazil. pp. 0–4.
- Gómez J., Schobbenhaus C., Montes N. E. and Compilers (2019) *Geological Map of South America 2019. Scale 1:5 000 000.*
- Guinoiseau D., Fekiacova Z., Allard T., Druhan J. L., Balan E. and Bouchez J. (2021) Tropical Weathering History Recorded in the Silicon Isotopes of Lateritic Weathering Profiles. *Geophys. Res. Lett.* **48**.
- Hammen van der T. and Wymstra T. A. (1964) A Palynological study on the Tertiary and Upper Cretaceous of British Guiana. *Leidse Geol. Meded.* **30**, 183–241.
- Haq B. U., Hardenbol J. and Vail P. R. (1987) Chronology of fluctuating sea levels during the Triassic. *Science (80-)*. **235**, 1156–1167.
- Heim J. A., Vasconcelos P. M., Shuster D. L., Farley K. A. and Broadbent G. (2006) Dating paleochannel iron ore by (U-Th)/He analysis of supergene goethite, Hamersley province, Australia. *Geology* **34**, 173–176.
- Heller B. M., Riffel S. B., Allard T., Morin G., Roig J.-Y., Couëffé R., Aertgeerts G., Derycke A., Ansart C., Pinna-Jamme R. and Gautheron C. (2022) Reading the climate signals hidden in bauxite. *Geochim. Cosmochim. Acta* **323**, 40–73.
- Hofmann F., Reichenbacher B. and Farley K. A. (2017) Evidence for >5 Ma paleo-exposure of an Eocene–Miocene paleosol of the Bohnerz Formation, Switzerland. *Earth Planet. Sci. Lett.* **465**, 168–175.
- Hofmann F., Treffkorn J. and Farley K. A. (2020) U-loss associated with laser-heating of hematite and goethite in vacuum during (U-Th)/He dating and prevention using high O₂ partial pressure. *Chem. Geol.* **532**.
- Holdsworth R. E., Butler C. A. and Roberts A. M. (1997) The recognition of reactivation during continental deformation. *J. Geol. Soc. London.* **154**, 73–78.

- Hoorn C., Bogotá-A G. R., Romero-Baez M., Lammertsma E. I., Flantua S. G. A., Dantas E. L., Dino R., do Carmo D. A. and Chemale F. (2017) The Amazon at sea: Onset and stages of the Amazon River from a marine record, with special reference to Neogene plant turnover in the drainage basin. *Glob. Planet. Change* **153**, 51–65.
- Hoorn C., Rodda M., Dino R., Soares E., Uba C., Ochoa-Lozanom D. and Mapes R. (2010) The Amazonian craton and its influence on past fluvial systems (Mesozoic-Cenozoic, Amazonia). In *Amazonia: landscape and species evolution. A look into the past.* (eds. C. Hoorn and F. P. Wesselingh). Wiley-Blackwell. pp. 103–122.
- King L. C. (1962) *Morphology of the Earth.*, Oliver and Boyd Publ. House, London.
- Klein C. (2005) Some Precambrian banded iron-formations (BIFs) from around the world: Their age, geologic setting, mineralogy, metamorphism, geochemistry, and origin. *Am. Mineral.* **90**, 1473–1499.
- Lascelles D. F. (2006) The genesis of the hope downs iron ore deposit, Hamersley Province, Western Australia. *Econ. Geol.* **101**, 1359–1376.
- Lima M. da G. (2008) A História do Intemperismo na Província Borborema Oriental, Nordeste do Brasil. Universidade Federal do Rio Grande do Norte, Natal, Brazil.
- Lippolt H. J., Brander T. and Mankopf N. R. (1998) An attempt to determine formation ages of goethites and limonites by (U+Th)-⁴He dating. *Neues Jahrb. Mineral. Monatshefte*, 505–528.
- Lippolt H. J., Wernicke R. S. and Boschmann W. (1993) ⁴He diffusion in specular hematite. *Phys. Chem. Miner.* **20**, 415–418.
- Marzoli A., Renne P. R., Piccirillo E. M., Ernesto M., Bellieni G. and De Min A. (1999) Extensive 200-million-year-old continental flood basalts of the Central Atlantic Magmatic Province. *Science (80-)*. **284**, 616–618.
- Mathian M., Bueno G. T., Balan E., Fritsch E., Do Nascimento N. R., Selo M. and Allard T. (2020) Kaolinite dating from Acrisol and Ferralsol: A new key to understanding the landscape evolution in NW Amazonia (Brazil). *Geoderma* **370**.
- McConnell R. B. (1968) Planation Surfaces in Guyana. *Geogr. J.* **134**, 506–520.
- Melo L. V. de, Villas R. N., Soares J. W. and Faraco M. T. L. (2003) Geological setting and mineralizing fluids of the Amapari gold deposit, Amapa State, Brazil. *Géologie la Fr.*, 243–255.

- Mendes A. C., Truckenbrod W. and Nogueira A. C. R. (2012) Análise faciológica da formação Alter do Chão (Cretáceo, Bacia do Amazonas), próximo à cidade de Óbidos, Pará, Brasil. *Rev. Bras. Geociências* **42**, 39–57.
- Monteiro H. S., Vasconcelos P. M., Farley K. A., Spier C. A. and Mello C. L. (2014) (U-Th)/He geochronology of goethite and the origin and evolution of cangas. *Geochim. Cosmochim. Acta* **131**, 267–289.
- Monteiro H. S., Vasconcelos P. M. P., Farley K. A. and Lopes C. A. M. (2018) Age and evolution of diachronous erosion surfaces in the Amazon: Combining (U-Th)/He and cosmogenic ^3He records. *Geochim. Cosmochim. Acta* **229**, 162–183.
- Nogueira A. C. R., Amorim K. B., Góes A. M., Truckenbrodt W., Petri S., Nogueira A. A. E., Bandeira J., Soares J. L., Baía L. B., Imbiriba Júnior M., Bezerra I. S., Ribas C. C. and Cracraft J. (2021) Upper Oligocene-Miocene deposits of Eastern Amazonia: Implications for the collapse of Neogene carbonate platforms along the coast of northern Brazil. *Palaeogeogr. Palaeoclimatol. Palaeoecol.* **563**, 19.
- de Oliveira Carmo I. and Vasconcelos P. M. (2006) $^{40}\text{Ar}/^{39}\text{Ar}$ geochronology constraints on late miocene weathering rates in Minas Gerais, Brazil. *Earth Planet. Sci. Lett.* **241**, 80–94.
- Pidgeon R. T. (2003) Application of (U-Th)/He Geochronology To Date Hematite and Other Iron Minerals Produced During Weathering. *Advances*, 321–323.
- Putzer H. (1984) The geological evolution of the Amazon basin and its mineral resources. In *The Amazon: Limnology and Landscape Ecology of a Mighty Tropical River and its Basin* (ed. H. Sioli). Dr W. Junk Publishers, Dordrecht. pp. 15–46.
- Reiners P. W., Chan M. A. and Evenson N. S. (2014) (U-Th)/He geochronology and chemical compositions of diagenetic cement, concretions, and fracture-filling oxide minerals in mesozoic sandstones of the Colorado Plateau. *Bull. Geol. Soc. Am.* **126**, 1363–1383.
- Riffel S. B., Vasconcelos P. M., Carmo I. O. and Farley K. A. (2016) Goethite (U-Th)/He geochronology and precipitation mechanisms during weathering of basalts. *Chem. Geol.* **446**, 18–32.
- Rodger M., Watts A. B., Greenroyd C. J., Peirce C. and Hobbs R. W. (2006) Evidence for unusually thin oceanic crust and strong mantle beneath the Amazon Fan. *Geology* **34**, 1081–1084.

- Rossetti D. F. (2001) Late Cenozoic sedimentary evolution in northeastern Pará, Brazil, within the context of sea level changes. *J. South Am. Earth Sci.* **14**, 77–89.
- Rossetti D. F. (2004) Paleosurfaces from northeastern Amazonia as a key for reconstructing paleolandscapes and understanding weathering products. *Sediment. Geol.* **169**, 151–174.
- Rossetti D. F. (2014) The role of tectonics in the late Quaternary evolution of Brazil's Amazonian landscape. *Earth-Science Rev.* **139**, 362–389.
- Rossetti D. F., Bezerra F. H. R. and Dominguez J. M. L. (2013) Late oligocene-miocene transgressions along the equatorial and eastern margins of brazil. *Earth-Science Rev.* **123**, 87–112.
- Rudnick R. L. and Gao S. (2013) *Composition of the Continental Crust*. 2nd ed., Elsevier Ltd.
- Ruffet G., Innocent C., Michard A., Féraud G., Beauvais A., Nahon D. and Hamelin B. (1996) A geochronological $^{40}\text{Ar}/^{39}\text{Ar}$ and $^{87}\text{Rb}/^{87}\text{Sr}$ study of K-Mn oxides from the weathering sequence of Azul, Brazil. *Geochim. Cosmochim. Acta* **60**, 2219–2232.
- dos Santos Albuquerque M. F., Horbe A. M. C. and Danišík M. (2020) Episodic weathering in Southwestern Amazonia based on (U–Th)/He dating of Fe and Mn lateritic duricrust. *Chem. Geol.* **553**, 119792.
- Scarpelli W. and Horikava E. H. (2018) Chromium, iron, gold and manganese in Amapá and northern Pará, Brazil. *Brazilian J. Geol.* **48**, 415–433.
- Scarpelli W. and Horikava E. H. (2017) Gold, iron and manganese in central Amapá, Brazil. *Brazilian J. Geol.* **47**, 703–721.
- Shaw J. M., Evenstar L., Cooper F. J., Adams B. A., Hofmann F. and Farley K. A. (2021) A Rusty Record of Weathering and Groundwater Movement in the Hyperarid Central Andes Geochemistry , Geophysics , Geosystems. *Geochemistry, Geophys. Geosystems* **22**, 24.
- Shuster D. L., Farley K. A., Vasconcelos P. M., Balco G., Monteiro H. S., Waltenberg K. and Stone J. O. (2012) Cosmogenic ^3He in hematite and goethite from Brazilian “canga” duricrust demonstrates the extreme stability of these surfaces. *Earth Planet. Sci. Lett.* **329–330**, 41–50.
- Shuster D. L., Vasconcelos P. M., Heim J. A. and Farley K. A. (2005) Weathering geochronology by (U–Th)/He dating of goethite. *Geochim. Cosmochim. Acta* **69**, 659–673.
- van Soelen E. E., Kim J. H., Santos R. V., Dantas E. L., Vasconcelos de Almeida F., Pires J. P., Roddaz M. and Sinninghe Damsté J. S. (2017) A 30 Ma history of the Amazon River

- inferred from terrigenous sediments and organic matter on the Ceará Rise. *Earth Planet. Sci. Lett.* **474**, 40–48.
- Stanjek H. and Schwertmann U. (1992) The influence of aluminum on iron oxides. Part XVI: Hydroxyl and aluminum substitution in synthetic hematites. *Clays Clay Miner.* **40**, 347–354.
- Tardy Y. (1997) *Petrology of Laterites and Tropical Soils.*, Balkema, Rotterdam, The Netherlands.
- Tardy Y. and Nahon D. (1985) Geochemistry of laterites, stability of Al-goethite, Al-hematite, and Fe³⁺-Kaolinite in bauxites and ferricretes: an approach to the mechanism of concretion formation. *Am. J. Sci.* **285**, 865–903.
- Tardy Y. and Roquin C. (1998) *Dérive des continents paléoclimats et altérations tropicales.*, BRGM, Orléans, France.
- Théveniaut H. and Freyssinet P. (2002) Timing of lateritization on the Guiana Shield synthesis of paleomagnetic results. *Palaeogeogr. Palaeoclimatol. Palaeoecol.* **178**, 91–117.
- Toby B. H. (2006) R factors in Rietveld analysis: How good is good enough? . *Powder Diffraction*. **21**, 67–70.
- Trolard F. and Tardy Y. (1987) The stabilities of gibbsite, boehmite, aluminous goethites and aluminous hematites in bauxites, ferricretes and laterites as a function of water activity, temperature and particle size. *Geochim. Cosmochim. Acta* **51**, 945–957.
- von Uexküll H. R. and Mutert E. (1995) Global extent, development and economic impact of acid soils. *Plant Soil* **171**, 1–15.
- Vasconcelos P. M., Heim J. A., Farley K. A., Monteiro H. and Waltenberg K. (2013) ⁴⁰Ar/³⁹Ar and (U-Th)/He -⁴He/³He geochronology of landscape evolution and channel iron deposit genesis at Lynn Peak, Western Australia. *Geochim. Cosmochim. Acta* **117**, 283–312.
- Vasconcelos P. M., Renne P. R., Brimhall G. H. and Becker T. A. (1994) Direct dating of weathering phenomena by ⁴⁰Ar/³⁹Ar and K-Ar analysis of supergene K-Mn oxides. *Geochim. Cosmochim. Acta* **58**, 1635–1665.
- Vermeesch P., Seward D., Latkoczy C., Wipf M., Günther D. and Baur H. (2007) α-Emitting mineral inclusions in apatite, their effect on (U-Th)/He ages, and how to reduce it. *Geochim. Cosmochim. Acta* **71**, 1737–1746.

- Watts A. B., Rodger M., Peirce C., Greenroyd C. J. and Hobbs R. W. (2009) Seismic structure, gravity anomalies, and flexure of the amazon continental margin, NE Brazil. *J. Geophys. Res. Solid Earth* **114**, 1–23.
- Wells M. A., Danišik M., McInnes B. I. A. and Morris P. A. (2019) (U-Th)/He-dating of ferruginous duricrust: Insight into laterite formation at Boddington, WA. *Chem. Geol.* **522**, 148–161.
- Westerhold T., Marwan N., Drury A. J., Liebrand D., Agnini C., Anagnostou E., Barnet J. S. K., Bohaty S. M., De Vleeschouwer D., Florindo F., Frederichs T., Hodell D. A., Holbourn A. E., Kroon D., Laurentano V., Littler K., Lourens L. J., Lyle M., Pälike H., Röhl U., Tian J., Wilkens R. H., Wilson P. A. and Zachos J. C. (2020) An astronomically dated record of Earth's climate and its predictability over the last 66 million years. *Science (80-.)*. **369**, 1383–1388.
- Wolff B. and Carozzi A. V (1984) *Microfacies, depositional environments, and diagenesis of the Amapá carbonates (Paleocene-Middle Miocene), Foz do Amazonas basin, offshore NE Brazil.*, Rio de Janeiro, Brazil.
- Wong T. E. (1986) Outline of the stratigraphy and the geological history of the Suriname coastal plain. *Geol. en Mijnb.* **65**, 223–241.
- Wymstra T. A. (1971) The palynology of the Guiana coastal basin. University of Amsterdam.
- Zachos J. C., Dickens G. R. and Zeebe R. E. (2008) An early Cenozoic perspective on greenhouse warming and carbon-cycle dynamics. *Nature* **451**, 279–283.

VI French Guiana laterite and bauxite evolution through time and space

Abstract

This study investigates the mineralogical characteristics and age of three ferruginous to bauxitic lateritic duricrust systems from the area of Cayenne in French Guiana (Mount Baduel, Vidal and Petit Connétable island) and through combination with published data from French Guiana and Suriname we examine the spatial extent of weathering events on the northeastern rim of the Guiana shield. Nine bulk samples were analyzed mineralogically and geochemically, and macroscopically homogeneously subsamples were separated from six of them. 120 (U-Th)/He ages were obtained on microscopically pure hematite and goethite fragments of these subsamples. For the subsamples of Mount Baduel, mineralogical analyses were conducted in order to better characterize the dated material and its formation conditions.

Bulk analyses reveal that in the lateritic-bauxitic profile of Mount Baduel both bauxitic and ferruginous duricrusts coexist as indicated by contrasting gibbsite and kaolinite contents and strong variation in Al-substitution of goethite. Bulk samples from Connétable show a clear bauxitic signature, whereas samples from Vidal have a more ferruginous signature.

The data from Mount Baduel allow to constrain the evolution of its lateritic cover, which records weathering since at least the Middle Miocene and secondary bauxitization during the Late Neogene. Geochronological results from Vidal and Connétable indicate weathering since the Oligocene, possibly even since the Late Eocene. The comparison with two recently published datasets from French Guiana (Heller et al., 2022) and Suriname (Ansart, 2022) shows that Oligocene weathering and Late Neogene bauxitization were regional features and provoked by climatic rather than geomorphological changes. Our results show that the proposed geomorphological models need to be reassessed and that the morphology of this area is strongly influenced by its proximity to the coast.

VI.1 Introduction

Tropical weathering, as it occurs nowadays in in the intertropical belt of continental areas, leads to the formation of thick lateritic profiles. These weathering profiles are generally stratified and their composition is a function of climate, drainage and, to a lesser degree, parent rock composition (Valeton, 1983; Bardossy and Aleva, 1990; Schellmann, 1994; Tardy, 1997;

Tardy and Roquin, 1998). While seasonally contrasted tropical monsoonal climate leads to the formation of ferruginous laterites, characterized by a mineralogy composed primarily of kaolinite, iron (oxyhydr)oxides and residual quartz, humid tropical climate (without or with a very short dry period), leads to the formation of bauxitic laterites (here also referred to as bauxites), especially when coupled to good drainage conditions (Bardossy and Aleva, 1990; Tardy and Roquin, 1998). Different from ferruginous laterites, bauxitic profiles are characterized by a strong accumulation of aluminum in form of aluminum (hydr)oxides (principally gibbsite and, to a lesser degree, boehmite) and Al-rich Fe (oxyhydr)oxides, whereas kaolinite is rare or absent (Valeton, 1972; Bardossy and Aleva, 1990; Tardy, 1997). Normally, both ferruginous and bauxitic laterites contain at their top, below a generally thin topsoil, a several meters thick indurated layer, the iron duricrust. This duricrust is principally constituted by supergene hematite and goethite and contains equally some kaolinite (ferruginous duricrust) or gibbsite (here referred to as bauxitic duricrust). The bauxite layer *sensu strictu*, composed of nearly pure gibbsite is located below the Fe duricrust and can be small or absent (Valeton, 1972; Bardossy and Aleva, 1990; Patterson et al., 1994; Carvalho et al., 1997).

Due to their stability at Earth's surface conditions, notably in the intertropical zone, laterites can become very old and are thus records of past climate (Tardy and Roquin, 1998). Previous studies have shown that they formed episodically throughout the Earth's history, especially in areas of tectonic quiescence (Prasad, 1983; Vasconcelos et al., 1994; Retallack, 2010; Monteiro et al., 2014; Vasconcelos et al., 2015; Monteiro et al., 2018). However, as dating of this material is very challenging due to the absence or scarcity of datable minerals, many uncertainties remain regarding the temporal and spatial extent of these weathering events.

The Guiana shield is located in the northern part of the South American continent and is supposed to have been tectonically stable and in tropical latitudes since the Cretaceous. The existence of several paleosurfaces corresponding to different phases of peneplanation with ages from Late Cretaceous to recent has been proposed by several authors (Choubert, 1957; King, 1962; McConnell, 1968; Blancaneaux, 1981; Aleva, 1984; Bardossy and Aleva, 1990). According to these authors the highest elevation paleosurfaces are the oldest ones whereas those at low elevation are the most recent ones. Many of these paleosurfaces are covered by thick (ferruginous and bauxitic) lateritic profiles recording a long-lasting story of tropical weathering. However, the episodes of enhanced weathering are not well constrained in time and space as only few weathering age datasets exist and sedimentological constraints of the

lateritic profiles are restricted to a small area (Hammen and Wymstra, 1964; Wymstra, 1971). Two recent (U-Th)/He geochronological datasets from bauxitic laterites in French Guiana (Kaw Mountain) and Suriname (Brownsberg Mountain) indicate that weathering at the northeastern edge of the Guiana shield goes back to the Oligocene or possibly Late Eocene (Ansart, 2022; Heller et al., 2022). While data from Brownsberg Mountain indicates the existence of a phase of bauxitization predating 14 Ma, the dataset from Kaw Mountain indicates ferruginous lateritic conditions during the Oligocene and Early to Middle Miocene. Nevertheless, the latter site has a strong bauxitic signature indicated by the presence of gibbsite, the absence of kaolinite and very Al-rich goethite (Heller et al., 2022). The authors state that a bauxitic overprint of a formerly ferruginous lateritic duricrust occurred during the Late Neogene. However due to the strong mixing of older and younger material a precise determination of the beginning and duration of the Neogene bauxitization was not possible.

The aim of this study is to investigate, whether the weathering history recorded at Kaw mountain has a regional extent, and if the proposed geomorphological models are valid in the target area. In order to elucidate these questions, three lateritic duricrusts in the city of Cayenne (French Guiana) and its surroundings were sampled: i) Mount Baduel, a 100 m high hill inside the city of Cayenne with a bauxitic-lateritic cover previously studied by paleomagnetism (Theveniaut and Freyssinet 1999, 2002) and investigated in more detail here ii) Lycee Vidal, a 25 m high knoll with a supposedly ferruginous lateritic cover, 8 km southeast of Cayenne (equally studied Paleomagnetism by Theveniaut and Freyssinet (2002)) and iii) the island of Petit Connétable, a small piece of lateritic duricrust in the middle of Atlantic ocean (0-2 m a.s.l) 40 km southeast of Cayenne and northeast of Kaw mountain and approximately 15km NE from the coast. As the outcrop conditions were very limited and restricted to the duricrust at Vidal and Connétable, we tried to compare the geochemical properties of these duricrusts with the better characterized ones from Baduel. Our results show how both bauxitic and ferruginous duricrusts can coexist in a same profile, that weathering at the three sites, formerly suggested to be Quaternary in age, goes back to the Miocene and Oligocene and that the Late Neogene bauxitization event recorded at Kaw was of regional extent. This implicates that the landscape of the study area contains very old features and that the geomorphological setting is strongly influenced by its proximity to the coast, where a too simplified geomorphological model suggesting older ages for higher elevation paleosurfaces is not valid.

VI.2 Geology, geomorphology and climate of the Cayenne area

VI.2.1 Geological context

The Cayenne peninsula is located at the northeastern edge of the Guiana shield, the northern part of the Amazon craton (Fig. VI-1A). The Guiana shield comprises two Archean cores but was mainly formed during the Paleoproterozoic Transamazonian orogeny (2.2-1.95 Ga) and later accretionary events as its southwestern border (Cordani and Teixeira, 2007). To the south the Guiana shield is covered by the Paleozoic sediments of the west-east stretching Amazonas-Solimões basin, whereas its western limitation is buried under the Meso- and Cenozoic Llanos Basin. Towards north and east the Guiana shield turns into a passive continental margin which developed since the Mesozoic breakup of Pangea and the opening of the Atlantic ocean, which occurred during the Jurassic for the equatorial Atlantic. Three major geologic events affected the area during the Cenozoic: i) the uplift of the Andes which started in the early Cenozoic became more intense during the Late Oligocene and Miocene (~23 Ma) and was strongest during the Middle to Late Miocene (~12 Ma) and Early Pliocene (~4.5 Ma) (Hoorn et al., 2010; Sundell et al., 2019); ii) the transcontinentalization of the Amazon river during the Miocene (finished by ca. 9-8 Ma, (Figueiredo et al., 2009; Hoorn et al., 2017)) leading to massive sedimentary deposition (ca. 10 km) in the Amazon fan (Damuth and Flood, 1985; Piper et al., 1997; Lopez, 2001) and iii) the closure of the Panama isthmus during the Pliocene (~3.5 – 2.7 Ma, (Coates, 1992; Bartoli et al., 2005)).

Sedimentary successions in the Guiana basin, the on- and offshore basin in the north of French Guiana, Suriname and Guyana, yield information about the phases of sedimentation, erosion and weathering during the Meso- and Cenozoic. The oldest sediments of the Guiana basin which cover weathered basement rocks are Late Cretaceous in age and are weathered, too (Wong, 1994). Paleocene to Early Eocene sediments on the onshore part of the basin (coastal plains of Guyana, Suriname and, to a lesser degree, French Guiana) were deeply weathered during the Late Eocene and Oligocene, leading to the formation of the economically important coastal bauxites in Suriname and Guyana (Hammen and Wymstra, 1964; Wymstra, 1971; Bardossy and Aleva, 1990; Wong, 1994; Monsels and Van Bergen, 2019). In the offshore sequence of the basin this weathering episode produced the “Bauxite Hiatus”. Sedimentation continued during the Cenozoic but other Hiatus occurs near the base of the Miocene, at the Miocene-Pliocene, Pliocene-Pleistocene and the Pleistocene-Holocene boundaries (Wong, 1986; Wong, 1994). Large parts of the Miocene are actually missing in the sedimentary

record (Wong, 1986). The siliciclastic sedimentation in the Guiana basin was strongly controlled by numerous transgression and regression cycles and several times the coastline moved far South as for example at the beginning of the Pliocene (Wong, 1986 and references therein). Early Pleistocene successions in Suriname suggest that sea-level was first low but then rose during the Pleistocene and weathering was active during at least two periods of nondeposition (Wong et al., 2009). The Holocene sedimentation of clay-rich material happened together with continuously rising sea-level with a constant to receding shore line. Sea-level reached its present position about 6000 years B.P. (Wong, 1986). The present coast is under the influence of the Amazon river whose clayey and silty sediments are transported westwards along the coast of the Guianas and are deposited there (Wong et al., 2009 and references therein). It has been suggested that since the transcontinentalization of the Amazon during the Miocene (Figueiredo et al., 2009; Hoorn et al., 2017) this process was active during sea-level high stands whereas during sea-level lowstands the shelf was exposed and the muddy sediments from the Amazon were deposited in deeper water (Lopez, 2001; Wong et al., 2009).

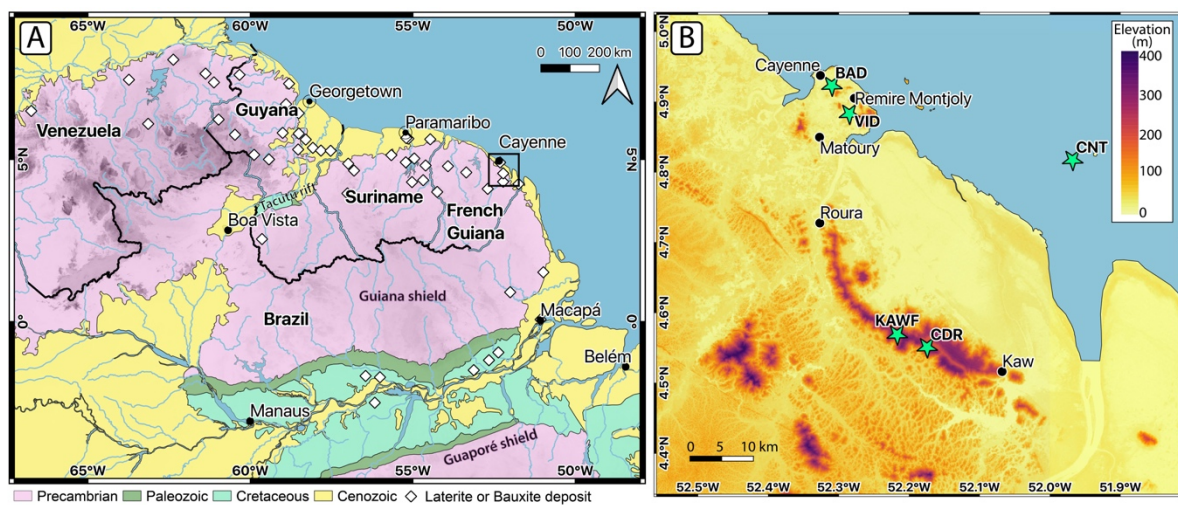


Figure VI-1: (A) Geological map of the Guyana Shield (after Gómez et al. (2019) modified according to Mendes et al. (2012) and Baker et al. (2015)) with documented laterite and bauxite deposits (white diamonds, after Bardossy and Aleva (1990)). The underlying Digital Elevation model indicates the relief (dark = high). (B) Digital Elevation model of northeastern French Guiana with sampling locations of Baduel (BAD), Vidal (VID) and Connétable (CNT)(stars). For comparison also the sampling location from Heller et al. 2022 (KAWF and CDR) are indicated.

VI.2.2 Geomorphological context

The structure of the Guiana shield is slightly domed and the Tacutu rift divides the shield into an eastern and a western domain (Fig. VI-1A). The occurrence of several planation surfaces of different elevations is one of the characteristics of the Guiana shield. The elevations of these surfaces are much higher in the western part (up to >2000 m) than in the eastern part (<1000 m). Several authors assign these planation surfaces to peneplanation events which happened

between the Cretaceous and recent times (Choubert, 1957; King, 1962; McConnell, 1968; Blancaneaux, 1981; Aleva, 1984; Bardossy and Aleva, 1990). The authors suggest that the highest paleosurfaces correspond to the oldest peneplanation events whereas the lower paleosurfaces relate to younger peneplanation events. Ages have been assigned to these surfaces, but they differ between the authors and the lack of absolute age data complicates the validation of the models (Choubert, 1957; King, 1962; McConnell, 1968; Blancaneaux, 1981; Aleva, 1984; Bardossy and Aleva, 1990).

In French Guiana the highest mountains (i.e. paleosurfaces) with elevations of up to 800 m can be found in its southern part. Towards the coast the mountains tend to be lower. Nevertheless elevations of 200-400 m can be found in close distance to the coast (<50 km, Fig. VI-1B). In the Cayenne area several more or less flat hills of 20-200 m elevation with steep slopes crop out of a generally low landscape (Fig. VI-1B).

VI.2.3 Climate

French Guiana is located in tropical latitudes north of the equator and most of the country has a tropical rainforest climate (“Af”) after the Köppen climate classification (Beck et al., 2018). In the Cayenne area mean annual rainfall is between 2600 and 3200 mm/y and mean annual temperature between 26 and 27°C with little monthly variation (< 2°C) (Groussin, 2001). French Guiana has two rainy seasons, one from May to June/July and another one in December and January. The main dry season is from July to November; from February to April rain is reduced but French Guiana lacks a second dry period (Groussin, 2001; Bovolo et al., 2012). On a regional scale, temperatures are quite constant over the Guianas, whereas precipitation shows a large variability in this region (Bovolo et al., 2012).

VI.3 Samples

Table VI-1 summarizes the studied samples and yields geographical information for the three study sites. The sites are briefly presented in the following.

VI.3.1 Baduel

Five samples were taken on a hill called Mount Baduel in the city of Cayenne (Fig. VI-1B), where a bauxitic-lateritic cover has developed on top of the high grade metamorphic rocks of the Paleoproterozoic Cayenne suite (~2.2 Ga, (Delor et al., 2003)). According to Delor et al. (2003) the basement of Mount Baduel consists of trondhjemitic rocks, whereas Vanderhaeghe

et al. (1998) propose a migmatitic gneiss which is consistent with our observations. The lateritic cover of Mount Baduel was previously studied by Girard et al. (2002) and Théveniaut and Freyssinet (1999). A lateritic profile crops out in an abandoned quarry (base of the quarry ca. 55 m a.s.l.), but due to surface erosion processes the different facies described by Théveniaut and Freyssinet (1999) were hardly visible in the quarry and some parts of the quarry (notably its top) were not accessible (Figure VI-2A and VI-2B). The top of Mount Baduel (ca. 100 m a.s.l.) was inaccessible, too and sampling and exploration of the site were hampered by religious activities occurring in the area.

One sample corresponds to the saprolite which crops out at the bottom of the quarry (BAD18-02) and four samples are lateritic duricrusts (BAD18-1B, BAD18-1C(A), BAD18-3A and BAD18-B3) (Fig. VI-2). Two massive duricrust samples were taken inside the quarry (BAD18-1B and BAD18-1C(A), in the following referred to as “quarry samples”) and two other duricrusts, a massive (BAD18-3A) and a pisolitic (BAD18-B3) one were sampled close to the top of the quarry (accessed from the other side) at slightly higher elevation of ca. 65m a.s.l (the latter two samples are here referred to as “top samples”). For detailed description of the samples see Table VI-1. Due to complicated outcrop and sampling conditions only two of the four duricrust samples could be sampled in situ (BAD18-1B and BAD18-3A). The other two duricrust samples (BAD18-1C(A) and BAD18-B3) were collected from large blocks (0.2-1 m³). We assume that the pisolitic block, from which BAD18-B3 was sampled, corresponds to the pisolitic top unit described by Theveniaut and Freyssinet (1999) (Fig. VI-2A) and rolled the hill some meters down. Note that sample BAD18-1C was splitted into a homogeneous central part (BAD18-1CA, used for the bulk analyses here) and a brecciated part (BAD18-1CB, not presented here) (see also Fig. VI-1E).

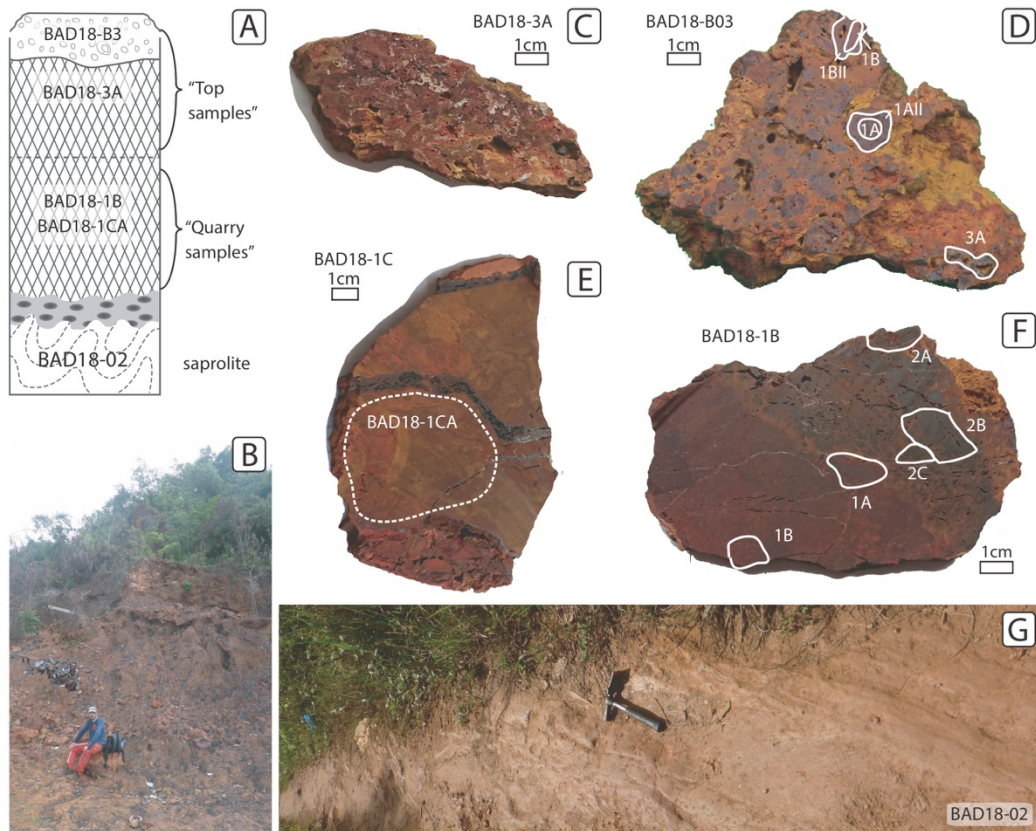


Figure VI-2: Mount Baduel field pictures and samples. (A) Schematic sketch of the profile modified after Théveniaut and Freyssinet (1999). (B) Abandoned quarry, see sitting person for scale. Samples BAD18-3A (C) and BAD18-B3 (D) were taken some meters uphill from the little tree group seen in (B). Samples BAD18-1C (E) and BAD18-1B (F) were taken in the quarry, BAD18-1C from the block serving as chair in (B) and BAD18-1B in the upper area of the quarry ca. 20m left of the shown section. (G) shows the outcropping saprolite along a path next the quarry, corresponding to its baselevel. The dashed white are in (E) indicates the sample area "1CA" used for the bulk analyses. The white areas marked in (D) and (F) indicate the separated subsamples. Note that subsample BAD18-B3_1D was separated from another slice and is not visible in (D). For picture see Fig. D-1 of the supplementary material.

VI.3.2 Vidal

The site "Lycee Vidal" (here referred to as Vidal) corresponds to a smooth hill of about 24 m elevation located on the Cayenne peninsula about 8 km southeast of the city center of Cayenne and 2 km west of the Mahoury mountain. According to Vanderhaeghe et al. (1998) the hill is composed of a Tonalite Granodiorite of the Paleoproterozoic Cayenne suite. The lateritic cover of the site has been previously studied by Girard et al. (2002) and Théveniaut and Freyssinet (2002) and is described as a ferruginous (not bauxitic) duricrust but no geochemical data is presented in the literature (Théveniaut and Freyssinet, 2002). Unfortunately, the outcrop conditions were very poor and no complete profile was visible. Two lateritic duricrust samples were taken at Vidal, unfortunately none of them in situ. Sample VID-1 (Fig. VI-3B) was at collected the surface and is very massive and extremely homogeneous. Sample VID18-1B (Fig. VI-3C) was sampled in an open construction pit (Fig. VI-3A) of about 1 m depth where

lateritic duricrust was cropping out. The sample corresponds to a dm sized block lying the in pit. For sample description see Table VI-1.

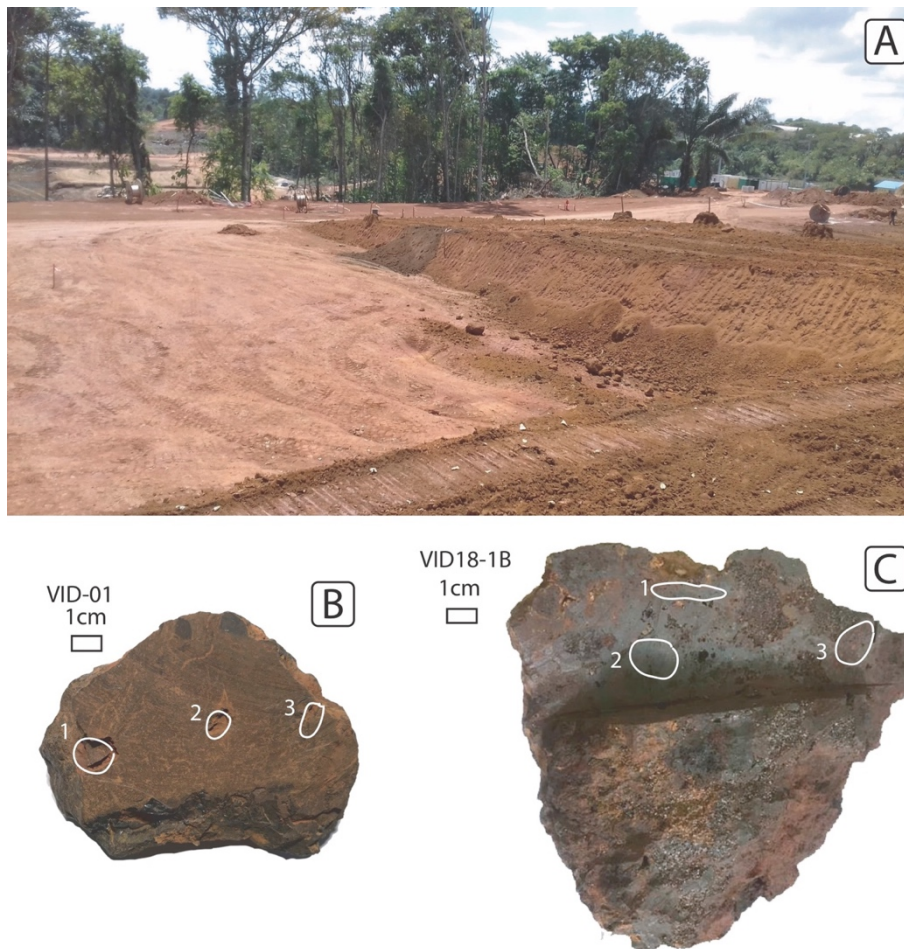


Figure VI-3: Vidal field and sample pictures. (A) Construction pit showing the rather poor outcrop conditions. (B) Sample VID-01 with separated subsamples. (C) Sample VID18-1B with separated subsamples.

VI.3.3 Connétable

The small island of “Petit Connétable” with a surface of ca. 2 ha lies in the Connétable Marine Reserve about 40 km southeast of Cayenne in the Atlantic ocean approximately 15 km northeast of the coast close to mouth of the Approuague river. The bigger island of the reserve, called “Grand Connétable” has a size of 200 x 170 m and culminates at 56 m. It is made up by a Paleoproterozoic quartzitic diorite which is crosscut by a Mesozoic dolerite dyke (Longueville et al., 2021). Above the fresh rocks a lateritic-bauxitic weathering profile developed (C. Gautheron, pers. comm.). Aluminum phosphates formed from the reaction of bird guano, infiltrated by rain from the top, with the weathering minerals. In contrast, the island of “Petit Connétable” (Figs. VI-4A and VI-4B) with a size of 2 ha and several meters of elevation is uniquely

composed of a lateritic duricrust and does not contain any vegetation. Partially the duricrust is covered by an algae film. Erosional structures linked to rain and seawater are visible. Samples GC21-01 (Fig. 4C) and GC21-03 (Fig. VI-4D) were collected in situ at the surface at two different spots of the “Petit Connétable” island. Both samples have a massive texture, are reddish to ochre brown colored and contain some greyish fine grained aggregates in cm-sized cavities (Figs. VI-4C and VI-4D).

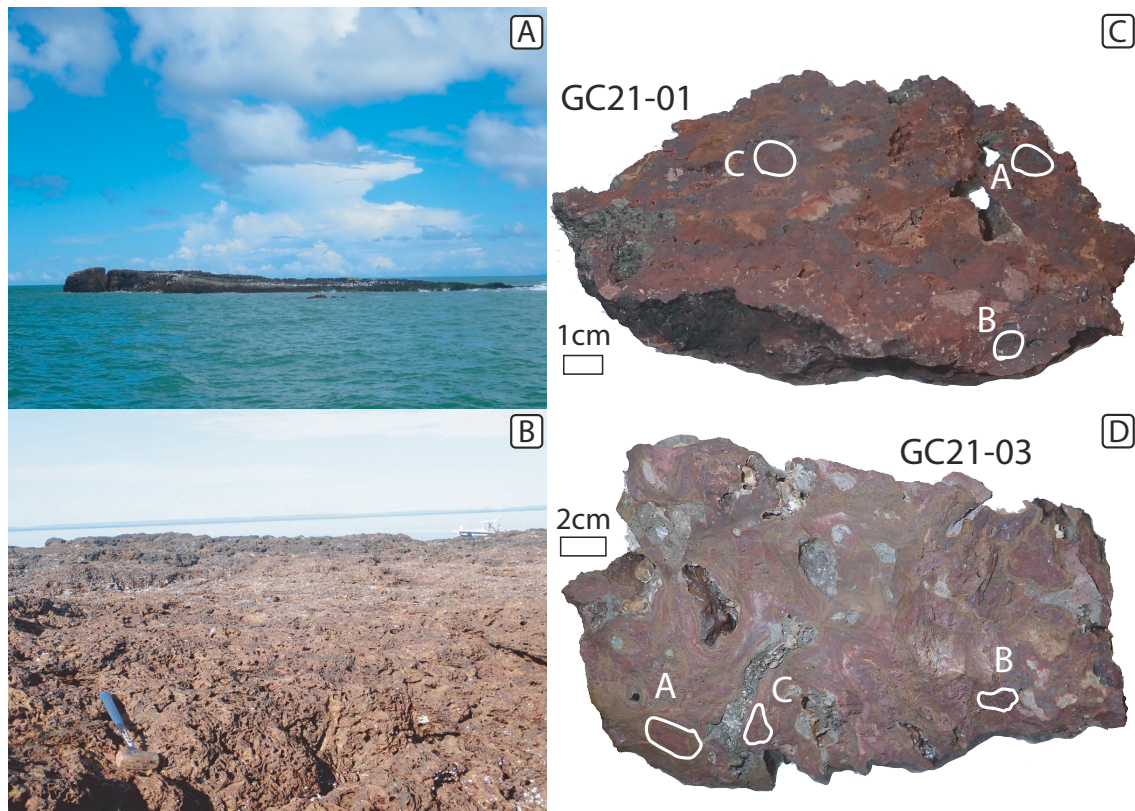


Figure VI-4: (A) Island of Petit Connetable seen from the sea. (B) lateritic duricrust on Petit Connetable island, see hammer for scale. (C) Sample GC21-01 with zones of subsamples. Subsample GC21-01_D was taken on the backside of the sampleslice. (D) Sample GC21-03 with zones of subsamples. Pictures by A. Heuret.

Table VI-1: Sample locations and description and overview of the methods applied to the samples

Site	Sample	Location	Elevation	Description	in situ?	Unit	Figure	Bulk analyses	(U-Th)/He	Subsample Mineralogy
Baduel	BAD18-02	4.9235°N / 52.3101°W	55m	saprolite with cm-thick red-white banding. Probably developed on top of a migmatite	yes	saprolite	2G	yes	no	no
	BAD18-1B	4.9233°N / 52.3097°W	ca. 60m	massive duricrust composed of ca. 10cm large "bands", one anthracite colored, the other red	yes	"quarry", ferruginous duricrust	2F	yes	yes	yes
	BAD18-1CA	4.9233°N / 52.3097°W	55m	massive duricrust with a ochre-red central part (analyzed here, 1CA), locally crosscut by foamy black veins and a more reddish brecciated part (not analyzed)	no, sampled from a ca. 1m ³ sized block in the quarry	"quarry", ferruginous duricrust	2E	yes	no	no
Baduel	BAD18-B3	4.9233°N / 52.3097°W	65m	pisolitic duricrust composed of 0.1 to 2 cm sized pisoliths of red to black colour cemented in a yellow ochre matrix	no, sampled from a 0.5x0.5x0.5 m sized rounded block	"top", bauxitic duricrust	2D	yes	yes	yes
	BAD18-3A	4.9233°N / 52.3097°W	65m	reddish to whitish, sometimes ochre colored duricrust with large pores	yes	"top", bauxitic duricrust	2C	yes	no	no
	VID-01	4.8831°N / 52.2849°W	ca. 25m	massive and very homogeneous dark brown duricrust	no, collected at surface	ferruginous duricrust ?	3B	yes	yes	no
Vidal	VID18-1B	4.8831°N / 52.2849°W	ca. 25m	blackish red duricrust with massive to pseudo-pisolitic textures with rounded reddish, sometime quartz-bearing aggregates which are cemented by a blackish coating	no, dm-sized block from bottom of an open construction pit where duricrust crops out	ferruginous duricrust ?	3C	yes	yes	some
	Connétable	4.8173°N / 51.9676°W	0-2m	massive duricrust reddish to ochre brown colored with greyish fine grained aggregates in cm-sized cavities	yes	bauxitic duricrust	4C	yes	yes	no
Connétable	GC21-03	4.8173°N / 51.9676°W	0-2m	massive duricrust reddish to ochre brown colored with greyish fine grained aggregates in cm-sized cavities	yes	bauxitic duricrust	4D	yes	yes	no

VI.4 Methods

VI.4.1 Bulk sample analyses

All samples were sawed into 1-2 cm thick slices and observed macroscopically. One slice per samples was crushed in a steel mortar and finely ground in an agate mortar or a planetary ball mill.

Powder X-ray diffraction pattern of the bulk samples were obtained as described in Heller et al. (2022). Rietveld refinement was done using the XND code (Berar and Baldinozzi, 1998) and the crystal parameters described in Heller et al. (2022) and Chapter V. Fe-Al substitution in goethite was calculated after Schulze (1984). The error given for our data includes the error of the Rietveld refinement and the error of the calibration of ± 2.6 given by Schulze (1984). The ratio hematite goethite was calculated as $RHG = \text{hematite} / (\text{hematite} + \text{goethite})$.

VI.4.2 Subsample analyses

Samples considered to be “datable” were selected for subsample preparation. Therefore, macroscopically homogeneous subsamples were separated from samples BAD18-1B, BAD18-B3, VID-1, VID-01B, GC21-01 and GC21-03 using a Dremel multi tool and named systematically (Figs. VI-2-4). The subsamples were crushed in a steel mortar and cleaned in an ultrasonic bath using milliQ water and ethanol. For mineralogical and geochronological analyses (apparently) homogeneous fragments (here referred to as grains) of 0.1 to 2mm size were selected by handpicking under a binocular microscope. The subsamples are briefly described in Table D-1 of the supplementary material. Table VI-1 indicates which methods were applied to the (sub)samples.

VI.4.2.1 Mineralogical analyses

Scanning Electron Microscopy (SEM) analyses and micro-XRD analyses were performed for most subsamples from samples BAD18-1B and BAD18-B3. Micro-XRD analyses were equally obtained for the subsamples of sample VID18-01B. Rietveld refinement was done for all micro-XRD patterns. For analytical procedures of SEM and micro-XRD analyses see Heller et al. (2022). In the future, additional SEM images and micro-XRD pattern will be obtained for all other samples to complete the dataset.

VI.4.2.2 (U-Th)/He dating

(U-Th)/He geochronological ages were obtained for all separated subsamples and from 3 to 12 aliquots were dated per subsample. Analytical procedures are described in Heller et al. (2022). He diffusion correction factors adapted to the mineralogy and alpha dose of the samples were applied as proposed in Chapters III and V. For the subsamples of sample VID-01 no micro-XRD data was available, but based on the extreme homogeneity of the bulk sample we used the bulk sample composition as base for the diffusion correction. Unfortunately for the samples from Connétable neither micro-XRD nor SEM analyses could be performed on time. As the bulk sample analyses indicate that the samples are predominantly composed of hematite, and goethite is Al-rich in GC21-03 and Al-poorer in GC21-01 (but no good fit could be obtained for goethite in that sample), we used a correction factor of 5% for the Connétable subsamples.

VI.5 Results

VI.5.1 Bulk sample mineralogy and geochemistry

VI.5.1.1 *Baduel*

Goethite (11.8 ± 3.6 to 59.1 ± 1.1 wt%), hematite (7.3 ± 4.4 to 57.2 ± 1.4 wt%), gibbsite (3.4 ± 1.4 to 48.2 ± 0.7 wt%) and rutile are present in all five samples whereas kaolinite is present only in two of the duricrust samples (the “quarry” samples BAD18-1B and BAD18-1CA) and in the saprolite sample where it composes the main mineral (70.4 ± 0.5 wt%) (Fig. VI-5B). The latter sample equally contains some quartz (3.6 ± 0.8 wt%). The Ratio Hematite-Goethite (RHG) ranges from 0.19 to 0.63. Al-substitution in goethite varies considerably between the samples from the top (21.6 ± 6.6 and 28.2 ± 4.7 mol%) and the quarry (4.9 ± 5.6 and 6.6 ± 3.5 wt%) and was not possible to calculate for the saprolite sample due to too low goethite concentrations.

The four iron duricrust samples (only two were dated) are composed primarily of Fe_2O_3 (40.3 to 77.2 wt%) and Al_2O_3 (6.2 to 34.7 wt%) and contain little SiO_2 (0.6 to 7.0 wt%), some TiO_2 (1.9 to 2.9 wt%), P_2O_5 (0.2 to 1.0 wt%), and MnO (0.02 to 0.07 wt%) whereas MgO , Na_2O , and K_2O concentrations are below the limit of detection (Fig. VI-5C). The saprolite sample BAD18-02 has a different composition with a high amount of SiO_2 (38.6 wt%) and Al_2O_3 (28.1

wt%), some Fe₂O₃ (17.7 wt%), TiO₂ (1.4 wt%), MnO (0.15 wt%), and little P₂O₅ (0.2 wt%) as well as MgO, Na₂O and K₂O concentrations below the limit of detection.

Bulk U concentrations are generally low in the Baduel dataset with concentrations between 1.4 and 2.1 ppm which are relatively similar in between the samples (Fig. VI-5D). In contrast, Th concentrations differ considerably with higher concentrations (14.6 to 17.2 ppm) in samples BAD18-B3 and -3A from the top, lower concentrations (1.0 to 1.5 ppm) in the quarry samples (BAD18-1B and -1CA) and a low to intermediate concentration in the saprolite sample (6.7 ppm) BAD18-02 (Fig. VI-5D). Note that the saprolite sample has a high Zr concentration (754 ppm) compared to the duricrust samples (149 to 333 ppm) and the mean of the upper continental crust (193 ppm) (Rudnick and Gao, 2013) (Fig. VI-5D). The compositional differences between the samples from the top, the quarry and the saprolite are also visible in the rare earth element (REE) pattern (Fig. VI-6) where the top samples (BAD18-B3 and -3A) show rather flat pattern with a slight relative depletion in the middle REEs (Eu to Dy) whereas the quarry and the saprolite samples show an enrichment in the heavy REE (Gd to Lu) and, in the case of BAD18-02 and BAD18-1CA, a depletion in light REE (La to Eu). Samples BAD18-1B and -02 show pronounced positive Ce anomalies whereas BAD18-1CA shows a slight negative anomaly.

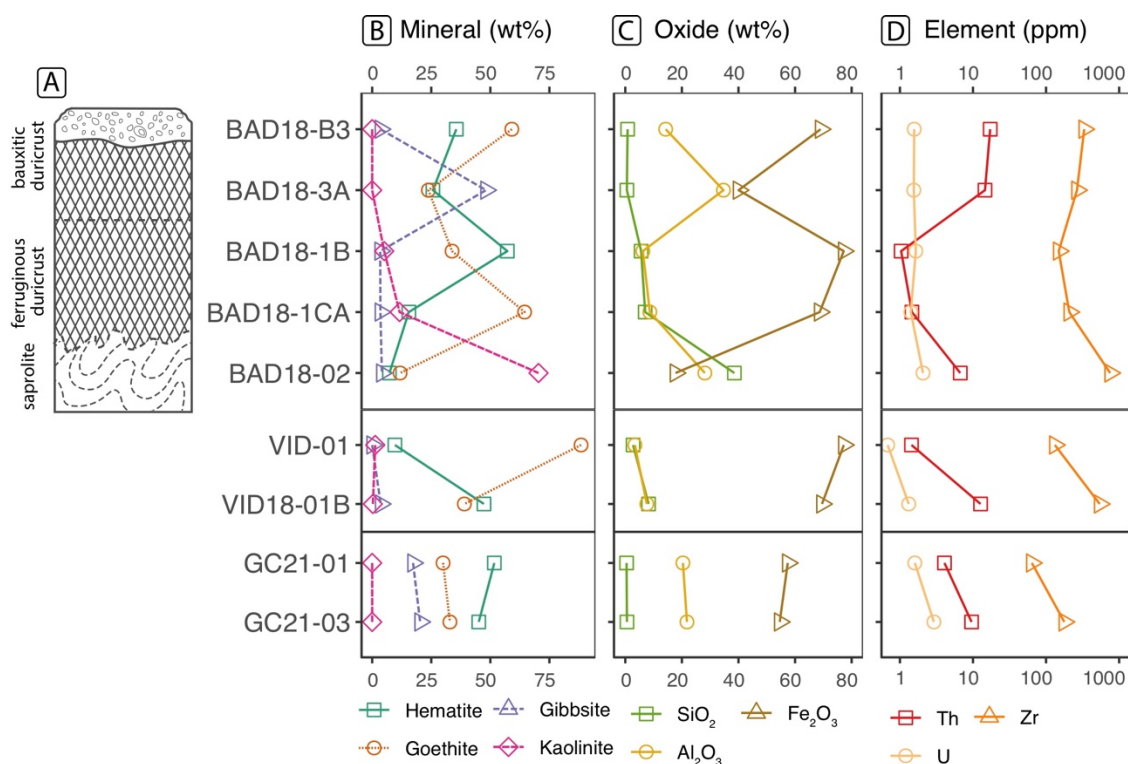


Figure VI-5: Bulk mineralogy and geochemistry of the analyzed samples. (A) Schematic profile of the lateritic cover of Mount Baduel, reinterpreted and adapted from Théveniaut and Freyssinet (1999). (B) Mineralogical composition of all samples, for data see Table VI-2. The Baduel samples correspond to the units of the profile in A at same vertical position. (C) Major element composition for the three most important oxides. (D) Concentrations of selected trace elements. For chemical data see Table VI-2.

VI.5.1.2 Vidal

The two samples from the Vidal site have slightly different compositions. VID-01 is predominantly composed of goethite (88.4 ± 0.3 wt%), some hematite (9.6 ± 0.9 wt%) and small amounts of kaolinite, anatase, rutile and quartz (see Fig. VI-5B and Table VI-1). In contrast, VID18-1B contains similar amounts of hematite (47.3 ± 1.3 wt%) and goethite (39.0 ± 1.8 wt%), some quartz (8.0 ± 0.3 wt%) and small amounts of gibbsite, anatase and kaolinite (Fig. VI-5B). The goethite of both samples has low Al-substitution (4.9 to 7.4 mol%). The major element composition reflects with mineralogy with high Fe₂O₃ contents (69.5 to 77.2 wt%) low Al₂O₃ (6.2 to 8.7 wt%) and SiO₂ (2.7 to 8.2 wt%) contents similar to the quarry samples from Baduel (Fig. VI-5C). For other major element data see Table VI-2. As in the Baduel samples, U concentrations are low (0.7 and 1.3 ppm) and Th concentrations lie at 1.4 and 12.7 ppm for VID-01 and VID18-1B, respectively (Fig. VI-5D). VID18-1B has the highest Zr concentration of the duricrust samples in this study (542 ppm). The REE pattern presented in Figure VI-6 show very different shapes for the two samples with VID-01 showing a depletion in LREE and an enrichment in HREE and VID18-1B presenting a rather flat pattern with a slight depletion in HREE relative to the LREE.

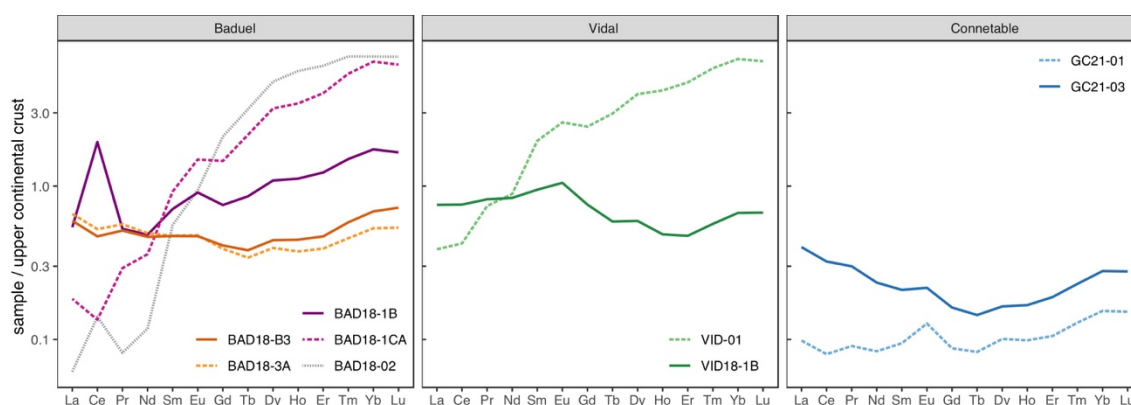


Figure VI-6: Rare earth element patterns of the analyzed samples from Baduel, Vidal and Petit Connétable normalized for the upper continental crust (Rudnick and Gao, 2013). Line colors correspond to the samples. For Baduel samples solid lines are dated samples and dashed lines correspond to samples analyzed only by bulk methods, for Vidal and Connétable this is only for better visibility.

VI.5.1.3 Connétable

The two samples from Connétable have a very similar bulk mineralogy composed mainly of hematite (45.1 ± 1.2 and 51.7 ± 0.9 wt%), goethite (30.0 ± 4.1 and 32.9 ± 1.8 wt%) and gibbsite (17.3 ± 0.7 and 20.3 ± 0.5 wt%) (Fig. VI-5B). Small amounts of anatase, boehmite and rutile are present (Table VI-1) whereas kaolinite and quartz were not detected in these samples. Al-substitution in goethite is 17.3 ± 5.0 mol% for sample GC21-03 and 7.4 ± 8.0 mol% for GC21-01 but note that Rietveld refinement of goethite presented some problems in GC21-01 and the real error of the goethite Al-substitution might be even greater. As for the samples from the top of Mount Baduel and indicated by the mineralogical composition, Fe_2O_3 (54.5 and 57.4 wt%) and Al_2O_3 (20.4 and 21.8 wt%) are the main components of the Connétable samples whereas SiO_2 contents are very low (0.4 and 0.6 wt%) (Fig. VI-5C). TiO_2 contents (3.3 and 4.8 wt%) are higher than in the other samples of the dataset whereas P_2O_5 and MnO contents are similar to the other samples (Table VI-2). The two samples from Connétable are the only ones of the dataset containing measureable amounts of MgO (0.15 and 0.79 wt%) and Na_2O (0.14 and 0.18 wt%). U (1.6-2.9 ppm) and Th (4.0-9.6 ppm) concentrations lie in the same range as those of the other samples (Figs. VI-5D and -5E). The REE pattern presented in Figure VI-6 show relatively flat REE pattern similar to the samples from the top of Baduel but with lower absolute concentrations (especially GC21-01). GC21-03 shows some depletion in MREE.

French Guiana laterite and bauxite evolution through time and space

Table VI-2: Mineralogical and geochemical composition of the bulk samples.

		BAD18-02	BAD18-1B	BAD18-1CA	BAD18-3A	BAD18-B3	VID-01	VID18-01B	GC21-01	GC21-03
Hematite	wt%	7.3	57.2	15.5	25.7	35.6	9.6	47.3	51.7	45.1
abs. error	wt%	4.4	1.4	1.7	2.4	1.3	0.9	1.3	0.9	1.2
Goethite	wt%	11.8	33.8	64.5	23.8	59.1	88.4	39.0	30.0	32.9
abs. error	wt%	3.6	2.2	0.9	2.7	1.1	0.3	1.8	4.1	1.8
Gibbsite	wt%	4.1	3.4	3.5	48.2	3.5	bld	3.6	17.3	20.3
abs. error	wt%	1.5	1.4	1.7	0.6	0.3	0.4	0.8	0.7	0.5
Anatase	wt%	2.7	0.5	5.0	2.4	1.8	0.3	1.8	0.7	1.1
abs. error	wt%	1.3	0.4	0.4	0.4	0.3	0.3	0.3	0.3	0.3
Kaolinite	wt%	70.4	5.1	11.6	bld	bld	1.3	0.3	bld	bld
abs. error	wt%	0.5	1.3	1.6	bld	bld	0.7	0.5	bld	bld
Rutile	wt%	bld	bld	bld	bld	bld	0.1	bld	bld	0.3
abs. error	wt%	bld	bld	bld	bld	bld	0.2	bld	bld	0.3
Boehmite	wt%	bld	bld	bld	bld	bld	bld	bld	0.3	0.3
abs. error	wt%	bld	bld	bld	bld	bld	bld	bld	0.3	0.2
Quartz	wt%	3.6	bld	bld	bld	bld	0.2	8.0	bld	bld
abs. error	wt%	0.8	bld	bld	bld	bld	0.2	0.3	bld	bld
RHG¹		0.38	0.63	0.19	0.52	0.38	0.10	0.55	0.63	0.58
abs. error		0.22	0.02	0.02	0.05	0.01	0.01	0.02	0.04	0.02
Goethite Al-substitution	mol%	22.7	4.9	6.6	21.6	28.2	7.4	4.9	7.4	17.2
abs. error (total)	mol%	20.2	5.6	3.5	6.6	4.7	5.1	5.5	8.0	5.0
abs. error (refinement)	mol%	17.6	3.0	0.9	4.0	2.1	2.5	2.9	5.4	2.4
Hematite Al-substitution	mol%	bld	5.4	8.2	5.5	12.8	bld	5.4	3.1	7.4
abs. error	mol%	bld	2.6	3.1	3.7	2.5	bld	2.4	1.2	1.9
R_{wp} value²		0.075	0.016	0.014	0.033	0.014	0.011	0.019	0.018	0.017
Fe₂O₃	wt%	17.7	77.2	68.7	40.0	69.0	77.2	69.5	57.4	54.6
Al₂O₃	wt%	28.1	6.2	8.7	34.7	14.3	3.4	7.6	20.4	21.8
SiO₂	wt%	38.6	5.6	7.0	0.6	0.8	2.7	8.2	0.4	0.6
TiO₂	wt%	1.42	1.87	2.87	2.23	1.94	0.98	3.87	4.81	3.33
P₂O₅	wt%	0.18	0.95	0.90	0.21	0.43	1.90	0.58	0.35	0.44
MnO	wt%	0.15	0.07	0.03	0.03	0.02	0.04	0.07	0.10	0.05
MgO	wt%	bld	bld	bld	bld	bld	bld	bld	0.15	0.79
CaO	wt%	bld	bld	bld	bld	bld	bld	bld	0.60	0.50
Na₂O	wt%	bld	bld	bld	bld	bld	bld	bld	0.14	0.18
K₂O	wt%	0.05	bld	bld	bld	bld	bld	bld	bld	bld
LOI³	wt%	12.8	8.2	11.8	22.4	13.8	13.6	9.3	14.5	17.3
U	ppm	2.1	1.7	1.4	1.6	1.6	0.7	1.3	1.6	2.9
Th	ppm	6.7	1.0	1.5	14.6	17.2	1.4	12.7	4.1	9.6
Zr	ppm	754	149	208	265	333	132	542	64	178

RHG¹: ratio hematite goethite; R_{wp}-value²: indicator of the goodness of fit, for details see Toby (2016) ; LOI³: loss of ignition

VI.5.2 Subsample mineralogy

VI.5.2.1 Baduel

Grains from all subsamples of samples BAD18-1B and -B3 were observed by SEM and nearly all subsamples were investigated by micro-XRD. Representative grains and textures of

the analyzed hematite and goethite subsamples are presented in Figure VI-7, results of the micro-XRD are presented in Table VI-3 and integrated in Figure VI-12.

VI.5.2.1.1 Sample BAD18-1B

The subsamples of sample BAD18-1B are predominantly composed of very pure hematite and goethite. Figures VI-7A-7C show typical hematite grains and textures of subsample BAD18-1B_1AM (Figs. VI-7A and VI-7B) and BAD18-1B_1AB (Fig. VI-7C). BAD18-1B_1AM is composed of very pure hematite with some pores but nearly no inclusions (Figs. 7A). Mounted grains show often small holes with shapes typical for kaolinite booklets (Fig. VI-7B). These “kaolinite phantoms” or “kaolinite dissolution features” have sizes of ca. 2-10 μm . The micro-XRD pattern obtained on one grain of this subsamples indicates nearly pure hematite (96.4 wt%) poor in Al (ca. 1.7 mol% substitution) and the presence of minor amounts of goethite (3.6 wt %). Interestingly subsample BAD18-1B_1B contains considerable amounts of kaolinite, Rietveld refinement indicates a composition of 82.6 ± 0.2 wt% Al-poor hematite (0% Al-substitution) and 17.3 ± 0.6 wt% kaolinite. SEM images show intact kaolinites but no kaolinite dissolution features (Fig. VI-7C). Some bigger pores in this subsample are mineralized with kaolinite. Intact kaolinite booklets in BAD18-1B_1B have a size of ca. 2-10 μm , thus approximately the same as the kaolinite phantoms in BAD18-1B_1AM. Furthermore subsample BAD18-1B_1B shows some empty pores (in our case filled with epoxy) with shapes reminding angular mineral inclusions (Fig. VI-7C). Subsample BAD18-1B_1AV (not presented) is composed of mainly botryoidal dense and pure hematite (78.6 ± 0.4 wt%) sometimes mixed with botryoidal goethite (21.3 ± 0.6 wt%), both phases lack any Al-substitution.

The three analyzed goethite subsamples of sample BAD18-1B (i.e. BAD18-1B_2A, BAD18-1B_2B, and BAD18-1B_2A) resemble each other a lot. They are very dense and homogeneous and generally inclusion free (Figs. VI-7D and VI-7E). Some grains show botryoidal growth features (not shown here) but are as homogeneous as the massive grains. Occasionally kaolinite dissolution features occur in the goethite (Fig. VI-7F). μXRD and Rietveld refinement of two grains indicate pure goethite (99.8 and 100 wt%) with little Al-substitution (0.8 and 1.7 mol%).

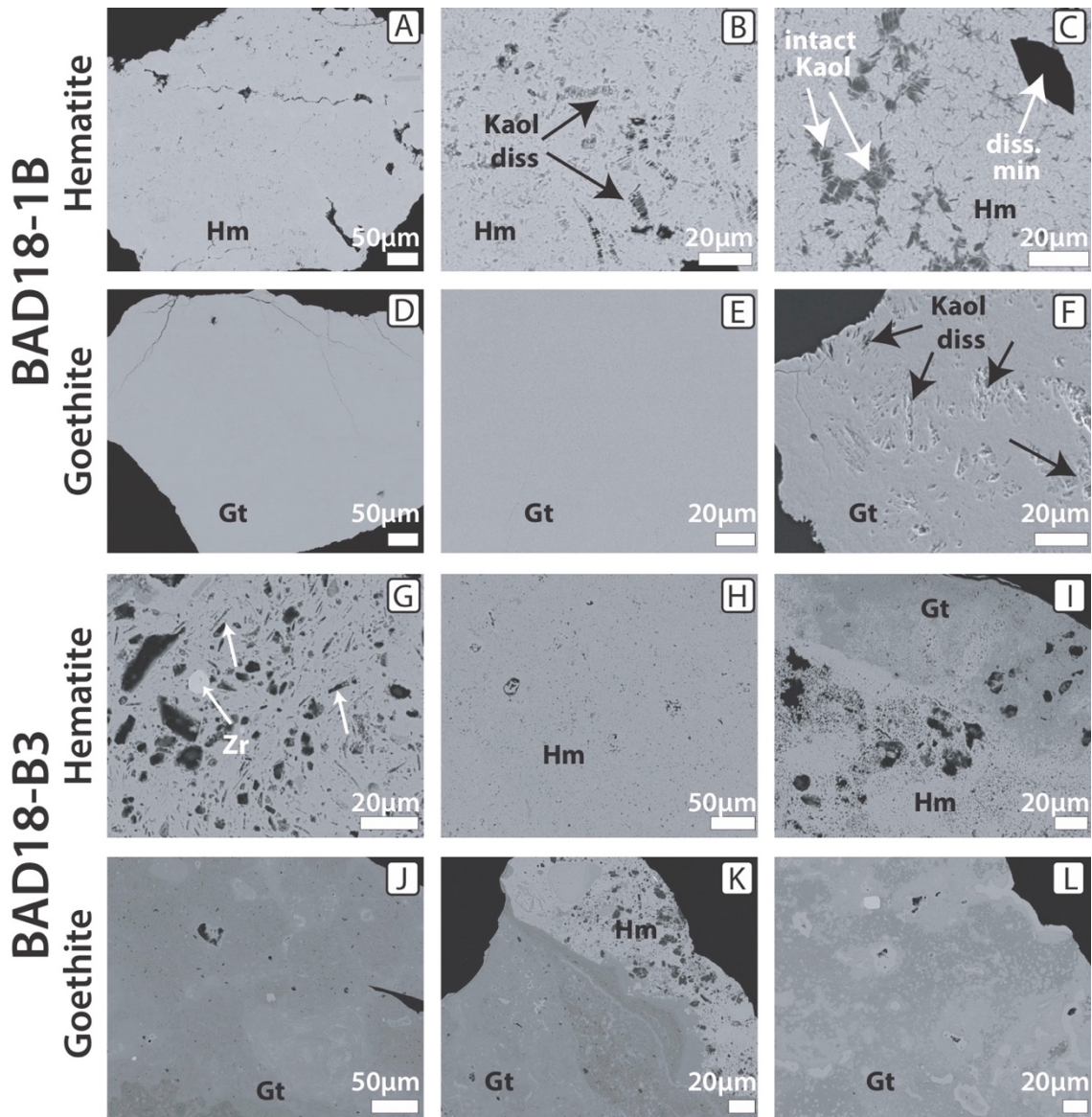


Figure VI-7: Backscattered Electron images obtained by Scanning Electron Microscopy (SEM) of hematite (Hm) and goethite (Gt) grains from Mount Baduel. (A) Dense and homogeneous hematite (BAD18-1B_1AM). (B) Zoom of (A) showing small kaolinite dissolution features inside the hematite (BAD18-1B_1AM). (C) Hematite containing intact kaolinite booklets as well as angular pores (black) indicating dissolution of primary minerals. (D) Typical goethite grain from sample BAD18-1B (BAD18-1B_2B). (E) Zoom of (D) showing the extreme homogeneity and purity of the goethite grains (BAD18-1B_2B). (F) Locally kaolinite dissolution features exist in the dense goethite grains of BAD18-1B (BAD18-1B_2C, secondary electron image). (G) Hematite of subsample BAD18-B3_1A containing numerous pores with shapes resembling primary mineral grains. Some pores (2 unnamed white arrows) are probably due to kaolinite dissolution. Zircon inclusions (Zr) are common in this subsample (BAD18-B3_1A). (H) Homogeneous hematite with small pores, typical for subsamples BAD18-B3_1B(II) and -1D (BAD18-B3_1B). (I) Hematite (Hm) showing locally hydration into goethite (Gt) (BAD18-B3_1D). (J) Al-rich goethite containing some small inclusions (BAD18-B3_3A). (K) Goethite grain with some heterogeneous hematite attached to it (BAD18-B3_3A). (L) Goethite grain showing different generations of goethite indicating multiple processes of precipitation (BAD18-B3_3A).

VI.5.2.1.1 Sample BAD18-B3

The subsamples of BAD18-B3 show very different features from sample BAD18-1B. The hematite subsamples can be split in two groups. Subsamples BAD18-B3_1A and BAD18-B3_1AII (deriving from the same pisolith) are very porous and heterogeneous (Fig. VI-7G). Many pores have angular shapes reminding dissolved mineral inclusions. Pores in shape of kaolinite

booklets are also common (Fig. VI-7G). Zircon inclusions are very common in this subsample (Fig. VI-7G). Although many of them are rather small (<10 μm) some zircon inclusions reach sizes up to 26 μm along the c-axis. Large anatase inclusions (up to 70 μm) were also observed in these subsamples. Micro-XRD and Rietveld refinement of one grain of subsample BAD18-B3_1A indicate predominance of hematite (88 wt%) containing some Al-substitution (ca. 5 mol%) with some goethite (11%) and small amounts of gibbsite and anatase (Table VI-3).

In contrast, subsamples BAD18-B3_1B, BAD18-B3_1BII and BAD18-B3_1D show overall very homogeneous textures (Fig. VI-7H). These hematite subsamples have generally a very fine porosity, bigger pores are sometimes present (Fig. VI-7I). Small (<10 μm) zircon and anatase inclusions occur occasionally. Some areas show transformation into goethite indicated by darker tones of gray (Fig. VI-7I). Only one grain of BAD18-B3_1D was analyzed by micro-XRD yielding a composition of 74.8 wt% hematite (containing ca. 2.7 mol% Al-substitution), 24.3 wt% goethite (with 16.7 mol% Al-substitution) and 0.9 wt% anatase.

Late stage goethite cementing hematite pisoliths is represented by subsample BAD18-B3_3A. Under the microscopy black and brownish grains were observed. Figures VI-6J to -6L show pictures of black goethite grains. The goethite is very fine grained, contains small pores and some small inclusions, sometimes composed of zircon (Fig. VI-7J). Occasionally pieces of hematite are attached to the goethite grains (Fig. VI-7K). Different shades of gray visible in many grains (Fig. VI-7L but also VI-7J and VI-7K) indicate the presence of different generations or types of goethite inside the grains and eventual mixture with fine grained gibbsite. Two grains of black goethite and one grain of brownish goethite were analyzed by micro-XRD. All three grains are composed predominantly of goethite (≥ 90 wt%) contain some gibbsite (4.0 to 4.7 wt%) and some anatase (0.7 – 2 wt%). Two grains contain some hematite (3.2-3.9 wt%). The goethite is extremely Al-rich with 24-25 mol% Al-substitution in the black goethite grains and 29 mol% Al substitution in the brown goethite grain.

Table VI-3: Results of the Rietveld refinement of the micro-XRD analyses.

Bulk sample	BAD18-1B	BAD18-1B	BAD18-1B	BAD18-1B	BAD18-1B	BAD18-B3	BAD18-B3	BAD18-B3	BAD18-B3	BAD18-B3	BAD18-B3	BAD18-B3	VID18-1B	VID18-1B	VID18-1B	VID18-1B
micro-XRD aliquot	B1B1AM_XRD1	B1B1AV_XRD1	B1B1B_XRD1	B1B2A_XRD1	B1B2C_XRD1	B31A_XRD1	B31D_XRD1	B33A_XRD1 ³	B33A_XRD2 ³	B33A_XRD1 ⁴	B33Abro_XRD1 ⁴	B33A_XRD1 ³	V1B1_XRD1	V1B3_XRD1	V1B3_XRD1	V1B3_XRD1
Subsample	BAD18-1B_1AM	BAD18-1B_1AV	BAD18-1B_1B	BAD18-1B_2A	BAD18-1B_2C	BAD18-B3_1A	BAD18-B3_1D	BAD18-B3_3A	BAD18-B3_3A	BAD18-B3_3A	BAD18-B3_3A	BAD18-B3_3A	VID18-1B_1	VID18-1B_1	VID18-1B_1	VID18-1B_3
Hematite	96.4	78.6	82.6	bid	0.2	88.1	74.8	bid	3.2	3.9	43.4	bid	43.4	bid	93.7	93.7
abs. error	0.1	0.4	0.2	bid	0.2	0.3	0.6	bid	0.3	0.2	0.8	bid	0.8	bid	0.1	0.1
Goethite	3.6	21.3	bid	100.0	99.8	10.7	24.3	95.2	90.4	90.0	55.3	95.2	55.3	90.0	5.6	5.6
abs. error	0.9	0.6	bid	bid	0.0	1.0	0.2	0.1	0.1	0.1	1.0	0.1	1.0	0.1	0.5	0.5
Gibbsite	bid	bid	bid	bid	bid	0.2	bid	4.0	4.4	4.7	bid	4.0	bid	4.7	bid	bid
abs. error	bid	bid	bid	bid	bid	0.7	bid	0.7	0.3	0.2	bid	0.7	bid	0.2	bid	bid
Anatase	bid	bid	0.1	bid	bid	1.1	0.9	0.7	2.0	1.5	1.3	0.7	1.3	1.5	0.6	0.6
abs. error	bid	bid	0.2	bid	bid	0.4	0.4	0.1	0.3	0.3	0.2	0.1	0.2	0.3	0.3	0.3
Kaolinite	bid	bid	17.3	bid	bid	bid	bid	bid	bid	bid	bid	bid	bid	bid	bid	bid
abs. error	bid	bid	0.6	bid	bid	bid	bid	bid	bid	bid	bid	bid	bid	bid	bid	bid
Rutile	bid	bid	bid	bid	bid	bid	bid	bid	bid	bid	bid	bid	bid	bid	bid	bid
abs. error	bid	bid	bid	bid	bid	bid	bid	bid	bid	bid	bid	bid	bid	bid	bid	bid
Quartz	bid	bid	bid	bid	bid	bid	bid	bid	bid	bid	bid	bid	bid	bid	bid	bid
abs. error	bid	bid	bid	bid	bid	bid	bid	bid	bid	bid	bid	bid	bid	bid	bid	bid
RHG ¹	0.96	0.79	1.00	0.00	0.00	0.89	0.75	0.00	0.03	0.04	0.44	0.00	0.44	0.04	0.94	0.94
abs. error	0.01	0.01	0.00	0.00	0.00	0.01	0.00	0.00	0.00	0.00	0.01	0.00	0.01	0.00	0.00	0.00
Goethite Al-substitution	bid	bid	bid	0.8	2.4	8.2	16.7	24.2	24.8	29.1	15.6	24.2	15.6	29.1	7.6	7.6
abs. error total	bid	bid	bid	2.9	3.1	6.2	7.2	3.5	3.0	2.9	3.5	3.5	3.5	2.9	9.8	9.8
abs. error refinement	bid	0.3	bid	0.3	0.5	3.6	4.6	0.9	0.4	0.3	0.9	0.9	0.9	0.3	7.2	7.2
Gt c-parameter	bid	3.0262	bid	3.0230	3.0203	3.0101	2.9952	2.9822	2.9811	2.9737	2.9972	2.9822	2.9972	2.9737	3.0112	3.0112
Hematite Al-substitution	1.7	bid	bid	bid	bid	4.7	2.7	bid	bid	18.1	7.7	bid	7.7	18.1	8.5	8.5
abs. error	0.6	bid	bid	bid	bid	0.7	1.3	bid	bid	2.9	0.7	bid	0.7	2.9	0.6	0.6
Ht a-parameter	5.0385	5.0422	5.0408	bid	bid	5.0349	5.0373	bid	bid	5.0184	5.0311	bid	5.0311	5.0184	5.0302	5.0302
R _{wp} value ²	0.0419	0.0429	0.0322	0.0338	0.0432	0.0565	0.0543	0.0432	0.0358	0.0306	0.0411	0.0432	0.0411	0.0306	0.0457	0.0457

RHG¹: ratio hematite goethite; R_{wp}-value²: indicator of the goodness of fit, for details see Toby (2016); ³: black grain; ⁴: brown grain

VI.5.2.2 Vidal

For sample VID18-1B one grain of each of the three subsamples was analyzed by micro-XRD but only two of them (VID18-1B_1 and VID18-1B_3) could be refined successfully by Rietveld refinement. The results, presented in Table VI-3, indicate a mixture of Al-rich hematite (43.4 wt% with 7.8 mol% Al-substitution) and Al-rich goethite (55.3 wt% with 15.6 mol% Al substitution) for VID18-1B_1 and rather pure hematite (93.7 wt%) rich in Al (ca. 8.5 mol%) with some goethite (5.6 wt%) for VID18-1B_3 and. Both grains contain some anatase and neither gibbsite nor kaolinite. The Rietveld refinement of VID18-1B_2 did not yield a satisfying fit but a composition of ca. 80 wt% hematite and 20 wt% goethite could be estimated.

SEM images of the Vidal samples and mineralogical analyses (SEM and micro-XRD) of Connétable samples could not be obtained on time but are planned for the near future.

VI.5.3 Geochronological results

120 (U-Th)/He ages were obtained successfully. The obtained ages range from 48.4 ± 4.8 Ma to <0.8 Ma. The results are presented in Table VI-3 and Figures VI-8 to VI-12. One outlying age, aliquot VID11A, with an age of 48.4 considered to be an outlier (see Section VI.5.3.2 for details) is not presented in Figure VI-8 and other figures including age data and was excluded from the interpretation. U concentrations are generally low in the dataset with concentrations between 0.2 and 5.9 ppm (median = 0.76 ppm) (Fig. VI-8B). Th concentrations cover a larger range with concentrations from below the limit of detection to 36.1 ppm (median = 5.4 ppm) (Fig. VI-8C). Sm concentrations range from below the limit of detection to 17.3 ppm (median = 1.94 ppm) (Fig. VI-8D).

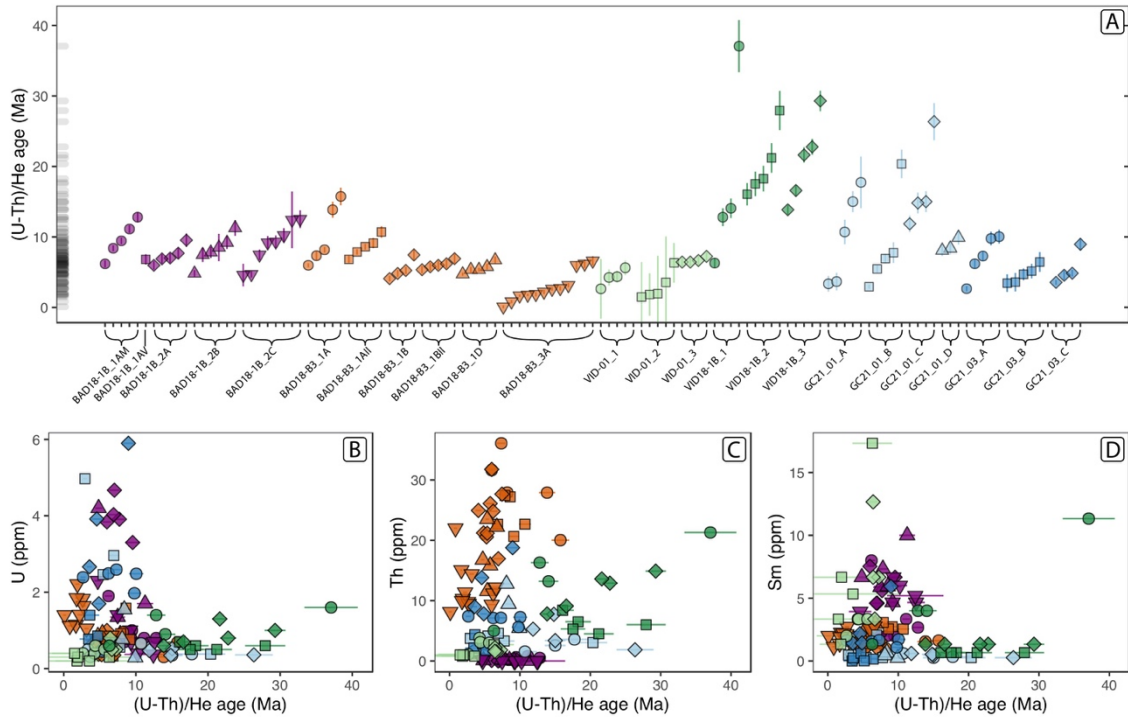


Figure VI-8: (U-Th)/He ages of supergene hematite and goethite obtained in this study. (A) Ranked order plot of all age data. Colors are specific for sites and samples, shapes correspond to subsamples. (B), (C) and (D) show the (U-Th)/He ages versus the concentrations of U, Th and Sm, respectively. Colors and shapes are as in (A).

VI.5.3.1 Baduel

61 ages ranging from 15.8 ± 1.3 Ma to <0.8 Ma were obtained for the two selected duricrust samples from Mount Baduel. The data is presented in more detail in Figure VI-9. The two samples, which show important differences regarding their mineralogy and geochemistry (see above) yield generally similar geochronological results. The age range covered by sample BAD18-1B is smaller with ages ranging from 12.8 ± 0.7 Ma to 4.6 ± 1.6 Ma. All subsamples of this sample show a considerable age spread which exceeds analytical uncertainty (Fig. VI-8A). The data shows a twofold negative correlation with U (pink datapoints in Fig. VI-9A). Th concentrations are extremely low in this sample ($\text{Th} < 1$ ppm in all but two aliquots) whereas Sm concentrations are higher with concentrations between 2 and 10 ppm (Figs. VI-9B and VI-9C). Both elements are uncorrelated with the ages.

In contrast to BAD18-1B, sample BAD18-B3 contains several subsamples yielding more reproducible results, notably BAD18-B3_1B(II) and BAD18-B3_1D. In these subsamples 8 out of 14 aliquots yield ages between 5.3 ± 0.5 and 6.2 ± 0.6 Ma whereas the other aliquots are slightly older or younger with ages between 4.1 ± 0.4 and 7.5 ± 0.7 Ma (Fig. VI-8A). BAD18-B3_1D shows a significant correlation with the Th/U ratio ($R^2 = 0.97$, $p\text{-value} = 0.003$, not plotted here),

whereas the (slight) age spread in subsamples BAD18-B3_1B (II) does not show any correlation with U, Th, Th/U or Sm. In subsample BAD18-B3_3A 7 of the 12 dated aliquots yield very similar results between 3.2 ± 0.3 and 1.7 ± 0.2 Ma whereas 3 aliquots yield ages (and U concentrations) similar to the other subsamples of this sample with ages of 6.6 ± 0.7 to 6.0 ± 0.6 Ma and two aliquots yield ages <0.9 Ma (Figs VI-8A and VI-9). Subsamples BAD18-B3_1A and BAD18-B3_1A(II) yield generally higher and more spread ages between 6.0 ± 0.5 and 15.8 ± 1.3 Ma. While the subsample BAD18-B3_1A shows a slight negative correlation with Th concentration ($R^2 = 0.66$, p-value= 0.09), no other correlation with U, Th or Sm was observed for these two subsamples.

Comparison of the age data with the mineralogical data shows that ages between 16 and 4 Ma are acquired on both hematite and goethite, whereas all ages <4 Ma correspond to goethite (Fig. VI-10A). Th concentrations are generally higher in hematite (Fig. VI-10B). Al-substitution in goethite shows a positive correlation with Th and increases towards younger ages (Figs. VI-10D and VI-10C).

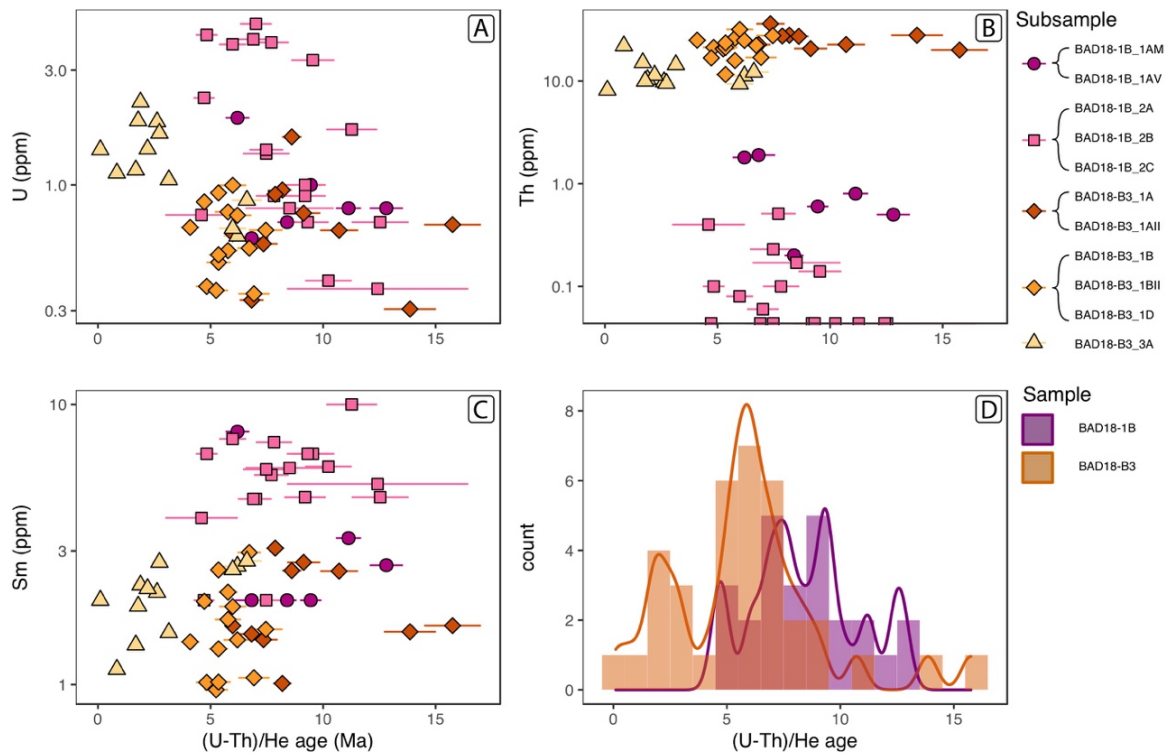


Figure VI-9: (U-Th)/He ages from Baduel versus U (A), Th (B), and Sm (C) concentrations. Colors and shapes correspond to subsamples which were grouped if they resemble a lot. (D) shows a histogram and a Kernel density plot for the two analyzed samples.

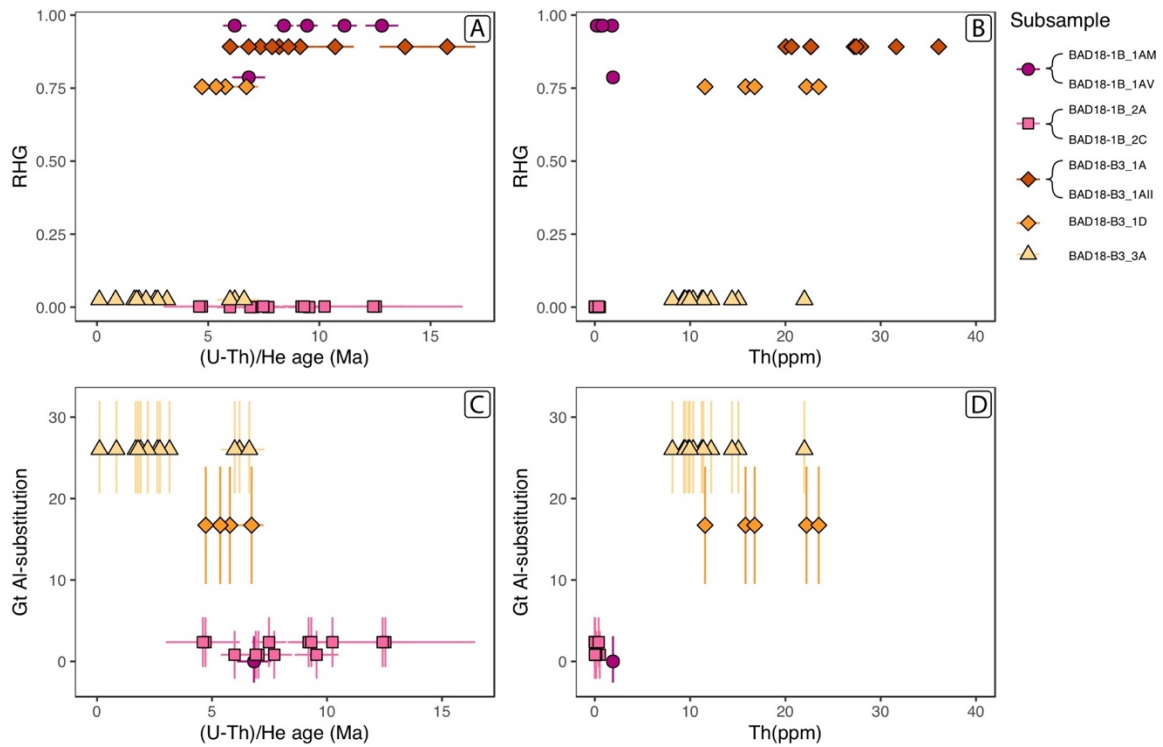


Figure VI-10: (U-Th)/He ages and Th concentrations from Mont Baduel versus the Ratio Hematite-Goethite (RHG) and Al-substitution in goethite obtained from micro-XRD pattern. Note that not for all subsamples micro-XRD pattern were obtained. For subsample BAD18-B3_3A three μ XRD pattern were obtained and mean values are presented. Similar subsamples are grouped together. Note that subsample BAD18-B3_1D is composed primarily of hematite (see D) and the Al-substitution value corresponds only to 25% goethite contained in this subsample.

VI.5.3.2 Vidal

The 28 ages of the Vidal site range from 48.4 ± 4.8 Ma to 1.5 ± 5.0 Ma and show very different results for the two samples. The results are presented in detail in Fig. VI-12. Sample VID-01 yields overall ages between 7.2 ± 0.72 and 1.5 ± 5.0 Ma, but one aliquot, VID11A, yields an age of 48.4 ± 4.8 Ma at similar U and Th concentrations and is therefore considered an outlier and excluded from the interpretation. All aliquots with ages <4.2 Ma (including all aliquots of subsample VID-01_2) have very large errors, mainly related to extremely low ^4He concentrations. Intra-subsample ages overlap with in error in the three subsamples. Regarding only the ages with relative errors $<100\%$ the ages range from 4.3 ± 1.2 to 7.2 ± 0.72 Ma with tendentially older ages in subsample VID-01_3 (median = 6.6 Ma) than VID-01_1 (median = 4.4 Ma). The well constrained ages (relative error $<100\%$) show a negative correlation with the Th concentration ($R^2 = 0.76$, p-value= 0.005, Fig. VI-10B).

Sample VID18-1B yield ages from 37.1 ± 3.7 Ma to 6.3 ± 0.7 Ma but most ages (12 out of 14) lie between 29.3 ± 1.5 Ma and 12.8 ± 1.3 Ma. The ages show a considerable spread and overlap only partly within error inside the three subsamples (Fig. VI-8A). Subsample VID18-1B_3 shows a positive correlation of age with Th concentration ($R^2 = 0.90$, p-value= 0.014, Fig.

VI-11B), and a tendency towards lower U concentrations at younger ages ($R^2 = 0.63$, p-value= 0.2, i.e. not significant) (Fig. VI-10A). While subsamples VID18-1B_3 shows similar (though insignificant) tendencies this is not the case for VID18-1B_1. VID18-1B_2 and VID18-1B_3, composed predominantly of hematite, yield generally higher ages than VID18-1B_1, which is composed primarily of goethite.

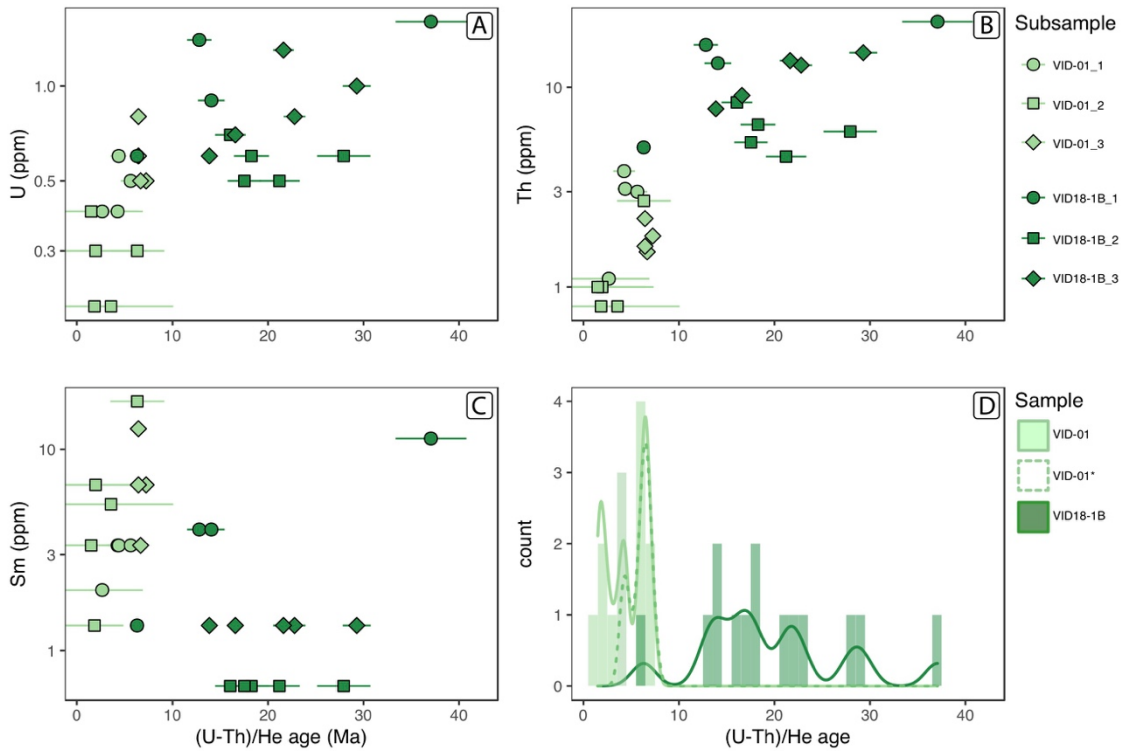


Figure VI-11: (U-Th)/He ages from Vidal versus U (A), Th (B), and Sm (C) concentrations. Colors correspond to samples and shapes to subsamples. (D) shows a histogram and a Kernel density plot for the two analyzed samples. The dashed line in (D) represents a Kernel Density plot when only ages with an error of <100% are considered.

VI.5.3.3 Connétable

The 31 (U-Th)/He ages obtained for the two duricrust samples from Connétable range from 26.4 ± 2.6 Ma to 2.6 ± 0.4 Ma (Figs. VI-8A and VI-12). GC21-01 yields ages from 26.4 ± 3.6 Ma to 2.9 ± 0.3 Ma and in three of the four analyzed subsamples age variation exceeds analytical uncertainty with only some of the ages overlapping within error. Subsample GC-01_A shows a poor positive correlation of age with Th ($R^2 = 0.70$, p-value= 0.078, Fig. VI-12B), GC-01_B a slight correlation of age with $\log(U)$ ($R^2 = 0.67$, p-value= 0.09) and GC-01_C a correlation with Sm ($R^2 = 0.96$, p-value= 0.021, Fig. VI-12C) whereas the other subsample-element pairs

show no correlations. Taking all subsamples together sample GC21-01 shows a poor but significant negative correlation of age with U and log(U) ($R^2 = 0.28$, p -value= 0.03, Fig. VI-12A).

Sample GC21-03 yields generally younger ages ranging from 10.0 ± 1.0 Ma to 2.7 ± 0.4 Ma. While in subsample GC21-03_B most ages overlap within error and yield results between 6.5 and 3.5 Ma the other two subsamples yield more spread ages. No correlations of age with U, Th or Sm are observed.

When the two samples are looked at together, they show generally low concentrations of U, Th and Sm for the older ages (>10 Ma) and both low and high concentrations of U, Th and Sm for the younger ages (<10 Ma) (Fig. VI-12A-C).

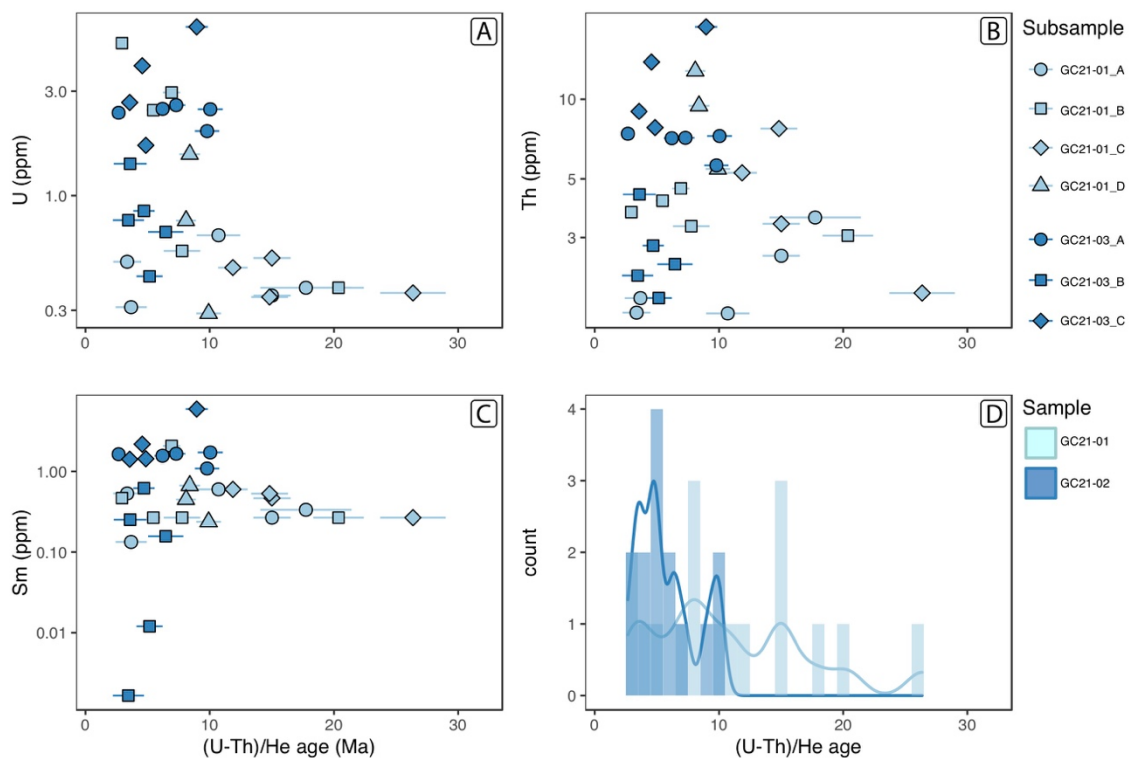


Figure VI-12: (U-Th)/He ages from Connetable versus U (A), Th (B), and Sm (C) concentrations. Colors correspond to samples and shapes to subsamples. (D) shows a histogram and a Kernel density plot for the two analyzed samples.

VI.6 Discussion

VI.6.1 Sampling

The selection of the samples in the field, with some samples that could not be taken in situ, is a major limitation for this study. The outcrop conditions of lateritic profiles, especially when they occur on mountain tops are often very poor in French Guiana (and in Amazonia

generally). On the one hand duricrusts are often covered by a soil layer hindering their observation and on the other hand the often very dense forest cover complicates access to the sites. Sampling in Cayenne was difficulted by the locally dense habitation. The sites of Mount Baduel and Vidal had been chosen because they had previously been studied by paleomagnetism (Théveniaut and Freyssinet, 1999; Théveniaut and Freyssinet, 2002). However since that study Mount Baduel turned into a habituated area, limiting the possibilities of sampling and site exploration.

At the moment of sampling and at the beginning of the analyses it was thought that only very pure and metallic Fe (oxyhydr)oxides were adapted for dating. This influenced the sampling, the sample selection and the subsampling procedure. More recent results (Chapter V) have shown that this belief might not be true as also more “ugly” duricrusts can yield highly reproducible (U-Th)/He ages. Furthermore, selection of samples containing either kaolinite or gibbsite facilitate characterization of the weathering conditions. While there is little doubt that the block samples from Baduel are representative of that profile, it would be good to confirm the results from Vidal with an in situ sample. At least for the bulk composition this is foreseen for the near future.

VI.6.2 Bulk sample composition

The bauxitic-lateritic profile of Baduel has previously been studied and described by Théveniaut and Freyssinet (1999). While our samples can be assigned macroscopically to their presented units of a pisolitic duricrust at the top, a massive duricrust and a saprolite, our mineralogical results show differences when compared to these authors. Unfortunately a direct comparison was difficulted by the fact that the outcrop conditions were rather poor at the moment of sampling for this study. Our two samples from the top (BAD18-B3 and -3A) resemble in their mineralogy and texture to what Théveniaut and Freyssinet (1999) describe as pisolitic duricrust (BAD18-B3) and massive duricrust (BAD18-3A). In their study, the authors present the entire massive duricrust to be very rich in gibbsite (> 50 %), similar to our sample BAD18-3A. In contrast, our two samples from the abandoned quarry, samples BAD18-1B and BAD18-1CA contain only small amounts of gibbsite and more important amounts of kaolinite (17% in BAD18-1CA). The low Al-substitutions in this goethite are also more indicative of ferruginous duricrust than bauxitic duricrust and we consider them therefore in the following as massive ferruginous duricrusts. The mineralogy of the saprolite sample analyzed here, with little

gibbsite, is compatible with the results of Théveniaut and Freyssinet (1999) which show variations of gibbsite content throughout the saprolitic part of the profile.

Differences of the ferruginous and bauxitic duricrusts are also visible when regarding the selected trace element and rare earth element concentrations in these 5 samples. As expected, Th and Zr concentrations are higher in the bauxitic samples when compared to the ferruginous samples. However, Zr and Th concentrations are surprisingly high in the saprolite (where they would be expected to be the lowest). This might be linked to an excess in zircon in the saprolite sample due to heterogeneities in the parental rock (a migmatite) and unrepresentative sampling. Furthermore the sampling point is slightly offset from the locations of the other samples. The REE pattern (Fig. VI-6) indicate that the ferruginous samples have more similarity with the saprolite than the bauxitic samples. These results support that the bauxitic and the ferruginous duricrusts sampled here represent different parts of the bauxitic-lateritic profile of Baduel.

Although the three lateritic covers presented in this study did not form on the same rocks (but all parental rocks are supposed to be intermediate basement rocks), comparing the bulk compositions of the duricrust samples from Vidal and Connétable with the Baduel samples allows to differentiate these samples. For the two samples from the Vidal site, described as ferruginous profile in the literature (Théveniaut and Freyssinet, 2002), the formation conditions cannot be deduced that easily from the bulk composition. Sample VID-01 is primarily composed of Al-poor goethite and contains minor amounts of kaolinite and quartz. This suggests formation under ferruginous lateritic conditions but the absence of other minerals and visible textures cannot prove this. The sample shows some similarities with sample BAD18-1B, which contains equally a large amount of Al-poor goethite, such as low Th concentration and a relative enrichment of HREE. In both samples goethite (and hematite?) might have formed from transported iron, possibly imported laterally or from the top. The pureness of the samples, the absence or low concentrations of Al and Th and high Fe/Al ratios indicate this.

Sample VID18-1B has a high Si/Al ratio, rather typical for ferruginous duricrusts. However, the mineralogical analyses show that this high Si/Al ratio is not related to the presence of kaolinite but to a strong presence of quartz. The sample stands equally out for its rather high Zr concentrations possibly indicating major presence of zircon in this sample. This might influence the concentrations of some other important trace elements such as Th. The REE pattern of VID18-1B shows no clear similarity neither with the bauxitic nor with the

ferruginous duricrusts from Baduel. From the given data it is therefore not possible say whether sample VID18-1B represents a ferruginous or bauxitic duricrust but the data is clearly compatible with the ferruginous characteristics proposed in the literature.

The samples from Connétable are devoid of kaolinite and quartz and rich in gibbsite indicating bauxitic conditions. The presence of MgO and Na₂O can be explained by the fact that the duricrust is in the middle of the sea and bathed by the waves. This “seawater imprint” is therefore not at all related to the weathering which created the duricrust. The REE pattern as well as concentrations of several weathering indicative trace elements (e.g. Th) underline the similarities with the bauxitic samples from the top of Mount Baduel. Although the parental material of the two sites might not be the same, the chemical signatures indicate similar formation conditions.

VI.6.3 Robustness and distribution of the (U-Th)/He ages of the different samples

The dataset presented in this study shows (U-Th)/He ages ranging from the Paleogene to the Quaternary, indicating a long weathering record in the Cayenne area. In the following the robustness of the data and the age distribution for every site will be discussed

VI.6.3.1 *Baduel*

VI.6.3.1.1 BAD18-1B

Sample BAD18-1B yields very continuous data from 12.8 to 4.6 Ma without a major age density peak (Fig. 9 VI-D). Overlapping maximum ages in three of the subsamples (Fig. VI-8A) indicate that these ages likely have a geological significance (Monteiro et al., 2014). Although the subsamples show a remarkable pureness and are basically inclusion free, ages within each subsample are relatively spread. The correlation with U visible in the data could indicate that phase mixing lead to the spread of the data (Heller et al., 2022). However the massive texture of the bulk sample (Fig. VI-2E) and the grains (Figs. VI-7A, -7D, -7E) do not suggest the presence of significantly different generations of iron minerals. The only observed features were botryoidal precipitations which have a similar composition as the massive grains. However, the few botryoidal grains analyzed (aliquots B1B1AV1, B1B2B4, B1B2C5, B1B2C5) tend to yield slightly younger ages than the massive grains. This might indicate that maybe different “generations” of goethite coexist but they resemble each other a lot in their texture and composition and resulted from the same precipitation processes. The lack of Al and Th in this sample might indicate that the Fe from which this sample precipitated was leached somewhere

else (e.g. at the top of the profile), was transferred and reprecipitated in form of the pure Fe oxides found in sample BAD18-1B. The rather continuous age distribution might also indicate that this process lasted several Myr and hematite and goethite precipitated continuously over this time interval. The lack of ages <4.6 Ma suggest that formation of this sample was mostly finished at that time. The presence of kaolinite dissolution features (Figs. VI-6B and VI-6F) and intact kaolinite (Fig. VI-7C) in the sample indicates that hematite and goethite precipitated while kaolinite was stable. While some of the kaolinite was lixiviated after hematite and goethite precipitation as indicated by dissolution features in both minerals this process was not pervasive as kaolinite remained stable in some parts of the sample. However, presence of angular pores (Fig. VI-7C) indicate that other minerals were lixiviated from these parts of the sample

VI.6.3.1.2 BAD18-B3

Sample B18-B3 yield slightly older maximum ages than sample BAD18-1B. The oldest ages occur in subsample BAD18-B3_1A(II) and correspond to the inner part of a large pisolith (Fig. VI-2D). The widespread presence of zircon in this subsample (Fig. VI-7G) suggests that He deriving from zircon inclusions (which are generally not dissolved in out acid mix) might have led to too old ages in this subsample. Theoretical studies for apatite (Vermeesch et al., 2007) imply that for rare and small actinide rich inclusions (ca. 1% of host mineral size) the impact on the age is relatively negligible (<10%), but it can be more important if inclusions are large and common. Zircon inclusions in BAD18-B3 All are frequent and sometimes relatively big. More detailed calculations would be needed in order to determine from which size and quantity on, they became problematic for (U-Th)/He dating of supergene hematite and goethite. We can therefore not decide whether the ages the two oldest aliquots are geologically meaningful or not. However, the textures observed in these two subsamples might also support an older age when compared to the other hematite subsamples. The abundance of dissolution features and the overall “chaotic” texture (Fig. VI-7G) suggest that that the analyzed pisolith experienced several cycles of dissolution and reprecipitation processes.

The other hematite subsamples show much more homogeneous ages and textures (Figs. VI-7H and VI-8A). Goethite detected by micro-XRD (Table VI-3) and SEM (Fig. VI-7I) as well as the age-Th/U correlation in subsample BAD18-B3_1D suggest that the hematite was partially rehydrated and transformed into goethite and the ages might be affected by phase mixing. Nevertheless, and despite of the presence of small zircon inclusions, the hematite subsamples

BAD18-3A_1B(II) and BAD18-3A_1D yield reproducible results with an age peak at 7-5 Ma (Fig. VI-9D).

The goethite cementing and coating the hematite pisoliths yield ages from 6.6 to <0.8 Ma with a strong major peak at 2 Ma (Fig. VI-9D). The three oldest aliquots very probably result from phase mixing with older hematite as indicated by higher U concentrations similar to hematite (Fig. VI-9A) and hematite material attached to goethite grains (Fig. VI-7K). Whether the youngest ages results from very more recent weathering activity or He loss due to retentivity problems cannot be solved here. However, the fact that 2 aliquots yield ages < 1 Ma and the favorable climatic conditions existing nowadays could indicate that weathering might have continued during the Quaternary.

VI.6.3.2 Vidal

VI.6.3.2.1 VID-01

When regarding only the ages with relative errors <100%, the Vidal age distribution shows a peak at 6.4 Ma similar to the one observed in sample BAD18-B3 and a smaller one at 4.4 Ma (dashed lined in Fig. VI-11D). When all ages are considered the sample shows a third age peak at 1.9 Ma similar to the goethite of sample BAD18-B3 (Fig. VI-11D).

As for sample BAD18-1B the rather homogeneous ages and the overall homogeneous texture and the composition of Al poor goethite might indicate that this sample could have precipitated from laterally or horizontally transported Fe rich solutions.

VI.6.3.2.2 VID18-1B

VID18-1B shows a very different age distribution from sample VID-01 with most of the data ranging from 12.8 to 29.3 Ma (Figs. VI-8A and VI-11D). One aliquot yields a significantly older age of 37 Ma. Since this aliquot has also the highest U and Th concentrations and given the fact that in 2 of the 3 analyzed subsamples Th and U decrease towards younger ages, this aliquot is likely the oldest endmember (Figs. VI-11A and VI-11B). However, high Zr concentration in the bulk sample (542 ppm versus 193 ppm in the mean UCC (Rudnick and Gao, 2013)) indicating the important presence of zircon in this sample suggest that the old age might also be related to He implantation from zircon inclusions questioning its significance. The oldest ages of the other two subsamples yield overlapping (U-Th)/He ages of 28-29 Ma. The rest of the data range from 22.7 to 6.3 Ma without indication of discrete events. The youngest aliquot in this sample yields an age of 6.3 Ma similar to most ages of sample VID-01 which it resembles

also regarding its Th, U and Sm concentrations. The observed age-Th and age-U correlations and the fact that all three grains analyzed by μ XRD show the presence of both hematite and goethite indicate that phase mixing might be responsible for some of the age spread in this sample. Possible endmembers could be ca. 30-40 Ma old hematite and younger goethite <7 Ma as the one from sample VID-01. While the micro-XRD data indicate presence of more Al-rich goethite (15 mol%) in subsample VID18-1B_1, the bulk sample contains generally Al-poor goethite (4.9 mol%), similar to the one of VID-01 (7 mol% Al-substitution). Zircon inclusions might have additionally disturbed the ages.

The results show that the sample records weathering probably since the Oligocene, possibly since the Late Eocene.

VI.6.3.3 Connétable

VI.6.3.3.1 GC21-01

GC21-01 yields rather spread ages which sometimes correlate with Th and U. The oldest age of 26 ± 2.6 Ma overlaps within error with two aliquots from sample VID18-1B (Fig. VI-8A). There is no reason to doubt the reliability of this age. Zr concentrations are low in the bulk sample (63 ppm) indicating no important presence of zircons. The age data does not indicate any discrete weathering events but shows some slight density increase around 15, 8 and 3.5 Ma (Fig. VI-12D). The indiscrete age distribution probably derives from complex phase mixing as also elsewhere observed for bauxitic duricrusts (Heller et al., 2022).

VI.6.3.3.2 GC21-03

GC21-03 shows only younger ages than GC21-01 and indicates more discrete weathering with one age peak at 10 Ma and a bigger and larger one between 7 and 3.5 Ma which peaks at 4.6 Ma (Fig. VI-12D). The main peak is about 1 to 1.5 Ma shifted when compared to Baduel. The youngest age of 2.7 ± 0.4 Ma which possibly indicates the end of Fe mineral precipitation overlaps within error with the youngest age from GC21-01. Unfortunately no complementary data which would allow to better characterize the samples and the related processes exist so far.

French Guiana laterite and bauxite evolution through time and space

Table VI-4: (U-Th)/He data of all obtained ages

Bulk Sample	subsample	aliquot	weight µg	⁴ He mol	⁴ He error mol	²³⁸ U ng	²³² Th ng	¹⁴⁷ Sm ng	²³⁸ U ppm	²³² Th ppm	¹⁴⁷ Sm ppm	Sm (total) ppm	Th/U	raw age Ma	corrected age Ma	age error Ma	corr. factor ¹ %	predominant mineral
BAD18-1B	BAD18-1B_1AM	B1B1AM1	31	2.36E-15	1.07E-16	7.63E-11	0.06	0.06	1.90	1.80	1.20	8.0	0.9	5.9	6.2	0.5	5	Ht
BAD18-1B	BAD18-1B_1AM	B1B1AM2	59	3.75E-15	1.12E-16	6.35E-11	0.05	0.03	0.80	0.50	0.40	2.7	0.7	12.2	12.8	0.7	5	Ht
BAD18-1B	BAD18-1B_1AM	B1B1AM3	176	9.37E-15	6.69E-17	5.32E-11	0.17	0.10	1.00	0.60	0.30	2.0	0.6	9.0	9.5	0.5	5	Ht
BAD18-1B	BAD18-1B_1AM	B1B1AM4	76	2.36E-15	6.25E-17	3.11E-11	0.05	0.02	0.70	0.20	0.30	2.0	0.4	8.0	8.4	0.4	5	Ht
BAD18-1B	BAD18-1B_1AM	B1B1AM5	146	8.03E-15	7.14E-17	5.50E-11	0.11	0.12	0.80	0.80	0.50	3.3	1.0	10.6	11.1	0.6	5	Ht
BAD18-1B	BAD18-1B_1AV	B1B1AV1	72	2.50E-15	1.12E-16	3.47E-11	0.04	0.13	0.60	1.90	0.30	2.0	3.4	6.5	6.8	0.7	5	Ht
BAD18-1B	BAD18-1B_2A	B1B2A10	60	6.69E-15	3.75E-16	1.12E-10	0.23	0.00	3.84	0.08	1.13	7.5	0.0	5.2	6.0	0.6	15	Gt
BAD18-1B	BAD18-1B_2A	B1B2A6	98	1.52E-14	3.93E-16	1.55E-10	0.46	0.01	4.67	0.06	0.69	4.6	0.0	6.1	7.0	0.7	15	Gt
BAD18-1B	BAD18-1B_2A	B1B2A7	107	1.56E-14	4.10E-16	1.46E-10	0.42	0.05	3.91	0.51	0.84	5.6	0.1	6.7	7.7	0.8	15	Gt
BAD18-1B	BAD18-1B_2A	B1B2A8	111	1.65E-14	3.70E-16	1.49E-10	0.37	0.02	3.30	0.14	1.00	6.7	0.0	8.3	9.5	1.0	15	Gt
BAD18-1B	BAD18-1B_2A	B1B2A9	140	1.83E-14	4.28E-16	1.31E-10	0.56	0.00	4.03	0.00	0.69	4.6	0.0	6.0	6.9	0.7	15	Gt
BAD18-1B	BAD18-1B_2B	B1B2B1	92	3.48E-15	6.69E-17	3.78E-11	0.08	0.00	0.90	0.00	0.70	4.7	0.0	8.0	9.2	0.9	15	Gt
BAD18-1B	BAD18-1B_2B	B1B2B2	46	4.24E-15	4.91E-17	9.21E-11	0.08	0.00	1.70	0.00	1.50	10.0	0.0	9.8	11.3	1.1	15	Gt
BAD18-1B	BAD18-1B_2B	B1B2B3	47	1.65E-15	6.25E-17	3.51E-11	0.04	0.00	0.90	0.10	1.10	7.3	0.1	6.8	7.8	0.8	15	Gt
BAD18-1B	BAD18-1B_2B	B1B2B4	43	4.06E-15	5.35E-17	9.44E-11	0.18	0.00	4.20	0.10	1.00	6.7	0.0	4.2	4.8	0.5	15	Gt
BAD18-1B	BAD18-1B_2B	B1B2B5	74	3.66E-15	3.79E-16	4.94E-11	0.10	0.02	1.35	0.23	0.88	5.9	0.2	6.5	7.5	1.0	15	Gt
BAD18-1B	BAD18-1B_2B	B1B2B6	56	1.87E-15	3.75E-16	3.35E-11	0.04	0.01	0.80	0.17	0.89	5.9	0.2	7.4	8.5	2.0	15	Gt
BAD18-1B	BAD18-1B_2C	B1B2C1	67	2.77E-15	7.14E-17	4.13E-11	0.06	0.00	1.00	0.00	0.70	4.7	0.0	8.0	9.2	0.9	15	Gt
BAD18-1B	BAD18-1B_2C	B1B2C2	69	2.28E-15	7.58E-17	3.30E-11	0.05	0.00	0.70	0.00	1.00	6.7	0.0	8.1	9.3	0.9	15	Gt
BAD18-1B	BAD18-1B_2C	B1B2C3	114	2.10E-15	7.58E-17	1.84E-11	0.04	0.00	0.40	0.00	0.90	6.0	0.1	8.9	10.2	1.0	15	Gt
BAD18-1B	BAD18-1B_2C	B1B2C4	63	2.50E-15	8.92E-17	3.97E-11	0.04	0.00	0.70	0.00	0.70	4.7	0.1	10.9	12.5	1.3	15	Gt
BAD18-1B	BAD18-1B_2C	B1B2C5	87	4.46E-15	1.03E-16	5.13E-11	0.20	0.00	2.30	0.00	0.30	2.0	0.0	4.1	4.7	0.5	15	Gt
BAD18-1B	BAD18-1B_2C	B1B2C6	90	4.46E-15	4.24E-17	4.96E-11	0.13	0.00	1.40	0.00	0.30	2.0	0.0	6.5	7.5	0.7	15	Gt
BAD18-1B	BAD18-1B_2C	B1B2C7	56	1.20E-15	3.57E-16	2.15E-11	0.02	0.00	0.37	0.00	0.78	5.2	0.0	10.8	12.4	4.0	15	Gt
BAD18-1B	BAD18-1B_2C	B1B2C8	59	1.07E-15	3.52E-16	1.81E-11	0.04	0.02	0.75	0.40	0.59	3.9	0.5	4.0	4.6	1.6	15	Gt
BAD18-B3	BAD18-B3_1A	B31A1	36	1.25E-14	1.25E-16	3.47E-10	0.02	1.30	0.57	36.08	0.22	1.4	63.4	7.0	7.4	0.6	5	Ht
BAD18-B3	BAD18-B3_1A	B31A2	61	2.68E-14	2.68E-16	4.39E-10	0.04	1.22	0.68	20.03	0.24	1.6	29.3	15.0	15.8	1.3	5	Ht
BAD18-B3	BAD18-B3_1A	B31A4	66	3.26E-14	3.26E-16	4.93E-10	0.02	1.84	0.30	27.90	0.23	1.5	91.5	13.2	13.9	1.2	5	Ht
BAD18-B3	BAD18-B3_1A	B31A3	115	2.90E-14	2.89E-16	2.52E-10	0.07	3.64	0.63	31.63	0.24	1.6	50.4	5.7	6.0	0.3	5	Ht
BAD18-B3	BAD18-B3_1A	B31A7	112	3.57E-14	3.55E-16	3.19E-10	0.11	3.13	0.95	27.91	0.15	1.0	29.3	7.8	8.2	0.4	5	Ht
BAD18-B3	BAD18-B3_1AI1	B31AI1	63	1.65E-14	1.65E-16	2.62E-10	0.05	1.30	0.76	20.64	0.41	2.7	27.0	8.7	9.1	0.7	5	Ht
BAD18-B3	BAD18-B3_1AI1	B31AI2	64	1.29E-14	1.29E-16	2.02E-10	0.02	1.45	0.33	22.65	0.23	1.5	68.2	6.5	6.8	0.5	5	Ht
BAD18-B3	BAD18-B3_1AI1	B31AI5	53	1.74E-14	1.74E-16	3.28E-10	0.03	1.20	0.65	22.67	0.38	2.5	35.0	10.2	10.7	0.8	5	Ht
BAD18-B3	BAD18-B3_1AI1	B31AI3	37	1.29E-14	1.31E-16	3.50E-10	0.06	1.01	1.58	27.21	0.38	2.6	17.2	8.2	8.6	0.4	5	Ht
BAD18-B3	BAD18-B3_1AI1	B31AI4	58	1.74E-14	1.75E-16	3.00E-10	0.05	1.59	0.91	27.43	0.46	3.1	30.0	7.5	7.9	0.4	5	Ht
BAD18-B3	BAD18-B3_1B	B31B1	77	1.03E-14	1.03E-16	1.33E-10	0.03	1.63	0.36	21.22	0.15	1.0	56.0	4.6	4.8	0.5	5	Ht
BAD18-B3	BAD18-B3_1B	B31B2	109	1.52E-14	1.52E-16	1.39E-10	0.04	2.24	0.36	20.56	0.14	1.0	56.4	5.0	5.3	0.5	5	Ht
BAD18-B3	BAD18-B3_1B	B31B3	51	7.09E-15	7.09E-17	1.39E-10	0.03	1.27	0.67	24.94	0.21	1.4	37.5	3.9	4.1	0.4	5	Ht
BAD18-B3	BAD18-B3_1B	B31B5	46	1.27E-14	1.27E-16	2.76E-10	0.03	1.27	0.65	27.66	0.24	1.6	42.6	7.1	7.5	0.7	5	Ht
BAD18-B3	BAD18-B3_1BI1	B31BI2	73	1.12E-14	1.12E-16	1.53E-10	0.03	1.24	0.35	16.95	0.16	1.1	48.0	6.6	6.9	0.7	5	Ht
BAD18-B3	BAD18-B3_1BI1	B31BI1	50	1.03E-14	1.03E-16	2.05E-10	0.04	1.30	0.77	26.10	0.26	1.7	33.8	5.5	5.8	0.6	5	Ht

continued on next page

French Guiana laterite and bauxite evolution through time and space

Bulk Sample		subsample	aliquot	weight	⁴ He mol	⁴ He error	⁴ He mol/g	²³⁸ U ng	²³² Th ng	¹⁴⁷ Sm ng	²³⁸ U ppm	²³² Th ppm	¹⁴⁷ Sm ppm	Sm (total) ppm	Th/U	raw age Ma	corrected age Ma	error corr. age Ma	diff. corr. factor ¹ %	predominant mineral
BAD18-B3	BAD18-B3_1B1	B31B1B3	80	1.20E-14	1.20E-16	1.51E-10	0.04	1.69	0.01	0.48	21.18	0.15	1.0	44.5	5.1	5.4	0.5	5	Ht	
BAD18-B3	BAD18-B3_1B1	B31B1B4	29	7.58E-15	7.54E-17	2.62E-10	0.03	0.92	0.01	1.00	31.76	0.28	1.9	31.9	5.7	6.0	0.6	5	Ht	
BAD18-B3	BAD18-B3_1B1	B31B1B5	34	7.14E-15	7.09E-17	2.10E-10	0.03	0.84	0.01	0.75	24.80	0.22	1.4	33.2	5.9	6.2	0.6	5	Ht	
BAD18-B3	BAD18-B3_1D	B31D1	50	6.25E-15	6.25E-17	1.25E-10	0.03	0.79	0.02	0.53	15.81	0.32	2.1	29.6	5.5	5.8	0.4	5	Ht	
BAD18-B3	BAD18-B3_1D	B31D2	55	4.91E-15	4.91E-17	8.92E-11	0.03	0.64	0.01	0.51	11.57	0.20	1.3	22.6	5.1	5.4	0.4	5	Ht	
BAD18-B3	BAD18-B3_1D	B31D3	40	8.03E-15	8.03E-17	2.01E-10	0.02	0.89	0.02	0.55	22.21	0.44	3.0	40.7	6.4	6.7	0.5	5	Ht	
BAD18-B3	BAD18-B3_1D	B31D4	61	1.07E-14	1.09E-16	1.76E-10	0.06	1.43	0.02	0.93	23.50	0.38	2.6	25.4	5.1	5.4	0.3	5	Ht	
BAD18-B3	BAD18-B3_1D	B31D5	37	4.28E-15	4.30E-17	1.16E-10	0.03	0.62	0.01	0.85	16.77	0.30	2.0	19.7	4.5	4.7	0.2	5	Ht	
BAD18-B3	BAD18-B3_3A	B33A1	111	4.46E-15	4.46E-17	4.02E-11	0.13	1.67	0.02	1.15	15.07	0.21	1.4	13.1	1.6	1.7	0.2	5	Gt	
BAD18-B3	BAD18-B3_3A	B33A2	133	1.38E-14	1.38E-16	1.04E-10	0.08	1.49	0.05	0.61	11.22	0.40	2.6	18.3	5.9	6.2	0.6	5	Gt	
BAD18-B3	BAD18-B3_3A	B33A3	65	5.80E-15	5.80E-17	8.92E-11	0.04	0.61	0.03	0.66	9.35	0.39	2.6	14.2	5.7	6.0	0.6	5	Gt	
BAD18-B3	BAD18-B3_3A	B33A4	71	8.97E-15	8.97E-17	1.26E-10	0.06	0.87	0.03	0.86	12.21	0.41	2.8	14.1	6.3	6.6	0.7	5	Gt	
BAD18-B3	BAD18-B3_3A	B33A11	100	7.14E-15	2.36E-16	7.14E-11	0.10	1.44	0.02	1.05	14.40	0.23	1.5	13.7	3.0	3.2	0.3	5	Gt	
BAD18-B3	BAD18-B3_3A	B33A12	48	1.29E-16	1.78E-16	2.70E-12	0.07	0.39	0.01	1.40	8.14	0.30	2.0	5.8	0.1	0.1	0.2	5	Gt	
BAD18-B3	BAD18-B3_3A	B33A13	33	9.37E-16	1.74E-16	2.84E-11	0.04	0.73	0.01	1.42	21.99	0.17	1.1	19.6	0.8	0.8	0.2	5	Gt	
BAD18-B3	BAD18-B3_3A	B33A14	65	2.99E-15	3.57E-16	4.60E-11	0.14	0.67	0.02	2.21	10.32	0.34	2.3	4.7	1.8	1.9	0.3	5	Gt	
BAD18-B3	BAD18-B3_3A	B33A15	95	5.35E-15	2.50E-16	5.64E-11	0.17	0.93	0.03	1.83	9.80	0.32	2.1	5.4	2.5	2.6	0.3	5	Gt	
BAD18-B3	BAD18-B3_3A	B33A16	38	2.10E-15	2.01E-16	5.52E-11	0.06	0.36	0.02	1.64	9.48	0.41	2.7	5.8	2.6	2.7	0.3	5	Gt	
BAD18-B3	BAD18-B3_3A	B33A17	43	2.01E-15	1.87E-16	4.67E-11	0.06	0.49	0.01	1.41	11.39	0.33	2.2	8.1	2.1	2.2	0.3	5	Gt	
BAD18-B3	BAD18-B3_3A	B33A7	48	1.87E-15	1.88E-17	3.90E-11	0.09	0.48	0.01	1.85	9.96	0.29	1.9	5.4	1.7	1.8	0.2	5	Gt	
VID-01	VID-01_1	VID011A	68	1.47E-14	3.93E-16	2.17E-10	0.03	0.15	0.02	0.40	2.20	0.30	2.0	5.2	42.1	48.4	4.8	15	Gt	
VID-01	VID-01_1	VID011B	64	1.70E-15	3.97E-16	2.65E-11	0.03	0.25	0.03	0.40	3.80	0.50	3.3	9.7	3.7	4.3	1.2	15	Gt	
VID-01	VID-01_1	VID011C	31	2.54E-16	3.93E-16	8.20E-12	0.01	0.04	0.01	0.40	1.10	0.30	2.0	3.0	2.3	2.6	0.3	15	Gt	
VID-01	VID-01_1	VID011D	50	1.38E-15	1.87E-16	2.77E-11	0.03	0.16	0.03	0.60	3.10	0.50	3.3	5.2	3.8	4.4	0.8	15	Gt	
VID-01	VID-01_1	VID011E	47	1.47E-15	1.87E-16	3.13E-11	0.02	0.14	0.03	0.50	3.00	0.50	3.3	6.2	4.9	5.6	1.0	15	Gt	
VID-01	VID-01_2	VID012A	23	1.52E-16	1.83E-16	6.60E-12	0.00	0.02	0.02	0.20	0.80	0.80	5.3	3.6	3.1	3.6	6.5	15	Gt	
VID-01	VID-01_2	VID012B	51	1.78E-16	1.87E-16	3.50E-12	0.01	0.04	0.01	0.20	0.80	0.20	1.3	4.1	1.6	1.8	3.0	15	Gt	
VID-01	VID-01_2	VID012C	21	6.25E-16	1.87E-16	2.97E-11	0.01	0.06	0.06	0.30	2.70	2.60	17.3	8.1	5.5	6.3	2.8	15	Gt	
VID-01	VID-01_2	VID012D	20	9.82E-17	1.87E-16	4.91E-12	0.01	0.02	0.02	0.30	1.00	1.00	6.7	3.7	1.7	2.0	5.4	15	Gt	
VID-01	VID-01_2	VID012E	17	7.58E-17	1.83E-16	4.46E-12	0.01	0.02	0.01	0.40	1.00	1.00	3.3	2.3	1.3	1.5	5.0	15	Gt	
VID-01	VID-01_3	VID013A	109	3.44E-15	2.10E-16	3.15E-11	0.05	0.20	0.11	0.50	1.80	1.00	6.7	3.6	6.3	7.2	0.7	15	Gt	
VID-01	VID-01_3	VID013C	127	4.37E-15	2.59E-16	3.44E-11	0.08	0.28	0.25	0.60	2.20	1.90	12.7	3.7	5.6	6.4	0.6	15	Gt	
VID-01	VID-01_3	VID013D	121	3.39E-15	2.54E-16	2.80E-11	0.06	0.19	0.06	0.50	1.50	0.50	3.3	2.9	5.8	6.7	0.7	15	Gt	
VID-01	VID-01_3	VID013E	130	4.91E-15	2.36E-16	3.78E-11	0.11	0.21	0.13	0.80	1.60	1.00	6.7	2.0	5.6	6.4	0.6	15	Gt	
VID18-1B	VID18-1B_1	VID181A	166	2.10E-13	5.80E-16	1.26E-09	0.26	3.53	0.29	1.60	21.30	1.70	11.3	13.4	35.3	37.1	3.7	5	Gt	
VID18-1B	VID18-1B_1	VID181B	95	3.26E-14	3.97E-16	3.43E-10	0.13	1.55	0.06	1.40	16.30	0.60	4.0	11.9	12.2	12.8	1.3	5	Gt	
VID18-1B	VID18-1B_1	VID181C	126	3.66E-14	4.24E-16	2.90E-10	0.12	1.66	0.08	0.90	13.20	0.60	4.0	14.4	13.4	14.1	1.4	5	Gt	
VID18-1B	VID18-1B_1	VID181D	79	4.46E-15	4.06E-16	5.65E-11	0.05	0.39	0.02	0.60	5.00	0.20	1.3	8.6	6.0	6.3	0.7	5	Gt	
VID18-1B	VID18-1B_2	VID182A	133	3.79E-14	3.84E-16	2.85E-10	0.08	0.80	0.01	0.60	6.00	0.10	0.7	10.4	26.6	27.9	2.8	5	Ht	
VID18-1B	VID18-1B_2	VID182B	71	1.38E-14	3.84E-16	1.95E-10	0.04	0.46	0.01	0.60	6.50	0.10	0.7	11.6	17.4	18.3	1.8	5	Ht	
VID18-1B	VID18-1B_2	VID182C	197	3.44E-14	4.02E-16	1.74E-10	0.10	0.89	0.02	0.50	4.50	0.10	0.7	8.7	20.2	21.2	2.1	5	Ht	

continued on next page

French Guiana laterite and bauxite evolution through time and space

continuation

Bulk Sample	subsample	aliquot	weight µg	⁴ He mol	⁴ He error mol	⁴ He mol/g	²³⁸ U ng	²³² Th ng	¹⁴⁷ Sm ng	²³⁸ U ppm	²³² Th ppm	¹⁴⁷ Sm ppm	Sm (total) ppm	Th/U raw age Ma	corrected age Ma	error Ma	corr. age Ma	diff. corr. factor ¹ %	predominant mineral
VID18-1B	VID18-1B_2	VID182D	258	5.80E-14	2.14E-16	2.25E-10	0.17	2.18	0.02	0.70	8.40	0.10	0.7	12.7	15.3	16.1	1.6	5	Ht
VID18-1B	VID18-1B_2	VID182E	119	1.83E-14	3.93E-16	1.54E-10	0.05	0.63	0.01	0.50	5.30	0.10	0.7	11.7	16.7	17.5	1.8	5	Ht
VID18-1B	VID18-1B_3	VID183A	140	9.37E-14	4.24E-16	6.69E-10	0.14	2.08	0.03	1.00	14.90	0.20	1.3	15.4	27.9	29.3	1.5	5	Ht
VID18-1B	VID18-1B_3	VID183B	126	5.80E-14	4.46E-16	4.60E-10	0.11	1.62	0.02	0.80	12.90	0.20	1.3	15.2	21.7	22.8	1.1	5	Ht
VID18-1B	VID18-1B_3	VID183C	173	2.99E-14	4.02E-16	1.73E-10	0.10	1.35	0.04	0.60	7.80	0.20	1.3	12.9	13.2	13.9	0.7	5	Ht
VID18-1B	VID18-1B_3	VID183D	181	9.37E-14	4.91E-16	5.18E-10	0.24	2.46	0.04	1.30	13.60	0.20	1.3	10.2	20.6	21.6	1.1	5	Ht
VID18-1B	VID18-1B_3	VID183E	149	3.57E-14	3.97E-16	2.40E-10	0.10	1.35	0.02	0.70	9.10	0.20	1.3	13.7	15.8	16.6	0.8	5	Ht
GC21-01	GC21-01_A	GC01A1	17	1.92E-15	3.39E-16	1.13E-10	0.01	0.06	0.00	0.38	3.57	0.05	0.3	9.4	16.9	17.7	3.7	5	unclear
GC21-01	GC21-01_A	GC01A2	28	1.56E-15	1.78E-16	5.58E-11	0.02	0.04	0.00	0.66	1.55	0.09	0.6	2.4	10.2	10.7	1.7	5	unclear
GC21-01	GC21-01_A	GC01A3	52	8.03E-16	1.83E-16	1.54E-11	0.03	0.08	0.00	0.50	1.56	0.08	0.5	3.1	3.2	3.4	1.1	5	unclear
GC21-01	GC21-01_A	GC01A4	127	9.37E-15	2.05E-16	7.38E-11	0.04	0.33	0.01	0.35	2.56	0.04	0.3	7.4	14.3	15.0	1.5	5	unclear
GC21-01	GC21-01_A	GC01A5	56	7.58E-16	2.14E-16	1.35E-11	0.02	0.10	0.00	0.31	1.77	0.02	0.1	5.7	3.5	3.7	1.3	5	unclear
GC21-01	GC21-01_B	GC01B1	125	1.12E-14	4.46E-16	8.92E-11	0.62	0.47	0.01	4.97	3.74	0.07	0.5	0.8	2.8	2.9	0.3	5	unclear
GC21-01	GC21-01_B	GC01B2	42	2.28E-15	3.57E-16	5.42E-11	0.02	0.14	0.00	0.56	3.31	0.04	0.3	5.9	7.4	7.8	1.5	5	unclear
GC21-01	GC21-01_B	GC01B3	59	8.48E-15	2.14E-16	1.44E-10	0.17	0.27	0.02	2.96	4.60	0.31	2.1	1.6	6.6	6.9	0.7	5	unclear
GC21-01	GC21-01_B	GC01B4	98	1.12E-14	4.10E-16	1.14E-10	0.04	0.30	0.00	0.38	3.05	0.04	0.3	8.0	19.4	20.4	2.0	5	unclear
GC21-01	GC21-01_B	GC01B5	103	9.82E-15	4.28E-16	9.53E-11	0.25	0.43	0.00	2.46	4.13	0.04	0.3	1.7	5.2	5.5	0.5	5	unclear
GC21-01	GC21-01_C	GC01C1	83	8.48E-15	4.19E-16	1.02E-10	0.04	0.28	0.01	0.52	3.38	0.07	0.5	6.5	14.3	15.0	1.5	5	unclear
GC21-01	GC21-01_C	GC01C2	115	1.25E-14	4.42E-16	1.09E-10	0.04	0.21	0.00	0.36	1.85	0.04	0.3	5.2	25.1	26.4	2.6	5	unclear
GC21-01	GC21-01_C	GC01C4	67	7.14E-15	3.61E-16	1.07E-10	0.03	0.35	0.01	0.47	5.27	0.09	0.6	11.2	11.3	11.9	1.2	5	unclear
GC21-01	GC21-01_C	GC01C5	101	1.67E-14	3.86E-16	1.65E-10	0.03	0.78	0.01	0.34	7.74	0.08	0.5	22.4	14.1	14.8	1.5	5	unclear
GC21-01	GC21-01_D	GC01D1	101	1.64E-14	4.52E-16	1.63E-10	0.16	0.95	0.01	1.55	9.44	0.10	0.7	6.1	8.0	8.4	0.8	5	unclear
GC21-01	GC21-01_D	GC01D2	234	3.68E-14	4.35E-16	1.57E-10	0.18	2.99	0.02	0.77	12.78	0.07	0.4	16.6	7.7	8.1	0.8	5	unclear
GC21-01	GC21-01_D	GC01D3	172	1.38E-14	4.16E-16	8.03E-11	0.05	0.94	0.01	0.29	5.45	0.04	0.2	18.8	9.4	9.9	1.0	5	unclear
GC21-03	GC21-03_A	GC03A1	38	5.06E-15	3.76E-16	1.33E-10	0.09	0.27	0.01	2.49	7.12	0.23	1.6	2.9	5.9	6.2	0.6	5	unclear
GC21-03	GC21-03_A	GC03A2	48	1.04E-14	4.18E-16	2.17E-10	0.12	0.35	0.01	2.48	7.25	0.26	1.7	2.9	9.6	10.0	1.0	5	unclear
GC21-03	GC21-03_A	GC03A3	80	1.33E-14	4.98E-16	1.66E-10	0.16	0.45	0.01	1.97	5.62	0.16	1.1	2.9	9.3	9.8	1.0	5	unclear
GC21-03	GC21-03_A	GC03A4	73	4.14E-15	4.63E-16	5.67E-11	0.17	0.54	0.02	2.39	7.40	0.24	1.6	3.1	2.5	2.7	0.4	5	unclear
GC21-03	GC21-03_A	GC03A5	100	1.60E-14	4.64E-16	1.60E-10	0.26	0.71	0.02	2.59	7.14	0.25	1.7	2.8	7.0	7.3	0.7	5	unclear
GC21-03	GC21-03_B	GC03B1	32	7.28E-16	1.94E-16	2.28E-11	0.02	0.07	0.00	0.77	2.15	0.00	0.0	2.8	3.3	3.5	1.3	5	unclear
GC21-03	GC21-03_B	GC03B2	16	7.19E-16	2.17E-16	4.49E-11	0.02	0.07	0.00	1.40	4.37	0.04	0.3	3.1	3.4	3.6	1.3	5	unclear
GC21-03	GC21-03_B	GC03B3	29	1.20E-15	2.15E-16	4.13E-11	0.02	0.07	0.00	0.68	2.38	0.02	0.2	3.5	6.2	6.5	1.4	5	unclear
GC21-03	GC21-03_B	GC03B4	40	1.46E-15	2.24E-16	3.66E-11	0.03	0.11	0.00	0.85	2.80	0.09	0.6	3.3	4.5	4.7	0.9	5	unclear
GC21-03	GC21-03_B	GC03B5	67	1.50E-15	2.61E-16	2.24E-11	0.03	0.12	0.00	0.43	1.77	0.00	0.0	4.1	4.9	5.2	1.1	5	unclear
GC21-03	GC21-03_C	GC03C2	19	3.20E-15	3.81E-16	1.69E-10	0.07	0.26	0.01	3.92	13.81	0.33	2.2	3.5	4.4	4.6	0.7	5	unclear
GC21-03	GC21-03_C	GC03C3	40	3.51E-15	2.08E-16	8.77E-11	0.11	0.36	0.01	2.66	8.99	0.21	1.4	3.4	3.4	3.6	0.4	5	unclear
GC21-03	GC21-03_C	GC03C4	31	1.47E-14	2.32E-16	4.76E-10	0.18	0.58	0.03	5.90	18.77	0.89	5.9	3.2	8.5	9.0	0.9	5	unclear
GC21-03	GC21-03_C	GC03C5	101	8.93E-15	2.47E-16	8.85E-11	0.17	0.79	0.02	1.70	7.80	0.21	1.4	4.6	4.6	4.9	0.5	5	unclear

diff. corr. factor¹: diffusion correction factor used for age correction

VI.6.4 Duricrust formation processes of Baduel

The results from the two dated duricrust samples from Mount Baduel allow to better constrain the evolution of the lateritic system. A schematic model of the proposed evolution is presented in Figure VI-13. The mineralogical and geochemical results of the bulk and the subsamples show, that both samples studied in detail represent different parts of the lateritic system, with BAD18-1B representing the massive ferruginous duricrust located between a saprolite and a duricrust richer in Al and BAD18-B3 represents the uppermost part of the profile, the pisolitic duricrust with bauxitic signature (without being a bauxite *sensu strictu* as iron oxides are predominant relative to Al (hydr)oxides). Thermochronological results from northeastern French Guiana indicate that the basement rock in this area are close to the surface since ca. 90 Ma (Derycke et al., 2021) (Fig. VI-13A). Our data does not allow to constrain the onset of weathering (Fig. 13B) but as discussed in Section VI.6.3.1, the oldest hematite and goethite subsamples are at least 12.8 ± 0.7 Ma old, possibly even 15.7 ± 1.3 Ma. This means that by that time (or earlier) a duricrust system had been set in place (Fig. VI-13C). The data suggest that lateritic weathering is rather continuous until ca. 7 Ma, indicating no specific periods of enhanced weathering. Kaolinite dissolution features in both studied samples indicate that the oldest iron (oxyhydr)oxides preserved precipitated while kaolinite was still stable. Possibly weathering was continuous during this time interval. In an dynamic duricrust system, the duricrust is dismantled at its top and formed at its bottom (Tardy, 1997; Beauvais, 2009). Fe is released from the top of the duricrust at the interface with the soil, probably through interactions with the biosphere and by pH reduction related to organic acids. The released Fe is transferred to the bottom of the duricrust at the interface with the mottled zone where it reprecipitates (e.g. due to redox changes), leading to downward migration of a ferruginization front with formation of new duricrust. Like this the duricrust is constantly rejuvenated at the bottom and younger than the one at the top (Fig. VI-13D). This process of Fe cycling was probably active since the formation of the duricrust at Mount Baduel. The very continuous ages in sample BAD18-1B support the durability of this process. The data of this sample shows furthermore an increase in U contents from 12 to 5 Ma. This might indicate that U cycling accompanied the Fe cycling (Fig. VI-13E). This is possible because U forms very mobile uranyl under oxidizing conditions.

In our dataset most of the hematite subsamples from the pisolitic sample BAD18-B3 yield an age of ca. 6 Ma. The increase of age data at that time documents a period of enhanced

weathering. The hematite precipitated at that time shows no signs of kaolinite preservation. It is thus possible that at 6 Ma kaolinite was not stable anymore at the top of the profile and that the conditions were already bauxitic. However, bauxitic conditions would probably favor the precipitation of goethite rather than hematite. The absence of kaolinite traces in the 6 Ma hematite could also be due to the fact that the kaolinite was very fine grained (<2 μm) or that there was little kaolinite in the system.

Fe (oxyhydr)oxide ages are generally reduced between 5 and 3 Ma and absent in sample BAD18-1B. This could indicate a phase of less favorable precipitation conditions and a period dominated by dismantling of the duricrust. After this (eventual) gap goethite precipitated more massively at 3-2 Ma and the Al-rich goethite of subsample BAD18-B3_3A precipitated (Figs. VI-9, VI-10 and VI-13F). The high Al-contents in this goethite indicate that goethite precipitation was probably linked to kaolinite dissolution (Tardy and Nahon, 1985). Due to strong drainage, probably linked to high precipitations, kaolinite became unstable and was dissolved. The released Al was incorporated into Gt and precipitated to gibbsite while silica was lixiviated from the system (Fig. VI-13F). Pre-existing hematite was hydrated through this process to form goethite. This hydration is visible in some of the hematite grains (Fig. VI-7I). These processes led to the cementation of the pisolitic duricrust. In the entire upper part of the duricrust kaolinite was dissolved and replaced by gibbsite leading to the bauxitization of the upper part of the duricrust of Mount Baduel. This is in line with observations of Theveniaut and Freyssinet (1999) who propose that the bauxitization of Mount Baduel was a secondary process.

Several meters below the surface, the bauxitization process, which heavily affected the top of the profile, was much less pervasive. Some kaolinite and other minerals, as for example quartz, were dissolved but a large proportion of the kaolinite remained intact as indicated by high kaolinite contents in duricrust sample BAD18-1CA (Fig. VI-5B).

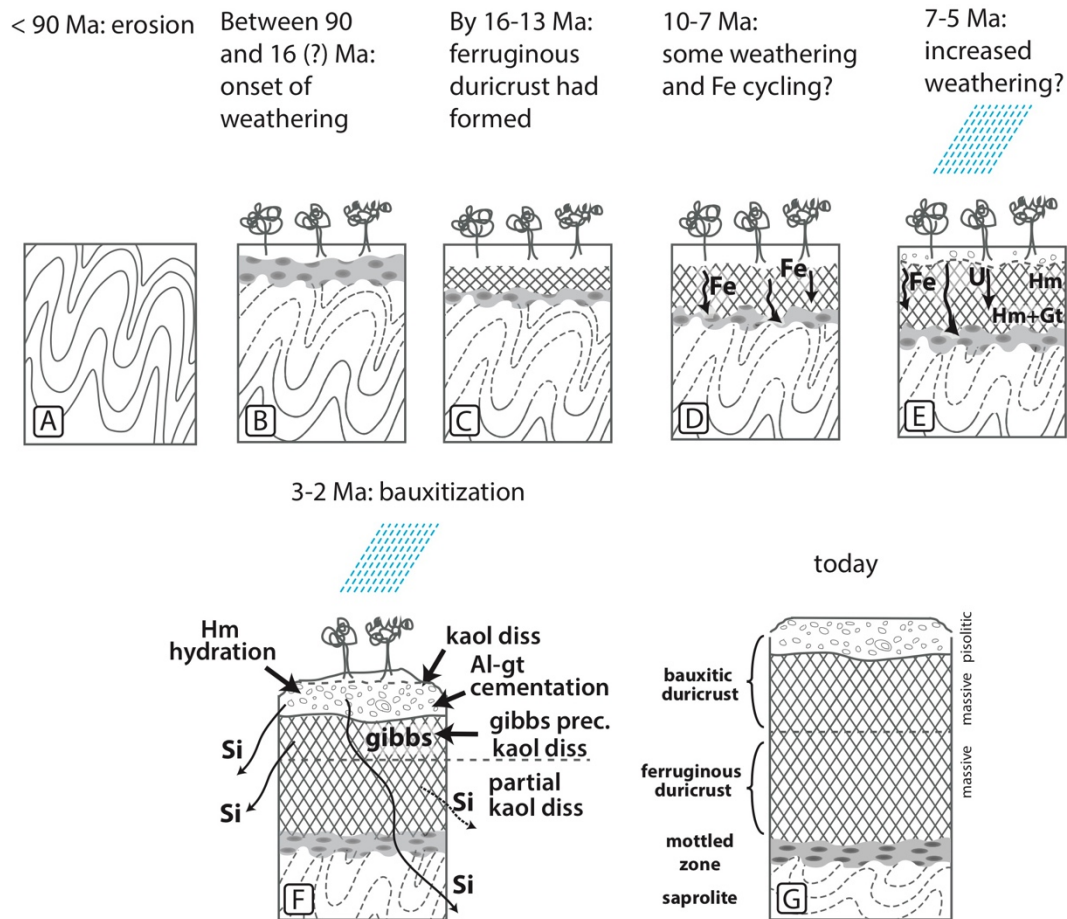


Figure VI-13: Evolution model of the lateritic profile of Mount Baduel. (A) Erosion and possibly peneplanation of the basement rocks happened after 90 Ma. (B) Weathering started between 90 and 16 Ma. (C) By 16-13 Ma a first, ferruginous duricrust had formed. (D) In the active duricrust system Fe is mobilized at the top of the duricrust and transported to the bottom where it reprecipitates. (E) Weathering increased around 6 Ma. Fe cycling probably continued and possibly included also U transfer. (F) Intense precipitation at 3-2 Ma led to bauxitization of the duricrust with gibbsite precipitation and silica lixiviation. (G) Shows a sketch of the duricrust in its present shape. Signatures are the same throughout the figure.

VI.6.5 Lateritization and bauxitization in the Cayenne area and its surroundings

The presented dataset is a new piece of puzzle shedding light on the weathering history of the northern rim of South America and complements two existing (U-Th)/He datasets from Kaw mountain in French Guiana (Heller et al., 2022) and Brownsberg in Suriname (Ansart, 2022). Weathered Late Cretaceous sediments overlaying weathered basement rocks in the Guiana basin confirm that weathering occurred since the beginning of the Cenozoic (Wong, 1986). Paleomagnetic studies by Theveniaut and Freyssinet (1999, 2002) indicate that weathering might date back to the Eocene at Kaw mountain and Mount Baduel, but due to the small latitudinal shift of South America during the Cenozoic these ages need to be interpreted with caution.

The maximum ages obtained in this study of ca. 30 Ma years, possibly even 37 Ma (see Section VI.6.3.2.2), are in accordance with the two studies by Heller et al. (2022) and Ansart (2022) which record weathering from the Late Eocene / Early Oligocene to the Quaternary. Figures VI-14 and 15 compare our new data with these datasets as well as other weathering (U-Th)/He age datasets from Amazonia (Shuster et al., 2005; Allard et al., 2018; Monteiro et al., 2018; dos Santos Albuquerque et al., 2020). These maximum ages correspond to the Late Eocene - Oligocene age proposed for the coastal bauxites in Suriname and Guyana (Hammen and Wymstra, 1964; Wymstra, 1971). The Bauxite Hiatus in the Guiana basin (Fig. VI-14) indicates that weathering lasted during the entire Oligocene (Wong, 1986). The beginning and the end of the Bauxite Hiatus are not well constrained but it has been proposed that it lasted even until the beginning of the Miocene (Wong, 1986 and references therein). Oligocene weathering ages appear in numerous weathering age datasets from Amazonia and South America (Lima, 2008; Monteiro et al., 2014; Monteiro et al., 2018) indicating that favorable weathering conditions were widespread at that time.

During the Oligocene temperatures were generally higher than today but lower than during the Eocene (Zachos et al., 2008; Westerhold et al., 2020). Some excursions towards higher temperatures are recorded during the Oligocene but whether they are prone to enhance the weathering activity on the Guiana shield cannot be decided. In any case for intense weathering high precipitations are more crucial than high temperature.

The absence of ages >30 or 37 Ma and notably also the absence of ages >16 Ma at Mount Baduel could be related to several things. Either could that mean that the nowadays weathered surfaces were not yet exposed by that time. Indeed, geomorphological models do not propose Eocene exposure of the paleosurfaces studied here (Choubert, 1957; Blancaneaux, 1981). On the other hand the absence of older ages could be related to the fact that secondary minerals formed in the early times of old weathering signatures were not preserved. As explained earlier, active duricrust systems are rejuvenated slowly but continuously. This also means that the oldest material might be recycled in some moment. Furthermore the absence of old ages could be linked to unrepresentative sampling as only few samples were studied. The results from the three sites presented here show that maximum ages might differ in between samples from the same site suggested to have experienced the same weathering history.

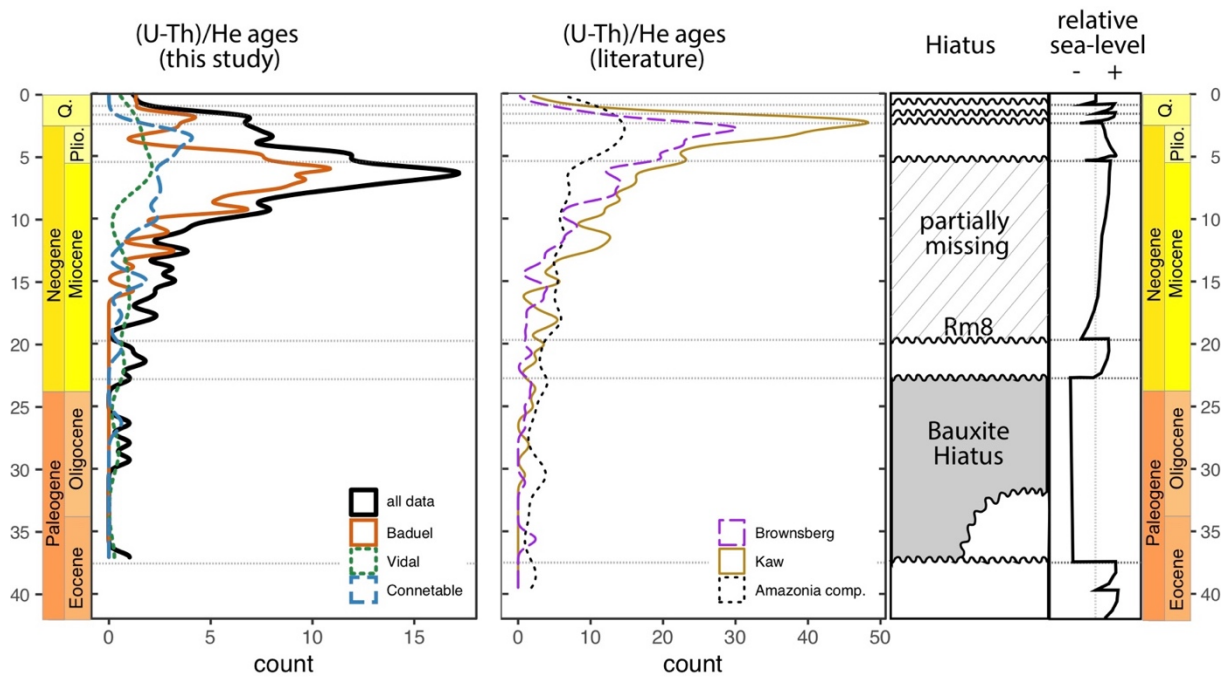


Figure VI-14: Comparison of data from this study with (U-Th)/He data on duricrusts published in the literature. Kernel density plots of data from this study (all data = black dense line, Baduel = brown line, Vidal = green finely dashed line, Connetable = blue largely dashed line) and Kernel density plots for published (U-Th)/He datasets: Ansart (2022) (purple dashed line), Heller et al. (2022) (golden dense line), and compilation with all Amazonian (U-Th)/He data (dashed black line) including data from (Shuster et al., 2012; Allard et al., 2018; Monteiro et al., 2018; dos Santos Albuquerque et al., 2020). Note that for better visibility only data <40 Ma of the compilation curve is shown. The right hand side shows the major hiatus surfaces from the sediment sequences in the Guiana basin and the relative sea level, from Wong (1986). Note that the age of most hiatus surfaces is not well defined and only approximative.

The dataset from Kaw, as well as data from the eastern rim of the Guiana shield (Chapter V) and ^{39}Ar - ^{40}Ar data from the Brazilian shield (Vasconcelos et al., 1994) show a an important peak at ca. 12 Ma. The here presented dataset does not show a significant peak at that time. Nevertheless, the maximum ages of sample BAD18-1B correspond to that age and samples GC21-01 and VID18-1B show some age concentrations around 15 Ma. The fact that most samples analyzed here were affected by phase mixing could have diluted the signal of that weathering event. Middle Miocene weathering could actually correspond to one prominent hiatus (“Rm8”, see Fig. VI-14) located near the base of the Miocene in the sedimentary successions of the Guiana basin (Wong, 1986; Wong, 1994). Similar to the Kaw dataset, and also to the data by Ansart (2022), overall age density of our samples increases since 10 Ma and samples BAD18-1B and GC21-03 show age density peaks at that time. However this feature could also result from mixing of multiple phases. Unfortunately the number of analyses is too small to decide whether this density increase has a geological meaning or not. Some of the Paleomagnetic ages of Theveniaut and Freyssinet (1999, 2002) from the Cayenne area yield Mid to Late Miocene ages, too, but the uncertainty of these ages is too big to allow a real comparison. Nevertheless, the sedimentary record of the Guiana basin indicates, that large

parts of the Miocene are actually missing in the sedimentary record (Hammen and Wymstra, 1964; Wong, 1986). This could indicate ongoing continental surface weathering during that time.

The main peak of this dataset is at ca. 6 Ma although there is a slight offset when regarding individual samples (Fig. VI-14, but also Figs. VI-9D, -11D and -12D). At Kaw this peak does not stand out but a shoulder is visible in the dataset at 6-5 Ma (Fig. VI-14). The dataset by Ansart 2022 shows a first peak between 8 and 6 Ma, also visible in the larger literature data compilation, and a next one at ca. 4 Ma. The weathering age peak at 6-5 Ma is synchronous with the hiatus at the Miocene-Pliocene boundary in the Guiana basin (Fig. VI-14).

The two datasets of Ansart (2022) and Heller et al. (2022) have their principal age peaks at 3.5-2 Ma. Although this is not the case for our dataset, it yields numerous ages at that time and the age densities curves are biased by the subsampling and the especially by the amount of analyzed aliquots. The more detailed analysis of the samples from Mount Baduel (Section VI-6.4) suggest furthermore that the minerals precipitated at that time, notable very Al-rich goethite, formed under bauxitic conditions.

Figure VI-15 compares the data of Connétable, Vidal and Baduel with the data of from Kaw. Interestingly the data from Connétable, and to a lesser degree Baduel, show a very similar distribution regarding age, U, Th and Sm when compared to Kaw. As element mobilities are influenced by the weathering conditions, this possibly suggests a very similar weathering history at Kaw, Connétable and Baduel, just the timing of high Th and Sm phases at Baduel is shifted to slightly older ages.

The comparison of the datasets shows that Late Neogene bauxitization has a regional extent. Although the new data presented here do not allow to better constrain the onset of the bauxitic conditions, it shows that latest during the Pliocene and Early Pleistocene bauxitic conditions prevailed in the study area and overprinted the already existing lateritic profiles at Baduel, Kaw, Connétable, and Brownsberg in Suriname. Despite the lack of clearly bauxitic signatures at Vidal, we cannot decide whether bauxitic weathering affected Vidal or not. The data from Baduel show that bauxitization might have not been completely pervasive everywhere and that different portions of the lateritic system could keep a ferruginous lateritic signature. The two samples from Vidal might represent samples unaffected by the bauxitization. The absence of Late Neogene ages, notably in sample VID18-1B, supports this.

The study by Heller et al. (2022) proposes both geomorphologic / geodynamic and climatic changes as possible triggers for bauxitization. They suggest that bauxitization might be linked to an increase in precipitation, possibly related to the mid Pliocene Warm Period (mPWP, Haywood et al. (2013)), to increased incision and thus drainage through an continental uplift in response to sedimentary loading in the Amazon fan, or to a combination of these factors with uplift leading to enhanced precipitation. The fact that Late Neogene bauxitization appears as a regional feature independent of local morphology and elevation strongly suggests that climate is the driving force responsible for this bauxitization. As suggested by Heller et al., (2022), bauxitization could be related to the mPWP. However, bauxitization might already have started before the mPWP. Lariviere et al., (2012) show that during the Late Miocene global climate was, despite of low CO₂ concentrations, generally warmer than during the Pliocene and today, with extended tropical warmth resulting in enhanced subtropical evaporation, greenhouse warming from water vapor, and warming from an increase in subtropical high 'greenhouse clouds'. These conditions could have been very favorable for the formation of bauxites on the northeastern Guyana shield. While the precise reason for the Late Neogene bauxitization cannot be identified yet, this study allows to exclude uplift as a possible reason.

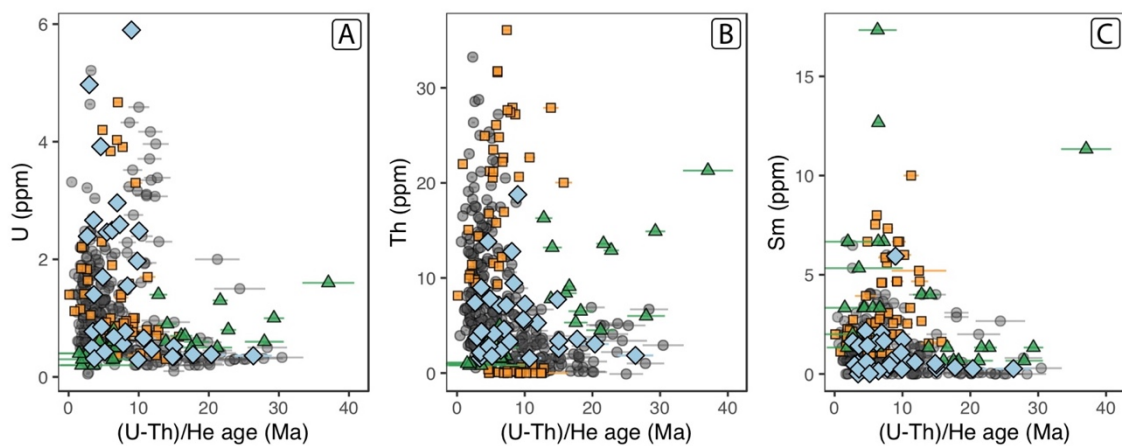


Figure VI-15: (U-Th)/He age data from Connetable (blue diamonds), Vidal (green triangles), Baduel (orange squares) and Kaw (grey circles, Heller et al., 2022) versus U (A), Th (B), and Sm (C) concentration. Note that the overall distribution of the data from Connetable, and to a lesser degree from Baduel, resembles the distribution from Kaw a lot.

VI.6.6 Geodynamic and geomorphological implications

The weathering age results from the northeastern Guiana shield allow to reassess the geomorphological models proposed for the Guiana shield. Several authors have suggested that the Guiana shield has 4-5 planation surfaces with different ages ranging from the late

Cretaceous to the Quaternary (Choubert, 1957; King, 1962; McConnell, 1968; Blancaneaux, 1981; Aleva, 1984; Bardossy and Aleva, 1990). These models were established mainly for the central areas of the shield. Figure VI-16A presents the model by McConnell (1968) adapted to the landscape of French Guiana. The figure shows that the too simplified reading “higher elevation = older age”, possibly true for the central areas of the shield, is probably not valid for coastal areas. McConnell (1968) proposes the existence of a coastal monocline where the different surfaces converge and are eventually inverted (see Fig. VI-16). This means on the one hand that “old planation surfaces” might occur at much lower elevations near the coast and on the other hand that planation surfaces of different ages might have similar absolute elevations near the coast.

Our dataset, together with those of Ansart (2022) and Heller et al. (2022), show that indeed the studied surfaces do not correspond to the too simplified model “higher elevation = older age”. The weathering ages show that a Quaternary age for the hills of the Cayenne area, once proposed by Choubert, (1957) and Blancaneaux (1981), is not possible because weathering traces back to the Miocene and Oligocene. However, the data is in concordance with the existence of a coastal monocline, as proposed by McConell (1968), where the surfaces converge near the coast and similar ages occur at different elevations (Fig. VI-16). The very similar ages obtained at Kaw (300m a.s.l.) and Connétable (0-2 m a.s.l.) which have a distance of about 40 km are the best example for similar ages at different elevations of a same paleosurface (Fig. VI-16B). Whether the proposed geomorphological models and peneplanation surface ages are valid for the central areas of the Guiana shield cannot be decided from our data. In order to answer this question, paleosurfaces from the inner area of the Guiana shield would be needed to be studied. In any case our results show that the landscape of the Cayenne area contains very old features and apart from some erosion likely did not change a lot during the last Myr.

The data from Petit Connétable Island allow to draw new conclusions of the geological evolution of the island and yields some information of the subsidence of the Guiana basin. Our data reveals that the lateritic duricrust of Petit Connétable has a bauxitic signature. New results show equally the presence of a well-developed bauxitic profile on the nearby island of Grand Connétable (C. Gautheron, pers. Communication). While bauxites often occur nearby the sea, they cannot form inside the sea (literally inside the water). This means that bauxitization of the Petit Connétable duricrust must have happened before the duricrust was drowned into the sea.

The youngest aliquot in the Connétable duricrust yields an age of 2.7 ± 0.4 Ma. This means that the position of the island relative to the sea-level was higher until that time. Whether drowning occurred due to subsidence of the Guiana basin or due to eustatic sea level rise is difficult to determine. The global sea level fluctuated a lot during the last 3 Ma in relation with the glaciation cycles (Bartoli et al., 2005; Miller et al., 2005). However the glaciations lead to rather short scale changes (10s to 100s kyr). Relative to modern day sea-level, mean global sea-levels were similar or lower since the Pliocene. However, the relative sea-level in the Guiana basin changed a lot but was predominantly higher since the beginning of the Pliocene, with exception of the Holocene (Fig. VI-15 and Wong 1986 and references therein). According to Wong (1986) the relative sea-level (which was lower before) reached its current position in the Guiana basin ca. 6000 yr. B. P. This means that without much vertical movement of the Connétable island, lateritization could even have continued during sea-level lowstands of the last 3 Ma and final drowning could have been very recent due to global sea level rise related to the current interglacial. Nevertheless as the relative sea-level was generally higher since the Pliocene, a geodynamic explication of the drowning of Connétable is also imaginable. Since ca. 2.4 Ma important amounts of sediments coming from the Andes have been deposited in the Amazon fan east of the Guiana shield, leading to a sediment pile of totally up to 10km (Lopez, 2001; Figueiredo et al., 2007; Figueiredo et al., 2009). Several authors have proposed that the sediment loading pushed down the shelf and oceanic plate and possible led to an uplift of the continental margin (Driscoll and Karner, 1994; Rodger et al., 2006; Figueiredo et al., 2009; Watts et al., 2009). Watts et al. (2009) explain that stresses and flexure created through the load of the Amazon fan extend for some hundreds of kilometers. Increased subsidence of the Guiana basin related to sediment loading from the Amazon fan sediments during the last 2-3 Ma could have brought the Connétable islands to their current vertical position. Prograding Pliocene and Pleistocene sediments in the Guiana basin described by Sapin et al., (2016) could be related to this process. However, the position of the Connétable islands close to the coast and overall west of the Amazon fan do not necessarily suggest an influence of the Amazon fan on the subsidence of Connétable. Thus, we cannot decide which of the aforementioned mechanisms lead to the drowning of the lateritic duricrust of Petit Connétable, but the weathering data indicates that this process happened since 2-3 Ma.

French Guiana laterite and bauxite evolution through time and space

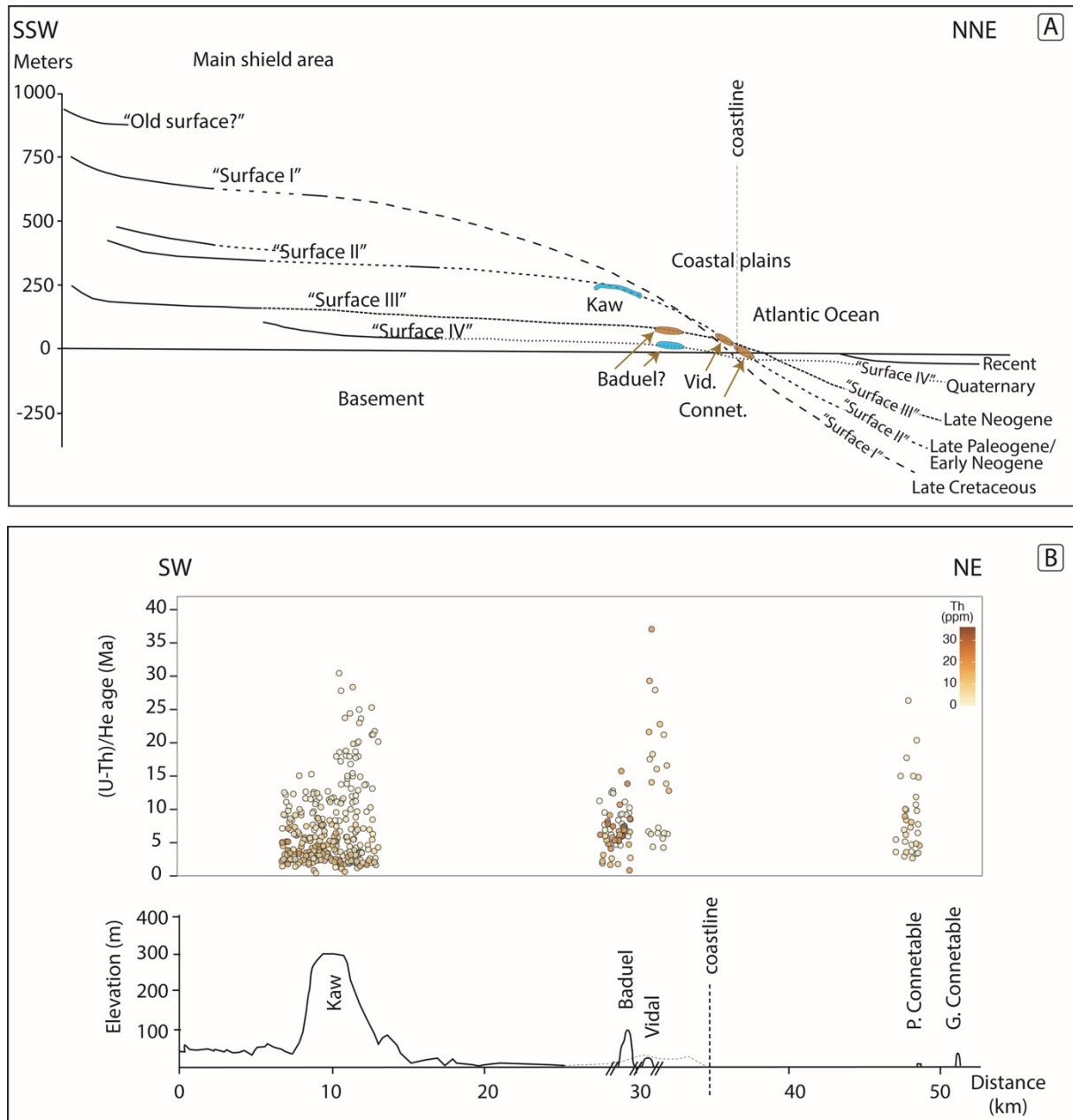


Figure VI-16: (A) Geomorphological model of the Guiana shield from McConnell, (1968) and Blancaneaux (1981) with the planation surfaces proposed for the Guianas. Elevations are strongly exaggerated. Proposed ages are on the right hand side. The top of Kaw mountain is suggested to belong to "Surface II", whereas Baduel and other low elevation hills are proposed to belong to "Surface IV" according to Blancaneaux (1981) and Choubert, (1957) (marked in blue). While the model makes sense for Kaw mountain this is not the case for Baduel. Orange ellipses shows how the new ages obtained for Baduel, Vidal and Connettable could fit into the proposed model with Baduel corresponding to "Surface III" and Vidal and Connettable corresponding to "Surface II" as Kaw mountain. (B) shows a schematic cross section from Kaw to Connettable. Note that Baduel and Vidal do not lie on this cross-section and were added according to their position relative to the coast. Obtained ages including those from Heller et al. (2022) are represented for the four studied sites. Note that for better visualization the data is plotted with a gentle x-spread and ages at Kaw were plotted separately for the northern and southern flank. Color of the datapoints relates to Th concentration which tends to be higher for bauxitic subsamples.

VI.7 Conclusions

This study shows that weathering in French Guiana (Cayenne area, Petit Connétable island, Kaw) goes back to the Miocene and Oligocene, possibly even to the late Eocene and is thus much older than previously proposed by some authors. New mineralogical and geochemical bulk data coupled to geochronological data from Mount Baduel allow to establish an evolution model for the bauxitic-lateritic profile of Mount Baduel which shows secondary bauxitization of a previously ferruginous lateritic profile. This process leads to the coexistence of both bauxitic and ferruginous duricrusts in the Baduel profile. The data from the three studied sites (Baduel, Vidal and Connétable) record a similar weathering history when compared to the lateritic cover of the nearby Kaw mountain in French Guiana (Heller et al. 2022) and Brownsberg mountain in Suriname (Ansart, 2022). The results indicate that Oligocene weathering was widespread in the area and happened on top of surfaces which nowadays have different elevations. Furthermore they show that Neogene bauxitization shown for Kaw by Heller et al. (2022) was a regional phenomenon and probably generated by climatic forcing. The data implicate that a too simplified geomorphologic model resumed as “high elevations correspond to old planation surfaces” is not valid in the area, but a coastal monocline leading to convergence and eventual flip of the surfaces near the coast could account for the observed pattern.

References

- Aleva G. J. J. (1984) Lateritization, bauxitization and cyclic landscape development in the Guiana Shield. In *Bauxite* (ed. L. Jacob Jr). A.I.M.E, New York, USA. pp. 297–318.
- Allard T., Gautheron C., Bressan Riffel S., Balan E., Soares B. F., Pinna-Jamme R., Derycke A., Morin G., Bueno G. T. and do Nascimento N. (2018) Combined dating of goethites and kaolinites from ferruginous duricrusts. Deciphering the Late Neogene erosion history of Central Amazonia. *Chem. Geol.* **479**, 136–150.
- Ansart C. (2022) Evolution des latérites du bouclier Amazonien, rapport de Mineralogie, géochronologie et géochimie. Université Paris Saclay, France.
- Baker P. A., Fritz S. C., Silva C. G., Rigsby C. A., Absy M. L., Almeida R. P., Caputo M., Chiessi C. M., Cruz F. W., Dick C. W., Feakins S. J., Figueiredo J., Freeman K. H., Hoorn C., Jaramillo C., Kern A. K., Latrubesse E. M., Ledru M. P., Marzoli A., Myrbo A., Noren A., Piller W. E., Ramos M. I. F., Ribas C. C., Trnadade R., West A. J., Wahnfried I. and

- Willard D. A. (2015) Trans-Amazon Drilling Project (TADP): Origins and evolution of the forests, climate, and hydrology of the South American tropics. *Sci. Drill.* **20**, 41–49.
- Bardossy G. and Aleva G. J. J. (1990) *Lateritic Bauxites*. Developmen., Elsevier Science, Amsterdam, The Netherlands.
- Bartoli G., Sarnthein M., Weinelt M., Erlenkeuser H., Garbe-Schönberg D. and Lea D. W. (2005) Final closure of Panama and the onset of northern hemisphere glaciation. *Earth Planet. Sci. Lett.* **237**, 33–44.
- Beauvais A. (2009) Ferricrete biochemical degradation on the rainforest-savannas boundary of Central African Republic. *Geoderma* **150**, 379–388.
- Beck H. E., Zimmermann N. E., McVicar T. R., Vergopolan N., Berg A. and Wood E. F. (2018) Present and future köppen-geiger climate classification maps at 1-km resolution. *Sci. Data* **5**, 1–12.
- Berar J. F. and Baldinozzi G. (1998) XND code: From X-ray laboratory data to incommensurately modulated phases. *Rietveld Model. complex Mater. CPD Newsl.* **20**, 3–5.
- Blancaneaux P. (1981) *Essai sur le milieu naturel de la Guyane Française.*, Paris.
- Bovolo C. I., Pereira R., Parkin G., Kilsby C. and Wagner T. (2012) Fine-scale regional climate patterns in the Guianas, tropical South America, based on observations and reanalysis data. *Int. J. Climatol.* **32**, 1665–1689.
- Carvalho A., Boulangé B., Melfi A. J. and Lucas Y. (1997) *Brazilian Bauxites*. eds. A. Carvalho, B. Boulangé, A. J. Melfi, and Y. Lucas, USP, FAPESP, ORSTOM, São Paulo, Paris.
- Choubert B. (1957) *Essai sur la morphologie de la Guyane.*, Paris.
- Coates A. G. (1992) Closure of the Isthmus of Panama: the near-shore marine record of Costa Rica and western Panama. *Geol. Soc. Am. Bull.* **104**, 814–828.
- Cordani U. G. and Teixeira W. (2007) Proterozoic accretionary belts in the Amazonian Craton. In *4-D Framework of Continental Crust: Geological Society of America Memoir 200* (eds. R. D. J. Hatcher, M. P. Carlson, J. H. McBride, and J. . Martínez-Catalán). Geological Society of America, Boulder, CO. pp. 297–320.
- Damuth J. E. and Flood R. D. (1985) Amazon Fan, Atlantic Ocean. In *Submarine Fans and Related Turbidite Systems* (ed. A. H. Bouma). Springer, New York, USA.
- Delor C., Lahondère D., Egal E., Lafon J. M., Cocherie A., Guerrot C., Rossi P., Truffert C., Théveniaut H., Phillips D. and Avelar V. G. de (2003) Transamazonian crustal growth

- and reworking as revealed by the 1:500,000-scale geological map of French Guiana (2nd edition). *Geol. la Fr.* **2-3-4**, 5–57.
- Derycke A., Gautheron C., Barbarand J., Bourbon P., Aertgeerts G., Simon-Labric T., Sarda P., Pinna-Jamme R., Boukari C. and Haurine F. (2021) French Guiana margin evolution: From Gondwana break-up to Atlantic opening. *Terra Nov.*, 1–8.
- Driscoll N. W. and Karner G. D. (1994) Flexural deformation due to Amazon Fan loading: A feedback mechanism affecting sediment delivery to margins. *Geology* **22**, 1015–1018.
- Figueiredo J., Hoorn C., van der Ven P. and Soares E. (2009) Late Miocene onset of the Amazon River and the Amazon deep-sea fan: Evidence from the Foz do Amazonas Basin. *Geology* **37**, 619–622.
- Figueiredo J. J. P., Zalán P. V. and Soares E. F. (2007) Bacia da foz do Amazonas. *Bol. Geociencias da Petrobras* **15**, 299–309.
- Girard J. P., Freyssinet P. and Morillon A. C. (2002) Oxygen isotope study of Cayenne duricrust paleosurfaces: Implications for past climate and laterization processes over French Guiana. *Chem. Geol.* **191**, 329–343.
- Gómez J., Schobbenhaus C., Montes N. E. and Compilers (2019) *Geological Map of South America 2019. Scale 1:5 000 000.*,
- Groussin J. (2001) Le Climat Guyanais. In *Atlas illustré de la Guyane* (ed. J. Barret). Laboratoire de Cartographie de la Guyane; Institut d'Enseignement Supérieur de Guyane. pp. 46–49.
- Hammen van der T. and Wymstra T. A. (1964) A Palynological study on the Tertiary and Upper Cretaceous of British Guiana. *Leidse Geol. Meded.* **30**, 183–241.
- Haywood A. M., Hill D. J., Dolan A. M., Otto-Bliesner B. L., Bragg F., Chan W. L., Chandler M. A., Contoux C., Dowsett H. J., Jost A., Kamae Y., Lohmann G., Lunt D. J., Abe-Ouchi A., Pickering S. J., Ramstein G., Rosenbloom N. A., Salzmann U., Sohl L., Stepanek C., Ueda H., Yan Q. and Zhang Z. (2013) Large-scale features of Pliocene climate: Results from the Pliocene Model Intercomparison Project. *Clim. Past* **9**, 191–209.
- Heller B. M., Riffel S. B., Allard T., Morin G., Roig J.-Y., Couëffé R., Aertgeerts G., Derycke A., Ansart C., Pinna-Jamme R. and Gautheron C. (2022) Reading the climate signals hidden in bauxite. *Geochim. Cosmochim. Acta* **323**, 40–73.
- Hoorn C., Bogotá-A G. R., Romero-Baez M., Lammertsma E. I., Flantua S. G. A., Dantas E. L., Dino R., do Carmo D. A. and Chemale F. (2017) The Amazon at sea: Onset and stages

- of the Amazon River from a marine record, with special reference to Neogene plant turnover in the drainage basin. *Glob. Planet. Change* **153**, 51–65.
- Hoorn C., Wesselingh F. P., ter Steege H., Bermudez M. A., Mora A., Sevink J., Sanmartín I., Sanchez-Meseguer A., Anderson C. L., Figueiredo J. P., Jaramillo C., Riff D., Negri F. R., Hooghiemstra H., Lundberg J., Stadler T., Särkinen T. and Antonelli A. (2010) Amazonia Through Time : Andean Uplift, Climate Change, Landscape Evolution and Biodiversity. *Science* (80-). **330**, 927–931.
- King L. C. (1962) *Morphology of the Earth.*, Oliver and Boyd Publ. House, London.
- Lariviere J. P., Ravelo A. C., Crimmins A., Dekens P. S., Ford H. L., Lyle M. and Wara M. W. (2012) Late Miocene decoupling of oceanic warmth and atmospheric carbon dioxide forcing. *Nature* **486**, 97–100.
- Lima M. da G. (2008) A História do Intemperismo na Província Borborema Oriental, Nordeste do Brasil. Universidade Federal do Rio Grande do Norte, Natal, Brazil.
- Longueville F., Aertgeerts G. and Lanson M. (2021) *Géologie structurale et cartographie des fonds marins des îles de la réserve du Grand- Connétable en Guyane.*,
- Lopez M. (2001) Architecture and depositional pattern of the quaternary deep-sea fan of the Amazon. *Mar. Pet. Geol.* **18**, 479–486.
- McConnell R. B. (1968) Planation Surfaces in Guyana. *Geogr. J.* **134**, 506–520.
- Mendes A. C., Truckenbrod W. and Nogueira A. C. R. (2012) Análise faciológica da formação Alter do Chão (Cretáceo, Bacia do Amazonas), próximo à cidade de Óbidos, Pará, Brasil. *Rev. Bras. Geociencias* **42**, 39–57.
- Miller K. G., Kominz A., Browning J. V, Wright J. D. and Mountain G. S. (2005) The Phanerozoic record of sea level change. *Science* (80-). **310**, 1293–1298.
- Monsels D. A. and Van Bergen M. J. (2019) Bauxite formation on Tertiary sediments in the coastal plain of Suriname. *J. South Am. Earth Sci.* **89**, 275–298.
- Monteiro H. S., Vasconcelos P. M., Farley K. A., Spier C. A. and Mello C. L. (2014) (U-Th)/He geochronology of goethite and the origin and evolution of cangas. *Geochim. Cosmochim. Acta* **131**, 267–289.
- Monteiro H. S., Vasconcelos P. M. P., Farley K. A. and Lopes C. A. M. (2018) Age and evolution of diachronous erosion surfaces in the Amazon: Combining (U-Th)/He and cosmogenic ³He records. *Geochim. Cosmochim. Acta* **229**, 162–183.

- Patterson S. H., Kurtz H. F., Olson J. C. and Neeley C. L. (1994) *World Bauxite Resources - Geology and Resources of Aluminum*. U.S. Geolo., U.S. Geological Survey, Washington.
- Piper D. J. W., Pirmez C., Manley. P. L., Long D., Flood R. D., Normark W. R. and Showers W. (1997) Mass-transport deposits of the Amazon Fan. *Proc. Ocean Drill. Program, 155 Sci. Results* **155**.
- Prasad G. (1983) A review of the early Tertiary bauxite event in South America, Africa and India. *J. African Earth Sci.* **1**, 305–313.
- Retallack G. J. (2010) Lateritization and bauxitization events. *Econ. Geol.* **105**, 655–667.
- Rodger M., Watts A. B., Greenroyd C. J., Peirce C. and Hobbs R. W. (2006) Evidence for unusually thin oceanic crust and strong mantle beneath the Amazon Fan. *Geology* **34**, 1081–1084.
- Rudnick R. L. and Gao S. (2013) *Composition of the Continental Crust*. 2nd ed., Elsevier Ltd.
- dos Santos Albuquerque M. F., Horbe A. M. C. and Danišik M. (2020) Episodic weathering in Southwestern Amazonia based on (U–Th)/He dating of Fe and Mn lateritic duricrust. *Chem. Geol.* **553**, 119792.
- Sapin F., Davaux M., Dall’asta M., Lahmi M., Baudot G. and Ringenbach J.-C. (2016) Post-rift subsidence of the French Guiana hyper-oblique margin: From rift-inherited subsidence to Amazon deposition effect. *Geol. Soc. Spec. Publ.* **431**, 125–144.
- Schellmann W. (1994) Geochemical differentiation in laterite and bauxite formation. *Catena* **21**, 131–143.
- Schulze D. G. (1984) The influence of aluminium on iron oxides. VIII. Unit-cell dimensions of Al-substituted goethites and estimation of Al from them. *Clays Clay Miner.* **32**, 36–44.
- Shuster D. L., Farley K. A., Vasconcelos P. M., Balco G., Monteiro H. S., Waltenberg K. and Stone J. O. (2012) Cosmogenic ³He in hematite and goethite from Brazilian “canga” duricrust demonstrates the extreme stability of these surfaces. *Earth Planet. Sci. Lett.* **329–330**, 41–50.
- Shuster D. L., Vasconcelos P. M., Heim J. A. and Farley K. A. (2005) Weathering geochronology by (U–Th)/He dating of goethite. *Geochim. Cosmochim. Acta* **69**, 659–673.
- Sundell K. E., Saylor J. E., Lapen T. J. and Horton B. K. (2019) Implications of variable late Cenozoic surface uplift across the Peruvian central Andes. *Sci. Rep.* **9**, 1–12.
- Tardy Y. (1997) *Petrology of Laterites and Tropical Soils.*, Balkema, Rotterdam, The Netherlands.

- Tardy Y. and Nahon D. (1985) Geochemistry of laterites, stability of Al-goethite, Al-hematite, and Fe³⁺-Kaolinite in bauxites and ferricretes: an approach to the mechanism of concretion formation. *Am. J. Sci.* **285**, 865–903.
- Tardy Y. and Roquin C. (1998) *Dérive des continents paléoclimats et altérations tropicales.*, BRGM, Orléans, France.
- Théveniaut H. and Freyssinet P. (1999) Paleomagnetism applied to lateritic profiles to assess saprolite and duricrust formation processes: The example of Mont Baduel profile (French Guiana). *Palaeogeogr. Palaeoclimatol. Palaeoecol.* **148**, 209–231.
- Théveniaut H. and Freyssinet P. (2002) Timing of lateritization on the Guiana Shield synthesis of paleomagnetic results. *Palaeogeogr. Palaeoclimatol. Palaeoecol.* **178**, 91–117.
- Valeton I. (1972) *Bauxites. Developmen.*, Elsevier, Amsterdam, The Netherlands.
- Valeton I. (1983) Palaeoenvironment of lateritic bauxites with vertical and lateral differentiation. *Geol. Soc. Spec. Publ.* **11**, 77–90.
- Vanderhaeghe O., Ledru P., Thiéblemont D., Egal E., Cocherie A., Tegye M. and Milési J. P. (1998) Contrasting mechanism of crustal growth. Geodynamic evolution of the Paleoproterozoic granite-greenstone belts of French Guiana. *Precambrian Res.* **92**, 165–193.
- Vasconcelos P. M., Reich M. and Shuster D. L. (2015) The paleoclimatic signatures of supergene metal deposits. *Elements* **11**, 317–322.
- Vasconcelos P. M., Renne P. R., Brimhall G. H. and Becker T. A. (1994) Direct dating of weathering phenomena by ⁴⁰Ar-³⁹Ar and K-Ar analysis of supergene K-Mn oxides. *Geochim. Cosmochim. Acta* **58**, 1635–1665.
- Vermeesch P., Seward D., Latkoczy C., Wipf M., Günther D. and Baur H. (2007) α-Emitting mineral inclusions in apatite, their effect on (U-Th)/He ages, and how to reduce it. *Geochim. Cosmochim. Acta* **71**, 1737–1746.
- Watts A. B., Rodger M., Peirce C., Greenroyd C. J. and Hobbs R. W. (2009) Seismic structure, gravity anomalies, and flexure of the amazon continental margin, NE Brazil. *J. Geophys. Res. Solid Earth* **114**, 1–23.
- Westerhold T., Marwan N., Drury A. J., Liebrand D., Agnini C., Anagnostou E., Barnet J. S. K., Bohaty S. M., De Vleeschouwer D., Florindo F., Frederichs T., Hodell D. A., Holbourn A. E., Kroon D., Laurentano V., Littler K., Lourens L. J., Lyle M., Pälike H., Röhl U., Tian J., Wilkens R. H., Wilson P. A. and Zachos J. C. (2020) An astronomically dated record of

Earth's climate and its predictability over the last 66 million years. *Science* (80-.). **369**, 1383–1388.

Wong T. (1994) The Paleocene-Eocene succession in the Guiana Basin. *Bull. la Société belge Géologie* **T.103**, 281–291.

Wong T. E. (1986) Outline of the stratigraphy and the geological history of the Suriname coastal plain. *Geol. en Mijnb.* **65**, 223–241.

Wong T. E., de Kramer R., de Boer P. L., Langereis C. and Sew-A-Tjon J. (2009) The influence of sea-level changes on tropical coastal lowlands; the Pleistocene Coropina Formation, Suriname. *Sediment. Geol.* **216**, 125–137.

Wymstra T. A. (1971) The palynology of the Guiana coastal basin. University of Amsterdam.

Zachos J. C., Dickens G. R. and Zeebe R. E. (2008) An early Cenozoic perspective on greenhouse warming and carbon-cycle dynamics. *Nature* **451**, 279–283.

VII EPR spectroscopic study of kaolinites from two lateritic profiles of the northeastern and eastern Guiana shield (Kaw mountain, French Guiana and Tucano mine, Amapá, Brazil)

Abstract

We present electron paramagnetic resonance (EPR) spectroscopy data from 28 purified kaolinite fractions from two lateritic profiles developed on top of Paleoproterozoic schists of the Guiana shield. The profiles correspond to a 75 m drill core from the bauxitic-lateritic cover of Kaw mountain in French Guiana, where the record of tropical weathering traces back to at least the Oligocene, and to a 120 m deep profile, sampled in the Tucano gold mine in northern Brazil, where ferruginous duricrusts record weathering since the Late Cretaceous or Early Paleogene. Samples from both profiles were characterized using standard mineralogical and geochemical techniques and kaolinite was purified from 16 and 12 samples from Kaw and Tucano, respectively. The Gaité index, which expresses a degree of crystalline disorder, was measured from the EPR signal of structural Fe^{3+} . It ranges from 4 to 24, i.e. close to the maximum range known for natural kaolinites. It indicates that kaolinite formed under nearly identical conditions throughout the 75 m of the Kaw profile, whereas results from the Tucano mine suggest different formation conditions for the kaolinites from the saprolite, the soil and the duricrust. The concentration of structural Fe^{3+} in the studied kaolinites ranges from ca. 430 to 2450 ppm and is independent of the bulk Fe_2O_3 compositions of the samples. In the strongly lateritized Kaw profile, kaolinite Fe^{3+} concentrations show correlations with the SiO_2 content and the Index of Lateritization of the bulk samples. Quantification of radiation-induced defects in kaolinite was complicated by a strong vanadyl interference in the Kaw samples but spectra correction by subtraction of a reference vanadyl signal yields acceptable results, allowing one to fit artificial dosimetry curves obtained through He^+ -particle-irradiation and subsequently estimate the paleodoses. Dosimetry curves of 22 kaolinite samples indicate different dose accumulation behaviors for nearly all samples with resulting paleodoses ranging from 70 to 266 kGy and from 15 to 510 kGy for Kaw and Tucano, respectively. Preliminary age without usual corrections (e.g. U microscopic mapping, average water content, impact of quartz) could be estimated for all irradiated samples. The results indicate kaolinite ages of several Ma to tens of Ma, which are in the same order of magnitude as (U-Th)/He ages obtained on supergene

hematite and goethite from the duricrusts of both profiles. For the Kaw profile, the oldest ages, which exceed those of the iron (oxyhydr)oxides, are found in the upper saprolite (< 35 m depth). For the Tucano mine, the preliminary age results suggest that old kaolinite was mostly preserved in the lower saprolite whereas matrix kaolinites at the top of the profile were rejuvenated relatively recently. Kaolinite captured in the lateritic duricrust was protected from this rejuvenation event, which post-dates the youngest hematite and goethite (U-Th)/He ages.

VII.1 Introduction

Kaolinite is a phyllosilicate widespread in the weathering environment as it forms by intense weathering of aluminous silicates such as feldspars or micas and is extremely stable in numerous conditions at the Earth's surface (Nahon, 1991). In ferruginous lateritic weathering profiles, kaolinite is present in all horizons, from the bottom, at the interface with the parental rock, up to the ferruginous duricrust and the topsoil (Tardy, 1997). Under bauxitic conditions, characterized by very humid climatic regimes and strong drainage, kaolinite starts to get instable and is dissolved (Tardy and Nahon, 1985; Bardossy and Aleva, 1990; Schellmann, 1994). While most of the silica is generally released during in this process and aluminum commonly reprecipitates in form of gibbsite and aluminous iron oxides, owing to the relatively low solubility of these phases, some of the mobilized Al and Si may also reaccumulate to form amorphous phases or crystalline kaolinite in lower parts of the profile (Schellmann, 1994). Kaolinite is thus an important component of the lateritic weathering system, but its very small grain size (ca. 100 μm to <2 μm) limits the number of methods that can be used to study such grains (see e.g. Varajao et al., 2001; Beauvais and Bertaux, 2002). Moreover, owing to the composition of kaolinite, no "classical" radiometric geochronological method can be applied to this clay mineral, restricting the possibilities to date it.

Intensive studies over the last three decades have shown that electron paramagnetic resonance spectroscopy (EPR) is a very sensitive method to characterize kaolinite (Gaite et al., 1993; Allard et al., 1994; Clozel et al., 1994; Balan et al., 1999). The EPR signal allows the detection, characterization and quantification of small impurities such as structural Fe^{3+} replacing Al^{3+} ions and thus yields information on the structural ordering and the crystal chemistry of the kaolinite (Gaite et al., 1993; Gaite et al., 1997; Balan et al., 1999; Balan et al., 2000). Furthermore, the EPR spectrum of kaolinite enables the quantification of radiation-induced defects (RIDs), that are electron holes on oxygen atoms in the kaolinite structure

EPR spectroscopic study of kaolinites from two lateritic profiles of the northeastern and eastern Guiana shield (Kaw mountain, French Guiana and Tucano mine, Amapá, Brazil) produced by ambient radioactivity (Allard et al., 1994; Clozel et al., 1994; Allard et al., 2012). Four types of radiation induced defects have been described, including the so-called A-, A'- B-centers, and one of them, the A-center, has been shown to be stable over geologic timescales ($T_{1/2}$ ca. 10^{12} a) as extrapolated to low temperature from the Earth's surface (Allard et al., 1994; Clozel et al., 1994; Allard et al., 2012). This means that these defects accumulate over the lifetime of the kaolinite, allowing to trace past radionuclide migration (Allard and Muller, 1998) and to estimate the defect accumulation duration, i.e. the age of formation of the kaolinite (Balan et al., 2005). For the latter application, the absolute radiation dose received by the kaolinite (paleodose) and the ambient dose rate produced by the surrounding radioactive elements (notably U, Th and K) need to be determined. Since the first study by Balan et al., (2005) the method has been refined recently and applied several times (Allard et al., 2018; Mathian et al., 2019; Allard et al., 2020; Mathian et al., 2020). Different types of kaolinite may have different dosimetry parameters and thus systematic artificial irradiation of each sample should be preferred to estimate the paleodose. In addition, several corrections should be applied on the dose rate to determine meaningful ages. These corrections concern, (i) the U spatial distribution assessed from induced-fission tracks method which requires thermal neutron irradiations (ii) the degree of aperture of the radioactive system assessed by gamma spectrometry, (iii) the average water content, (iv) a balance of dose rate derived from the geometry of quartz grain volume.

This study presents an EPR investigation of purified kaolinite fractions from two lateritic profiles of the Guiana shield. Ferruginous duricrusts of both profiles have been previously studied using (U-Th)/He dating of supergene hematite and goethite yielding important age constraints on the weathering history of the two sites (Heller et al., 2022 and Chapter V). However, that information is restricted to the duricrusts at the top lateritic profiles. Kaolinite, which is present throughout the near totality of the two profiles, will potentially bring important insight into the formation and evolution of the entire sampled range of the profiles and is therefore the target of this study.

The two studied profiles correspond to a 75 m drill core from the bauxitic-lateritic cover of Kaw mountain in French Guiana, where tropical weathering traces back to at least the Oligocene (Heller et al., 2022) and a 120 m deep profile sampled in the open pit Tucano gold mine in the Northern Brazilian state of Amapá, where ferruginous duricrusts record weathering since the Late Cretaceous or Early Paleogene (Chapter V). The crystal chemistry and structural

properties of purified kaolinite samples were explored by analysis of the structural Fe³⁺ EPR signal, which is sensitive to the conditions of formation of the clay. In addition, owing to strong interferences from the vanadyl signal and in some case baseline due to iron oxides, we tested a method of fitting the spectra with an inhouse code of Hamiltonian calculation to determine the concentration of A-centers. As this approach appeared too difficult to implement for some samples, we used a simplified approach that allowed us to satisfactorily determine paleodoses in the whole profiles together with preliminary ages that provide the base for further geochronological investigations.

VII.2 Background

VII.2.1 EPR spectroscopy

Electron resonance paramagnetic spectroscopy is a method based on the interaction of microwaves with material under a magnetic field. The absorbance of incident microwaves at a stable frequency is measured at the resonance conditions under a changing magnetic field. The EPR spectrum represents the derivative intensity of the absorbance spectrum. The effective spectroscopic factor g can be derived from the resonance condition: $h\nu = g\beta H$ where h is the Planck constant, ν is the hyperfrequency (GHz), β the Bohr Magneton and H the magnetic field. It corresponds to a tensor and may present an anisotropy specific of the paramagnetic species in its crystalline environment. For more details on the methods, see Chapter II.

VII.2.2 Kaolinite and its structure

Kaolinite ($\text{Al}_2\text{Si}_2\text{O}_5(\text{OH})_4$) is a layered clay mineral with a structure composed of octahedral and tetrahedral sheets which host Al^{3+} and Si^{4+} , respectively (Fig. VII-1). Al^{3+} can be substituted by Fe^{3+} and concentrations of hundreds to thousands of ppm Fe^{3+} can be found in natural kaolinite samples (Balan et al., 2000). Furthermore the Al^{3+} ions can be replaced by divalent cations such as Fe^{2+} , Mg^{2+} or Mn^{2+} , which creates a local charge imbalance.

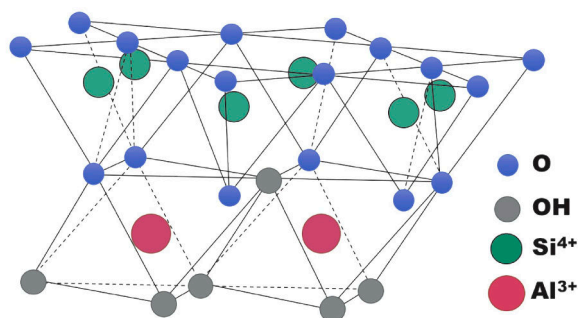


Figure VII-1: Schema of the crystal structure of kaolinite composed of a tetrahedra layer hosting Si^{4+} and an octahedra layer hosting Al^{3+} . Note that the size of the atoms is not scaled.

VII.2.3 The EPR spectrum of kaolinite

VII.2.3.1 Structural Fe^{3+}

Figure VII-2A represents a typical EPR spectrum of a natural kaolinite sample, GB1 (Cases et al., 1982), used as internal standard. Note that the absolute magnetic field values of the EPR spectra depend on the incident frequency set at the resonance and unless the spectra are corrected for the frequency (generally not done for the spectra presented therein), the x-values might differ. Note however, that all spectra presented here and measured for this thesis were acquired in the same conditions (same cavity, room temperature and glass tubes) and the frequency differences between samples are generally small (due to different volumes of sample for instance).

The EPR spectrum of the GB1 kaolinite is characterized by a first small peak around $g=8.6$ (here at ca. 900 gauss), a triplet in the area around $g=4.3$ and a doublet at $g=2$ (here in the range of 3500 gauss) (Fig. VII-2A). The first part of the signal is related to paramagnetic Fe^{3+} ions substituted for Al^{3+} in the kaolinite structure (here referred to as structural Fe) and can show additional weak peaks in well-ordered samples (not shown here). According to Gaité et al. (1993) and Balan et al. (1999) the structural Fe^{3+} represents two contributions, referred to as $\text{Fe}^{3+}_{(I)}$ and $\text{Fe}^{3+}_{(II)}$ (Fig. VII-2A). The relative contribution of the $\text{Fe}^{3+}_{(II)}$ signal decreases as a function of disorder in natural kaolinites as it is related to sites within low-defect kaolinite. In contrast, the $\text{Fe}^{3+}_{(I)}$ signal is produced by changes in the site symmetry due to the random distribution of vacant octahedral sites in successive layers (Balan et al., 1999). This difference between the $\text{Fe}^{3+}_{(II)}$ and the $\text{Fe}^{3+}_{(I)}$ signals allows one to estimate the local crystalline disorder of the kaolinite from the EPR spectra (Gaité et al., 1997). The structural iron can also be used to determine contributions of endmembers (if any can be distinguished) with contrasting

EPR spectroscopic study of kaolinites from two lateritic profiles of the northeastern and eastern Guiana shield (Kaw mountain, French Guiana and Tucano mine, Amapá, Brazil) degrees of disorder by linear decomposition of the EPR spectra and imply different conditions of formation within a same profile (Balan et al., 2007). Furthermore it is possible to calculate the concentration of structural Fe³⁺ through double integration of the EPR signal and calibration using a kaolinite standard with known content of structural iron (Balan et al., 2000). Note that apart from the structural, paramagnetic Fe³⁺, superparamagnetic Fe³⁺, probably in form of nanometric iron oxides and oxyhydroxides might be present in the kaolinite EPR spectra. Such superparamagnetic Fe³⁺ creates large peaks in the area of g=2. Both hematite and goethite produce relatively strong signals, for more details see (Guskos et al., 2002; Carbone et al., 2005; Valezi et al., 2016).

VII.2.3.2 Radiation induced defects

The area at g=2 represents a doublet (Fig. VII-2A), present in all natural kaolinite samples studies by EPR but absent in synthetic kaolinites (Jones et al., 1974; Angel et al., 1977). The doublet corresponds to the radiation induced defects (RIDs). It is generally composed of three different components which superpose each other (Fig. VII-2B and VII-2C). The different components are the A-center, the A' -center and the B-center. Their g-factors are $g_x = 2.001$, $g_y = 2.006$, $g_z = 2.049$ for the A-center, $g_{//} = 2.039$ and $g_z = 2.006$ for A', and $g_x = 2.002$, $g_y = 2.02$, $g_z = 2.04$ for the B-center (Clozel et al., 1994). A fourth signal, generally not present, was recently proposed by Goodman et al. (2016). The A-center corresponds to an electron hole located on a π orbital of an oxygen atom. It shows a parallel and a perpendicular component at X-band, but Q-band (34 GHz) measurement reveals a third rhombic component (see g parameters above). It is produced by any radiation, including α , β , γ -rays and recoil nuclei and it is stable over geological periods. Its half-life time has been estimated to 10^{12} years at ambient temperature. It is annealed from 450°C (2h), the temperature where kaolinite starts to dehydroxylate (Clozel et al., 1994). The A'-center is preferentially formed by heavy ion implantation. Its thermal stability is lower that of the A-center with annealing at temperatures >400°C and at ambient condition its stability has been estimated to about 1000 years . The B-center (Fig. VII-2B and VII-2C) is most easily formed with ionizing radiations and consists of an electron hole located on an oxygen atom bound to 2 Aluminum atoms (Allard et al., 2012). Consequently it has a superhyperfine structure (see Chapter II) with 11 peaks on each principal component of the anisotropic signal (Clozel et al., 1994; Fig. VII-2C). The B-center is not stable over geological timescales. At ambient conditions its proposed lifetime is in the range of 10-100 years and it is unstable over 2 hours at temperatures >250-300°C.

EPR spectroscopic study of kaolinites from two lateritic profiles of the northeastern and eastern Guiana shield (Kaw mountain, French Guiana and Tucano mine, Amapá, Brazil)

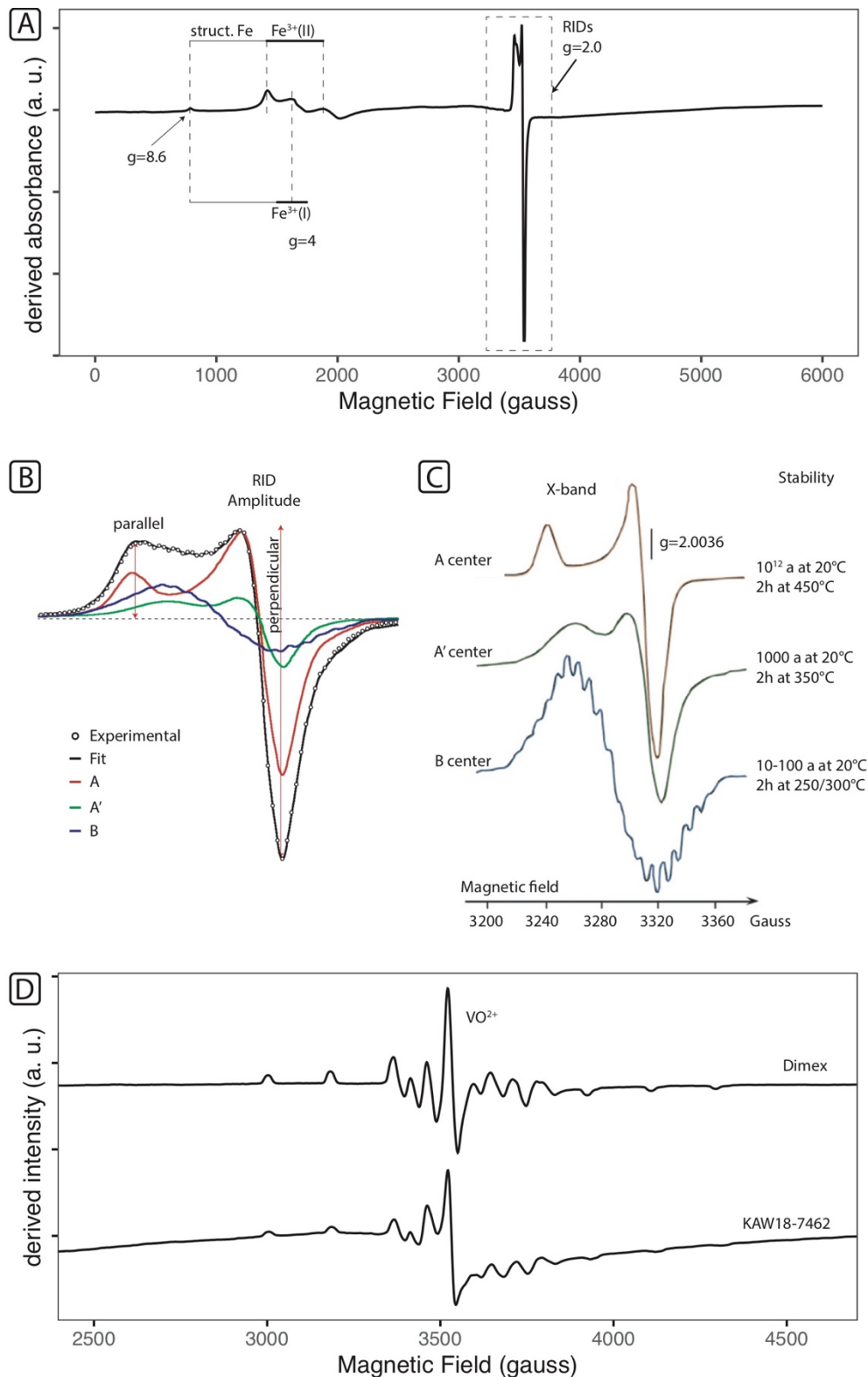


Figure VII-2: The EPR spectrum of kaolinite. (A) Total spectrum of reference kaolinite GB1 (Cases, 1982) indicating the regions of the structural Fe³⁺ and of the radiation-induced defects (RIDs). Note that the spectrum is not corrected for field shift. (B) Enlarged view of the RID area at $g=2$ for the Barrails kaolinite with linear composition of A (red), A' (green) and B (blue) centers spectra. White circles are experimental data, black dense line corresponds to the fit. (courtesy of T. Allard). (C) Isolated EPR spectra of A, A' and B centers with their stability characteristics (after Allard et al., 2012). (D) EPR spectrum of the vanadyl signal of the vanadyl-rich reference dickite Dimex (see Muller and Calas, 1993 for identification of the vanadyl signal) and sample KAW18-7462 of this study where the vanadyl signal interferes with the RID signal.

VII.2.3.1 Vanadyl

Vanadyl, VO^{2+} , is a common impurity in kaolinite (Muller and Calas, 1993). Figure VII-2D presents an EPR spectrum of a vanadyl-rich reference dickite (dickite is a kaolinite polymorph with a different stacking pattern of the dioctahedral sheets) from Mexico, named Dimex (from Wards company), similar to Nowa Ruda dickite (Premović et al., 2012). The VO^{2+} signal in dickite (and kaolinite) is located at $g=2$ and has a nearly axial hyperfine structure with outermost 8 parallel and 8 central perpendicular components. Due to their similar position at $g=2$, the VO^{2+} and RIDs signals overlap each other if both are present (Fig. VII-2D).

VII.3 Samples

For this study, kaolinite-bearing samples from two sites already studied by (U-Th)/He dating were investigated: Kaw mountain in French Guiana and the Tucano mine in Amapá, Northern Brazil. For the geological, geomorphological and climatic contexts of the two sites see Chapters IV and V, respectively.

VII.3.1 Kaw (French Guiana)

The basement of Kaw mountain belongs to the Paleoproterozoic Paramaca formation which is composed of intermediate schists representing metamorphosed volcano-sedimentary rocks. The samples investigated here were sampled from a 75 m deep drill-core drilled at the top of Kaw mountain at ca. 307 m elevation next to a place called “Camp-Caiman” (4.56897° N/ 52.21697° W). The drill-core exposes the upper 75 m of the lateritic cover and at its bottom the parent rock is still strongly weathered. Figure VII-3 shows pictures and a sketch of the drill core. The first 45 cm of the core are composed of an ochre colored soil containing pieces of a disaggregated duricrust. Note that at the beginning of the drilling a lot of water was needed and a part of the soft material of the first 1-2 m was possibly washed out. Below the soil, from ca. 0.5 to 4.8 m depth, is a lateritic-bauxitic duricrust, composed of harder pieces of variable size and blackish, red, ochre, and sometimes whitish color, which are surrounded by a soft reddish to ochre-brown matrix. Below the duricrust the material gets softer, the color gets more violet and variable and subvertical structures appear. A mottled zone *sensu stricto* is absent, but we assigned the region from 4.7 to 7.5 m to a “transition zone”. From 7.5 to 75 m the core is composed of saprolite. The saprolite has a subvertical structure (dip ca. 60°) and is generally very heterogeneous. The colors vary from violet-red to ochre brown, gray and white

EPR spectroscopic study of kaolinites from two lateritic profiles of the northeastern and eastern Guiana shield (Kaw mountain, French Guiana and Tucano mine, Amapá, Brazil) (Fig. VII-3C). The softness varies with depth, too, and sometimes a banding, foliation or crenulation is visible. A complete log of the drill-core can be found in Table E-1 of the supplementary material. 33 samples were taken from this core. During sampling it was paid attention to capture the different units of the core and to take samples in regular distances. Table VII-1 summarizes the sample description for the samples chosen after XRD analyses for geochemical analyses and kaolinite purification. Note that during sample preparation heterogeneous samples were split into two fractions, >1 mm and <1 mm, and both fractions were treated separately.

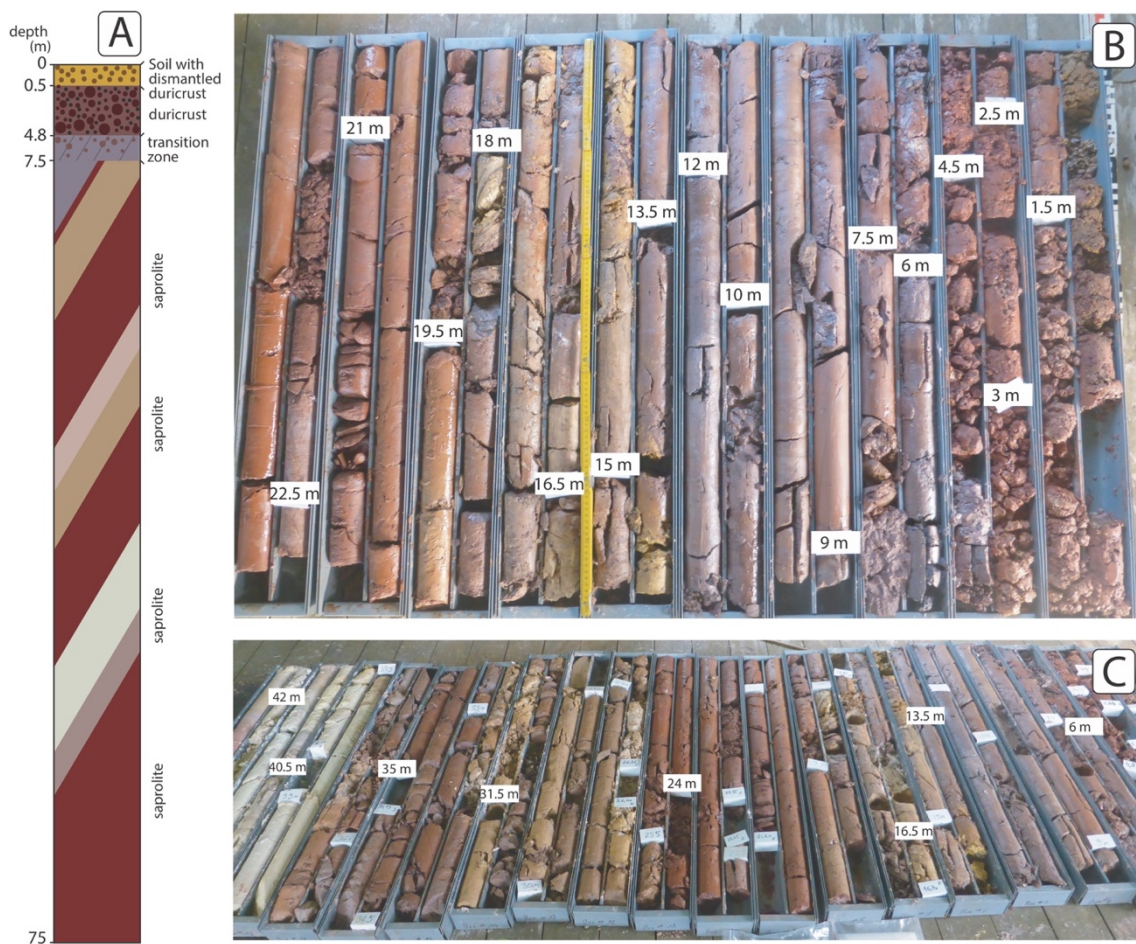


Figure VII-3: Drill core taken at Kaw mountain. (A) Schematic overview of the drillcore. Colors are simplified and only approximative. (B) upper 23 m of the drillcore with depth indications. (C) upper 43m of the drillcore showing the heterogeneity of the saprolite. Holes and missing core are (mainly) due to sampling.

EPR spectroscopic study of kaolinites from two lateritic profiles of the northeastern and eastern Guiana shield (Kaw mountain, French Guiana and Tucano mine, Amapá, Brazil)

Table VII-1. Description of the samples from the Kaw drill core. Minerals detected by XRD (Qz = quartz, Kl = kaolinite, Hm = hematite, Gt = goethite, Gi = gibbsite, Rt = rutile, An = anatase, and Ms = muscovite) were not quantified, but the x[~] x[~] indicate the estimated relative quantities ranging from few (x) to very abundant (xxxx).

Sample	depth (m)	description	Fraction	Minerals detected by XRD									#CBD cycles						
				Qz	Kl	Hm	Gt	Gi	Rt	An	Ms	purified		irradiation					
KAW18 - 10A			<1mm	xx	xx			xxx	x	x				x					5
KAW18 - 10B1	0.10		>1mm, red nodules					xxx											
KAW18 - 10B2		yellow brown soil with colluvium from duricrust	>1mm, black nodules					xxx	xxx	x									
KAW18 - 65BA	0.65		<1mm	xx	xx			xxx		x									
KAW18 - 65B2		red duricrust pieces, surrounded by clay minerals, some yellow material	>1mm	x	xx			xxx		x									
KAW18 - 275A	2.75		<1mm	xx	xx			xxx	x	x									
KAW18 - 275B		heterogenous duricrust, in pieces, with soft material	>1mm	xx	xx			xx	x	x									
KAW18 - 480A	4.80		<1mm	xxx	xx			xxx	xxx	x									6
KAW18 - 480B		red to nearly black cuirasse, more pieces, often pebble size or bigger	>1mm	xx	xxx			xxx	xxx	x									11
KAW18 - 525	5.25	softer material with less pieces, write and bordeaux, "mottled zone" / "bariolé"?																	
KAW18 - 750	7.50	saprolite with visible structures, slightly reddisher than before						xxx	xx	x									9
KAW18 - 945	9.45	saprolite with shistosity, purple gray-red fine, mm-sized layers with Fe-oxides						xxx	xx	xx									5
KAW18 - 1405	14.05	heterogeneous saprolite, reddish purple with yellow and stms white material. Some qtz grains. Shistosity less but still visible						xxxx	x	x									3
KAW18 - 2235	22.35	purple/violett saprolite, clay-rich, no shistosity, some greenish/ grey veins visible		xxx	xxx				x										3
KAW18 - 3040	30.40	brown violettish saprolite, rather massiv however some shistosity and broken into disks, rocky, locally qtz-veins																	4
KAW18 - 3135	31.35	beige white saprolite, softer than material above, + homogeneous red-beige saprolite																	2
KAW18 - 3235	32.35	white homogeneous saprolite with shistosity, clayrich																	4
KAW18 - 4217	42.17	red violett saprolite, clayrich, with shistosity, hardness: knife enters																	1
KAW18 - 4985	49.85	red violett (pretty red) saprolite with shistosity. Inclination of shistosity steeper than before, rather soft																	3
KAW18 - 6034	60.34	saprolite with shistosity, more heterogeneous material, red violett ochre stms white, qtz grains						xxx	xx	x									3
KAW18 - 6875	68.75	softer red violett saprolite, less shistosity, fine white minerals, pretty soft (however one harder piece with better shistosity in between)						xxx	xx	x									2
KAW18 - 7462	74.62			xx	xxx														2

VII.3.2 Tucano mine (Amapá, Brazil)

In the TAB2 pit of the Tucano mine, located at 0.84570° S/ 51.87718° W, both weathered schists and banded iron formations crop out (Fig. VII-4). For this study, a vertical profile of ca. 120 m was sampled in the altered schists. Sample depths and descriptions can be found in Table VII-2. The top of the profile, located at ca. 260 m a.s.l., is composed of a ochre-brown topsoil containing some pieces of disaggregated duricrust. Below the soil is a ca. 1.5-2 m thick layer composed of lateritic pisoliths of variable size which are surrounded by a fine grained matrix (Fig. VII-4B). A mottled zone is absent and a red-violet clay-rich horizon is located just below the pisolitic layer (Fig. VII-4B). The clay horizon turns quickly into a vertically dipping banded saprolite. Down to the last accessible point at ca. 140 m a.s.l., i.e. 120 m below the surface, saprolite crops out. The saprolite often shows a banding and its colors vary from red to ochre-yellow and white. Occasionally the relatively fine grained schist-saprolite is crosscut by weathered felsic dykes. Saprolite samples were taken at ca. 6.5, 16, 55, and 120 m below the surface and in two cases different lithologies were sampled at the same elevation. Moreover, a duricrust sample (TUC19-1E), taken ca. 150 m away from the profile and dated by (U-Th)/He dating, was analyzed. Sample descriptions can be found in Table VII-2.

EPR spectroscopic study of kaolinites from two lateritic profiles of the northeastern and eastern Guiana shield (Kaw mountain, French Guiana and Tucano mine, Amapá, Brazil)

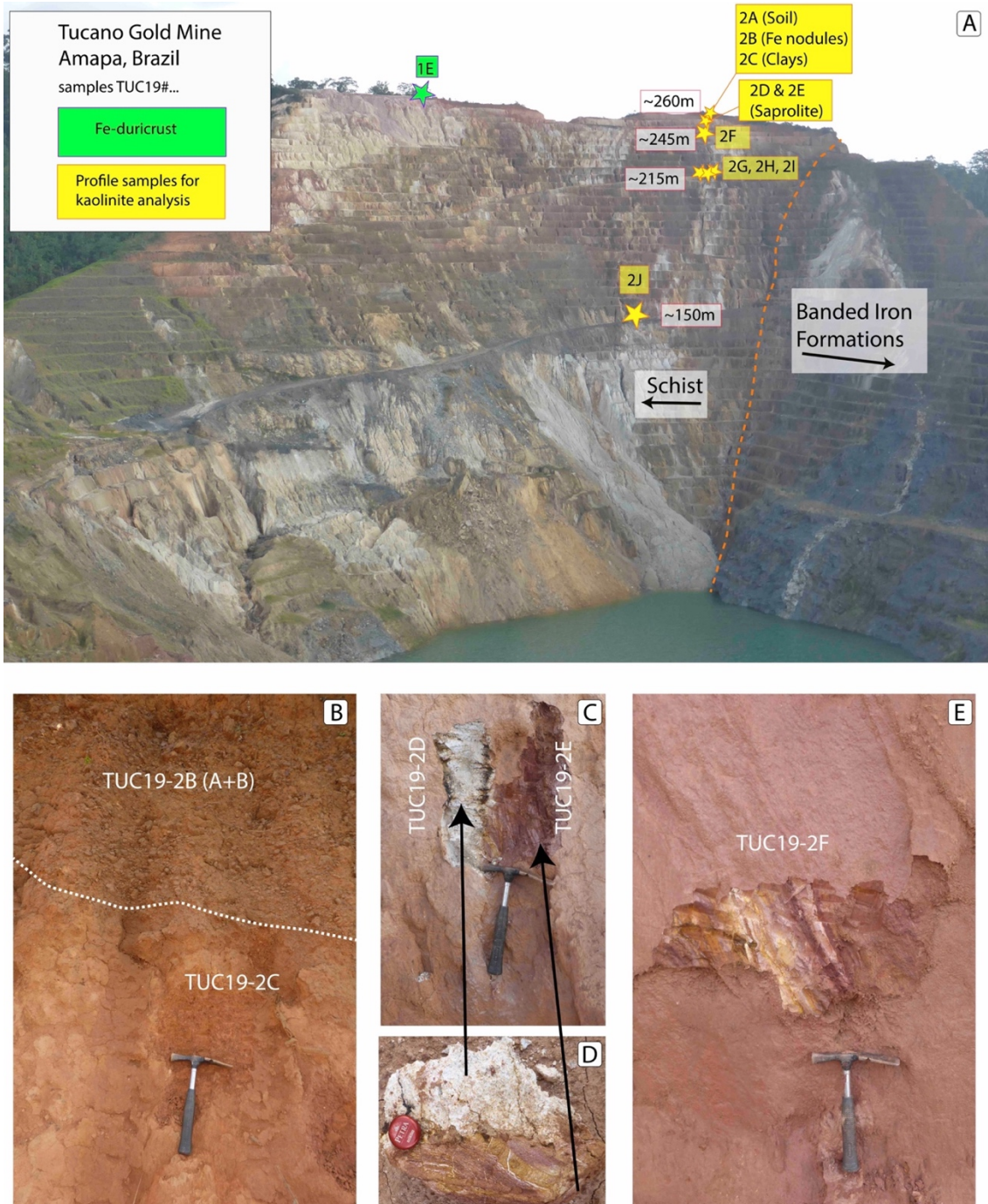


Figure VII-4: Tucano samples. (A) overview of the mining pit with indication of the sampling spots and their elevation. The dashed orange line indicates the limit between the schist and the banded iron formations. (B) Picture of the upper part of the profile with the pisolith layer (TUC19-2B) above the dashed line and the clay-rich layer (TUC19-2C) below the dashed line. (C) and (D) show samples TUC19-2D and -2E in the outcrop and in the hand specimen. (E) shows the cleaned wall where sample TUC19-2F was taken. Note the vertical banding of the saprolite.

EPR spectroscopic study of kaolinites from two lateritic profiles of the northeastern and eastern Guiana shield (Kaw mountain, French Guiana and Tucano mine, Amapá, Brazil)

Table VII-2: Description of Tucano mine samples. Minerals detected by XRD (Kl = kaolinite, Qz = quartz, Ms = muscovite, Gt = goethite, Hm = hematite, An = anatase, and Gib = gibbsite) were not quantified but the "x" indicate the estimated relative quantities ranging from few (x) to very abundant (xxxx).

Sample	Elevation a.s.l.	Depth below Surface	Description Bulk Sample	Subsample	Fraction	Minerals detected by XRD						#CBD cycles	
						Kl	Qz	Ms	Gt	Hm	An		Gi
TUC19-01E	ca. 260	1.5	Ochre yellow red duricrust in situ, more or less pisolitic structure with red pisoliths in a yellow ochre solid matrix - Sampled ca. 150m offset from the other samples of the profiles (see Fig. 3)			xx	x	xxx	xx	x	x	x	11
TUC19-02A	ca. 260	0.2	Ochre brown soil containing some pisoliths	TUC19-2AA TUC19-2AB	<1 mm >1m m	xxx	xx	xx	x	x	x	x	7
TUC19-02B		1	Pisolith horizon with cm-sized ochre-brown pisoliths contained in a fine grained ochre brown soft matrix	TUC19-2BA TUC19-2BB	<1mm >1m m	xxx	xx	x	xx	x	x	x	5
TUC19-02C		2	red-violet clays			xx	xx	x	x	x	x	x	6
TUC19-02D		6.5	White saprolite with large white micas and some black minerals (Mn oxides?)			xxx	xx	xxx	x	x	x	x	2
TUC19-02E		6.5	Yellow-red Saprolite (weathered shist) with banding and foliation sampled directly next to TUC19-01D			xx	x	xxx	x	x	x	x	5
TUC19-02F		16	Reddish saprolite (weathered shist) with banding and foliation			xxx	x	xx	x	x	x	x	4
TUC19-02G		ca. 55	Ochre yellow saprolite, more felsic			xxx	x	xx	x	x	x	x	4
TUC19-02H		ca. 55	Whitish pink saprolite with some foliation. Harder than TUC19-01G. Granitic parent rock?			xxx	xxx	x	x	x	x	x	3
TUC19-02I	ca. 215	ca. 55	reddish saprolite (weathered shist) with red-white banding (mm to cm-sized bands)	TUC19-2Ia TUC19-2Ib	red bands	xxx	x	xx	x	xx	x	x	7
TUC19-02J	ca. 140	120	reddish saprolite on shist, harder than previous samples and more coarse grained	TUC19-2Ic	white bands	xxxx	x	x	x	x	x	x	4
						x	xxxx	xxx	x	x	x	x	5

The location of the sampling site is Lat = 0°50,742'S, Long = 51°52,631'W.

VII.4 Methods

VII.4.1 Bulk sample analyses

VII.4.1.1 XRD analyses

All 33 samples taken from the Kaw drill-core, as well as the 12 samples of the Tucano profile were analyzed by XRD. As mentioned above, very heterogeneous samples were split into two fractions, >1mm and <1 mm, and analyzed separately. The aim of this separation was to compare the kaolinites imprisoned in indurated material with the kaolinite in the fine grained matrix. *Circa* 30g of sample material were finely ground using a agate mortar. In order to make sure that kaolinite minerals were not damaged, no planetary ball mill was used. For XRD analyses, the sample material was filled into hollowed inox sample holders (32 mm diameter and 3 mm depth) and analyzed using the same measurement conditions as in Chapter IV.

VII.4.1.2 Geochemical analyses

Considering their depth in the profiles and the presence of kaolinite, samples were selected for kaolinite purification and geochemical analyses. Geochemical analyses of major and trace elements were performed by the SARM at Nancy. For details on the analytical procedures and uncertainties see Chapter IV and www.sarm.fr.

VII.4.1.3 Thin sections

Thin sections were obtained for 22 selected samples, but due to major delays for their preparation, they could unfortunately not be studied on time and therefore are not described here.

VII.4.2 Kaolinite purification

16 samples from Kaw and 12 samples from Tucano were selected for kaolinite purification based on the abundant presence of kaolinite detected through XRD and their depth in the profiles. Deferration was performed following the citrate-bicarbonate- dithionite (CBD) procedure of Mehra and Jackson (1960) and the clay fraction was separated by centrifugation (for details see Chapter II). All EPR analyses were performed on these purified fine fractions.

VII.4.3 Fine fraction XRD

XRD diffractograms were obtained on the separated fine fractions using the same measurement setting as explained for the bulk samples but smaller sample holders with diameters of 27 mm and 20 mm and 0.5 or 1 mm depth were used.

VII.4.4 Artificial irradiation

11 samples of each profile were selected for artificial irradiations based on their EPR spectra. Therefore, 210 mg of kaolinite sample material were brought into solution with 42 ml MilliQ water. This suspension was agitated during 24h. If necessary the material was put for 5-10 minutes in a ultrasonic bath and 10 μ l of NaOH were added in order to disperse the clay minerals. Afterwards 6 ml of suspension were transferred to circular hollowed inox plates and air dried during 48 h until complete dryness. 6 plates were prepared for each sample. Ideally this procedure creates a kaolinite layer with a constant thickness of 4 μ m.

The kaolinite samples were irradiated with He⁺ ions (to simulate α -particles and more extensively ionizing effects) at the ARAMIS linear accelerator (Orsay, France) using 6 different doses of 3 \times 10¹¹, 6 \times 10¹¹, 1 \times 10¹², 3 \times 10¹², 6 \times 10¹², 10¹³ ions / cm² corresponding to irradiation doses of 69 to 2308 kGy. After irradiation, the sample material was scrapped off the inox plates, wrapped into Al foil and heated during 2h at 250°C in order to anneal unstable irradiation defects.

VII.4.5 EPR measurements

For EPR analyses, the purified kaolinite was filled into 16 cm long tubes made of ultrapure suprasil glass. 20-100 mg sample material were filled into the tubes and the weight and the height (ideally 15-20 mm) of the material were determined.

EPR spectra were recorded at room temperature at X-Band (9.44 GHz) using a Bruker EMXplusTM spectrometer equipped with a high sensibility cavity. Acquisition was done with a microwave power of 40 mW and a magnetic field modulation with frequency of 100 kHz and an amplitude of 5 of 3 gauss for total spectra and defect (and vanadyl) spectra, respectively. Three types of spectra were acquired: i) total spectra covering the range of 0-6000 gauss (obtained for all purified samples on unirradiated material); ii) spectra of the region from 3290 to 3690 Gauss including the radiation induced defects (done for all samples and irradiated

EPR spectroscopic study of kaolinites from two lateritic profiles of the northeastern and eastern Guiana shield (Kaw mountain, French Guiana and Tucano mine, Amapá, Brazil) and iii) spectra covering the range of 2800-4500 gauss which contains the vanadyl signal. The vanadyl spectra were acquired for Kaw samples only, generally on the unirradiated material and, for sample KAW18-7462, on both unirradiated and irradiated material. In order to avoid machine drift effects, defect spectra were acquired in a block for all doses of each sample. The internal kaolinite standard GB1 was measured twice in every measurement session (at the beginning and the end) in order to check for the stability of the recording conditions. The Nowa Ruda dickite which shows a strong vanadyl signal but no RIDs was measured with the conditions of setting ii.

In order to compare the intensities and related concentration of paramagnetic species, all EPR spectra were normalized using the following equation:

$$I_{norm} = \frac{I_{measured}}{m \times RG \times F_c} \quad (VII-1)$$

With m the sample mass, RG the recording gain and F_c a sample height (h) correction factor which is $F_c = 1.2864 - 0.014318 \times h$ for the used cavity.

VII.4.6 Gaité index and structural Fe³⁺ calculation

From the total EPR spectra, the Gaité index, which is a dimensionless parameter of disorder was calculated according to (Gaité et al., 1997). As illustrated in Figure VII-5A, the position and width of the 1Y peak (g=8.6) and the position of 3Z peak (g=4.3) were determined and the Gaité Index E was calculated as $E=L/D$ with L=full width at half maximum (1Y) and D the distance between the two peaks. The concentration of structural Fe³⁺ substituting Al³⁺ ions was calculated in absolute units by double integration after Balan et al. (2000). Figure VII-5B visualizes the procedure and shows the integrated signal of the structural Fe³⁺ (assimilated to absorbance). The integration of the absorbance of structural Fe³⁺ was calibrated using a linear correlation between several kaolinite standards measured in the same conditions and described in Balan et al. (2000).

EPR spectroscopic study of kaolinites from two lateritic profiles of the northeastern and eastern Guiana shield (Kaw mountain, French Guiana and Tucano mine, Amapá, Brazil)

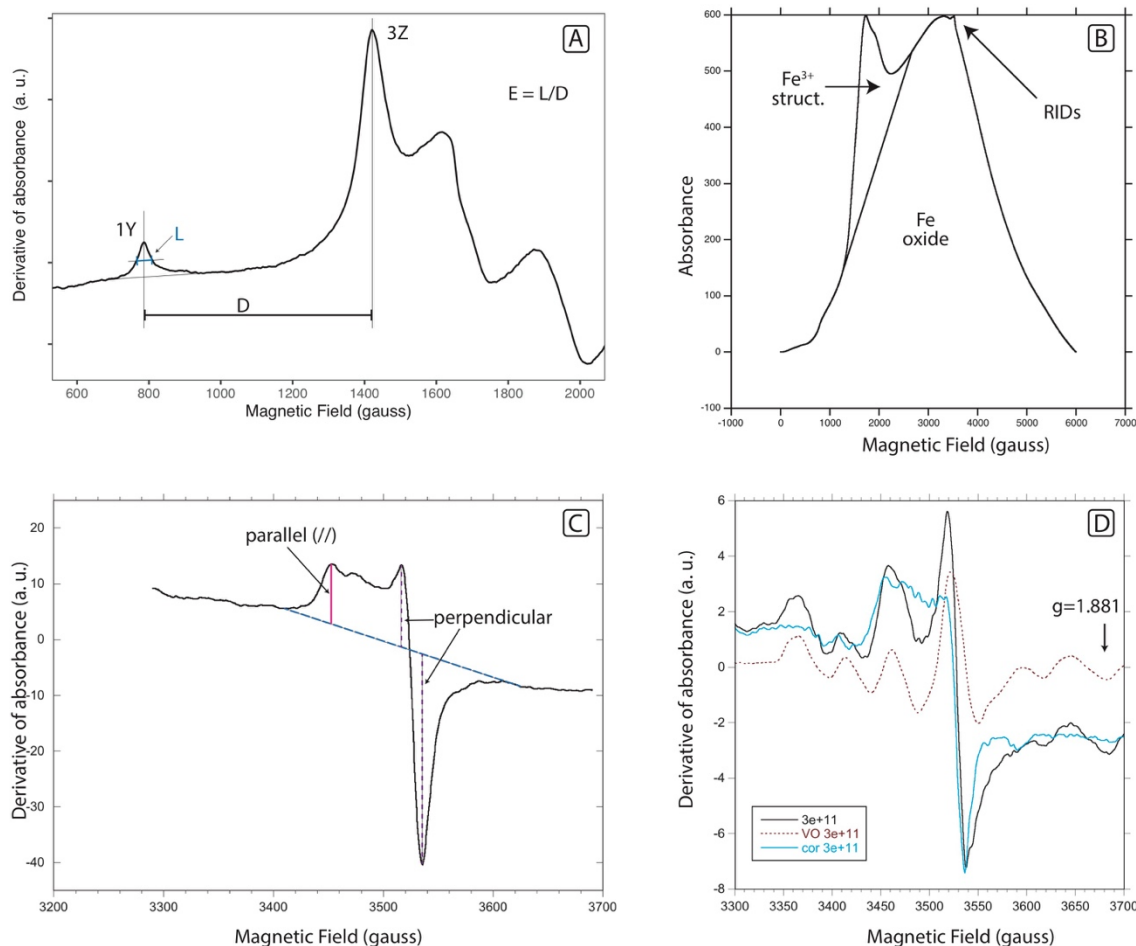


Figure VII-5: Illustration of the calculations applied to the kaolinite EPR spectra. (A) The Gaité Index is calculated from the full width at half maximum of the 1Y peak at $g \approx 9$ ("L") and divided by the distance of between the 1Y and the 3Z peak ("D"). (E) Integrated EPR spectra of sample TUC19-2BA indicating the area used for structural Fe^{3+} calculation. The integration of the derivative of absorbance (normally used as y-axis) is the actual absorbance. (C) RID are of the $6 \cdot 10^{11}$ dose of sample TUC19-2F showing the used baseline and the measured amplitudes of the parallel and the perpendicular components. (D) RID spectrum of the $6 \cdot 10^{11}$ dose of sample KAW18-7462 showing the measured spectrum (black line), the vanadyl component (dashed brown line) whose contribution was estimated from the intensity at $g=1.881$ and the corrected RID spectra (blue line) used for estimating the A-center concentration.

VII.4.7 Fitting of the RID EPR spectra using ZFSFIT

In order to test automated fitting of the RID spectra, the software ZFSFIT (Morin and Bonnin, 1999) was used. Therefore the values of magnetic field were transformed into Tesla (1 Tesla = 10 000 gauss), and corrected for the magnetic field shift (-16.84 Gauss) and the frequency. A, A' and B-center parameters were calibrated for GB1 kaolinite. Fitting of sample spectra was tried by varying scale factors and widths of the centers. The baseline was estimated using a spline function fixed at 5 points. If this did not allow a satisfying fit then peaks characteristics, peak shape and g-factors were also modified. The tested procedures are explained in more details in Section 5.6 of this chapter.

VII.4.8 Concentration of A-centers and Paleodose estimation

For the estimation of the paleodose, the amplitudes of the RID signals were measured from the EPR spectra of the natural and artificially irradiated samples (Figure VII-5C). Where possible, the RID concentration was estimated from the perpendicular component, related principally to the A-center as this defect is a dominant species (Figs. VII-2B and VII-2C). This simplified procedure is satisfying as long as the shape of the RID signal remains the same between samples. The analytical error of the amplitude is ca. 15% (Mathian et al., 2019).

Samples showing a strong vanadyl interference were corrected by subtracting the Vanadyl spectrum of the Nowa Ruda reference dickite (Premović et al., 2012). The intensity of the vanadyl signal was estimated from isolated resonances assigned to VO^{2+} only (Figs VII-2D and VII-5D) such as those at low and high field values from either side of the RID signal. Vanadyl correction was performed for every spectrum individually. In order to reduce the effect of the VO^{2+} correction, the RID amplitude was measured from the parallel component in these samples.

Dosimetry curves were least-square fitted using two functions. An exponential function, as proposed and applied by Allard et al. (1994); Allard and Muller (1998); Balan et al. (2005):

$$C = C_s(1 - \exp^{-\lambda(D+P)}) \quad (\text{VII-2})$$

as well as an exponential function with a linear component as proposed by Duval (2012):

$$C = C_s(1 - \exp^{-\lambda(D+P)}) + Fl \times (D + P) \quad (\text{VII-3})$$

with C the defect concentration of the irradiated sample, C_s the defect concentration at saturation, D the radiation dose used, P the naturally accumulated dose (paleodose), and Fl a linear factor (for detail see Duval, 2012). The efficiency of radiation, i.e., the quantity of defects created per unit dose for low radiation doses, is then defined by the product λC_s (Allard et al., 1994; Allard and Muller, 1998; Balan et al., 2005). For every sample both formulas were tested and the best fit with the smallest residue was selected for the determination of the paleodose.

VII.4.9 Dose-rate and preliminary age calculation

Raw dose-rates were calculated using the relation between dose rates and concentration of radioactive isotopes (U, Th, K) provided by Adamiec and Aitken (1998) for closed systems at the secular equilibrium.

Preliminary ages were calculated as $Age = \frac{Paleodose}{Dose-rate}$. The error and needed corrections are discussed in Section 5.9.

VII.5 Results and Discussion

VII.5.1 Bulk mineralogy and geochemistry

VII.5.1.1 Kaw drill core

The XRD patterns from the Kaw mountain drill core are summarized in Figure E-1 of the supplementary material and Table VII-2 (only XRD data for samples selected for further analyses are presented). The samples from the upper 8m show a considerable variation regarding their mineralogical composition. The upper 5 m are primarily composed of hematite, goethite and gibbsite, with intermediate to small amounts of kaolinite and minor amounts of anatase and rutile, and correspond to the topsoil and the lateritic-bauxitic duricrust of Kaw mountain. Below 5 m the samples are principally composed of kaolinite and quartz with some hematite and / or goethite and minor amounts of muscovite. The proportions of kaolinite and quartz, which were not quantified, vary throughout the profile. The observed color differences ranging from red, violet to ochre-brown, gray and white underline the variability of the nature and concentration of iron minerals. Table VII-3 and Figure VII-6 show the major element quantities of samples analyzed geochemically (n=22). SiO₂ concentrations vary from 0.4 to 71 wt% and are generally higher in the saprolite (> 40 wt%) and low in the duricrust and the Soil (≤ 26 wt%). Fe₂O₃ contents range from 0.3% to 81 wt% with high concentrations in the soil and duricrust nodules (> 60 wt%), the corresponding <1 mm fractions (20-40 wt%) and rather low and relatively constant in the saprolite (mostly 10-14 wt%) (Fig. VII-6A). Al₂O₃ contents show less variation ranging from 7 to 42 wt%. The highest concentrations can be found in the finer fractions (< 1mm) of the soil and the duricrust whereas the >1 mm fraction of the same samples show the lowest concentrations. In the saprolite concentrations vary between 18 and 34 wt % and are generally anticorrelated with the SiO₂ concentrations (Fig. VII-6A). This anticorrelation is probably due to different proportions of kaolinite and quartz. TiO₂ concentrations range from 0.3 to 5 wt% and show a general increase towards the top of the profile (Fig. VII-6B). The highest concentrations can be found in the <1 mm fractions of the upper 3 m. K₂O concentrations range from 0.08 to 2.1% in the upper 10m of the profile and are often below the limit of detection in the rest of the profile. Na₂O, MgO and MnO show a very similar pattern. K₂O, Na₂O MgO show

EPR spectroscopic study of kaolinites from two lateritic profiles of the northeastern and eastern Guiana shield (Kaw mountain, French Guiana and Tucano mine, Amapá, Brazil)

their highest concentrations at 9.45 m depth with values often 3 or 4 times higher than in the surrounding samples (Fig. VII-6B). CaO concentrations are generally low throughout the profile (<0.1 wt%) whereas P₂O₅ concentrations are below the limit of detection for all but three samples. The Si/Al ratio shows variations between 1 and 4 in the saprolite (Fig. VII-6C) and drops below 1 on in the duricrust. The Index of Lateritization was calculated after (Babechuk et al., 2014) as

$$IOL = 100 \times \frac{Al_2O_3 + Fe_2O_3}{Al_2O_3 + Fe_2O_3 + SiO_2} \quad (VII-4)$$

The obtained Lateritization Indices range from 22.4 to 99.9 (median = 54) and show an increase towards the top of the profile (Fig. VII-6D). Note however, that the highest values (>88) were obtained in the >1mm fractions whereas the fractions <1mm yield indices up to 86. In any case the obtained values represent the strong lateritization of the top of the profile which is correlated to Si loss, whereas the saprolitic part of the profile can be characterized as “kaolinitised” (Schellmann, 1982).

The XRD and geochemical results are typical of a lateritic profile with a mixed ferruginous-bauxitic top. The results are in concordance with the descriptions of (Choubert, 1956) who studied the lateritic cover of Kaw mountain in detail. The depletion of alkali and earth alkali elements (relative to the upper continental crust, where mean Na₂O, K₂O, CaO, and MgO, concentrations range from 2.5-3.6 wt%, Rudnick and Gao, 2013) is a typical characteristic of lateritic profiles and has been observed all over the tropical zone (Tardy, 1997). The surprisingly elevated concentrations of alkali and earth alkali elements at 9.45m depth are probably related to the presence of muscovite which has been detected in the XRD patterns. The overall TiO₂ enrichment towards the top of the profile is also expected as Ti is a very immobile element. The duricrust exposed in this drill core is slightly different from the duricrusts presented by Heller et al. (2022), as it contains a relatively high proportion of soft, not indurated material. The presence of gibbsite in the first 3 m of the profile represent the bauxitic signature of the profile. Heller et al. (2022) show that bauxitization was a secondary process which overprinted a previously ferruginous duricrust. The profile does not show the “classical” bauxitic sequence with a rather pure bauxite layer rich in gibbsite underlying an iron duricrust (Bardossy and Aleva, 1990). However, our results are in line with the observations of Choubert (1956) who describes that the bauxitization of the lateritic cover of Kaw is very heterogeneous in space and intensity. The duricrust thickness of ca. 4-5 m observed here is similar to mean duricrust thickness of ca 5.5m described by Choubert (1956).

EPR spectroscopic study of kaolinites from two lateritic profiles of the northeastern and eastern Guiana shield (Kaw mountain, French Guiana and Tucano mine, Amapá, Brazil)

The drill-core reveals a strong heterogeneity of color and softness in the saprolite. We assume that this macroscopic heterogeneity is linked to lithologic variations of the parental rock, which belong to the volcano-sedimentary Paramaca formation (Choubert, 1956; Vanderhaeghe et al., 1998; Delor et al., 2003). Compositional differences of the volcano-sedimentary layers with variable amounts of mafic and felsic minerals can easily explain the observed heterogeneity. However this heterogeneity complicates reconstruction of the weathering history and is the reason why no mass balances were calculated for this profile.

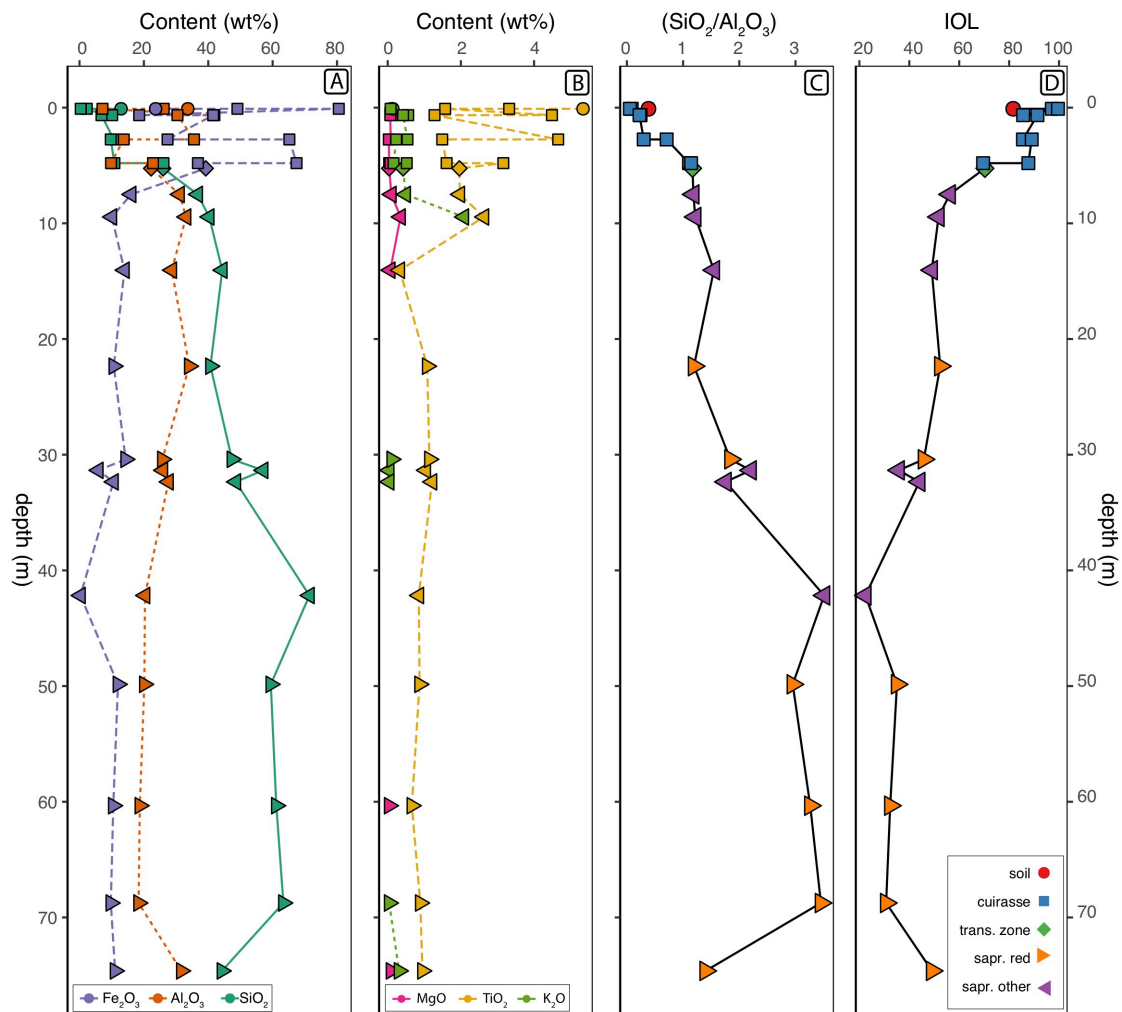


Figure VII-6: Major element composition of the samples from the Kaw mountain drill-core. (A) Concentrations of the three most abundant oxides. (B) Concentrations of selected less abundant oxides. Colors in (A) and (B) are according to the oxide (see legend at the bottom), shapes are according to the sample-type and as (C and D). (C) shows the Si/Al ratio whereas (D) shows the index of lateritization, calculated after Babeuchuk et al., (2014). Colors and shapes are representative of the sample-type.

EPR spectroscopic study of kaolinites from two lateritic profiles of the northeastern and eastern Guiana shield (Kaw mountain, French Guiana and Tucano mine, Amapá, Brazil)

Table VII-3: Bulk composition of the samples from the Kaw drillcore.

Sample	Depth m	Sample Type	SiO ₂ wt%	Al ₂ O ₃ wt%	Fe ₂ O ₃ wt%	MnO wt%	MgO wt%	CaO wt%	Na ₂ O wt%	K ₂ O wt%	TiO ₂ wt%	P ₂ O ₅ wt%	LOI ¹ wt%	Sum wt%	IOI ²
KAW18-10A	0.10	soil	12.9	33.7	23.6	0.05	0.09	0.12	0.03	0.14	5.34	0.16	23.6	99.7	81.6
KAW18-10B1	0.10	cuirasse	2.2	26.2	49.1	0.02	bid	bid	bid	0.08	3.32	bid	17.3	98.2	97.1
KAW18-10B2	0.10	cuirasse	0.4	7.1	80.5	0.04	bid	0.05	bid	bid	1.57	0.3	9.9	99.9	99.6
KAW18-65B2	0.65	cuirasse	6.8	30.4	41.5	bid	0.07	bid	bid	0.42	1.28	bid	18.7	99.2	91.3
KAW18-65BA	0.65	cuirasse	10.2	41.9	18.5	0.02	0.12	bid	0.03	0.56	4.49	bid	23.1	98.9	85.6
KAW18-275A	2.75	cuirasse	10.6	35.6	27.4	0.02	0.08	bid	0.02	0.54	4.66	bid	19.9	98.8	85.5
KAW18-275B	2.75	cuirasse	9.7	13.7	65.2	bid	0.03	bid	bid	0.23	1.49	bid	9.2	99.6	89.0
KAW18-480A	4.80	cuirasse	26.1	22.8	36.8	0.02	0.07	0.08	0.03	0.52	3.16	bid	11.1	100.7	69.6
KAW18-480B	4.80	cuirasse	10.8	9.8	67.4	0.05	0.04	0.08	bid	0.16	1.61	bid	9.4	99.4	87.7
KAW18-525	5.25	trans.zone	26.0	22.3	39.2	0.03	0.04	0.08	bid	0.42	1.96	bid	10.0	100.0	70.3
KAW18-750	7.50	saprolite	36.7	31.1	16.0	0.04	0.1	bid	0.02	0.49	1.97	bid	12.6	99.0	56.2
KAW18-945	9.45	saprolite	40.3	33.1	10.0	0.02	0.35	0.09	0.05	2.08	2.63	bid	11.4	100.0	51.7
KAW18-1405	14.05	saprolite	44.4	28.7	14.0	0.03	0.07	0.08	bid	bid	0.33	0.31	12.9	100.7	49.0
KAW18-2235	22.35	saprolite (red)	40.7	34.1	10.7	bid	bid	0.08	bid	bid	1.08	bid	13.4	100.0	52.4
KAW18-3040	30.40	saprolite (red)	47.4	25.7	14.3	bid	bid	bid	bid	0.11	1.14	bid	10.6	99.2	45.8
KAW18-3135	31.35	saprolite	57.0	25.9	5.8	bid	bid	0.08	bid	0.04	1.04	bid	10.9	100.8	35.8
KAW18-3235	32.35	saprolite	48.6	27.6	10.6	bid	bid	0.04	bid	0.04	1.21	bid	11.5	99.5	44.0
KAW18-4217	42.17	saprolite	71.4	20.4	0.3	bid	bid	0.08	bid	bid	0.85	bid	8.0	101.0	22.4
KAW18-4985	49.85	saprolite (red)	59.4	20.1	12.0	bid	bid	0.08	bid	bid	0.87	bid	8.6	101.1	35.1
KAW18-6034	60.34	saprolite (red)	61.1	18.7	10.5	bid	0.04	0.08	bid	bid	0.66	bid	8.3	99.5	32.3
KAW18-6875	68.75	saprolite (red)	63.3	18.4	9.7	bid	bid	0.08	bid	0.04	0.89	bid	8.0	100.5	30.7
KAW18-7462	74.62	saprolite (red)	44.3	31.6	11.1	bid	0.09	0.08	bid	0.31	0.95	bid	12.6	101.0	49.1

LOI¹: loss of ignition; IOI²: Index of Lateritization calculated after Babeuchuk et al. (2014)

VII.5.1.2 Tucano mine

12 samples from the Tucano mine were analyzed by XRD and geochemistry. In the two uppermost samples TUC19-2A and TUC19-2B the fractions >1 mm (TUC19-2AA and TUC19-2BA) and <1 mm (TUC19-2AB and TUC19-2BB) were analyzed separately and the banded sample TUC19-2I was split into a white part (2Iw) and a red part (2Ir). Figure E-2 of the supplementary material presents the XRD pattern of the Tucano bulk samples. At the top the samples are primarily composed of kaolinite and goethite with some quartz, hematite, anatase, muscovite and gibbsite (sample TUC19-1E only). The saprolite samples are generally composed of kaolinite and quartz with some goethite and hematite and certain samples (especially TUC19-2D, 2E) contain important amounts of muscovite. Table VII-4 and Figure VII-7 resume the bulk chemistry of these samples. SiO₂ concentrations range from 11 to 76 wt% and show a general decrease towards the top the profile. Fe₂O₃ contents vary between 3 and 62 wt% and show a general increase towards the top with the highest concentrations in the indurated duricrust samples (TUC19-2BB and TUC19-1E). Al₂O₃ contents show relatively little variation with values between 11 and 34 wt% throughout the profile (Fig. VII-7A). Thus, the distribution of SiO₂, Fe₂O₃ and Al₂O₃ are in line with those from the Kaw profile except that weathering is less intense (no bauxitization). Al₂O₃ and SiO₂ show a certain anticorrelation relative to Fe₂O₃ (Fig. VII-7A). TiO₂ concentrations show a considerable variation ranging from 0.06% in sample TUC19-2D to 6.7 wt% in the red bands of sample TUC19-1(r) (Fig. VII-7B). Interestingly there is a general TiO₂ decrease towards the top of the profile. K₂O concentrations range from below the limit of detection in the duricrust samples to 8.5 wt% in sample TUC19-2E (Fig. VII-7B). Note that in this sample muscovite was observed macroscopically and by XRD. Most other samples have lower K₂O concentrations ranging from 2.3 to 0.1 wt%. MgO shows a very similar pattern as K₂O whereas Na₂O concentrations are b.l.d. for most samples (but not TUC19-2E). P₂O₅ and MnO concentrations are generally low (< 0.5 and 0.3 wt%, respectively), but show considerably higher concentrations in sample TUC19-2D (Fig. VII-7C). Note that the latter sample corresponds to a weathered felsic dyke. The IOL varies from 18 to 87 and is the highest in the duricrust samples (Fig. VII-7D).

The geochemistry of the Tucano profile reflects its macroscopic heterogeneity. Geochemical variations between different saprolite lithologies sampled at the same depth support the hypothesis that an important amount of geochemical variation in this profile is linked to heterogeneities of the parental rock. As for Kaw, this primary heterogeneity limits the

EPR spectroscopic study of kaolinites from two lateritic profiles of the northeastern and eastern Guiana shield (Kaw mountain, French Guiana and Tucano mine, Amapá, Brazil)

possibilities of mass balance calculations (which were thus not done). Nevertheless, the profile shows typical characteristics of a lateritic profile with an important Fe accumulation in the duricrust and leaching of alkali and earth alkali elements (relative to the upper continental crust, Rudnick and Gao, 2013), except for the high K₂O content in sample TUC19-2E which is linked to the presence of white mica, as mentioned above. Relatively high P₂O₅ concentrations in sample TUC19-2D could be linked to the presence of (weathered?) phosphates, as sample TUC19-2D represents a weathered felsic dyke. Detailed analysis of the XRD spectrum could reveal this but was not done here as this is only of minor importance for this study. The overall decrease of TiO₂ concentrations towards the top of the profile is an unexpected feature and might be linked to heterogeneous distribution of Ti-bearing minerals in the parental material. Alternatively, this may be related to conditions favoring the mobility of Ti as first described by Cornu et al. (1999) in lateritic profiles from Amazonia. Different from Kaw, the Tucano profile is not bauxitized and kaolinite is present all over the profile while gibbsite is not a major component in any of the samples.

EPR spectroscopic study of kaolinites from two lateritic profiles of the northeastern and eastern Guiana shield (Kaw mountain, French Guiana and Tucano mine, Amapá, Brazil)

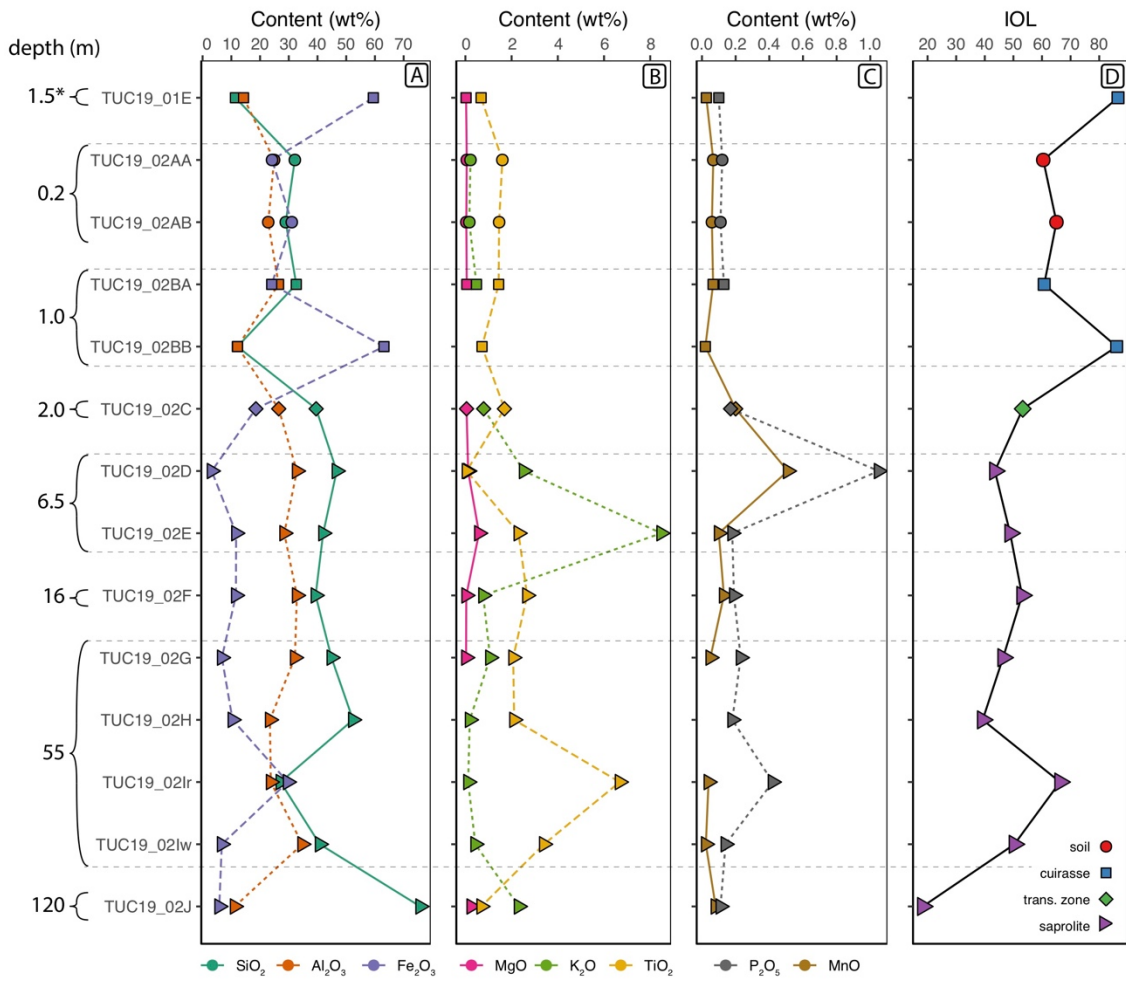


Figure VII-7: Major element composition of the samples from the Tucano profile. (A) Major element contents of the most abundant oxides. (B) and (C) show the concentrations of the less abundant "major" elements. Colors in (A-C) are according to the oxide (see legend at the bottom), shapes are according to the sample-type and as in (D). (D) shows the index of lateritization, calculated after Babechuk et al. (2014). Colors and shapes are representative of the sample-type. Horizontal dashed lines group samples taken at the same depth. *Sample TUC19-1E was taken with a lateral distance of ca. 150m from the other samples.

Table VI-4: Bulk composition of the samples from the Tucano mine.

Sample	Depth m	Sample Type	SiO ₂ wt%	Al ₂ O ₃ wt%	Fe ₂ O ₃ wt%	MnO wt%	MgO wt%	CaO wt%	Na ₂ O wt%	K ₂ O wt%	TiO ₂ wt%	P ₂ O ₅ wt%	LOI ¹ wt%	Sum wt%	IOI ²
TUC19_01E	1.5	cuirasse	11.4	14.3	59.4	0.03	0.03	0.05	bld	bld	0.68	0.10	13.0	99.0	86.6
TUC19_02AA	0.2	soil	32.1	24.9	24.2	0.07	0.06	bld	bld	0.22	1.60	0.12	16.2	99.5	60.4
TUC19_02AB	0.2	soil	29.0	22.9	31.0	0.06	0.04	bld	bld	0.17	1.46	0.11	15.2	99.9	65.1
TUC19_02BA	1	cuirasse	32.6	26.5	24.1	0.07	0.06	bld	bld	0.48	1.44	0.13	14.7	99.9	60.8
TUC19_02BB	1	cuirasse	12.1	12.2	63.2	0.02	bld	bld	bld	bld	0.72	bld	11.5	99.7	86.1
TUC19_02C	2	trans. zone	39.5	26.5	18.6	0.20	0.05	0.05	bld	0.79	1.69	0.17	12.1	99.6	53.3
TUC19_02D	6.5	saprolite	46.7	32.8	3.2	0.51	0.12	0.05	0.07	2.53	0.06	1.05	11.0	98.1	43.5
TUC19_02E	6.5	saprolite	42.0	28.4	11.7	0.10	0.59	bld	0.24	8.48	2.30	0.18	5.2	99.2	48.9
TUC19_02F	16	saprolite	39.4	32.8	11.6	0.13	0.04	bld	bld	0.77	2.67	0.19	12.7	100.3	53.0
TUC19_02G	55	saprolite	44.9	32.1	6.7	0.05	0.03	bld	bld	1.07	2.07	0.23	12.1	99.2	46.4
TUC19_02H	55	saprolite	52.4	23.4	10.4	bld	bld	0.04	bld	0.19	2.11	0.18	10.4	99.1	39.3
TUC19_02I _r	55	saprolite	27.1	23.8	29.7	0.04	bld	bld	bld	0.12	6.68	0.42	11.0	98.8	66.3
TUC19_02I _w	55	saprolite	40.8	34.7	6.7	0.02	bld	0.04	bld	0.43	3.40	0.14	13.3	99.5	50.4
TUC19_02J	120	saprolite	75.8	11.2	5.8	0.08	0.26	0.06	0.11	2.31	0.69	0.11	3.5	99.9	18.3

VII.5.2 Fine fraction mineralogy

Fine fraction XRD patterns are presented in Figures VII-8 and VII-9 for Kaw and Tucano, respectively. At Kaw most fine fractions are composed primarily of kaolinite with some quartz. The quartz proportion is variable; while some samples contain no detectable or very minor amounts of quartz (e.g. KAW18-2235 or -750), others contain more important amounts (e.g. KAW18-4217). Sample KAW18-10A comprises an important amount of gibbsite and some anatase. Very minor amounts of muscovite (e.g. KAW18-750, -7462) or anatase (KAW18-4217, -7462) have been detected in several samples (Fig. VII-8).

As for the Kaw samples, the fine fractions of the Tucano mine samples are generally composed primarily of kaolinite. Nearly all samples contain some quartz. Sample TUC19-2J contains a large amount of quartz (Fig. VII-9). Several samples contain important amounts of muscovite (especially TUC19-2E, and -2J but also, -2F, -2D, and 2G). Anatase is present in several samples (e.g. TUC19-2E, -2C, 2AA, 2lw) and sample TUC19-1E contains some gibbsite (Fig. VII-9). Two unidentified phases exist in the samples. One, already noticed in the bulk XRD pattern, detected in TUC19-2D (but also present in TUC19-2E, -2lw and -2G), and a second, which has a peak at the same position as goethite but which corresponds to an unidentified white hydrophobic phase present in TUC19-2J and -2E (and, in very minor amounts in -2G, -2F, -2D, and 2C).

The XRD results show that the applied purification method allows one to concentrate kaolinite but depending on the bulk composition other mineral phases might exist in relatively important proportion in the fine fractions. The possible "contamination" with quartz and muscovite is partially due to the separation procedure. It should be tested whether the applied procedure can be improved in order to obtain purer kaolinite separates. Likely, the observed contamination is related to very fine grained quartz and muscovite particles representing tiny mineral rests from partial dissolution and separation by physical methods is thus difficult to improve.

EPR spectroscopic study of kaolinites from two lateritic profiles of the northeastern and eastern Guiana shield (Kaw mountain, French Guiana and Tucano mine, Amapá, Brazil)

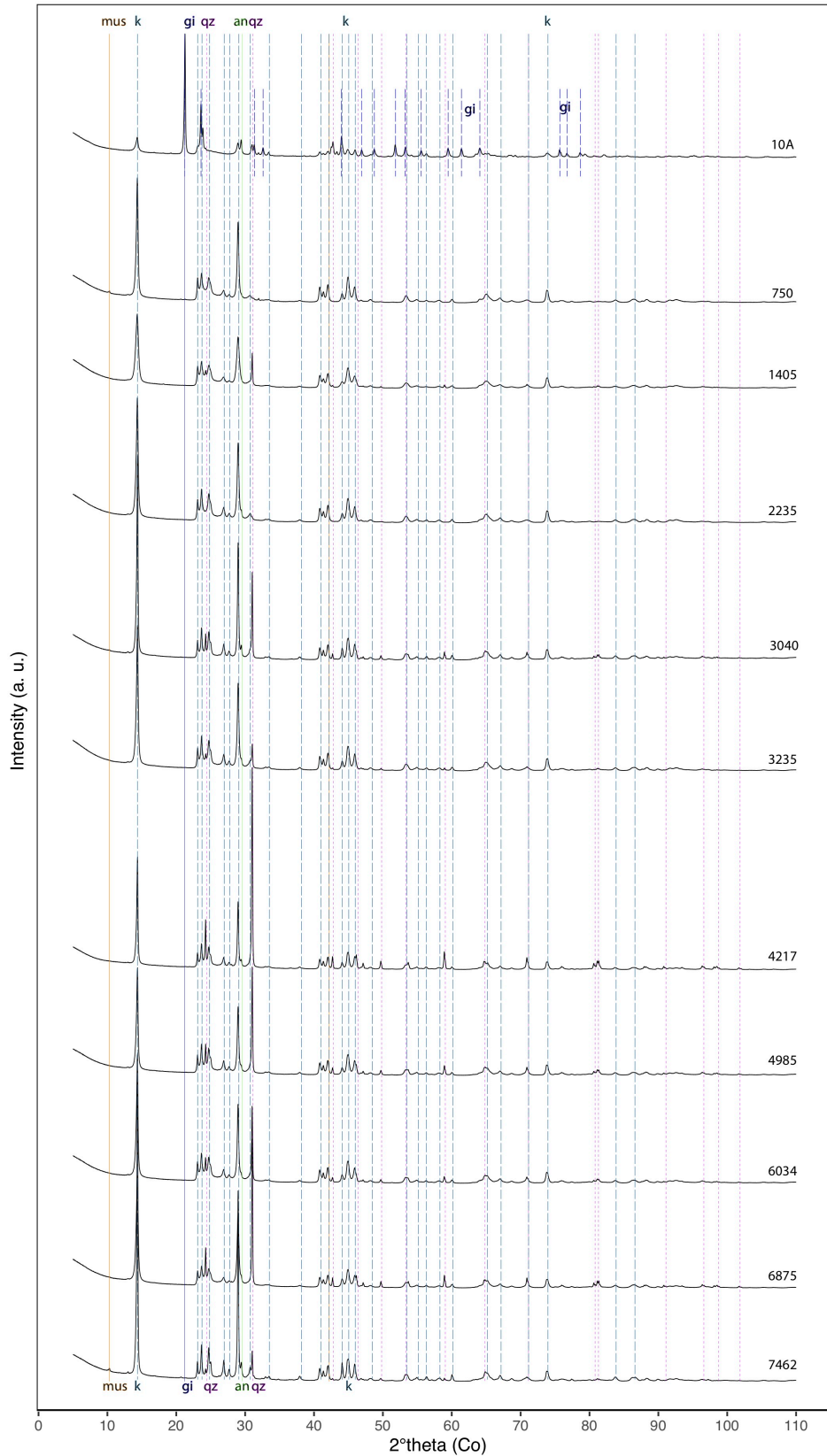


Figure VII-8: XRD pattern of the purified fine fractions of the Kaw samples. Vertical lines of the same color correspond to peaks of the same mineral (mus = muscovite (yellow solid line), k= kaolinite (dashed light blue lines), gi = gibbsite (solid dark blue line and shorter dark blue dashed lines in 10A), qz= quartz (pink finely dashed lines), an=anatase (bright green line)). The sample name corresponds to the depth in cm.

EPR spectroscopic study of kaolinites from two lateritic profiles of the northeastern and eastern Guiana shield (Kaw mountain, French Guiana and Tucano mine, Amapá, Brazil)

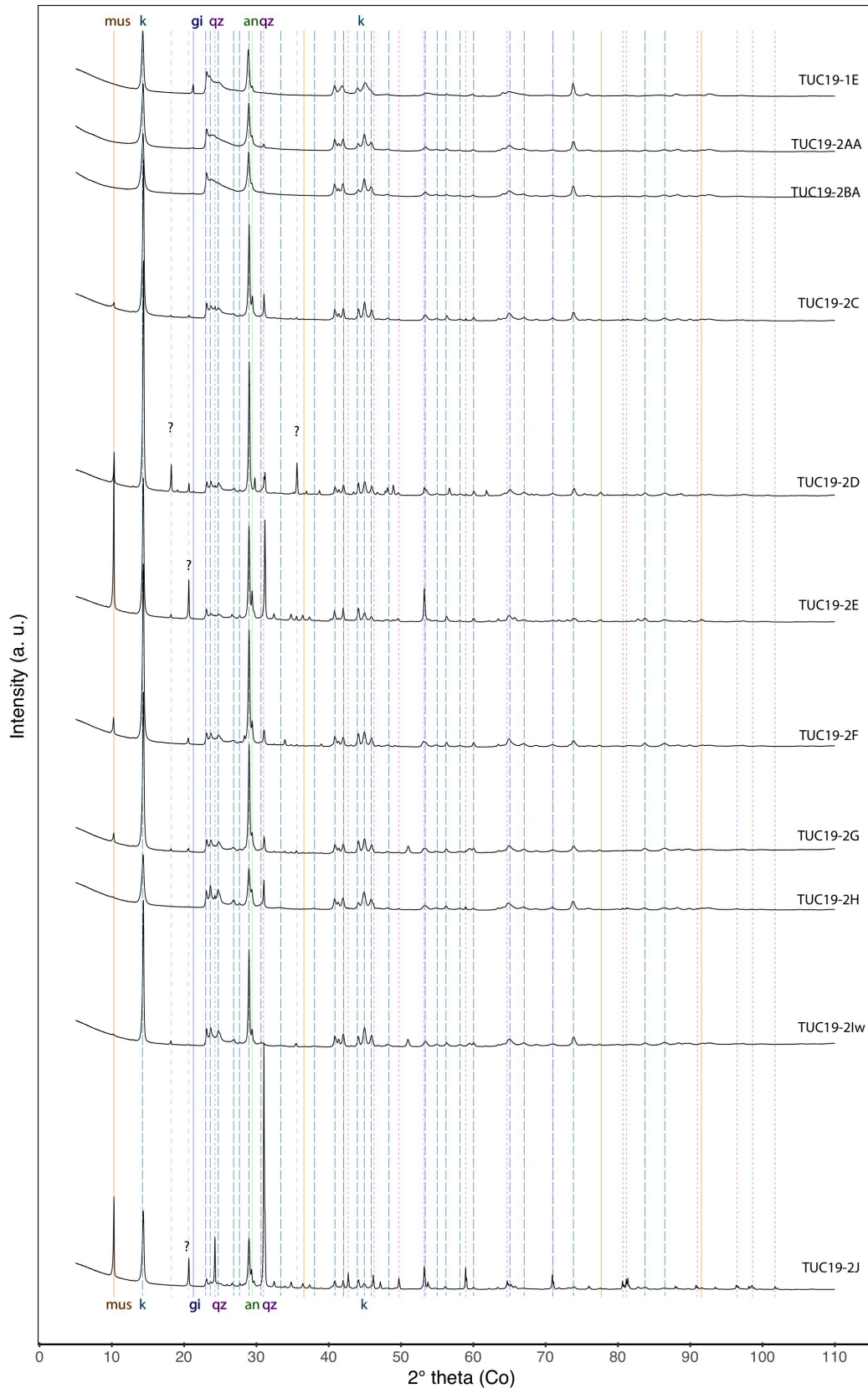


Figure VII-9: XRD pattern of the purified fine fractions of the Tucano mine samples. Vertical lines of the same color correspond to peaks of the same mineral. (mus = muscovite (yellow solid lines), k= kaolinite (dashed light blue lines), gi = gibbsite (solid dark blue line and shorter dark blue dashed lines in 10A), qz= quartz (pink finely dashed lines), an=anatase (bright green line)). Bright gray dashed lines correspond to unidentified phases (?).

VII.5.3 Gamma Spectrometry

The results of the gamma spectroscopy measured for 12 samples, 6 from each site, are presented in Table E-2 of the supplementary material. The results show that the radioactive decay chains of all samples are in secular equilibrium (C. Falguères, pers. comm.). This indicates that no radon was lost neither accumulated in the samples, at least recently. Indeed, the time required for the decay chain to reach equilibrium with equal activities between uranium and daughters is higher than 1 Ma, if the longest period of ^{238}U daughter (^{234}U , $T_{1/2} = 2.5 \cdot 10^5$ yrs) is considered.

VII.5.4 Total EPR spectra of the kaolinite samples

The total EPR spectra of all analyzed samples are presented in Figure VII-10. At Kaw most samples show the typical shape at $g \approx 4.3$ with the three apparent peaks of structural Fe^{3+} . Numerous samples show the RID signals at $g=2$, but many samples show also a strong vanadyl signal. In several samples (e.g. 480A, 480B, 3135, Fig. VII-10) the vanadyl signal does not allow identification of the RID signal, consequently they were not used for artificial irradiation. Baselines show often rather undulated and irregular shapes. Sample 10A for example shows a baseline jump in the area of the RID signal, whereas several samples, notably those with a strong vanadyl signal, such as for example 480B and 3135, show a wavy baseline at the beginning of the vanadyl signal. The baselines are probably linked to the presence of iron oxides and also possibly to iron clusters in the kaolinite structure. It is known that hematite and goethite have RPE signals in the area of $g = 2$ (Guskos et al., 2002; Carbone et al., 2005; Valezi et al., 2016). The baseline shapes observed in samples 480B and 3135 at $g=2$ resemble the EPR signal of synthetic goethite presented by Carbone et al. (2005). It cannot be excluded that albeit the numerous CBD cycles, some hematite and goethite present as nanophases remained trapped in the kaolinite particles. However, it is surprising that the most problematic baselines coincide with the strongest vanadyl signals. Three samples (KAW18-945, -3135 and -4217) show an unidentified signal of unknown origin between the $\text{Fe}^{3+}_{(I)}$ and the $\text{Fe}^{3+}_{(II)}$ peaks (Fig. VII-10). Sample KAW18-10A shows another small peak at slightly higher g -value, possibly related to gibbsite which has been detected in this sample.

The EPR spectra of the Tucano samples show very different pattern when compared to Kaw (Fig. VII-10). While some spectra have very typical structural iron signal in the area of $g=4.3$, such as for example TUC19-2Iw, TUC19-2G or TUC19-1E, several other samples, notably TUC19-2C, TUC19-2E and TUC19-2F, but also TUC19-2H, show a very intense baseline and a very noisy

EPR spectroscopic study of kaolinites from two lateritic profiles of the northeastern and eastern Guiana shield (Kaw mountain, French Guiana and Tucano mine, Amapá, Brazil) signal. As for Kaw it is possible that remaining (oxyhydr)oxides are the probable reason for the observed baselines. The baseline shape of sample TUC19-2F shows some similarity with the EPR signal of hematite (Guskos et al., 2002) but it is expected that parameters such as the size and nature of the iron (oxyhydr)oxides can influence the large signal of the baseline. In addition, since EPR is an extremely sensitive method, small amounts of such iron phases can produce a strong signal. Since the XRD of the fine fractions shows contribution of muscovite, quartz, anatase and (at least) two unknown phases it is possible that these phases might also have contributed to the baselines.

All Tucano samples show a typical RID signal in area of $g=2$ (Fig. VII-10B). The intensity between these signals varies a lot between the different samples. Several samples show an important baseline jump in the area of $g=2$ (e.g. TUC19-2Ir). A number of samples (e.g. TUC19-2G) show a pattern with the perpendicular component being smaller than the parallel component (see Figure VII-2B for attribution of these components). This feature could be linked to the observed baseline jump often observable in the same samples. Again this baseline shape could be linked to the presence of iron (oxyhydr)oxides.

EPR spectroscopic study of kaolinites from two lateritic profiles of the northeastern and eastern Guiana shield (Kaw mountain, French Guiana and Tucano mine, Amapá, Brazil)

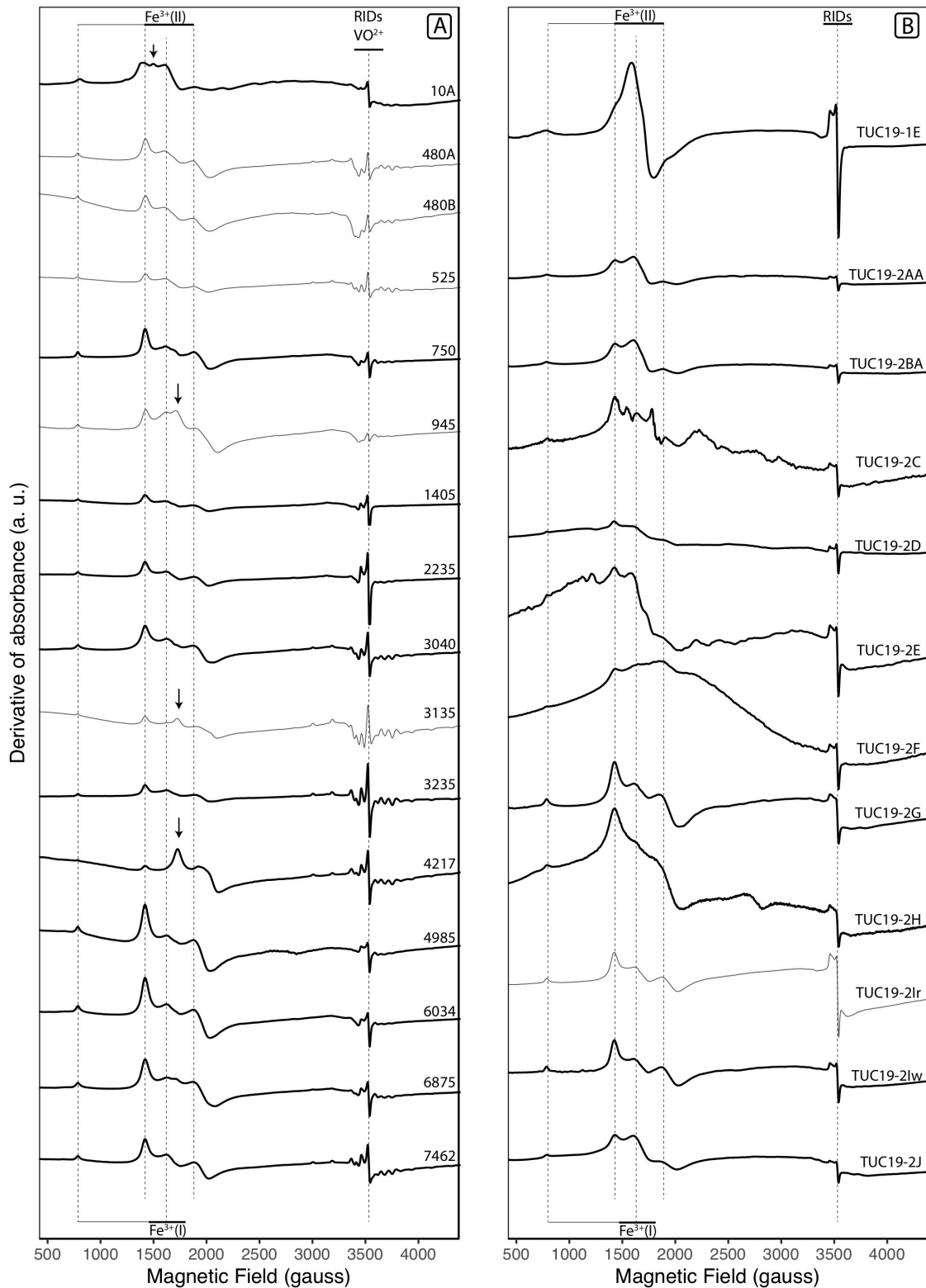


Figure VII-10: Total EPR spectra for samples of Kaw mountain (black arrows indicate unidentified components) (A) and Tucano mine (B). Thin gray lines correspond to samples which were purified but not irradiated. In A the shortened sample names correspond to the sample depth in cm. Note that the spectra were normalized in intensity but not in magnetic field (due to different cavity and frequency) which explains the difference in absolute x-values when compared to Figure VII-1B and VII-1C.

VII.5.5 Structural Fe³⁺

The results of the Gaité index and the concentration of structural Fe³⁺ calculated for the samples from Kaw and Tucano are presented in Table VII-5 and Figures VII-11 and VII-12 for Kaw and Tucano, respectively. Calculation of the Gaité index was possible for all samples except from TUC19-2E.

VII.5.5.1 Kaolinites from Kaw

Gaité Index of disorder

The obtained Gaité indices show rather constant values between 4 and 8, mainly between 4 and 6, representative of well-ordered kaolinite. The only sample showing a slightly higher value (11) is the soil matrix 10A at the top of the profile (Fig. VII-11A). The Gaité Index is not correlated with the IOL (not presented). The Kaw profile is mostly a saprolitic profile but the occurrence of well-ordered kaolinites in the saprolite and poorly ordered ones in the topsoil is fully in line with what was observed before in Amazonia from EPR data (Balan et al., 2005; Mathian et al., 2019; Mathian et al., 2020). Besides, Tardy (1997) or Lucas et al. (1996) also described that in a lateritic profile kaolinites are well ordered in the saprolite and become disordered towards the top of the profile, i.e. in the mottled zone, the duricrust and the soil. This contrast is not fully understood but Tardy (1997) explains it with the recrystallization of kaolinites in the mottled zone. The extremely homogeneous series of Gaité indices in the Kaw saprolite and the duricrust indicate near identical precipitation conditions for all kaolinites. These conditions are not yet identified but kinetics might have played a part. Indeed, Guinoiseau et al. (2021) propose from results of a reactive transport model that topsoil kaolinites derive from conditions of rapid water percolation whereas formation of saprolite kaolinites was longer. In addition, it is known from high temperature (200-240°C) syntheses of kaolinites that low pH produces well-ordered structure while at higher pH poorly ordered kaolinites are formed (Fialips et al., 2000). Consequently, pH should also be considered as a potential parameter influencing order-disorder during crystal growth. Such a process still has to be demonstrated at ambient temperature, but so far synthesis of kaolinite is not possible in these conditions. However, the pH in the profile, *circa* pH=5 at surface and even slightly higher in the saprolite is not consistent with this assumption.

EPR spectroscopic study of kaolinites from two lateritic profiles of the northeastern and eastern Guiana shield (Kaw mountain, French Guiana and Tucano mine, Amapá, Brazil)

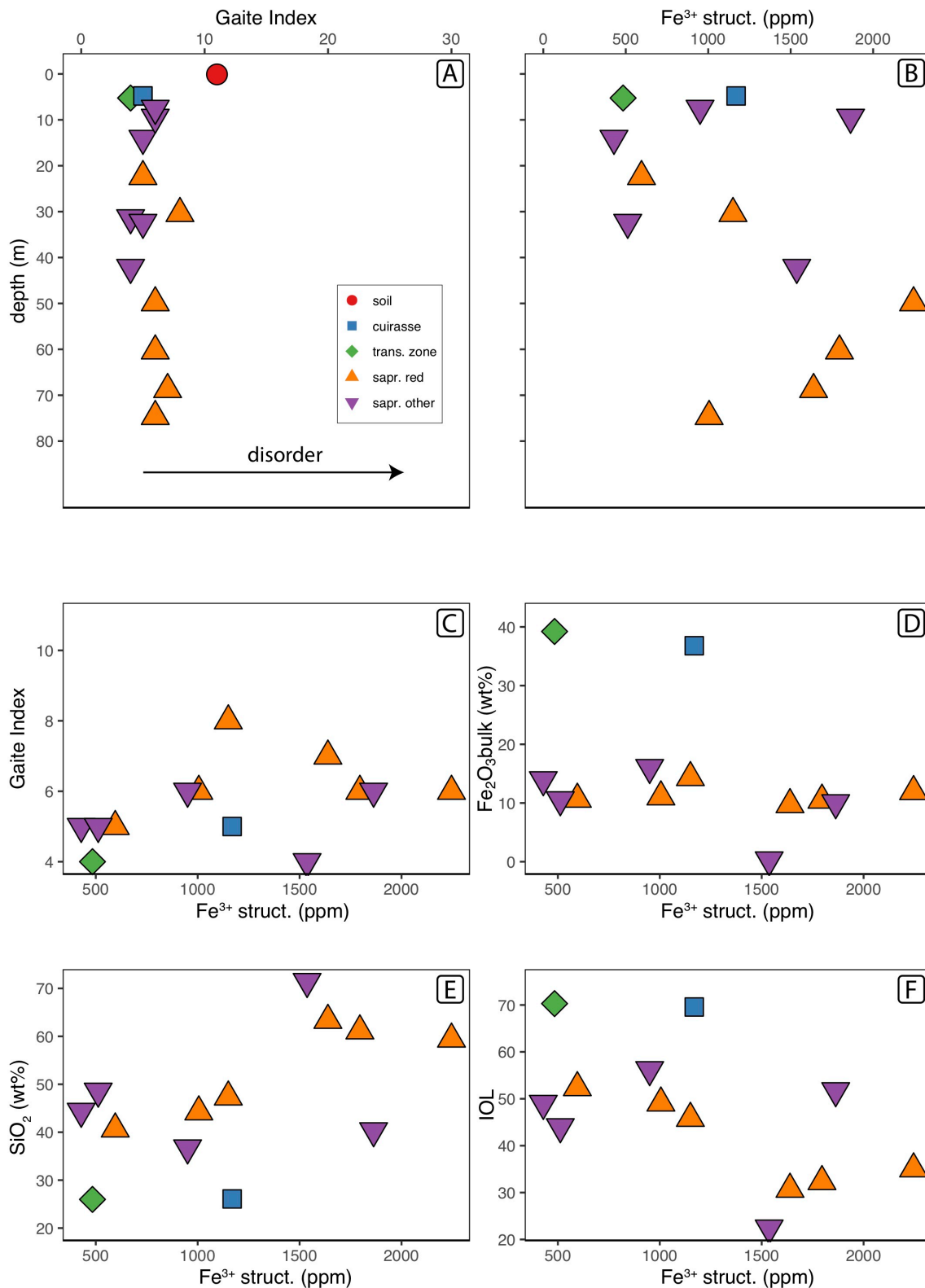


Figure VII-11: Kaolinite properties of the kaolinites from Kaw mountain (A) Gaité Index of the kaolinites as a function of depth. (B) Structural Fe as a function of depth. (C) Gaité index versus structural Fe³⁺. (D) Structural Fe of the kaolinites versus Fe₂O₃ content of bulk samples. (E) Structural Fe of the kaolinites versus SiO₂ content of bulk samples. (F) Structural Fe³⁺ of the kaolinite versus the index of lateritization (IOL) of the bulk samples.

Concentration of structural Fe³⁺

The concentration of structural Fe³⁺ covers a range from 429 to 2245 ppm (median = 1150 ppm) presenting a larger relative variation than the Gaité Index (Fig. VII-11B). Note that [Fe³⁺_{struct.}] was not measured in sample 10A from the top soil because of the likely interference of structural iron from gibbsite. Indeed 10A is the only sample with a strong gibbsite content (see Fig 8). Gaité Index and structural Fe³⁺ exhibit no significant correlation but there might be a tendency (p-value = 0.19) that less ordered kaolinites contain more structural Fe³⁺. Interestingly, the concentration of structural Fe³⁺ correlates with the SiO₂ concentration (R² = 0.32, p-value = 0.04, Fig. VII-11E) and with the Index of Lateritization of the bulk samples (R² = 0.56, p-value = 0.02, Fig. VII-11F). The structural Fe³⁺ shows no correlation with depth (Fig. VII-11B) neither with the amount of Fe₂O₃ in the bulk samples, which is relatively constant throughout the profile (Fig. VII-11D). Note in particular that the naturally white sample (KAW18-4217) has almost no associated iron content whereas the concentration of structural iron in kaolinite is relatively high, around 1550 ppm. The relation between the present iron content of raw samples and the structural Fe³⁺ in kaolinites suggests that the formation of kaolinite and the dynamics of iron in the profile are not connected. The Al-Fe substitution in kaolinite is mainly linked to the solubility of kaolinite, amount of Al, Fe and Si in solution and the activity of water (Didier et al., 1985; Trolard and Tardy, 1989). Since disordered kaolinite has a higher solubility than well-ordered kaolinite, this explains why disordered kaolinite can have higher Fe-Al substitutions (Trolard and Tardy, 1989), a feature that has been observed by several authors (e.g. Rengasamy et al., 1975). According to Tardy (1997), the larger kaolinites from the saprolite are dissolved in the mottled zone (i.e. below the duricrust) and recrystallize in form of small, disordered, Fe-rich kaolinite. We now know however, that the relation between structural iron, as measured from EPR, and crystalline disorder is not general. Indeed, the profiles studied near Manaus by Balan et al. (2005; 2007) present a large variation of kaolinite degree of disorder albeit with a constant concentration of structural iron (Balan et al., 2000; Balan et al., 2007). Consequently, other factors than trivalent iron influence crystalline disorder in kaolinites. Our data from Kaw show only a slight relation of disorder and Fe-substitution in kaolinite, and thus do not fully support the model proposed by Tardy (1997). There is no increase in Fe-substitutions towards the top of the profile and in contrast to the model proposed by Tardy (1997), Fe-substitution in kaolinite seems to decrease with increasing lateritization (IOL) in our samples, i.e. the weathering system tends to purify the kaolinite.

Nevertheless, the variation of structural Fe³⁺ throughout the saprolite can be explained by the amount of silica in the samples, as Trolard and Tardy (1989) have shown that at fixed water activity the Fe substitution in kaolinite increases when the dissolved silica activity increases. Here the total SiO₂ content of samples arising mostly from quartz and kaolinite is considered as a proxy for dissolved SiO₂ that was present when kaolinite crystallized. Since the SiO₂ content is included in the calculation of the index of lateritization and the two values correlate strongly in our dataset, the silica activity can explain the correlation of structural Fe with the IOL. Yet, little kaolinite exists from the duricrust and the upper 5 m of the profile. It is possible that recrystallized disordered kaolinite, which is more soluble than well-ordered kaolinite, was dissolved during the Late Neogene bauxitization which affected the profile. Selective dissolution could have led to the fact that only well-ordered kaolinite survived.

EPR spectroscopic study of kaolinites from two lateritic profiles of the northeastern and eastern Guiana shield (Kaw mountain, French Guiana and Tucano mine, Amapá, Brazil)

Table VII-5: Obtained Gaité indices and structural Fe³⁺ concentrations for the samples of both studied profiles.

Profile	Sample	Gaité Index	abs. error estimated	Structural Fe ³⁺ (ppm)
TUC19	1E	24	3	2448
TUC19	2AA	10	3	1139
TUC19	2BA	11	1	1505
TUC19	2C	9	3	not possible
TUC19	2D	5	0.5	not possible
TUC19	2E			not possible
TUC19	2F	10	2	not possible
TUC19	2G	7	1	2383
TUC19	2H	11	2	not possible
TUC19	2lw	6	0.5	1274
TUC19	2lr	7	1	950
TUC19	2J	9	0.5	1640
KAW18	10A	11	4	not possible
KAW18	480A	5	0.5	1169
KAW18	480B	5	0.5	not possible
KAW18	525	4	0.5	484
KAW18	945	6	1	950
KAW18	750	6	1	1863
KAW18	1405	5	1	428
KAW18	2235	5	1	595
KAW18	3040	8	1	1150
KAW18	3135	4	0.5	not possible
KAW18	3235	5	1	512
KAW18	4217	4	0.5	1537
KAW18	4985	6	1	2245
KAW18	6034	6	1	1796
KAW18	6875	7	1	1639
KAW18	7462	6	1	1005

VII.5.5.2 Kaolinites from Tucano

Gaité index of disorder

The kaolinites from the Tucano mine have generally higher and more variable Gaité indices ranging from 5 to 24 (Fig. VII-12A). This range almost covers the whole range for natural kaolinites as shown by Gaité et al. (1997). The samples from the saprolite present lower indices

from 5 to 11, the best-ordered kaolinite being the one from the weathered felsic dyke TUC19-2D. The samples from the top are less ordered with indices from 9 to 11 in the soil and duricrust matrices and the clay layer and a very high index of 24, indicative for disordered kaolinite, in the duricrust sample TUC19-1E. This indicates that the Fe duricrust did not form just after the saprolitization, in line with the nodule studied by Balan et al. (2005) but in opposition to the Kaw profile. This is in concordance with the processes proposed by Tardy (1997). The samples show a positive correlation of Gaité Index and IOL ($R^2 = 0.37$, p -value = 0.04, Fig. VII-12E), but this correlation disappears when taking the very different sample TUC19-1E out of consideration. Covering a larger range of Gaité indices, the results from Tucano resemble those of other lateritic profiles studied by Balan et al. (2005) or by Mathian et al. (2019; 2020). However, compared to the studies by Balan et al. (2005); Mathian et al. (2019; 2020); Allard et al., (2020), the degree of disorder of our kaolinites from the soil (TUC19-2AA) and the duricrust matrix (TUC19-2BA) are relatively lower. Balan et al. (2007) have shown that in lateritic profiles well-ordered saprolitic kaolinites and disordered newly formed kaolinites might be mixed. The partially ordered kaolinites from the soil and the top of the profile could thus be a mixture of well-ordered saprolitic kaolinite and disordered kaolinite as the one captured in the duricrust.

Concentration of structural Fe^{3+}

Calculation of the structural Fe^{3+} was not possible for all samples as several spectra, notably from the top of the saprolite, exhibited very complicated baselines. The obtained amounts of structural Fe^{3+} are generally higher than at Kaw with values ranging from 950 to 2448 ppm (median = 1505 ppm). They are neither correlated with depth nor the bulk Fe_2O_3 content (Fig. VII-12B and -D), but as for Kaw there might be a tendency towards higher amounts of structural Fe^{3+} in less ordered kaolinites ($R^2 = 0.33$, p -value = 0.18, Fig. VII-12C). Structural Fe^{3+} shows no correlation with the IOL or SiO_2 but except for the duricrust sample TUC19-1E the data plot in the same area as the Kaw data (Fig VII-12F). As only few structural Fe^{3+} data for Tucano could be obtained and the saprolitic kaolinites cover the entire range of structural Fe^{3+} concentrations, the data can neither prove nor refute the possibility of kaolinite mixing at the top of the profile.

EPR spectroscopic study of kaolinites from two lateritic profiles of the northeastern and eastern Guiana shield (Kaw mountain, French Guiana and Tucano mine, Amapá, Brazil)

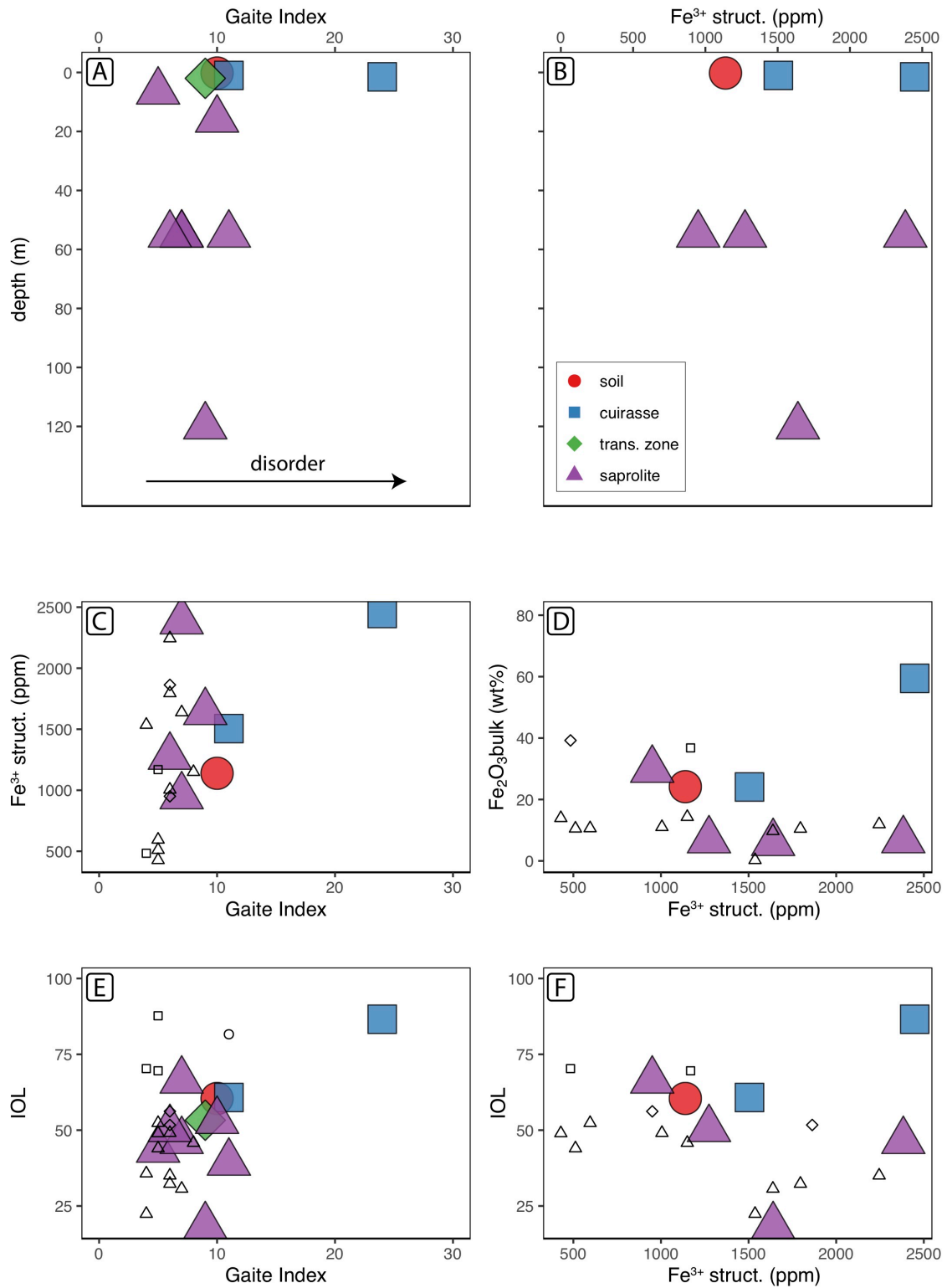


Figure VII-12: Properties of the kaolinites from the Tucano mine. (A) Gaité Index versus sample depth in the profile. Symbol shapes and colors correspond to the sample-type. (B) Structural Fe³⁺ of the kaolinites versus sample depth. Note that for several samples calculation of the structural Fe³⁺ was not possible. (C) Gaité Index versus structural Fe³⁺. (D) Structural Fe³⁺ of the kaolinites versus Fe₂O₃ content of the bulk samples. (E) Gaité Index versus the Index of Lateritization. (F) Structural Fe³⁺ versus the Index of Lateritization. In (C-F) big colored symbols correspond to kaolinites from the Tucano mine, whereas small symbols correspond to kaolinites from Kaw presented in Figure VII-11.

VII.5.6 Radiation-induced defects

VII.5.6.1 Automated fitting of the EPR spectra

In the framework of this study was tried to fit the RID area of kaolinite EPR spectra using the ZFSFIT code (Morin and Bonnin, 1999). Firstly, in order to obtain calibration parameters for the sample fitting, the well-studied GB1 kaolinite was fitted. This was done using the g-factors of the A, A' and B center from the literature. However, changing only the scale factors ("intensity"), widths and peak-shapes (proportion of Lorentzian versus Gaussian shape) of the A, A' and B centers did not yield a satisfying fit, and refinement of the g-factors of the three centers was necessary to obtain a good fit (Fig. VII-13A). The refined g-factors ($g_x = 2.00114$, $g_y = 2.00511$, $g_z = 2.04997$ for A-center ; $g_x = 2.00638$, $g_y = 2.00638$, $g_z = 2.03792$ for A'-center; $g_x = 2.01955$, $g_y = 1.99629$, $g_z = 2.04233$ for B-center) differ only very slightly from the literature values ($g_x = 2.001$, $g_y = 2.006$, $g_z = 2.049$ for A-center, $g_x = 2.039$, $g_z = 2.006$, for A'-center; $g_x = 2.002$, $g_y = 2.02$, $g_z = 2.04$ for B-center (Clozel et al., 1994)). The vanadyl signal was calibrated for the Nowa Ruda reference dickite, yielding in an acceptable but not perfect fit. Indeed, it appears that a second vanadyl spectrum has to be considered in dickite and kaolinite when looking in detail at the high field transitions, the relative amplitude of which is sample dependent, a complexity that adds to the complexity of the baseline.

With the parameters and g-factors obtained for GB1 and the Nowa Ruda dickite, it was tried to fit the sample spectra (RID and vanadyl areas).

For the Tucano samples, only the A, A' and B centers were used to fit the data. However, modifying only scale-factors and widths of the centers did not yield satisfying fits as often the shape of the data was not well reproduced (Fig. VII-13B). Refinement of the peak shapes, g-factors, and distribution of the perpendicular g component was needed in order to reproduce the measured spectra. This allowed us to obtain mathematically correct fits for some of the data but the resulting A, A' and B center shapes often differed from the known shapes obtained by linear decomposition. Furthermore, it was often not possible to fit the different irradiation doses of a same sample using the same parameters, and in several cases g-factors needed to be modified between the different doses. Moreover, the obtained solutions were not unique and differing the starting conditions (e.g. using the results of a higher or a lower dose) led to different results.

For some of the Kaw spectra it was tried to fit both the RIDs and the vanadyl signal. In order to obtain acceptable fits (Fig. VII-13C) forcing of extremely constrained baseline was necessary (Fig. VII-13D).

The attempt to fit the data showed the complexity of the signals and the difficulty to reproduce the data by automated fitting. Due to the strong signal overlap of the components in the area of $g=2$, the solutions are not unique and extraction of the parameters for paleodose calculation is therefore problematic. The fact that refinement of the g -factors needed to be done to fit different samples is not consistent as change of the g -factors in between kaolinite samples has not yet been observed. However, as the differences of the obtained g -factors were very small and the fitting is very sensitive to these changes it could be possible that such small differences have not yet been observed. However, the fact that refinement of the g -factor was needed in between different irradiation doses of the same sample raises some question on the methodology. As the same material was used for the different irradiation doses there is no reason why the g -factors would change between them. As EPR spectrometry is a highly sensible method, small differences in the spectra requiring modification of the g -factors might be related to small, heterogeneously distributed impurities or eventually sample orientation effects.

In addition, fitting attempts of the Kaw spectra suggest that the baselines of the spectra are very complex. Possibly other signals with resonances at $g=2$, such as minor iron oxides are contained in the spectra complicating them additionally.

To summarize this part, it appears that vanadyl and iron nano-oxides interferences together with unrelated signal shapes for RIDs hindered meaningful signal fitting with ZFSFIT code. More work would be needed in order to develop a reliable methodology to fit the types of complex EPR spectra encountered in laterites from Kaw and Tucano. Consequently a simplified approach was undertaken to estimate the concentration of A-centers in the purified kaolinites.

EPR spectroscopic study of kaolinites from two lateritic profiles of the northeastern and eastern Guiana shield (Kaw mountain, French Guiana and Tucano mine, Amapá, Brazil)

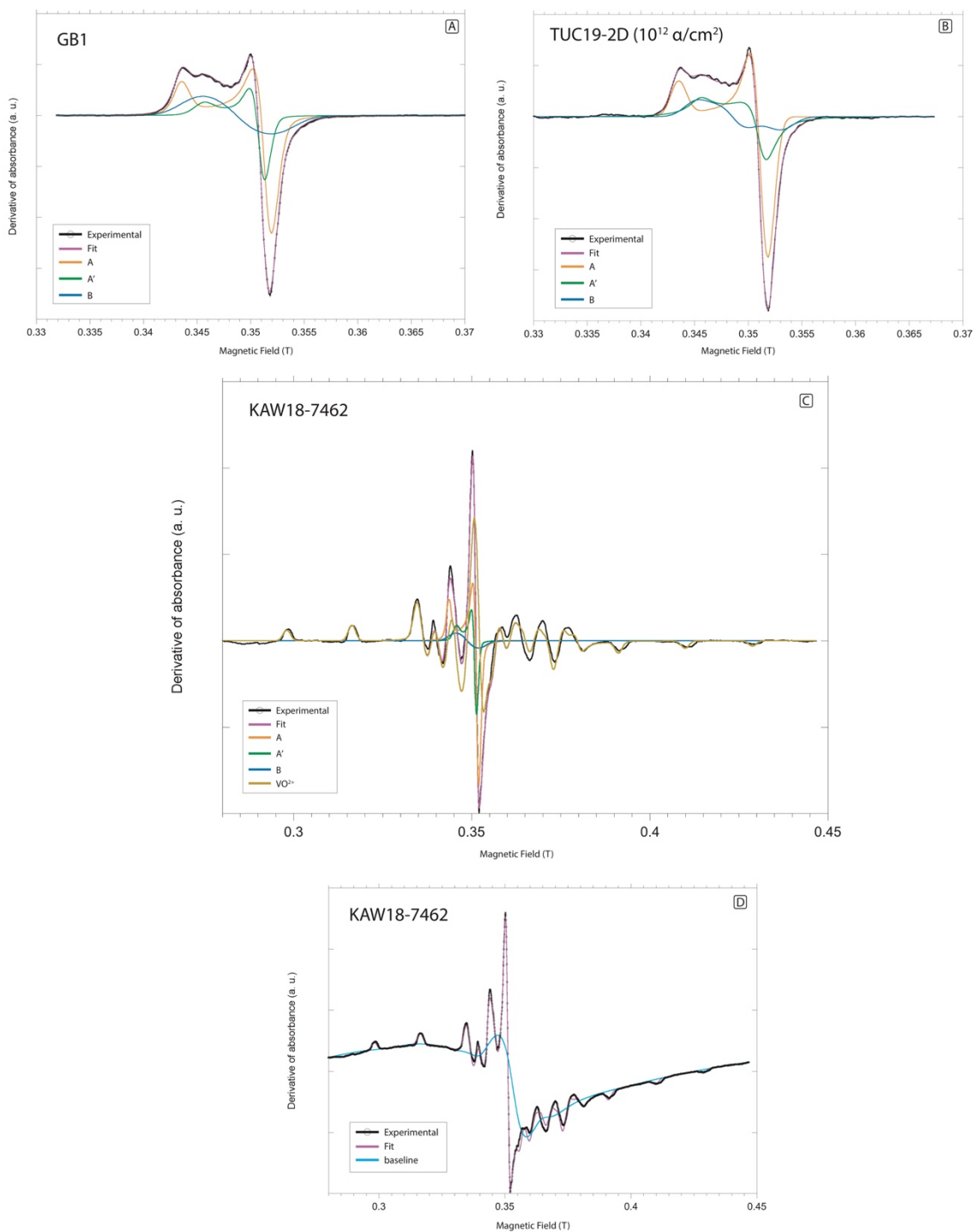


Figure VII-13: Results of the computed fitting of the EPR spectra using the ZFSFIT software. (A) Fitting of the RID signal of GB1 kaolinite (B) Fitting of sample TUC19-2D, irradiated with $10^{12} \text{ He}^+/\text{cm}^2$. Note that the A'-center and the B-center have atypical shapes when compared to GB1. (C) Baseline corrected fit of KAW18-7462 including fitting of the VO^{2+} signal. High field components suggest that an additional spectrum of vanadyl would be required to fit the kaolinite signal. (D) Forced baseline needed to produce the fit presented in (C).

VII.5.6.2 Estimate of [A-center] in the Tucano mine kaolinites

Figure VII-14 and Figure E-3 of the supplementary material show the RID spectra of the natural and irradiated samples from the Tucano mine after 250°C annealing. All samples show an increase of the RID signal at higher irradiation doses, confirming that the observed signals are RIDs. The RID intensity in the naturally irradiated samples shows an important variation throughout the profile (Figure VII-10). Some samples, e.g. TUC19-1J, have atypical RID shapes with a very poor upper peak of the perpendicular component. As explained in Section VII.5.4 this shape could be linked to a baseline jump due to small iron (oxyhydr)oxides. Several RID signals, especially those of higher doses, indicate the presence of remaining A' or B-centers, as seen from the component at $g = 2.039$. Note that 250°C heating is expected to anneal almost all B-centers. Compared to the RID signals in the studies by Mathian (2019, 2020), the RID signals from the Tucano mine are very strong and the baselines are of small amplitude in the RID area. For reasons of comparison, the amplitudes of both perpendicular and parallel component were measured for the Tucano samples (Fig. VII-5). The baseline is then considered linear at either side of the RID signal. Then the amplitude of the perpendicular component is measured at both side of the baseline, reducing the impact of the latter on the measured amplitude. The amplitude of the parallel component is measured only above the baseline. An unknown baseline shape is therefore more problematic of this measurement and induces a larger error onto the latter. For this reason, the perpendicular component was used for paleodose calculation if possible. Table E-3 and Fig. E-5 of the supplementary material present the obtained RID amplitudes and compare the RID amplitudes of the perpendicular and the parallel component.

EPR spectroscopic study of kaolinites from two lateritic profiles of the northeastern and eastern Guiana shield (Kaw mountain, French Guiana and Tucano mine, Amapá, Brazil)

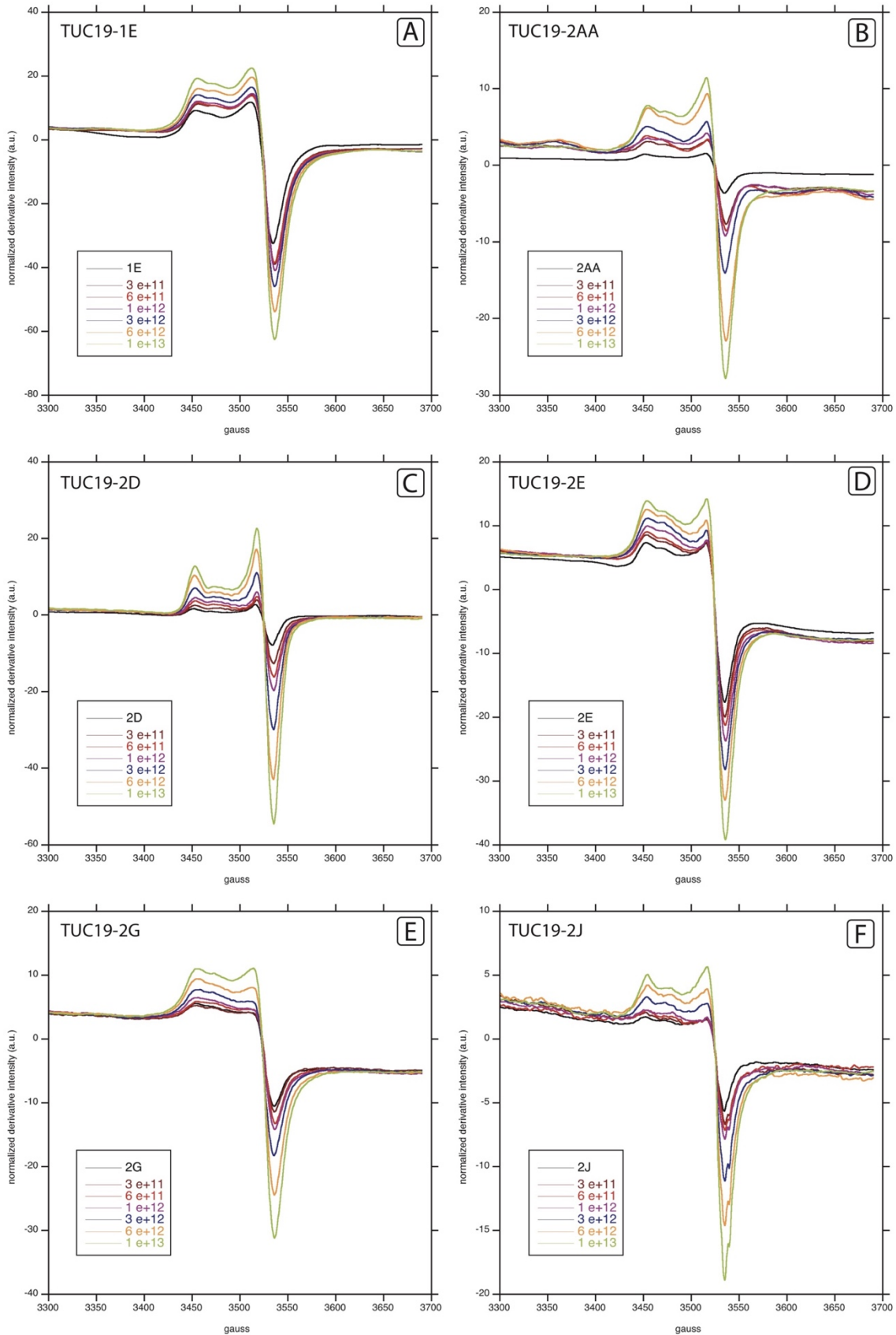


Figure VII-14: Radiation induced defects (RIDs) of selected kaolinite samples from the Tucano mine. Black lines correspond to the natural kaolinite, colored lines correspond to artificial irradiation doses. The legend indicates the irradiation dose in He^+ particles/cm². Similar plots for all other irradiated samples can be found in Figure E-3 of the supplementary material.

VII.5.6.3 Estimate of [A-center] in the Kaw kaolinites

Figure VII-5D shows an example of the vanadyl correction applied to most of the irradiated samples from Kaw. The RID spectra from Kaw, most of which are corrected for vanadyl, are presented in Figure VII-15 and Figure E-4 of the supplementary material. The corrected spectra show forms that are typical for kaolinites. Wavelet with hyperfine constant around 8 gauss in the area of 3500 gauss ($g=2.039$) indicate the presence of B-centers in some samples such as KAW18-7462 or KAW18-3235 (Figs. VII-15D and VII-15F). While most samples show very typical and strong RID signals, especially at high doses, sample KAW18-1A shows an atypical bump between the parallel and the perpendicular A-center components at ca. 3480 gauss (Fig. VII-15A) at high irradiation doses. This feature is not as large as a typical B-center (see Figs. VII-1A and -1B). It might be related to the significant presence of gibbsite in this sample (Fig. VII-8). RIDs in gamma irradiated synthetic gibbsite have been observed previously by EPR (Pushkareva et al., 2002) but no g -values, dosimetry nor thermal stability have been determined, which is a strong limitation for the discussion of the RIDs in KAW18-1A sample.

The applied vanadyl correction technique had already been employed in other studies (Allard et al., 2020; Mathian et al., 2020) but in that cases the vanadyl contributions were much lower and less omnipresent than in the Kaw samples. The successful application here shows that this method yields acceptable results even if the vanadyl contribution is relatively important. As the vanadyl signal is very strong at the position the perpendicular RID component and induces therefore an error onto the latter, the amplitude of the parallel component was measured and used for paleodose calculation in the vanadyl corrected spectra. To minimize error on the parallel component amplitude, the baseline was linearly extrapolated from the region before the RID spectrum.

EPR spectroscopic study of kaolinites from two lateritic profiles of the northeastern and eastern Guiana shield (Kaw mountain, French Guiana and Tucano mine, Amapá, Brazil)

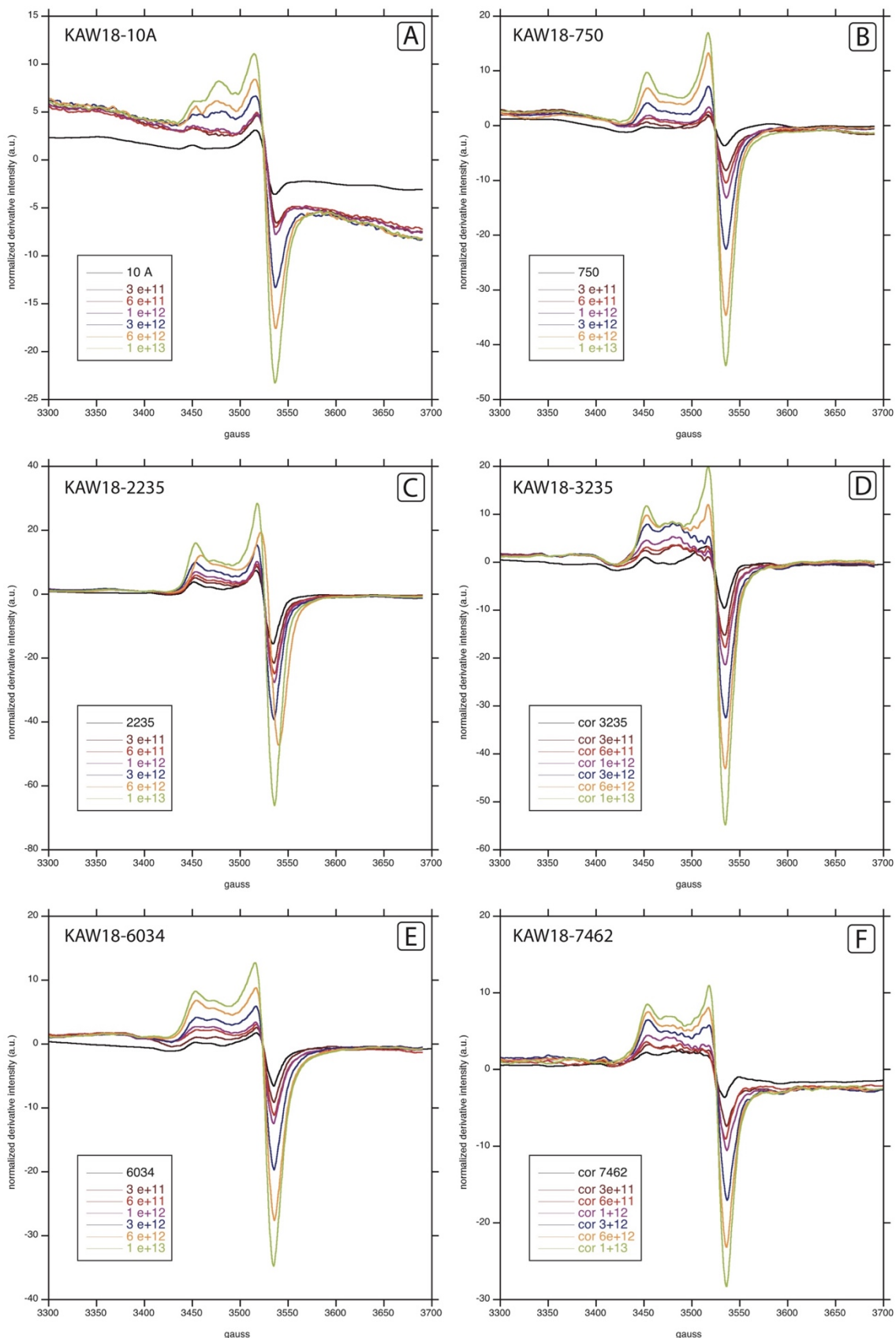


Figure VII-15: Radiation induced defects (RIDs) of selected kaolinite samples from the Kaw drill-core. Black lines correspond to the natural kaolinite, colored lines correspond to artificially irradiated material. The legend indicates the irradiation dose in alpha-particles/cm². Similar plots for all other irradiated samples can be found in Figure E-4 of the supplementary material. If legend indicates “cor” this means that the samples were corrected for vanadyl. Note that high doses in sample 10A show an atypical bump in the middle of the parallel and the perpendicular component. Samples 3235 and 7462 show finely undulated signals due to the B-centers.

VII.5.7 Paleodoses

As the fitting approach of the signal in the RIDs region was not yet acceptable, the simplified procedure was used to estimate the A-center signal amplitudes, which allowed the calculation of paleodoses for all irradiated samples. Following the methodology of the published studies (Balan et al., 2005; Allard et al., 2018; Mathian et al., 2019; Allard et al., 2020; Mathian et al., 2020), the perpendicular component was used for calculation of the Tucano paleodoses. As explained above this would have been problematic for the vanadyl corrected Kaw samples and thus the parallel component was used for paleodose estimation in these samples. In order to validate this procedure, paleodoses were also calculated using the parallel components of the Tucano samples. If the fits were calculated with the same formula (purely exponential or with linear contribution) and of comparable quality (similar residue), the results derived from perpendicular and parallel components were generally comparable.

The results of the paleodose calculations for both sites are presented in Figures VII-16 and VII-17 that show selected dosimetry curves for Kaw and Tucano, respectively. Used dosimetry curves of all other samples and function parameters can be found in Figures E-6 and E-7 and Table E-4 of the supplementary material. For most samples a dosimetry curve with linear component (eq. VII-3, Duval, 2012) yielded a better fit than a purely exponential curve. The fit with the smaller residue was chosen to determine the paleodose. Note however, that in some scarce cases, the residues of the fits with the two formulas are close while the paleodoses might differ a lot (e.g. Figs. VII-14E and E-7E of the Supplementary Material). In such cases, the best fit was also preferred. Other fits with the two functions can give similar paleodoses (Fig. VII-14F).

The dosimetry curves have very different shapes and their parameters show a considerable variation indicating that all samples have a different response to a given irradiation dose (Figs. VII-16 and VII-17). It shows that even samples with similar degrees of ordering (e.g. basically all Kaw samples) have different responses to a given dose (Fig. VII-16). While it has already been shown that different types of kaolinite with different degrees of ordering responded differently to a given dose (Allard et al., 1994), it had previously been assumed that inside one “family” of kaolinites with the same degree of disorder the response would be similar (Allard and Muller, 1998; Balan et al., 2005; Mathian et al., 2019). It was previously possible to correlate the saturation concentration of A-centers with the Gaité index, but this concerned a very limited set of contrasting reference samples exhibiting exponential

EPR spectroscopic study of kaolinites from two lateritic profiles of the northeastern and eastern Guiana shield (Kaw mountain, French Guiana and Tucano mine, Amapá, Brazil)
growth curves under He⁺ irradiation (Allard and Muller, 1998). Our results clearly show that this is not the case and that dosimetry curves should preferably be obtained for all samples.

The obtained paleodoses range from 70 to 266 kGy for Kaw and from 15 to 574 kGy for the Tucano profile. Mathian et al. (2019) estimate the error for the Paleodose to 36% based on the combined errors on RID concentrations and curve fitting. Note however that impact of the formula selection (exponential or exponential with linear component) can be considerably bigger than 36%.

The obtained paleodoses for Kaw and Tucano are higher than those obtained by Mathian et al. (2019) (2-44 kGy), Mathian et al. (2020) (0-110 kGy), Allard et al. (2020) (11-134 kGy) but resemble those obtained by Allard et al. (2018) for Fe-duricrust embedded kaolinites (64 and 398 kGy) and are similar to smaller than those by Balan et al. (2005) (100-1000 kGy). Note however, that the latter authors used two dosimetry curves to model the dosimetry curves for the rest of their dataset according to their degree of disorder.

The paleodose values obtained in this study lie thus in the range of previously studied kaolinites.

EPR spectroscopic study of kaolinites from two lateritic profiles of the northeastern and eastern Guiana shield (Kaw mountain, French Guiana and Tucano mine, Amapá, Brazil)

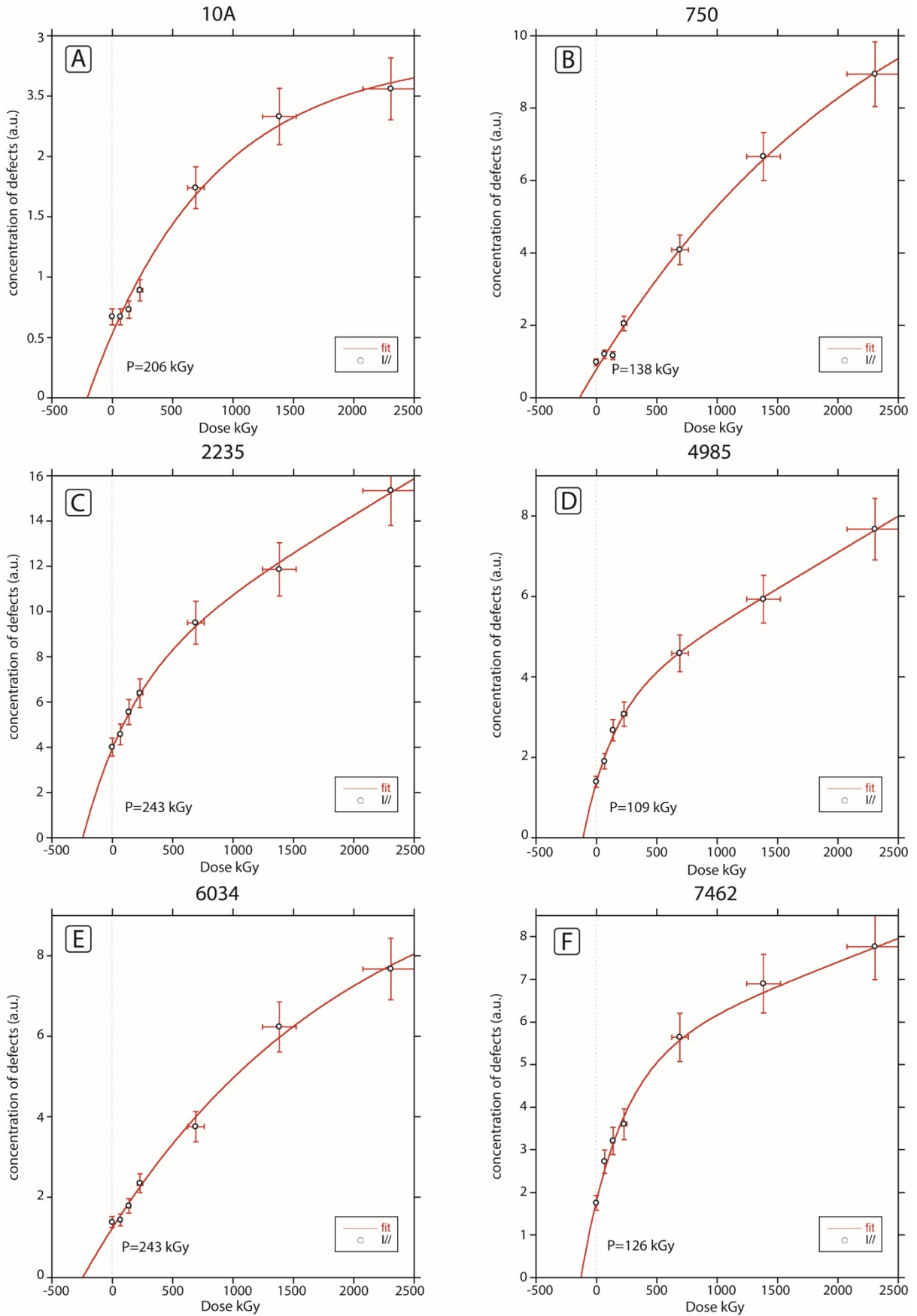


Figure VII-16: Dosimetry curves for selected kaolinite samples from Kaw. The concentration of defects is calculated from the RID signal amplitudes. P corresponds to the paleodose derived from the fit with exponential or exponential + linear functions. While for some samples very good fits were obtained (e.g. 2235, 4985), for others not all points could be well fitted (e.g. 10A, 750). Note that the knickpoint of the curves are different in between the samples.

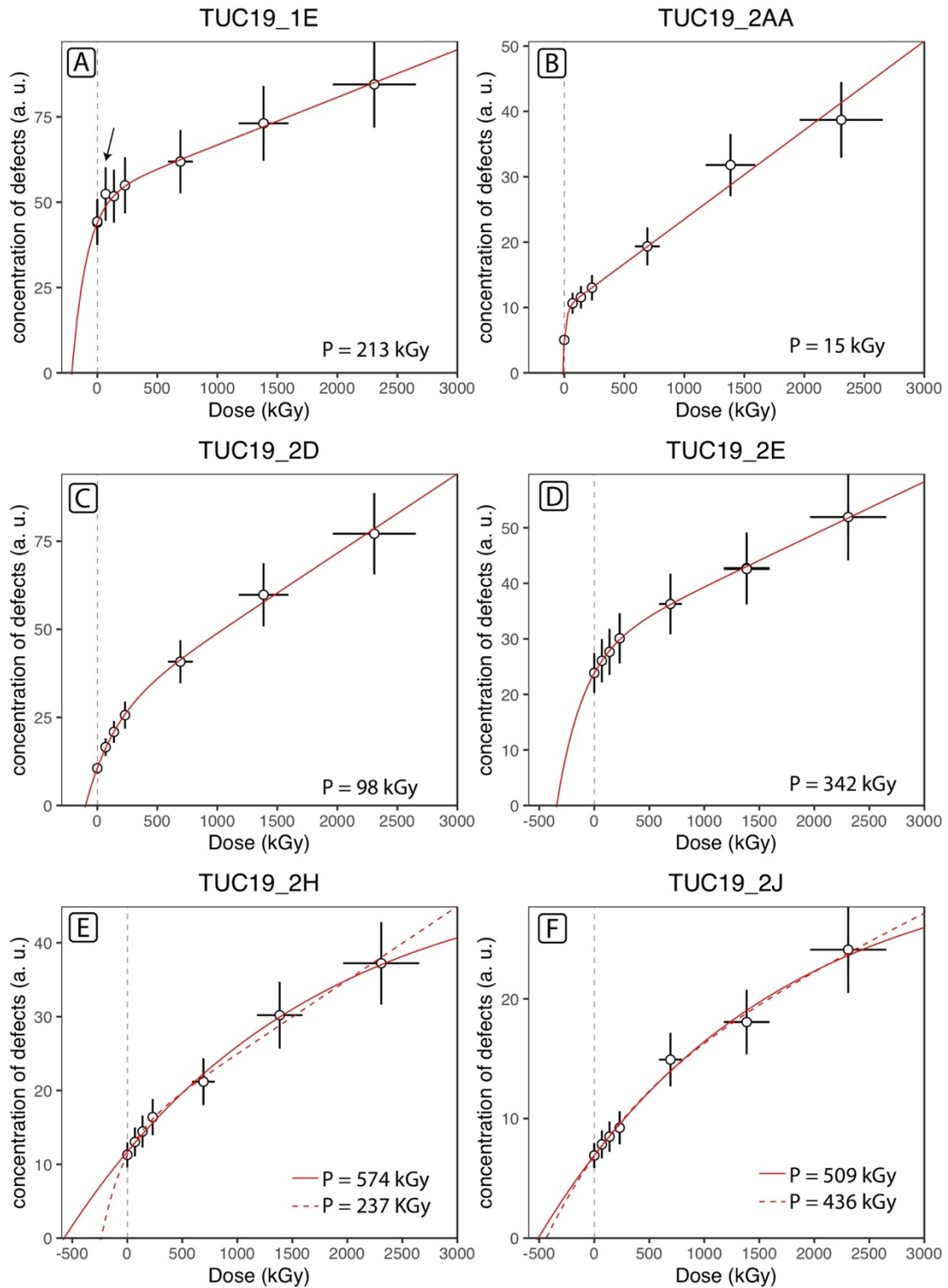


Figure VII-17: Dosimetry curves for selected kaolinite samples from the Tucano mine. The concentration of defects are measured from the RID signal amplitudes. P corresponds to the paleodose obtained by fitting with exponential or exponential + linear functions. (A-D) were fitted using an exponential curve with linear component as this yielded clearly the better fit when compared to a purely exponential function. In (E) and (F), purely exponential functions (solid lines) yielded a slightly better fit than exponential functions with linear components (dashed curves): In these cases paleodoses are given for both functions and yield very different paleodoses in (E) and similar results in (F). The arrow in (A) shows an outlier excluded from the fitting.

VII.5.8 Dose-rates

Figures VII-18 and VII-19 show the RID amplitudes (unirradiated samples) and radioelement (U, Th and K) concentrations for all samples from Kaw and Tucano, respectively. At Kaw, U and Th concentrations are generally higher in the deeper saprolite (>35m), lower in the upper saprolite (6-35m) and highest at the top in the soil sample (Fig. VII-18). Both elements show a similar pattern when compared to Zr indicating that zircon might be an important primary mineral host for the two elements. K concentrations are not presented as they are below the limit of detection for most samples (Fig. VII-6B). The RID amplitudes of the unirradiated Kaw samples show a different pattern when compared to the radioelements.

In the Tucano samples, U and Th concentrations are very constant in the upper two meters but show some important variation throughout the saprolite (Fig. VII-19). Both elements show an overall pattern that resembles the Zr pattern. An exception is sample TUC19-01E which has slightly higher U but lower in Zr concentrations when compared to the other 3 samples from the top (TUC19-2AA, 2BA and 2C) (Fig. VII-19). Furthermore sample TUC19-02F has a very high Th concentration but not a high U concentration. K₂O concentrations show a different pattern and are highest in the muscovite-rich sample TUC19-2E. RID amplitude variation shows some similarities with Th and U variation in the saprolite (e.g. high values in TUC19-2F but the RID pattern can be very different from the radioelement pattern with very low RID amplitudes in samples TUC19-2AA, -2BA and -2C and a very high RID amplitude in TUC19-1E (Fig. VII-19).

EPR spectroscopic study of kaolinites from two lateritic profiles of the northeastern and eastern Guiana shield (Kaw mountain, French Guiana and Tucano mine, Amapá, Brazil)

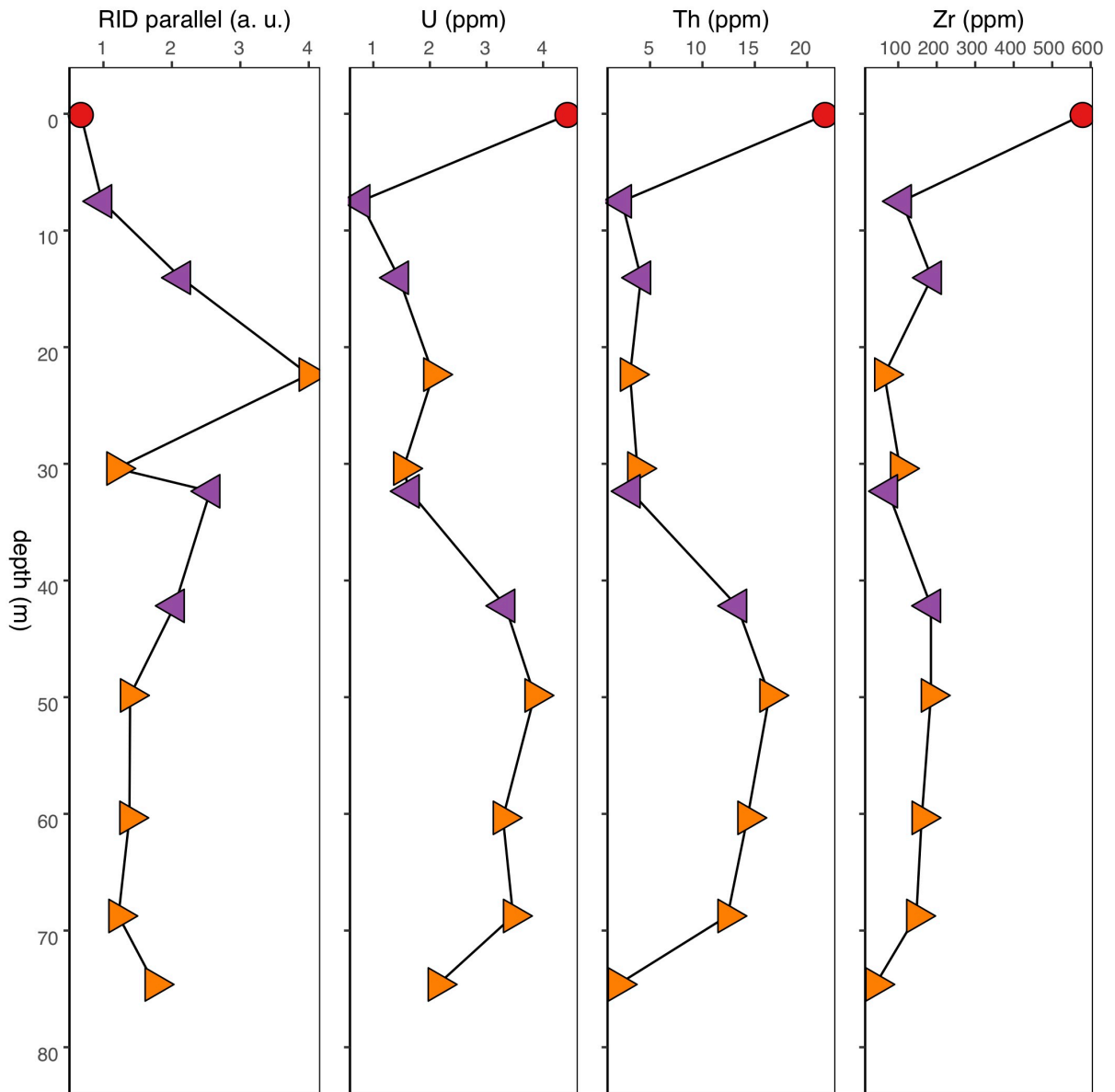


Figure VII-18: Variation of kaolinite RID amplitudes (parallel component, natural material), and bulk U, Th and Zr concentrations as a function of depth for the Kaw samples (red circle = soil, yellow triangle = red saprolite, violet triangle = other saprolite). U, Th and Zr show similar variation whereas the RID amplitudes show a different pattern.

EPR spectroscopic study of kaolinites from two lateritic profiles of the northeastern and eastern Guiana shield (Kaw mountain, French Guiana and Tucano mine, Amapá, Brazil)

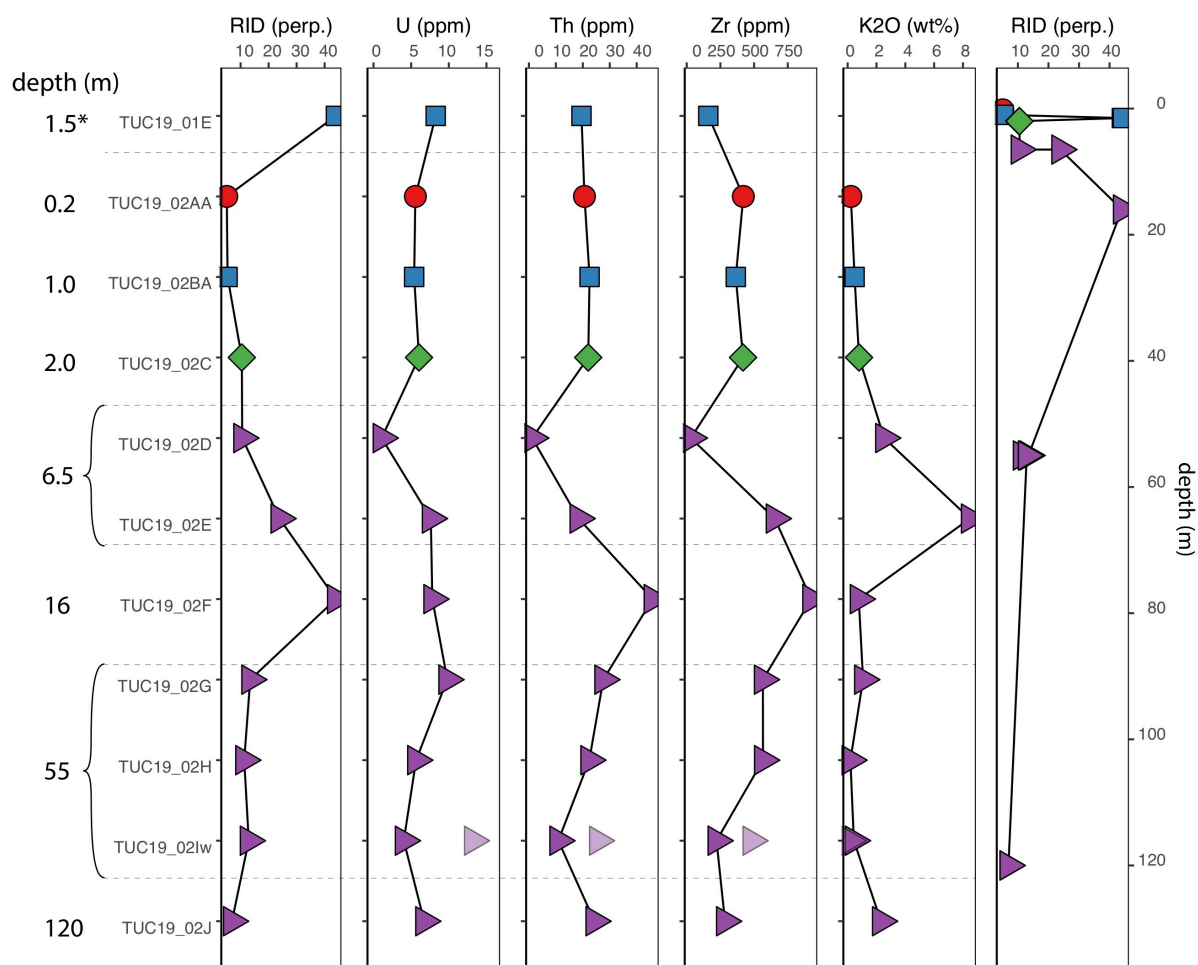


Figure VII-19: RID amplitudes of purified kaolinites and bulk radioelement concentrations for the Tucano samples. (red circle = soil, blue rectangle = duricrust layer, green diamond = transition zone, violet triangle = saprolite). The semi-transparent symbols for TUC19-02lw correspond to sample TUC19-2lr (= red bands of the same sample). The column at the right shows the same RID data as the one on the left but plotted versus a linear scale of depth.

Raw dose-rates were calculated from the U, Th and K concentrations of the bulk samples. They range from 0.005 to 0.031 Gy/a and 0.007 to 0.063 Gy/a for Kaw and Tucano, respectively. However these dose rates do not correspond to the effective dose rates experienced by the kaolinites due to four major factors that are discussed below :

- i. The role of the spatial distribution of the radioelements and thus the effective proportion of alpha radiation to the total dose-rate which corresponds to the largest uncertainty. Radioactive U and Th and their daughter products emit alpha, beta and gamma radiation. The sphere of action of these three types of radiation is very different with alpha particles affecting approximately the surrounding 20 μm in silicate and oxide materials, beta radiation affecting a radius of *circa* 3 mm and gamma radiation a radius of *circa* 30 cm. This means that the distribution of alpha-emitters influences how much of the material will be affected by alpha radiation. If all alpha-emitters (i.e. U and Th

- and some daughters) are concentrated in large and distant U and Th bearing phases, the bulk sample will not significantly experience alpha irradiation. If U and Th are distributed homogeneously in the sample e.g. absorbed onto clay minerals surfaces or contained in fine grained iron (oxyhydr)oxides, all kaolinite is possibly affected by the alpha radiation. Since alpha radiation corresponds to approximately 90% of the dose-rate of U and Th, the effective amount of alpha radiation experienced by the kaolinite minerals is crucial to correct the dose-rate. The distribution of U in a sample can be visualized by induced fission tracks (see Balan et al., 2005 and reference therein). This allows one to estimate the proportion of U concentrated in host minerals and distributed homogeneously in the matrix material. Previous studies have shown that in the lateritic materials this proportion can vary significantly but generally both diffuse and concentrated radioelements coexist (Mathian et al., 2019; Mathian et al., 2020). Since the Th distribution cannot be visualized by induced fission tracks, the distribution needs to be estimated or determined by more sophisticated methods (e. g. X-ray fluorescence in Synchrotron-radiation experiments). In our samples from Kaw and Tucano, there is a strong correlation between U, Th and Zr, zircon being one of the most important U, Th-bearing minerals in the continental crust. Therefore, a significant part of U and Th should be contained in zircons, and the size and abundance of these minerals will be a critical parameter. Unfortunately, the analysis of U fission tracks to produce microscopic mapping could not be performed on time for our samples.
- ii. Possible radon loss. Radon is a daughter product of the U et Th decay chains. As this element is a noble gas it can be lost or accumulated in the soil environment, leading to a disequilibrium in the decay chain of U an Th. In such situation the effective dose rate differs from the raw dose-rate. However our samples are in secular equilibrium, which indicates no gain or loss. We thus assume that this equilibrium existed all along the lifetime of kaolinite.
 - iii. Attenuation effects related to the water content of the samples (Hennig and Grün, 1983; Allard et al., 1994). Water contained in pore spaces of soils and saprolites impacts the effective dose experienced by the kaolinites as the water absorbs some of the radiation. Water thus lowers the effective dose-rate. To visualize roughly the effect of water, a water content of 20% induces a remaining dose rate of 80%. Therefore it is not the strongest correction.

- iv. Amounts and sizes of quartz grains in the samples. The amount of quartz, its distribution and grain size impact the efficiency of the alpha radiation. This can lead to either higher or lower effective dose-rates. The correction can be high if the quartz content is important. Unfortunately there was no time to study the thin sections petrologically. This will be needed in order to estimate the quartz contents and grains sizes of the different samples. As the samples studied here are often banded leading to heterogeneous quartz and kaolinite distributions it would be necessary to consider how this influences the “quartz effect” as such heterogeneity has not yet been included in applied quartz corrections (e.g. Allard et al., 2020).

While the amount of water and quartz can affect the dose-rate by some percent to tens of percent, the dose-rate uncertainty related to the spatial distribution of the radioelements is nearly of a factor 10 (for 0 % alpha dose rate). In order to estimate the minimum and maximum dose-rates, we calculated dose-rates considering 100 %, 50 % and 0 % alpha radiation. These extreme values probably include the uncertainties related to water and quartz content.

Dose rates including all alpha-particles range from 0.005 to 0.031 Gy/a and 0.007 to 0.063 Gy/a for Kaw and Tucano, respectively. Considering only 50% of the alpha radiation, the dose rates are considerably lower ranging from 0.004 to 0.017 Gy/a for Kaw and 0.005 to 0.03 Gy/a for Tucano. Assuming that no alpha radiation was effective yields dose-rates of 0.0007 to 0.003 Gy/a and 0.003 to 0.006 Gy/a for Kaw and Tucano, respectively. Correct dose rates are probably somewhere in between the values for all and no alpha radiation. The obtained dose-rates are reported on Table VII-6 and in Figures VII-20 and VII-21 for Kaw and Tucano, respectively.

EPR spectroscopic study of kaolinites from two lateritic profiles of the northeastern and eastern Guiana shield (Kaw mountain, French Guiana and Tucano mine, Amapá, Brazil)

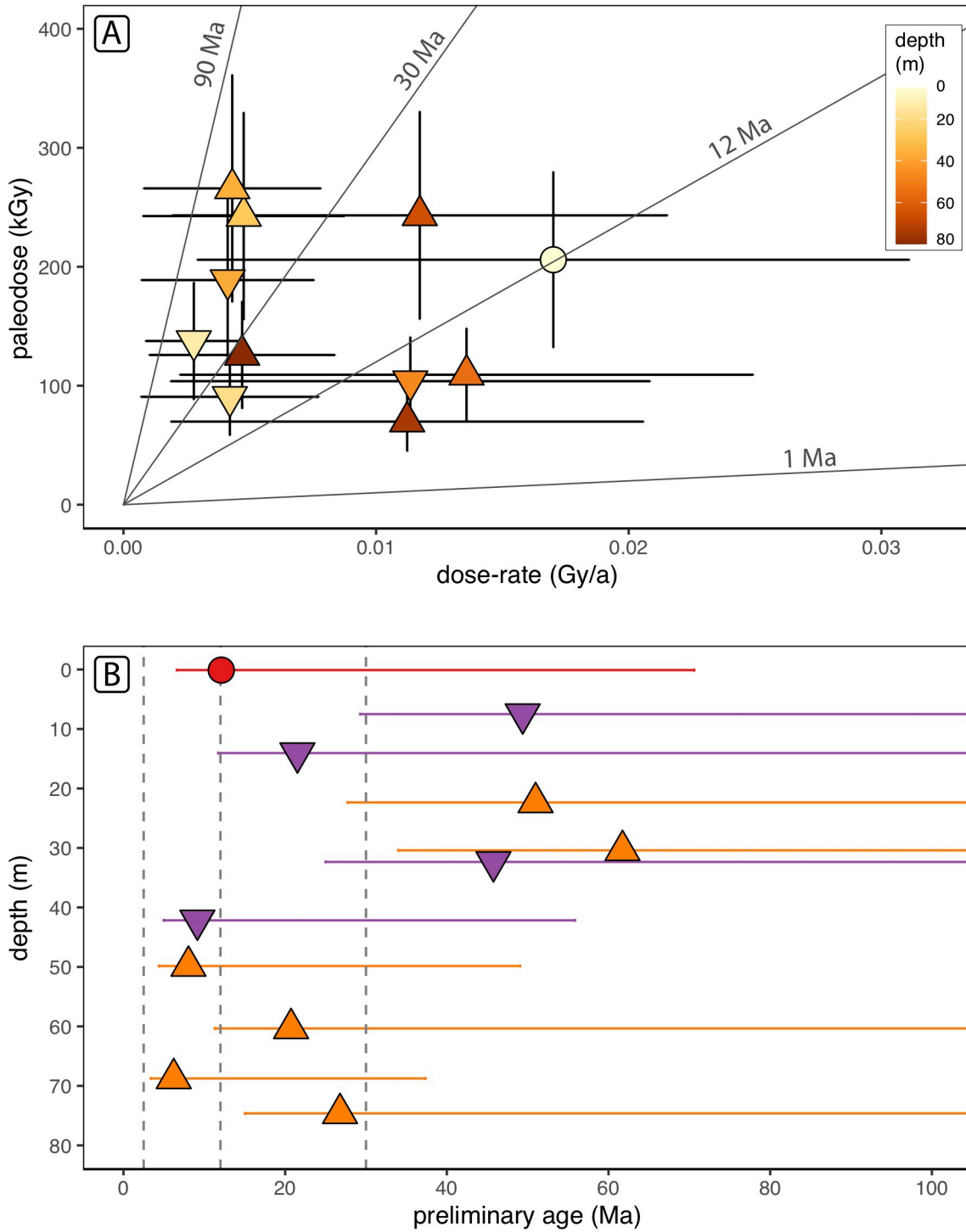


Figure VII-20: Preliminary dating of kaolinites from Kaw: (A) Dose-rates versus paleodoses. Total dose rates were calculated assuming 50% of alpha radiation dose rate. Errorbars of the dose rates consider all alpha (maximum) and no alpha (minimum) contributions. Colors correspond to the sample depth, shapes relate to the sample type and are as in most other figures (circle = soil, triangle = saprolite). Straight lines indicate isochrons (B) shows the preliminary kaolinite ages calculated with 50% alpha radiation versus sample depth for the Kaw samples. As in (A) errorbars correspond to scenarii of 100% and 0% alpha radiation yielding minimum and maximum ages, respectively (red circle = soil, yellow triangles = red saprolite, violet triangles = other saprolite). Gray dashed vertical lines correspond to 30, 12 and 2.5 Ma which are episodes of increased hematite and goethite precipitation in the Kaw duricrusts (Heller et al., (2022)).

VII.5.9 Preliminary ages

Due to the very large uncertainty of the dose-rates, calculation of precise absolute ages is rather illusory here. However, in order to have an idea of the orders of magnitude, preliminary ages were calculated using the obtained paleodoses and dose-rates for 0%, 50% and 100% alpha radiation. The results are presented in Table VII-6 and in Figures VII-20 and VII-21. Note that these preliminary ages do not include the error related to the paleodose which depends on the quality of the fitting of dosimetry data but was estimated to be ca. 36% in Mathian et al., (2019).

Despite the considerable profile heterogeneity, radionuclide distributions are possibly similar between the samples of a same profile. Thus, relative “age” differences contain probably information on the formation and evolution of the lateritic profiles. For this reason we report preliminary ages, given for all, 50% and no alpha-radiation, and discuss their relative differences.

For Kaw, the obtained preliminary ages spread from 6 to 62 Ma considering 50 % alpha radiation and range from 3 to 34 and 37 to 335 Ma considering all or no alpha, respectively. The preliminary age results thus indicate kaolinite ages of several Ma to tens of Ma. The obtained maximum ages (0% alpha) are unlikely because they would imply full hosting of alpha emitters in U,Th-bearing minerals, which was never observed yet in previous studies of induced fission track mapping. In addition, thermochronological studies indicate that the basement rocks of northeastern French Guiana are close to the surface since ca. 90 Ma (Derycke et al., 2021), giving maximum constraint for the onset of weathering. (U-Th)/He ages from the Fe duricrust indicate weathering since at least 30 Ma at Kaw with phases of increased iron (oxyhydr)oxide precipitation at 14-12 Ma and 6-2 Ma (Heller et al., 2022). The 50% alpha radiation ages are thus in the range of expected and possible results. Although all preliminary ages overlap “within error”, there is a trend showing that the highest ages are in the range of 7 to 8 m and 20 to 35m depth (Fig. VII-20). At the very top, at 14m and below 35m the obtained preliminary ages tend to be younger and are more disperse.

According to the models of the development of weathering profiles (Tardy, 1997) it is expected that the age of weathering decreases continuously from the top to the bottom due to the downwards movement of the weathering front. While some studies seem to have confirmed this (Théveniaut and Freyssinet, 1999), the study by Mathian et al., (2019) indicates that age depth relationships are probably more complicated as different parts of the profile

could have been affected by later weathering episodes whereas some areas might have been protected from such overprints.

The preliminary results from the Kaw saprolite indicate that the lower saprolite is overall younger than the upper saprolite. This could be related to the general downwards movement of the weathering front. If the observed variability between 35 and 75 m has any significance or not cannot be solved here due to the preliminary character of the ages. The soil and the saprolite sample at 14 m show lower paleodoses and preliminary ages. This could be related to a more recent rejuvenation at the top of the profile as this has previously been observed in several studies (Balan et al., 2005; Mathian et al., 2020) and has recently also been supported by modelling results of Si isotopes (Guinoiseau et al., 2021). Unfortunately most of the purified kaolinite samples from the duricrust could not be analyzed due to the strong vanadyl signal. However, this might possibly also indicate that the RIDs concentrations are relatively low in these samples with kaolinites tending to be younger than in the underlying saprolite. The preliminary ages obtained at 7-8 m and in between 20 and 35 m depth are relatively old compared to the (U-Th)/He ages obtained on the duricrust, even when considering the enormous error of the former. This possibly indicates that the early stages of weathering are better preserved in the saprolite than in the duricrust and that the onset of weathering at Kaw predates the Oligocene.

At Tucano, 50 % alpha radiation ages range from 0.8 to 30 Ma whereas 100% and 0% alpha radiation ages span from 0.4 to 16.2 and 5 to 172 Ma, respectively. For samples TUC19-2lw 2x3 ages (referring to TUC19-2lw and TUC19-2lw*) were calculated as the geochemical results show that the white and the red bands have different chemical compositions. The ages of TUC19-2lw were calculated using the radioelement compositions of TUC19-2lw and using 100%, 50% and 0% alpha radiation. The ages of TUC19-2lw* were calculated considering the alpha radiation (100, 50 or 0%) of TUC19-2lw but the beta and gamma radiation of TUC19-2lr. Since beta and gamma radiation affect a larger area (cm radius) beta and gamma radiation of the more radioactive red layers probably affected also the kaolinites in the white layers. Considering only the radioelements of the white layers leads thus to an underestimation of the dose rate and too old ages. The results of TUC19-2lw* are therefore more reasonable.

The preliminary results from the Tucano thus show some similarities and some important differences when compared to the Kaw profile. As for Kaw the highest paleodoses and also the oldest preliminary ages are preserved in the saprolite (Fig. VII-21). The top

EPR spectroscopic study of kaolinites from two lateritic profiles of the northeastern and eastern Guiana shield (Kaw mountain, French Guiana and Tucano mine, Amapá, Brazil)

samples, which are the soil matrix TUC19-2AA and the duricrust matrix TUC19-2BA and, to a lesser degree the clay horizon TUC19-2C show much lower paleodoses and preliminary ages. Interestingly this is not the case for the duricrust sample TUC19-1E, which has a higher paleodose and preliminary age (even when considering the large errorbars an age difference exists). This indicates that the top of the profile was recently rejuvenated but the kaolinite trapped in the duricrust was protected from this rejuvenation. This resembles the observation by Balan et al., (2005), who observed kaolinite in Fe-rich nodules was protected from later rejuvenation. However, in contrast to our results, in that study the kaolinite captured in the duricrust is very well-ordered and resembles the kaolinite of the saprolite. This is not the case here, where the duricrust kaolinite is the only very disordered kaolinite of the samples set. This indicates that in contrast to the study by Balan et al. (2005), three dominant groups of kaolinites are present in the Tucano profile: i) saprolite kaolinites which are well-ordered, old and possibly unaffected by major recent reworking ii) more or less well-ordered kaolinites which are very young and formed or recrystallized through recent rejuvenation found primarily in the soft material at the top of the profile and iii) disordered kaolinite with an age probably between the saprolite and the soil which was captured in the duricrust and was therefore protected from the recent rejuvenation. The very young ages obtained in the matrix kaolinites at the top of the profile refute the possibility, indicated by the Gaité indices, that these kaolinites are mixtures of well-ordered saprolitic and disordered duricrust kaolinites.

EPR spectroscopic study of kaolinites from two lateritic profiles of the northeastern and eastern Guiana shield (Kaw mountain, French Guiana and Tucano mine, Amapá, Brazil)

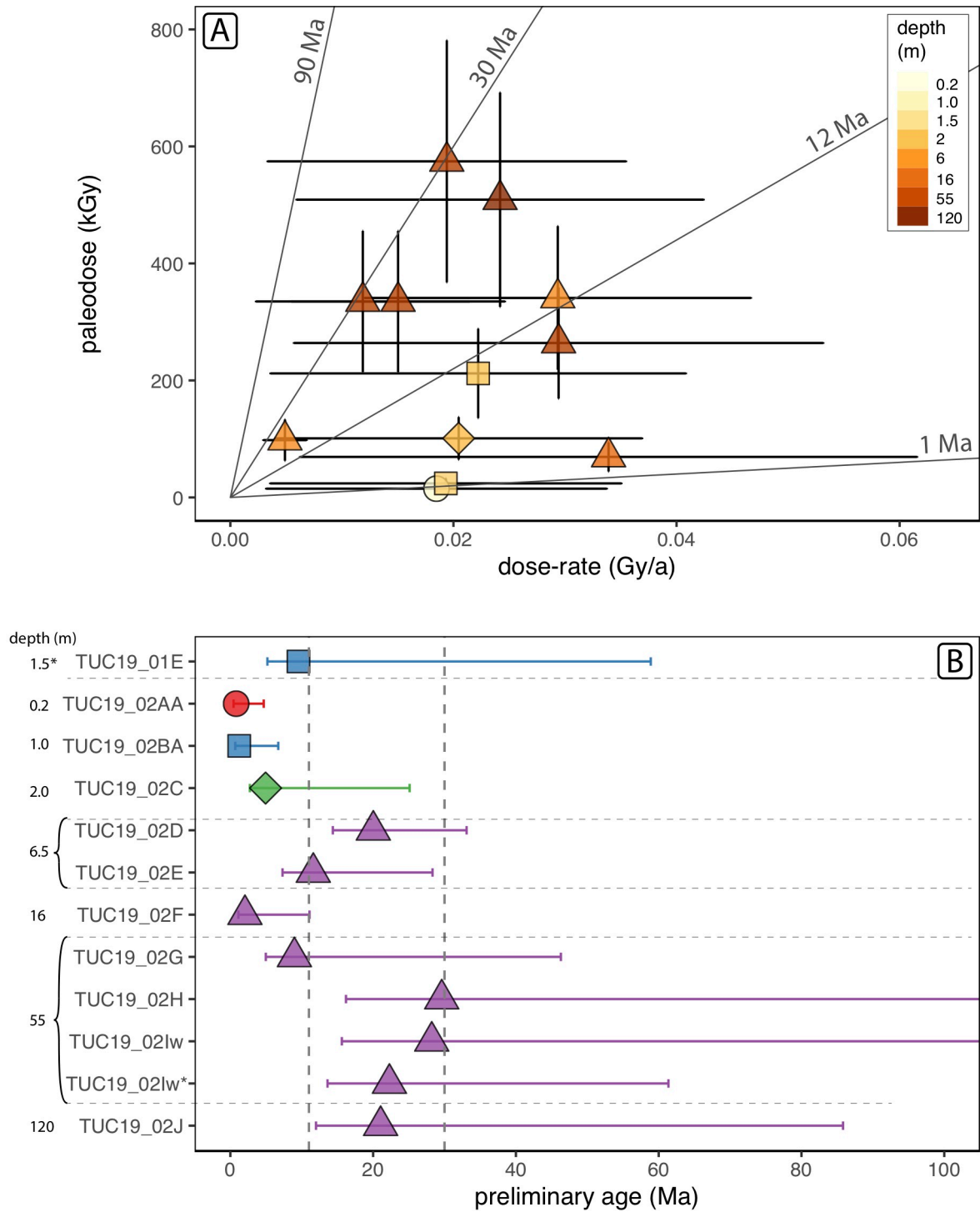


Figure VII-21: Preliminary dating of kaolinites from the Tucano mine: (A) Dose-rates versus paleodoses. Dose rates were calculated considering 50% alpha radiation. Errorbars of the dose rates consider all alpha (maximum) and no alpha (minimum) radiation. Note that for better visibility the x-axis is truncated at 110 Ma. Colors correspond to the sample depth, shapes relate to the sample type and are as in most other figures (circle = soil, rectangle = duricrust, diamond = transition zone, triangle = saprolite). Straight lines indicate specific isochrons. (B) shows the preliminary kaolinite ages calculated with 50% alpha radiation for each of the Tucano samples. Depths are given at the left. As in (A) errorbars correspond to scenarii of 100% and 0% alpha radiation yielding minimum and maximum ages, respectively (red circle = soil, yellow triangles = red saprolite, violet triangles = other saprolite). Gray dashed vertical lines correspond to 30 and 11 Ma which are episodes of increased hematite and goethite precipitation in the Tucano duricrusts (see Chapter V). The age of TUC19_02lw was calculated using the U, Th and K concentrations of TUC19_02lw whereas the age of TUC19_02lw* was calculated using the alpha radiation of TUC19_02lw and the beta and gamma radiation of TUC19_02lr (see text for mor details). Note that sample TUC19-01E was sampled with about 150m lateral offset.

EPR spectroscopic study of kaolinites from two lateritic profiles of the northeastern and eastern Guiana shield (Kaw mountain, French Guiana and Tucano mine, Amapá, Brazil)

The preliminary kaolinite ages obtained in the saprolite and the duricrust resemble those of the hematite and goethite (U-Th)/He ages obtained for this site, which range back to the Late Cretaceous / Early Paleogene and indicate the presence of two weathering events peaking at 30 and 11 Ma (dashed vertical lines in Figure VII-21). The kaolinite ages in the saprolite are likely not older than the (U-Th)/He ages from the duricrust, but due to the large error this cannot be assessed here. Nevertheless, the data allow us to conclude that a very recent weathering (< 5 Ma, i.e. maximum age of TUC19-2AA) affected the top of the profile but possibly did not lead to the (re)precipitation of Fe (oxyhydr)oxides since the youngest goethite minerals in the duricrusts were dated at 8 Ma.

The preliminary ages allow some first insights into the temporal evolution of the present profiles. However, it would be necessary to study the spatial distributions of the radioelements in the samples and to better investigate them petrologically in order to reduce the error in the dose rate and to obtain meaningful ages.

Table VII-6: Kaolinite age data for both studied profiles. Ages considering 50% alpha-radiation are likely the best estimates, ages considering 100% and 0% alpha-radiation can be considered as maximum errors of the ages.

Sample	Depth	U	Th	Zr	K ₂ O	Paleodose	Dose-rate 100% alpha	Dose-rate 50% alpha	Dose-rate 0% alpha	Age 100% alpha	Age 50% alpha	Age 0% alpha
	m	ppm	ppm	ppm	wt%	kGy	Gy/a	Gy/a	Gy/a	Ma	Ma	Ma
KAW18-10A	0.1	4.4	21.7	579	0.14	206	0.0311	0.0170	0.0029	6.6	12.1	70.6
KAW18-750	7.5	0.8	2.3	109	0.49	138	0.0047	0.0028	0.0009	29.3	49.4	157.4
KAW18-1405	14.1	1.5	4.1	187	bld	91	0.0077	0.0042	0.0007	11.7	21.5	132.3
KAW18-2235	22.4	2.1	3.1	64	bld	243	0.0088	0.0048	0.0008	27.7	51.0	317.1
KAW18-3040	30.4	1.5	3.8	105	0.11	266	0.0078	0.0043	0.0008	34.0	61.7	335.3
KAW18-3235	32.4	1.6	3.1	73	0.04	189	0.0076	0.0041	0.0007	25.0	45.8	269.6
KAW18-4217	42.2	3.3	13.3	185	bld	104	0.0209	0.0114	0.0019	5.0	9.1	55.9
KAW18-4985	49.9	3.9	16.4	185	bld	109	0.0249	0.0136	0.0022	4.4	8.0	49.1
KAW18-6034	60.3	3.3	14.3	161	bld	243	0.0215	0.0117	0.0019	11.3	20.7	126.4
KAW18-6875	68.8	3.5	12.4	147	0.04	70	0.0206	0.0112	0.0019	3.4	6.2	37.4
KAW18-7462	74.6	2.1	1.9	41	0.31	126	0.0084	0.0047	0.0010	15.0	26.8	123.8
TUC19_02AA	0.2	5.6	20.6	420	0.22	15	0.0337	0.0185	0.0032	0.4	0.8	4.7
TUC19_02BA	1.0	5.4	22.5	364	0.48	24	0.0351	0.0193	0.0036	0.7	1.2	6.7
TUC19_01E	1.5	8.3	19.5	160	bld	212	0.0408	0.0222	0.0036	5.2	9.5	58.9
TUC19_02C	2.0	6.0	22.0	418	0.79	101	0.0369	0.0205	0.0040	2.7	4.9	25.1
TUC19_02D	6.5	1.1	1.2	30	2.53	98	0.0068	0.0049	0.0030	14.4	20.0	33.1
TUC19_02E	6.5	7.6	18.4	653	8.48	341	0.0467	0.0294	0.0120	7.3	11.6	28.3
TUC19_02F	16.0	7.8	45.9	924	0.77	69	0.0616	0.0339	0.0062	1.1	2.0	11.1
TUC19_02G	55.0	9.8	27.6	565	1.07	264	0.0531	0.0294	0.0057	5.0	9.0	46.3
TUC19_02H	55.0	5.7	22.4	566	0.19	574	0.0355	0.0194	0.0033	16.2	29.6	172.1
TUC19_02Iw*	55.0	13.2	25.6	480	0.12	335	0.0246	0.0150	0.0055	13.6	22.3	61.4
TUC19_02Iw	55.0	4.0	10.9	221	0.43	335	0.0215	0.0119	0.0023	15.6	28.2	145.8
TUC19_02J	120.0	6.7	24.3	284	2.31	509	0.0424	0.0242	0.0059	12.0	21.1	85.8

VII.6 Conclusions

This study concentrates on purified kaolinites from two very deep lateritic profiles on the northeastern and eastern Guiana shield. Both profiles record strong tropical weathering and show an important protolith heterogeneity complicating their geochemical investigation. Investigation of the crystalline disorder of the kaolinites from the 75m Kaw drill core indicates that well-ordered clay minerals formed under near identical, possibly kinetic, conditions throughout the entire profile, excluding the topsoil where they are less ordered. Structural Fe^{3+} concentrations in these kaolinites is disconnected from bulk Fe_2O_3 compositions but shows a relation with the Index of Lateritization and dissolved SiO_2 concentration. Kaolinites from the 120m deep Tucano mine profile indicate more variable formation conditions and are very well-ordered throughout the saprolite and disordered in the duricrust at the top of the profile. Radiation induced defects (RIDs) are present in nearly all samples but often are overlapped by a strong vanadyl signal at Kaw. While computed spectra fitting yielded no satisfying results and would require further effort, spectra correction by manual subtraction of a vanadyl reference signal allowed extraction of the RID signals. Dosimetry curves obtained through artificial irradiation of 22 selected samples yield paleodoses ranging from ca. 15 to 575 kGy and show that all samples, even those with a very similar degree of structural ordering, have different dosimetry parameters. Dose-rates were calculated from radioelement concentrations and were used for calculation of preliminary kaolinite ages. Preliminary ages derived from 3 scenarii providing a frame of major uncertainties allow a first insight into the evolution of the two profiles. At Kaw, the oldest kaolinites can be found in the upper saprolite (< 35 m depth) and they could be older than the oldest remaining iron oxides preserved in the Fe duricrust from the top of the profile, which are Oligocene in age. In the Tucano mine, the oldest kaolinites with ages of several millions to tens of millions of years are preserved in the deeper parts of the profile. The soft material of the top of the profile experienced very recent rejuvenation but kaolinites captured in the duricrust were apparently protected from this process and yield older ages. Further investigation of the radioelement distribution will be needed in order to reduce the uncertainties of the dose rates and to obtain meaningful ages.

References

- Adamiec G. and Aitken M. (1998) Dose-rate conversion factors: update. *Anc. TL* **16**, 41–49.
- Allard T., Balan E., Calas G., Fourdrin C., Morichon E. and Sorieul S. (2012) Radiation-induced defects in clay minerals: A review. *Nucl. Instruments Methods Phys. Res. Sect. B Beam Interact. with Mater. Atoms* **277**, 112–120.
- Allard T., Gautheron C., Bressan Riffel S., Balan E., Soares B. F., Pinna-Jamme R., Derycke A., Morin G., Bueno G. T. and do Nascimento N. (2018) Combined dating of goethites and kaolinites from ferruginous duricrusts. Deciphering the Late Neogene erosion history of Central Amazonia. *Chem. Geol.* **479**, 136–150.
- Allard T. and Muller J. P. (1998) Kaolinite as an in situ dosimeter for past radionuclide migration at the earth's surface. *Appl. Geochemistry* **13**, 751–765.
- Allard T., Muller J. P., Dran J. C. and Ménager M. T. (1994) Radiation-induced paramagnetic defects in natural kaolinites: Alpha dosimetry with ion beam irradiation. *Phys. Chem. Miner.* **21**, 85–96.
- Allard T., Pereira L., Mathian M., Balan E., Taitson Bueno G., Falguères C. and do Nascimento N. R. (2020) Dating kaolinite from the Neogene Içá Formation and overlying laterites, central Amazonia, Brazil: Constraints for a stratigraphic correlation. *Palaeogeogr. Palaeoclimatol. Palaeoecol.* **554**.
- Angel B. R., Cuttler A. H., Richards K. S. and Vincent W. E. J. (1977) Synthetic kaolinites doped with Fe²⁺ and Fe³⁺ ions. *Clays Clay Miner.* **25**, 381–383.
- Babechuk M. G., Widdowson M. and Kamber B. S. (2014) Quantifying chemical weathering intensity and trace element release from two contrasting basalt profiles, Deccan Traps, India. *Chem. Geol.* **363**, 56–75.
- Balan E., Allard T., Boizot B., Morin G. and Muller J. P. (2000) Quantitative measurement of paramagnetic Fe³⁺ in kaolinite. *Clays Clay Miner.* **48**, 439–445.
- Balan E., Allard T., Boizot B., Morin G. and Muller J. P. (1999) Structural Fe³⁺ in natural kaolinites: New insights from electron paramagnetic resonance spectra fitting at X and Q-band frequencies. *Clays Clay Miner.* **47**, 605–616.
- Balan E., Allard T., Fritsch E., Sélo M., Falguères C., Chabaux F., Pierret M. C. and Calas G. (2005) Formation and evolution of lateritic profiles in the middle Amazon basin: Insights from radiation-induced defects in kaolinite. *Geochim. Cosmochim. Acta* **69**, 2193–2204.

- Balan E., Fritsch E., Allard T. and Calas G. (2007) Inheritance vs. neoformation of kaolinite during lateritic soil formation: A case study in the Middle Amazon basin. *Clays Clay Miner.* **55**, 253–259.
- Bardossy G. and Aleva G. J. J. (1990) *Lateritic Bauxites*. Developmen., Elsevier Science, Amsterdam, The Netherlands.
- Beauvais A. and Bertaux J. (2002) In situ characterization and differentiation of kaolinites in lateritic weathering profiles using infrared microspectroscopy. *Clays Clay Miner.* **50**, 314–330.
- Carbone C., Di Benedetto F., Marescotti P., Sangregorio C., Sorace L., Lima N., Romanelli M., Lucchetti G. and Cipriani C. (2005) Natural Fe-oxide and -oxyhydroxide nanoparticles: An EPR and SQUID investigation. *Mineral. Petrol.* **85**, 19–32.
- Cases J.-M., Lirtard O., Yvon J. and Delon J.-E. (1982) Etude des proprietes cristallographiques, morphologiques, superficielles de kaolinites desordonnees. *Bull. Minéralogie* **105**, 439–455.
- Choubert B. (1956) *Les Gisements de bauxite de la Guyane Française.*
- Clozel B., Allard T. and Muller J. P. (1994) Nature and stability of radiation-induced defects in natural kaolinites: New results and a reappraisal of published works. *Clays Clay Miner.* **42**, 657–666.
- Cornu S., Lucas Y., Lebon E., Ambrosi J. P., Luizão F., Rouiller J., Bonnay M. and Neal C. (1999) Evidence of titanium mobility in soil profiles, Manaus, central Amazonia. *Geoderma* **91**, 281–295.
- Delor C., Lahondère D., Egal E., Lafon J. M., Cocherie A., Guerrot C., Rossi P., Truffert C., Théveniaut H., Phillips D. and Avelar V. G. de (2003) Transamazonian crustal growth and reworking as revealed by the 1:500,000-scale geological map of French Guiana (2nd edition). *Geol. la Fr.* **2-3-4**, 5–57.
- Derycke A., Gautheron C., Barbarand J., Bourbon P., Aertgeerts G., Simon-Labric T., Sarda P., Pinna-Jamme R., Boukari C. and Haurine F. (2021) French Guiana margin evolution: From Gondwana break-up to Atlantic opening. *Terra Nov.*, 1–8.
- Didier P., Perret D., Tardy Y. and Nahon D. (1985) Equilibres entre kaolinites ferrifères, goethites alumineuses et hématites alumineuses dans les systèmes cuirassés. Rôle de l'activité de l'eau et de la taille des pores / Equilibria between Fe-kaolinites, Al-goethites and Al-hematites in ferricretes. Par. *Sci. Géologiques. Bull.* **38**, 383–397.

- Duval M. (2012) Dose response curve of the ESR signal of the Aluminum center in quartz grains extracted from sediment. *Anc. TL* **30**, 11–16.
- Fialips C. I., Petit S., Decarreau A. and Beaufort D. (2000) Influence of synthesis pH on kaolinite “crystallinity” and surface properties. *Clays Clay Miner.* **48**, 173–184.
- Gaite J.-M., Ermakoff P., Allard T. and Muller J.-P. (1997) Paramagnetic Fe³⁺: a Sensitive Probe for Disorder in Kaolinite Origins of Line Broadening. *Clays Clay Miner.* **45**, 496–505.
- Gaite J. M., Ermakoff P. and Muller J. P. (1993) Characterization and origin of two Fe³⁺ EPR spectra in kaolinite. *Phys. Chem. Miner.* **20**, 242–247.
- Goodman B. A., Worasith N. and Deng W. (2016) EPR spectra of a new radiation-induced paramagnetic centre in kaolins. *Clay Miner.* **51**, 707–714.
- Guinoiseau D., Fekiacova Z., Allard T., Druhan J. L., Balan E. and Bouchez J. (2021) Tropical Weathering History Recorded in the Silicon Isotopes of Lateritic Weathering Profiles. *Geophys. Res. Lett.* **48**.
- Guskos N., Papadopoulos G. J., Likodimos V., Patapis S., Yarmis D., Przepiera A., Przepiera K., Majszyk J., Typek J., Wabia M., Aidinis K. and Drazek Z. (2002) Photoacoustic, EPR and electrical conductivity investigations of three synthetic mineral pigments: Hematite, goethite and magnetite. *Mater. Res. Bull.* **37**, 1051–1061.
- Heller B. M., Riffel S. B., Allard T., Morin G., Roig J.-Y., Couëffé R., Aertgeerts G., Derycke A., Ansart C., Pinna-Jamme R. and Gautheron C. (2022) Reading the climate signals hidden in bauxite. *Geochim. Cosmochim. Acta* **323**, 40–73.
- Hennig G. J. and Grün R. (1983) ESR dating in quaternary geology. *Quat. Sci. Rev.* **2**, 157.238.
- Jones J. P. E., Angel B. R. and Hall P. L. (1974) Electron spin resonance studies of doped synthetic kaolinite. II. *Clay Miner.* **10**, 257–270.
- Lucas Y., Nahon D., Cornu S. and Eyrolles F. (1996) Genèse et fonctionnement des sols en milieu équatorial. *CR. Acad. Sci. Paris* **322**, 1–16.
- Mathian M., Aufort J., Braun J. J., Riotte J., Selo M., Balan E., Fritsch E., Bhattacharya S. and Allard T. (2019) Unraveling weathering episodes in Tertiary regoliths by kaolinite dating (Western Ghats, India). *Gondwana Res.* **69**, 89–105.
- Mathian M., Bueno G. T., Balan E., Fritsch E., Do Nascimento N. R., Selo M. and Allard T. (2020) Kaolinite dating from Acrisol and Ferralsol: A new key to understanding the landscape evolution in NW Amazonia (Brazil). *Geoderma* **370**.

- Mehra O. P. and Jackson M. L. (1960) Iron oxide removal from soils and clays by a dithionite-citrate system buffered with sodium bicarbonate. *Clays Clay Miner.* **7**, 317–327.
- Morin G. and Bonnin D. (1999) Modeling EPR Powder Spectra Using Numerical Diagonalization of the Spin Hamiltonian. *J. Magn. Reson.* **136**, 176–199.
- Muller J.-P. and Calas G. (1993) Genetic significance of paramagnetic centers in kaolinites. In *Kaolin Genesis and Utilization* (eds. H. H. Murray, W. Bundy, and C. Harvey). The Clay Minerals Society, Boulder, CO. pp. 261–289.
- Nahon D. (1991) *Introduction to the petrology of soils and chemical weathering.*, Wiley, New York, USA.
- Premović P., Ciesielczuk J., Bzowska G. and Dordević M. (2012) Geochemistry and electron spin resonance of hydrothermal dickite (Nowa Ruda, Lower Silesia, Poland): Vanadium and chromium. *Geol. Carpathica* **63**, 241–252.
- Pushkareva R., Kalinichenko E., Lytovchenko A., Pushkarev A., Kadochnikov V. and Plastynina M. (2002) Irradiation effect on physico-chemical properties of clay minerals. *Appl. Clay Sci.* **21**, 117–123.
- Rengasamy P., Krishna Murti G. S. R. and Sarma V. A. K. (1975) Isomorphous Substitution of Iron for Aluminium in Some Soil Kaolinites. *Clays Clay Miner.* **23**, 211–214.
- Rudnick R. L. and Gao S. (2013) *Composition of the Continental Crust*. 2nd ed., Elsevier Ltd.
- Schellmann W. (1982) Eine neue Lateritdefinition. *Geol. Jahrb.* **58**, 31–47.
- Schellmann W. (1994) Geochemical differentiation in laterite and bauxite formation. *Catena* **21**, 131–143.
- Tardy Y. (1997) *Petrology of Laterites and Tropical Soils.*, Balkema, Rotterdam, The Netherlands.
- Tardy Y. and Nahon D. (1985) Geochemistry of laterites, stability of Al-goethite, Al-hematite, and Fe³⁺-Kaolinite in bauxites and ferricretes: an approach to the mechanism of concretion formation. *Am. J. Sci.* **285**, 865–903.
- Théveniaut H. and Freyssinet P. (1999) Paleomagnetism applied to lateritic profiles to assess saprolite and duricrust formation processes: The example of Mont Baduel profile (French Guiana). *Palaeogeogr. Palaeoclimatol. Palaeoecol.* **148**, 209–231.
- Trolard F. and Tardy Y. (1989) A model of Fe³⁺-kaolinite, Al³⁺-goethite, Al³⁺-hematite equilibria in laterites. *Clay Miner.* **24**, 1–21.

- Valezi D. F., Piccinato M. T., Sarvezuk P. W. C., Ivashita F. F., Paesano A., Varalda J., Mosca D. H., Urbano A., Guedes C. L. B. and Di Mauro E. (2016) Goethite (α -FeOOH) magnetic transition by ESR, Magnetometry and Mössbauer. *Mater. Chem. Phys.* **173**, 179–185.
- Vanderhaeghe O., Ledru P., Thiéblemont D., Egal E., Cocherie A., Tegye M. and Milési J. P. (1998) Contrasting mechanism of crustal growth. Geodynamic evolution of the Paleoproterozoic granite-greenstone belts of French Guiana. *Precambrian Res.* **92**, 165–193.
- Varajao A. F. D. C., Gilkes R. J. and Hart R. D. (2001) The Relationships between Kaolinite Crystal Properties and the Origin of Materials for a Brazilian Kaolin Deposit. *Clays Clay Miner.* **49**, 44–59.
- Yokoyama Y. and Nguyen H. V. (1980) Direct non-destructive dating of marine sediments, manganese nodules and corals by high-resolution gamma-ray spectrometry. In *Isotope Marine Chemistry* (eds. E. D. Goldberg, Y. Horibe, and i K. Saruhash). Uchida Rokakuho Pub. Co. Ltd, Tokyo. pp. 259– 736.

VIII Conclusions and perspectives

VIII.1 Conclusions

This thesis allows one to draw a number of conclusions regarding the applied techniques and the evolution of the studied profiles and areas. This section aims to summarize the principal outcomes and will concentrate first on the methodologic aspects and then on the regional aspects.

Firstly, the theoretical study on He diffusion in goethite shows that He diffusion is unidimensional along the *b*-axis (*Pnma* spacegroup) in pure goethite and He is not retained in defect free goethite or Al-goethite. We demonstrate that the He retentiveness observed in natural goethite can only be linked to crystal defect, radiation damage and pathway obstruction. The review of He diffusion data in natural goethite deduced from under-vacuum degassing studies shows that the He retentivity increases with growing radiation damage and higher Al content. Growth structures such as botryoidal growth play an additional role as they can result in pathway obstruction. Adapted He-loss correction factors scaled on content of radiation damage and Al-content are proposed.

Secondly, our study revealed unexpectedly reproducible ages in materials that were previously discarded for the dating exercise. Indeed, reproducible (U-Th)/He age results are not common in the field of hematite and goethite (U-Th)/He geochronology. In the supergene context, where different phases and generations of Fe (oxyhydr)oxides become mixed through multiple cycles of dissolution and (re)precipitation, phase mixing can be a major source of age spreading and heavily affect the age reproducibility. The impact of phase mixing upon the obtained ages depends on the ages and actinide concentrations of the endmember phases. Regarding maximum and minimum ages of individual (sub)samples can help to extract geologic meaningful information from mixed age datasets. Since the weathering conditions control the (re)dissolution and (re)precipitation of existing phases, the weathering history of a profile has a strong impact on the age distribution and reproducibility. Simple weathering histories with discrete weathering events and less intense weathering probably favor better defined and more reproducible ages. In contrast, complex weathering histories including phases of very intense (bauxitic) weathering lead to more complex age distributions related to more intense mixing and possibly stronger actinide concentration gradients. However, the very reproducible ages obtained in the Tucano mine show that highly reproducible results can be obtained from very fine-grained material, even with a certain porosity and when intergrown with fine-grained

kaolinite. There is no need for very metallic, hard and pore-free material as previously assumed. This widens the field of applicability of (U-Th)/He geochronology to subsamples that were not selected in previous studies. As the method suffers from a bias due to subjective subsample selection, this opens new possibilities to reduce the possible distortion of goethite and hematite ages.

This thesis shows on several sites of lateritic and bauxitic duricrusts from Brazil and French Guiana that an approach coupling quantitative mineralogy, petrological observations, geochemical and geochronological analyses of supergene Fe (oxyhydr)oxides allows one to extract important information on the evolution of the weathering conditions and thereby on the past climate.

The thick (>75 m) lateritic cover of Kaw mountain which was studied in detail in this thesis records weathering since at least the Oligocene. Analysis of kaolinites from a 75m drill-core show that this mineral formed under near identical conditions over 70m of the core. Preliminary kaolinite EPR ages indicate that the oldest material is preserved in the upper 30 m of the saprolite and that the onset of weathering might predate the Oligocene. Results from Fe(oxyhydr)oxides from the lateritic-bauxitic duricrusts indicate that ferruginous lateritic conditions existed at least since the Oligocene with an increase in Fe(oxyhydr)oxide precipitation during the middle Miocene. During the Late Neogene, weathering at Kaw mountain intensified and the previously ferruginous cover was bauxitized. This led to widespread dissolution of kaolinite, precipitation of gibbsite and Th and Al enrichment of the Fe minerals. The newly formed Fe (oxyhydr)oxide phases became mixed with and partially replaced the preexisting Fe minerals, leading to very complex textures and very spread age distributions.

Comparison with other lateritic covers in northeastern French Guiana and Suriname shows that Oligocene weathering is a regional feature. The laterites in French Guiana possibly developed synchronously to the coastal bauxites in Suriname and Guyana but differences in local climate and drainage might have led to the formation of bauxites in Suriname and Guyana and to the formation of ferruginous laterites in French Guiana. (U-Th)/He from Mont Baduel, one of the studied site in French Guiana, allow the identification of two weathering peaks at ca. 6 and 3-2 Ma which possibly correspond to hiatus in the Guiana basin. At least the second of the two events is linked to the bauxitization of that site.

(U-Th)/He results from the lateritic-bauxitic duricrust from the Petit Connétable island, located in the Atlantic ocean ca. 15km from the coast and about 40km NE of Kaw mountain, show a very similar age-U-Th distribution when compared to Kaw mountain. This suggests very similar weathering histories for the two sites and underlines the regional character of the Late Neogene bauxitization event. The combination of the (U-Th)/He results from French Guiana allows a reassessment of the geomorphological models and indicates that the morphology of the studied region is strongly influenced by its proximity to the coast.

The weathering profile exposed in the Tucano mine records weathering going back to the Late Cretaceous or Early Paleogene. Kaolinites formed under more variable conditions in this profile but as at Kaw, the oldest kaolinites seem to be preserved in the saprolite. The ferruginous duricrust formed at the top of the profile records two discrete weathering events at ca. 30 and 12 Ma with durations of ca. 6 Ma each. Highly reproducible hematite and goethite (U-Th)/He ages allow to establish a precipitation chronology of different phases of hematite and goethite and thereby a deeper insight into the duricrust formation processes. Kaolinites from the soft material in the upper meters of the profile record a relatively recent (< 5 Ma) rejuvenation, i.e. recrystallisation event, that seems to have had no major impact on the indurated Fe (oxyhydr)oxides and the kaolinites captured inside the duricrust.

Comparison of the data obtained of this thesis with existing weathering chronology datasets indicates that Oligocene and Mid-Miocene weathering are regional scale features with possible continental scale importance.

VIII.2 Perspectives

This thesis yields some answers to a number of questions but on the same time it raises new questions and gives ideas of possible future work that could be done. Some of these aspects shall be explained in this section.

On the methodologic side, several issues could be developed and regarded in detail.

It would be important to calculate the real impact that zircon inclusions can have on the age of supergene hematite and goethite. Among possible contaminants, zircon inclusions are often used to explain too old ages. However, from which size, quantity and actinide concentration are they actually interfering with iron oxides *s.l.* (U-Th)/He ages ? A quantitative modelling for zircon inclusions with different sizes and actinide concentrations in an iron (oxyhydr)oxide matrix, similar to the iron oxide phase mixing model presented in chapter IV, could allow us to estimate the impact of such inclusions onto the (U-Th)/He ages in zircon-rich supergene phases.

Bulk duricrust samples analyzed in this thesis show an important variability of trace elements and rare earth elements. Preliminary, multielement in-situ LA-ICPMS data obtained on mounted hematite and goethite subsamples indicate that important variation exists also between the subsamples of the duricrusts. Analytical development allowing the measurement of trace and rare earth elements on the (U-Th)/He dated aliquots could give important additional insight into the processes of duricrust formation. Since several trace elements (e.g. Ce, V, Cr, Mn) are very sensitive to redox processes, such data could yield information on the precipitation conditions through time. As laterites are important primary resources for a number of critical elements (e.g Sc, Ni, REE, Nb, Au) an improved understanding of the temporal and spatial dynamics of these elements in the lateritic duricrust system could yield important information for their exploration.

In the framework of the RECA project to which this thesis belongs, Fe isotopes measurements were obtained by Z. Fekiacova (CEREGE, France) on subsample grains of the Kaw lateritic duricrust. The $\delta^{56}\text{Fe}$ results, presented in Figure VIII-1, show a very strong fractionation, much stronger than what has been observed in laterites in the literature so far (Poitrasson et al., 2008; Li et al., 2017; Ratié et al., 2021). The fractionation correlates with the ages of the subsamples and increases towards younger ages, while seeming not linked to the mineralogical phase (i. e. hematite or goethite). The results raise the question about what leads to this strong fractionation and if this is linked to the kinetics of the iron (oxyhydr)oxide

formation, to the duration of the weathering, to the intensity of the weathering or if biological processes play a role in the Fe cycling. Comparison of the results with modelling of Fe fractionation through repeated dissolution and reprecipitation cycles might yield insight into the recycling rates of Fe in the duricrusts.

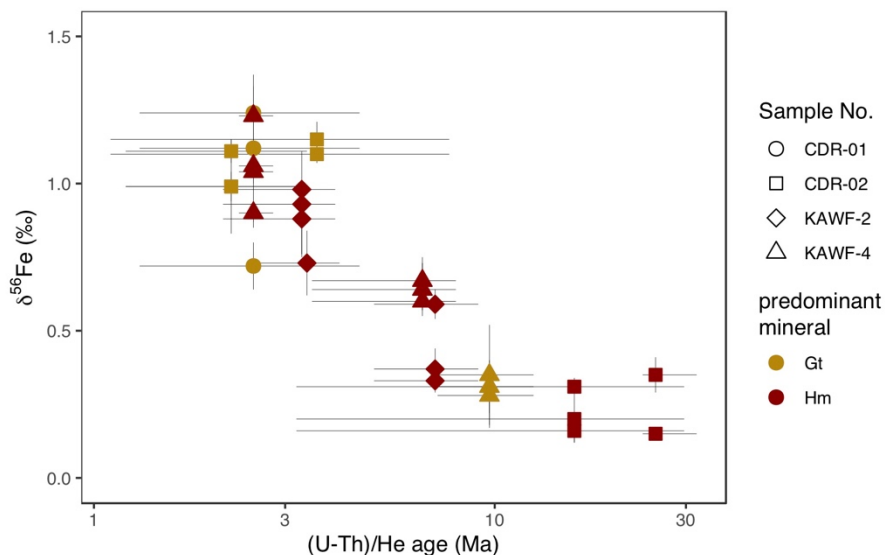


Figure VIII-1: Fe-isotope fractionation of individual subsample grains from selected subsamples. Symbol colors correspond to the mineral, symbol shapes to the sample. Note that the x-axis is logarithmic. Ages are given as median ages of the subsamples with maximum and minimum subsample ages as error bars.

Chapter VII suggests that the kaolinites of the studied profiles may be old, possibly older than the oldest preserved Fe (oxyhydr)oxides. In order to confirm (or refute) this first estimate, it will be necessary to better study the petrology of the analyzed samples and to obtain information on the microscopic distribution of radioelements in order to properly calculate the dose-rates. This can be performed through induced fission tracks for uranium and X-ray fluorescence for thorium. Finally, this will allow us to lower the uncertainty on the kaolinite ages and thereby enable a deeper insight into the evolution and formation of the profiles, especially of their saprolitic parts. Ages of kaolinites will be confronted with those on iron (oxyhydr)oxides originating from the associated duricrusts.

The oldest (U-Th)/He ages of supergene hematite and goethite obtained in this study are generally considered to date the minimum age of the ferruginous duricrust (or maybe something we could call a “proto-duricrust”?) and thereby a minimum age for the onset of weathering. While the kaolinite ages can be one hint to constrain the earlier phases of weathering it would also be good to examine, how much time it takes, to form a “proto duricrust” in which the Fe minerals are sufficiently crystallized to retain He in their structure.

This would allow us to have a better idea of what the oldest He ages obtained in this thesis actually represent. This could be done by studying very young profiles (few Myr) developed on top of Late Cenozoic rocks of known formation of exposure age. Targeting not only completely indurated material but also more friable ferruginous parts like soft nodular layers could be tested. Comparison of ferruginous (proto-?) duricrusts developed on top of different lithologies with variable iron contents might furthermore elucidate the impact of the rock type onto the duration of duricrust formation, as our results indicate that important differences might exist between iron-rich and iron-poor rocks.

The results of this study have shown that along the coast of French Guiana the geomorphological evolution seems to be strongly influenced by the proximity of the coastline. In order to verify whether the geomorphological models proposed for the Guiana shield (Choubert, 1957; King, 1962; McConnell, 1968; Blancaneaux, 1981; Aleva, 1984; Bardossy and Aleva, 1990) are valid for the interior of the shield, it would be very interesting to study duricrusts from paleosurfaces with different elevations from the central areas of the shield. The southern regions of French Guiana and Guyana could be possible targets as lateritic duricrusts have been described for these areas (Bardossy and Aleva, 1990). This could furthermore reveal whether Late Neogene bauxitization was restricted to the coastal areas or had a larger extent.

The highest and supposedly oldest paleosurfaces of the Guiana shield are the so called “tepuis” in Venezuela and its bordering regions of Guyana and Brazil with elevations of more than 2000 m. The top of the tepuis is often shaped by karstic landforms resulting from the weathering of the quartzites of the Roraima Supergroup (Yanes and Briceño, 1993; Piccini and Mecchia, 2009). Although thick lateritic profiles have not yet been reported for these paleosurfaces, ferruginous duricrusts developed on top of crosscutting dolerite dykes have been observed (Briceño and Schubert, 1990). Investigation of these duricrusts using the coupled approach developed in this thesis could yield very interesting information on the age and the evolution of this very unique landscape and the geomorphological evolution of the Guiana shield.

The evaluation of the data obtained in this thesis has shown that the identified weathering events are generally regional features albeit with some intensity differences when regarding different areas of the Guiana shield. This raises the question about the possible triggers of such events. Are they linked to regional tectonic rearrangements and to global climatic changes? What is the importance of the proximity to the coast and of the sea-level for

the laterite and more specifically bauxite formation? Comparison with results from other regions of the South American continent shows that some of the weathering events detected on the Guiana shield might even have had a continental scale impact. In order to detect whether these periods of enhanced weathering were of global importance it would be necessary to compare the obtained results with those from other continents, notably from Africa, and possibly from Southeast Asia and Australia. This could also give hints regarding the triggers of such weathering events. Are the main phases of lateritization linked to phases of high temperature coupled to high humidity as proposed by Prasad (1983), to phases of high humidity only or are they linked to short-lived atmospheric changes of the greenhouse gas contents as for example proposed by Retallack (2010)? Since the field of weathering chronology is still in progress, some of these questions might be answered in the future. Finally, the quantification of consumed CO₂ during weathering of silicate at a continental scale during the identified weathering phases could be interesting to better understand the carbon cycle and retroaction on paleoclimates.

References

- Aleva G. J. J. (1984) Lateritization, bauxitization and cyclic landscape development in the Guiana Shield. In *Bauxite* (ed. L. Jacob Jr). A.I.M.E, New York, USA. pp. 297–318.
- Bardossy G. and Aleva G. J. J. (1990) *Lateritic Bauxites*. Developmen., Elsevier Science, Amsterdam, The Netherlands.
- Blancaneaux P. (1981) *Essai sur le milieu naturel de la Guyane Française.*, Paris.
- Briceño H. O. and Schubert C. (1990) Geomorphology of the Gran Sabana, Guayana Shield, southeastern Venezuela. *Geomorphology* **3**, 125–141.
- Choubert B. (1957) *Essai sur la morphologie de la Guyane.*, Paris.
- King L. C. (1962) *Morphology of the Earth.*, Oliver and Boyd Publ. House, London.
- Li M., He Y. S., Kang J. T., Yang X. Y., He Z. W., Yu H. M. and Huang F. (2017) Why was iron lost without significant isotope fractionation during the lateritic process in tropical environments? *Geoderma* **290**, 1–9.
- McConnell R. B. (1968) Planation Surfaces in Guyana. *Geogr. J.* **134**, 506–520.
- Piccini L. and Mecchia M. (2009) Solution weathering rate and origin of karst landforms and caves in the quartzite of Auyan-tepui (Gran Sabana, Venezuela). *Geomorphology* **106**, 15–25.

- Poitrasson F., Viers J., Martin F. and Braun J. J. (2008) Limited iron isotope variations in recent lateritic soils from Nsimi, Cameroon: Implications for the global Fe geochemical cycle. *Chem. Geol.* **253**, 54–63.
- Prasad G. (1983) A review of the early Tertiary bauxite event in South America, Africa and India. *J. African Earth Sci.* **1**, 305–313.
- Ratié G., Garnier J., Vieira L. C., Araújo D. F., Komárek M., Poitrasson F. and Quantin C. (2021) Investigation of Fe isotope systematics for the complete sequence of natural and metallurgical processes of Ni lateritic ores: Implications for environmental source tracing. *Appl. Geochemistry* **127**.
- Retallack G. J. (2010) Lateritization and bauxitization events. *Econ. Geol.* **105**, 655–667.
- Yanes C. E. and Briceño H. O. (1993) Chemical weathering and the formation of pseudo-karst topography in the Roraima Group, Gran Sabana, Venezuela. *Chem. Geol.* **107**, 341–343.

A. Supplementary material for Chapter III

Helium Diffusion experiments used in this study

For the purpose of this study data from under-vacuum helium diffusion experiments published by Deng et al. (2017), Heim et al. (2006), Shuster et al. (2005) and Vasconcelos et al. (2013) were re-evaluated and activation energy were calculated from the latter. The following figures show for every re-evaluated experiment which steps were used for linear regression and extraction of the diffusion parameters. For experiments where mean-values were calculated individual and mean regression lines are presented. Only steps with $10^4/T < 19.1 \text{ K}^{-1}$ (corresponding to 250°C, indicated by vertical gray line) were used for calculation as goethite transforms into hematite at ca. 250 °C at ambient pressure. Consequently, only steps with $10^4/T < 18 \text{ K}^{-1}$ (corresponding to 282°C) are displayed. The extracted activation energy can be found in Table III-1 of the manuscript.

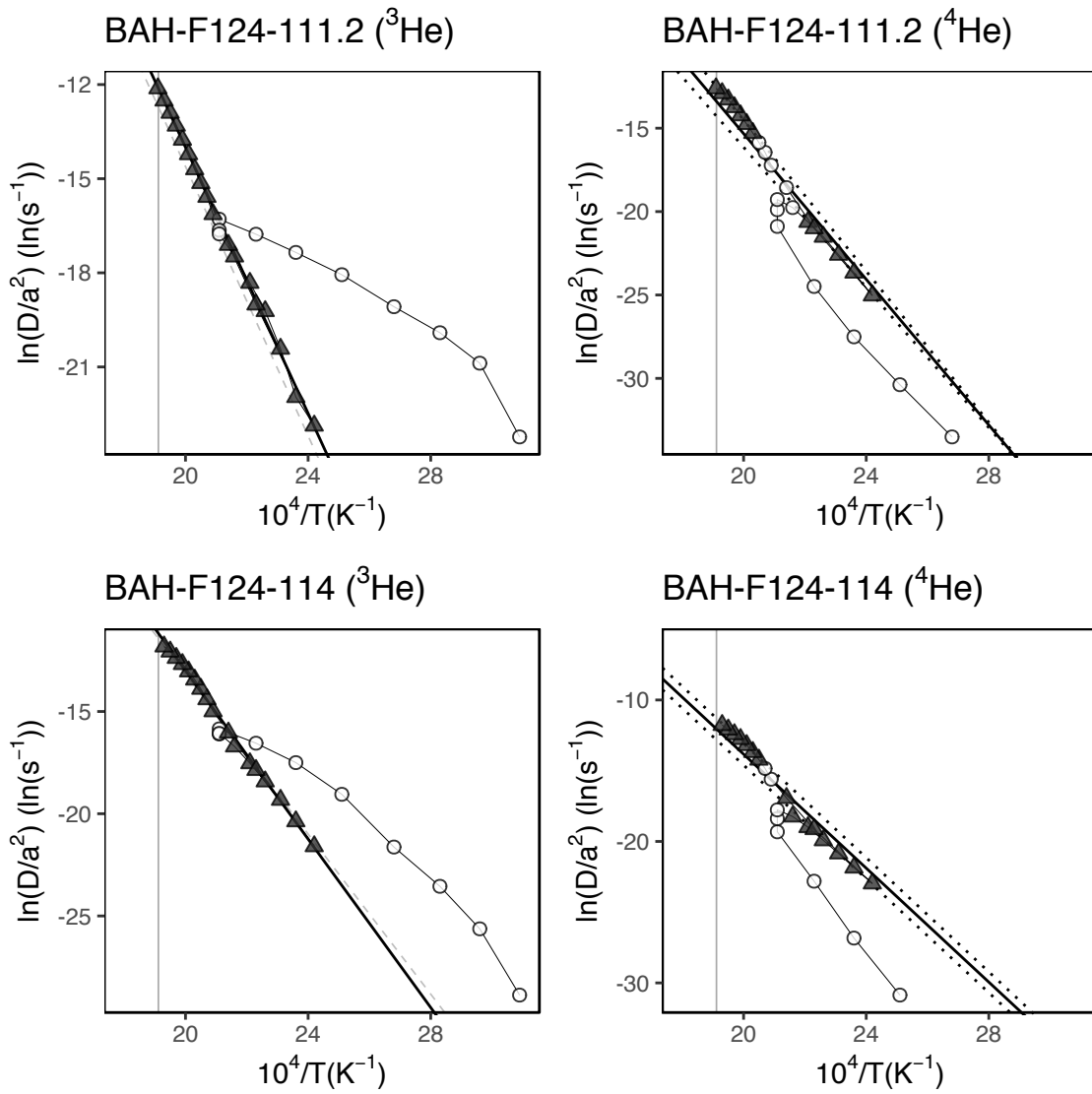


Figure A-1: He diffusion data from Shuster et al. (2005). Gray triangles correspond to steps used for regression; empty circles were not used. Black solid lines are regressions used for calculation of the activation energy; dotted lines correspond to regressions used for calculation of mean values. Grey dashed lines correspond to diffusion parameters presented by the authors. The gray vertical lines indicate $10^4/T = 19.1 \text{ K}^{-1}$ (i.e. 250°C).

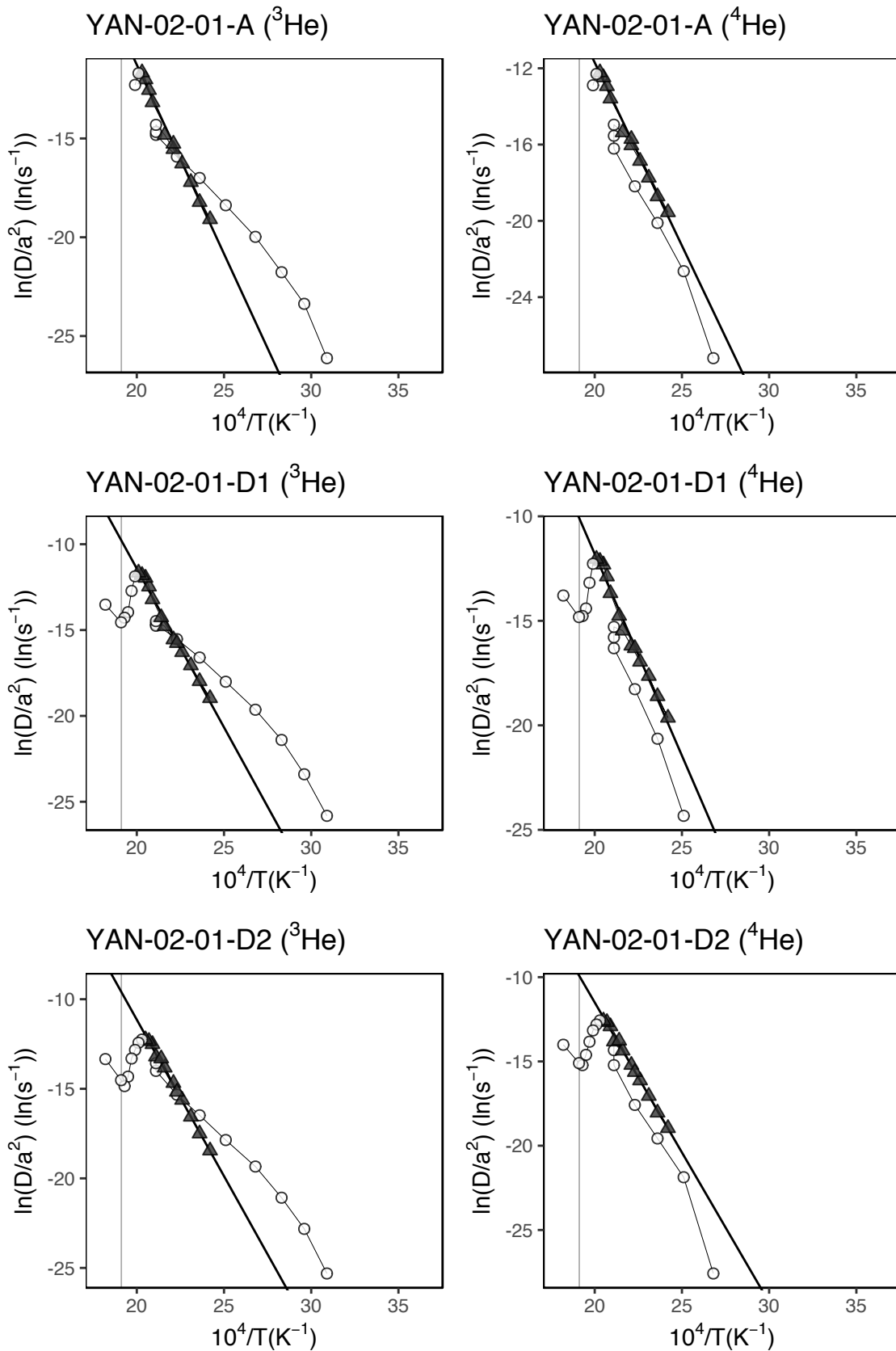


Figure A-2: He diffusion data from Heim et al. (2006). Gray triangles correspond to steps used for regression (black solid lines) used for calculation of the activation energy.

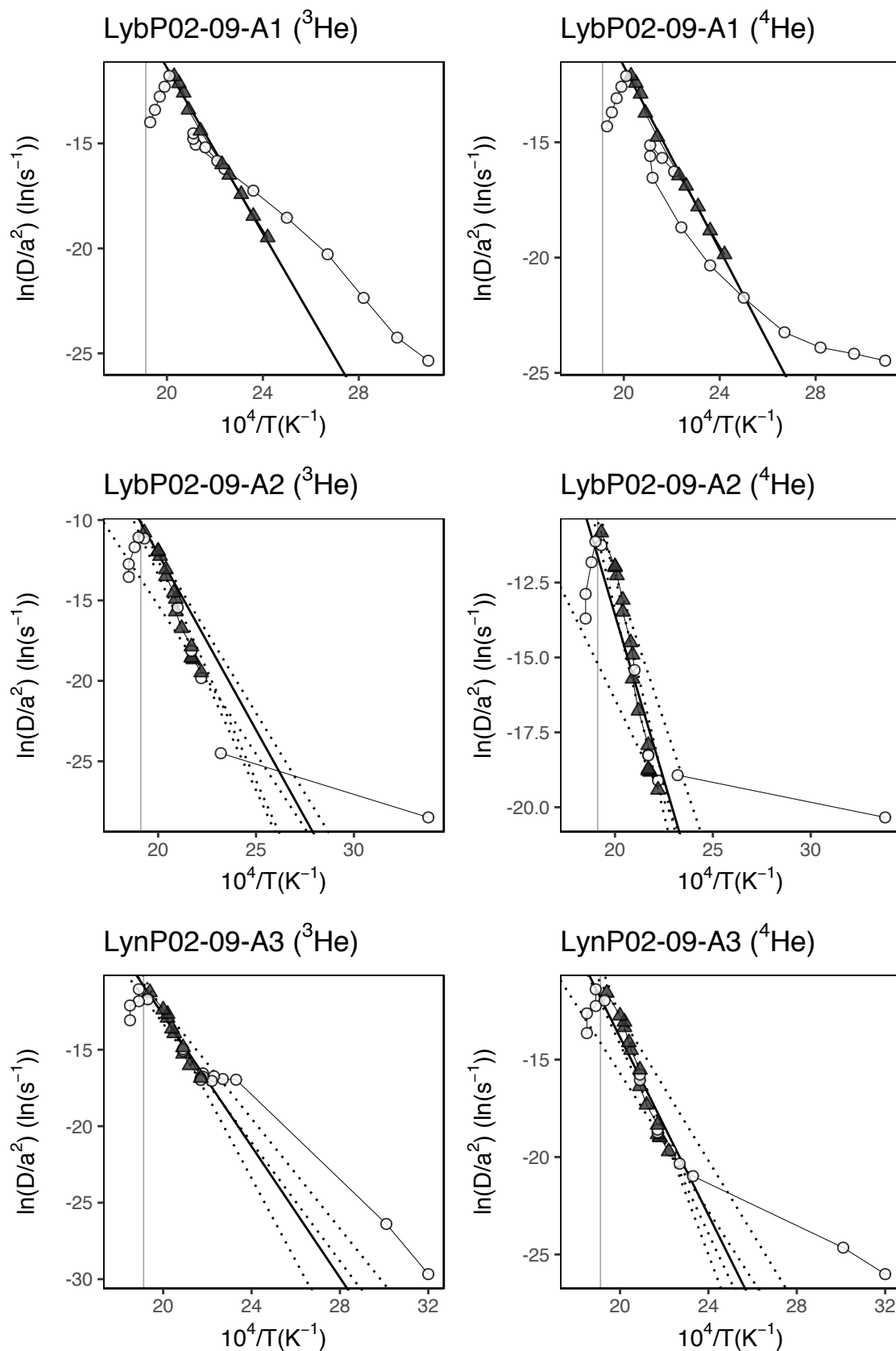


Figure A-3: He diffusion data from Vasconcelos et al. (2013). Gray triangles correspond to steps used for regression; empty circles were not used. Black solid lines are (mean) regressions used for calculation of the activation energy, dotted lines correspond to regressions used for calculation of mean values. The gray vertical lines indicate $10^4/T = 19.1 \text{ K}^{-1}$ (i.e. 250°C).

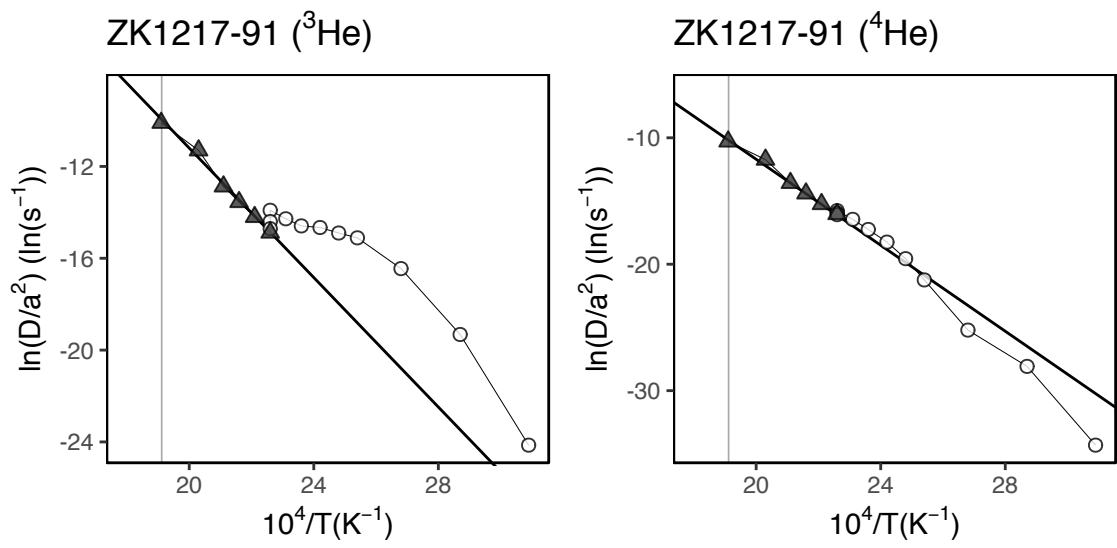


Figure A-4: He diffusion data from Deng et al. (2017). Gray triangles correspond to steps used for regression; empty circles were not used. Black solid lines are regressions used for calculation of the activation energy. The gray vertical lines indicate $10^4/T = 19.1 \text{ K}^{-1}$ (i.e. 250°C).

B. Supplementary material for Chapter IV

Figures



Figure B1: (A) Outcropping duricrust along the KAWF transect. (B) Sampling location of KAWF-2 and KAWF-3

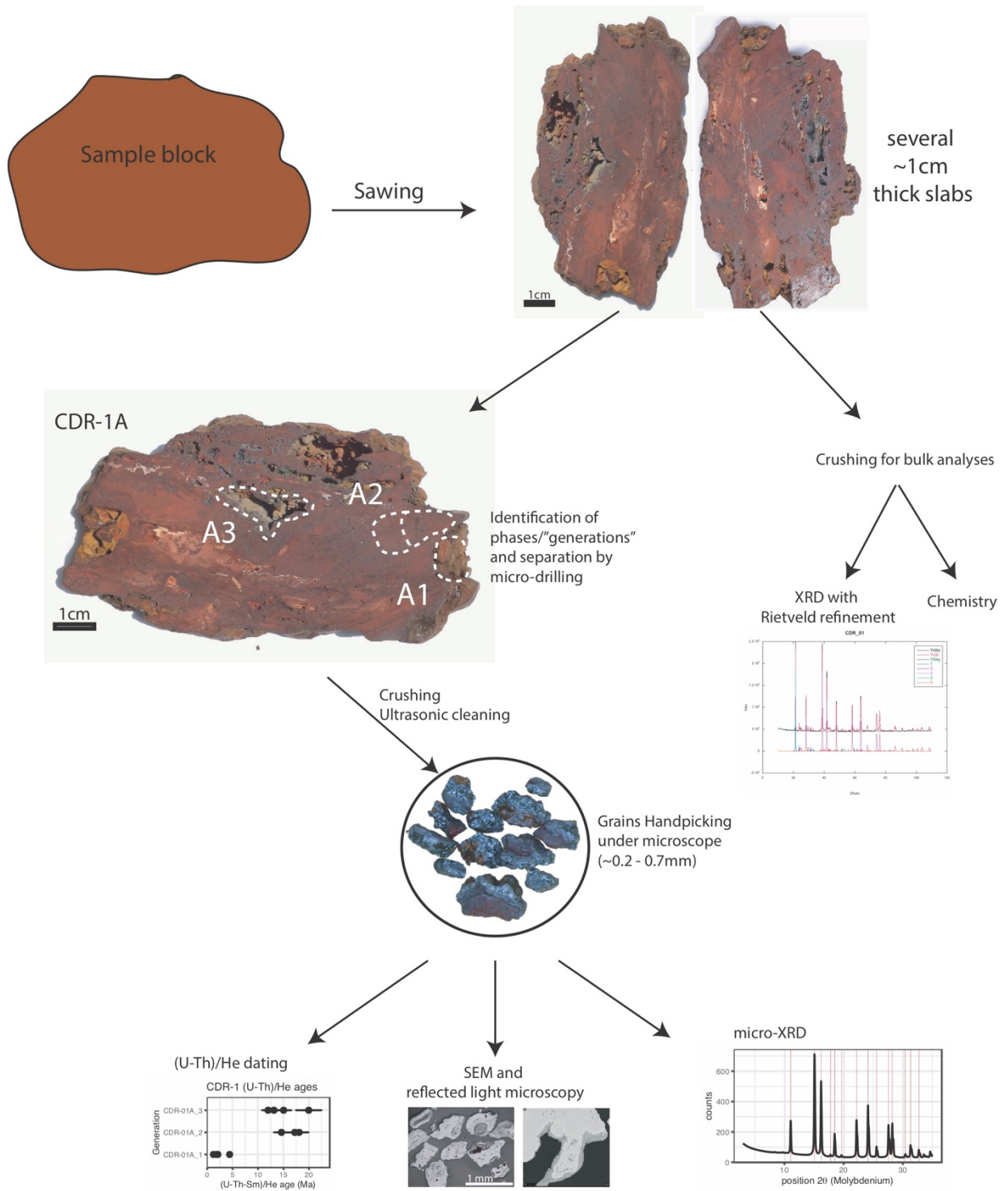


Figure B2: Schema of the sample processing. Note that this figure is already presented in Chapter II but for reasons of consistency it is included again here.

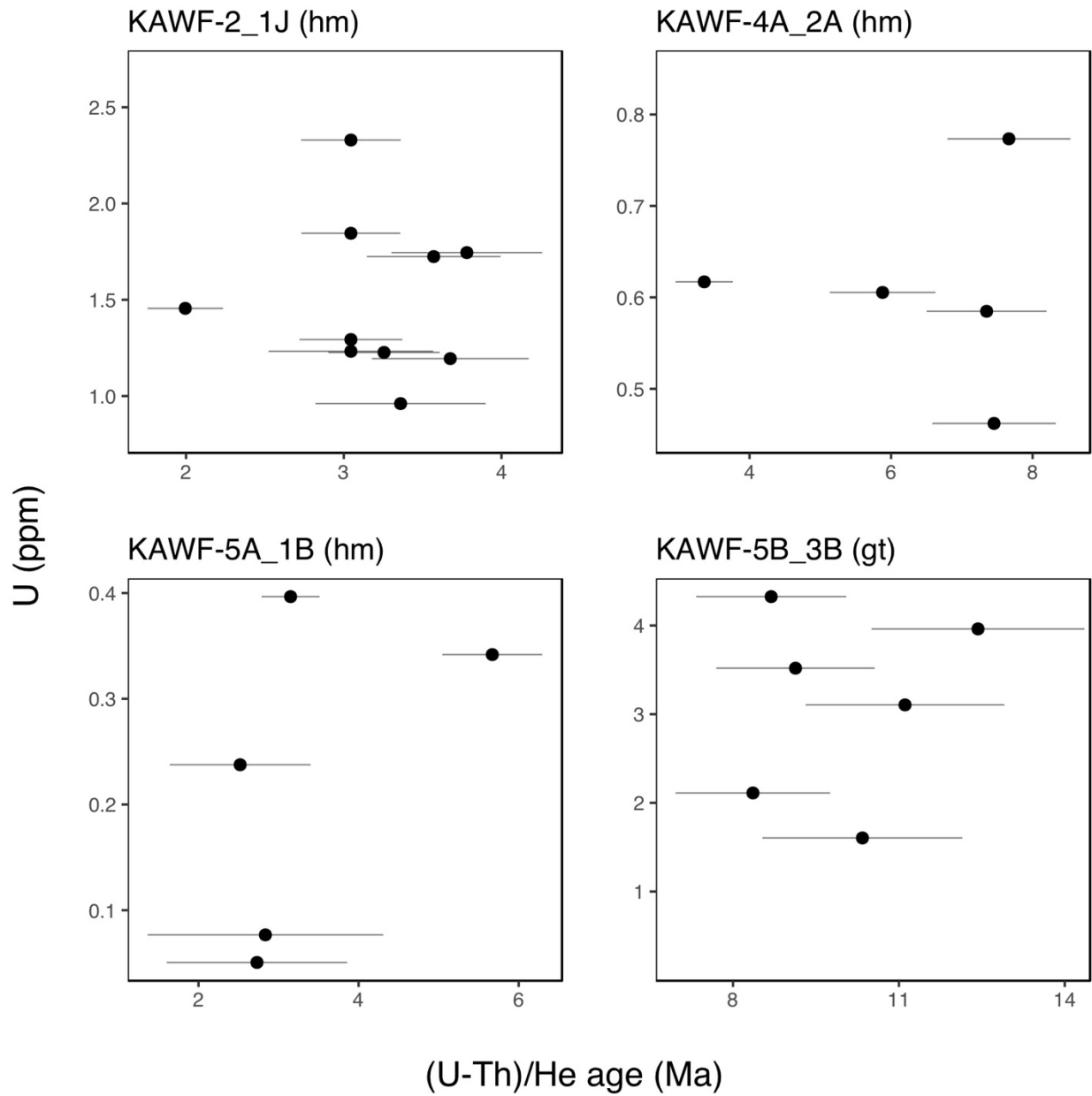


Figure B3: (U-Th)/He ages and U concentrations of three hematite (hm) subsamples and one goethite (gt) subsample. The absence of a negative correlation of (U-Th)/He ages with U and presence of a positive correlation for KAWF-5B_3B indicate that no major U loss occurred during degassing of the samples.

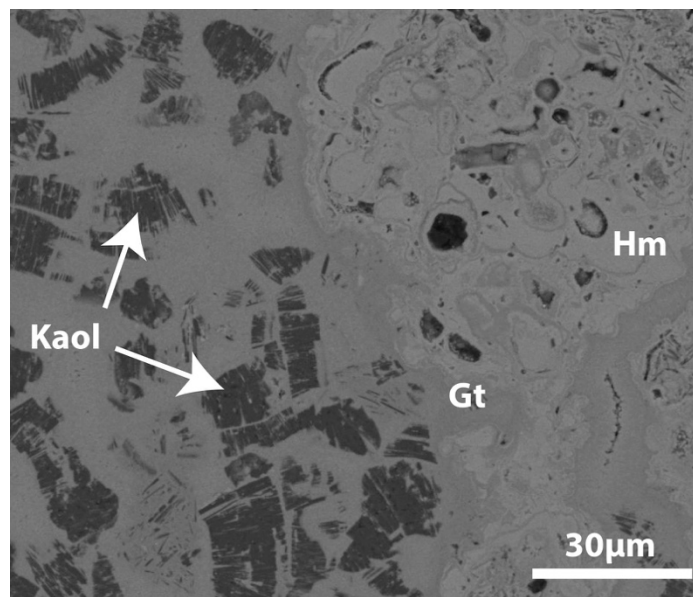
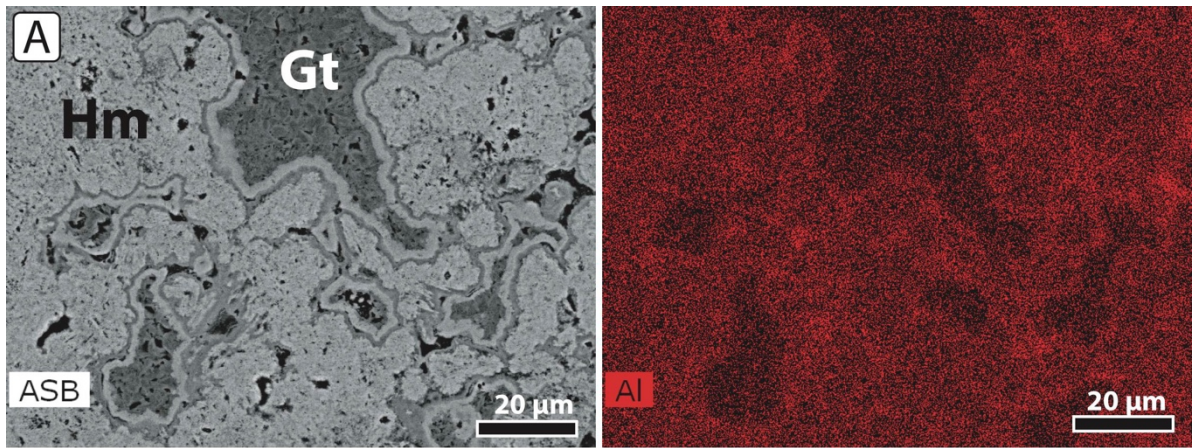
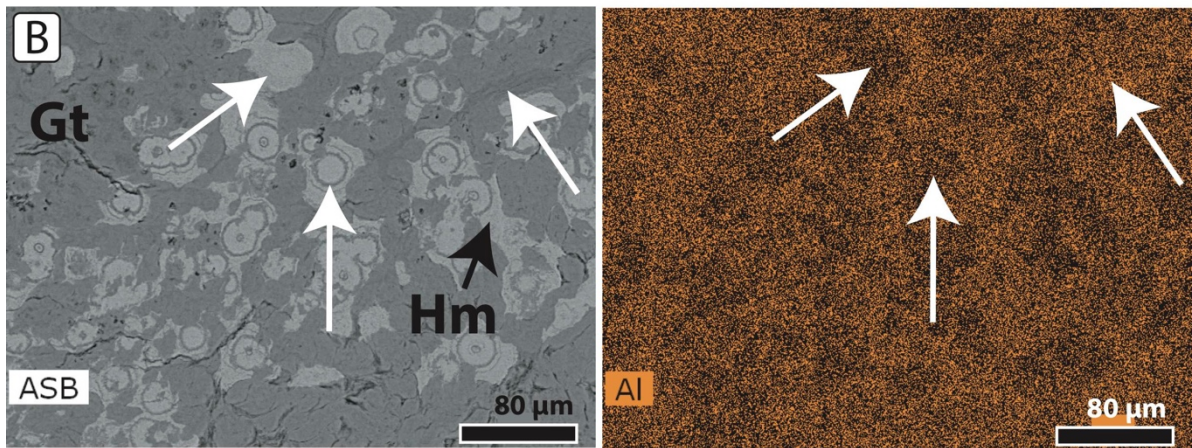


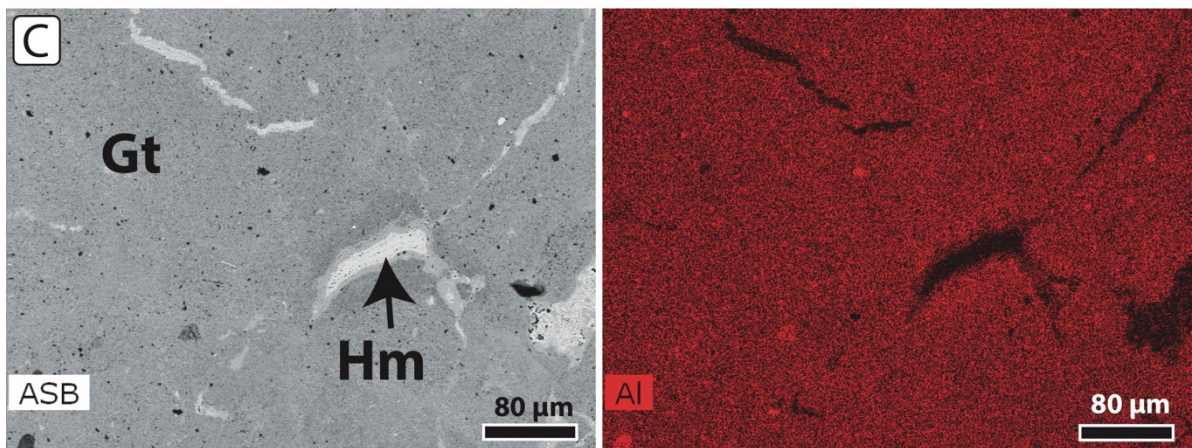
Figure B4: Scanning electron microscopy image of intact kaolinites in a goethite-hematite matrix in generation KAWF-1A_5BII.



Generation CDR-02_2D



Generation KAWF-5B_2All



Generation KAWF-2_3DB

Figure B5: Examples of Al element maps obtained by SEM-EDS of different generations. Left pictures show back scattered electron images, right images Al distribution. White arrows in B point to the same areas in both pictures.

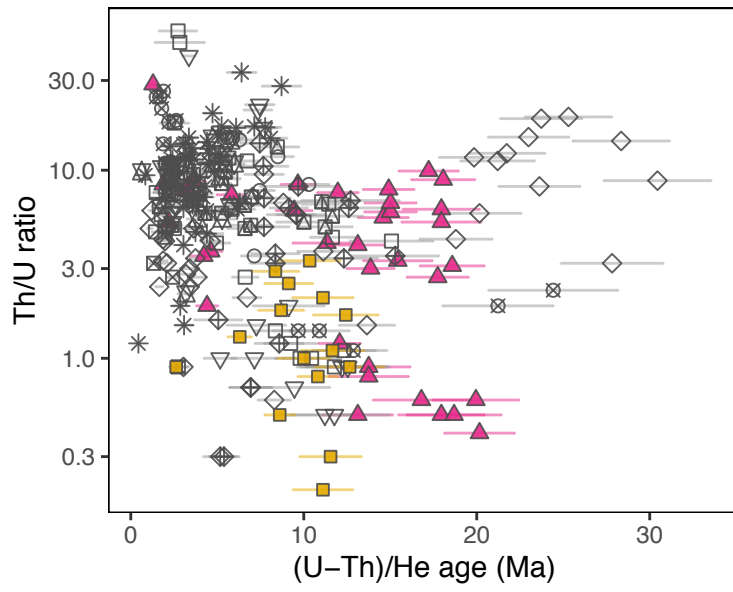


Figure B6A: (U-Th)/He age versus Th/U ratio of the analyzed samples. Shapes and colors are as in Figure 5 of the manuscript.

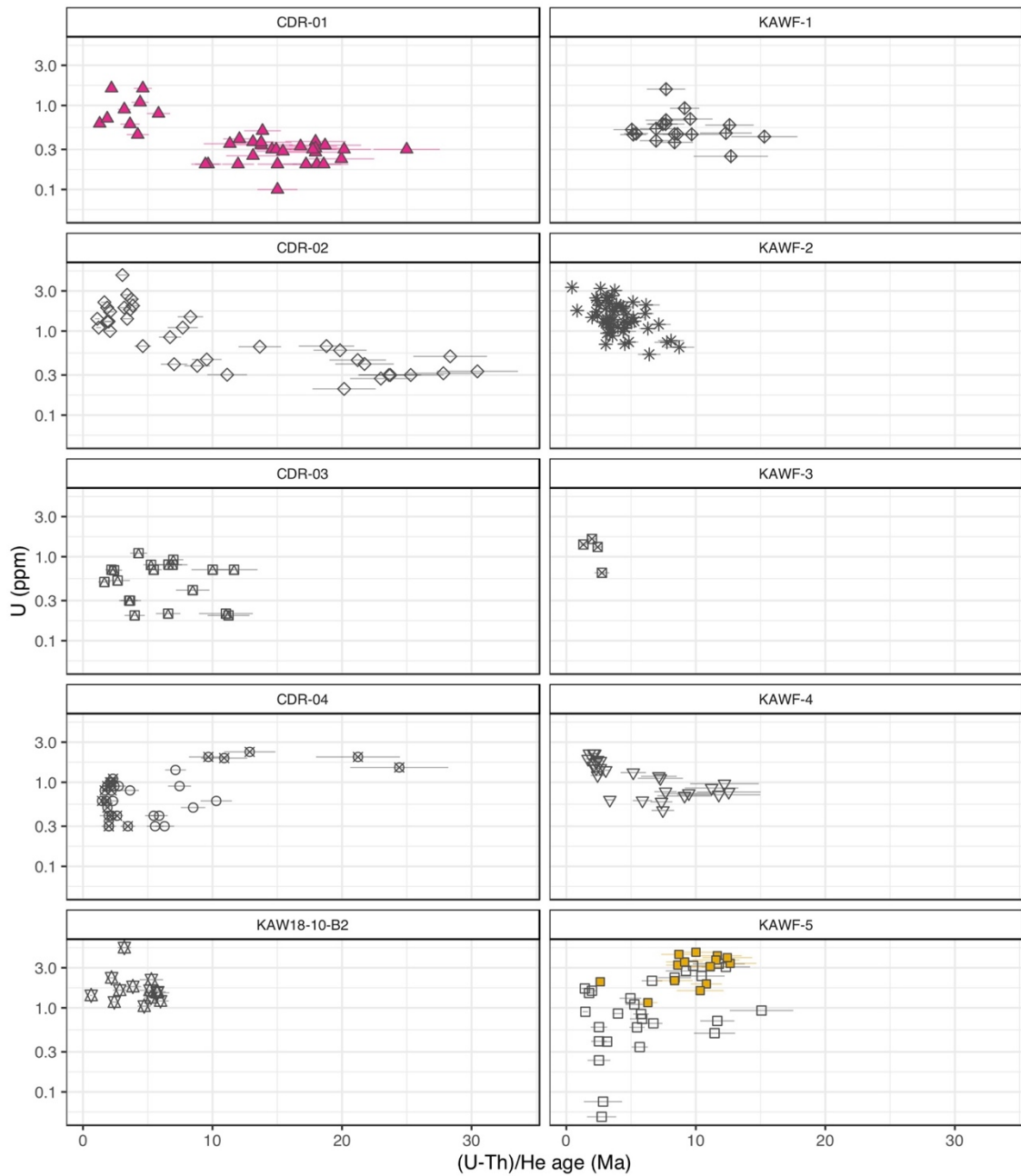


Figure B6B: (U-Th)/He age versus U concentration for all samples separately. Shapes and colors are as in Figure 5 of the manuscript.

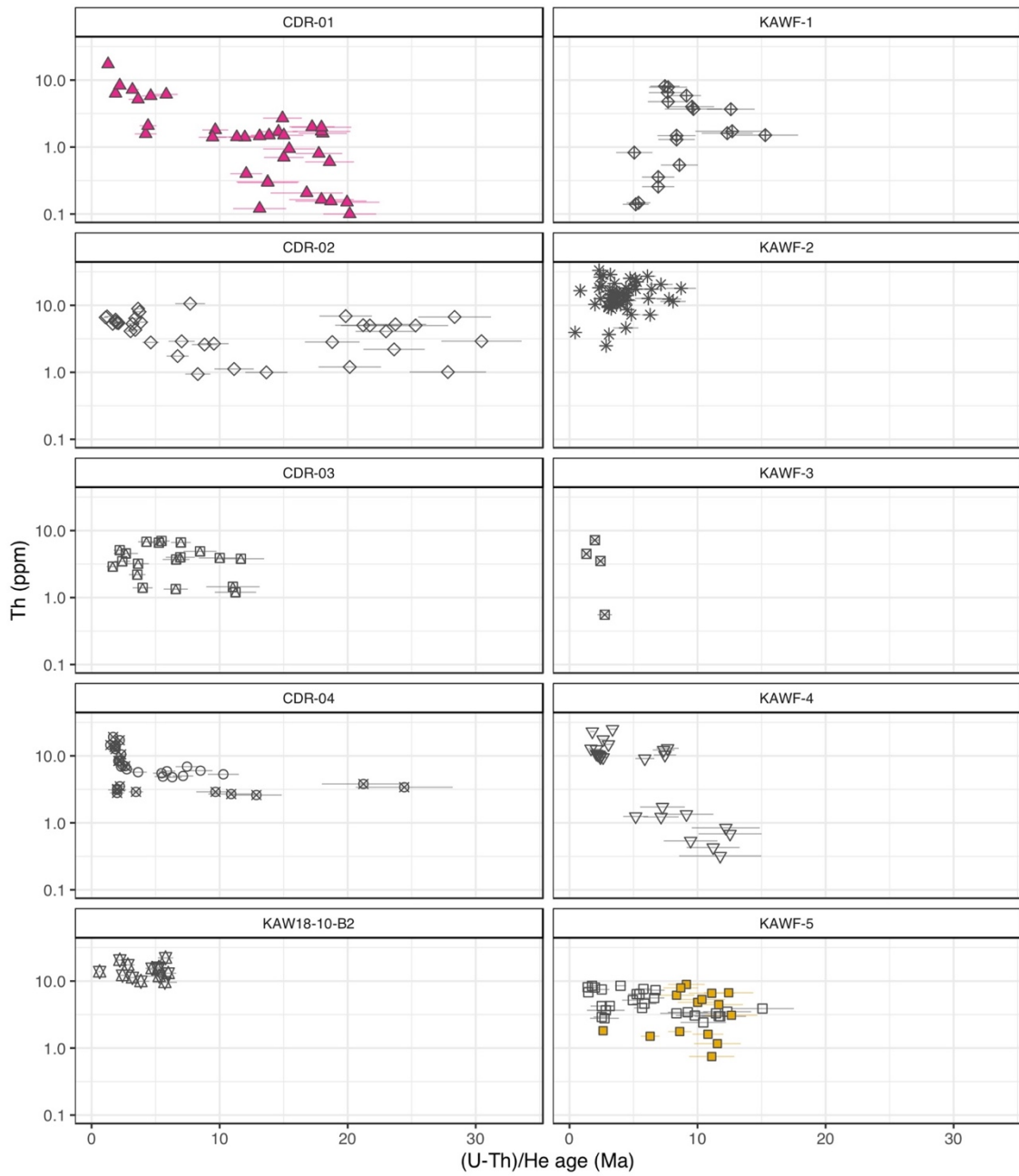


Figure B6C: (U-Th)/He age versus Th concentration for all samples separately. Shapes and colors are as in Figure 5 of the manuscript.

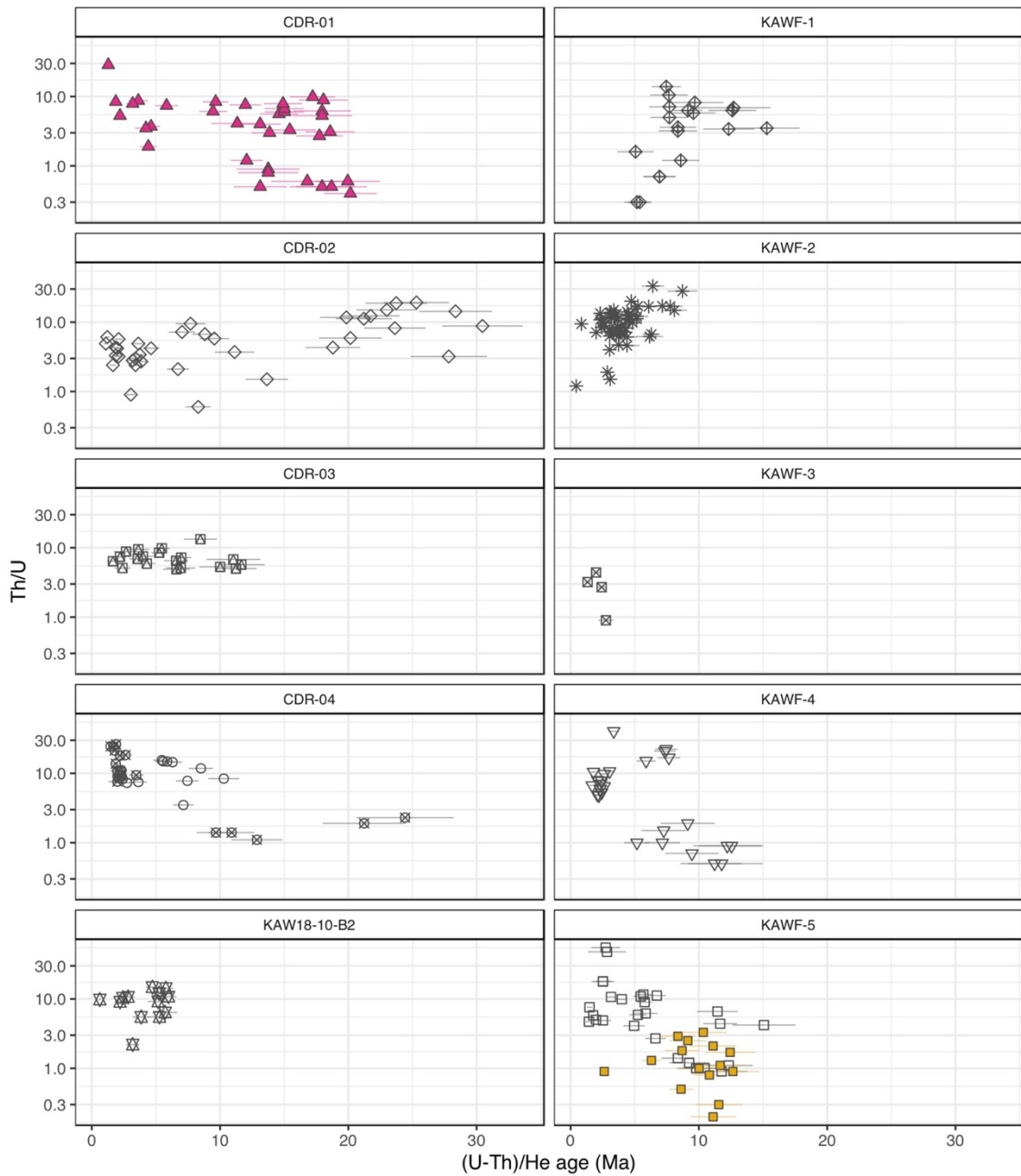


Figure B6D: (U-Th)/He age versus Th/U ratio for all samples separately. Shapes and colors are as in Figure 5 of the manuscript.

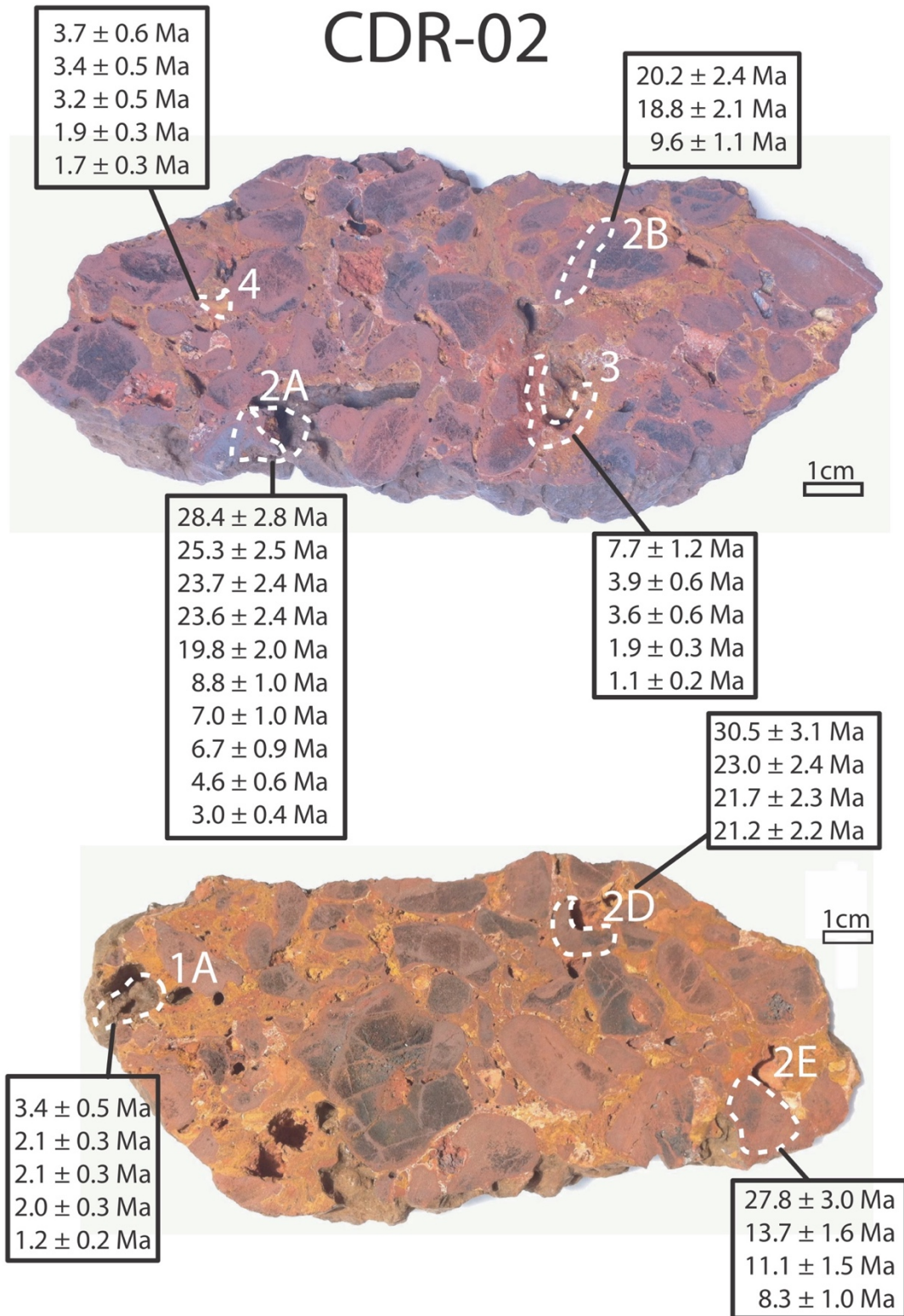


Figure B7A: sample pictures indicating the separated generations with obtained (U-Th)/He ages

CDR-03

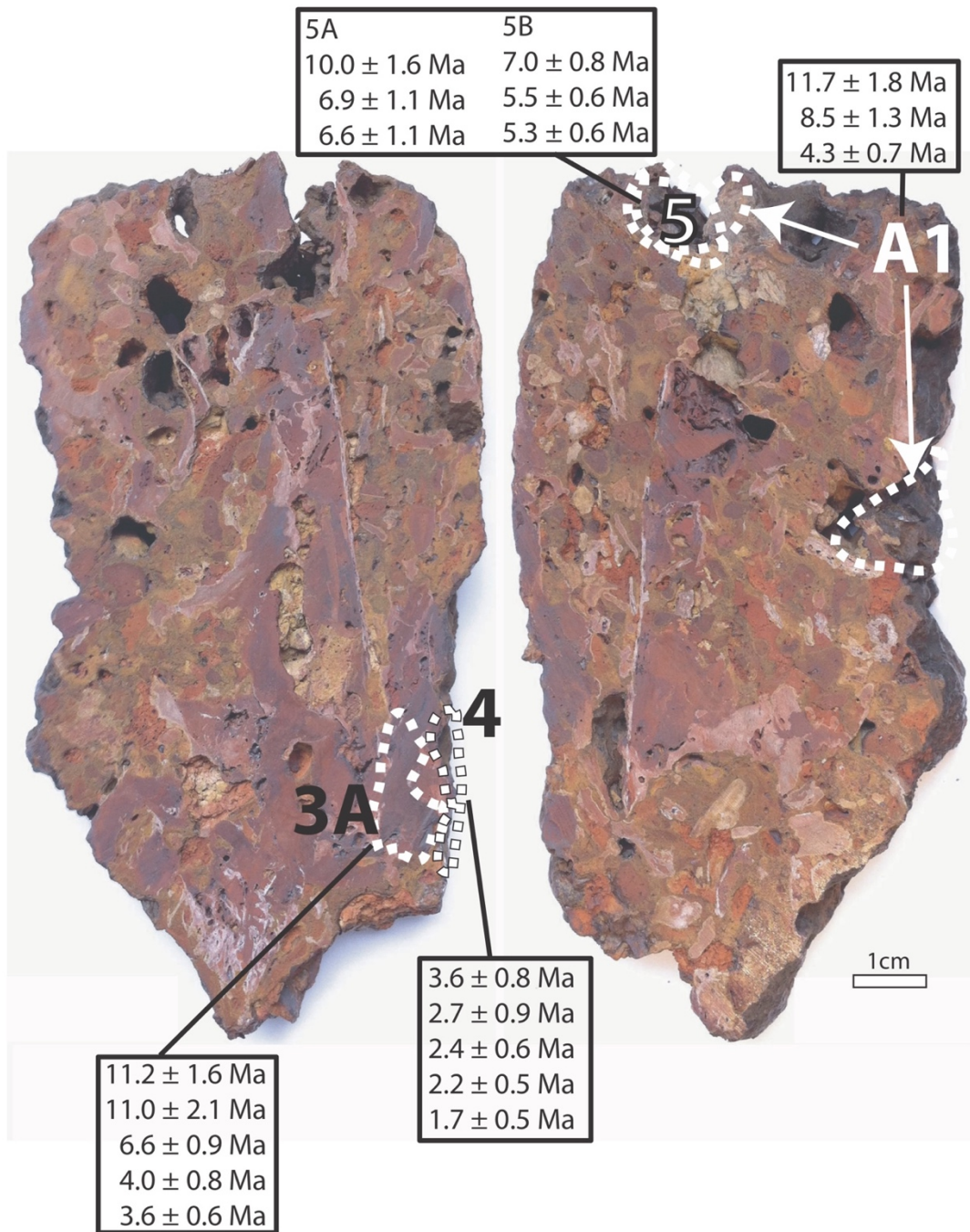


Figure B7B: sample pictures indicating the separated generations with obtained (U-Th)/He ages

CDR-04

CDR-04A

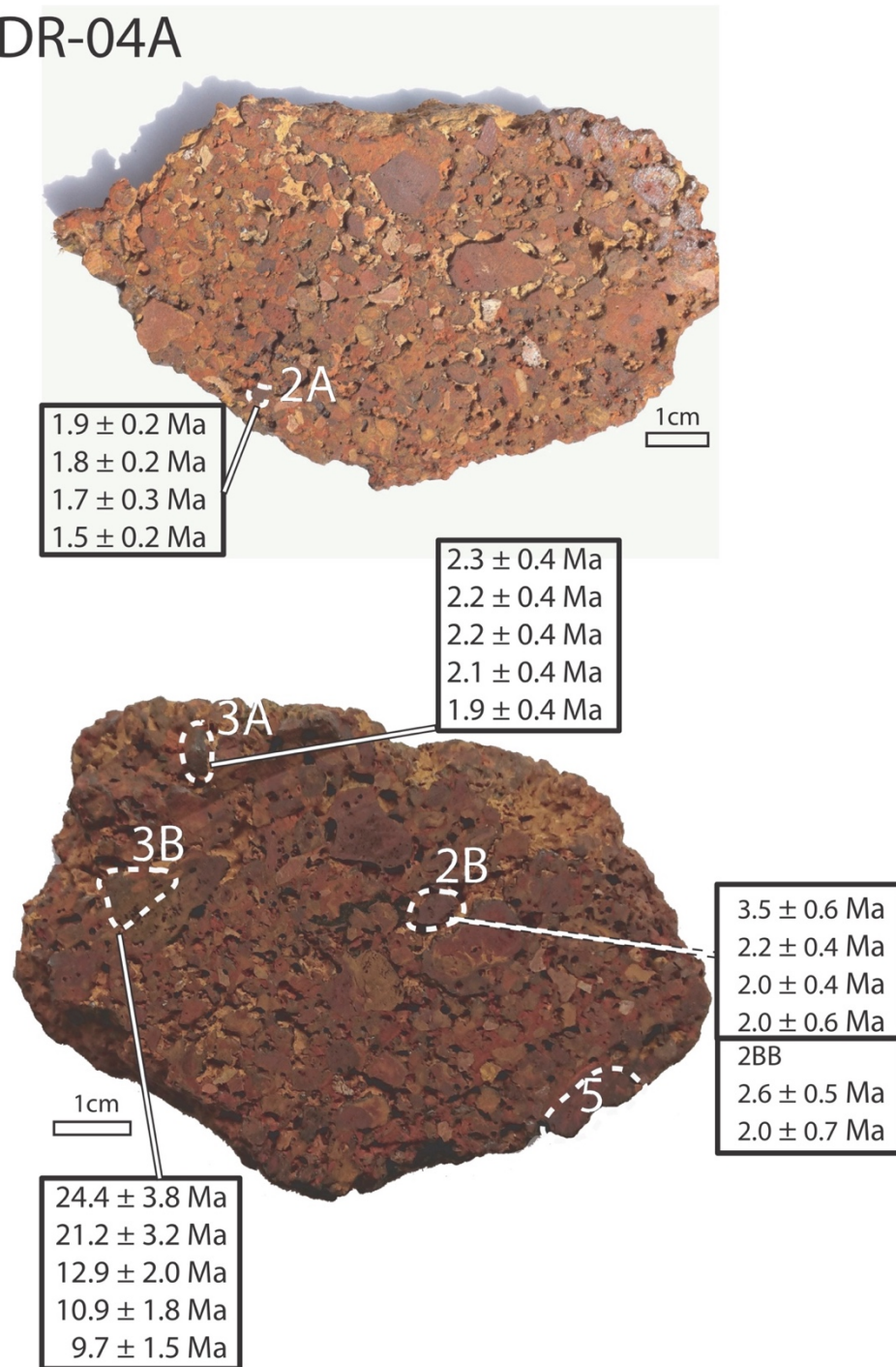


Figure B7C: sample pictures indicating the separated generations with obtained (U-Th)/He ages

CDR-04

CDR-04C

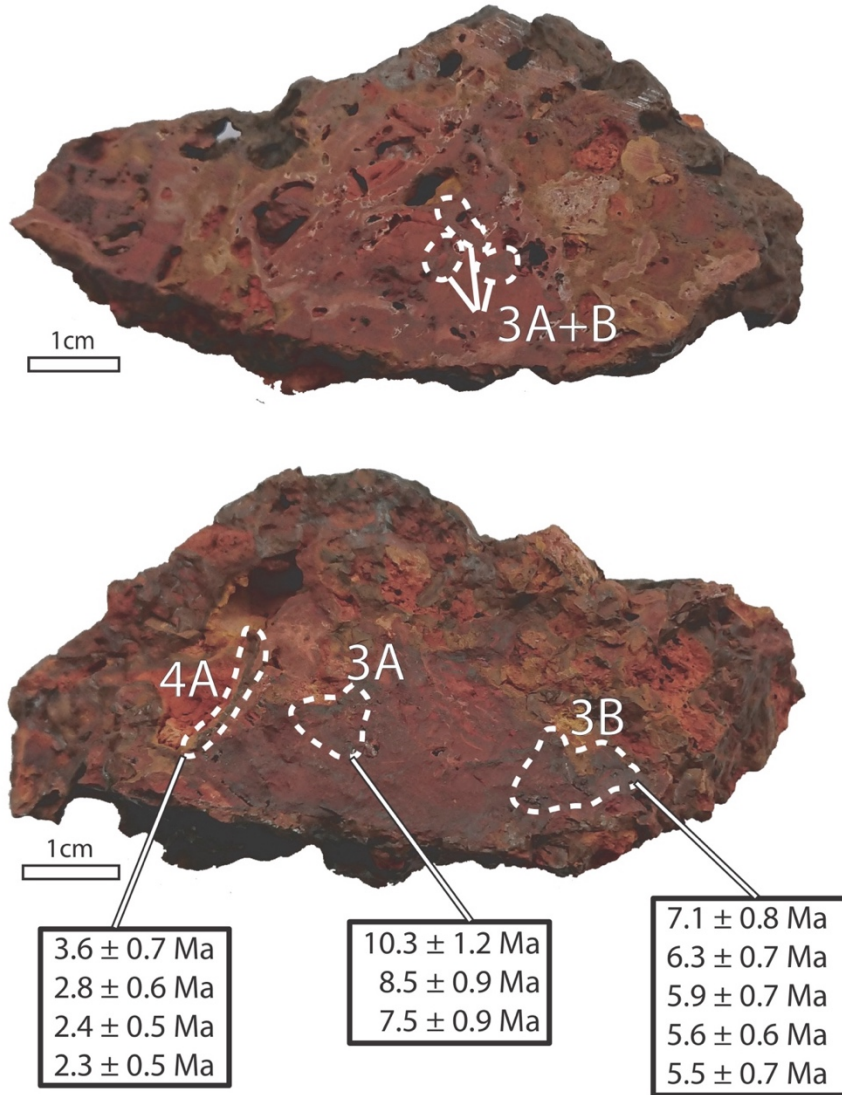
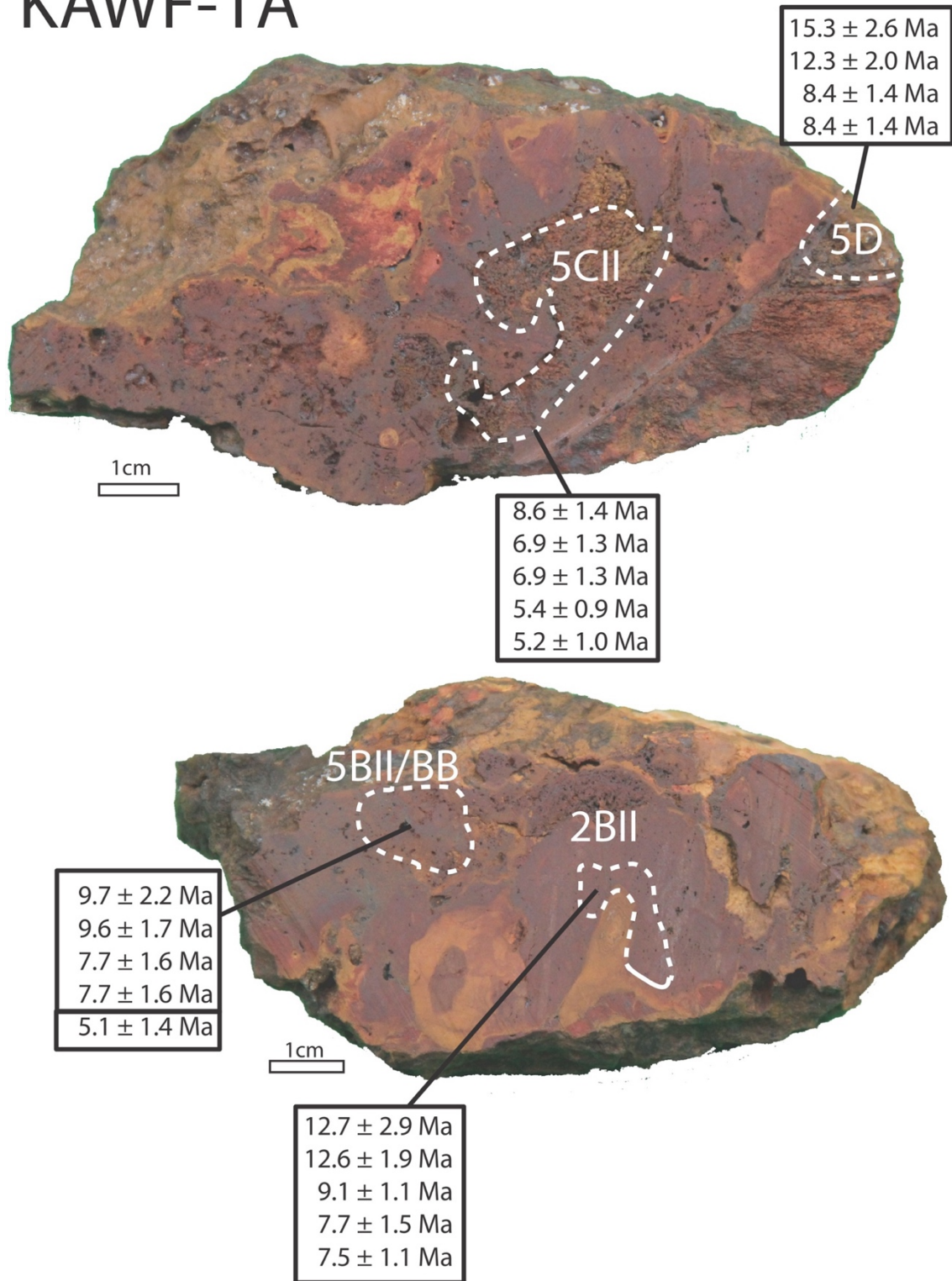


Figure B7D: sample pictures indicating the separated generations with obtained (U-Th)/He ages

KAWF-1A



B7E: sample pictures indicating the separated generations with obtained (U-Th)/He ages

Figure

KAWF-2

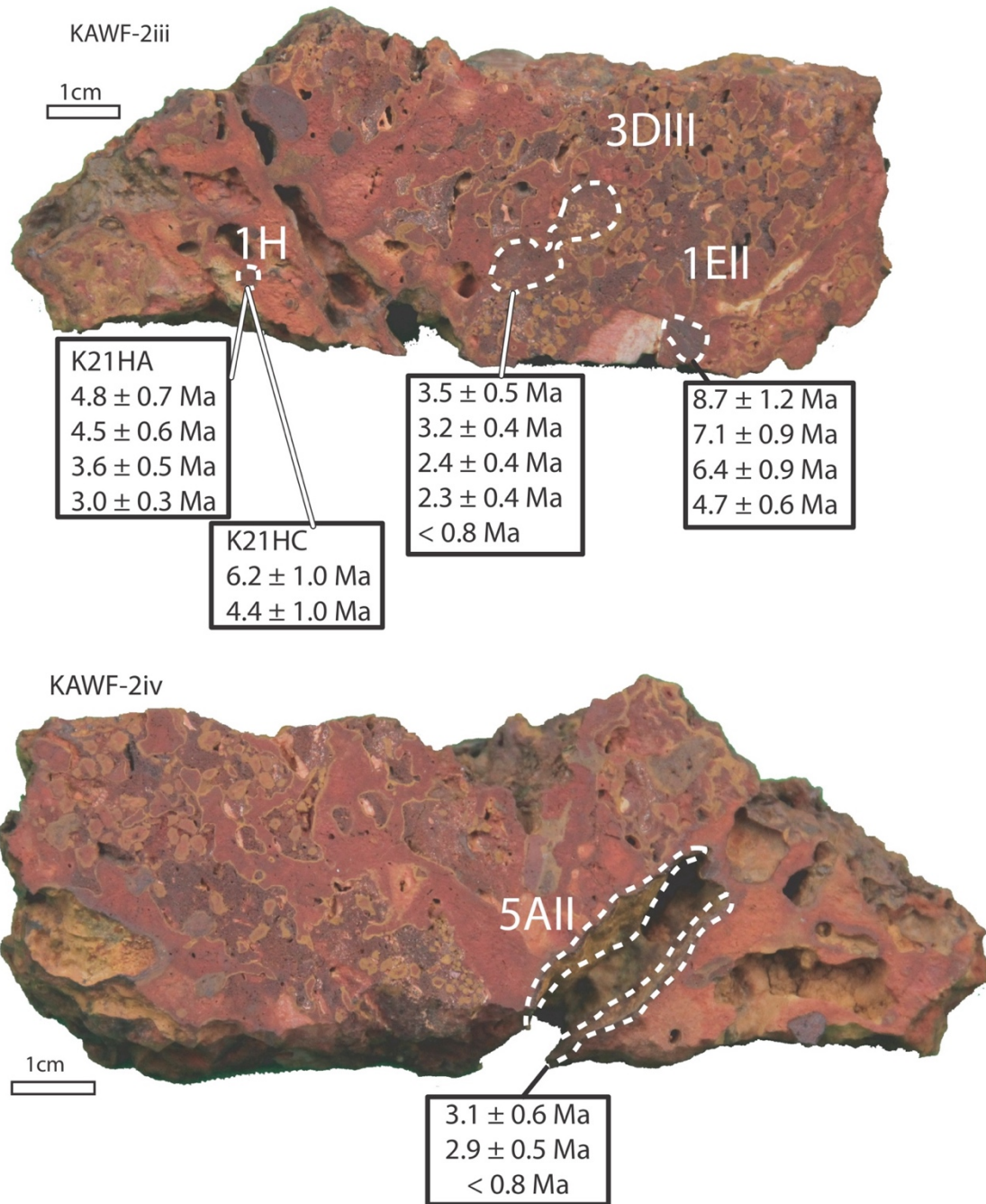


Figure B7F: sample pictures indicating the separated generations with obtained (U-Th)/He ages

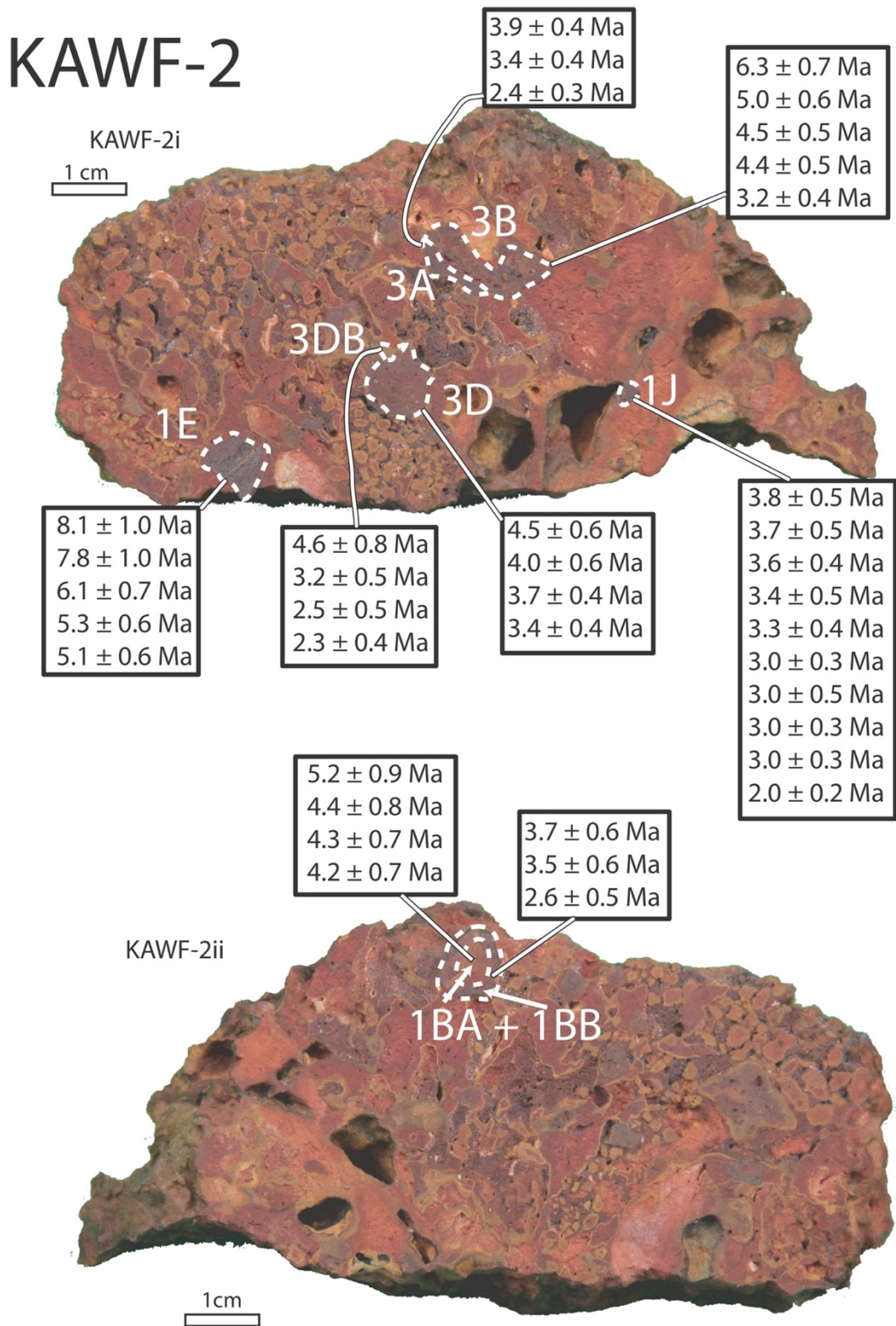


Figure B7G: sample pictures indicating the separated generations with obtained (U-Th)/He ages

KAWF-3

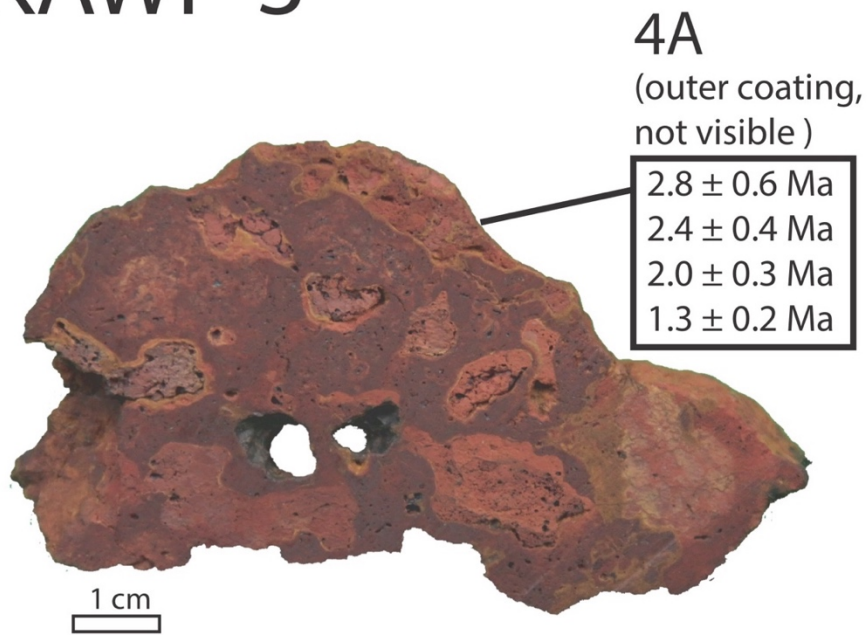


Figure B7H: sample pictures indicating the separated generations with obtained (U-Th)/He ages

KAWF-4

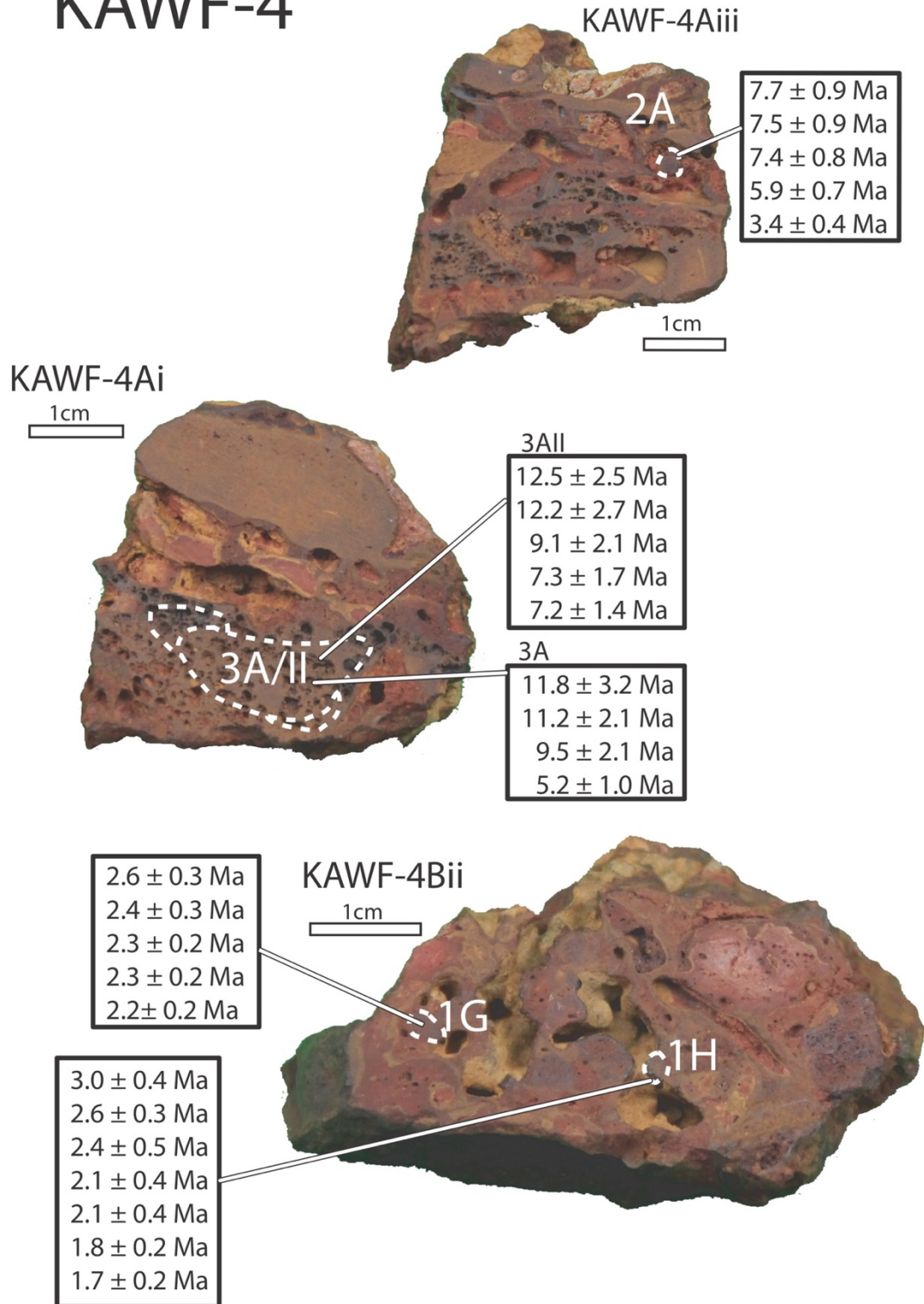


Figure B7I: sample pictures indicating the separated generations with obtained (U-Th)/He ages

KAW18-10B2



Pisolite A

AA (inside)
 4.7 ± 0.5 Ma
 2.8 ± 0.5 Ma
 2.4 ± 0.3 Ma
 2.2 ± 0.4 Ma
 < 0.8 Ma

AB (coating)
 5.7 ± 0.9 Ma
 5.3 ± 0.9 Ma
 3.9 ± 0.6 Ma

Pisolite B

BA (inside)
 6.0 ± 0.6 Ma
 5.8 ± 0.6 Ma
 5.3 ± 0.5 Ma

BB (coating)
 5.2 ± 0.8 Ma
 3.2 ± 0.5 Ma

Exemplary pisolites of sample KAW18-10B2 similar to the two analyzed ones

Figure B7J: sample pictures indicating the separated generations with obtained (U-Th)/He ages

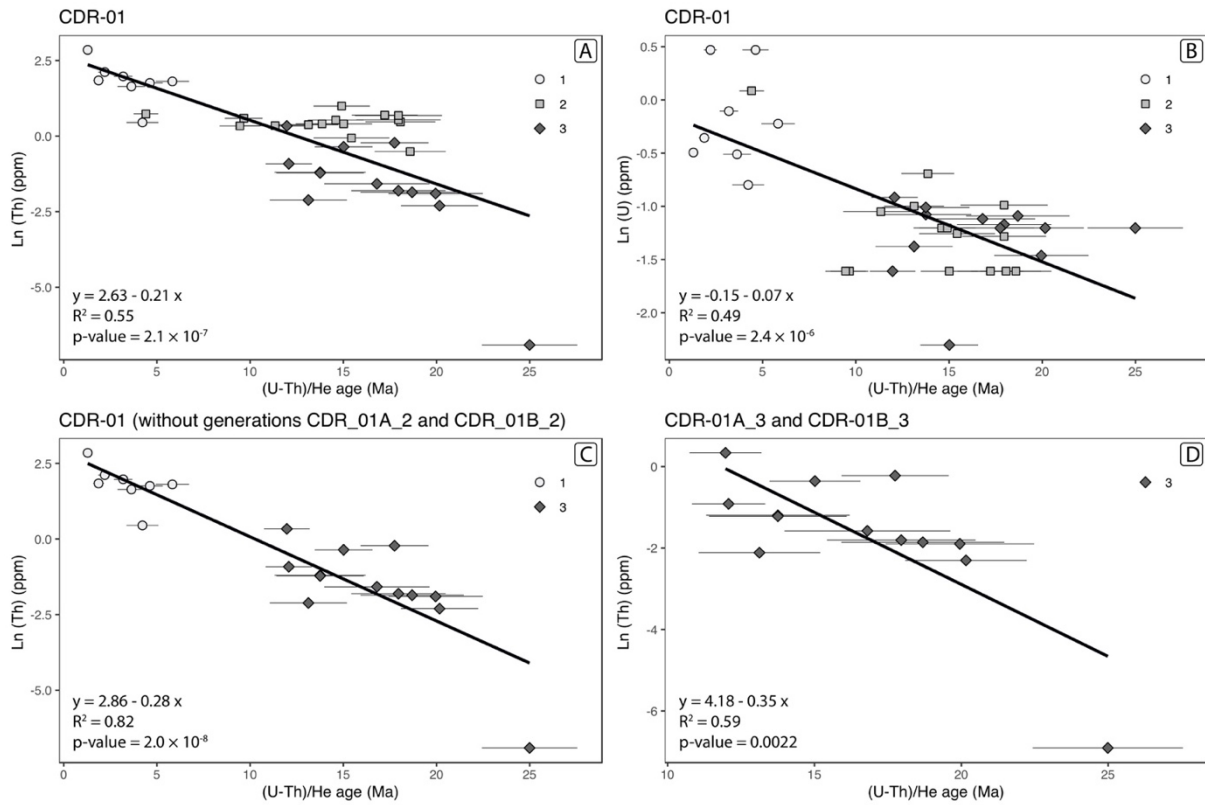


Figure B8: (U-Th)/He age versus log-transformed U and Th concentrations and calculated regressions for sample CDR-01 and selected subsamples. As the relations of age vs Th and U are generally not linear due to phase mixing and the fact that He production is an exponential process, log-correlations show the correlations better. The Th concentration of aliquot CDR#01B3_g1 which is below the limit of detection was replaced by 0.001ppm in order to include the value in the regression calculation. All presented correlations are significant with $p\text{-values} < 0.05$ (for details on the significance of correlations see e.g. Dalgaard, P., 2008. *Introductory Statistics with R, Statistics. ed. Springer, New York, USA*). Shapes and colors are as in Figure 6 of the manuscript.

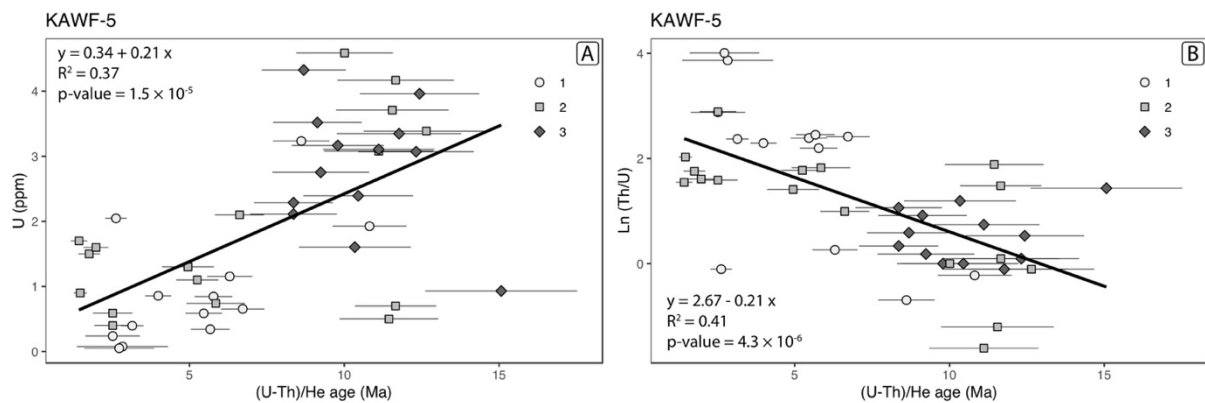


Figure B9: KAWF-5 (U-Th)/He age versus U and Ln(Th/U) with calculated regressions. Shapes and colors are as in Figure 6 of the manuscript.

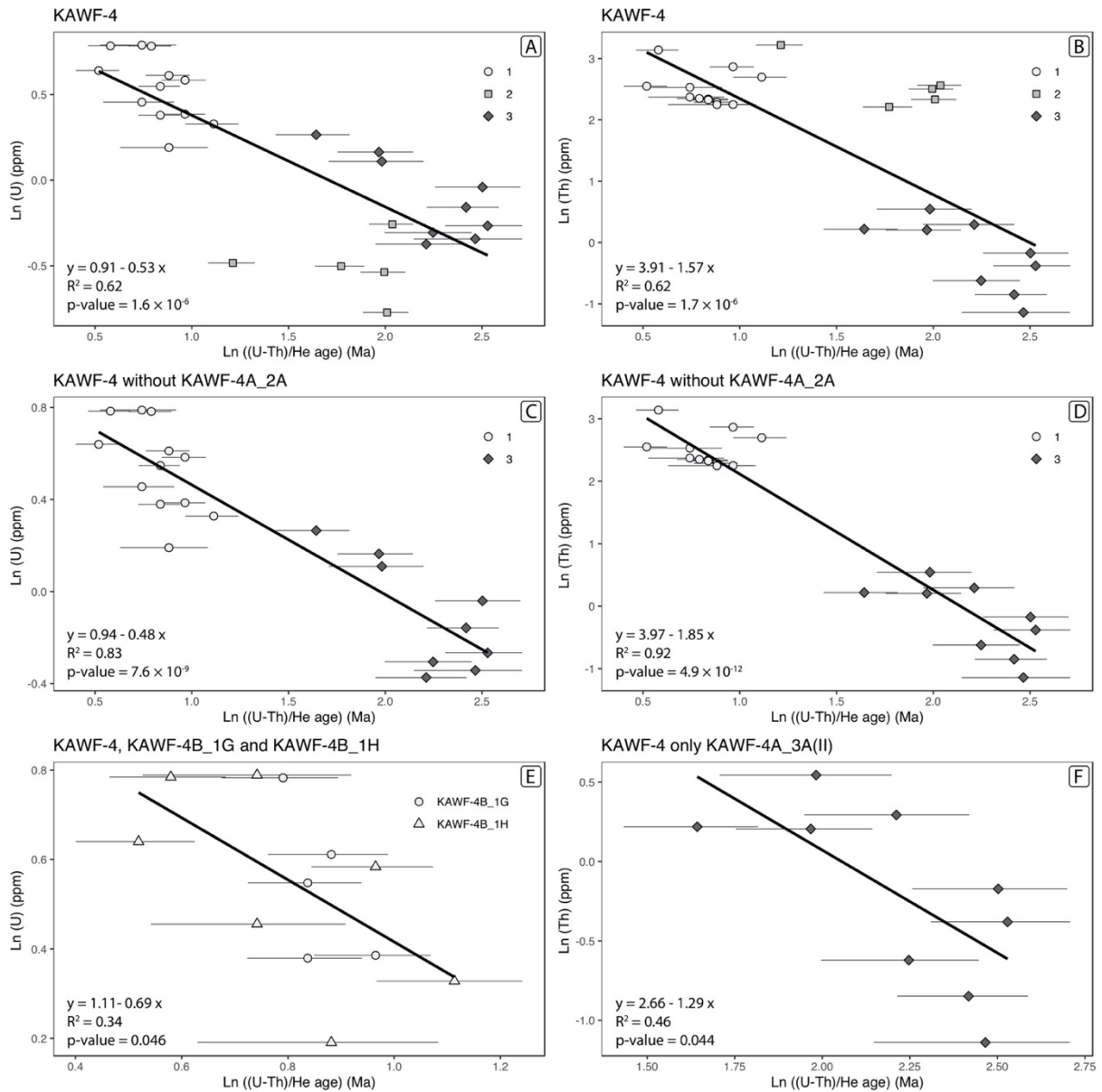


Figure B10: Logarithmic relations of (U-Th)/He ages and Th and U concentrations and calculated regressions for sample KAWF-4 and selected subsamples. Colors and shapes of the symbols indicate the subsamples. As the relations of age vs Th and U are generally not linear due to phase mixing and the fact that He production is an exponential process, log-correlations show the correlations better. Ln(age) vs Ln(Th) and Ln(U) correlations are more significant when subsample K4A_2A (medium gray squares in A and B) is excluded as this subsample composes clearly a different chemistry and is not a mixtures of the other subsamples (compare A with C and B with D).

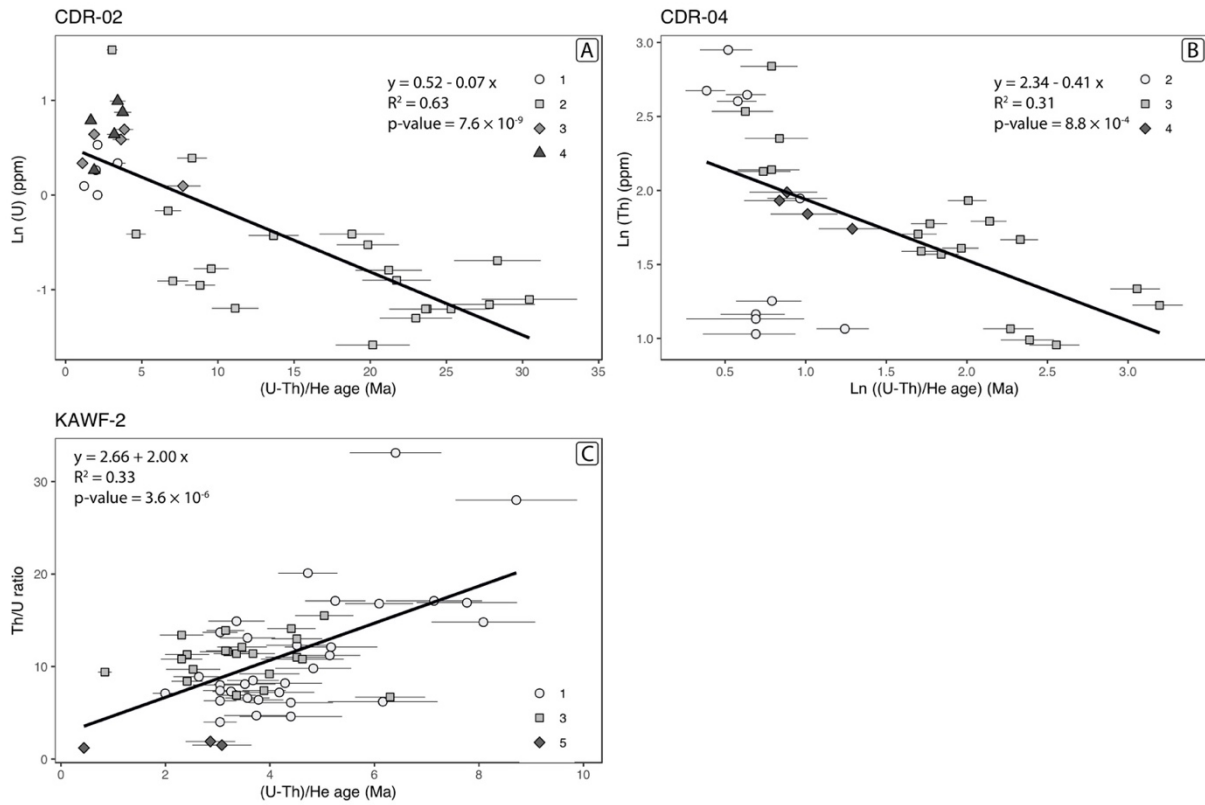


Figure B11: $(U-Th)/He$ age versus $\ln(U)$, $\ln((U-Th)/He \text{ age})$ versus $\ln(Th)$ and $(U-Th)/He$ age vs Th/U ratio for selected samples with calculated regressions. Colors and shapes indicate the subsamples. Note that as a function of the Th and U concentrations and the mixing, log-transformed values might show the correlations (which are thus log-correlations) better than the untransformed values.

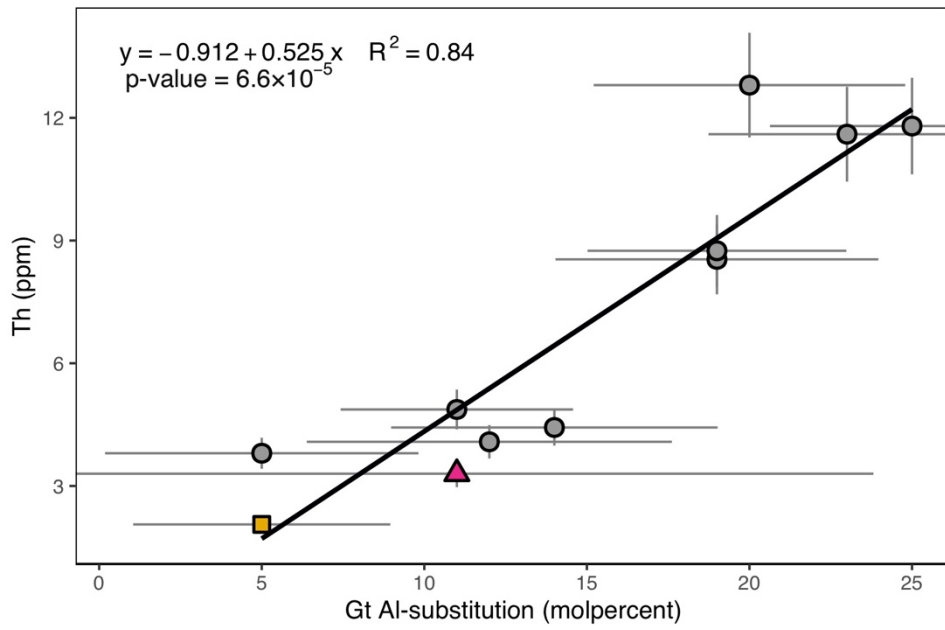


Figure B12: Goethite Al-substitution versus Th concentration for bulk samples with calculated linear regression corresponding to Figure 7B. Shapes and colors are as in Fig. 7B.

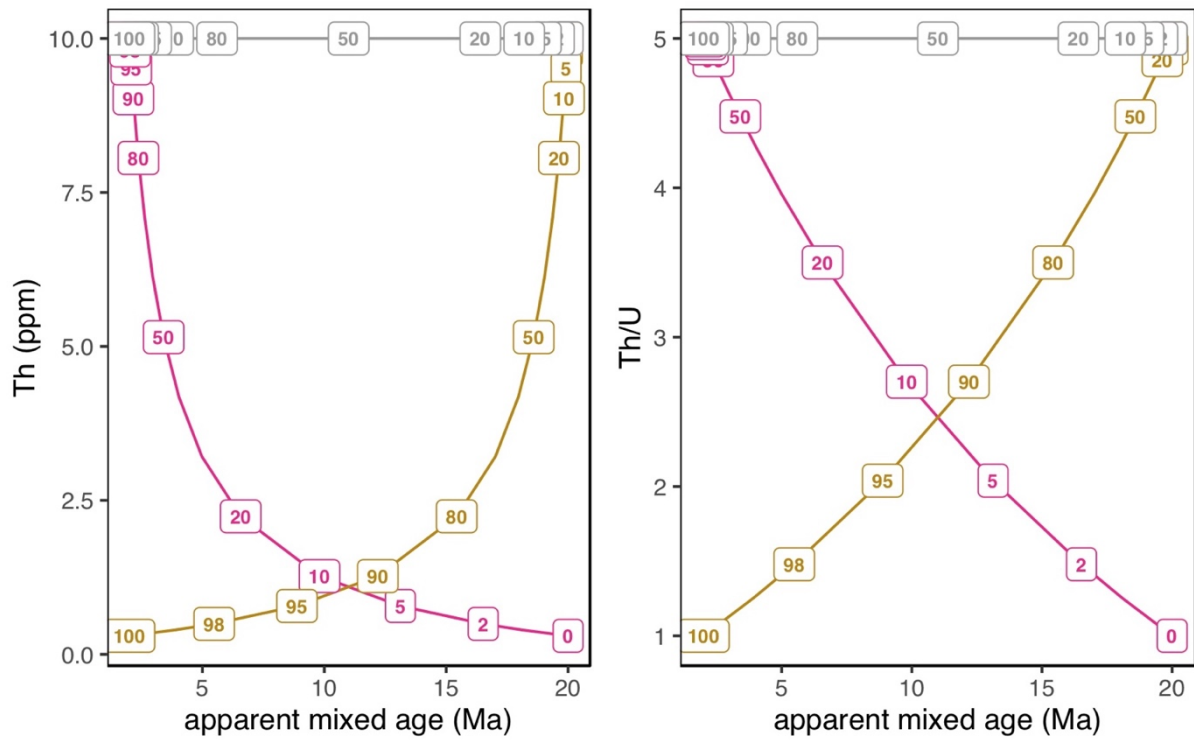


Figure B13: Supplementary figures for the age mixing model. For legend and explanations see Figure 8 and section 6.1 of the article.

Tables

Table B1: description of the separated subsamples

LOC	Sample No.	Subsample	predominant mineral phase	colour	luster	short description
CDR	CDR-01A	CDR-01A_1	Gt	black	metallic to semi-metal	outermost coating
CDR	CDR-01A	CDR-01A_2	Hm	reddish brown	dull	massive matrix, sometimes with mm sized cavities filled with gen CDR-01A_3
CDR	CDR-01A	CDR-01A_3	Hm	black	metallic	botryoidal filling of small cavities
CDR	CDR-01B	CDR-01B_1	Gt	black	metallic to semi-metal	outermost coating
CDR	CDR-01B	CDR-01B_2	Hm	reddish brown	dull	massive matrix, sometimes with mm sized cavities filled with gen CDR-01A_3
CDR	CDR-01B	CDR-01B_2A	Hm	reddish brown	dull	picked from CDR-01B_2, massive homogeneous grains
CDR	CDR-01B	CDR-01B_2B	Hm	reddish brown	dull	picked from CDR-01B_2 but grains with wormlike structure
CDR	CDR-01B	CDR-01B_3	Hm	black	metallic	botryoidal filling of cavities, often small pieces of matrix attached
CDR	CDR-02	CDR-02_1A	Gt	black	metallic	outermost coating
CDR	CDR-02	CDR-02_2A	Hm	reddish brown	dull	more metallic and hard matrix at rim of pisolith, pourous
CDR	CDR-02	CDR-02_2B	Hm	grey	metallic	metallic vein inside altered pisolith, pourous
CDR	CDR-02	CDR-02_2D	Hm	grey	metallic	more metallic and hard matrix at rim of pisolith, pourous
CDR	CDR-02	CDR-02_2E	Hm	grey	metallic	more metallic and hard matrix of outer part of pisolith, pourous
CDR	CDR-02	CDR-02_3A	Gt	black	metallic	botryoidal cavity filling between pisoliths
CDR	CDR-02	CDR-02_4A	Gt	brownish	glassy	matrix / cavity filling between pisoliths
CDR	CDR-03A	CDR-03A_1	Gt	black	metallic	outermost coating and filling of voids
CDR	CDR-03	CDR-03_3	Hm	red	dull to semi-metallic	most metallic parts of matrix
CDR	CDR-03	CDR-03_4	Gt	reddish black	glassy	outermost coating next to red matrix
CDR	CDR-03	CDR-03_5A	Gt	black	glassy	outer coating and coating surrounding small pisoliths, no pores
CDR	CDR-03	CDR-03_5B	Gt-Hm-mix	black	semi-metallic	picked from same material as CDR-03_5A but less glassy under microscope, eventually rest of small pisoliths
CDR	CDR-04A	CDR-04A_2A	Hm	red	dull	bean shaped rather dense pisolith (5x2mm) with some pores
CDR	CDR-04A	CDR-04A_2B	Hm	red	dull	bean shaped pisolith (5x2mm) with some pores, less dense than CDR-04A_2A
CDR	CDR-04A	CDR-04A_2BB	Hm	red	semi-metallic	botryoidal filling pieces of pisolith CDR-04A_2B
CDR	CDR-04A	CDR-04A_3A	Gt	black reddish	glassy	vermiforme structure, interior red+more pourous; rest denser+black/browner. blackish parts analysed
CDR	CDR-04A	CDR-04A_3B	Gt	black orange	dull	big triangular "clast" or matrix, massive with some pores
CDR	CDR-04C	CDR-04C_3A	Hm	silvery red	metallic	massive matrix with some small pores
CDR	CDR-04C	CDR-04C_3B	Hm	silvery red	metallic	massive matrix with some small pores
CDR	CDR-04C	CDR-04C_4A	Gt	black brown	glassy	dense layered vein without pores
KAW18-10	KAW18-10B2	KAW18-10B2_AA	Hm	red	dull	inner part if pisolit KAW18-10B2_A, with some pores
KAW18-10	KAW18-10B2	KAW18-10B2_AB	Gt	black	glassy	outer part if pisolit KAW18-10B2_A, rather dense
KAW18-10	KAW18-10B2	KAW18-10B2_BA	Hm	red	dull	inner part if pisolit KAW18-10B2_B, with some pores
KAW18-10	KAW18-10B2	KAW18-10B2_BB	Gt	black	glassy	outer part if pisolit KAW18-10B2_B, rather dense
KAWF	KAWF-1A	KAWF-1A_2BII	Hm	red	dull	red matrix
KAWF	KAWF-1A	KAWF-1A_5BB	Gt	black	glassy	black botryoidal pieces of subsample KAWF-1A_5BII
KAWF	KAWF-1A	KAWF-1A_5BII	Gt	brown	dull to glassy	brown porous rather hard matrix
KAWF	KAWF-1A	KAWF-1A_5CII	Gt	black	glassy	botryoidal glassy filling of big void/coating, massive to wormlike with concoidal fractures
KAWF	KAWF-1A	KAWF-1A_5D	Gt-Hm-mix	purple-reddish-black	dull	massive vein or matrix close to outer surfacem very dense and hard, rather homogeneous no pores, breaks concoidally
KAWF	KAWF-2	KAWF-2_1BA	Gt	red-orange	rather dull	inner part of big (ca.1.5 cm) pisolith
KAWF	KAWF-2	KAWF-2_1BB	Gt-Hm-mix	red-orange-black	glassy	outer part of big (ca.1.5 cm) pisolith
KAWF	KAWF-2	KAWF-2_1E	Hm	darkred-darkgrey	semi-metallic	inner part of slightly angular nodule with some pores, not completely dense; some material slightly less consolidated with less pores
KAWF	KAWF-2	KAWF-2_1EII	Hm	darkred-darkgrey	semi-metallic	inner part of slightly angular nodule with some pores, not completely dense; some material slightly less consolidated with less pores
KAWF	KAWF-2	KAWF-2_1HA	Gt-Hm-mix	reddish	rather dull	inner slightly pourous part of vermiforme structure (0.7x1cm)
KAWF	KAWF-2	KAWF-2_1HC	Gt	black	glassy	outer dense part of vermiforme structure (0.7x1cm)
KAWF	KAWF-2	KAWF-2_1J	Hm	red	half-metallic	pisolith with few pores
KAWF	KAWF-2	KAWF-2_1JA	Hm	red	dull	harder, elongated part of matrix, dark homogeneous material picked
KAWF	KAWF-2	KAWF-2_1JB	Hm	black	metallic	hard metallic vein in matrix/subsample KAWF-2_1JA with pores
KAWF	KAWF-2	KAWF-2_1JD	Hm	red	dull	red matrix
KAWF	KAWF-2	KAWF-2_1JDB	Gt	yellow	dull	yellow (mm wide) rim around matrix of subsample KAWF-2_1JD
KAWF	KAWF-2	KAWF-2_1DIII	Hm	red	dull	red matrix
KAWF	KAWF-2	KAWF-2_1SAII	Gt	brown	glassy	layered coating of big void/cavity
KAWF	KAWF-3	KAWF-3_4A	Gt	black	glassy	outermost coating
KAWF	KAWF-4A	KAWF-4A_2A	Hm	red-black	dull to semi-metallic	bean shaped nodule (3mm) with some pores
KAWF	KAWF-4A	KAWF-4A_3A	Gt	yellow brown dark-grey	dull	spongy matrix-like material, rather hard with many, often big pores but denser unporous aras also exist
KAWF	KAWF-4A	KAWF-4A_3AII	Gt	yellow brown dark-grey	dull	spongy matrix-like material, rather hard with many, often big pores but denser unporous aras also exist
KAWF	KAWF-4B	KAWF-4B_1G	Hm	red-black	semi-metallic	bean shaped small pisolit (1.5*3mm), dense without visible pores
KAWF	KAWF-4B	KAWF-4B_1H	Hm	red-black	semi-metallic	rounded / bean shaped small pisolith, rather dense with some pores
KAWF	KAWF-5A	KAWF-5A_1A	Hm	red-black	semi-metallic	rounded pisolith (2.5*4mm) with some pores in gibbsitic matrix
KAWF	KAWF-5A	KAWF-5A_1B	Hm	black	semi-metallic	rounded dense pisolith (3*3mm) with few pores in gibbsitic matrix
KAWF	KAWF-5A	KAWF-5A_2A	Gt	grey-black	semi-metallic	dense cement/ matrix coating / sourrounding the small pisoliths. black and glassy pieces
KAWF	KAWF-5A	KAWF-5A_2B	Gt-Hm-mix	grey	semi-metallic	dense cement/ matrix coating / sourrounding the small pisoliths but different colour from 2A (more reddish und less glassy)
KAWF	KAWF-5A	KAWF-5A_2C	Hm	grey	metallic	separated from same material as 2A and 3B but more porous and more metallic, grey silvery material. possibly corresponding to small pisoliths
KAWF	KAWF-5A	KAWF-5A_3AII	Gt	black	glassy to semi-metallic	2-3mm thick vein, matrixlike without pores
KAWF	KAWF-5B	KAWF-5B_1B	Gt-Hm-mix	black	glassy	thick vein /matrix (?), nearly massive in between gibbsite
KAWF	KAWF-5B	KAWF-5B_2AII	Gt	dark grey	rather dull	massive matrix-like "band" close to outer rum of sample crosscut by some gibbsitic veins
KAWF	KAWF-5B	KAWF-5B_3B	Gt	grey	glassy	very homogeneous coating without pores covering a cavity and the outside of the sample

Supplementary material for Chapter IV

Table B2 : Trace element and rare earth element concentrations of the dated duricrusts. All values are given in $\mu\text{g/g}$ (ppm)

Element\Sample	CDR-01	CDR-02	CDR-03	CDR-04A	CDR-04C	KAWF-1	KAWF-2	KAWF-3	KAWF-4	KAWF-5A	KAWF-5B
As	51.2	121	136	223	127	66.8	130	141	192	53.5	37.3
Ba	bld	bld	bld	14.3	bld	15.4	10.9	7.1	7.7	7.9	6.9
Be	bld	0.14	0.13	0.38	0.12	0.38	0.36	0.32	0.26	0.95	2.46
Bi	0.1	0.43	0.16	0.48	0.14	0.24	0.43	0.46	0.52	0.17	bld
Cd	0.05	0.04	0.05	0.03	0.06	0.04	0.09	0.05	0.06	0.08	0.09
Co	12.7	1.94	2.15	6.42	2.01	6.54	10.8	3.83	4.91	15.8	13.3
Cr	331	1390	566	688	475	180	705	639	1133	289	414
Cs	bld	bld	bld	0.05	bld	0.04	bld	0.02	bld	0.04	bld
Cu	216	58.2	84.2	80.5	102	75.1	74.9	73.5	60.8	333	679
Ga	25.9	47.9	41.8	35.1	38.7	23.5	43.6	40.4	42	61.3	26.3
Ge	1.72	4.61	1.19	0.98	1.06	2.4	1.46	1.81	2.02	0.93	1.09
Hf	3.82	3.83	4.09	3.97	3.32	2.82	5.96	5.92	6.85	6.73	4.21
In	0.15	0.37	0.19	0.24	0.17	0.13	0.28	0.27	0.27	0.16	0.19
Mo	2.35	5.23	5.82	6.87	5.26	3.92	6	6.28	7.06	3.39	1.45
Nb	9.08	8.93	10.3	10.8	8.8	5.43	13.7	13.1	16.6	16	8.34
Ni	15.3	18.3	7.6	25.2	9.3	35.8	12.6	9.3	9.7	52.3	111
Pb	8.94	17.4	19.6	33.2	30.9	42.2	40.3	16.2	13.7	9.37	6.51
Rb	bld	bld	bld	0.48	bld	0.25	0.24	bld	bld	bld	bld
Sb	0.93	2.85	3.45	7.07	2.87	1.63	4.29	4.32	7.75	1.06	0.58
Sc	23.31	43.12	18.28	18.59	16.51	28.34	45.79	33.49	35.49	73.42	145.3
Sn	1.96	2.42	2.35	2.85	2.08	1.74	5.79	4.43	4.74	3.74	1.92
Sr	5.8	7.2	7.6	12.3	7.4	8	14.9	13.3	12.8	5.8	bld
Ta	0.67	0.69	0.83	0.85	0.7	0.48	1.12	1.08	1.32	1.3	0.68
Th	3.3	8.54	4.43	8.75	4.08	4.87	12.8	11.8	11.6	3.8	2.06
U	0.43	0.85	0.77	1.24	0.7	1.13	1.94	1.55	1.7	1.69	2.61
V	1335	1403	2244	3572	2086	736	1288	1519	1681	1447	839
W	bld	1.25	0.85	1.19	bld	2.01	3.92	4.08	10.6	1.14	0.97
Y	1.95	3.6	4.37	12.1	3.8	5.71	9.27	8.22	11.3	3.77	3.34
Zn	131	20	13.1	85.3	13.5	89.9	34.9	23.6	26	66.5	83
Zr	142	140	152	150	125	104	219	220	265	259	161
La	35.7	5.86	9.24	11	8.41	8.99	15.2	13.6	12.8	7.05	1.58
Ce	50.2	9.21	13	19.5	11.8	15.1	24.6	23.5	20.8	9.04	3.13
Pr	7.92	1.14	1.72	2.42	1.55	1.6	3.04	2.69	2.55	1.36	0.435
Nd	20	4	5.74	8.99	4.94	5.53	10.9	9.65	8.84	4.62	1.82
Sm	2.25	0.726	0.889	2.03	0.842	1.04	1.92	1.73	1.67	0.874	0.73
Eu	0.441	0.189	0.247	0.598	0.225	0.269	0.501	0.447	0.432	0.222	0.227
Gd	0.931	0.597	0.724	2.02	0.656	0.917	1.56	1.43	1.54	0.691	0.656
Tb	0.114	0.104	0.127	0.365	0.114	0.157	0.256	0.236	0.283	0.128	0.146
Dy	0.632	0.73	0.844	2.41	0.753	1.09	1.74	1.56	1.93	0.836	1.01
Ho	0.119	0.165	0.189	0.513	0.17	0.231	0.37	0.34	0.447	0.191	0.217
Er	0.387	0.531	0.644	1.42	0.528	0.745	1.15	1.05	1.36	0.587	0.645
Tm	0.0634	0.0931	0.118	0.212	0.0948	0.13	0.189	0.171	0.217	0.101	0.109
Yb	0.551	0.804	1.05	1.5	0.853	1.06	1.45	1.42	1.7	0.813	0.889
Lu	0.099	0.138	0.22	0.237	0.171	0.191	0.258	0.25	0.282	0.122	0.127

Table B3: Main results of Rietveld refinement of the subsamples (powders and single grains) XRD patterns. Unreported raw values include scale factors and line-width parameters that were refined for goethite, hematite, anatase and rutile only. Anisotropic line-shapes and iron site occupancy factors were refined for goethite and hematite only (see Materials and Method). Uncertainties on each values were obtained from the XRD code (except for gt-Fe-Al substitution, see Materials and Methods).

Sample	subsample	XRD aliquot	Hematite	wt%	abs. error	Goethite	wt%	abs. error	Gibbsite	wt%	abs. error	Anatase	wt%	abs. error	Rutile	wt%	abs. error	Kaolinite	wt%	abs. error	Hm/(Hm+Gt)	RHG	Gt-c	abs. error	Gt-Fe-Al substitution	abs. error	R _{wp}	XRD method
CDR-01A	CDR-01A_1	CDR_01A1_powder2nd	18.3	2.145	77.1	0.8415	3.3	0.35	1.3	0.4	bid	bid	bid	1.00	0.19	2.9908	0.0026	19.2	4.1	0.013	powder XRD							
CDR-01A	CDR-01A_3	C1A3sp_XRD1	100	0	bid	bid	bid	bid	bid	bid	bid	bid	bid	1.00	0.82	3.0069	0.0124	10.1	9.7	0.014	single grain XRD							
CDR-01B	CDR-01B_2	CDR_01B2_powder2nd	77.5	0.405	17.2	2.46	3.8	0.4	1.5	0.3	bid	bid	bid	0.98	0.98	3.0451	0.0118	0.0	0.048	single grain XRD								
CDR-01B	CDR-01B_3	C1B3_XRD1	98.2	0	1.8	0	bid	bid	bid	bid	bid	bid	bid	0.16	2.9799	0.0028	25.5	4.2	0.012	powder XRD								
CDR-02	CDR-02_1A	CDR_02A1_powder2nd	14.3	1.245	76.6	0.505	7.1	0.2	2.1	0.25	bid	bid	bid	0.82	3.0130	0.0181	6.6	12.9	0.014	powder XRD								
CDR-02	CDR-02_2A	CDR_02A2_powder2nd	80.8	0.49	18.2	3.2	0.6	0.3	0.4	0.4	bid	bid	bid	0.96	3.0083	0.0085	9.3	7.5	0.035	single grain XRD								
CDR-02	CDR-02_2D	C2D2_XRD1	92.1	0.05	3.6	0.45	4.4	0.3	bid	bid	bid	bid	bid	0.01	2.9919	0.0005	18.7	2.9	0.031	single grain XRD								
CDR-02	CDR-02_3A	C2A3_XRD1	0.8	0.1	93.4	0.05	5	0.2	0.8	0.1	bid	bid	bid	0.82	2.9731	0.0056	29.4	5.8	0.029	single grain XRD								
CDR-04A	CDR-04A_2A	C4A2A_XRD1	81.73	0.25	18.26	1.3	bid	bid	bid	bid	bid	bid	bid	1.00	0.05	2.9970	0.0004	15.7	2.9	0.028	single grain XRD							
CDR-04A	CDR-04A_2B	C4A2B_XRD1	98.8	0.02	bid	bid	bid	bid	bid	1.2	0.3	bid	bid	0.05	3.0198	0.0004	2.7	2.8	0.029	single grain XRD								
CDR-04A	CDR-04A_3A	C4A3A_XRD1	4.5	0.5	95.2	0	bid	bid	bid	bid	bid	bid	bid	0.84	3.0168	0.0131	4.4	10.1	0.044	single grain XRD								
CDR-04A	CDR-04A_3B	C4A3B_XRD1	bid	bid	100	0	bid	bid	bid	bid	bid	bid	bid	0.81	3.0096	0.0016	8.5	3.5	0.035	single grain XRD								
CDR-04C	CDR-04C_3A	C4C3A_XRD1	81.2	0.35	15.3	2.8	bid	bid	3.4	0.85	bid	bid	bid	0.21	3.0094	0.0005	8.6	2.9	0.031	single grain XRD								
KAWF-1A	KAWF-1A_2BII	K1A2BII_XRD1	68.5	0.35	16.2	0.967	0.001	bid	bid	1.1	0.25	14.2	0.55	0.81	3.0096	0.0016	8.5	3.5	0.035	single grain XRD								
KAWF-1A	KAWF-1A_5BII	K1A5BII_XRD1	19.5	0.55	74.2	0.295	bid	2.4	2.4	0.3	bid	bid	bid	0.26	3.0196	0.0005	2.8	2.9	0.034	single grain XRD								
KAWF-1A	KAWF-1A_5CII	K1A5CII_XRD1	bid	bid	100	0	bid	bid	bid	bid	bid	bid	bid	0.00	3.0240	0.0015	0.3	3.5	0.044	single grain XRD								
KAWF-1A	KAWF-1A_5D	K1A5D_XRD1	26.3	0.65	73.7	0.3	bid	bid	bid	bid	bid	bid	bid	0.26	3.0196	0.0005	2.8	2.9	0.034	single grain XRD								
KAWF-2	KAWF-2_1BA	K21BA_XRD1	bid	bid	99.8	0.0045	bid	0.2	0.2	0.2	bid	bid	bid	0.00	2.9898	0.0009	19.8	3.1	0.041	single grain XRD								
KAWF-2	KAWF-2_1BB	K21BB_XRD1	46.9	0.5	52.2	0.633	bid	0.8	0.1	bid	bid	bid	bid	0.47	2.9922	0.0010	18.5	3.2	0.030	single grain XRD								
KAWF-2	KAWF-2_1E	K21E_XRD3	84	0.15	14.2	0.6555	bid	1.8	1.8	0.25	bid	bid	bid	0.86	3.0144	0.0078	5.8	7.1	0.032	single grain XRD								
KAWF-2	KAWF-2_1J	K21J_XRD3	67.2	0.4	31.9	1.126	bid	0.5	0.2	0.4	0.15	bid	bid	0.68	2.9913	0.0018	19.0	3.6	0.031	single grain XRD								
KAWF-2	KAWF-2_3A	K23A_XRD3	46.7	0.45	45.7	0.6815	7.6	0.25	bid	bid	bid	bid	bid	0.51	2.9876	0.0011	21.1	3.2	0.029	single grain XRD								
KAWF-2	KAWF-2_3B	K23B_XRD1	74	0.4	22	1.663	4	0.35	bid	bid	bid	bid	bid	0.77	3.0034	0.0042	12.1	5.0	0.038	single grain XRD								
KAWF-2	KAWF-2_5AII	K25AII_XRD1	bid	bid	99.2	0.01	bid	bid	bid	0	0.8	0.5	0.00	3.0006	0.0007	13.7	3.0	0.033	single grain XRD									
KAWF-4A	KAWF-4A_2A	K4A2A_XRD3	82.3	0.25	17.2	0.6	bid	0.6	bid	bid	bid	bid	bid	0.83	3.0076	0.0033	9.7	4.5	0.047	single grain XRD								
KAWF-4A	KAWF-4A_3AII	K4A3AII_XRD3	bid	bid	100	0	bid	bid	bid	bid	bid	bid	bid	0.00	3.0153	0.0003	5.3	2.8	0.028	single grain XRD								
KAWF-4B	KAWF-4B_1G	K4B1G_XRD3	3.4	0.6	93	0.1	bid	3.6	0.2	bid	bid	bid	bid	0.04	3.0141	0.0003	6.0	2.8	0.030	single grain XRD								
KAWF-4B	KAWF-4B_1G	K4B1G_XRD3	50.2	0.95	49.5	1.55	bid	0.4	0.25	bid	bid	bid	bid	0.50	2.9918	0.0019	18.7	3.7	0.046	single grain XRD								
KAWF-4B	KAWF-4B_1G	K4B1G_XRD4	49.6	0.95	49.9	1.5	bid	0.5	0.25	bid	bid	bid	bid	0.50	2.9892	0.0018	20.2	3.6	0.053	single grain XRD								
KAWF-4B	KAWF-4B_1H	K5B1H_XRD1	76.8	0.4	15.5	1.605	5.4	0.4	2.3	bid	bid	bid	bid	0.83	2.9936	0.0060	17.6	6.0	0.031	single grain XRD								
KAWF-5A	KAWF-5A_1A	K5A1A_XRD1	74.6	0.55	25	2.05	bid	0.4	0.2	bid	bid	bid	bid	0.75	2.9909	0.0038	19.2	4.8	0.037	single grain XRD								
KAWF-5A	KAWF-5A_1B	K5A1B_XRD1	83.3	0.3	16.6	1.8	bid	0.1	0.2	bid	bid	bid	bid	0.83	3.0002	0.0049	13.9	5.4	0.036	single grain XRD								
KAWF-5A	KAWF-5A_3AII	K5A3AII_XRD1	bid	bid	100	0	bid	bid	bid	bid	bid	bid	bid	0.00	3.0161	0.0008	4.8	3.0	0.045	single grain XRD								
KAWF-5B	KAWF-5B_1B	K5B1B_XRD1	50.9	0.45	49.1	0.55	bid	bid	bid	bid	bid	bid	bid	0.51	3.0166	0.0007	4.5	3.0	0.033	single grain XRD								
KAWF-5B	KAWF-5B_2AII	K5B2AII_XRD1	12.6	0.45	83.1	0.15	bid	4.4	0.2	bid	bid	bid	bid	0.13	3.0179	0.0004	3.8	2.8	0.026	single grain XRD								
KAWF-5B	KAWF-5B_3B	K5B3B_XRD1	bid	bid	99.6	0.0055	bid	0.4	0.15	bid	bid	bid	bid	0.00	3.0157	0.0004	5.0	2.8	0.034	single grain XRD								

Supplementary material for Chapter IV

Table B5: theoretically calculated mixed ages for 3 different scenarios as presented in Figure 8

scenario	phase 1 (wt%)	phase 2 (wt%)	apparent mixed age (Ma)	U total (ppm)	Th total (ppm)	Th/U ratio
1	100	0	20	0.3	0.3	1
1	99	1	18.86	0.32	0.4	1.25
1	98	2	17.84	0.33	0.49	1.48
1	95	5	15.32	0.39	0.79	2.04
1	90	10	12.33	0.47	1.27	2.7
1	80	20	8.74	0.64	2.24	3.5
1	70	30	6.66	0.81	3.21	3.96
1	60	40	5.3	0.98	4.18	4.27
1	50	50	4.34	1.15	5.15	4.48
1	40	60	3.63	1.32	6.12	4.64
1	30	70	3.09	1.49	7.09	4.76
1	20	80	2.65	1.66	8.06	4.86
1	10	90	2.29	1.83	9.03	4.93
1	5	95	2.14	1.92	9.52	4.97
1	2	98	2.05	1.97	9.81	4.99
1	1	99	2.03	1.98	9.9	4.99
1	0	100	2	2	10	5
2	100	0	20	2	10	5
2	99	1	19.97	1.98	9.9	4.99
2	98	2	19.95	1.97	9.81	4.99
2	95	5	19.86	1.92	9.52	4.97
2	90	10	19.71	1.83	9.03	4.93
2	80	20	19.35	1.66	8.06	4.86
2	70	30	18.91	1.49	7.09	4.76
2	60	40	18.37	1.32	6.12	4.64
2	50	50	17.66	1.15	5.15	4.48
2	40	60	16.7	0.98	4.18	4.27
2	30	70	15.34	0.81	3.21	3.96
2	20	80	13.26	0.64	2.24	3.5
2	10	90	9.67	0.47	1.27	2.7
2	5	95	6.68	0.39	0.79	2.04
2	2	98	4.16	0.33	0.49	1.48
2	1	99	3.14	0.32	0.4	1.25
2	0	100	2	0.3	0.3	1
3	100	0	20	2	10	5
3	99	1	19.82	2	10	5
3	98	2	19.64	2	10	5
3	95	5	19.1	2	10	5
3	90	10	18.2	2	10	5
3	80	20	16.4	2	10	5
3	70	30	14.6	2	10	5
3	60	40	12.8	2	10	5
3	50	50	11	2	10	5
3	40	60	9.2	2	10	5
3	30	70	7.4	2	10	5
3	20	80	5.6	2	10	5
3	10	90	3.8	2	10	5
3	5	95	2.9	2	10	5
3	2	98	2.36	2	10	5
3	1	99	2.18	2	10	5
3	0	100	2	2	10	5

C. Supplementary material for Chapter V

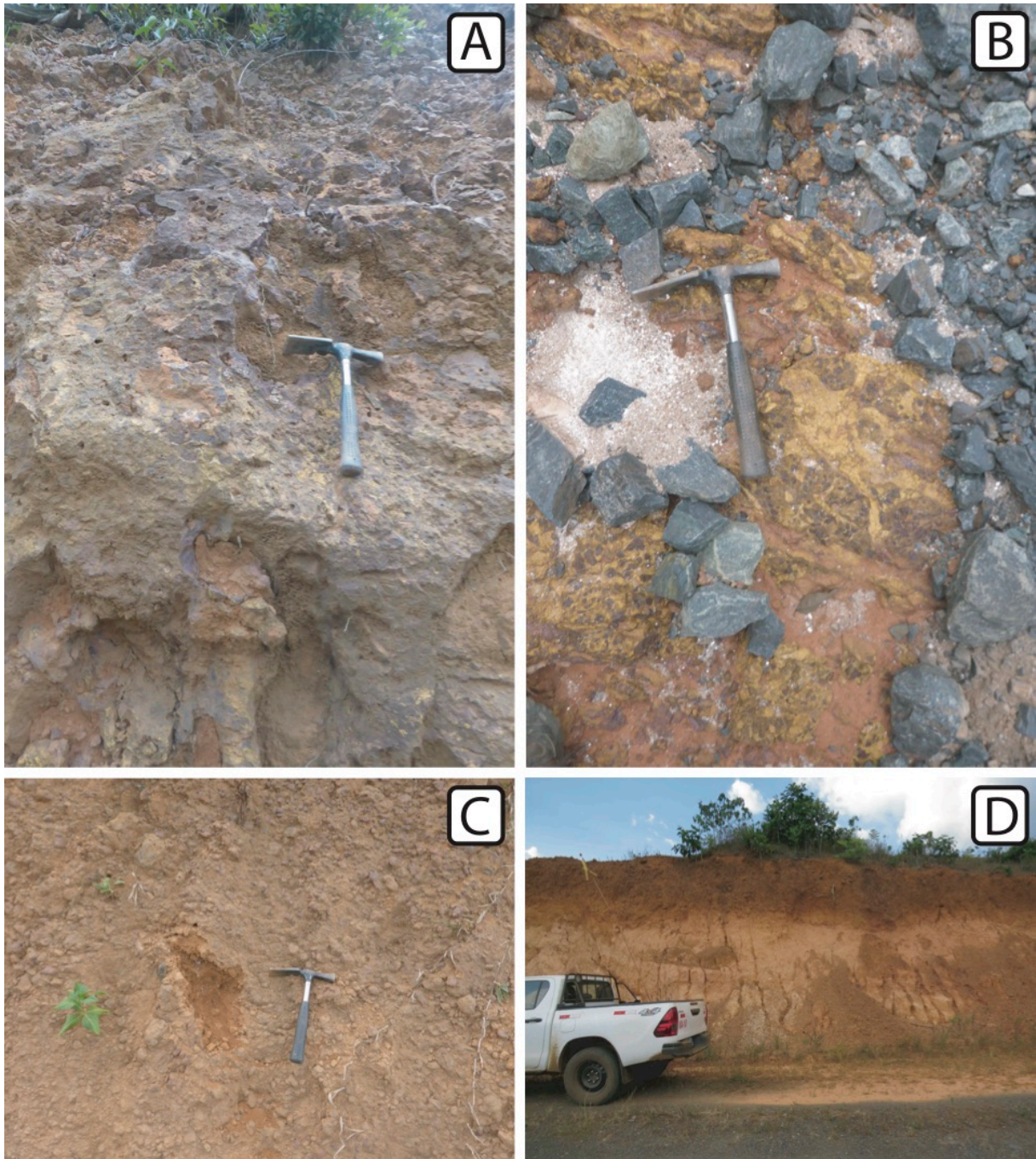


Figure C-1: Field pictures from the Tucano mine. (A) TUC19-1D, (B) TUC19-1E, (C) pisolith layer from which TUC19-1C was samples and (D) upper meters of the profile some meters away.

TUC19_1D (II)

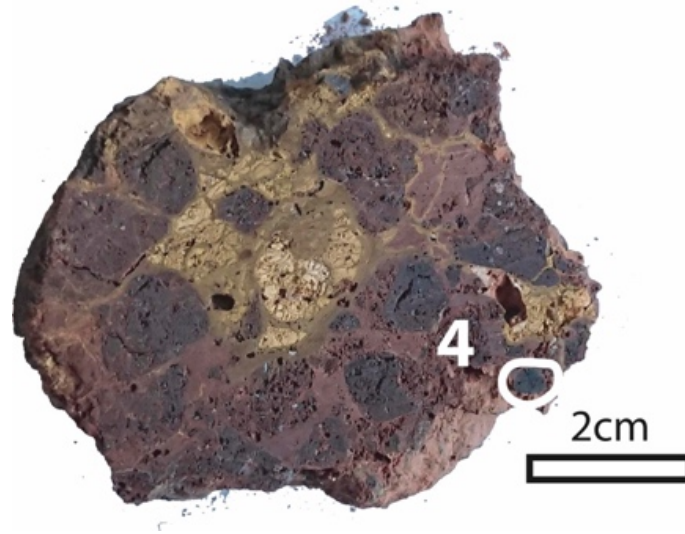


Figure C-2: Slice of sample TUC19-1D with indicated subsample TUC19-1D_4 (white).

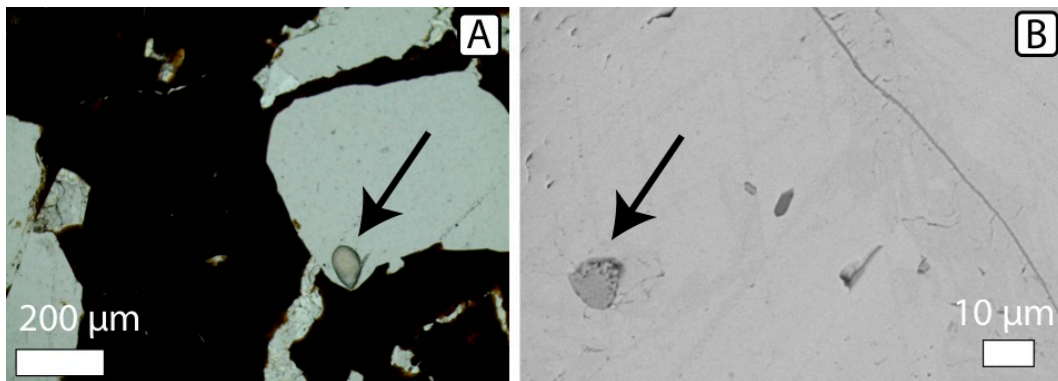


Figure C-3: (A) Polarized light microscopic image of an angular pore within hematite containing a rounded mineral rest. (B) Back scattered electron image of a kaolinite filled pore (black arrow) in subsample TUC19-1F_1A.

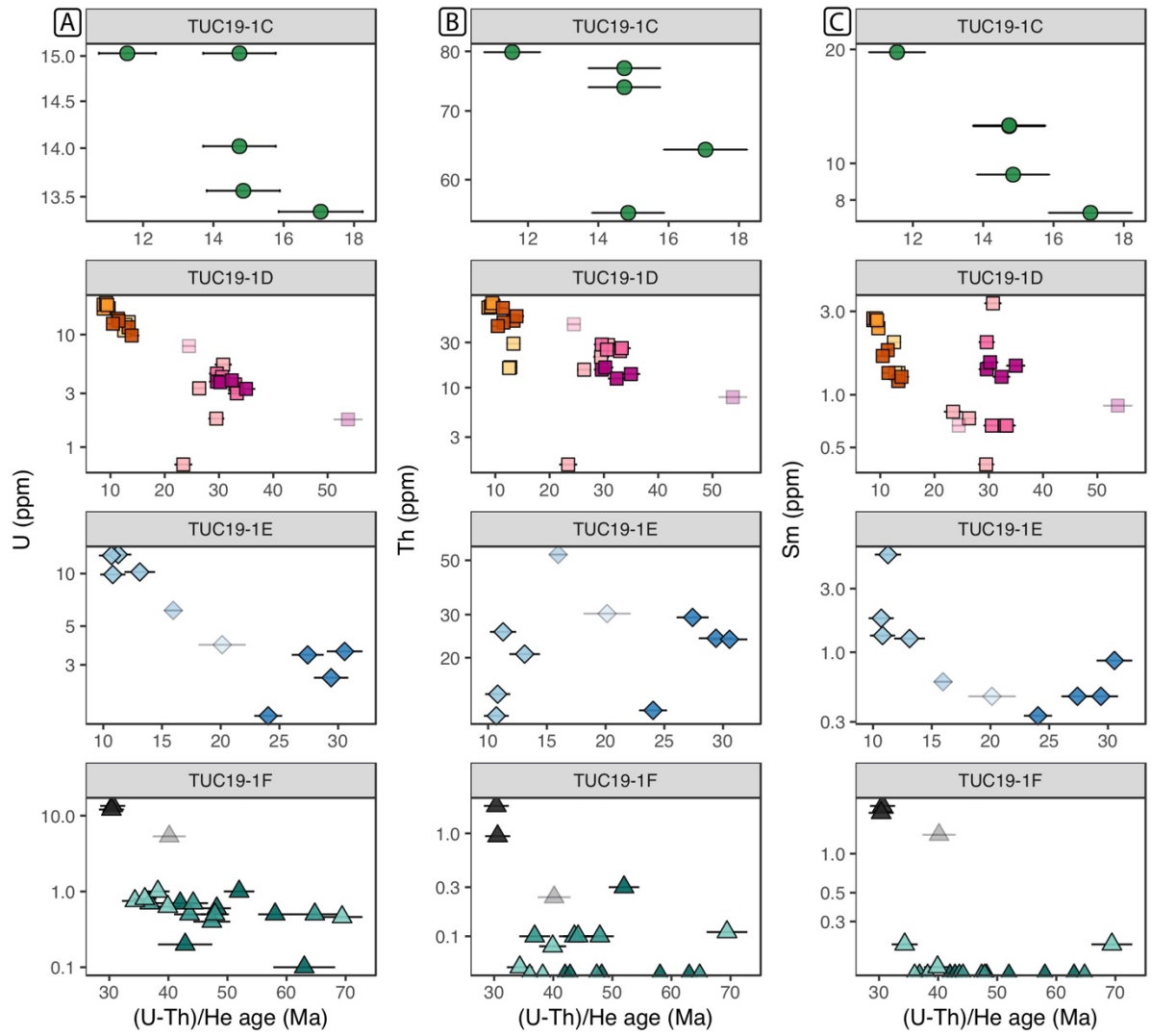


Figure C-4: (U-Th)/He ages versus U (A), Th (B) and Sm (C) concentrations. As figure 6B-D of manuscript but \log_{10} y-scales and x-scales adapted for every plot.

TUC19-1F

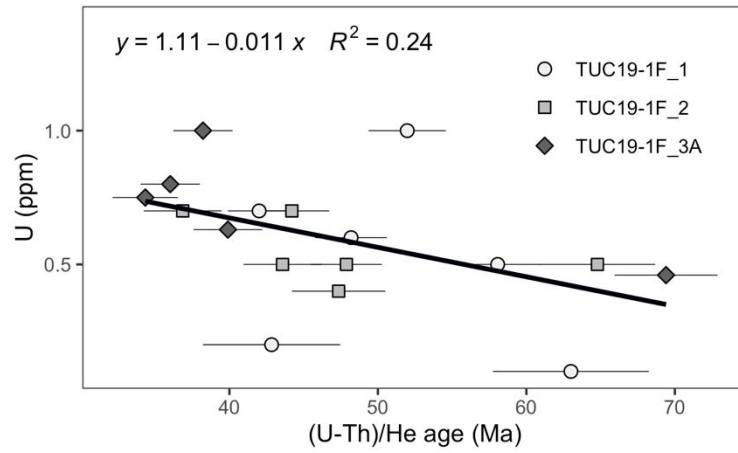


Figure C-5: Linear correlation of (U-Th)/He age and U concentration for the hematite subsamples of sample TUC19-1F. Although the correlation coefficient R^2 which describes the correlation is relatively low with 0.24, the correlation is significant as the p -value of the correlation is 0.048 (The p -value is a statistic measure which varies between 0 and 1 and indicates the probability if the null hypothesis (i.e. random distribution of the data) is true or not. Commonly p -values <0.005 (i.e. the probability that the null hypothesis is true is 5%) are considered as significant. (see e.g. Dalgaard, P., 2008, "Introductory to Statistics with R", Springer, 363 p.)).

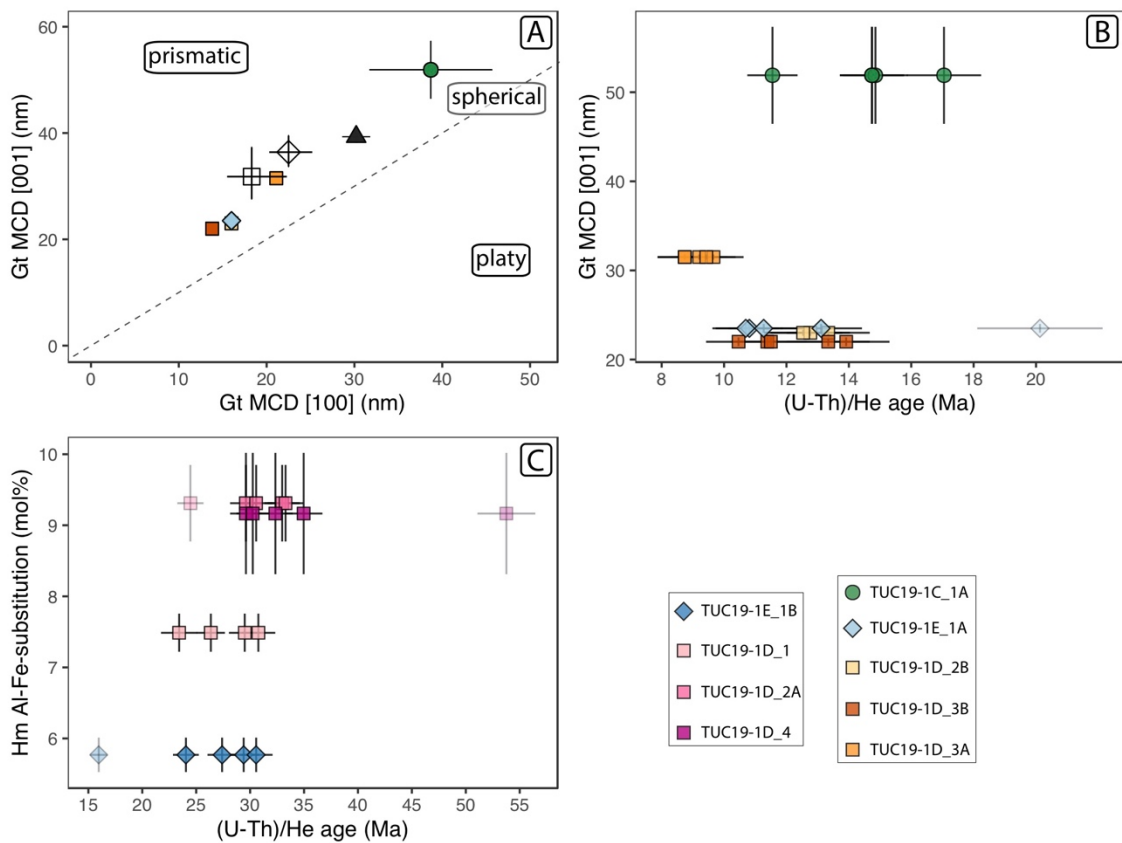


Figure C-6: Supplementary figures of the mineralogical properties of the subsamples and their relation with the (U-Th)/He ages. (A) Zoomed area of figure 4E with the goethite crystallite sizes in [100] and [001] directions. The dashed line indicates the 1-1 line which corresponds to approximately spherical crystallites. All presented subsamples have slightly anisotropic prismatic shapes. (B) Goethite crystallite sizes in [001] direction versus (U-Th)/He ages. (C) Hematite Fe-Al substitution versus obtained (U-Th)/He ages. In (B) and (C) only data from duricrusts above the schist are presented.

Supplementary observations

Interestingly a number of inclusions, some of them being composed of highly mobile elements such as Ca, Mg, were preserved in the canga sample. This means that these minerals were still (partly) stable and not completely dissolved when the canga layer formed and additionally it might imply that the canga layer protected these inclusions from being dissolved better than the hematite in the massive duricrust. The presence of these phases can be explained by the association of carbonates, iron, magnesium and calcium silicates with the BIFs (Scarpelli and Horikava, 2017).

Table C-1: Description of the separated subsamples

Bulk Sample	Subsample	Description	predominant mineral
TUC19-1B	TUC19-1B_1	black, stms anthrazit, metallic, rarely more glassy luster, "crystal" growth surfaces visible (structures similar to K5B2A)	Ht
TUC19-1C	TUC19-1C_1A	yellow ochre outer coating of pisolit, +- dense but some big holes with shape of former grains, often black mini veins, some small brighter patches, not ideal not perfectly pures	Gt
TUC19-1C	TUC19-1C_1B	inside of pisolith, red matrix rather soft and pourous pores coated with botryoidal gt	Ht
TUC19-1D	TUC19-1D_1	not very pure, pourous, rather soft (?) reddish brown material, locally clays attached?, rather ugly	Ht
TUC19-1D	TUC19-1D_2A	hard to pick, black spongy material, many pores, stms slightly dirty (?) some clays on surface? slightly glassy luster	Ht
TUC19-1D	TUC19-1D_2B	brown denser material, fine grained, no pores visible, slightly concoidal fractures	Gt
TUC19-1D	TUC19-1D_3A	ochre coloured material, rather dense and dull	Gt
TUC19-1D	TUC19-1D_3B	black veins, dense, slightly (but not completely) glassy, often not completely pure, clayey matrix attached	Gt
TUC19-1D	TUC19-1D_4	black, big pores, rather glassy luster	Ht
TUC19-1E	TUC19-1E_1A	very difficult to pick, brown black material when black denser than brown some small pores, surrounding of pisolites?	Gt
TUC19-1E	TUC19-1E_1B	very difficult to pick, red blackish, dense + slightly spongy, densest grains for He	Ht
TUC19-1F	TUC19-1F_1	magnetic, metallic luster, botryoidal black, at first glance metallic under good light rather	Ht
TUC19-1F	TUC19-1F_1botr ¹	black botryoidal slightly glassy material picked from the TUC19-1F_1 but more botryoidal	Ht-Gt-mix
TUC19-1F	TUC19-1F_2	very similar to 1, black +- glassy, very dense and homogeneous	Ht
TUC19-1F	TUC19-1F_3A	black, dense, rather glassy (often) botryoidal visible. A fragments often "spherical"	Ht
TUC19-1F	TUC19-1F_3B	black dense botryoidal layers visible	Gt

TUC19-1F_1botr¹: botryoidal goethite of subsample TUC19-1F_1

Supplementary material for Chapter V

Table C-2: Trace element composition of the analyzed bulk samples.

Element		TUC19-1C	TUC19-1D	TUC19-1E	TUC19-1F	TUC19-1C(matrix)
As	µg/g	123.6	130.9	126.0	25.7	18.3
Ba	µg/g	7.9	bld	bld	bld	40.7
Be	µg/g	1.24	1.29	2.02	5.97	2.03
Bi	µg/g	1.1	0.7	0.8	0.2	0.9
Cd	µg/g	0.07	0.03	0.03	0.07	0.09
Co	µg/g	3.2	4.7	8.3	8.9	3.8
Cr	µg/g	359.2	128.0	115.0	4.8	103.0
Cs	µg/g	0.10	0.05	0.20	0.05	2.47
Cu	µg/g	53	72	64	89	32
Ga	µg/g	27.2	27.8	30.8	1.1	48.4
Ge	µg/g	3.3	7.2	3.0	2.4	2.8
Hf	µg/g	9.5	3.2	4.3	0.1	9.9
In	µg/g	0.17	0.14	0.15	bld	0.18
Mo	µg/g	6.3	3.7	3.8	1.8	2.9
Nb	µg/g	12.9	14.1	13.8	2.8	42.8
Ni	µg/g	21.1	14.7	30.0	39.6	26.6
Pb	µg/g	28.3	51.9	53.7	31.5	46.2
Rb	µg/g	0.70	0.49	0.71	0.15	45.80
Sb	µg/g	3.5	2.8	3.0	0.6	1.6
Sc	µg/g	16.9	20.9	27.3	1.4	21.3
Sn	µg/g	6.0	13.9	8.7	1.4	32.3
Sr	µg/g	2.7	1.8	3.3	1.1	24.6
Ta	µg/g	1.26	1.62	1.53	0.32	5.86
Th	µg/g	25.7	22.3	19.5	0.5	22.5
U	µg/g	8.0	5.3	8.3	2.1	5.4
V	µg/g	236	294	317	32	145
W	µg/g	4.59	4.85	3.93	16.29	14.10
Y	µg/g	6.3	4.3	5.5	9.7	16.1
Zn	µg/g	76.2	32.8	68.7	94.2	47.6
Zr	µg/g	383	130	160	7	364
La	µg/g	5.6	5.1	10.1	1.6	58.2
Ce	µg/g	7.7	7.7	13.0	3.4	90.4
Pr	µg/g	1.26	0.85	1.50	0.41	12.50
Nd	µg/g	4.6	3.0	5.0	1.8	44.9
Sm	µg/g	1.08	0.68	1.18	0.53	7.81
Eu	µg/g	0.27	0.18	0.29	0.20	1.58
Gd	µg/g	0.97	0.65	1.04	0.78	5.03
Tb	µg/g	0.19	0.12	0.19	0.14	0.71
Dy	µg/g	1.31	0.88	1.31	1.07	3.87
Ho	µg/g	0.28	0.19	0.26	0.28	0.69
Er	µg/g	0.86	0.54	0.76	0.88	1.84
Tm	µg/g	0.14	0.09	0.13	0.14	0.28
Yb	µg/g	1.14	0.67	0.94	0.95	2.01
Lu	µg/g	0.18	0.10	0.14	0.16	0.30

D. Supplementary material for Chapter VI

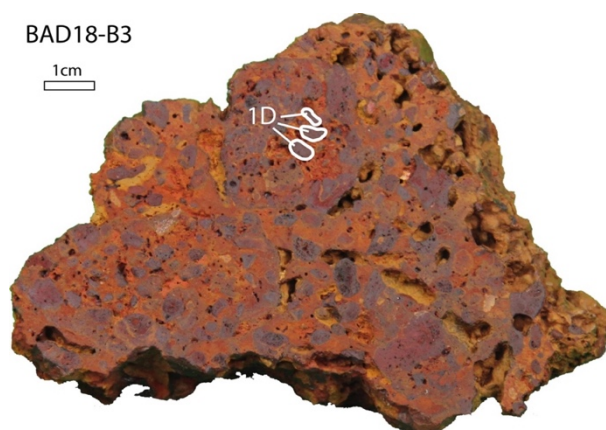


Figure D-1: Subsample BAD18-B3_1D, selected from another slice than the other subsamples

Table D-1: Description of the separated subsamples

Bulk sample	Subsample	predominant mineral	Macroscopic Description
BAD18-1B	BAD18-1B_1AM	Hm	silver, metallic, massive matrix material with some pores
BAD18-1B	BAD18-1B_1AV	Hm	silver, metallic, botryoidal void/ vein filling without pores
BAD18-1B	BAD18-1B_1B	Hm	silver-red dull massive matrix material, porous
BAD18-1B	BAD18-1B_2A	Gt	dark-gray semi-metallic massive matrix material, rather pore-free
BAD18-1B	BAD18-1B_2B	Gt	dark-gray semi-metallic massive matrix material, rather pore-free
BAD18-1B	BAD18-1B_2C	Gt	dark-gray semi-metallic massive matrix material, rather pore-free
BAD18-B3	BAD18-B3_1A	Hm	dark red, sometimes slightly brown, dull, inner part of a large (1.5 cm) pisolith. contains larger pores (100-200 μ m)
BAD18-B3	BAD18-B3_1AII	Hm	dark red, sometimes slightly brown, dull, central to outer part of a large (1.5 cm) pisolith. contains larger pores (100-200 μ m)
BAD18-B3	BAD18-B3_1B	Hm	red dull elongated pisolith, rather dense with some pores
BAD18-B3	BAD18-B3_1BII	Hm	red dull elongated pisolith, rather dense with some pores
BAD18-B3	BAD18-B3_1D	Hm	red-black dull bean-shaped pisoliths (n=3), rather dense with little pores
BAD18-B3	BAD18-B3_3A	Gt	grey slightly glassy material, void filling (?) without pores. Under microscope black and ochre brown, with concoidal fractures
VID-01	VID-01_1	Gt	brown homogeneous relatively soft material
VID-01	VID-01_2	Gt	brown homogeneous relatively soft material
VID-01	VID-01_3	Gt	brown homogeneous relatively soft material
VID18-1B	VID18-1B_1	Gt	black relatively dense and hard material, metallic luster
VID18-1B	VID18-1B_2	Hm?	black relatively dense and hard material, metallic luster
VID18-1B	VID18-1B_3	Hm	red material, softer than subsamples 1 and 2
GC21-01	GC21-01_A	unclear	red-violet blackish matrix material, rather dull
GC21-01	GC21-01_B	unclear	red-violet blackish matrix material, rather dull
GC21-01	GC21-01_C	unclear	red-violet blackish matrix material, rather dull
GC21-01	GC21-01_D	unclear	red-violet matrix material, metallic luster
GC21-03	GC21-03_A	Hm?	red-violet matrix material, relatively soft
GC21-03	GC21-03_B	Hm?	red-violet matrix material, relatively soft
GC21-03	GC21-03_C	Hm?	red-violet matrix material, harder than A and B

Supplementary material for Chapter VI

Table D-2: Trace element concentrations including rare earth element concentrations of the bulk samples. Note that the rare earth element concentrations are not normalized to the upper continental crust.

Element		BAD18-02	BAD18-1B	BAD18-1CA	BAD18-3A	BAD18-B3	VID-01	VID18-01B	GC21-01	GC21-03
As	µg/g	2.3	3.4	2.6	26.9	58.9	3.2	15.3	10.0	35.9
Ba	µg/g	115.0	11.3	bld	13.8	9.2	20.3	33.3	6.8	9.4
Be	µg/g	0.48	1.74	3.45	0.13	0.27	6.17	0.88	0.10	0.15
Bi	µg/g	0.1	bld	0.1	0.6	0.9	bld	0.7	0.3	1.3
Cd	µg/g	0.15	0.03	0.05	0.05	0.04	0.18	0.20	0.15	0.17
Co	µg/g	11.9	43.7	17.9	4.6	2.0	17.7	18.6	28.4	8.7
Cr	µg/g	16.2	96.9	40.1	217.0	294.0	19.9	204.0	293.0	771.0
Cs	µg/g	0.38	0.10	0.12	0.03	0.04	0.09	0.03	bld	bld
Cu	µg/g	107	398	205	70	46	408	233	192	106
Ga	µg/g	45.0	15.3	19.0	58.3	78.2	6.7	44.6	42.9	46.3
Ge	µg/g	1.3	4.6	1.9	0.8	0.9	1.0	1.0	0.7	0.7
Hf	µg/g	20.6	3.9	5.3	7.3	9.6	3.3	13.3	1.7	4.7
In	µg/g	0.20	0.09	0.11	0.37	0.50	0.04	0.28	0.11	0.16
Mo	µg/g	bld	4.1	5.8	4.8	12.7	3.0	4.9	11.2	12.1
Nb	µg/g	18.2	8.9	12.4	22.2	24.5	7.9	30.9	5.4	11.0
Ni	µg/g	11.1	15.7	27.5	2.7	2.7	25.5	10.7	69.2	9.7
Pb	µg/g	29.1	33.6	8.9	14.8	14.4	3.7	9.4	10.0	15.0
Rb	µg/g	1.80	0.33	0.47	bld	0.15	0.81	bld	bld	0.19
Sb	µg/g	0.1	0.1	0.1	0.5	1.0	0.6	0.8	0.8	1.9
Sc	µg/g	38.6	68.7	58.6	16.1	15.1	15.1	35.0	16.8	34.7
Sn	µg/g	3.5	1.8	2.7	5.6	7.9	1.2	8.1	1.7	1.7
Sr	µg/g	bld	7.1	bld	18.2	16.5	2.2	44.3	347.0	73.3
Ta	µg/g	2.01	0.68	0.96	1.91	2.02	0.63	3.24	0.49	1.06
Th	µg/g	6.7	1.0	1.5	14.6	17.2	1.4	12.7	4.1	9.6
U	µg/g	2.1	1.7	1.4	1.6	1.6	0.7	1.3	1.6	2.9
V	µg/g	191	1025	411	676	1709	173	1278	3189	3666
W	µg/g	bld	bld	bld	0.91	1.10	bld	1.48	3.22	8.87
Y	µg/g	127.0	15.8	40.1	7.3	8.7	64.7	7.8	1.8	3.7
Zn	µg/g	416.0	54.0	142.0	67.6	31.2	250.0	131.0	39.6	35.1
Zr	µg/g	754	149	208	265	333	132	542	64	178
La	µg/g	1.9	16.7	5.7	20.4	18.4	12.0	23.4	3.1	12.4
Ce	µg/g	8.9	122.0	8.5	33.0	29.6	26.6	47.7	5.1	20.3
Pr	µg/g	0.58	3.74	2.07	4.00	3.64	5.26	5.82	0.64	2.13
Nd	µg/g	3.2	13.0	9.7	13.3	12.6	24.0	22.6	2.3	6.3
Sm	µg/g	2.62	3.33	4.33	2.23	2.22	9.27	4.45	0.44	0.99
Eu	µg/g	0.94	0.91	1.49	0.48	0.47	2.60	1.05	0.13	0.22
Gd	µg/g	8.40	3.01	5.83	1.56	1.64	9.76	3.03	0.35	0.65
Tb	µg/g	2.22	0.60	1.51	0.24	0.27	2.08	0.41	0.06	0.10
Dy	µg/g	18.70	4.24	12.50	1.54	1.73	15.50	2.31	0.39	0.64
Ho	µg/g	4.67	0.93	2.87	0.31	0.37	3.49	0.40	0.08	0.14
Er	µg/g	14.00	2.82	9.27	0.90	1.08	10.90	1.09	0.24	0.43
Tm	µg/g	2.10	0.45	1.62	0.14	0.17	1.76	0.17	0.04	0.07
Yb	µg/g	13.70	3.40	12.70	1.04	1.34	13.20	1.31	0.30	0.55
Lu	µg/g	2.16	0.51	1.92	0.17	0.22	2.02	0.21	0.05	0.09

E. Supplementary material for Chapter VII

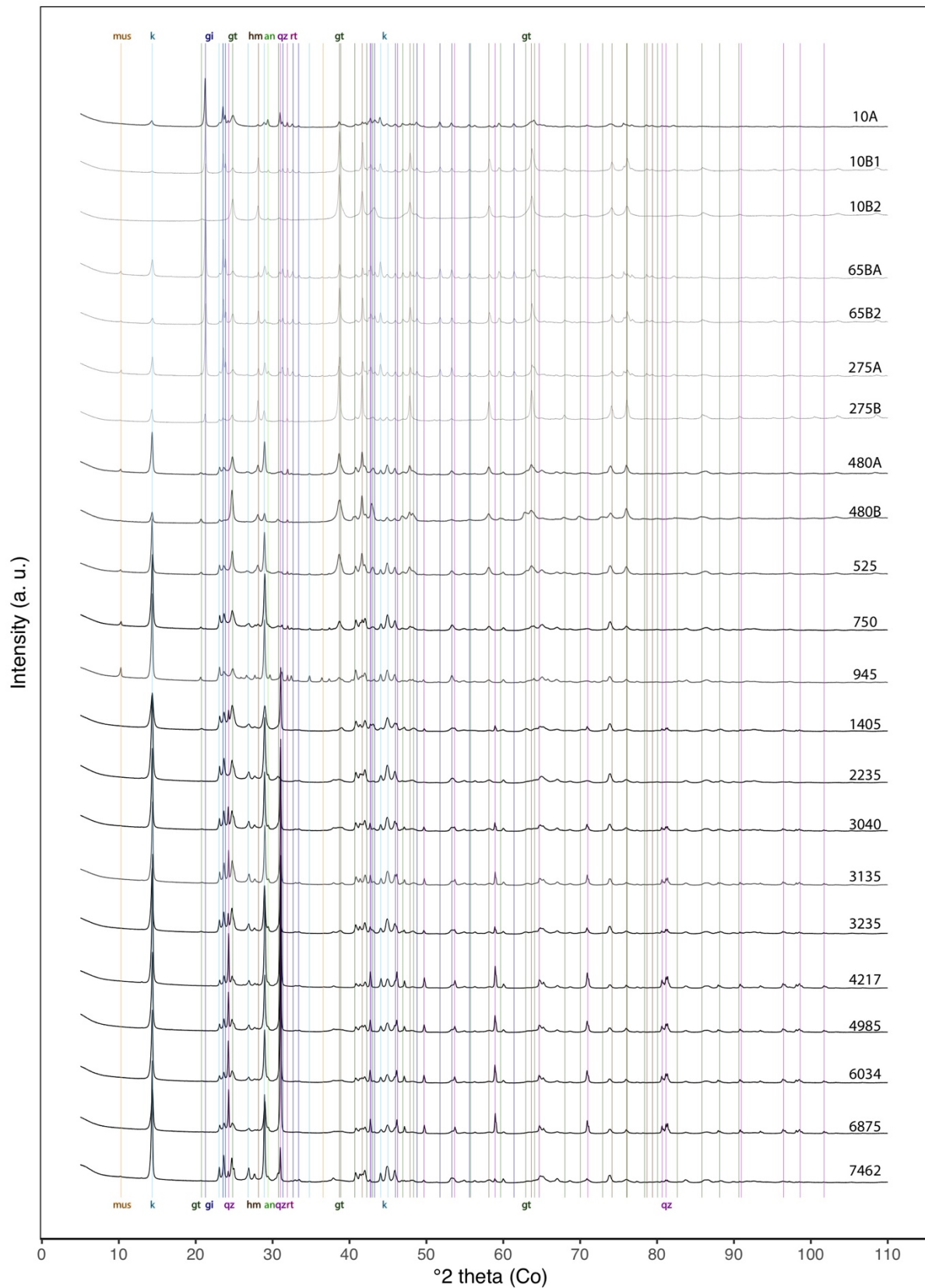


Figure E-1: XRD-pattern of the bulk samples of the Kaw drillcore. Mus = muscovite, k= kaolinite, gt=goethite, gi = gibbsite, hm= hematite, qz= quartz, an=anatase, rt=rutile. Vertical lines of the same color correspond to peaks of the same mineral. The sample name corresponds to the depth in cm. XRD pattern of all samples analyzed geochemically are presented. Black solid pattern correspond to samples investigated by EPR, bright gray pattern correspond to samples investigated by geochemistry only.

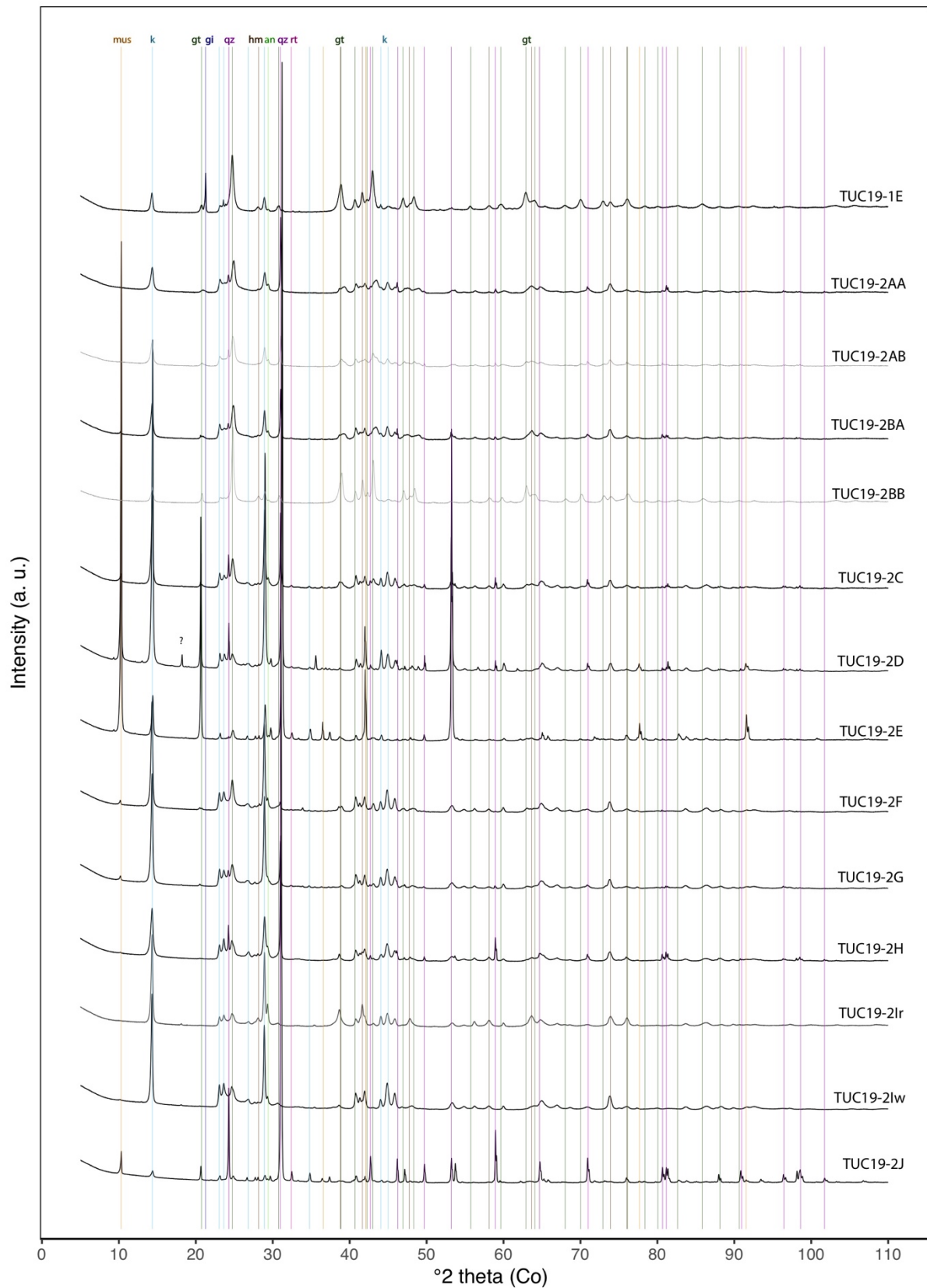


Figure E-2: XRD-pattern of the bulk samples of the Tucano profile. Mus = muscovite, k= kaolinite, gt=goethite, gi = gibbsite, hm= hematite, qz= quartz, an=anatase, rt=rutile. Vertical lines of the same color correspond to peaks of the same mineral. Black solid pattern correspond to samples investigated by EPR, bright gray pattern correspond to samples investigated by geochemistry only.

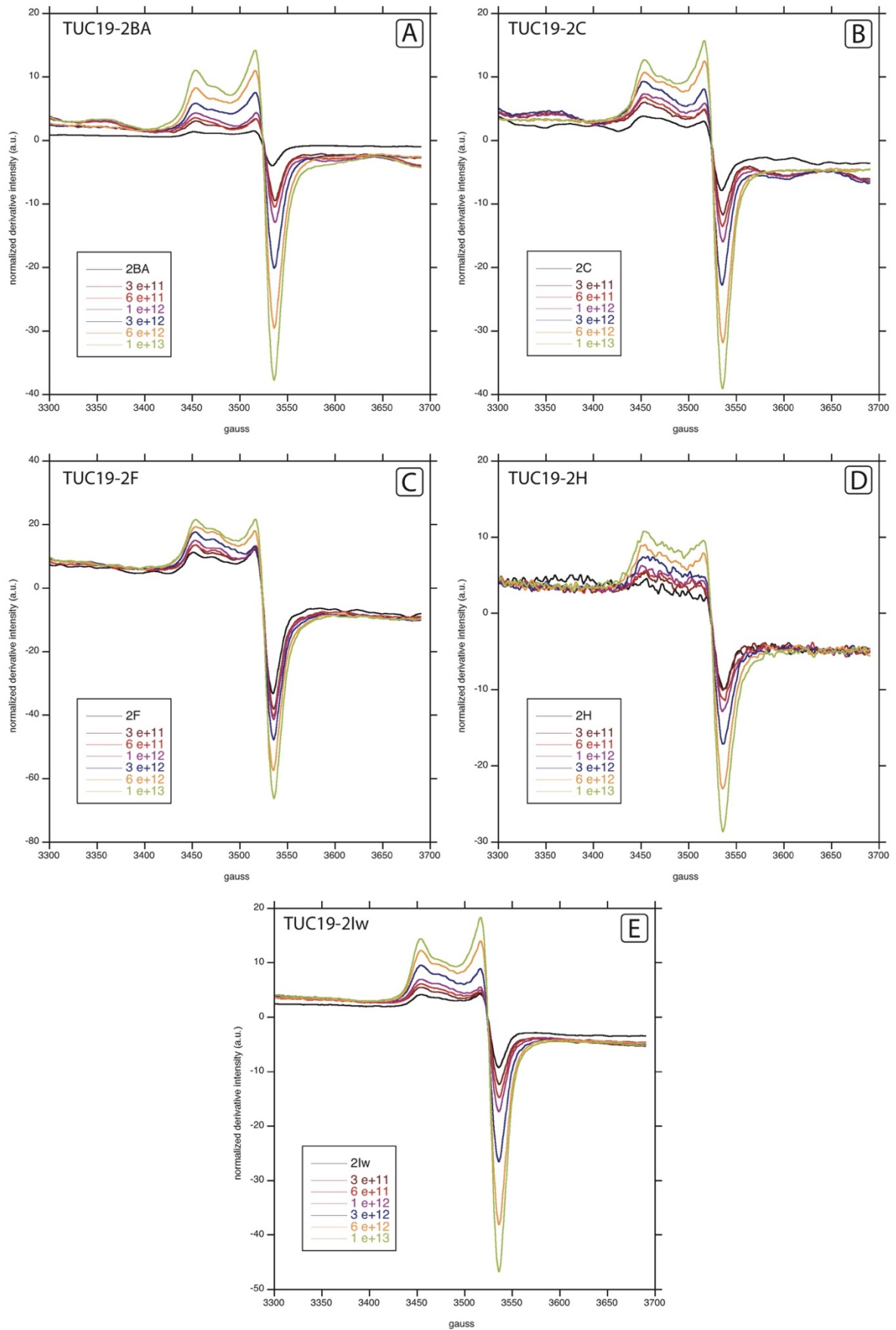


Figure E-3: Radiation induced defects (RIDs) of remaining kaolinite samples from the Tucano mine. Black lines correspond to the natural kaolinite, colored lines correspond to artificial irradiation doses. The legend indicates the irradiation fluence in He⁺ particles/cm²

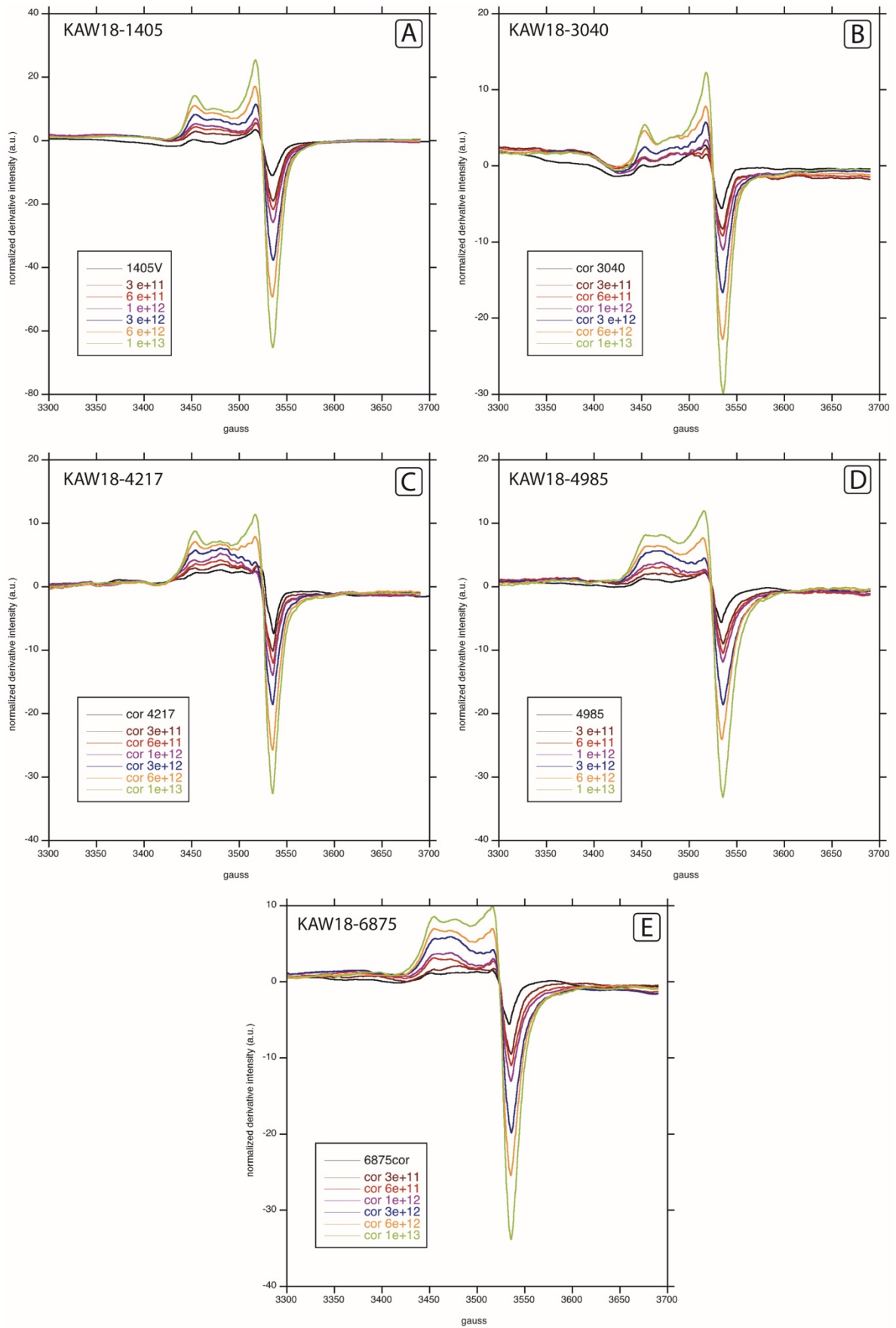


Figure E-4: Radiation induced defects (RIDs) of remaining kaolinite samples from the Kaw drill core. Black lines correspond to the natural kaolinite, colored lines correspond to artificial irradiation doses. The legend indicates the irradiation dose in He^+ -particles/ cm^2 . If legend indicates "cor" this means that the samples were corrected for vanadyl.

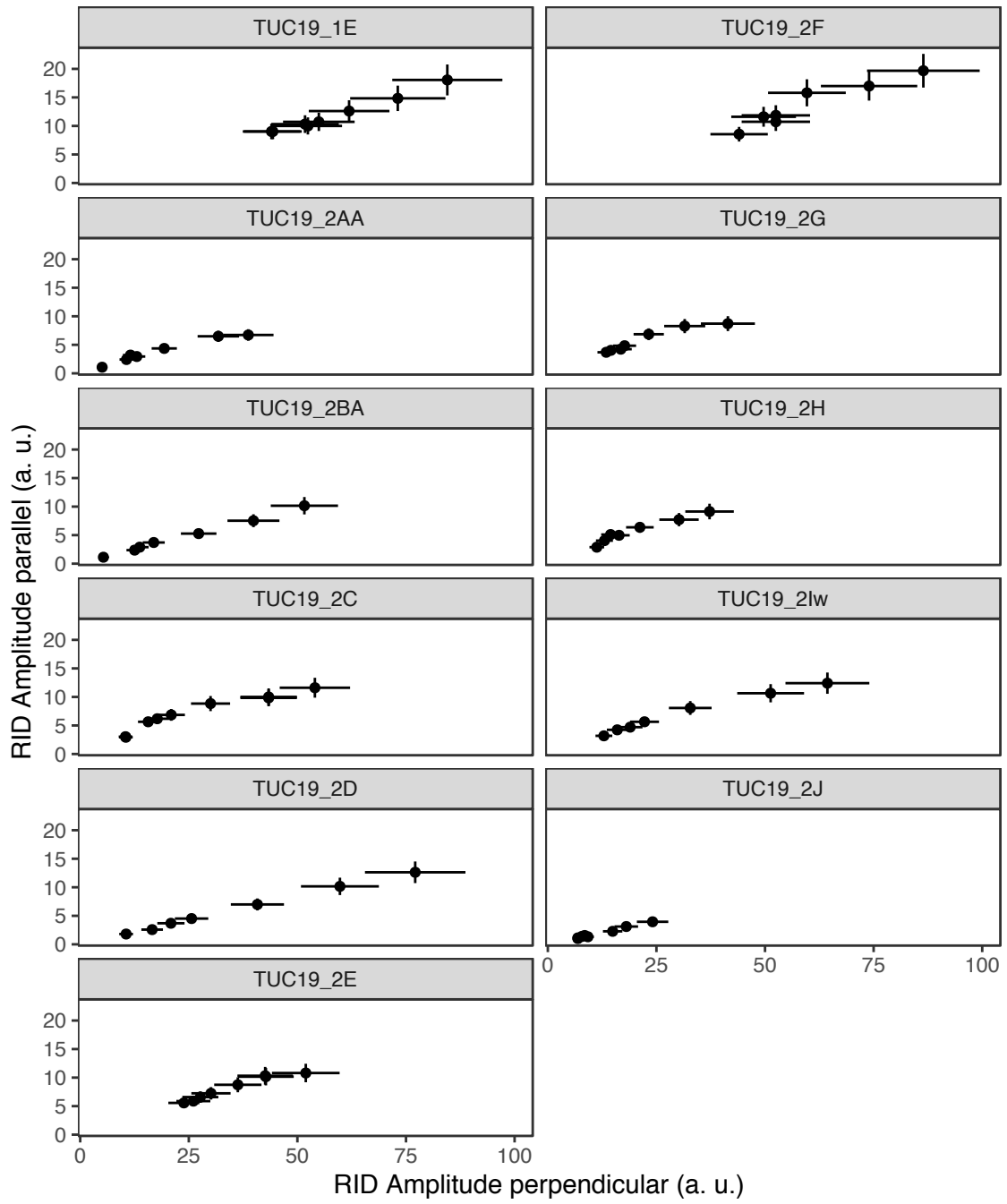


Figure E-5: Radiation induced defect (RID) signal amplitude of perpendicular versus parallel components for the Tucano samples.

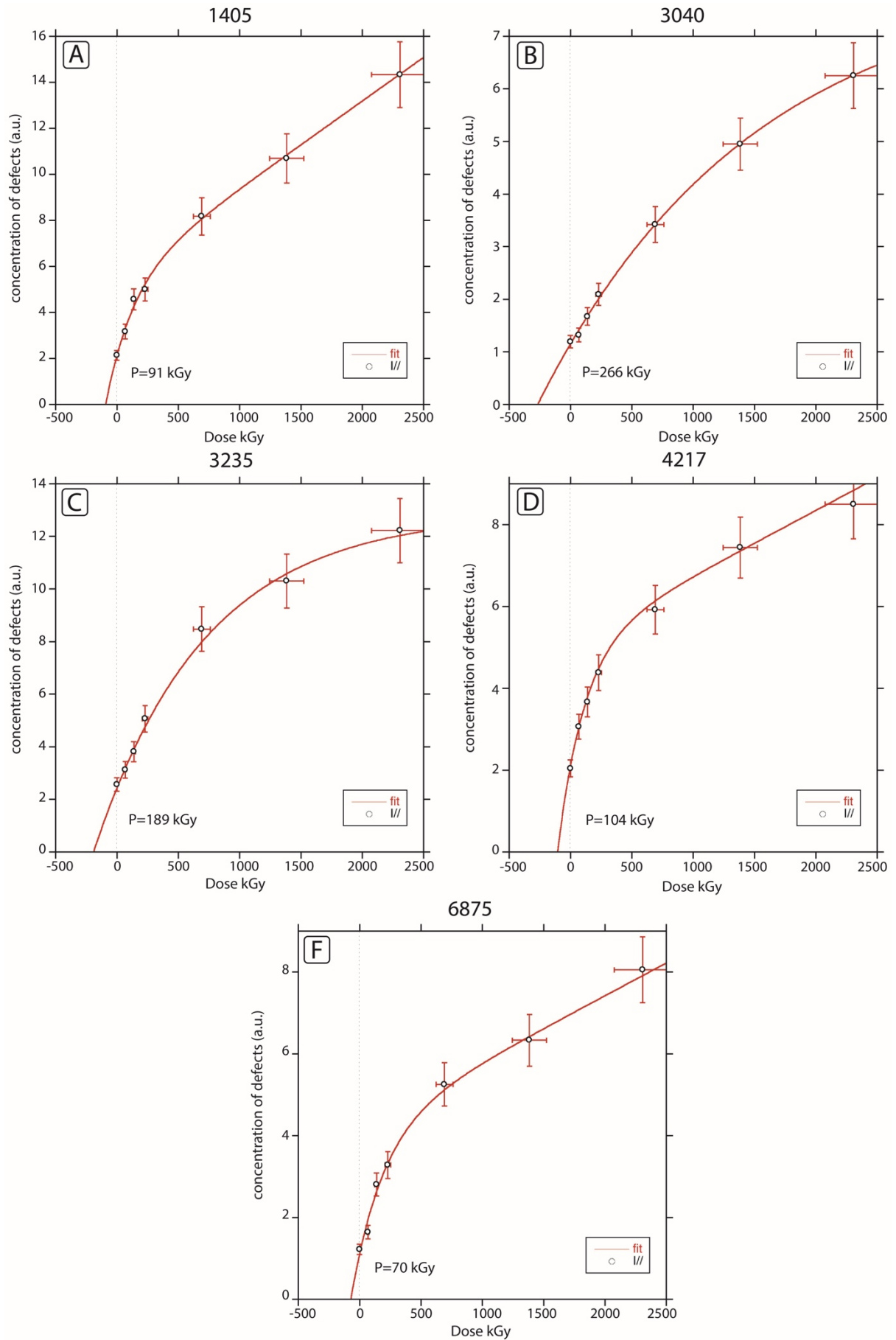


Figure E-6: Dosimetry curves for remaining kaolinite samples from Kaw. Concentration of defects are calculated from the RID amplitudes (arbitrary units). P corresponds to the paleodose obtained through the fitting shown.

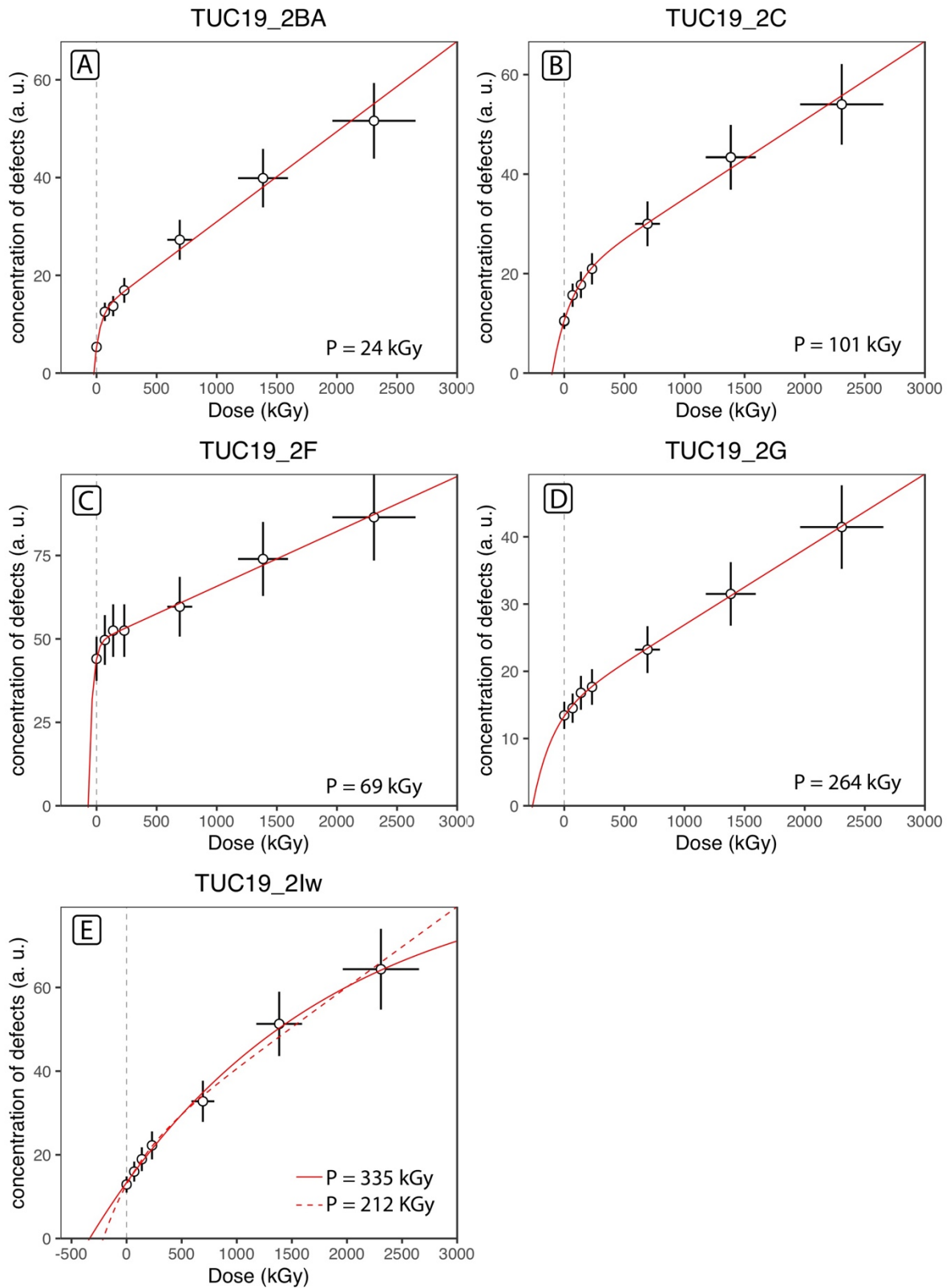


Figure E-7: Dosimetry curves for remaining kaolinite samples from the Tucano mine. Concentration of defects is calculated from the RID amplitudes (arbitrary units). P corresponds to the paleodose obtained through the fitting shown. In (E) a purely exponential function (solid curve) yielded a slightly better fit than an exponential function with linear components (dashed curve). Paleodoses are given for both functions and differ more than the 36% analytical error.

Supplementary material for Chapter VII

Table E-1: Log of the Kaw mountain drill-core.

Unit Start (m)	Unit End (m)	Sample	Description
0.00	0.25	10	yellow brown soil with colluvium from duricrust (Munsell 7.5YR 5/6)
0.25	0.45		transition from soil to cuirasse
0.45	1.50		red-yellow-dark cuirasse, heterogenous, with red clay (Munsell 10R 4/6, 10R 4/8)
1.50	2.35		red cuirasse pieces, less clay, some yellow material
2.35	4.50		heterogenous cuirasse (Munsell 10R 4/8, 10R 5/8, 10R 4/6, 10R 4/8)
4.50	5.00	480	red to nearly black cuirasse, more pieces, often pebble size or bigger (Munsell 7.5R 5/6)
5.00	5.30	525	softer material with less pieces, write and bordeaux, "mottled zone" / "bariolé"? (Munsell 7.5R 4/3, 7.5R 4/4)
5.30	7.50		saprolite like, heterogeneous material containing clays and Fe oxides. Gray, violett, bordeaux, locally white or red (Munsell 7.5R)
7.50	8.10	750	saprolite with visible structures, slightly reddish than before (Munsell 2.5YR 4/6)
8.10	10.10	945	saprolite with shistosity, purple gray-red fine, mm-sized layers with Fe-oxides
10.10	11.00		clay-rich saprolite, reddish
11.00	13.00		saprolite with color variations. purple-reddish parts alternate with nearly black and white parts. Sometimes pieces in between
13.00	13.85		saprolite, reddish purple brown with some yellow material
13.85	14.70	1405	heterogeneous saprolite, reddish purple with yellow and stms white material. Some qzt grains. Shistosity less but still visible (Munsell 7.5R 6/6 (yellow material))
14.70	15.20		saprolite, reddish stms yellow with color variations at cm-scale (Munsell 5YR 6/6 to 2.5YR 5/4)
15.20	15.65		saprolite with shistosity, red violett brown
15.65	15.80		heterogenic saprolite with white material
15.80	16.70		yellow ochre brown clay-rich
16.70	17.10		yellowish saprolite, rocky ("rocheuse")
17.10	17.70		heterogenous clay-rich saprolite, shistosity and bands visible
17.70	18.00		reddish-purple saprolite with shistosity (continuation)
18.00	18.30		yellow, rocky saprolite, visible bands yellow and dark brown (up to 0.5cm thickness), sometimes greenish
18.30	19.95		reddish saprolite, structures well visible rocky, already harder
19.95	20.50		red homogeneous saprolite, clayrich
20.50	21.75		red homogeneous saprolite with shistosity, less clay, harder
21.75	22.30		red homogeneous saprolite, shistosity well visible, rocky
22.30	22.70	2235	purple/violett saprolite, clay-rich, no shistosity, some greenish/ grey veins visible
22.70	22.80		heterogeneous saprolite rocky, purple white gray orange
22.80	23.60		red saprolite with strong shistosity, rocky but also some clays (not too hard)
23.60	24.90		red homogeneous saprolite, rocky with some clays, not too hard
24.90	25.50		red-violett saprolite with shistosity, rocky, + homogeneous
25.50	25.70		violett beige, stms orange saproliteheterogenous, rocky, no visible shistosity
25.70	25.95		very heterogenous beige red white dark saprolite with some hard dark pieces
25.95	26.60		white beige saprolite, partly rocky partly clay-rich, no shistosity, often homogeneous
26.60	26.80		brown homogeneous saprolite with shistosity
26.80	27.80		brown, slightly violettish saprolite, only very slight shistosity, homogeneous and rather massiv, tiny patches (former grains?) visible
27.80	29.25		brown, slightly violettish saprolite, only very slight shistosity, homogeneous and rather massiv, tiny patches (former grains?) visible
29.25	29.95		white-beige massiv saprolite with very little shistosity
29.95	30.00		saprolite with beige and red bands, foliation and folds visible
30.00	31.00	3040	brown violettish saprolite, rather massiv however some shistosity and broken into disks, rocky, locally qtz-veins
31.00	31.60	3135	beige white saprolite, softer than material above, + homogeneous
31.60	31.83		beige white saprolite, harder than material directly above, some beige white layering visible, some shistosity
31.83	32.08		white beige, stms brown saprolite, some shistosity, rather heterogenous
32.08	32.15		hard piece, brownish, with visible shistosity, maybe qtz-rich
32.15	32.25		white beige brown heterogenous saprolite with shistosity

Supplementary material for Chapter VII

Unit Start (m)	Unit End (m)	Sample	Description
32.25	32.35	3235?	hard piece with shistosity
32.35	32.48	3235?	white clay layer, abrupt change to underlying unit
32.48	33.60		reddish violett slightly brownish saprolite, strong shistosity /fine foliation, homogeneous. From 32.80-32.95m more violett
33.60	35.45		red violett homogeneous saprolite, strong shistosity
35.45	36.15		red violett homogeneous saprolite, strong shistosity
36.15	36.40		violett but brighter saprolite, strong shistosity
36.40	36.90		core fractured, reddish violett saprolite with shistosity
36.90	37.05		gray-beige, slightly reddish material with shistosity, swollen ("gonflant")
37.05	37.45		reddish gray saprolite, clay-rich, shistosity, pretty soft
37.45	37.50		reddish to white saprolite with shistosity, pretty soft
37.50	39.35		white homogeneous material, stms slightly greenish, good shistosity
39.35	39.75		white saprolite with shistosity and some clay
39.75	40.50		white gray slightly purple with shistosity, +- hard, rocky
40.50	40.90		soft portion, white with some violett, clay with some darker pieces in between
40.90	41.13		white red-brownish material, some shistosity, harder than material before but still pretty soft
41.13	41.90		white homogeneous saprolite with shistosity
41.90	42.87	4217	white homogeneous saprolite with shistosity, clayrich
42.87	43.20		transition zone from white-beige to violett-red/gray material, all with shistosity
43.20	43.55		red violett saprolite with foliation. red and violett layers, tiny folding visible
43.55	44.25		red-grayish saprolite with good shistosity, clay-rich but rather competent / compact
44.25	45.00		red (red-brown intense) saprolite with shistosity, clay-rich
45.00	45.48		red violett saprolite, clay-rich, good shistosity, compact
45.48	47.40		red violett saprolite, clay-rich, good shistosity, compact, only slight colour variations
47.40	49.45		red violett saprolite with good shistosity. some slight colour variation between bands. Attention: surface colour sthms too red due to fine grained drill material
49.45	51.05	4985	red violett saprolite, clayrich, with shistosity, hardness: knife enters
51.05	51.30		red violett saprolite, clayrich, with shistosity, harder than above
51.30	53.10		red violett saprolite with shistosity (slightly undulated), again harder (not totally hard though), homogeneous, as m before
53.10	55.00		red violett saprolite with shistosity (continuation)
55.00	55.55		red violett saprolite with shistosity, rather hard but still with clays
55.55	56.77		red violett saprolite to shist, harder material than before. At 56.28-56.40m fault (?) crossing, incl. ca. 70°, steeper than shistosity, rock next to it has brittle fractures parallel to it
56.77	57.00		red violett saprolite with shistosity, not too hard
57.00	57.67		red violett to beige saprolite, more heterogeneous, softer, with shistosity and stms folded, stms reaching yellow to blueish colors
57.67	58.05		red violett saprolite with shistosity, harder again
58.05	58.33		red violett beigeish saprolite with shistosity, slightly more massiv
58.33	58.68		red violett saprolite, more reddish, better shistosity, harder
58.68	59.20		red violett (pretty red) saprolite with shistosity. Inclination of shistosity steeper than before, rather soft
59.20	59.28		one hard piece
59.28	61.05	6034	red violett (pretty red) saprolite with shistosity. Inclination of shistosity steeper than before, rather soft
61.05	61.95		red violett saprolite with steep inclination (near 90°), no remarkable variation, rather soft
61.95	62.55		red violett gray (general colour brighter) saprolite, more gray fine material, maybe folded
62.55	63.27		red violett saprolite with shistosity, slightly more reddish again
63.27	64.10		red beige violett saprolite, clayrich, rather soft, strong shistosity
64.10	64.25		harder portion, same colour, less shistosity (still visible though)
64.25	64.40		heterogeneous material with yellow-white veins and some qtz-rich veins
64.40	64.50		red violett saprolite with shistosity, harder (knife nearly does not enter)
64.50	64.55		slightly softer than before, one yellow-ochre layer

Supplementary material for Chapter VII

Unit Start (m)	Unit End (m)	Sample	Description
64.55	65.40		homogeneous weathered rock with shistosity, red brown/violett (slightly darker than overlying), pretty hard (sound when knocking with knife)
65.40	65.55		harder material, red to red brown
65.55	66.10		red violett saprolite with fine layers (mm-sized) of different tonalities visible, from darker purple brown to gray and orange. Good shistosity, rather soft
66.10	67.00		weathered rock (harder, sound when knocking with knife), good shistosity, slight color variations between small bands
67.00	67.40		more massiv saprolite, less shistosity, red gray with some white minerals, rather soft and crumbly
67.40	67.50		violett reddish with white and ochre spots ("tache"), clayrich, soft, rather massiv, little shistosity
67.50	68.10		violett reddish with white and ochre spots ("tache"), clayrich, soft, better shistosity than before
68.10	68.40		harder, well foliated saprolite / weathered rock, dark red violett, no white stuff
68.40	68.73		violett red saprolite with some shistosity (not very strong) with small (<2mm) white and bigger ochre patches
68.73	69.20	6875	saprolite with shistosity, more heterogeneous material, red violett ochre stms white, qtz grains
69.20	69.40		red violett saprolite, clay-rich, good shistosity, few white patches / tiny veins, some ochre veins / patches
69.40	70.10		clayrich saprolite / weathered rock, dominantly red-violett but also white and ochre bands, good shistosity /foliation
70.10	70.50		red violett weathered rock (hard saprolite), color more homogeneous, some ochre on foliation planes, good shistosity
70.50	71.30		hard weathered rock red bordeaux, less violett, ochre on foliation /shistosity planes, generally homogeneous
71.30	73.42		hard weathered rock, often broken, some portions slightly softer, some bright layers. Good shistosity, pretty red, stms ochre bands or ochre on shistosity planes
73.42	74.40		red violett gray saprolite with good foliation, stms white or ochre fine bands, +- hard
74.40	75.00	7462	softer red violett saprolite, less shistosity, fine white minerals, pretty soft (however one harder piece with better shistosity in between)

Table E-2: Results of the Gamma-spectroscopy of the selected bulk samples from both profiles.

Sample	Mass (g)	U dpm/g	abs. error	U ppm	abs. error	Ra dpm/g	abs. error	Rn dpm/g	abs. error	Th dpm/g	abs. error	Th ppm	abs. error	K %	abs. error
KAW18_750	73.15	0.53	0.05	0.71	0.07	0.60	0.11	0.55	0.02	0.57	0.03	2.34	0.11	0.50	0.01
KAW18_1405	79.91	1.04	0.06	1.39	0.08	0.84	0.12	0.75	0.02	0.92	0.03	3.81	0.12	<	0.01
KAW18_3040	82.74	1.19	0.06	1.60	0.08	1.26	0.12	1.11	0.02	0.90	0.03	3.71	0.12	0.02	0.01
KAW18_4217	80.57	2.66	0.09	3.56	0.12	2.38	0.17	2.31	0.03	3.30	0.05	13.61	0.21	<	0.01
KAW18_6034	86.36	2.29	0.06	3.08	0.08	2.53	0.11	2.24	0.02	3.43	0.03	14.15	0.14	<	0.00
KAW18_7462	84.4	1.75	0.07	2.35	0.09	2.20	0.14	2.18	0.03	0.64	0.03	2.63	0.12	0.23	0.01
TUC19_02A	85.79	3.82	0.11	5.12	0.14	4.59	0.19	3.76	0.04	4.93	0.06	20.31	0.25	0.14	0.09
TUC19_02D	94.04	0.67	0.05	0.90	0.06	1.07	0.10	1.11	0.02	0.27	0.02	1.10	0.08	2.66	0.02
TUC19_01E	96.38	3.77	0.10	5.05	0.14	5.30	0.19	4.39	0.04	5.00	0.06	20.60	0.24	<	0.01
TUC19_02G	92.91	8.23	0.14	11.03	0.19	8.37	0.25	8.15	0.05	8.15	0.08	33.59	0.31	0.83	0.02
TUC19_02I(w)	39.66	4.42	0.12	5.92	0.16	6.02	0.26	5.32	0.05	4.68	0.07	19.27	0.30	0.32	0.02
TUC19_02J	109.25	4.98	0.08	6.68	0.10	4.62	0.14	4.50	0.03	5.16	0.04	21.26	0.16	2.44	0.02

dpm = disintegrations per minute

Table E-3: Measured RID amplitudes for dosimetry curves of both samples

Sample	Dose	Dose	Parallel component a.u.	Perpendicular component a.u.	Sample	Dose	Dose	Parallel component a.u.
	(H ⁺ ions/cm ²)	kGy				(H ⁺ ions/cm ²)	kGy	
TUC19_01E	natural	0.0	9.0	44.0	KAW18-10A	natural	0.0	0.67
TUC19_01E	3×10 ¹¹	69.2	10.0	52.4	KAW18-10A	3×10 ¹¹	69.2	0.67
TUC19_01E	6×10 ¹¹	138.5	10.3	51.8	KAW18-10A	6×10 ¹¹	138.5	0.73
TUC19_01E	1×10 ¹²	230.8	10.7	54.9	KAW18-10A	1×10 ¹²	230.8	0.89
TUC19_01E	3×10 ¹²	692.3	12.6	61.9	KAW18-10A	3×10 ¹²	692.4	1.74
TUC19_01E	6×10 ¹²	1385.0	14.8	73.1	KAW18-10A	6×10 ¹²	1385.0	2.33
TUC19_01E	1×10 ¹³	2308.0	18.1	84.5	KAW18-10A	1×10 ¹³	2308.0	2.56
TUC19_02AA	natural	0.0	1.1	5.0	KAW18-750	natural	0.0	0.98
TUC19_02AA	3×10 ¹¹	69.2	2.4	10.6	KAW18-750	3×10 ¹¹	69.2	1.20
TUC19_02AA	6×10 ¹¹	138.5	3.2	11.6	KAW18-750	6×10 ¹¹	138.5	1.16
TUC19_02AA	1×10 ¹²	230.8	2.9	13.0	KAW18-750	1×10 ¹²	230.8	2.05
TUC19_02AA	3×10 ¹²	692.3	4.4	19.3	KAW18-750	3×10 ¹²	692.4	4.09
TUC19_02AA	6×10 ¹²	1385.0	6.5	31.8	KAW18-750	6×10 ¹²	1385.0	6.66
TUC19_02AA	1×10 ¹³	2308.0	6.7	38.7	KAW18-750	1×10 ¹³	2308.0	8.94
TUC19_02BA	natural	0.0	1.1	5.3	KAW18-1405	natural	0.0	2.13
TUC19_02BA	3×10 ¹¹	69.2	2.4	12.5	KAW18-1405	3×10 ¹¹	69.2	3.16
TUC19_02BA	6×10 ¹¹	138.5	2.9	13.7	KAW18-1405	6×10 ¹¹	138.5	4.57
TUC19_02BA	1×10 ¹²	230.8	3.7	16.9	KAW18-1405	1×10 ¹²	230.8	5.00
TUC19_02BA	3×10 ¹²	692.3	5.3	27.3	KAW18-1405	3×10 ¹²	692.4	8.17
TUC19_02BA	6×10 ¹²	1385.0	7.5	39.9	KAW18-1405	6×10 ¹²	1385.0	10.69
TUC19_02BA	1×10 ¹³	2308.0	10.2	51.6	KAW18-1405	1×10 ¹³	2308.0	14.33
TUC19_02C	natural	0.0	2.9	10.5	KAW18-2235	natural	0.0	4.00
TUC19_02C	3×10 ¹¹	69.2	5.6	15.7	KAW18-2235	3×10 ¹¹	69.2	4.57
TUC19_02C	6×10 ¹¹	138.5	6.2	17.7	KAW18-2235	6×10 ¹¹	138.5	5.55
TUC19_02C	1×10 ¹²	230.8	6.9	21.0	KAW18-2235	1×10 ¹²	230.8	6.39
TUC19_02C	3×10 ¹²	692.3	8.8	30.0	KAW18-2235	3×10 ¹²	692.4	9.50
TUC19_02C	6×10 ¹²	1385.0	10.0	43.4	KAW18-2235	6×10 ¹²	1385.0	11.86
TUC19_02C	1×10 ¹³	2308.0	11.6	54.0	KAW18-2235	1×10 ¹³	2308.0	15.34
TUC19_02D	natural	0.0	1.8	10.6	KAW18-3040	natural	0.0	1.19
TUC19_02D	3×10 ¹¹	69.2	2.6	16.6	KAW18-3040	3×10 ¹¹	69.2	1.32
TUC19_02D	6×10 ¹¹	138.5	3.7	20.9	KAW18-3040	6×10 ¹¹	138.5	1.67
TUC19_02D	1×10 ¹²	230.8	4.5	25.6	KAW18-3040	1×10 ¹²	230.8	2.09
TUC19_02D	3×10 ¹²	692.3	7.0	40.8	KAW18-3040	3×10 ¹²	692.4	3.42
TUC19_02D	6×10 ¹²	1385.0	10.2	59.8	KAW18-3040	6×10 ¹²	1385.0	4.95
TUC19_02D	1×10 ¹³	2308.0	12.6	77.1	KAW18-3040	1×10 ¹³	2308.0	6.25
TUC19_02E	natural	0.0	5.6	23.9	KAW18-3235	natural	0.0	2.56
TUC19_02E	3×10 ¹¹	69.2	5.9	26.0	KAW18-3235	3×10 ¹¹	69.2	3.12
TUC19_02E	6×10 ¹¹	138.5	6.6	27.7	KAW18-3235	6×10 ¹¹	138.5	3.81
TUC19_02E	1×10 ¹²	230.8	7.2	30.1	KAW18-3235	1×10 ¹²	230.8	5.06
TUC19_02E	3×10 ¹²	692.3	8.7	36.3	KAW18-3235	3×10 ¹²	692.4	8.47
TUC19_02E	6×10 ¹²	1385.0	10.2	42.7	KAW18-3235	6×10 ¹²	1385.0	10.30
TUC19_02E	1×10 ¹³	2308.0	10.8	51.9	KAW18-3235	1×10 ¹³	2308.0	12.22
TUC19_02F	natural	0.0	8.6	44.0	KAW18-4217	natural	0.0	2.04
TUC19_02F	3×10 ¹¹	69.2	11.6	49.7	KAW18-4217	3×10 ¹¹	69.2	3.06
TUC19_02F	6×10 ¹¹	138.5	10.7	52.5	KAW18-4217	6×10 ¹¹	138.5	3.67
TUC19_02F	1×10 ¹²	230.8	11.9	52.5	KAW18-4217	1×10 ¹²	230.8	4.38
TUC19_02F	3×10 ¹²	692.3	15.8	59.6	KAW18-4217	3×10 ¹²	692.4	5.92
TUC19_02F	6×10 ¹²	1385.0	17.0	74.0	KAW18-4217	6×10 ¹²	1385.0	7.44
TUC19_02F	1×10 ¹³	2308.0	19.7	86.5	KAW18-4217	1×10 ¹³	2308.0	8.50
TUC19_02G	natural	0.0	3.7	13.4	KAW18-4985	natural	0.0	1.39
TUC19_02G	3×10 ¹¹	69.2	4.0	14.5	KAW18-4985	3×10 ¹¹	69.2	1.90
TUC19_02G	6×10 ¹¹	138.5	4.2	16.8	KAW18-4985	6×10 ¹¹	138.5	2.67
TUC19_02G	1×10 ¹²	230.8	4.8	17.7	KAW18-4985	1×10 ¹²	230.8	3.07
TUC19_02G	3×10 ¹²	692.3	6.9	23.2	KAW18-4985	3×10 ¹²	692.4	4.58
TUC19_02G	6×10 ¹²	1385.0	8.3	31.5	KAW18-4985	6×10 ¹²	1385.0	5.93
TUC19_02G	1×10 ¹³	2308.0	8.7	41.5	KAW18-4985	1×10 ¹³	2308.0	7.67
TUC19_02H	natural	0.0	2.9	11.3	KAW18-6034	natural	0.0	1.38
TUC19_02H	3×10 ¹¹	69.2	4.0	13.0	KAW18-6034	3×10 ¹¹	69.2	1.43
TUC19_02H	6×10 ¹¹	138.5	5.1	14.4	KAW18-6034	6×10 ¹¹	138.5	1.78
TUC19_02H	1×10 ¹²	230.8	5.0	16.4	KAW18-6034	1×10 ¹²	230.8	2.34
TUC19_02H	3×10 ¹²	692.3	6.4	21.2	KAW18-6034	3×10 ¹²	692.4	3.75
TUC19_02H	6×10 ¹²	1385.0	7.7	30.2	KAW18-6034	6×10 ¹²	1385.0	6.23
TUC19_02H	1×10 ¹³	2308.0	9.1	37.2	KAW18-6034	1×10 ¹³	2308.0	7.67
TUC19_02Iw	natural	0.0	3.2	12.9	KAW18-6875	natural	0.0	1.22
TUC19_02Iw	3×10 ¹¹	69.2	4.2	16.0	KAW18-6875	3×10 ¹¹	69.2	1.64
TUC19_02Iw	6×10 ¹¹	138.5	4.7	19.0	KAW18-6875	6×10 ¹¹	138.5	2.80
TUC19_02Iw	1×10 ¹²	230.8	5.6	22.3	KAW18-6875	1×10 ¹²	230.8	3.28
TUC19_02Iw	3×10 ¹²	692.3	8.1	32.8	KAW18-6875	3×10 ¹²	692.4	5.25
TUC19_02Iw	6×10 ¹²	1385.0	10.6	51.3	KAW18-6875	6×10 ¹²	1385.0	6.33
TUC19_02Iw	1×10 ¹³	2308.0	12.4	64.4	KAW18-6875	1×10 ¹³	2308.0	8.05
TUC19_02J	natural	0.0	1.1	6.9	KAW18-7462	natural	0.0	1.75
TUC19_02J	3×10 ¹¹	69.2	1.4	7.8	KAW18-7462	3×10 ¹¹	69.2	2.72
TUC19_02J	6×10 ¹¹	138.5	1.5	8.5	KAW18-7462	6×10 ¹¹	138.5	3.21
TUC19_02J	1×10 ¹²	230.8	1.3	9.2	KAW18-7462	1×10 ¹²	230.8	3.60
TUC19_02J	3×10 ¹²	692.3	2.3	14.9	KAW18-7462	3×10 ¹²	692.4	5.64
TUC19_02J	6×10 ¹²	1385.0	3.1	18.1	KAW18-7462	6×10 ¹²	1385.0	6.90
TUC19_02J	1×10 ¹³	2308.0	4.0	24.1	KAW18-7462	1×10 ¹³	2308.0	7.77

Supplementary material for Chapter VII

Table E-4: Regression parameters of the dosimetry curves of both sites. Note that for the Tucano samples only the perpendicular RID amplitudes were used for paleodose calculation. The results for the parallel components are given for comparison but were not used. Note that for Kaw two different slightly codes were used for regression which explains the sometimes large, negative residues.

Sample	RID Component used	Formula	Regression Parameter				Residue
			Cs	m2	Paleodose	Fl	
TUC19_1E	perpendicular	exp+lin	49.8	0.0082	213	0.0140	0.0052
TUC19_1E	parallel	exp+lin	9.3	0.0077	270	0.0034	0.0018
TUC19_2AA	perpendicular	exp+lin	9.7	0.0463	15	0.0136	0.2007
TUC19_2BA	perpendicular	exp+lin	12.1	0.0215	24	0.0185	0.2607
TUC19_2BA	parallel	exp+lin	3.0	0.0093	43	0.0031	0.0508
TUC19_2C	perpendicular	exp+lin	17.7	0.0071	101	0.0158	0.0864
TUC19_2D	perpendicular	exp+lin	24.3	0.0043	98	0.0225	0.0299
TUC19_2D	parallel	exp+lin			104		0.1209
TUC19_2E	perpendicular	exp+lin	26.7	0.0043	342	0.0094	0.0028
TUC19_2F	perpendicular	exp+lin	48.2	0.0319	69	0.0165	0.0218
TUC19_2G	perpendicular	exp+lin	12.7	0.0064	264	0.0112	0.0303
TUC19_2H	perpendicular	exp+lin	12.6	0.0051	238	0.0100	0.0521
TUC19_2H	perpendicular	exp	50.5	0.0005	574		0.0452
TUC19_2lw	perpendicular	exp+lin	17.6	0.0033	212	0.0192	0.0866
TUC19_2lw	perpendicular	exp	88.5	0.0005	335		0.0557
TUC19_2lw	parallel	exp+lin			196		0.0493
TUC19_2lw	parallel	exp			269		0.0513
TUC19_2J	perpendicular	exp+lin	12.0	0.0012	437	0.0045	0.1144
TUC19_2J	perpendicular	exp	31.9	0.0005	509		0.0550
KAW18-10A	parallel	exp	2.8	0.0010	206		-0.9870
KAW18-750	parallel	exp	14.2	0.0004	138		-0.9969
KAW18-1405	parallel	exp+lin	5.2	0.0045	91	0.0038	-0.9982
KAW18-2235	parallel	exp+lin	7.1	0.0024	243	0.0032	0.0439
KAW18-3040	parallel	exp	8.1	0.0006	266		0.0360
KAW18-3235	parallel	exp	12.9	0.0011	189		0.0628
KAW18-4217	parallel	exp+lin	5.0	0.0047	104	0.0016	0.0312
KAW18-4985	parallel	exp+lin	3.3	0.0040	109	0.0018	0.0943
KAW18-6034	parallel	exp	10.9	0.0005	243		-0.9952
KAW18-6875	parallel	exp+lin	4.1	0.0039	70	0.0016	-0.9954
KAW18-7462	parallel	exp+lin	5.1	0.0031	126	0.0011	0.1357

Résumé étendu en langue française

Introduction

Les latérites sont d'épais profils d'altération, de la dizaine à centaine de mètres d'épaisseur qui se développent dans les conditions climatiques tropicales et subtropicales que l'on rencontre couramment sur la surface continentale de la Terre. Elles se forment à l'interface entre la géosphère, l'hydrosphère, la biosphère et l'atmosphère et leurs caractéristiques dépendent des propriétés de ces quatre sphères et d'une cinquième, le temps. Les latérites (désignées ici comme l'ensemble du profil d'altération, y compris la saprolite, la cuirasse ferrugineuse et le sol) représentent l'altération d'une roche aux conditions (sub)tropicales de la surface terrestre et sont principalement composées de minéraux secondaires, appelés supergènes, qui se forment au cours de l'altération, tels que les argiles et plus particulièrement la kaolinite, les (oxyhydr)oxydes de fer (i.e. hématite et goethite) et les (oxy)hydroxydes d'aluminium, minéraux qui sont très stables dans un tel contexte climatique (Tardy, 1997). La transformation des minéraux silicatés primaires en minéraux secondaires supergènes comprend la libération et la lixiviation des éléments alcalins et alcalino-terreux (Na, K, Ca, Mg) et la transformation du CO₂ en acide carbonique dissous influençant le bilan géochimique et atmosphérique global (Berner et al., 1983; Nahon, 1991; Lasaga et al., 1994). L'altération tropicale intense conduit à l'accumulation résiduelle d'éléments immobiles tels que Fe et Al mais aussi d'éléments traces comme Ni, Au, Nb, Sc ou les terres rares (REE) pour lesquels les latérites sont des ressources économiquement importantes (Patterson et al., 1994; Butt et Cluzel, 2013; Butt, 2016; Giovannini et al., 2017; Chassé et al., 2019). La composition géochimique et minéralogique d'une latérite est fortement influencée par les conditions climatiques dans lesquelles elle se forme, alors que la composition du matériau parent joue un rôle secondaire (Bardossy et Aleva, 1990; Schellmann, 1994; Tardy, 1997). Le climat tropical de mousson, contrasté selon les saisons, favorise la formation de latérites ferrugineuses, "classiques", dominées par la kaolinite, l'hématite, la goethite (et le quartz, selon le protolithe) (Tardy et Roquin, 1998). Un climat tropical très humide lié à des conditions très bien drainées peut conduire au développement de bauxites latéritiques, des latérites enrichies en Al dans lesquelles la kaolinite n'est plus stable et qui sont caractérisées par une désilication et une accumulation d'Al sous forme d'(oxy)hydroxydes d'Al (Valeton, 1972; Bardossy et Aleva, 1990; Carvalho et al., 1997; Valeton, 1999). En raison de leur stabilité à long terme dans toute la zone intertropicale, qui couvre environ 44% de la surface continentale de la Terre, les latérites sont

des archives des climats passés (Tardy et Roquin, 1998). Il a été proposé que les latérites se sont formées épisodiquement tout au long de l'histoire de la Terre dans des périodes au climat très favorable, mais on sait peu de choses sur la durée, la fréquence et l'étendue spatiale de ces événements d'altération (Prasad, 1983; Vasconcelos et al., 1994; Tardy et Roquin, 1998; Retallack, 2010; Vasconcelos et al., 2015). Plusieurs études ont montré que les latérites peuvent être très anciennes, notamment dans les zones de quiescence tectonique, mais il existe encore peu d'informations concernant leur évolution temporelle et leur réponse aux changements climatiques et géodynamiques (Vasconcelos et al., 1994; Beauvais et al., 2008; Monteiro et al., 2014; Allard et al., 2018; Mathian et al., 2019). Comme différents signaux climatiques sont potentiellement superposés dans des latérites anciennes et constamment exposées aux conditions climatiques, le démêlage des informations paléoclimatiques préservées dans ces archives est une tâche complexe (Beauvais, 1999; Vasconcelos, 1999; Girard et al., 2000; Balan et al., 2005; Monteiro et al., 2014; Mathian et al., 2019).

Alors que les processus contrôlant la géochimie des éléments majeurs sont connus (voir par exemple l'altération des silicates primaires ; Nahon, 1991), un défi majeur dans l'étude des latérites est de résoudre le manque de contraintes temporelles. On sait déjà que plusieurs générations d'un même minéral secondaire peuvent coexister dans un profil, mais comme elles sont principalement composées de minéraux argileux, d'(oxyhydr)oxydes de fer et d'(oxy)hydroxydes d'aluminium, la plupart des méthodes géochronologiques classiques ne peuvent pas être appliquées aux latérites. Les datations K/Ar et $^{39}\text{Ar}/^{40}\text{Ar}$ ont été appliquées avec succès aux oxydes de Mn supergènes provenant des cuirasses latéritiques (Vasconcelos et al., 1994; Ruffet et al., 1996; Beauvais et al., 2008; Beauvais et Chardon, 2013; Beauvais et al., 2016; Bonnet et al., 2016; Vasconcelos et Carmo, 2018) et ont fourni un premier cadre temporel pour des périodes d'altération distinctes au Brésil, en Afrique et en Inde. Cependant, les datations K/Ar et $^{39}\text{Ar}/^{40}\text{Ar}$ nécessitent la présence de phases porteuses de potassium telles que les oxydes de Mn qui sont relativement rares dans les latérites par rapport aux oxydes de fer sensu lato, aux (oxy)hydroxydes d'aluminium et à la kaolinite. En ciblant les principaux composants de la latérite, il est possible d'obtenir une compréhension plus complète et plus approfondie de leur formation et de leur évolution. Le paléomagnétisme a été appliqué avec succès aux parties ferrugineuses de certains profils latéritiques mais cette méthode devient très imprécise si le décalage latitudinal était faible dans l'intervalle de temps d'intérêt, comme, par exemple, pour le craton amazonien au cours de la période cénozoïque (Schmidt et

Embleton, 1976; Schmidt et al., 1983; Kumar, 1986; Théveniaut et Freyssinet, 1999; Théveniaut et Freyssinet, 2002).

L'hématite et la goethite sont les principaux constituants de la cuirasse ferrugineuse présente dans la plupart des profils latéritiques (Bardossy et Aleva, 1990; Tardy, 1997). Ces minéraux peuvent être datés par la méthode (U-Th)/He car ils retiennent quantitativement l'He dans leurs structures cristallines (Lippolt et al., 1993 ; Shuster et al., 2005; Heim et al., 2006; Vasconcelos et al., 2013; Reiners et al., 2014; Balout et al., 2017; Deng et al., 2017; Hofmann et al., 2017; Farley, 2018). Cette méthode a été utilisée avec succès par un nombre croissant d'études au cours des trois dernières décennies pour contraindre les âges des (oxyhydr)oxydes de fer supergènes, mais certains aspects essentiels de la méthode, tels que les paramètres de diffusion de l'He dans la goethite, restent mal compris (Lippolt et al, 1998; Pidgeon et al., 2004; Monteiro et al., 2014; Riffel et al., 2016; Allard et al., 2018; Monteiro et al., 2018; Wells et al., 2019; dos Santos Albuquerque et al., 2020).

La kaolinite est présente dans la (quasi) totalité de la plupart des profils latéritiques, y compris les cuirasses ferrugineuses dans certains cas, et est le constituant majeur de la saprolite qui compose généralement la partie la plus épaisse du profil latéritique. Contrairement aux oxydes de Mn et aux oxydes de Fe, les kaolinites ne révèlent pas de générations à l'échelle des assemblages minéraux mais sont représentatifs de l'ensemble du profil à l'échelle macroscopique. Les kaolinites naturelles contiennent des défauts ponctuels créés par le rayonnement radioactif ambiant, défauts qui sont stables sur des échelles de temps géologiques et peuvent être détectés par spectroscopie de résonance paramagnétique électronique (RPE) (Clozel et al., 1994; Allard et al., 2012). Balan et al. (2005) ont été les premiers à utiliser ces défauts pour dater la formation de kaolinite avec une méthodologie complète, et depuis, cette approche a été appliquée pour dater des kaolinites provenant de latérites et de sols latéritiques (Allard et al., 2018; Mathian et al., 2019; Allard et al., 2020; Mathian et al., 2020).

Le bouclier guyanais, c'est-à-dire la partie nord du craton amazonien, présente un intérêt particulier pour l'étude des latérites et des bauxites car il est tectoniquement stable et se trouve à des latitudes tropicales depuis le Crétacé, favorisant le développement de profils latéritiques profonds. Les modèles géomorphologiques proposent que sa surface a été façonnée par une série d'événements de pénéplanation qui ont alterné avec des phases dominées par l'altération, conduisant à un paysage en escalier (Choubert, 1957; King, 1962;

McConnell, 1968; Blancaneaux, 1981; Aleva, 1984). Les données géochronologiques des oxydes supergènes de Mn et de Fe du bouclier brésilien, partie sud du craton amazonien, indiquent une altération épisodique tout au long du Cénozoïque (Vasconcelos et al., 1994; Ruffet et al., 1996; Monteiro et al., 2018). Pour le bouclier guyanais, seules quelques contraintes d'âge d'altération très imprécises existent, indiquant un enregistrement de l'altération depuis le Cénozoïque inférieur à moyen (Hammen et Wymstra, 1964; Wymstra, 1971; Théveniaut et Freyssinet, 1999; Théveniaut et Freyssinet, 2002). En raison de la rareté des carbonates et des sédiments lacustres, il existe peu des contraintes paléoclimatiques pour l'Amazonie, ce qui complique la compréhension de l'évolution de cette région qui abrite la plus grande biodiversité du monde (par exemple Hoorn et al., 2010). L'étude des latérites et bauxites du bouclier guyanais a donc le potentiel de fournir des informations importantes sur l'histoire géologique et paléoclimatique de cette région et d'en savoir plus sur la formation et l'évolution des anciens profils latéritiques et bauxitiques.

Les principaux objectifs de cette thèse sont :

- i) améliorer la compréhension de la formation et de l'évolution des latérites en plaçant les processus minéralogiques et géochimiques dans un cadre temporel,
- ii) trouver une méthode pour démêler les signaux climatiques cachés dans les latérites et les cuirasses latéritiques et
- iii) permettre une nouvelle compréhension de l'évolution climatique et géomorphologique du bouclier guyanais.

Afin de contribuer à ces objectifs, deux zones d'étude ont été sélectionnées : a) le bord nord-est du bouclier guyanais en Guyane française où plusieurs profils latéritiques-bauxitiques se sont prétendument développés depuis l'Éocène et le Miocène (Choubert, 1957 ; Théveniaut et Freyssinet, 2002) et où le climat actuel est extrêmement humide avec plus de 4000 mm de précipitations / an (Groussin, 2001) et b) la bordure orientale du bouclier guyanais dans l'état brésilien de l'Amapá, où des profils latéritiques ferrugineux se sont développés possiblement depuis le Crétacé supérieur (Bardossy et Aleva, 1990) et où le climat actuel est plus contrasté saisonnièrement avec environ 2300 mm de précipitations / an. Les deux profils étudiés plus en détail, la montagne de Kaw en Guyane française et la mine de Tucano au Brésil, présentent des similitudes importantes telles que leurs roches parentales, leur altitude et l'épaisseur de leurs profils (>70 m), mais différent par leur cadre géomorphologique, leur proximité de la mer et la quantité actuelle des précipitations.

Cette thèse contient cinq chapitres majeurs (III-VII) et trois chapitres plus petits (I, II et VIII). Le chapitre II reprend les approches minéralogiques analytiques (microscopie électronique à balayage et diffraction des rayons X avec affinement Rietveld), géochimiques et géochronologiques ((U-Th)/He et RPE) utilisées dans cette étude et explique certaines subtilités dans le contexte de ce travail. Le chapitre III présente une étude théorique interdisciplinaire qui examine les contrôles de la diffusion de l'He dans la goethite en comparant les données expérimentales de diffusion de ^3He et ^4He publiées et réévaluées avec les calculs théoriques ab-initio. Le chapitre IV présente une étude détaillée de la cuirasse latéritique-bauxitique de la montagne de Kaw en Guyane française. Je montre comment les conditions d'altération et les signaux climatiques peuvent être extraits d'un ensemble de données vaste et complexe en couplant les données géochronologiques, minéralogiques et géochimiques. Dans le chapitre V, cette approche est appliquée aux cuirasses ferrugineuses de la deuxième zone cible, la mine de Tucano dans l'Amapá, au Brésil. Les résultats montrent des caractéristiques très contrastées par rapport à ceux de la montagne de Kaw en Guyane française et permettent d'approfondir la compréhension des processus à petite échelle qui se produisent lors d'événements d'altération discrets. Dans le chapitre VI, je présente une étude des cuirasses latéritiques de trois autres sites dans le nord-est de la Guyane française, donnant un aperçu de l'évolution de ces sites et permettant des conclusions importantes sur l'évolution climatique et géomorphologique régionale.

Deux profils latéritiques profonds (> 70 m) de la montagne de Kaw et de la mine de Tucano sont étudiés dans le chapitre VII. J'examine les données RPE des kaolinites provenant de différents niveaux de ces profils, ainsi que la géochimie globale. Le chapitre VIII résume les résultats finaux de cette thèse et présente les perspectives pour les études futures.

Les sections suivantes résument les différents chapitres majeurs en bref.

Résumé du Chapitre III : Révélation de l'impact des dommages radiogéniques et de la teneur en Al sur la diffusion de l'He dans la goethite

Depuis plusieurs dizaines d'années, la méthode géochronologique (U-Th)/He sur la goethite est de plus en plus appliquée pour dater la formation et l'évolution des latérites ou la formation des dépôts miniers. Cependant, des questions subsistent sur la perte possible d'He par diffusion en raison de la structure polycristalline de la goethite et la sous-estimation associée de l'âge (U-Th)/He. La perte d'hélium a été estimée entre 2 et 30%, mais aucune

relation ou modèle n'a été produit pour expliquer de telles valeurs. Pour clarifier la situation, nous avons d'abord effectué une revue complète des données expérimentales de diffusion de l'He dans la goethite naturelle, qui révèle le lien entre l'énergie d'activation et la perte d'He avec la dose de dommage. Pour comprendre le comportement de diffusion de l'He dans la goethite et modéliser la perte d'He, les défauts naturels et les dommages alpha ainsi que l'effet de la composition chimique et de la structure de croissance sur la diffusion de l'He ont été étudiés grâce à une étude multi-échelle. Nous avons utilisé des simulations numériques combinant la théorie de la fonction de densité à l'échelle atomique et des simulations cinétiques de Monte Carlo à l'échelle macroscopique. Nous avons trouvé que la diffusion de l'He est purement anisotrope le long de l'axe préférentiel allongé (i.e. l'axe b) et que l'He fuit facilement dans la goethite et l'Al-goethite sans défaut. La conséquence de cette anisotropie est que les défauts cristallographiques et les dommages alpha diminuent fortement la diffusivité de l'He dans la goethite et l'Al-goethite en obstruant le canal de diffusion ou en piégeant l'He le long de l'axe b. L'impact des défauts et des dommages sur la diffusion de l'He est encore plus important pour la goethite riche en Al. Les paramètres de diffusion de l'He obtenus pour la goethite contenant des défauts et des dommages sont similaires à l'énergie d'activation et à la perte de diffusion de l'He obtenues dans la goethite naturelle dans la littérature. Ceci permet de démontrer la dépendance systématique du coefficient de diffusion avec la dose de dommage et l'impact de l'Al sur la rétention de He. Les atomes de He ne sont retenus qu'à la faveur d'obstructions bloquant la diffusion et de lacunes les piégeant dans la structure de la goethite. La conséquence de ce comportement diffusif est qu'une partie de l'He diffuse hors du cristal jusqu'à ce qu'une quantité suffisante de dommages soit accumulée le long de l'axe b. La taille du domaine de diffusion est la longueur du canal le long de l'axe b plutôt que la taille totale de la cristallite. Pour corriger la perte de He, cette étude propose une estimation de la rétention de He et des corrections nécessaires pour différents types de goethite avec une correction de la perte d'He allant de $15\pm 10\%$ à $5\pm 5\%$ pour la goethite contenant peu d'Al en fonction de la dose de dommage, et $5\pm 5\%$ pour la goethite contenant une grande quantité d'Al.

Résumé du Chapitre IV : Lire les signaux climatiques cachés dans la bauxite

La dynamique de l'altération tropicale au cours du temps avec la formation et l'évolution à long terme des latérites associée aux forçages climatiques et géodynamiques est

encore une question peu explorée. Pour mieux y accéder, nous nous sommes concentrés sur des cuirasses latéritiques-bauxitiques provenant de la montagne de Kaw, bien explorée et haute de 300 m, dans le nord-est de la Guyane française. Des sous-échantillons composés (oxyhydr)oxydes de fer et macroscopiquement homogènes ont été séparés de 10 blocs d'échantillons. Les échantillons et les sous-échantillons ont été étudiés par des analyses minéralogiques (microscopie électronique à balayage et (micro-)diffraction des rayons X avec affinement Rietveld) et géochimiques et par la géochronologie (U-Th)/He. Les échantillons montrent une grande hétérogénéité à l'échelle macro et microscopique, reflétant les différentes étapes de la formation et de l'évolution des cuirasses par des processus de dissolution et de (re)précipitation des (oxyhydr)oxydes de Fe. Les 284 âges (U-Th)/He obtenus sur goethite, α -(Fe, Al)OOH, et l'hématite, α -Fe₂O₃, vont de 30.5 ± 3.1 à <0.8 Ma et montrent une grande variabilité au sein d'un échantillon. Les sous-échantillons les plus anciens d'hématite et de goethite pauvre en Al ont précipité depuis 30 Ma et se sont formés alors que la kaolinite était stable. La précipitation des minéraux de fer a augmenté depuis 14-12 Ma mais s'est toujours produite dans des conditions ferrugineuses latéritiques et non bauxitiques. L'accélération des cycles de dissolution et (re)précipitation des minéraux de Fe, la substitution d'Al dans la goethite, et l'enrichissement global en Th, ainsi que la précipitation de gibbsite indiquent une intensification de l'altération et une évolution vers des conditions bauxitiques depuis la fin du Miocène. Les minéraux de fer riches en Th et en U formés pendant cette phase tardive d'altération intense se sont mélangés aux minéraux de fer préexistants, ce qui a entraîné une forte dispersion des âges (U-Th)/He. Nous proposons que cet épisode d'altération intensifiée, qui a atteint son apogée à environ 6-2 Ma, correspond à la bauxitisation de la couverture latéritique de la montagne de Kaw.

Le modèle que nous proposons, avec une latéritisation depuis au moins 30 Ma et une bauxitisation depuis la fin du Miocène, fournit de nouvelles contraintes sur l'échelle de temps et l'intensité de l'altération de la montagne de Kaw. Le début de la latéritisation en Guyane française (région de Kaw) est potentiellement plus ancien que 30 Ma environ et la comparaison avec les bauxites voisines indique que le début de l'altération à Kaw pourrait être synchrone avec la formation des bauxites côtières du Suriname et de la Guyane. L'intensité différente de l'altération paléogène qui a produit des bauxites sur les roches sédimentaires du Suriname et de la Guyane et une couverture latéritique ferrugineuse sur les roches du socle de Kaw pourrait être due aux différentes capacités de drainage du matériau parental.

L'événement de bauxitisation du Néogène supérieur que nous observons dans nos données n'a pas encore été décrit dans la région. La bauxitisation à Kaw pourrait avoir été causée soit par un changement régional ou global des précipitations, soit par un soulèvement en flexion dû à la charge sédimentaire dans l'éventail amazonien, entraînant une incision accrue et donc un drainage plus important, soit par une combinaison de ces processus avec un soulèvement entraînant des changements dans le schéma local des précipitations.

Enfin, nous confirmons qu'une combinaison détaillée de résultats géochronologiques couplés à des analyses minéralogiques et géochimiques améliore notre compréhension des processus d'altération tropicaux et de la formation des cuirasses en plaçant les processus minéralogiques et géochimiques dans un cadre temporel.

Résumé du Chapitre V : Chronologie de la précipitation de l'hématite et de la goethite dans des cuirasses latéritiques du Brésil équatorial

Nous présentons un nouvel ensemble de données géochronologiques, minéralogiques et géochimiques couplées (U-Th)/He d'hématite et de goethite supergènes provenant d'un profil latéritique développé sur des schistes et des formations ferrifères rubanées (BIFs) paléoprotérozoïques dans la région de Serra do Navio, Amapá, Brésil. Les âges (U-Th)/He présentent des âges généralement reproductibles pour chaque sous-échantillon, l'âge des hématites allant de 69.4 ± 3.5 à 16.0 ± 0.8 Ma et celui des goethites de 40.2 ± 2.8 à 8.7 ± 0.9 Ma. Ces résultats montrent que l'altération dans la zone orientale du bouclier guyanais a commencé probablement au Crétacé supérieur ou au Paléogène inférieur, ce qui indique que cette zone correspond peut-être à la surface dite "Gondwana" proposée dans la littérature. Fondamentalement, tous les âges anciens se produisent dans une couche de canga formée au-dessus des BIF, tandis que les échantillons de cuirasse ferrugineuse développés au sommet des schistes n'enregistrent l'altération que depuis le Paléogène supérieur. Cela pourrait éventuellement indiquer que la production d'une cuirasse latéritique est plus facile et plus rapide au sommet des BIFs qui sont par définition riches en fer qu'au sommet des schistes. L'ensemble de données se distingue par sa remarquable reproductibilité de l'âge qui permet de distinguer deux événements d'altération à 30 Ma et 12 Ma qui ont probablement duré environ 6 Ma chacun et correspondent à la précipitation de grandes quantités d'hématite à 30 Ma et de goethite à 12 Ma. Les analyses Rietveld des sous-échantillons datés permettent de comprendre l'évolution minéralogique de la cuirasse et montrent que pendant les deux

événements d'altération, la taille des cristallites d'hématite et de goethite augmente vers des âges plus jeunes. Quatre sous-échantillons de goethite bien définis montrent que sur un court intervalle de temps, la goethite devient de plus en plus riche en Al, U, Th et Sm et se mélange de plus en plus avec la kaolinite. Les événements d'altération enregistrés ici apparaissent également dans d'autres ensembles de données d'âge d'altération du nord de l'Amérique du Sud et représentent probablement des phases de climat tropical contrasté relativement chaud et/ou sec à 30 Ma et un climat tropical contrasté comparativement plus frais et/ou plus humide à 12 Ma. Entre ces deux événements et depuis 8 Ma, les précipitations de minéraux de Fe semblent avoir cessé. Ceci pourrait être dû soit à des changements climatiques vers des conditions climatiques moins favorables au maintien actif du système de cuirasse, soit être lié à une baisse significative de la nappe phréatique, liée à un soulèvement continental ou à une baisse du niveau de la mer et évoquant l'érosion au lieu de la formation de cuirasse. L'altération généralisée observée dans la région au cours du Néogène tardif ou même plus tard suggère qu'une baisse de la nappe phréatique est une explication plus probable.

Résumé du Chapitre VI : Évolution des latérites et bauxites de Guyane française à travers le temps et l'espace

Cette étude examine les caractéristiques minéralogiques et l'âge de trois systèmes des cuirasses latéritiques ferrugineux à bauxitiques de la région de Cayenne en Guyane française (Mont Baduel, Vidal et île du Petit Connétable). En combinant ces données avec celles publiées en Guyane française et au Suriname, nous examinons l'extension spatiale des événements d'altération sur la bordure nord-est du bouclier guyanais. Neuf échantillons de cuirasses ferrugineuses et saprolite ont été analysés minéralogiquement et géochimiquement, et des sous-échantillons macroscopiquement homogènes ont été séparés de six cuirasses d'entre eux. 120 âges (U-Th)/He ont été obtenus sur des fragments d'hématite et de goethite microscopiquement purs de ces sous-échantillons. Pour les sous-échantillons du Mont Baduel, des analyses minéralogiques ont été réalisées afin de mieux caractériser le matériel daté et ses conditions de formation.

Les analyses des roches totales révèlent que dans le profil latéritique-bauxitique du Mont Baduel coexistent des cuirasses bauxitiques et ferrugineux, comme l'indiquent les teneurs contrastées en gibbsite et kaolinite et la forte variation de la substitution en Al de la

goethite. Les échantillons de Connétable montrent une signature bauxitique claire, alors que les échantillons du Vidal ont une signature plus ferrugineuse.

Les données du Mont Baduel permettent de contraindre l'évolution de sa couverture latéritique, qui enregistre une altération depuis au moins le Miocène moyen et une bauxitisation secondaire pendant le Néogène supérieur. Les résultats géochronologiques de Vidal et Connétable indiquent une altération depuis l'Oligocène, peut-être même depuis l'Éocène supérieur. Ceci montre que ces couvertures d'altération sont donc beaucoup plus anciennes que ce qui avait été proposé par certains auteurs. Les données des trois sites étudiés (Mont Baduel, Vidal et Connétable) enregistrent une histoire d'altération similaire lorsqu'on les compare à la couverture latéritique de la montagne de Kaw en Guyane française (Heller et al. 2022) et de la montagne de Brownsberg au Suriname (Ansart, 2022). Les résultats indiquent que l'altération à l'Oligocène était répandue dans la région et s'est produite sur des surfaces qui ont aujourd'hui des élévations différentes. De plus, ils montrent que la bauxitisation néogène montrée pour Kaw par Heller et al. (2022) était un phénomène régional et probablement généré par un forçage climatique. Les données impliquent qu'un modèle géomorphologique trop simplifié, repris sous la forme "les élévations plus élevées correspondent aux surfaces de pénéplaine plus anciennes", n'est pas valable dans la région, mais qu'une monocline côtière conduisant à la convergence et au basculement éventuel des surfaces près de la côte pourrait expliquer la configuration observée.

Résumé du Chapitre VII : Étude spectroscopique RPE des kaolinites de deux profils latéritiques du bouclier nord-est et est guyanais (montagne de Kaw, Guyane française et mine de Tucano, Amapá, Brésil)

Nous présentons les données de résonance paramagnétique électronique (RPE) de 28 fractions de kaolinite purifiée provenant de deux profils latéritiques développés au sommet des schistes paléoprotérozoïques du bouclier guyanais. Les profils correspondent à une carotte de 75 m de la couverture bauxitique-latéritique de la montagne de Kaw en Guyane française, où les traces d'altération tropicale remontent au moins à l'Oligocène, et à un profil de 120 m de profondeur, échantillonné dans la mine d'or de Tucano au nord du Brésil, où des cuirasses ferrugineuses témoignent d'une altération depuis le Crétacé supérieur ou le Paléogène inférieur. Les échantillons des deux profils ont été caractérisés à l'aide de techniques minéralogiques et géochimiques standards et la kaolinite a été purifiée pour 16 et 12

échantillons de Kaw et Tucano, respectivement. L'indice de Gaite, qui exprime un degré de désordre cristallin, est mesuré à partir du signal RPE du Fe^{3+} structural. Il est compris entre 4 et 24, c'est-à-dire proche de la plage maximale connue pour les kaolinites naturelles.

L'étude du désordre cristallin des kaolinites de la carotte de 75 m de Kaw indique que des minéraux argileux bien ordonnés se sont formés dans des conditions quasi identiques, probablement cinétiques, dans tout le profil, à l'exception du sol où ils sont moins ordonnés. Les concentrations structurales de Fe^{3+} dans ces kaolinites sont déconnectées des compositions de Fe_2O_3 sur roche totale mais montrent une relation avec l'indice de latéritisation et la concentration de SiO_2 des roches totales. Les kaolinites provenant du profil de la mine Tucano indiquent des conditions de formation plus variables et sont très bien ordonnées dans l'ensemble de la saprolite et désordonnées dans la cuirasse au sommet du profil. Les défauts induits par le rayonnement (RID) sont présents dans presque tous les échantillons mais sont souvent recouverts par un fort signal vanadyle à Kaw. Alors que le fitting automatisé des spectres calculés n'a pas donné de résultats satisfaisants et nécessitait des efforts supplémentaires, la correction des spectres par soustraction manuelle d'un signal de référence vanadyle a permis d'extraire les signaux RID. Les courbes de dosimétrie obtenues par irradiation artificielle de 22 échantillons sélectionnés donnent des paléodoses allant d'environ 15 à 575 kGy et montrent que tous les échantillons, même ceux ayant un degré d'ordonnement structural très similaire, ont des paramètres dosimétriques différents. Les débits de dose ont été calculés à partir des concentrations de radioéléments et ont été utilisés pour le calcul des âges préliminaires (sans les corrections habituelles comme par exemple, cartographie microscopique U, teneur moyenne en eau, impact du quartz) des kaolinites. Les âges préliminaires calculés pour 3 scénarii encadrant les principales incertitudes permettent d'avoir un premier aperçu de l'évolution des deux profils. A Kaw, les kaolinites les plus anciennes se trouvent dans la saprolite supérieure (< 35 m de profondeur) et elles sont peut-être plus anciennes que les oxydes de fer les plus anciens conservés dans la cuirasse de Fe du sommet du profil, qui sont d'âge oligocène. Dans la mine de Tucano, les kaolinites les plus anciennes, dont l'âge varie de plusieurs millions à plusieurs dizaines de millions d'années, sont conservées dans les parties les plus profondes du profil. Le matériau meuble du haut du profil a subi un rajeunissement très récent, qui est postérieur aux plus jeunes âges de l'hématite et de la goethite (U-Th)/He, mais les kaolinites capturées dans la cuirasse ont apparemment été protégées de ce processus et donnent des âges plus anciens. Une étude plus approfondie de la

distribution des radioéléments sera nécessaire afin de réduire les incertitudes des débits de dose et d'obtenir des âges significatifs.

Conclusions

L'intégration des résultats de cette thèse permet de tirer un certain nombre de conclusions concernant les techniques appliquées et l'évolution des profils et des zones étudiés. Cette section vise à résumer les principaux résultats et se concentrera d'abord sur les aspects méthodologiques et ensuite sur les aspects régionaux.

Cette étude a révélé des âges reproductibles inattendus dans des matériaux qui avaient été précédemment rejetés pour la méthode de datation (U-Th)/He. En effet, les résultats reproductibles des âges (U-Th)/He ne sont pas courants dans le domaine de la géochronologie sur hématite et goethite. Dans le contexte supergène, où différentes phases et générations d'(oxyhydr)oxydes de Fe se mélangent au cours de multiples cycles de dissolution et de (re)précipitation, le mélange des phases peut être une source majeure de dispersion des âges et affecter fortement leur reproductibilité. L'impact du mélange des phases sur les âges obtenus dépend des âges et des concentrations en actinides des phases extrêmes. La détermination des âges maximum et minimum des (sous-)échantillons individuels peut aider à extraire des informations géologiques significatives à partir d'ensembles de données d'âges mélangés. Comme les conditions d'altération contrôlent la (re)dissolution et la (re)précipitation des phases existantes, l'histoire de l'altération d'un profil a un fort impact sur la distribution et la reproductibilité des âges. Des histoires d'altération simples avec des événements d'altération discrets et une altération moins intense favorisent probablement des âges mieux définis et plus reproductibles. En revanche, des histoires d'altération complexes comprenant des phases d'altération très intense (bauxitique) conduisent à des distributions d'âges plus complexes liées à un mélange plus intense et éventuellement à des gradients de concentration en actinides plus forts. Cependant, les âges très reproductibles obtenus dans la mine de Tucano montrent que des résultats hautement reproductibles peuvent être obtenus à partir de matériaux à cristallites très fins, même avec une certaine porosité et lorsqu'ils sont mélangés avec de la kaolinite à grains fins. Il n'est pas nécessaire d'avoir un matériau très métallique, dur et sans pores, comme on le supposait auparavant. Cela élargit le champ d'application de la géochronologie (U-Th)/He à des sous-échantillons qui n'ont pas été sélectionnés dans les études précédentes. Comme la méthode souffre d'un biais dû à la sélection subjective des sous-

échantillons, cela ouvre de nouvelles possibilités pour réduire la distorsion possible des âges obtenues sur la goethite et de l'hématite.

Concernant le régime d'altération régionale, la comparaison entre les couvertures latéritiques du nord-est de la Guyane française et du Suriname montre que l'altération Oligocène est une caractéristique régionale. Les latérites de la Guyane française se sont probablement développées de manière synchrone avec les bauxites côtières du Suriname et de la Guyane, mais des différences dans le climat et le drainage locaux ont pu conduire à la formation de bauxites au Suriname et en Guyane et à la formation de latérites ferrugineuses en Guyane française et au nord du Brésil. La comparaison des données obtenues dans le cadre de cette thèse avec les ensembles de données chronologiques d'altération existants indique que l'altération de l'Oligocène et du Miocène moyen sont des caractéristiques d'échelle régionale avec une importance possible à l'échelle continentale. L'évènement de bauxitization au Néogène tardif semble être au moins de caractère régional sur la côte nord-est du bouclier guyanais. Une comparaison avec des ensembles de données provenant d'autres régions du monde serait nécessaire afin d'étudier l'étendue spatiale de ces événements d'altération. Cela pourrait en outre fournir des informations sur les déclencheurs potentiels de tels événements d'altération.

Références

- Aleva G. J. J. (1984) Lateritization, bauxitization and cyclic landscape development in the Guiana Shield. In *Bauxite* (ed. L. Jacob Jr). A.I.M.E, New York, USA. pp. 297–318.
- Allard T., Balan E., Calas G., Fourdrin C., Morichon E. et Sorieul S. (2012) Radiation-induced defects in clay minerals: A review. *Nucl. Instruments Methods Phys. Res. Sect. B Beam Interact. with Mater. Atoms* **277**, 112–120.
- Allard T., Gautheron C., Bressan Riffel S., Balan E., Soares B. F., Pinna-Jamme R., Derycke A., Morin G., Bueno G. T. et do Nascimento N. (2018) Combined dating of goethites and kaolinites from ferruginous duricrusts. Deciphering the Late Neogene erosion history of Central Amazonia. *Chem. Geol.* **479**, 136–150.
- Allard T., Pereira L., Mathian M., Balan E., Taitson Bueno G., Falguères C. et do Nascimento N. R. (2020) Dating kaolinite from the Neogene Içá Formation and overlying laterites, central Amazonia, Brazil: Constraints for a stratigraphic correlation. *Palaeogeogr. Palaeoclimatol. Palaeoecol.* **554**.

- Ansart C. (2022) Evolution des latérites du bouclier Amazonien, rapport de mineralogie, géochronologie et géochimie. Université Paris Saclay, France.
- Balan E., Allard T., Fritsch E., Sélo M., Falguères C., Chabaux F., Pierret M. C. et Calas G. (2005) Formation and evolution of lateritic profiles in the middle Amazon basin: Insights from radiation-induced defects in kaolinite. *Geochim. Cosmochim. Acta* **69**, 2193–2204.
- Balan E., Fritsch E., Allard T. et Calas G. (2007) Inheritance vs. neoformation of kaolinite during lateritic soil formation: A case study in the Middle Amazon basin. *Clays Clay Miner.* **55**, 253–259.
- Balout H., Roques J., Gautheron C., Tassan-Got L. et Mbongo-Djimbi D. (2017) Helium diffusion in pure hematite ($\alpha\text{-Fe}_2\text{O}_3$) for thermochronometric applications: A theoretical multi-scale study. *Comput. Theor. Chem.* **1099**, 21–28.
- Bardossy G. et Aleva G. J. J. (1990) *Lateritic Bauxites*. Developmen., Elsevier Science, Amsterdam, The Netherlands.
- Beauvais A. (1999) Geochemical balance of lateritization processes and climatic signatures in weathering profiles overlain by ferricretes in Central Africa. *Geochim. Cosmochim. Acta* **63**, 3939–3957.
- Beauvais A., Bonnet N. J., Chardon D., Arnaud N. et Jayananda M. (2016) Very long-term stability of passive margin escarpment constrained by $^{40}\text{Ar}/^{39}\text{Ar}$ dating of K-Mn oxides. *Geology* **44**, 299–302.
- Beauvais A. et Chardon D. (2013) Modes, tempo, and spatial variability of Cenozoic cratonic denudation: The West African example. *Geochemistry, Geophys. Geosystems* **14**, 1590–1608.
- Beauvais A., Ruffet G., Hénocque O. et Colin F. (2008) Chemical and physical erosion rhythms of the West African Cenozoic morphogenesis: The ^{39}Ar - ^{40}Ar dating of supergene K-Mn oxides. *J. Geophys. Res. Earth Surf.* **113**, 1–15.
- Berner R. A., Lasaga A. C. et Garrels R. M. (1983) Carbonate-silicate geochemical cycle and its effect on atmospheric carbon dioxide over the past 100 million years. *Am. J. Sci.* **283**, 641–683.
- Blancaneaux P. (1981) *Essai sur le milieu naturel de la Guyane Française.*, Paris.
- Bonnet N. J., Beauvais A., Arnaud N., Chardon D. et Jayananda M. (2016) Cenozoic lateritic weathering and erosion history of Peninsular India from $^{40}\text{Ar}/^{39}\text{Ar}$ dating of supergene K-Mn oxides. *Chem. Geol.* **446**, 33–53.

- Butt C. R. M. (2016) The development of regolith exploration geochemistry in the tropics and sub-tropics. *Ore Geol. Rev.* **73**, 380–393.
- Butt C. R. M. et Cluzel D. (2013) Nickel laterite ore deposits: Weathered serpentinites. *Elements* **9**, 123–128.
- Carvalho A., Boulangé B., Melfi A. J. et Lucas Y. (1997) *Brazilian Bauxites*. eds. A. Carvalho, B. Boulangé, A. J. Melfi, et Y. Lucas, USP, FAPESP, ORSTOM, São Paulo, Paris.
- Chassé M., Griffin W. L., O'Reilly S. Y. et Calas G. (2019) Australian laterites reveal mechanisms governing scandium dynamics in the critical zone. *Geochim. Cosmochim. Acta* **260**, 292–310.
- Choubert B. (1957) *Essai sur la morphologie de la Guyane.*, Paris.
- Clozel B., Allard T. et Muller J. P. (1994) Nature and stability of radiation-induced defects in natural kaolinites: New results and a reappraisal of published works. *Clays Clay Miner.* **42**, 657–666.
- Deng X. D., Li J. W. et Shuster D. L. (2017) Late Mio-Pliocene chemical weathering of the Yulong porphyry Cu deposit in the eastern Tibetan Plateau constrained by goethite (U–Th)/He dating: Implication for Asian summer monsoon. *Earth Planet. Sci. Lett.* **472**, 289–298.
- Farley K. A. (2018) Helium diffusion parameters of hematite from a single-diffusion-domain crystal. *Geochim. Cosmochim. Acta* **231**, 117–129.
- Giovannini A. L., Bastos Neto A. C., Porto C. G., Pereira V. P., Takehara L., Barbanson L. et Bastos P. H. S. (2017) Mineralogy and geochemistry of laterites from the Morro dos Seis Lagos Nb (Ti, REE) deposit (Amazonas, Brazil). *Ore Geol. Rev.* **88**, 461–480.
- Girard J. P., Freyssinet P. et Chazot G. (2000) Unraveling climatic changes from intraprofile variation in oxygen and hydrogen isotopic composition of goethite and kaolinite in laterites: An integrated study from Yaou, French Guiana. *Geochim. Cosmochim. Acta* **64**, 409–426.
- Groussin J. (2001) Le Climat Guyanais. In *Atlas illustré de la Guyane* (ed. J. Barret). Laboratoire de Cartographie de la Guyane; Institut d'Enseignement Supérieur de Guyane. pp. 46–49.
- Guinoiseau D., Fekiacova Z., Allard T., Druhan J. L., Balan E. et Bouchez J. (2021) Tropical Weathering History Recorded in the Silicon Isotopes of Lateritic Weathering Profiles. *Geophys. Res. Lett.* **48**.

- Hammen van der T. et Wymstra T. A. (1964) A Palynological study on the Tertiary and Upper Cretaceous of British Guiana. *Leidse Geol. Meded.* **30**, 183–241.
- Heim J. A., Vasconcelos P. M., Shuster D. L., Farley K. A. et Broadbent G. (2006) Dating paleochannel iron ore by (U-Th)/He analysis of supergene goethite, Hamersley province, Australia. *Geology* **34**, 173–176.
- Heller B. M., Riffel S. B., Allard T., Morin G., Roig J.-Y., Couëffé R., Aertgeerts G., Derycke A., Ansart C., Pinna-Jamme R. et Gautheron C. (2022) Reading the climate signals hidden in bauxite. *Geochim. Cosmochim. Acta* **323**, 40–73.
- Hofmann F., Reichenbacher B. et Farley K. A. (2017) Evidence for >5 Ma paleo-exposure of an Eocene–Miocene paleosol of the Bohnerz Formation, Switzerland. *Earth Planet. Sci. Lett.* **465**, 168–175.
- Hoorn C., Wesselingh F. P., ter Steege H., Bermudez M. A., Mora A., Sevink J., Sanmartín I., Sanchez-Meseguer A., Anderson C. L., Figueiredo J. P., Jaramillo C., Riff D., Negri F. R., Hooghiemstra H., Lundberg J., Stadler T., Särkinen T. et Antonelli A. (2010) Amazonia Through Time : Andean Uplift, Climate Change, Landscape Evolution and Biodiversity. *Science (80-.)*. **330**, 927–931.
- King L. C. (1962) *Morphology of the Earth.*, Oliver et Boyd Publ. House, London.
- Kumar A. (1986) Palaeolatitudes and the age of Indian laterites. *Palaeogeogr. Palaeoclimatol. Palaeoecol.* **53**, 231–237.
- Lasaga A. C., Soler J. M., Ganor J., Burch T. E. et Nagy K. L. (1994) Chemical weathering rate laws and global geochemical cycles. *Geochim. Cosmochim. Acta* **58**, 2361–2386.
- Lippolt H. J., Brander T. et Mankopf N. R. (1998) An attempt to determine formation ages of goethites and limonites by (U+Th)-⁴He dating. *Neues Jahrb. Mineral. Monatshefte*, 505–528.
- Lippolt H. J., Wernicke R. S. et Boschmann W. (1993) ⁴He diffusion in specular hematite. *Phys. Chem. Miner.* **20**, 415–418.
- Mathian M., Aufort J., Braun J. J., Riotte J., Selo M., Balan E., Fritsch E., Bhattacharya S. et Allard T. (2019) Unraveling weathering episodes in Tertiary regoliths by kaolinite dating (Western Ghats, India). *Gondwana Res.* **69**, 89–105.
- Mathian M., Bueno G. T., Balan E., Fritsch E., Do Nascimento N. R., Selo M. et Allard T. (2020) Kaolinite dating from Acrisol and Ferralsol: A new key to understanding the landscape evolution in NW Amazonia (Brazil). *Geoderma* **370**.

- McConnell R. B. (1968) Planation Surfaces in Guyana. *Geogr. J.* **134**, 506–520.
- Monteiro H. S., Vasconcelos P. M., Farley K. A., Spier C. A. et Mello C. L. (2014) (U-Th)/He geochronology of goethite and the origin and evolution of cangas. *Geochim. Cosmochim. Acta* **131**, 267–289.
- Monteiro H. S., Vasconcelos P. M. P., Farley K. A. et Lopes C. A. M. (2018) Age and evolution of diachronous erosion surfaces in the Amazon: Combining (U-Th)/He and cosmogenic ^3He records. *Geochim. Cosmochim. Acta* **229**, 162–183.
- Nahon D. (1991) *Introduction to the petrology of soils and chemical weathering.*, Wiley, New York, USA.
- Patterson S. H., Kurtz H. F., Olson J. C. et Neeley C. L. (1994) *World Bauxite Resources - Geology and Resources of Aluminum.* U.S. Geolo., U.S. Geological Survey, Washington.
- Pidgeon R. T., Brander T. et Lippolt H. J. (2004) Late Miocene (U+Th)- ^4He ages of ferruginous nodules from lateritic duricrust, Darling Range, Western Australia. *Aust. J. Earth Sci.* **51**, 901–909.
- Prasad G. (1983) A review of the early Tertiary bauxite event in South America, Africa and India. *J. African Earth Sci.* **1**, 305–313.
- Reiners P. W., Chan M. A. et Evenson N. S. (2014) (U-Th)/He geochronology and chemical compositions of diagenetic cement, concretions, and fracture-filling oxide minerals in mesozoic sandstones of the Colorado Plateau. *Bull. Geol. Soc. Am.* **126**, 1363–1383.
- Retallack G. J. (2010) Lateritization and bauxitization events. *Econ. Geol.* **105**, 655–667.
- Riffel S. B., Vasconcelos P. M., Carmo I. O. et Farley K. A. (2016) Goethite (U-Th)/He geochronology and precipitation mechanisms during weathering of basalts. *Chem. Geol.* **446**, 18–32.
- Ruffet G., Innocent C., Michard A., Féraud G., Beauvais A., Nahon D. et Hamelin B. (1996) A geochronological $^{40}\text{Ar}/^{39}\text{Ar}$ and $^{87}\text{Rb}/^{87}\text{Sr}$ study of K-Mn oxides from the weathering sequence of Azul, Brazil. *Geochim. Cosmochim. Acta* **60**, 2219–2232.
- dos Santos Albuquerque M. F., Horbe A. M. C. et Danišík M. (2020) Episodic weathering in Southwestern Amazonia based on (U-Th)/He dating of Fe and Mn lateritic duricrust. *Chem. Geol.* **553**, 119792.
- Schellmann W. (1994) Geochemical differentiation in laterite and bauxite formation. *Catena* **21**, 131–143.

- Schmidt P. W. et Embleton B. J. J. (1976) Palaeomagnetic Results From Sediments of the Perth Basin, Western Australia, and their bearing on the timing of regional lateritization. *Palaeogeogr. Palaeoclimatol. Palaeoecol.* **19**, 257–273.
- Schmidt P. W., Prasad V. et Ramam P. K. (1983) Magnetic ages of some Indian laterites. *Palaeogeogr. Palaeoclimatol. Palaeoecol.* **44**, 185–202.
- Shuster D. L., Vasconcelos P. M., Heim J. A. et Farley K. A. (2005) Weathering geochronology by (U-Th)/He dating of goethite. *Geochim. Cosmochim. Acta* **69**, 659–673.
- Tardy Y. (1997) *Petrology of Laterites and Tropical Soils.*, Balkema, Rotterdam, The Netherlands.
- Tardy Y. et Roquin C. (1998) *Dérive des continents paléoclimats et altérations tropicales.*, BRGM, Orléans, France.
- Théveniaut H. et Freyssinet P. (1999) Paleomagnetism applied to lateritic profiles to assess saprolite and duricrust formation processes: The example of Mont Baduel profile (French Guiana). *Palaeogeogr. Palaeoclimatol. Palaeoecol.* **148**, 209–231.
- Théveniaut H. et Freyssinet P. (2002) Timing of lateritization on the Guiana Shield synthesis of paleomagnetic results. *Palaeogeogr. Palaeoclimatol. Palaeoecol.* **178**, 91–117.
- Valeton I. (1972) *Bauxites. Developmen.*, Elsevier, Amsterdam, The Netherlands.
- Valeton I. (1999) Saprolite-bauxite facies of ferralitic duricrust on paleosurfaces of former Pangaea. In *Palaeoweathering, Palaeosurfaces and Related Continental Deposits* (eds. M. Thiry et R. Simon-Coignon). Blackwell Science Ltd. pp. 153–188.
- Vasconcelos P. M. (1999) K-Ar and $^{40}\text{Ar} / ^{39}\text{Ar}$ Geochronology of weathering processes. *Annu. Rev. Earth Planet. Sci.* **27**, 183–229.
- Vasconcelos P. M. et Carmo I. de O. (2018) Calibrating denudation chronology through $^{40}\text{Ar}/^{39}\text{Ar}$ weathering geochronology. *Earth-Science Rev.* **179**, 411–435.
- Vasconcelos P. M., Heim J. A., Farley K. A., Monteiro H. et Waltenberg K. (2013) $^{40}\text{Ar}/^{39}\text{Ar}$ and (U-Th)/He - $^4\text{He}/^3\text{He}$ geochronology of landscape evolution and channel iron deposit genesis at Lynn Peak, Western Australia. *Geochim. Cosmochim. Acta* **117**, 283–312.
- Vasconcelos P. M., Reich M. et Shuster D. L. (2015) The paleoclimatic signatures of supergene metal deposits. *Elements* **11**, 317–322.
- Vasconcelos P. M., Renne P. R., Brimhall G. H. et Becker T. A. (1994) Direct dating of weathering phenomena by $^{40}\text{Ar}/^{39}\text{Ar}$ and K-Ar analysis of supergene K-Mn oxides. *Geochim. Cosmochim. Acta* **58**, 1635–1665.

Wells M. A., Danišík M., McInnes B. I. A. et Morris P. A. (2019) (U-Th)/He-dating of ferruginous duricrust: Insight into laterite formation at Boddington, WA. *Chem. Geol.* **522**, 148–161.

Wymstra T. A. (1971) The palynology of the Guiana coastal basin. University of Amsterdam.

Curriculum Vitae

Beatrix Heller

Date of Birth: March 25th, 1991
 Place of Birth: Heidelberg, Germany
 Nationality: German

Academic Education

2018-2022	<p>PhD Student Université Paris Saclay and Sorbonne Université Project <i>“Temporal evolution of Amazonian laterites reconstructed from mineralogy, geochemistry and geochronology”</i> Supervisors: Pr. Cécile Gautheron, Dr. Thierry Allard</p>
2014-2017	<p>Master of Science in Geosciences Georg-August-Universität Göttingen, Germany Thesis: <i>“Low T–thermochronology of the Archean, ore–bearing Hattu schist belt in Karelia, Finland”</i></p>
2016	<p>Study Abroad (5 months) Charles University Prague, Czech Republic</p>
2010-2014	<p>Bachelor of Science in Geosciences Georg-August-Universität Göttingen, Germany Thesis: <i>“U–Pb Geochronology and Hf–Isotopes in Zircons from basement rocks of Luís Alves Craton (Santa Catarina, Southern Brazil)”</i></p>
2014	<p>Study Abroad (5 months) Universidade de São Paulo, São Paulo, Brazil</p>
2012-2013	<p>Study Abroad (1 year) Universidade de São Paulo, São Paulo, Brazil</p>

Publications

- **Heller, B. M.**, Bressan Riffel, S., Allard, T., Morin, M., Roig, J., Coueffé, R., Aertgeerts, G., Derycke, A., Ansart, C., Pinna-Jamme, R. and Gautheron, C. (2022): “Reading the climate signals hidden in bauxite”, *Geochimica et Cosmochimica Acta* (323), DOI: 10.1016/j.gca.2022.02.017
- Ansart, C., Quantin, C., Calmels, D., Allard, T., Roig, J., Coueffé, R., **Heller, B.**, Pinna-Jamme, R., Nouet, J., Reguer, S., Vantelon, D., Gautheron, C. (2022) : “(U-Th)/He geochronology constraints on lateritic duricrust formation on the Guiana Shield”. *Frontiers in Earth Science* (10), 888993, DOI: 10.3389/feart.2022.888993
- Gautheron, C., Hueck, M., Ternois, S., **Heller, B.**, Schwartz, S., Sarda, P., Tassan-Got, L., (2022) : “Investigating the shallow to mid-depth (>100-300°C) continental crust

evolution with (U-Th)/He thermochronology: A Review”, *Minerals* (12.5), DOI: 10.3390/min12050563

- Hueck, M., Oriolo, S., Basei, M. A. S., Oyhantcabal, P., **Heller, B. M.**, Wemmer, K., Siegesmund, S. (2022): “Archean to early Neoproterozoic crustal growth of the southern South American Platform and its wide-reaching “African” origins”, *Precambrian Research* (369), DOI: 10.1016/j.precamres.2021.106532
- **Heller, B. M.**, Hueck, M., Passarelli, C.R., Basei, M. A. S. (2021): “Zircon U-Pb geochronology and Hf isotopes of the Luís Alves Terrane: Archean to Paleoproterozoic evolution and Neoproterozoic overprint”, *Journal of South American Earth Sciences* (106), DOI: 10.1016/j.jsames.2020.103008
- **Heller, B.M.**, Lünsdorf, N.K., Dunkl, I., Molnar, F. and von Eynatten, H. (2019): “Estimation of radiation damage in titanites using Raman spectroscopy”, *American Mineralogist* (104), 857-868 DOI:10.2138/am-2019-6681
- Hueck, M., Dunkl, I., **Heller, B.**, Basei, M.A.S., and Siegesmund, S. (2018): “(U-Th)/He thermochronology and zircon radiation damage in the South American passive margin: thermal overprint of the Paraná LIP?”, *Tectonics*, (37): 1–18. DOI: 10.1029/2018TC005041
- Cukrov N., Barišić D., **Heller B.**, Lojen S. and Cukrov N. (2013): “Importance of representative sediment sample for environmental interpretation: a case study in the Krka river, Croatia”, *Natura Montenegrina, Podgorica* 12 (3–4): 787–792.

Presentations and conference participations

- **Heller, B.**, “*Temporal evolution of Amazonian laterites reconstructed from mineralogy, geochemistry and geochronology*” Seminary Talk 03/2022, ISTERRE, Grenoble, France.
- Milanes Fernandez, V., de Stucky Quay, G., **Heller, B.** (Conveners) “*Quantifying Drivers of Landscape Evolution*” Session at AGU 2021, New Orleans, USA, and online.
- **Heller, B.**, Bressan-Riffel, S., Gautheron, C., Allard, T., Morin, G., Roig, J. and Coueffe, R., “*Constraints on past climate and geomorphological evolution through laterite dating*” Oral presentation, AGU 2021, New Orleans, USA, and online.
- **Heller, B.**, Bressan-Riffel, S., Gautheron, C., Allard, T., Morin, G., Roig, J. and Coueffe, R., “*Detailed study of a lateritic cover in NE French Guiana: dynamic evolution through time extracted from mineralogy, geochemistry and geochronology*” Oral presentation, Goldschmidt 2021 Virtual conference.
- **Heller, B.**, Bressan-Riffel, S., Gautheron, C., Allard, T., Morin, G., Roig, J. and Coueffe, R., “*(U-Th-Sm)/He dating of supergene Fe duricrusts in NE French Guiana: Implications of a multiproxy approach*” EGU 2020 Virtual conference.
- **Heller, B.**, Bressan Riffel, S., Gautheron, C., Allard, T., Morin, G., Roig, J., Coueffé, R., “*Dating of weathering surfaces in French Guiana using the (U-Th-Sm)/He method to determine ages of supergene iron oxides and oxyhydroxides*” Poster presentation, AGU 2019, San Francisco, USA.
- **Heller, B.**, Bressan-Riffel, S., Gautheron, C., Allard, T., Morin, G., Roig, J. and Coueffe, R. “*Insights into Fe-duricrust evolution in French Guiana using (U-Th-Sm)/He dating of supergene iron oxides and oxyhydroxides*” Poster presentation, Geomünster 2019, Münster, Germany.
- **Heller, B. M.**, Dunkl, I., Lünsdorf, K., Molnár, F., Huhma, H. and von Eynatten, H., “*Titanite “Crystallinity” Determination for Thermochronology*”, Poster Presentation, Goldschmidt 2018, Boston, USA.